NASA Technical Memorandum 84489

Measured Pressure Distributions, Aerodynamic Coefficients, and Shock Shapes on Blunt Bodies at Incidence in Hypersonic Air and CF_4

Charles G. Miller III

SEPTEMBER 1982

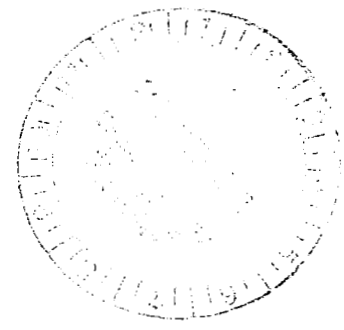

NASA

NASA Technical Memorandum 84489

Measured Pressure Distributions, Aerodynamic Coefficients, and Shock Shapes on Blunt Bodies at Incidence in Hypersonic Air and CF_4

Charles G. Miller III
Langley Research Center
Hampton, Virginia

National Aeronautics
and Space Administration

**Scientific and Technical
Information Office**

1982

INTRODUCTION

Over the last two decades, considerable effort has been directed toward understanding the supersonic-hypersonic aerothermodynamic phenomena associated with a vehicle entering the atmosphere of Earth or another planet. During the Apollo period of the 1960's, a mostly experimental data base was used to design, or verify the performance of, an Earth entry vehicle. Ground-based facilities, each capable of simulating the Mach number and Reynolds number of a portion of the entry trajectory, collectively established this data base. As interest expanded beyond Earth entry to entry into the atmosphere of Mars in the late 1960's, ground-based facilities continued to contribute directly toward understanding the flow characteristics encountered by a blunt probe entering an atmosphere other than that of Earth. However, as this interest in scientific exploration expanded toward Venus and the outer planets, designers of aeroshells for the probes relied more on flow fields predicted with analytical methods. This reliance on prediction was necessary because existing facilities were not capable of simulating or duplicating the severe environment encountered by a vehicle entering the atmosphere of Venus or an outer planet. Even so, ground-based facilities played an important role in establishing a data base for Earth and planetary entry during the 1970's, for example, during the Space Shuttle development.

Often, the support provided by ground-based facilities is indirect. As analytical methods emerge from the developmental stage, their predictions are often compared with measurements. Consider the hypothetical development of a numerical method for computing supersonic and hypersonic flow characteristics about a blunt body. The first phase of this development may be to compute the inviscid flow field about the blunt body at zero incidence with ideal-gas behavior assumed. These predictions may be compared with measured shock detachment distance and surface pressure distributions on the blunt body. After verification of this inviscid ideal-gas method, the effects of viscosity may be incorporated, and predicted and measured convective heat-transfer rates may be compared to validate the method. Next, the capability of predicting flow conditions about the body at incidence may be included, and predictions again compared with measurement. As development of the code continues, complex phenomena such as turbulence, massive blowing simulating surface material lost due to ablation, and real-gas chemistry including nonequilibrium effects and radiation are added. At this point in the development, ground-based facilities begin to fall short of providing a credible experimental data base for comparison. The scarcity of experimental data on real-gas flow characteristics about blunt bodies at incidence motivated, in part, the present study.

Synonymous with real-gas effects are large values of the normal-shock density ratio, which is the primary parameter governing the flow about a blunt body at hypersonic speeds (refs. 1 and 2). This high density ratio is due to excitation of vibration, dissociation, and ionization energy modes of the atmospheric gas passing through the bow shock. To illustrate the difference in density ratios existing between conventional wind tunnels and flight, a ratio of only 5 to 6 is produced in a conventional hypersonic tunnel using air or nitrogen as the test medium, whereas a vehicle encounters ratios 3 times larger on entering the atmosphere of Earth and 4 times larger on entering the predominantly CO_2 atmosphere of Venus. Duplication of

real-gas phenomena in hypersonic flow in a ground-based facility is a formidable task. A few operational facilities can generate very high velocities at hypersonic conditions, but for extremely short run times (for example, see refs. 2 to 6). Although these impulse-type facilities are valuable tools in the study of real-gas effects, they lack many of the advantages (particularly in the area of data acquisition) of a conventional wind tunnel. An alternative method of generating high normal-shock density ratios is to use a test gas with a low ratio of specific heats in a conventional wind tunnel (refs. 1, 7, and 8). With such a test medium, high density ratios can be generated at relatively low enthalpies, and thus complex real-gas chemistry can be avoided. For example, the Langley Hypersonic CF_4 Tunnel (ref. 9) generates a density ratio of 12 at a Mach number of 6, whereas the Langley 20-Inch Mach 6 Tunnel (refs. 10 and 11) generates a density ratio of 5.3 in air.

The Langley Research Center has been developing sophisticated computer programs to predict the flow conditions about planetary probes. Because of Langley's hypersonic facility complex (refs. 12 and 13), including the only high-density-ratio conventional wind tunnel (CF_4 tunnel) operating in the United States, researchers have the opportunity to validate their numerical techniques with data from these facilities. Thus, a study was conducted on several blunt bodies at incidence in a number of hypersonic facilities over a range of Mach number, Reynolds number, and density ratio, and various predictions were compared with this experimental data base.

The purpose of this report is to present shock shapes, pressure distributions, and aerodynamic coefficients measured on analytical shapes (hyperboloid with an asymptotic angle of 45°, "sonic-corner" paraboloid, and paraboloid with an angle of 27.6° at the base), a Viking aeroshell generated in a generalized orthogonal coordinate system (ref. 14), and a family of cones having a 45° half-angle and different nose shapes (spherical, flattened, concave, and cusp) corresponding to predicted heat shield losses during Jovian entry. These data, obtained in the Langley Continuous-Flow Hypersonic Tunnel, 20-Inch Mach 6 Tunnel, and Hypersonic CF_4 Tunnel, cover a Mach number range from 6 to 10, a free-stream unit Reynolds number range from 2×10^6 to 27×10^6 m^{-1}, a density ratio range from 5.3 to 12, and an angle of attack range from 0° to 20°. Limited heat-transfer data obtained on the hyperboloid and paraboloid in Mach 6 air are presented in the appendix. Also presented are comparisons between measurements and predictions from simple theories and numerical flow field programs.

SYMBOLS

A model base area, m^2

C_A axial-force coefficient, Axial force/$q_\infty A$

C_D drag coefficient, $C_N \sin \alpha + C_A \cos \alpha$

C_L lift coefficient, $C_N \cos \alpha - C_A \sin \alpha$

C_m pitching-moment coefficient, Pitching moment/$q_\infty A d_b$

C_N normal-force coefficient, Normal force/$q_\infty A$

d diameter, m

g acceleration due to gravity, 9.8 m/sec^2

L/D	lift-drag ratio, C_L/C_D
M	Mach number
N_{Re}	unit Reynolds number, m^{-1}
p	pressure, Pa
q	dynamic pressure, Pa
$\dot{q}$	heat-transfer rate, W/m^2
r	radius or radius of curvature of outer surface, m
s	surface length from geometric stagnation point at zero incidence, m
T	temperature, K
U	velocity, m/sec
x,y	rectangular coordinates
α	angle of attack, deg
β	coordinate in generalized orthogonal coordinate system, equal to 180° at the nose
γ	ratio of specific heats
η	acute angle between axis of symmetry and tangent to outer surface
θ	cone half-angle or asymptotic angle of analytical model, deg
ρ	density, kg/m^3
τ	skin thickness, m
ϕ	circumferential angle (0° leeward, 180° windward)

Subscripts:

b	model base or corner
calc	calculated
eff	effective
m	measured
n	nose
s	surface
sph	sphere

w	wall
∞	free stream
2	static conditions behind normal portion of bow shock
t,1	reservoir stagnation conditions
t,2	stagnation conditions behind normal portion of bow shock

FACILITIES AND TEST METHODS

Langley Hypersonic CF_4 Tunnel

The Langley Hypersonic CF_4 Tunnel is a conventional blowdown wind tunnel that uses Dupont Freon 14 (tetrafluoromethane (CF_4)) as the test gas. This facility, shown schematically in figure 1(a), is described in detail in reference 9. Two lead-bath heaters connected in parallel, each containing 9.1 Mg of lead and 440-volt resistance heaters, are used to heat the CF_4 to the desired temperature. The high-pressure heated CF_4 is introduced into the settling chamber and subsequently expanded through an axisymmetric contoured nozzle. Approximately 3 seconds are required to establish steady flow at the nozzle exit, and for the present tests, the total run time was 10 seconds. After testing, the contents of the vacuum sphere are exhausted into a CF_4 reclaimer system that liquefies the CF_4, exhausts gaseous impurities to the atmosphere, passes the compressed liquid through a vaporizer, and stores the high-pressure gaseous CF_4 in bottles.

The model is positioned at the nozzle exit by a pneumatically driven injection mechanism with the center of pitch rotation fixed on the nozzle center line. The angle of attack may be varied over $\pm 20°$ with a straight sting. The injection time (time required for the model to move from the prerun position to the nozzle center line) is approximately 1.5 seconds and retraction time is approximately 2 seconds.

Pitot-pressure surveys measured at the nozzle exit and downstream of the exit for nominal reservoir temperatures of 608, 717, and 815 K and a range of reservoir pressure from 6.9 to 17.6 MPa are presented in reference 9. These surveys demonstrate the existence of a uniform test core having a diameter of approximately 28 cm (0.55 times the nozzle exit diameter) at the maximum test values of reservoir pressure and temperature. The contoured axisymmetric nozzle was designed for a reservoir pressure of 17.6 MPa and a temperature of 811 K. When the facility is operated at off-design reservoir conditions, spikes and dips in the pitot-pressure profiles occur near the nozzle center line (ref. 9). The average pitot pressure across the test core decreased 3 to 4 percent with an axial variation of 20.3 cm downstream of the nozzle exit (ref. 9), with the corresponding free-stream Mach number variation being about 0.3 percent. Flow conditions vary negligibly over the axial distance occupied by the present models.

Langley 20-Inch Mach 6 Tunnel

The Langley 20-Inch Mach 6 Tunnel (refs. 10 and 11) is a blowdown wind tunnel that uses dry air as the test gas. Air is supplied at 4.14 MPa and heated to a maximum temperature of 560 K by an electrical resistance heater. The maximum reservoir pressure is 3.5 MPa. The general arrangement of this facility is shown schematically in figure 1(b). A fixed-geometry two-dimensional contoured nozzle is used. The parallel sidewalls form a 0.86-cm by 50.8-cm throat section and 52.1-cm by 50.8-cm test section, and the length from the nozzle throat to the test section window center line is 2.27 m. This tunnel is equipped with a movable second minimum and exhausts either into a vacuum sphere or to the atmosphere through an annular air ejector. The maximum run time is 2 minutes with the sphere and 20 minutes with the ejector.

Models were mounted on the injection system located below the test section. This system includes a remote-controlled sting support system capable of moving the model through an angle of attack range from -5° to +55°; the sideslip angle range is from 0° to -10°. For the pressure tests, the model was positioned in the test section at the desired angle of attack during tunnel start because of insufficient length of pressure tubing. For force and moment tests, the model was injected into the test section after steady flow had been achieved. Injection time over the last 24.9 cm was about 0.9 second with a maximum 2g acceleration. Angle of attack for the force and moment tests and for some of the pressure tests was varied during the run. Angle of attack was set optically by using a point light source adjacent to the test section and a small lens-prism mounted on the tapered cylindrical section extending behind the force models or mounted perpendicular to the base of the pressure models. The image of the source was reflected by the prism and focused by the lens onto a calibration board, which was viewed with a closed-circuit video system. The accuracy of determining angle of attack in this manner is estimated to be ±0.25°. For force tests, measurements were made at eight angles of attack (0°, 20°, 16°, 12°, 8°, 4°, 0°, -4°) during each test.

A single pitot-pressure probe was inserted into the tunnel from the top of the test section and positioned 6.35 mm downstream of the center of the schlieren window and 10.2 cm above and to the right (looking upstream) of the nozzle center line. The leading edges of the pressure models at zero incidence were positioned in the same plane as the pitot probe; the leading edges of the force models were approximately 3.8 cm upstream of this plane, because of the more aft location of the small lens-prism mounted on the tapered cylindrical section behind the force models. Pitot-pressure surveys at the center of the schlieren window show the existence of a 27-cm by 33-cm test core for reservoir pressures from 0.5 to 3 MPa (ref. 10). For this range of pressure, the Mach number variation across the core was less than 0.03, corresponding to a pitot-pressure variation of about 2 percent. The flow conditions change negligibly over the axial space occupied by the present models.

Langley Continuous-Flow Hypersonic Tunnel

The Langley Continuous-Flow Hypersonic Tunnel (ref. 12) was operated in the blowdown mode for the present tests. The CFHT, shown schematically in figure 1(c), uses a water-cooled three-dimensional contoured nozzle to generate a nominal Mach number of 10 with dry air as the test gas. The nozzle throat is 2.54 cm square and the test section is 78.7 cm square. Air for the settling chamber is supplied at 34.5 MPa, and the maximum operating reservoir pressure is 15.2 MPa. The maximum reservoir stagnation temperature of the air, heated by a 15-MW electric resistance tube heater, is 1060 K. A low-pressure preheat of the nozzle walls is performed

prior to a run. The maximum run time in the blowdown mode, using two, 12.2-m-diameter vacuum spheres, is 60 to 80 seconds.

Before a run, the model is positioned in an injection chamber on the side of the tunnel. This chamber allows access to the model without opening the test section to the atmosphere or shutting the tunnel down during the continuous operating mode. The injection system can rapidly (about 0.5 sec) insert a model for heat-transfer tests or insert a model at low acceleration for force tests. This system is capable of changing the angle of attack of a model 5° per second for a range of ±90°.

MODELS

Expressions describing the surface coordinates of the models tested are as follows (because these models were fabricated from expressions in which the quantities x and y were in inches, x and y are also in inches in the following equations; the angle β is in degrees):

Model 1 - Hyperboloid

$$y = \sqrt{x^2 + x} \tag{1a}$$

where the model nose is located at the origin (x = 0, y = 0).

Model 2 - Sonic-corner paraboloid

$$\left.\begin{aligned} &\text{Forebody:} \quad y = 2.0466\sqrt{x} \\ &\text{Afterbody:} \quad y = \sqrt{7.647535 - 3.81968x} \end{aligned}\right\} \tag{1b}$$

Model 3 - Paraboloid

$$y = 1.4472\sqrt{x} \tag{1c}$$

Model 4 - Viking aeroshell (in generalized orthogonal coordinate system (ref. 14))

$$\left.\begin{aligned} x &= 0.90021326 \cos\beta + 0.07515984 \cos 2\beta + 0.07121531 \cos 3\beta \\ &\quad - 0.05382820 \cos 4\beta \\ y &= 1.90412851 \sin\beta - 0.07515984 \sin 2\beta - 0.07121531 \sin 3\beta \\ &\quad + 0.05382820 \sin 4\beta \end{aligned}\right\} \tag{1d}$$

where $\beta = 180°$ corresponds to the nose and β varies from 0° to 180° over the body. (These expressions for x and y approximate a spherically blunted cone forebody with a half-angle of 70°.)

Model 5 - 45° cone with spherical nose, with $r_n/r_b = 0.5$ and $r_b = 2.0$ in.

$$\left.\begin{aligned} x &= 1 - \sqrt{1 - y^2} && (x < 0.29289 \text{ in.}) \\ x &= y - 0.41421 && (x > 0.29289 \text{ in. (cone section)}) \end{aligned}\right\} \quad (1e)$$

Model 6 - 45° cone with flattened nose

$$\left.\begin{aligned} \frac{x}{r_b} &= 0.07352 - 0.05983\,\frac{y}{r_b} + 1.56443\left(\frac{y}{r_b}\right)^2 - 13.37559\left(\frac{y}{r_b}\right)^3 \\ &\quad + 48.21829\left(\frac{y}{r_b}\right)^4 - 47.45473\left(\frac{y}{r_b}\right)^5 \\ &&& (x < 0.29289 \text{ in.},\ r_b = 2.0 \text{ in.}) \\ x &= y - 0.41421 && (x > 0.29289 \text{ in.}) \end{aligned}\right\} \quad (1f)$$

Model 7 - 45° cone with concave nose

$$\left.\begin{aligned} \frac{x}{r_b} &= 0.14512 + 0.03171\,\frac{y}{r_b} - 6.80355\left(\frac{y}{r_b}\right)^2 + 39.22126\left(\frac{y}{r_b}\right)^3 \\ &\quad - 78.127995\left(\frac{y}{r_b}\right)^4 + 59.77109\left(\frac{y}{r_b}\right)^5 \\ &&& (x < 0.29289 \text{ in.},\ r_b = 2.0 \text{ in.}) \\ x &= y - 0.41421 && (x > 0.29289 \text{ in.}) \end{aligned}\right\} \quad (1g)$$

Model 8 - 45° cone with cusp nose

$$\left.\begin{aligned}\frac{x}{r_b} &= -2.28402 \times 10^{-4} + 2.08333 \times 10^{-1}\,\frac{y}{r_b} - 1.25246 \times 10^{1}\left(\frac{y}{r_b}\right)^2 \\ &\quad + 2.56585 \times 10^{2}\left(\frac{y}{r_b}\right)^3 - 1.71023 \times 10^{3}\left(\frac{y}{r_b}\right)^4 + 5.153355 \times 10^{3}\left(\frac{x}{r_b}\right)^5 \\ &\quad - 7.182985 \times 10^{3}\left(\frac{y}{r_b}\right)^6 + 3.73900 \times 10^{3}\left(\frac{y}{r_b}\right)^7 \\ &\qquad\qquad (x < 0.29289 \text{ in.},\quad r_b = 2.0 \text{ in.}) \\ x &= y - 0.41421 \qquad\qquad (x \geq 0.29289 \text{ in.})\end{aligned}\right\} \quad (1h)$$

The base diameter for all models is 10.16 cm. Models were mounted on 2.54-cm-diameter stings, whose ratio of length to diameter always exceeded 3. Planform views of the models are shown in figure 2.

Pressure models were fabricated for the eight shapes, and force models were fabricated for models 1, 3, 5, 6, 7, and 8. The force models were machined from type 347 stainless steel, as was pressure model 1. Pressure models 2 to 8 were cast out of aluminum. A wooden pattern, 1.52 mm oversize to allow for shrinkage and machining, was made with the orifices located on it (fig. 3(a)). A sand mold was made from this pattern, stainless steel tubing was installed in the mold cavity and connected to the orifice locations (fig. 3(b)), and the cavity was filled with aluminum 355-T6. After solidifying, the cast model was removed from the sand mold and the surface machined to the required contour. Pressure orifices on the forebody were distributed along 4 rays (ϕ = 0°, 60°, 120°, and 180°); the stainless steel pressure tubing had an inside diameter of 1.02 mm. In general, the surface coordinates of these models measured to within 0.1 mm of the requested values of x and y. The surface finish for all models was 0.8 μm.

Prior to the fabrication of these force and pressure models, a pressure model and a heat-transfer model (see the appendix) were fabricated for the hyperboloid and paraboloid shapes. These models were spun from type 347 stainless steel with a die machined to specifications, and their surfaces polished to a 0.8 μm finish. The base plate was welded to the shell after installation of the pressure tubes or thermocouple wires. Unfortunately, the model surface coordinates were not measured after the base plates were welded in place. After the initial tests in the Mach 6 tunnel, discrepancies were observed between shock shapes measured on the pressure and the heat-transfer model of the same shape at the same flow conditions. Subsequent measurements of the surface coordinates of the models revealed deviations from the requested shape by as much as 2.16 mm. Nevertheless, pressure distributions and shock shapes are presented for these spun models, since they were the only models tested in both the Mach 6 tunnel and the CF_4 tunnel. To differentiate between these models and the more accurate machined models of the hyperboloid and paraboloid shapes, the spun models are designated as series 1 and the machined models as series 2.

Pressure distributions along various rays on the model surface are presented in terms of s, the surface length from the geometric stagnation point at zero incidence, nondimensionalized by s_b, the surface length from the stagnation point to the corner. This length is given in terms of x and y by

$$s = \int_0^x \sqrt{1 + \left(\frac{dy}{dx}\right)^2}\, dx \qquad \text{or} \qquad s = \int_0^y \sqrt{1 + \left(\frac{dx}{dy}\right)^2}\, dy \tag{2}$$

Thus, for the analytical models,

$$\frac{s}{s_b} = \frac{\displaystyle\int_0^x \sqrt{1 + \left(\frac{dy}{dx}\right)^2}\, dx}{\displaystyle\int_0^{x_b} \sqrt{1 + \left(\frac{dy}{dx}\right)^2}\, dx} \tag{3}$$

where

Model	dy/dx	x_b, in.
1	$(x + 0.5)/\sqrt{x^2 + x}$	1.56
2	$1.0233/\sqrt{x}$	.955
3	$0.7236/\sqrt{x}$	1.91

For the cone models (models 5 to 8)

$$\frac{s}{s_b} = \frac{\displaystyle\int_0^y \sqrt{1 + \left(\frac{dx}{dy}\right)_n^2}\, dy + \sqrt{1 + \frac{1}{\tan^2\theta}}(y_b - y)}{\displaystyle\int_0^{r_n \cos\theta} \sqrt{1 + \left(\frac{dx}{dy}\right)_n^2}\, dy + \sqrt{1 + \frac{1}{\tan^2\theta}}(y_b - r_n \cos\theta)} \tag{4}$$

where y_b is equal to 2 in.

Although a closed-form solution is possible for the paraboloid and cones (models 3 and 5 to 8), s/s_b for the hyperboloid (model 1) must be obtained numerically. Values of s/s_b presented herein were determined from numerical integration (Simpson's rule) for all models. Because pressure distributions are sometimes plotted in the literature as a function of s/r_n, values of both s_b and r_n are presented:

Model	s_b, cm (in.)	r_n, cm (in.)
1	6.5352 (2.5729)	1.2700 (0.5000)
2	5.7716 (2.2723)	5.3195 (2.0943)
3	7.3442 (2.8914)	2.6599 (1.0472)
5	6.6403 (2.6143)	2.5400 (1.0000)
6	6.5308 (2.5712)	
7	6.5682 (2.5859)	
8	6.6421 (2.6150)	

The equivalent nose radius for the hyperboloid (model 1) and the paraboloid (model 3) were determined from

$$r = \frac{\left[1 + \left(\frac{dy}{dx}\right)^2\right]^{3/2}}{\left|\frac{d^2y}{dx^2}\right|} \tag{5}$$

INSTRUMENTATION AND DATA ACQUISITION

Pressure

Model surface pressures were measured in the Mach 6 tunnel and the CFHT with variable-capacitance diaphragm transducers having seven ranges of pressure, the maximum being 133 kPa. Each facility had 20 such transducers available. The signal from a transducer was recorded on a magnetic tape by an analog-to-digital recording system. For tests in the Mach 6 tunnel, the output signals from 8 of the 20 pressure transducers were displayed on an oscillograph, and data were taken at selected times. This interaction with the system allowed data acquisition for a steady-state flow condition ($p_{t,1}$, $T_{t,1}$, and $p_{t,2}$ constant with time); also, pressure lag due to the long length of tubing (approximately 3 m) could be observed and data taken after the pressure became constant. Each data point represented the average of 20 samples made per second for each channel. To reduce the response time of the pressure measuring system, particularly for base pressure and afterbody pressure measurements, the transducers and reference manifold were subjected before the run to a pressure that was close to that expected on the model surface during the run. With a switching device referred to as a pinch bar, the 20 pressure transducers could be used to measure in excess of 40 surface pressures during a run. Again, to improve the response of the system, the pinch bar was hooked up so that pressure levels changed relatively little when the transducers were switched from one group of 20 orifices to another. In the CFHT, each orifice was connected directly to a pressure transducer; hence, two runs were required for each model at a given condition to obtain 40 surface pressure measurements.

In the CF_4 tunnel, 42 pressure transducers were available: 10 variable-capacitance type and 32 strain-gage type. Outputs from these pressure transducers were recorded on magnetic tape at a rate of 400 samples per second for each channel.

Shock Shapes

During the pressure and force tests in the Mach 6 tunnel, shock shapes were measured with a Z-pattern, single-pass schlieren system. A xenon light source was operated in a continuous mode during tunnel startup. Once steady flow was obtained over the model, a mirror was inserted into the schlieren system to reflect a short-duration light pulse from the lamp into a camera equipped with a fast opening shutter. Representative schlieren photographs are shown in figure 4 for models 5 and 8. Shock shapes were not obtained in the CFHT because this facility is not equipped with a flow visualization system.

Shock shapes were measured in the CF_4 tunnel with a dual-plate holographic interferometer system (ref. 15). Holograms, recorded using a pulsed ruby laser that provided a 50 mJ pulse for 20 nsec, were used to produce schlieren photographs and interferograms.

Forces and Moments

Forces and moments were measured in the Mach 6 tunnel and the CFHT with the same sting-supported, six-component strain-gage balance. This balance was water cooled and shielded from the flow to minimize the effect of heating (aerodynamic heating and conduction within the model and sting) on the strain gages. The strain-gage excitation voltage was 5 volts. Output for the normal-force, axial-force, and pitching-moment components was recorded by the analog-to-digital system at 40 samples per second.

DATA REDUCTION AND UNCERTAINTY

Pressure

Measured surface pressure distributions are nondimensionalized by the pressure at the stagnation point of the model at zero incidence. The pitot pressure was measured for all tests performed in the Mach 6 tunnel and the CF_4 tunnel. The ratio of the pitot pressure to the model stagnation point pressure at zero incidence was computed as a correction factor. For tests at incidence, the ratio of model surface pressure to pitot pressure was multiplied by this correction factor, which was less than 3 percent from unity for both the Mach 6 tunnel (ref. 16) and the CF_4 tunnel tests. For tests in the CFHT, the pitot pressure was calculated from the calibrated free-stream Mach number, the reservoir pressure, and correction factors accounting for imperfect-gas effects in the reservoir. The procedure for obtaining nondimensionalized surface pressures was the same except that the calculated pitot pressure was used instead of a measured value.

At low densities, the heat-transfer rate and orifice diameter may affect pressure measurements (ref. 17). This phenomenon, caused by unequal speed distributions for incoming and outgoing molecules near the orifice entrance, is evidenced by a decrease in the measured pressure with a decrease in the orifice diameter for a given density and heat-transfer rate. For the conditions of the present study, orifice effects are negligible (ref. 17). Considering errors resulting from calibration of the pressure transducers, transducer uncertainties, system response time, outgassing, and thermal creep, the present pressure measurements are believed to be accurate to within 3 percent. Data scatter in surface pressures measured on the models at zero incidence indicates an overall uncertainty of 3 to 5 percent.

PREDICTION OF FLOW CONDITIONS

Free-stream conditions and conditions behind the normal shock were determined for each run in the Mach 6 tunnel and CF_4 tunnel by assuming an isentropic expansion of the test gas through the nozzle. Reservoir thermodynamic properties were determined from the measured reservoir pressure $p_{t,1}$ and temperature $T_{t,1}$. For the range of test conditions in the Mach 6 tunnel, air behaves ideally. The tabulated data of reference 18 were curve fitted for $5.7 < M_\infty < 6.3$ to yield the following expression for M_∞ in terms of measured $p_{t,1}$ and $p_{t,2}$:

$$M_\infty = 8.30067582 - 106.1638176\left(\frac{p_{t,2}}{p_{t,1}}\right) + 963.5096163\left(\frac{p_{t,2}}{p_{t,1}}\right)^2 \tag{6}$$

The corresponding free-stream conditions and post-normal-shock conditions were obtained from the ideal-air relations and tables of reference 18.

Imperfect-gas (intermolecular-force) effects must be accounted for at the reservoir conditions of the CF_4 tunnel (refs. 1 and 9). Test section flow conditions in CF_4 were calculated from the imperfect CF_4 expressions of reference 19 and measured values of $p_{t,1}$, $T_{t,1}$, and $p_{t,2}$. From measured and calculated reservoir conditions, an isentropic nozzle expansion was performed to an initial estimate of the free-stream static temperature T_∞. A normal-shock crossing was performed and a value of $p_{t,2}$ was calculated by assuming the gas between the shock and the stagnation region to be isentropic. If the calculated value of $p_{t,2}$ was not within 0.05 percent of the measured value, T_∞ was iterated until this tolerance was achieved.

A parameter of interest for the CF_4 tunnel is the effective ratio of specific heats. Ideal-gas flow field programs can accurately predict inviscid flow about a blunt body at hypersonic speeds and high normal-shock density ratios provided that the density ratio is accounted for by using an effective ratio of specific heats (ref. 2). This effective value is determined from the ideal-gas normal-shock relation (ref. 18),

$$\gamma_{eff} = \frac{1 + \frac{\rho_2}{\rho_\infty}\left(1 - \frac{2}{M_\infty^2}\right)}{\frac{\rho_2}{\rho_\infty} - 1} \tag{7}$$

For Mach 6 and 10 air, $\gamma_{eff} = \gamma_\infty = 1.4$, and for CF_4, $\gamma_{eff} \approx 1.12$.

Imperfect-gas effects must also be considered in determining flow conditions for the CFHT (ref. 20). Because the pitot pressure at the test section was not measured in the CFHT, free-stream Mach number and Reynolds number for measured reservoir pressures and temperatures were obtained from a calibration study performed prior to the present study. (See fig. 7.) Along with these values of M_∞ were supplied correction factors (ratios of imperfect-gas to ideal-gas quantities, ref. 20 and fig. 7(c))

nozzle design conditions, in anticipation of possible tests of the present models in the CF_4 tunnel. (As discussed previously, the CF_4 tunnel must be run at nozzle design conditions ($p_{t,1} \approx 17.6$ MPa, $T_{t,1} \approx 811$ K) to avoid a degradation of the flow quality. At nozzle design conditions, the unit Reynolds number immediately behind a normal shock $N_{Re,2}$ is approximately 6.5×10^5 m^{-1}.)

Pressure models were tested over a range of angle of attack from 0° to either 16° or 20° in increments of 4°. To obtain a more detailed circumferential mapping of the surface pressure in the Mach 6 tunnel, the models were rolled 30° at angles of attack of 4° and 8°. This provided pressure distributions along rays of $\phi = 0°$, 30°, 60°, 90°, 120°, 150°, and 180°. Force models were tested over a range of angle of attack from -4° to 20°.

It should be noted that models tested in the Mach 6 tunnel at the highest value of reservoir pressure in the first series of tests were sandblasted. The source of the solid flow contaminants was attributed to deterioration of an acoustical muffler installed in the system. A fine grade of sandpaper was used to restore a smooth finish to the model surface after each run at high reservoir pressure. These solid contaminants in the flow were not expected to significantly affect the surface pressure measurements. The first model tested in the CFHT (hyperboloid pressure model) was also sandblasted and the source of these solid flow contaminants was traced to rust resulting from a leak in the water-cooled nozzle near the throat. This situation was corrected and models tested thereafter received little sandblasting.

PREDICTIONS

The present results for models 1, 3, and 5 at zero incidence are compared with predictions from a modified version of the computer code presented in reference 21. The method of reference 21 rapidly (in regard to computer time) predicts ideal-gas inviscid supersonic and hypersonic flow conditions about spheres, ellipsoids, paraboloids, and hyperboloids that may have conical afterbodies. An approximation that allows an independent evaluation of the pressure throughout the shock layer is made to the normal momentum equation. This approximation removes many of the usual mathematical problems associated with subsonic and supersonic regions. An iterative technique that scales the shock to the specified body in the subsonic and low supersonic region of the flow field is used. Since the publication of reference 21, a viscous package, providing the capability of predicting heat-transfer rates, has been added to the program. A listing of the original program and user instructions are presented in reference 21 along with a detailed discussion of the theory. Pressure distributions, heat-transfer distributions, and shock shapes presented herein and designated as being from reference 21 were generated by Ernest V. Zoby.

Predictions from two other flow field computer programs are compared with measurement. One is a time-dependent inviscid ideal-gas program for axisymmetric blunt bodies. This program does not appear in the open literature. Results from it were generated by Harris H. Hamilton of the Langley Research Center and are designated "unpublished" on the figures. The other code (ref. 22) is a time-dependent second-order-accurate finite-difference method which uses the viscous shock layer equations in body-oriented coordinates to describe the flow field. The results presented from this method were generated by either Ajay Kumar of the Langley Research Center or R. N. Gupta, NRC Senior Research Associate.

Surface pressure distributions for all eight model shapes were predicted with modified Newtonian theory (refs. 23 and 24), represented by the expression for the pressure coefficient

$$C_p = C_{p,stag} \sin^2\eta \tag{8}$$

where $C_{p,stag}$ is the pressure coefficient at the stagnation point behind a normal shock and η is the angle of inclination of the model surface to the axis of revolution ($\eta = 90°$ when perpendicular to the axis of revolution). For $5.7 < M_\infty < 10.2$, the value of $C_{p,stag}$ for air is 1.8235 with an uncertainty of 0.5 percent; for CF_4, $C_{p,stag}$ is 1.916. Thus, the ratio of surface pressure to model stagnation point pressure (pitot pressure) is given (ref. 16) for air by

$$\frac{p_s}{p_{t,2}} = 0.985 \sin^2\eta + \frac{p_\infty}{p_{t,2}} \tag{9a}$$

and for CF_4 by

$$\frac{p_s}{p_{t,2}} = 0.978 \sin^2\eta + \frac{p_\infty}{p_{t,2}} \tag{9b}$$

where leeward

$$\eta = \tan^{-1}\frac{dy}{dx} - \alpha \tag{10a}$$

and windward

$$\eta = \tan^{-1}\frac{dy}{dx} + \alpha \tag{10b}$$

Surface pressures on the cone sections of models 5 to 8 at incidence were also predicted with the semiempirical results of reference 25 and the equivalent-cone method of reference 26.

RESULTS AND DISCUSSION

The present study was performed in two series of tests. In the first series, the hyperboloid and paraboloid spun pressure models and heat-transfer models (see the section entitled "Models") were tested in the Langley 20-Inch Mach 6 Tunnel and the Langley Hypersonic CF_4 Tunnel. Shock shapes measured on these models are shown in figure 8. For a few tests, the shock shape was obtained in two ways: (1) by reading

the shock detachment distance from prints, as discussed in the section on data reduction (denoted in fig. 8 by open symbols) and (2) by using an enlarger which displayed the model over twice its size on the surface of a digitizer table. The general agreement between the shock detachment distances measured with these two methods lends credibility to the measured values. The shock shapes for the two hyperboloid models agree (fig. 8(a)), whereas the detachment distance for the pressure paraboloid model exceeds that for the heat-transfer paraboloid model (fig. 8(b)). Differences in the model shapes possibly caused this discrepancy. The second set of surface coordinate measurements, discussed in the section entitled "Models," revealed deviations from the requested analytical shape by as much as 2.16 mm.

A second series of tests were performed with more accurate hyperboloid and paraboloid models, along with two other analytical configurations and a family of 45° cones having different nose shapes. All the models tested in the second series were pressure or force models and were tested in the Mach 6 tunnel and the CFHT. Although the data obtained in the first series correspond to somewhat irregular model contours, they are presented nevertheless because they represent the only comparisons at two density ratios in Mach 6 flow.[1]

Shock Shapes

Shock shapes measured on a 10.16-cm-diameter sphere are shown in figure 9 and those measured on the hyperboloid (model 1) and paraboloid (model 3) at various angles of attack are shown in figures 10 and 11. The data of these figures, obtained in Mach 6 air and CF_4, illustrate the effect of normal-shock density ratio ρ_2/ρ_∞, or effective ratio of specific heats γ_{eff}, on shock detachment distance. For the sphere (fig. 9), the agreement between the shock detachment distances for the two air tests at different reservoir pressures (Reynolds numbers) indicates the absence of viscous effects over the operating range of reservoir pressure in the Mach 6 tunnel. Increasing the density ratio from 5.2 for air to 12.1 for CF_4 moves the shock closer to the surface of the sphere; in the stagnation region, this increase in density ratio decreases the detachment distance by a factor of about 2. The shock detachment distances predicted for air and CF_4 ($\gamma_{eff} = 1.123$) with the method of reference 21 agree well with measurements in the stagnation region of the sphere.

Predicted (ref. 21) and measured shock shapes at $\alpha = 0°$ in air and CF_4 are in good agreement for the hyperboloid (fig. 10(a)); fair agreement is observed for the paraboloid (fig. 11(a)), with prediction underestimating the shock detachment distance. The shock shapes over the surface of these two analytical models at all angles of attack are free of inflections in both test gases. Density ratio has a pronounced effect on shock detachment distance for these two models for the present range of angle of attack.

The effect of angle of attack on shock shape in air and CF_4 is shown for the hyperboloid in figure 12 and the paraboloid in figure 13. The shock detachment distance over the windward ($-1 \leq y/r_b \leq 0$) surface of the hyperboloid is relatively independent of angle of attack, particularly in CF_4 (fig. 12(b)). The effect of angle of attack on shock detachment distance is also small on the windward surface of the paraboloid (fig. 13) in both test gases, whereas on the leeward side, detachment

---

[1]The results of the first series are presented in figures 10 to 13 and 23 to 30.

distance significantly increases with increasing angle of attack. The effect of the flow expansion around the corner on the windward shock shape occurs closer to both models at the higher value of normal-shock density ratio.

Shock shapes obtained in the Mach 6 tunnel during the second series of tests are shown in figures 14 to 20 for a range of angle of attack. The shock shape over the forebody of the sonic-corner paraboloid (model 2) is shown in figure 14, over the paraboloid (model 3) in figure 15, over the Viking aeroshell (model 4) in figure 16, and over the cone models with different nose shapes (models 5 to 8) in figures 17 to 20. Note that the cone section of the cone models remains fixed in the x,y coordinate system as the nose changes shape. The predicted (ref. 21) and measured shock detachment distance from the more accurate paraboloid model used in this second series agree well at $\alpha = 0°$ (fig. 15(a)).

An inflection in the shock measured over the surface of the spherical-nose cone (model 5) is observed at $y/r_b \approx \pm 0.6$ and $\alpha = 0°$ (fig. 17(a)). This inflection, due to overexpansion of the flow from the spherical nose to the cone section, is discussed in reference 27 and illustrated subsequently. Shock shapes measured and predicted (refs. 21 and 22 and the unpublished time-dependent blunt-body program) for the spherical-nose cone at $\alpha = 0°$ (fig. 17(a)) are in good agreement.

The effect of angle of attack on the shock shape for the four cone models is shown in figure 21. The inflection in the shock shapes on models 5, 6, and 7 observed at the lower angles of attack does not appear at the highest angle of attack on either the windward or leeward sides. The shock detachment distance near the nose and in the plane of the base on the windward side is relatively insensitive to angle of attack for all four cone models. In figure 22, the shock shapes on the four cone models are compared with one another at angles of attack of 0°, 4°, and 20°. As in figures 17 to 21, the cone section of the models is fixed in the x,y coordinate system. Varying the nose shape from spherical has a small influence on the shock shape in the nose region at the lower angles of attack (figs. 22(a) and 22(b)), but little effect away from the nose region. This is also the case at $\alpha = 20°$ (fig. 22(c)) on the windward side; however, changing the nose from spherical increases the shock detachment distance on the leeward side.

An embedded shock within the leeward shock layer was observed for the cusp-nose cone (model 8) at angles of attack of 16° and 20°. This embedded shock may be observed from the schlieren photographs of figure 4 and was also observed for the flattened-nose cone (model 6) and concave-nose cone (model 7) at the highest angle of attack ($\alpha = 20°$). This embedded shock, which was not observed for the spherical-nose cone (model 5) at angles of attack up to 20°, originates on the cone surface just downstream of the nose-cone junction.

Pressure

Comparisons between air and CF_4 results (series 1).- Pressure distributions measured on the hyperboloid at various angles of attack and Reynolds numbers in air and CF_4 are shown in figures 23 and 26. The measured pressure distribution in air at $\alpha = 0°$ (fig. 23(a)) exhibits an unexpected overexpansion of the flow similar to that observed on spherically blunted cones (ref. 27). Also shown in figure 23(a) are the predictions of references 21 and 22 and modified Newtonian theory. Newtonian theory underpredicts the measured surface pressures at $\alpha = 0°$, whereas the predictions of references 21 and 22 are in reasonably good (about 6 percent) agreement with measurement. The surface pressure ratios $p/p_{t,2}$ for the hyperboloid reveal that

the flow is subsonic over the forebody at $\alpha = 0°$ and 4° and becomes supersonic on the leeward side for $\alpha > 4°$. (If the flow within the shock layer expands isentropically from the stagnation region, the flow becomes supersonic when $p/p_{t,2} < 0.528$ for air and $p/p_{t,2} < 0.575$ for CF_4.) Newtonian theory underpredicts the windward surface pressure at all angles of attack, but is in fairly good agreement with measured leeward surface pressures for $\alpha \geq 12°$. An influence of flow expansion at the corner is observed just upstream of the corner on the windward ray ($\phi = 180°$) for $\alpha \geq 12°$. Pressures measured on a 45° hyperboloid at Mach 10, but at a lower Reynolds number than in the present study, also exceeded Newtonian theory at $\alpha = 0°$ (ref. 28). It was speculated in reference 28 that analytical bodies having a sonic point at the end of the forebody surface would have experimental pressure distributions different from Newtonian theory. The results of figure 23 for the most windward ($\phi = 180°$) and leeward ($\phi = 0°$) rays tend to support this speculation. The data of figure 24 show that the factor of 17 variation in Reynolds number has no effect on surface pressure on the hyperboloid at all angles of attack.

As in air, an overexpansion of the CF_4 flow is observed for the hyperboloid at $\alpha = 0°$ (fig. 25(a)). In general, Newtonian theory and the method of reference 21 underpredict the surface pressure at $\alpha = 0°$; Newtonian theory underpredicts the windward surface pressure, which corresponds to an inviscid subsonic shock layer, and agrees fairly well with measurement on the leeward side for $\alpha \geq 8°$. The CF_4 results for the hyperboloid are compared with the air results at $N_{Re,\infty,d_b} = 0.2 \times 10^6$ in figure 26. In general, the pressure ratios for the CF_4, with a density ratio approximately twice that of air, are less than those for air. This trend of a lower surface pressure ratio for CF_4 is also predicted by the method of reference 21 at $\alpha = 0°$ (fig. 26(a)). The difference between measured surface pressure ratios for the two gases increases with increasing angle of attack and is about 30 percent on the leeward side at $\alpha = 20°$. Unlike air, the flow over the forebody of the hyperboloid in CF_4 may be both subsonic and supersonic at $\alpha = 0°$. Also, the CF_4 pressure distributions on the most windward ray do not exhibit an upstream influence of the flow expansion at the corner, as do the air results for $\alpha \geq 12°$.

Pressure distributions for the paraboloid (model 3) are shown in figures 27 to 30 for various angles of attack, Reynolds numbers, and test gases. At $\alpha = 0°$ in air (fig. 27(a)), the predictions of reference 21 and Newtonian theory agree reasonably well (6 to 7 percent) with measurement. As observed for the hyperboloid, Newtonian theory tends to underpredict the windward surface pressure at angles of attack, but is in good agreement with the leeward pressure distribution. This is also observed in CF_4 (fig. 29). The windward shock layer flow becomes subsonic along the entire $\phi = 180°$ ray for $\alpha \geq 12°$ in air and $\alpha \geq 16°$ in CF_4. As expected, there is no significant effect of Reynolds number on the surface pressure distribution for this relatively blunt body in Mach 6 air (fig. 28). The method of reference 21 predicts an effect of density ratio on surface pressure at $\alpha = 0°$ (fig. 30(a)). Although an effect of density ratio on the leeward surface pressure distribution for the paraboloid may exist (fig. 30), it is not as significant as that observed in figure 26 for the hyperboloid.

Mach 6 air results (series 2).- Pressure distributions on the sonic-corner paraboloid (model 2) in Mach 5.9 air are shown in figure 31 at various angles of attack. The pressure distribution on the forebody is predicted quite well by Newtonian theory for all angles of attack. The pressure distributions of figure 31 illustrate the rapid expansion of the flow around the corner. Except at $\alpha = 8°$, the pressures on the windward ($\phi = 180°$) and leeward ($\phi = 0°$) rays of the afterbody are relatively constant with s/s_b, are essentially the same value, and do not change appreciably with increasing angle of attack. The afterbody pressure is close to the

free-stream static pressure. The reason that the afterbody pressure distributions along $\phi = 0°$ and $180°$ are different at $\alpha = 8°$ from those of the other rays (fig. 31(c)) is unknown.

Pressure distributions on the more accurate (series 2) paraboloid (model 3) are shown in figure 32 for Mach 5.9 air. The surface pressure ratios $p/p_{t,2}$ for this model are somewhat lower than values measured on the model tested in the first series and are in good agreement with prediction (ref. 21 and Newtonian theory) at $\alpha = 0°$. Newtonian theory predicts the windward and leeward pressure distributions quite well at all angles of attack.

Figure 33 shows measured pressure distributions on the Viking aeroshell (model 4) in Mach 5.9 air. As with the sonic-corner paraboloid (fig. 31), the flow expands rapidly around the corner and the pressure becomes nearly constant over the afterbody surface. The afterbody pressure ratio is about the same at all angles of attack and is slightly higher than the free-stream static pressure.

Measured pressure distributions for the cones (models 5 to 8) in Mach 5.9 air are shown in figures 34 to 37 at various angles of attack. The predictions of references 21 and 22, the unpublished time-dependent blunt-body program, and Newtonian theory are compared with measurement in figure 34(a) for the spherical-nose cone at $\alpha = 0°$; also shown for $|s/s_b| > 0.3$ are predictions from the cone theories of references 25 and 26. The predictions of reference 22 and the unpublished program agree with measurement; the prediction of reference 21 agrees with measurement on the spherical section and aft portion of the cone section, but underpredicts the overexpansion of the flow from the spherical nose by about 10 percent. The flow at the surface of this cone at $\alpha = 0°$ becomes supersonic on the spherical section just upstream of the sphere-cone junction and, as observed in figure 34(a), becomes subsonic on the rear of the cone section. The theories of references 25 and 26, naturally, do not predict the overexpansion for the present cone models. Newtonian theory predicts the surface pressure distribution on the spherical nose, but underpredicts the pressure on the cone section. The theory of High and Blick (ref. 26) predicts the asymptotic cone pressure quite well, whereas the semiempirical method of Amick (ref. 25) overpredicts this pressure. The method of reference 25 was included herein because of its success when applied to larger cone angles and higher Mach numbers than those from which the semiempirical relations were derived (ref. 29). For all four cone models (figs. 34 to 37), Newtonian theory underpredicts the cone surface pressure on the windward side at all angles of attack, and agrees reasonably well with measured leeward-side pressures at the higher angles of attack ($\alpha > 12°$). As for the spherical-nose cone, Newtonian theory accurately predicts the pressure distribution on the flattened nose of model 6 (fig. 35); however, it does not predict the pressure distributions on the concave and cusp noses of models 7 and 8 (figs. 36 and 37).

The effect of nose shape of the cones on the pressure distribution in Mach 5.9 air is shown in figure 38 at several angles of attack. The data of figure 38 correspond to the most windward ($\phi = 180°$) and leeward ($\phi = 0°$) rays. The nose shape does not influence the windward or the leeward pressure distribution on the cone section for $0° < \alpha < 16°$; at $\alpha = 20°$, some effect of the nose shape is apparent on the leeward pressures close to the nose-cone junction. For all four nose shapes, an overexpansion of the flow from the nose to the cone section is observed on the windward side at the lower angles of attack ($\alpha < 12°$); this overexpansion also occurs on the leeward side for all angles of attack. The pressure distributions on the nose of the flattened-nose cone (model 6) and concave-nose cone (model 7) are approximately the same at the lower angles of attack, but depart from one another on the leeward

side at the higher angles of attack. The pressure distribution on the cusp-nose cone is indicative of flow separation and reattachment. The shock generated by reattachment was observed in the schlieren photographs (fig. 4).

The effect of angle of attack on measured windward and leeward pressure distributions for the four cone models in Mach 5.9 air is shown in figure 39. The overexpansion on the windward side of the spherical-nose cone (fig. 39(a)) occurs for effective cone angles ($\theta + \alpha$) less than or equal to 57°. Note that increasing the cone half-angle beyond the detachment angle, which is about 55° for Mach 6 air, causes the bow wave over the conical portion of a sphere cone to change from conical to spherical, and the flow changes from supersonic to completely subsonic along the cone (ref. 30). For $\alpha > 12°$, the windward surface pressure for all four cone models decreases as the flow approaches the base.

Circumferential pressure distributions on the cone section of the spherical-nose cone in Mach 5.9 air are shown in figure 40 at various angles of attack. These distributions correspond to $s/s_b = \pm 0.88$. Predicted distributions from Newtonian theory and the methods of references 25 and 26 are compared with measurement. At the lower angles of attack, the method of High and Blick (ref. 26) provides the most accurate prediction of the measured pressures, whereas Newtonian theory is more accurate at the higher angles of attack.

Mach 10 air results (series 2).- Pressure distributions measured on the hyperboloid (model 1), the sonic-corner paraboloid (model 2), the paraboloid (model 3), the Viking aeroshell (model 4), and the four cones (models 5 to 8) in the Langley Continuous-Flow Hypersonic Tunnel in Mach 10 air are shown in figures 41 to 48. The angle of attack was varied from 0° to 16° in 4° increments for these Mach 10 tests. In figure 41(a), the pressure distribution on the more accurate (series 2) hyperboloid is free of an overexpansion at $\alpha = 0°$. Unfortunately, this hyperboloid model was not tested in the Mach 6 tunnel; however, the results of figure 41(a) cast doubt on the validity of the overexpansion observed at Mach 6 (fig. 23(a)) on the less-accurate (series 1) hyperboloid model. At $\alpha = 0°$ (fig. 41(a)), the measured surface pressure is predicted quite well by the method of reference 21. As observed previously for Mach 6 air, Newtonian theory underpredicts the windward pressure distribution for the hyperboloid, but agreement between Newtonian theory and measurement improves on the leeward side with increasing angle of attack.

The pressure ratio on the afterbody of the sonic-corner paraboloid (fig. 42) is relatively constant as angle of attack varies from 0° to 16°. The pressure on the afterbody is about 1.75 to 2.5 times that of the free-stream static pressure. As observed in figure 31, the afterbody pressure was nearly the same as the free-stream static pressure at Mach 5.9. Hence, Mach number affects the afterbody pressure. Whereas the afterbody pressure was relatively constant with s/s_b for Mach 5.9 air (fig. 31), the afterbody pressure at Mach 10 increases with $|s/s_b|$ in the direction of the sting.

The methods of references 21 and 22 accurately predict the measured pressure distribution for the paraboloid at $\alpha = 0°$ (fig. 43(a)). As observed at Mach 5.9 (fig. 32), the measured pressure distributions for the paraboloid are predicted quite well by Newtonian theory at Mach 10 (fig. 43) for the present range of angle of attack. In figure 44, the afterbody pressure on the Viking aeroshell is essentially constant with s/s_b and is the same on the windward and leeward rays ($\phi = 180°$ and 0°) at $\alpha < 12°$. This was also the case for Mach 5.9 air (fig. 33). However, the afterbody pressure is about twice the free-stream static pressure at Mach 10, whereas it was approximately equal to the free-stream pressure at Mach 5.9.

The effect of free-stream Reynolds number on the pressure distribution on the hyperboloid, paraboloid, Viking aeroshell, and four cone models is shown in figures 49 to 55 at $\alpha = 0°$ and 16°. As expected, Reynolds number does not affect the forebody pressure distributions on these relatively blunt bodies. However, Reynolds number does influence afterbody pressure on the Viking aeroshell (fig. 51), the pressure decreasing with increasing Reynolds number at these two angles of attack. This trend is characteristic of the Reynolds number effect on base pressure observed for laminar flow (ref. 31). Surface pressures measured at Mach 10 on the hyperboloid (fig. 49) agree quite well with those measured on the hyperboloid tested in reference 28, which had the same equivalent nose radius.

Pressure distributions illustrating the effect of nose shape of the cone models at Mach 10 are shown in figure 56 at various angles of attack. As expected, these results are nearly the same as those observed at Mach 5.9 (fig. 38). The effect of Mach number on the pressure distributions on the spherical-nose cone is shown in figure 57 at $\alpha = 0°$ and 16°. Again, as expected (refs. 23 and 24), no effect of Mach number is apparent.

Forces and Moments

Aerodynamic coefficients (normal, axial, and pitching moment) are shown as a function of angle of attack in figure 58 for the hyperboloid (model 1), paraboloid (model 3), and spherical-nose cone (model 5) in Mach 10 air. Also shown in figure 58 are predicted (ref. 32) aerodynamic coefficients based on Newtonian theory, where the maximum pressure coefficient is assumed to equal 2, for the spherical-nose cone (model 5). The normal-force coefficients C_N for the paraboloid and cone match each other closely up to $\alpha = 16°$, whereas C_N for the hyperboloid is somewhat less than that for the other two models at a given angle of attack. The geometric similarity of the hyperboloid and cone is illustrated by the variation of axial-force coefficient C_A (fig. 58(b)), with C_A for the paraboloid being much less than that for the other two configurations. The pitching-moment coefficients C_m for all three models agree up to $\alpha = 8°$. At the highest angle of attack ($\alpha = 20°$), the pitching moments for the paraboloid and cone are in good agreement and that for the hyperboloid is higher than for the other two models. Newtonian theory for the cone (ref. 32) underpredicts C_N at $\alpha > 4°$, underpredicts C_A at $\alpha \leq 16°$, and predicts C_m with fair accuracy.

Aerodynamic coefficients measured on the four cone models in the Mach 6 tunnel and the CFHT are compared in figures 59 to 62. The aerodynamic coefficients measured in these two facilities are essentially the same for the present range of angle of attack; that is, no effect of Mach number or Reynolds number on the aerodynamic coefficients is observed. Normal-force and pitching-moment coefficients measured on a 45° spherically blunted cone ($r_n/r_b = 0.5$) in reference 33 agree with the present results, whereas the axial-force coefficients measured in reference 33 are about 4 to 5 percent lower. (As in the present study, no correction for the base pressure was applied to the results of ref. 33. Base pressures measured on the spherical-nose cone in Mach 5.9 air in the present study were approximately equal to the free-stream static pressure for $0° < \alpha < 20°$.)

The effect of nose shape of the cones on aerodynamic coefficients is shown in figure 63 for Mach 10 air. Normal-force and pitching-moment coefficients (figs. 63(a) and 63(c)) are the same for the flattened, concave, and cusp nose shapes (the normal-force coefficient for these three shapes is slightly less than that for the spherical-nose cone at the highest angle of attack (fig. 63(a)). There may be a small decrease in axial force as the nose shape is changed from a sphere, but this

change is within the experimental uncertainty. The drag and lift coefficients and lift-drag ratios for the hyperboloid and cone models are shown in figure 64 for Mach 5.9 and 10.1 air. The Reynolds number N_{Re,∞,d_b} is the same for the two Mach numbers.

CONCLUSIONS

Pressure distributions, aerodynamic coefficients, and shock shapes were measured on blunt bodies of revolution in hypersonic flow at angles of attack from 0° to 20° in 4° increments. Configurations tested were a hyperboloid with an asymptotic angle of 45°, a sonic-corner paraboloid, a paraboloid with an angle of 27.6° at the base, a Viking aeroshell generated in a generalized orthogonal coordinate system, and a family of 45° half-angle cones having spherical, flattened, concave, and cusp nose shapes. Real-gas effects were simulated for the hyperboloid and paraboloid by testing these models at Mach 6 in air and CF_4. The normal-shock density ratio was 5.3 for air and 12 for CF_4. Tests were also performed in Mach 10 air. Predictions from Newtonian theory, simple theories, and numerical flow field programs are compared with measurement. The results of this study led to the following conclusions:

1. A pronounced effect of density ratio on shock shape was observed for a sphere and for the hyperboloid and paraboloid, the shock detachment distance decreasing with increasing density ratio. The detachment distance on the windward side of the hyperboloid was relatively independent of angle of attack up to 20°. Shock shapes for the sphere and hyperboloid at zero incidence in Mach 6 air and CF_4 were predicted reasonably well by the ideal-gas method of Zoby and Graves (NASA TM X-2843, ref. 21) where an effective value of the ratio of specific heats for CF_4 was input to this method. An embedded shock within the bow shock layer on the leeward side was observed for the 45° cone models having flattened, concave, and cusp nose shapes at an angle of attack of 20°, but was not observed for the spherical-nose cone.

2. Surface pressure ratios on the most windward ray and especially the most leeward ray of the hyperboloid decreased with increasing density ratio; this effect of density ratio increases with increasing angle of attack. A smaller effect of density ratio on surface pressure was observed for the paraboloid. The decrease of surface pressure ratio with increasing density ratio for these two analytical models at zero incidence was predicted by the Zoby-Graves method.

3. The forebody pressure distribution on all models was independent of Mach number between 6 and 10 and of Reynolds number, which was varied by a factor of 17 at Mach 6. However, the afterbody pressure on the Viking aeroshell increased with increasing Mach number and decreasing Reynolds number. At Mach 6, the afterbody pressures on the most windward and leeward rays of the sonic-corner paraboloid and Viking aeroshell were approximately equal to the free-stream static pressure at all angles of attack.

4. The method of Zoby and Graves and the method of Kumar and Graves (AIAA Paper No. 77-172, ref. 22) accurately predicted the measured pressure distributions on the hyperboloid and paraboloid in Mach 6 and Mach 10 air. For the 45° spherical-nose cone, the Zoby-Graves method underpredicted the surface pressure just downstream of the sphere-cone junction. The surface pressure distribution on this cone at zero incidence in Mach 6 air was accurately predicted by an unpublished time-dependent blunt-body program of Harris H. Hamilton of the Langley Research Center and by the Kumar-Graves method. The windward and leeward pressures on the paraboloid were accurately predicted by Newtonian theory for the present range of angle of attack, as

was the leeward pressure on the hyperboloid at the higher angles of attack. Newtonian theory underpredicts the pressure on the windward side of the hyperboloid, which does not have a natural sonic point on the surface.

5. Changing nose shape of the 45° cones from spherical to flattened, concave, or cusp did not appreciably affect the aerodynamic coefficients in Mach 10 air. The 45° hyperboloid, which geometrically resembles the 45° spherical-nose cone, has a slightly smaller normal-force coefficient, about the same axial-force coefficient, and a slightly larger pitching-moment coefficient than does the 45° cone. Newtonian theory for the spherical-nose cone underpredicted the normal- and axial-force coefficients and predicted the pitching-moment coefficient reasonably well.

Langley Research Center
National Aeronautics and Space Administration
Hampton, VA 23665
June 22, 1982

APPENDIX

MEASURED HEAT-TRANSFER DISTRIBUTIONS ON HYPERBOLOID AND PARABOLOID

Convective heat-transfer rates were measured on the hyperboloid (model 1) and the paraboloid (model 3) in the Langley 20-Inch Mach 6 Tunnel. The convective heat-transfer rate to the model surface was obtained by using the transient calorimetry technique to measure the rate of heat storage in the model skin. These heat-transfer models were spun from type 347 stainless steel and had a wall thickness of 0.61 mm to 0.76 mm. Chromel-alumel thermocouples (30-gage wire, 0.25 mm in diameter) were welded to the inside surface of the shell; 44 thermocouples were distributed along 5 rays.

The models, originally at or below room temperature, were suddenly exposed to steady-state air flow by quick injection from a sheltered position below the floor of the tunnel test section. Injection was accomplished in 0.5 to 0.55 second, as determined from a 3-position switch attached to the injection mechanism, and the model remained in the flow for approximately 5 seconds before being retracted. The output signal from each thermocouple was recorded by the analog-to-digital system at 20 samples per second. After a test, the angle of attack was changed and the model was cooled by a jet of air. The model thermocouple outputs were scanned before the next test to verify that the model shell had returned to an isothermal state.

The data reduction procedure used for these continuous thin-skin models is discussed in detail in reference 34. Because of the difference in surface area between the inner and outer surfaces of the thin-skin model (refs. 35 and 36), a geometric correction factor ω must be applied to the measured skin thickness τ_m. The product $\tau_m\omega$, referred to as the effective skin thickness τ_{eff}, is defined as the ratio of the volume of the skin element to the area of the skin element subjected to aerodynamic heating. The curvature correction factor is given in reference 35 as

$$\omega = \left(1 - \frac{\tau_m \cos \eta}{2y}\right)\left(1 - \frac{\tau_m}{2r}\right) \tag{A1}$$

where

$$\eta = \tan^{-1} \frac{dy}{dx}$$

and

$$r = \frac{\left[1 + \left(\frac{dy}{dx}\right)^2\right]^{3/2}}{\left|\frac{d^2y}{dx^2}\right|}$$

APPENDIX

Values of ω at the thermocouple locations for the two heat-transfer models are

Hyperboloid (model 1)

s/s_b	ω
0	0.945
.046	.951
.0965	.961
.2075	.978
.324	.985
.4555	.989
.584	.992
.7215	.993
.849	.994
.9185	.995

Paraboloid (model 3)

s/s_b	ω
0	0.9735
.046	.974
.089	.975
.183	.978
.280	.982
.390	.985
.517	.988
.650	.990
.807	.991
.891	.992

Considering the possible errors in conduction effects (lateral conduction in the model shell and along the thermocouple wires), in effective skin thickness, in measured inner surface temperatures, and in the values of density and specific heat of the skin material, the values of heating rate presented herein are believed accurate to within 15 percent (ref. 34).

Heat-transfer distributions measured on the hyperboloid and paraboloid models are nondimensionalized by the predicted (ref. 37) value of heat transfer to the stagnation point of a sphere. The sphere radius is equal to the equivalent nose radius of the model (see section entitled "Models"). The value of wall temperature required in the prediction of the stagnation point heat-transfer rate was selected to force agreement between the measured heat-transfer rate at the nose ($s = 0$) of the model at zero incidence and the predicted heat-transfer rate to a sphere (that is, $\dot{q}/\dot{q}_{sph} = 1$ at $s/s_b = 0$ and $\alpha = 0°$). The resulting value of $T_w/T_{t,2}$ was used to predict $\dot{q}_{sph}$ for tests at $\alpha > 0°$. The values of $T_w/T_{t,2}$ used for the three reservoir pressures in the Mach 6 tunnel are

Nominal $p_{t,1}$, MPa	$T_w/T_{t,2}$ for -	
	Hyperboloid (model 1)	Paraboloid (model 3)
0.16	0.1805	0.158
.70	.258	.262
3.41	.325	.323

Heat-transfer distributions for the hyperboloid in Mach 6 air are shown in figure 65 at various angles of attack and the highest value of free-stream Reynolds number. Also shown in figure 65(a) are heating distributions predicted with the methods of references 21 and 22 at $\alpha = 0°$. These predictions agree reasonably well with measurement, except along $\phi = 180°$. The increase in heat-transfer rate occurring around $s/s_b = -0.5$ on this ray is attributed to transition of the boundary

layer from laminar to turbulent flow due to surface roughness. (Although the surface of this model was polished prior to any testing, it became somewhat rough during the tests because of sandblasting by solid contaminants in the flow.) Transition was also observed at $\alpha = 4°$ (fig. 65(b)) and may have occurred at $\alpha = 8°$ (fig. 65(c)). Near the base, the windward-surface heating rate increases only about 30 percent as angle of attack is increased from 0° to 20°, whereas the leeward heating rate decreases by a factor of 2.5 or so. The circumferential heating distributions imply that the flow remained attached on the leeward side as the angle of attack was increased to 20° (that is, no minima in the circumferential heating distributions were observed.)

The effect of free-stream Reynolds number on the heat-transfer distribution for the hyperboloid is shown in figure 66 for $\alpha = 0°$. The heat-transfer rate tends to increase with increasing Reynolds number in the region just downstream of the model stagnation point, but is essentially independent of Reynolds number for $s/s_b > 0.4$. (Because the sandblasting effect worsens with increasing reservoir pressure (Reynolds number) and this effect is expected to increase the heating rate on the model surface (ref. 38), no definite conclusion concerning the increase in heating with increasing Reynolds number is made.)

Heat-transfer distributions for the paraboloid in Mach 6 air are shown in figure 67 at various angles of attack. Like the hyperboloid data in figure 65, these data correspond to the highest value of free-stream Reynolds number. Unlike the data for the hyperboloid, no evidence of boundary layer tansition is observed for the paraboloid. The methods of references 21 and 22 overpredict the heating rate in the nose region at $\alpha = 0°$ (fig. 67(a)); the prediction of reference 21 agrees with measurement to within 15 percent for $|s/s_b| > 0.5$. The circumferential heating distribution gives no evidence of leeward flow separation at the higher angles of attack. The results of figure 68 illustrate the absence of a Reynolds number effect on the heating at $\alpha = 0°$.

REFERENCES

1. Jones, Robert A.; and Hunt, James L. (appendix A by James L. Hunt, Kathryn A. Smith, and Robert B. Reynolds, and appendix B by James L. Hunt and Lillian R. Boney): Use of Tetrafluoromethane To Simulate Real-Gas Effects on the Hypersonic Aerodynamics of Blunt Vehicles. NASA TR R-312, 1969.

2. Miller, Charles G., III: Shock Shapes on Blunt Bodies in Hypersonic-Hypervelocity Helium, Air, and CO_2 Flows, and Calibration Results in Langley 6-Inch Expansion Tube. NASA TN D-7800, 1975.

3. Trimpi, Robert L.: A Preliminary Theoretical Study of the Expansion Tube, A New Device for Producing High-Enthalpy Short-Duration Hypersonic Gas Flows. NASA TR R-133, 1962.

4. Miller, Charles G.: Operational Experience in the Langley Expansion Tube With Various Test Gases. NASA TM-78637, 1977.

5. Clemens, P. L., compiler: The Von Kármán Gas Dynamics Facility 1000-ft Hypervelocity Range - Description, Capabilities, and Early Test Results. AEDC-TR-66-197, U.S. Air Force, Nov. 1966. (Available from DTIC as AD 801 906.)

6. Hypersonic Shock Tunnel - Description and Capabilities. Calspan Corp., Sept. 1975.

7. Chapman, Dean R.: Some Possibilities of Using Gas Mixtures Other Than Air in Aerodynamic Research. NACA Rep. 1259, 1956. (Supersedes NACA TN 3226.)

8. Hunt, James L.; Jones, Robert A.; and Smith, Kathryn A.: Use of Hexafluoroethane To Simulate the Inviscid Real-Gas Effects on Blunt Entry Vehicles. NASA TN D-7701, 1974.

9. Midden, R. E.; and Miller, C. G.: Description and Preliminary Calibration Results for the Langley Hypersonic CF_4 Tunnel. NASA TM-78800, 1978.

10. Goldberg, Theodore J.; and Hefner, Jerry N. (appendix by James C. Emery): Starting Phenomena for Hypersonic Inlets With Thick Turbulent Boundary Layers at Mach 6. NASA TN D-6280, 1971.

11. Keyes, J. Wayne: Force Testing Manual for the Langley 20-Inch Mach 6 Tunnel. NASA TM-74026, 1977.

12. Schaefer, William T., Jr.: Characteristics of Major Active Wind Tunnels at the Langley Research Center. NASA TM X-1130, 1965.

13. Pirrello, C. J.; Hardin, R. D.; Heckart, M. V.; and Brown, K. R.: An Inventory of Aeronautical Ground Research Facilities. Volume I - Wind Tunnels. NASA CR-1874, 1971.

14. Gnoffo, Peter A.: Forebody and Afterbody Solutions of the Navier-Stokes Equations for Supersonic Flow Over Blunt Bodies in a Generalized Orthogonal Coordinate Sytem. NASA TP-1075, 1978.

15. Burner, Alpheus W.; and Midden, Raymond E.: Holographic Flow Visualization at the Langley CF_4 Tunnel. NASA TM-74051, 1977.

16. Miller, Charles G., III; and Gnoffo, Peter A.: Pressure Distributions and Shock Shapes for 12.84°/7° On-Axis and Bent-Nose Biconics in Air at Mach 6. NASA TM-83222, 1981.

17. Guy, R. W.; and Winebarger, R. M.: Effect of Orifice Size and Heat-Transfer Rate on Measured Static Pressures in a Low-Density Arc-Heated Wind Tunnel. NASA TN D-3829, 1967.

18. Ames Research Staff: Equations, Tables, and Charts for Compressible Flow. NACA Rep. 1135, 1953. (Supersedes NACA TN 1428.)

19. Properties and Applications of the "Freon" Fluorocarbons. Tech. Bull. X-88F, E. I. du Pont de Nemours & Co., Sept. 3, 1968. (Revised Feb. 3, 1969.)

20. Erickson, Wayne D.; and Creekmore, Helen S.: A Study of Equilibrium Real-Gas Effects in Hypersonic Air Nozzles, Including Charts of Thermodynamic Properties for Equilibrium Air. NASA TN D-231, 1960.

21. Zoby, Ernest V.; and Graves, Randolph A. Jr.: A Computer Program for Calculating the Perfect Gas Inviscid Flow Field About Blunt Axisymmetric Bodies at an Angle of Attack of 0°. NASA TM X-2843, 1973.

22. Kumar, Ajay; and Graves, R. A., Jr.: Numerical Solution of the Viscous Hypersonic Flow Past Blunted Cones at Angle of Attack. AIAA Paper No. 77-172, Jan. 1977.

23. Truitt, Robert Wesley: Hypersonic Aerodynamics. The Ronald Press Co., c.1959.

24. Hayes, Wallace D.; and Probstein, Ronald F.: Hypersonic Flow Theory. Volume I - Inviscid Flows, Second ed. Academic Press, Inc., 1966.

25. Amick, James L.: Pressure Measurements on Sharp and Blunt 5°- and 15°-Half-Angle Cones at Mach Number 3.86 and Angles of Attack to 100°. NASA TN D-753, 1961.

26. High, M. D.; and Blick, E. F.: Cone Pressure Distribution at Large and Small Angles of Attack. AIAA J., vol. 2, no. 11, Nov. 1964, pp. 2054-2055.

27. Cleary, Joseph W.: Effects of Angle of Attack and Nose Bluntness on the Hypersonic Flow Over Cones. AIAA Paper No. 66-414, June 1966.

28. Little, Herbert R.: An Experimental Investigation of Surface Conditions on Hyperboloids and Paraboloids at a Mach Number of 10. AEDC-TR-69-225, U.S. Air Force, Jan. 1970. (Available from DTIC as AD 698 755.)

29. Bushnell, Dennis M.; Jones, Robert A.; and Huffman, Jarrett K.: Heat-Transfer and Pressure Distributions on Spherically Blunted 25° Half-Angle Cone at Mach 8 and Angles of Attack up to 90°. NASA TN D-4792, 1968.

30. Stewart, David A.; and Marvin, Joseph G.: Convective Heat-Transfer Rates on Large-Angle Conical Bodies at Hypersonic Speeds. NASA TN D-5526, 1969.

31. Miller, Charles G., III: Experimental Base Pressures on 9° Spherically Blunted Cones at Mach Numbers From 10.5 to 20. NASA TN D-4800, 1968.

32. Wells, William R.; and Armstrong, William O.: Tables of Aerodynamic Coefficients Obtained From Developed Newtonian Expressions for Complete and Partial Conic and Spheric Bodies at Combined Angles of Attack and Sideslip With Some Comparisons With Hypersonic Experimental Data. NASA TR R-127, 1962.

33. Calloway, Robert L.; and White, Nancy H.: Measured and Predicted Shock Shapes and Aerodynamic Coefficients for Blunted Cones at Incidence in Air at Mach 5.9. NASA TP-1652, 1980.

34. Miller, Charles G., III: Comparison of Thin-Film Resistance Heat-Transfer Gages With Thin-Skin Transient Calorimeter Gages in Conventional-Hypersonic Wind Tunnels. NASA TM-83197, 1981.

35. Cooper, Morton; and Mayo, Edward E.: Measurements of Local Heat Transfer and Pressure on Six 2-Inch-Diameter Blunt Bodies at a Mach Number of 4.95 and at Reynolds Numbers Per Foot up to 81×10^6. NASA MEMO 1-3-59L, 1959.

36. Conti, Raul J.: Approximate Temperature Distributions and Streamwise Heat Conduction Effects in the Transient Aerodynamic Heating of Thin-Skinned Bodies. NASA TN D-895, 1961.

37. Fay, J. A.; and Riddell, F. R.: Theory of Stagnation Point Heat Transfer in Dissociated Air. J. Aeronaut. Sci., vol. 25, no. 2, Feb. 1958, pp. 73-85, 121.

38. Grabau, Martin; Smithson, H. K., Jr.; and Little, Wanda J.: A Data Reduction Program for Hotshot Tunnels Based on the Fay-Riddell Heat-Tansfer Rate Using Nitrogen at Stagnation Temperatures From 1500 to 5000°K. AEDC-TDR-64-50, U.S. Air Force, June 1964.

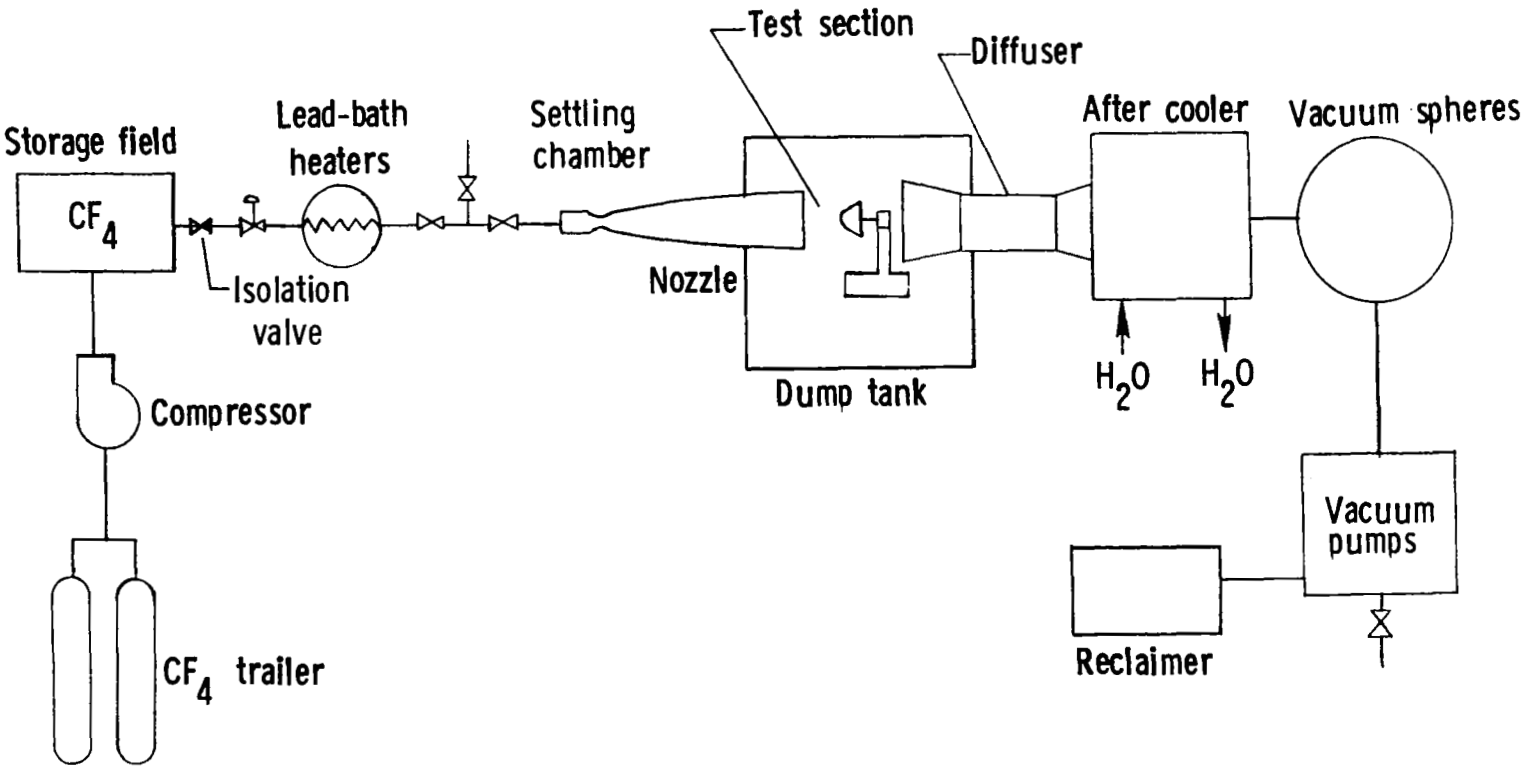

(a) Langley Hypersonic CF_4 Tunnel (taken from ref. 9).

Figure 1.- Schematics of wind tunnels used in the present study.

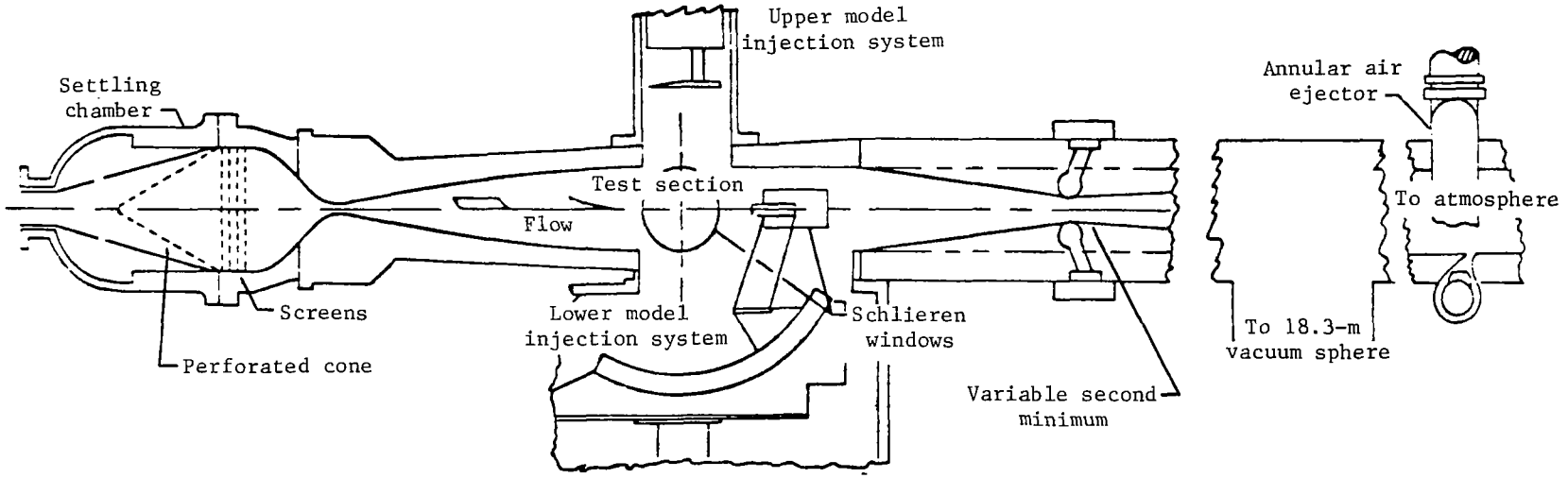

(b) Langley 20-Inch Mach 6 Tunnel (taken from ref. 10).

Figure 1.- Continued.

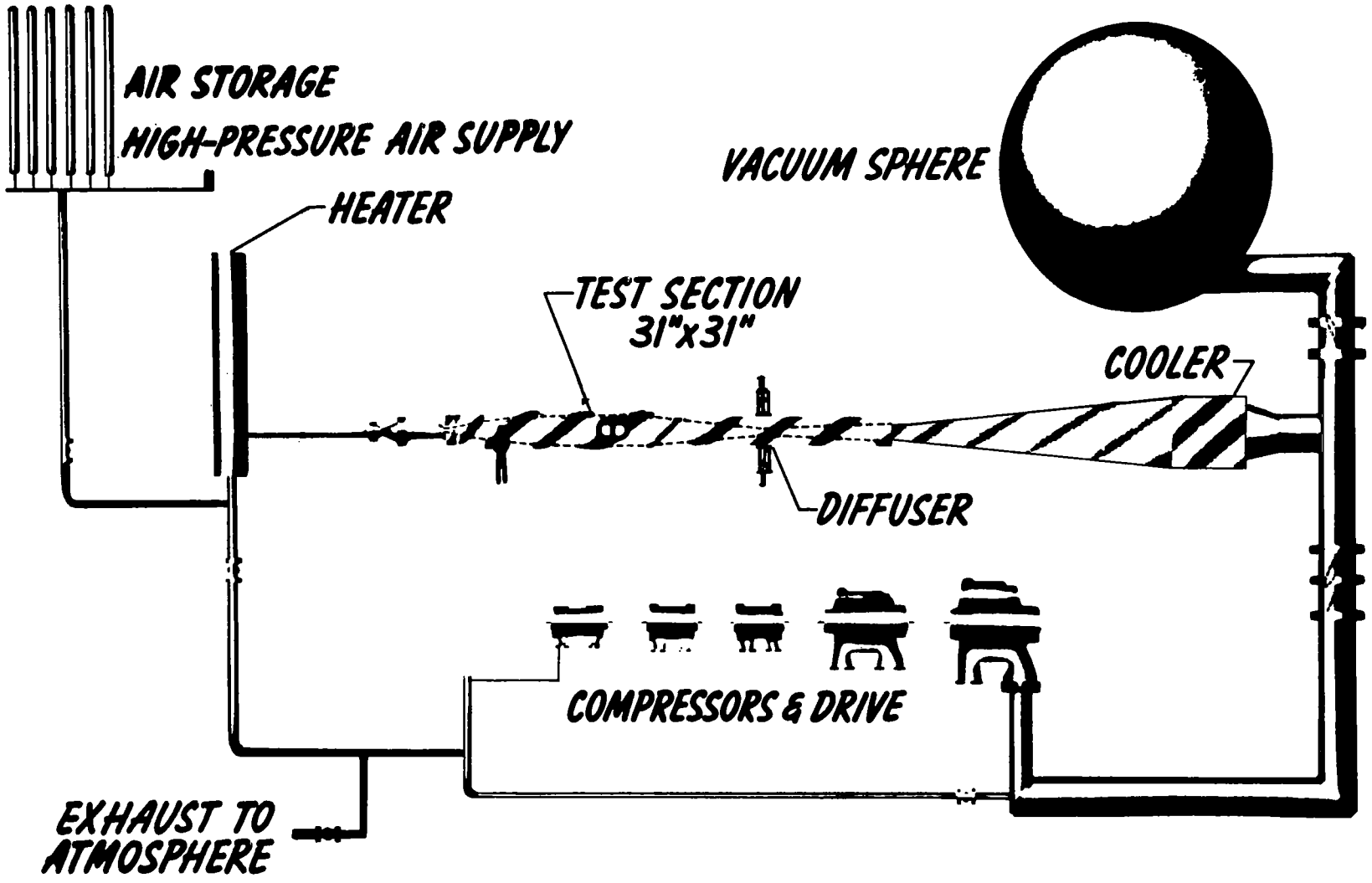

(c) Langley Continuous-Flow Hypersonic Tunnel (taken from ref. 34).

Figure 1.- Concluded.

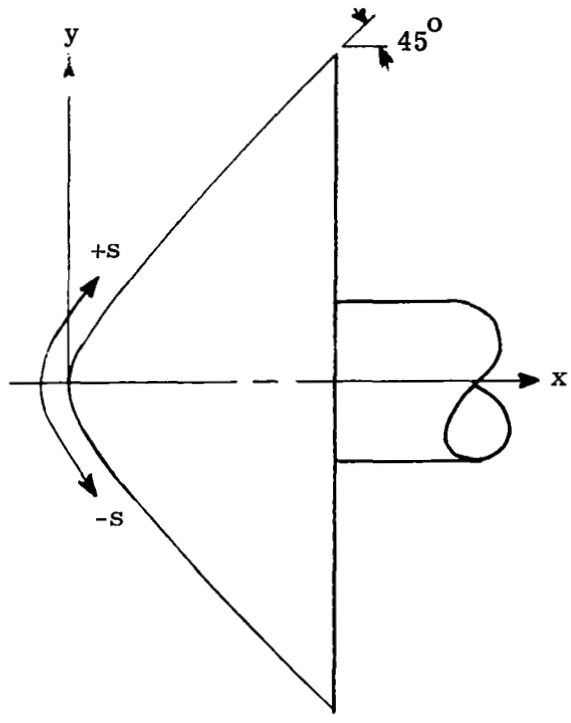

(a) Hyperboloid (model 1).

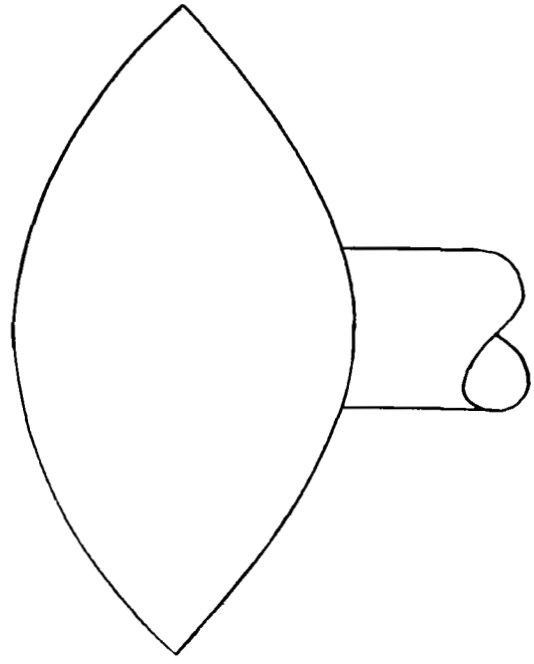

(b) Sonic-corner paraboloid (model 2).

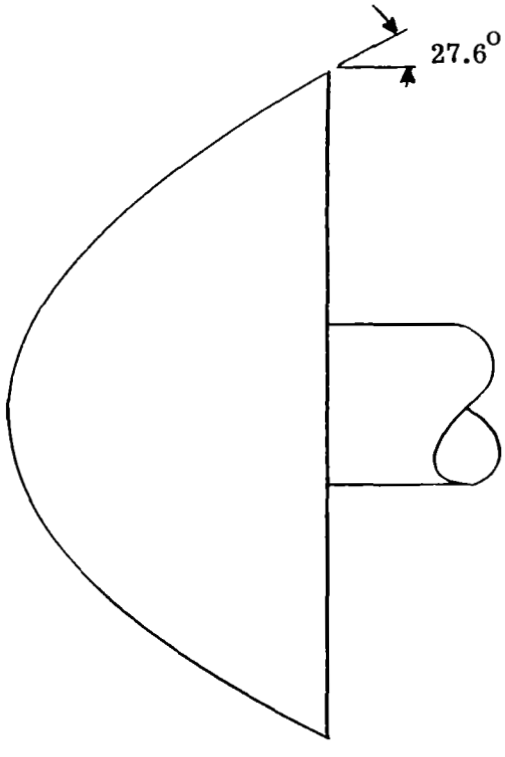

(c) Paraboloid (model 3).

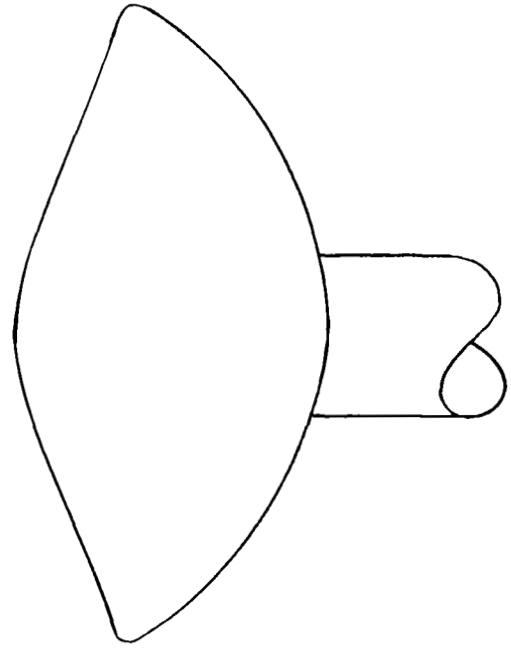

(d) Viking aeroshell (model 4).

Figure 2.- Planform views of configurations tested.

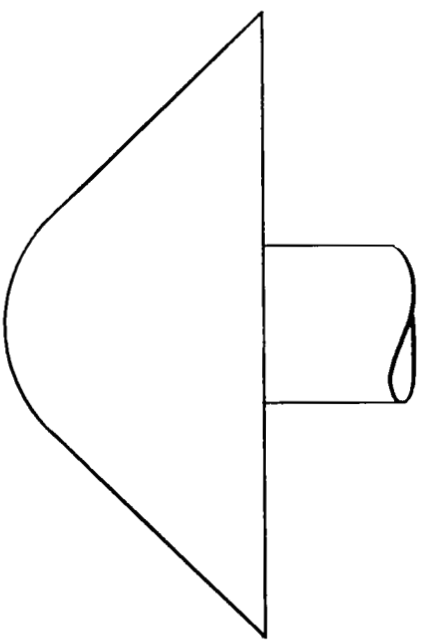

(e) 45° cone with spherical nose (model 5).

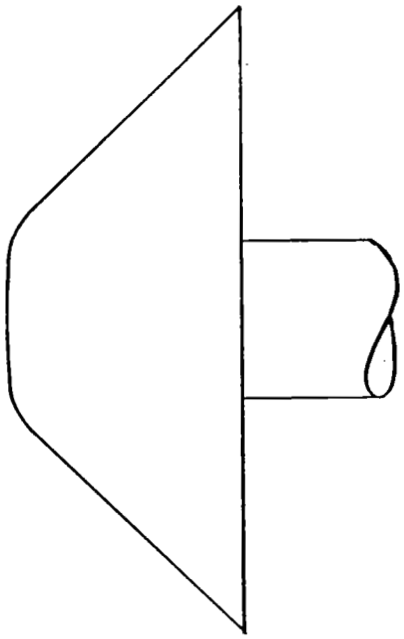

(f) 45° cone with flattened nose (model 6).

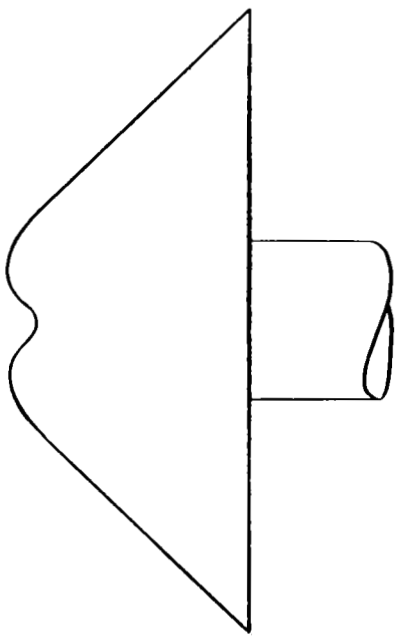

(g) 45° cone with concave nose (model 7).

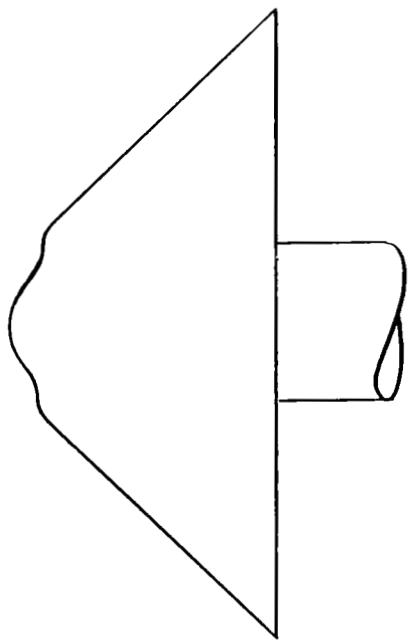

(h) 45° cone with cusp nose (model 8).

Figure 2.- Concluded.

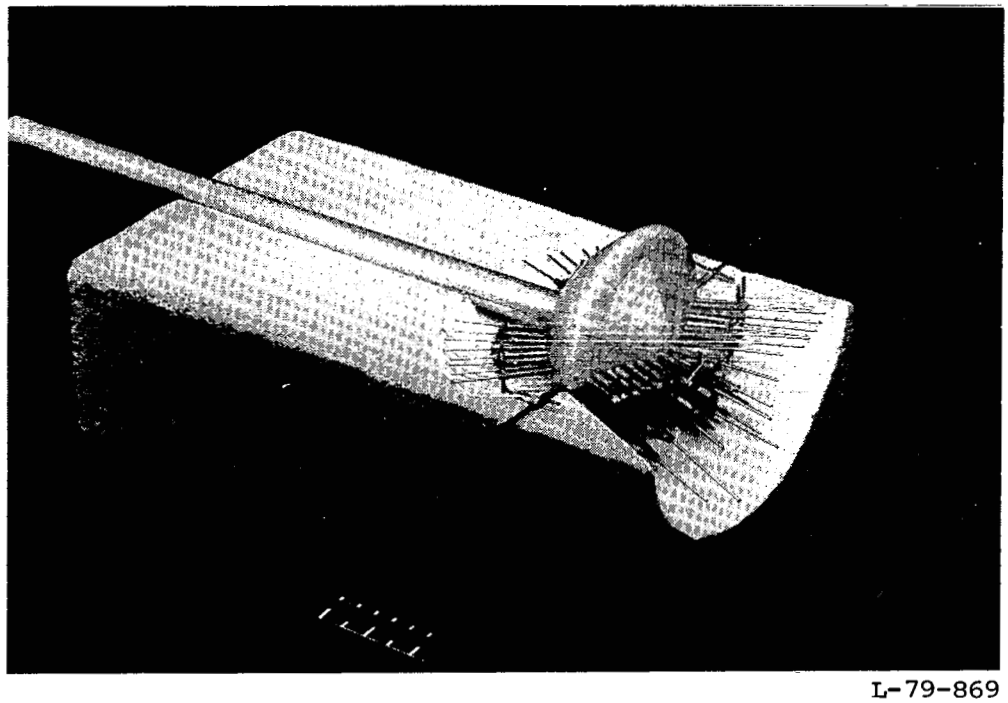

L-79-869

(a) Wooden pattern (model 4).

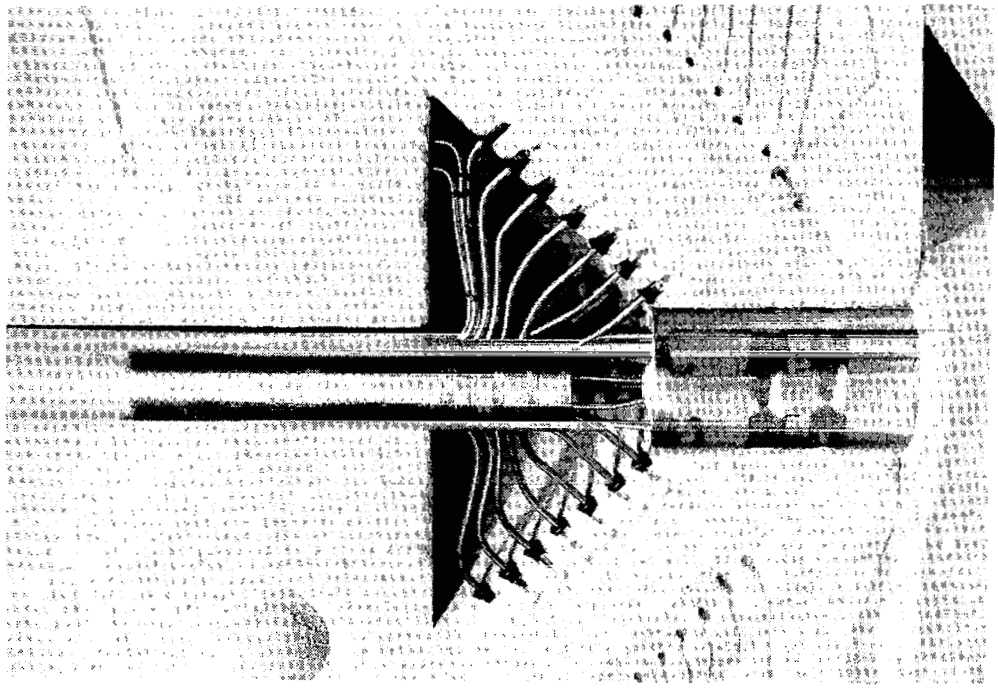

L-79-2891

(b) Sand mold (model 6).

Figure 3.- Photographs illustrating steps in casting of aluminum pressure models.

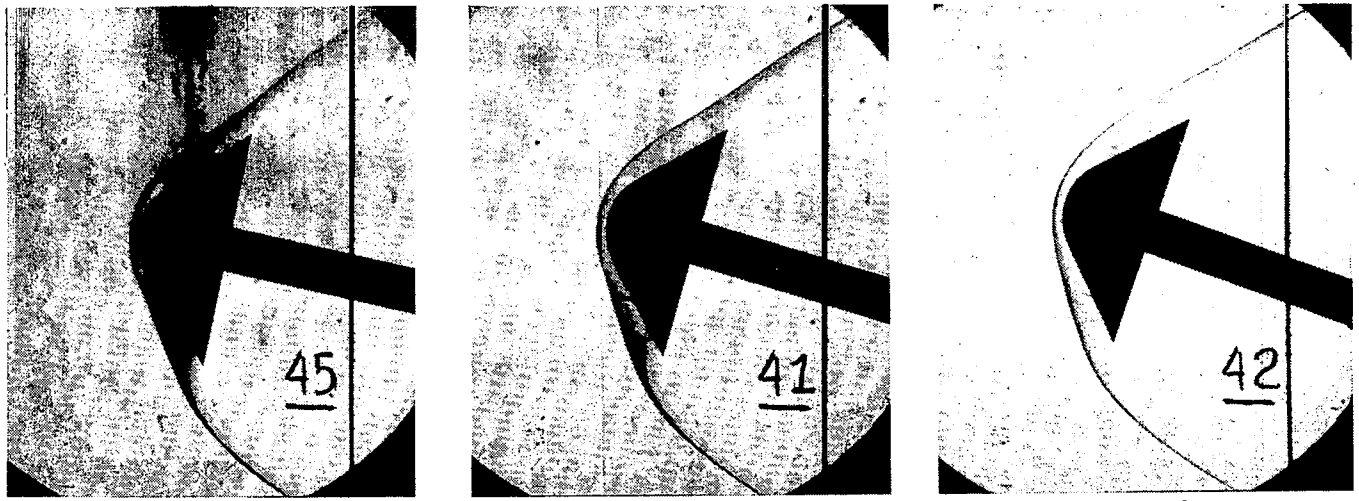

$\alpha = 12^{\circ}$ $\alpha = 16^{\circ}$ $\alpha = 20^{\circ}$

(a) Spherical-nose cone (model 5).

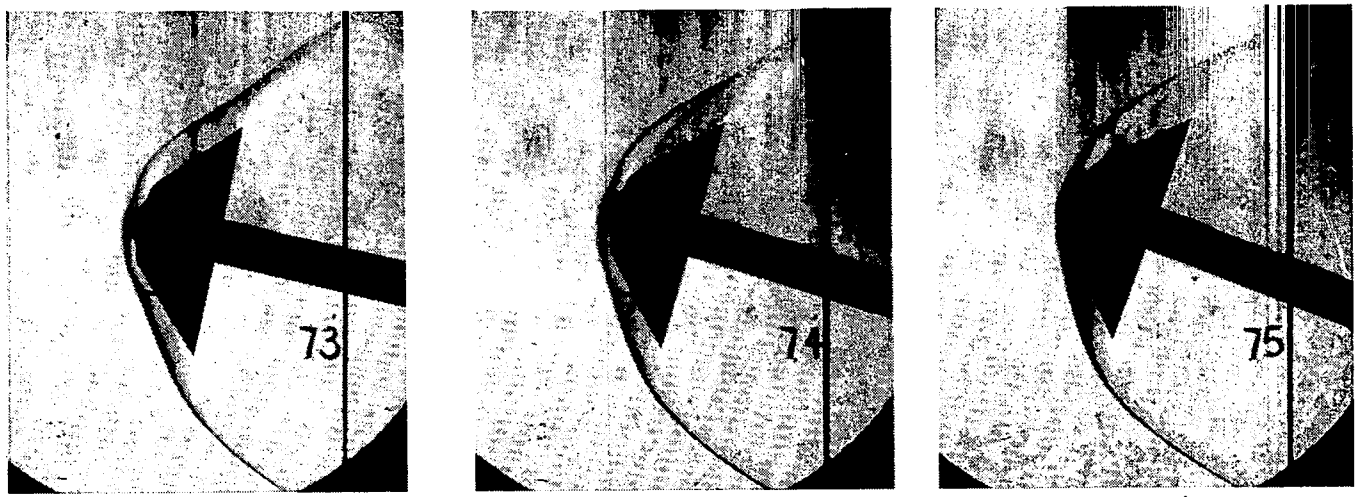

$\alpha = 12^{\circ}$ $\alpha = 16^{\circ}$ $\alpha = 20^{\circ}$

L-82-158

(b) Cusp-nose cone (model 8).

Figure 4.- Representative schlieren photographs for the spherical-nose cone (model 5) and cusp-nose cone (model 8) in Mach 5.92 air.

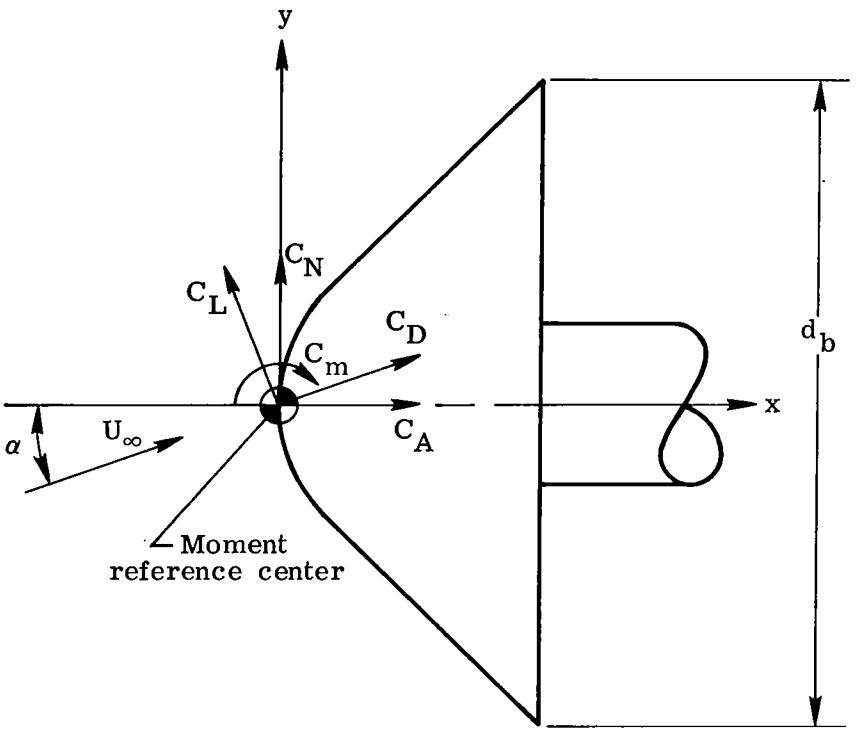

Figure 5.- Sketch illustrating location of the moment reference center for this study.

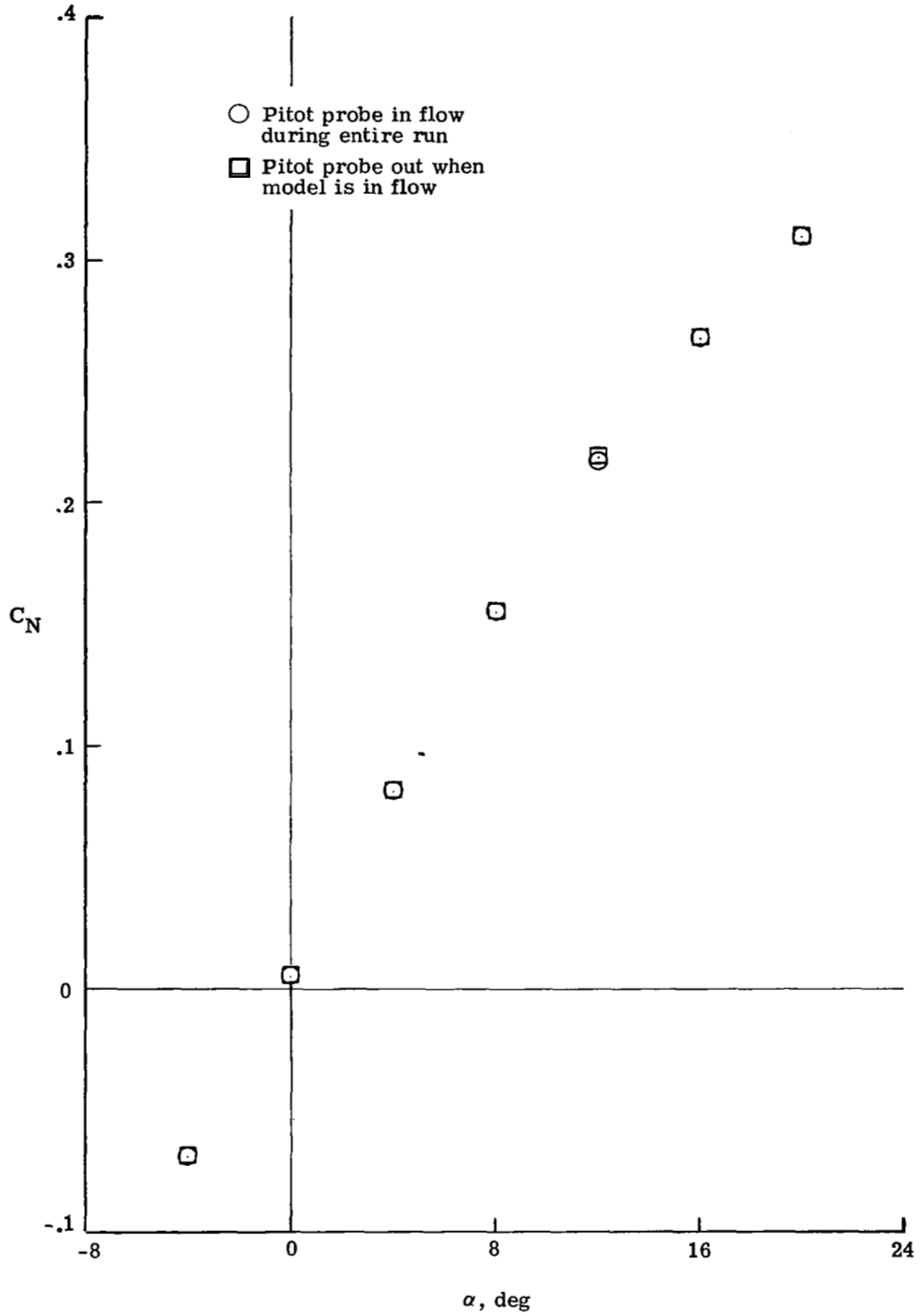

(a) Normal-force coefficient, model 5.

Figure 6.- Effect of the presence of a pitot-pressure probe on measured aerodynamic coefficients for models 5 and 7 in the Mach 6 tunnel.

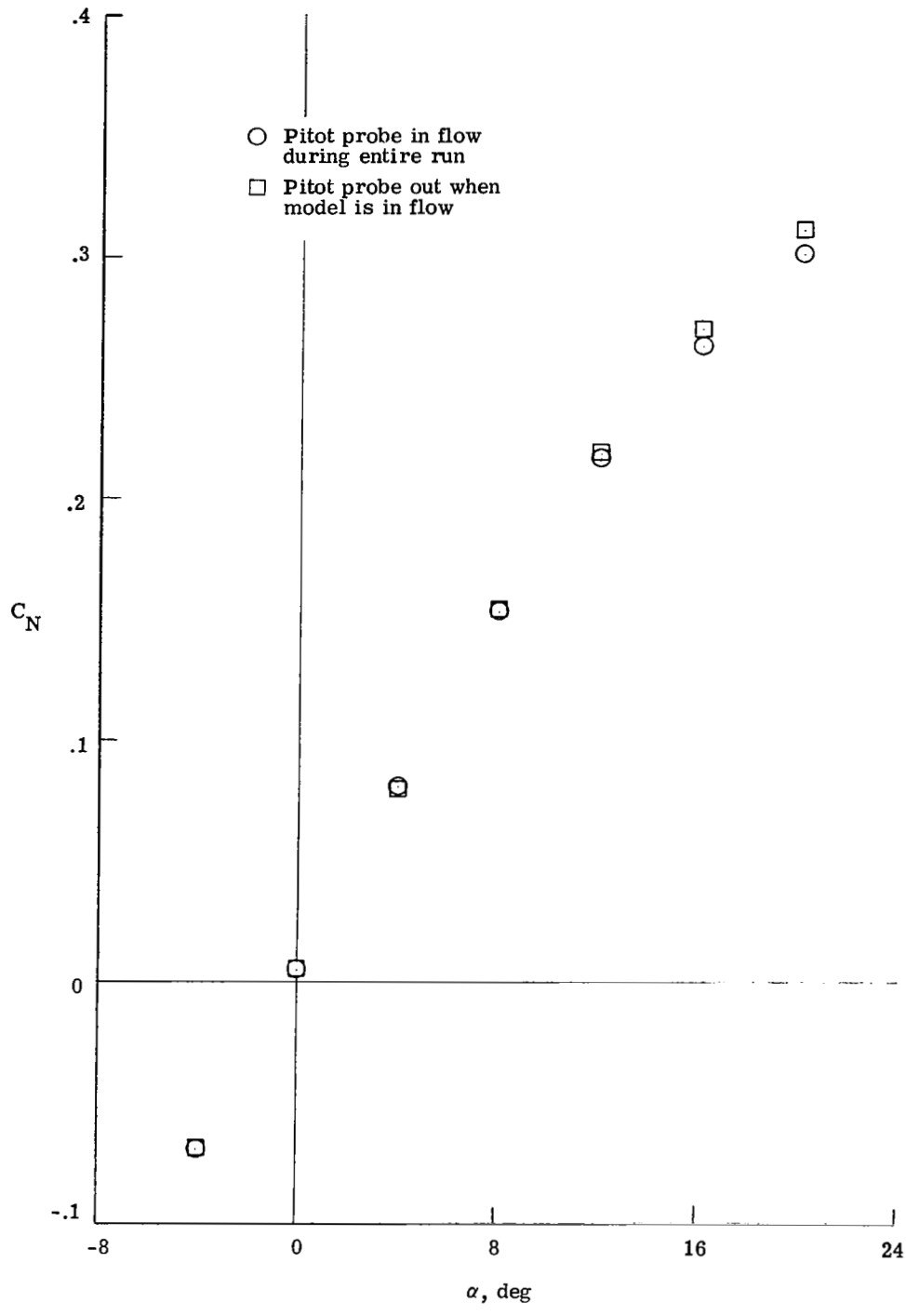

(b) Normal-force coefficient, model 7.

Figure 6.- Continued.

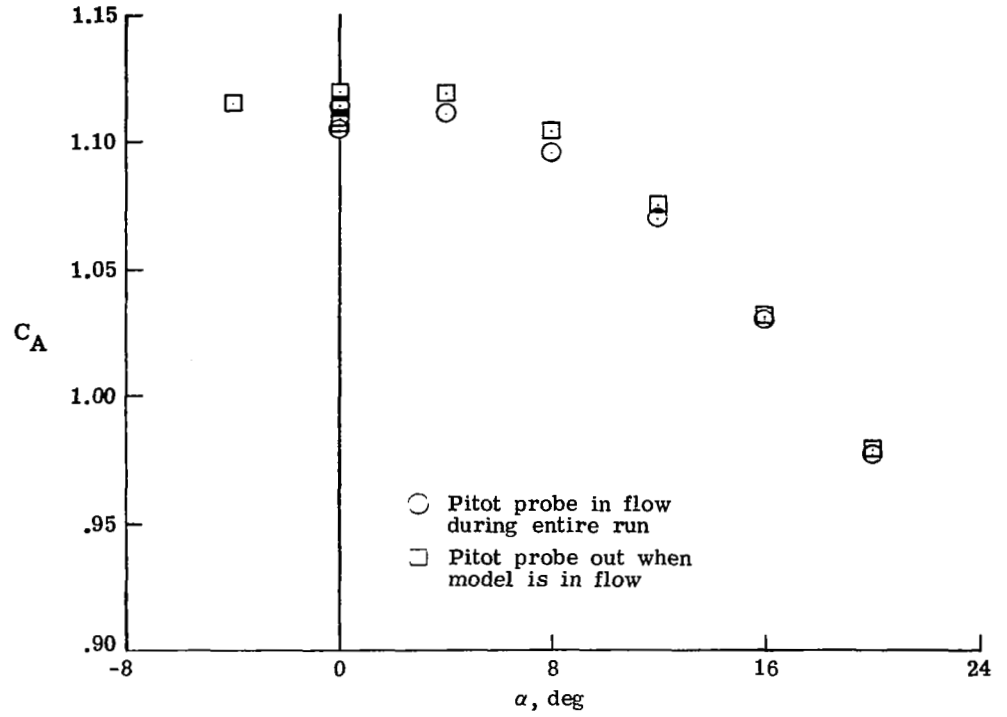

(c) Axial-force coefficient, model 5.

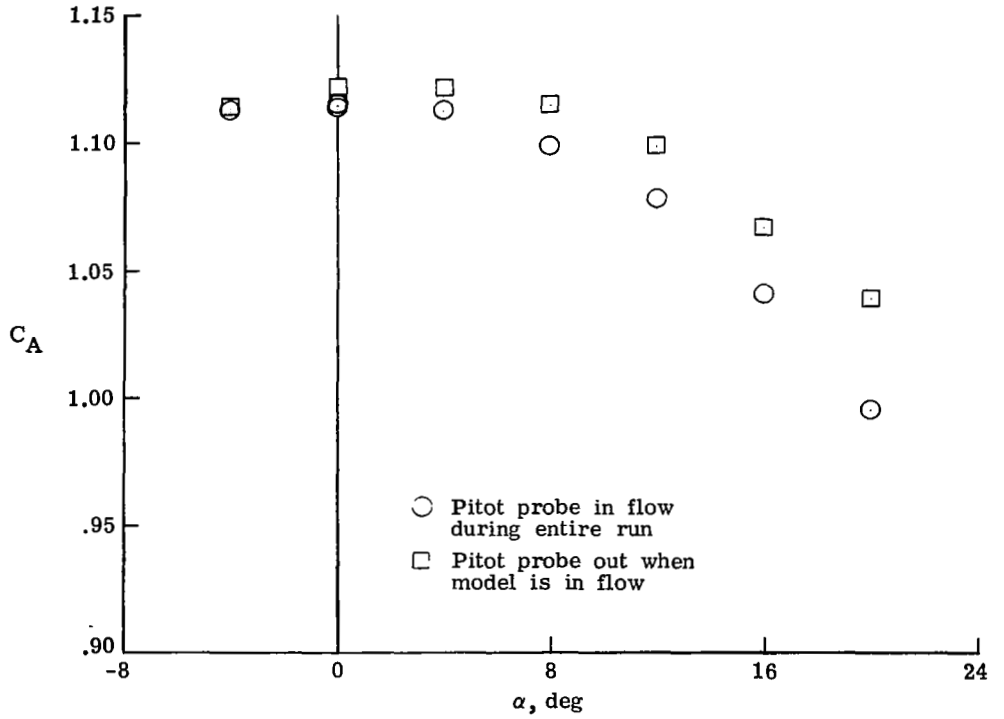

(d) Axial-force coefficient, model 7.

Figure 6.- Continued.

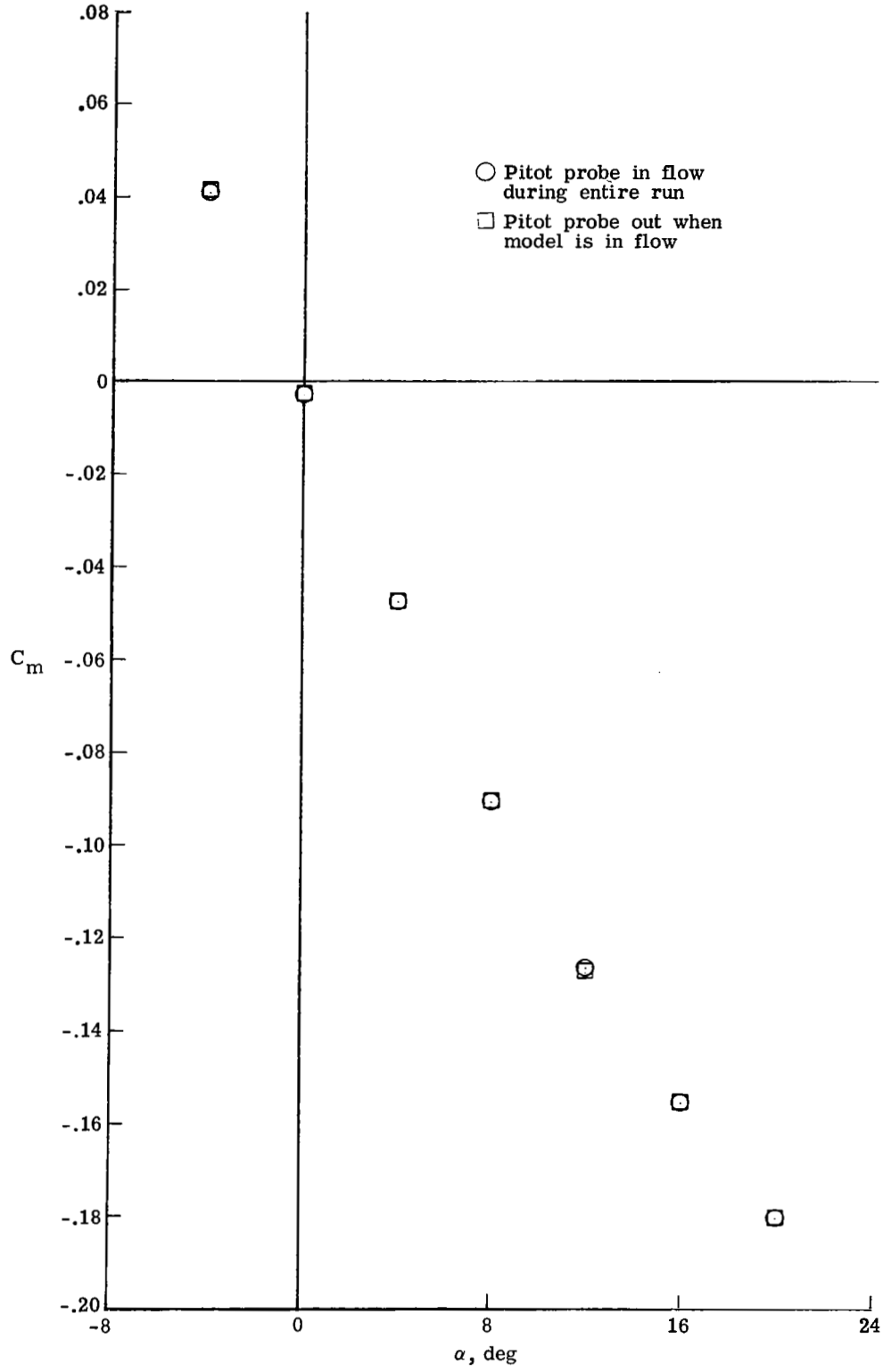

(e) Pitching-moment coefficient, model 5.

Figure 6.- Continued.

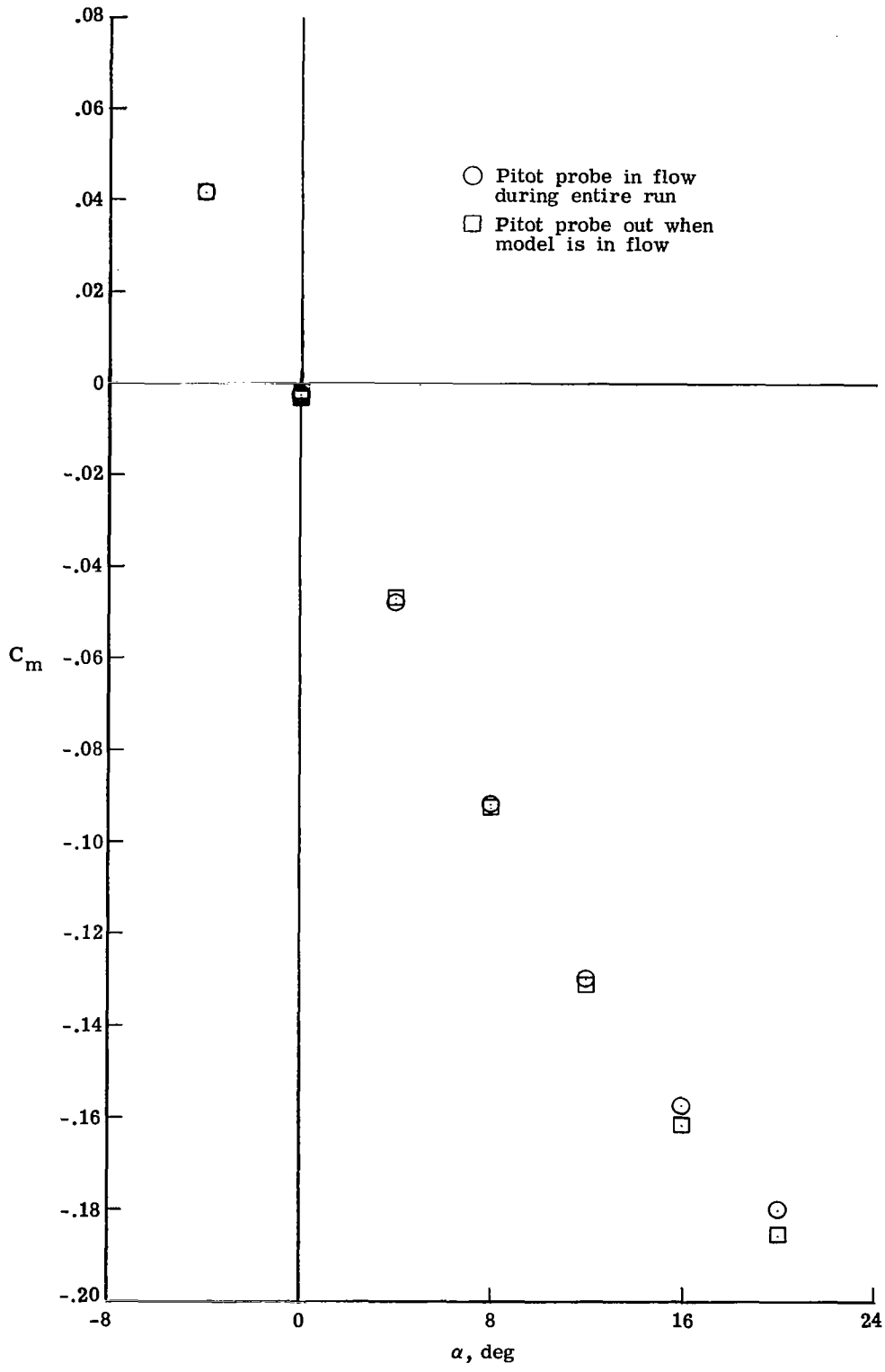

(f) Pitching-moment coefficient, model 7.

Figure 6.- Concluded.

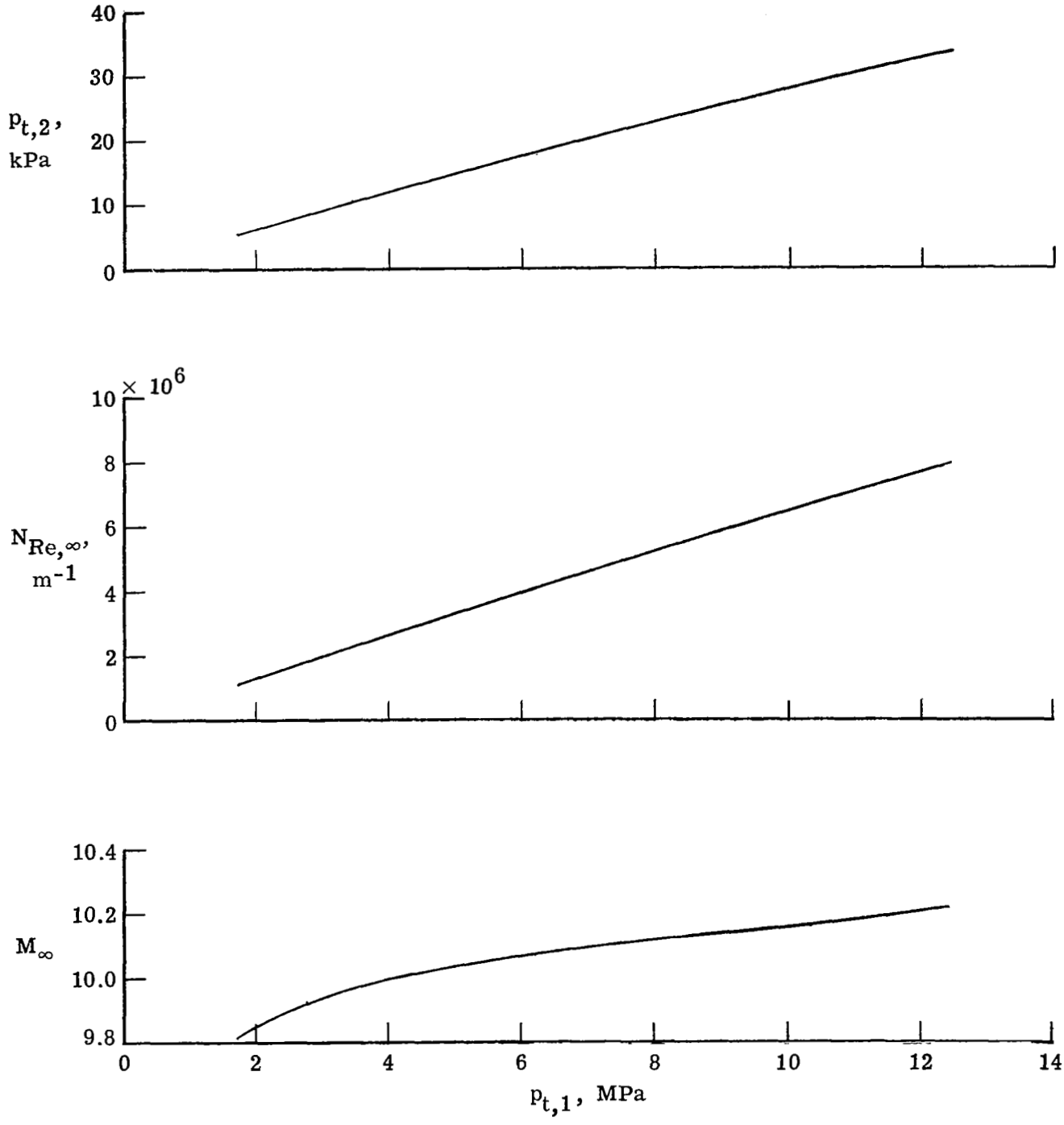

(a) Flow conditions.

Figure 7.- Calibration results for CFHT.

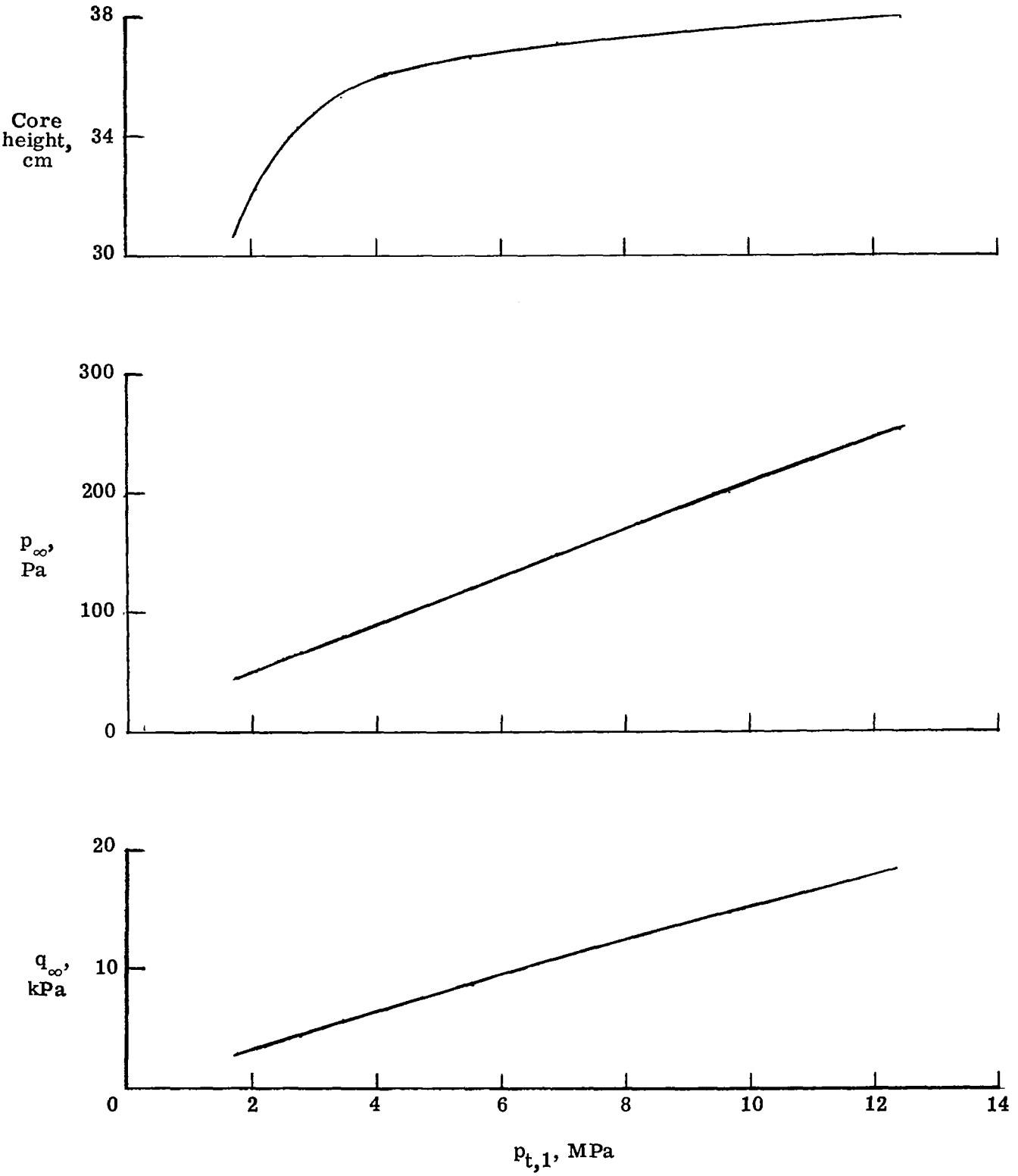

(a) Flow conditions - concluded.

Figure 7.- Continued.

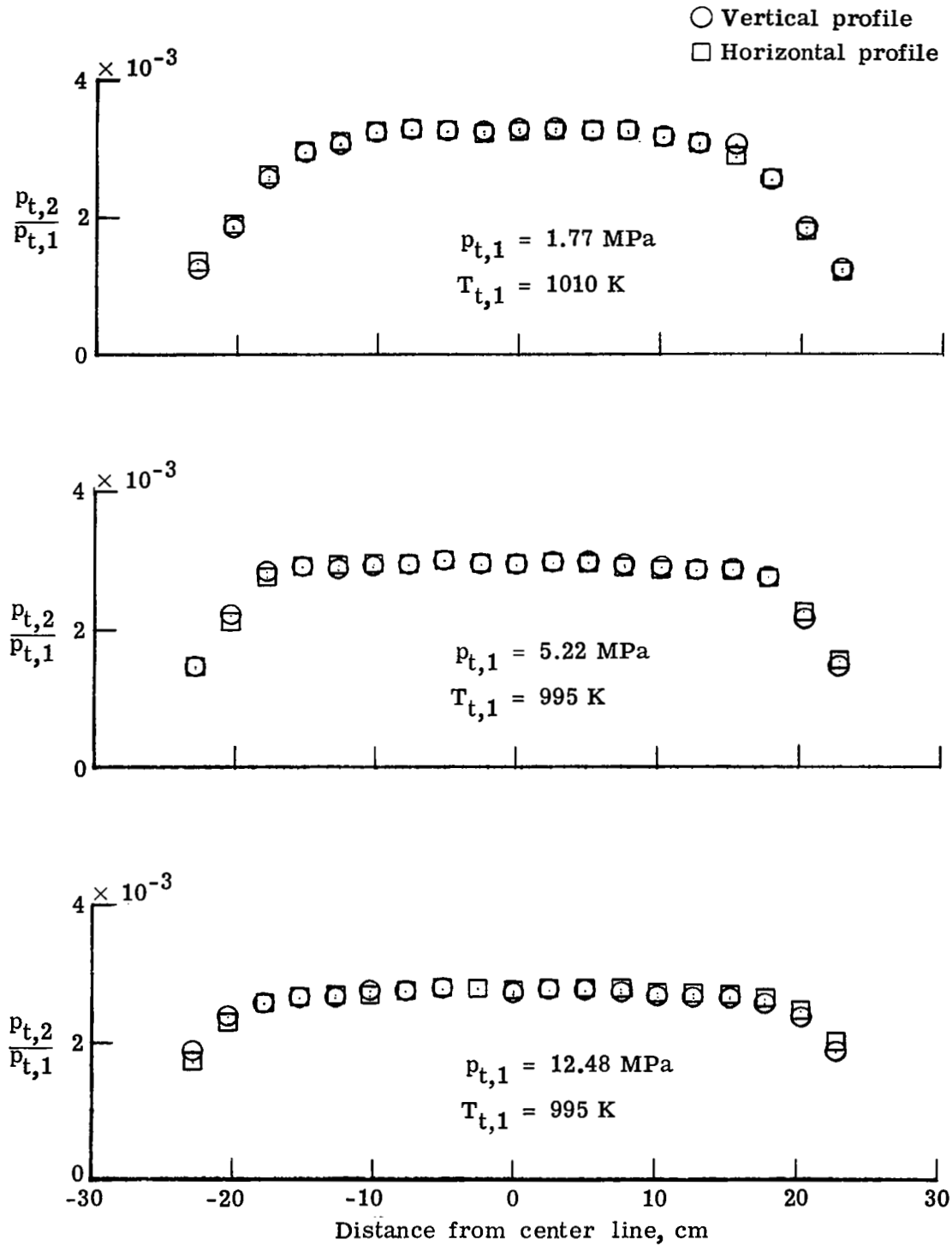

(b) Vertical and horizontal pitot-pressure surveys at an axial station equal to zero.

Figure 7.- Continued.

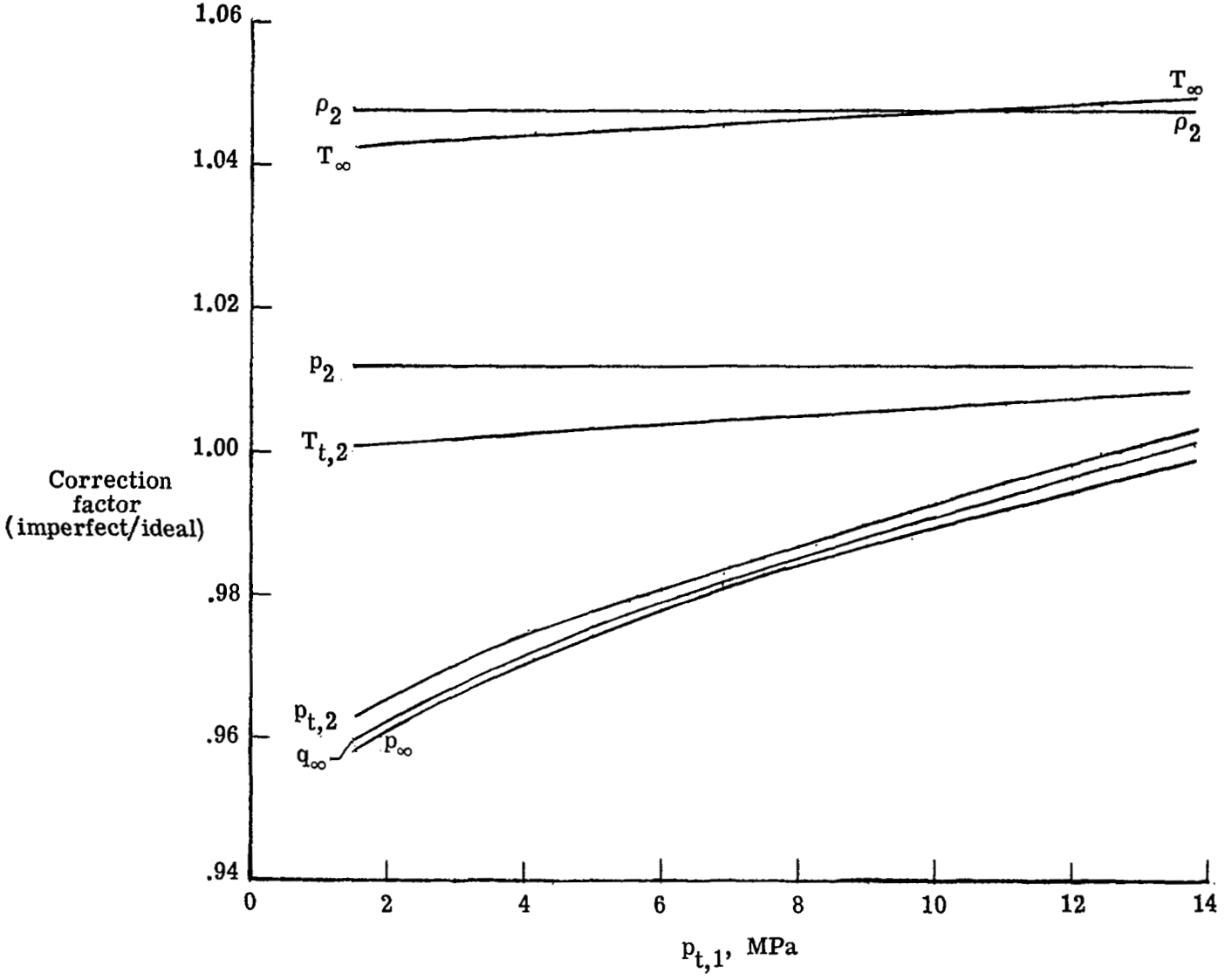

(c) Imperfect-air correction factors for $T_{t,1} = 1005$ K.

Figure 7.- Concluded.

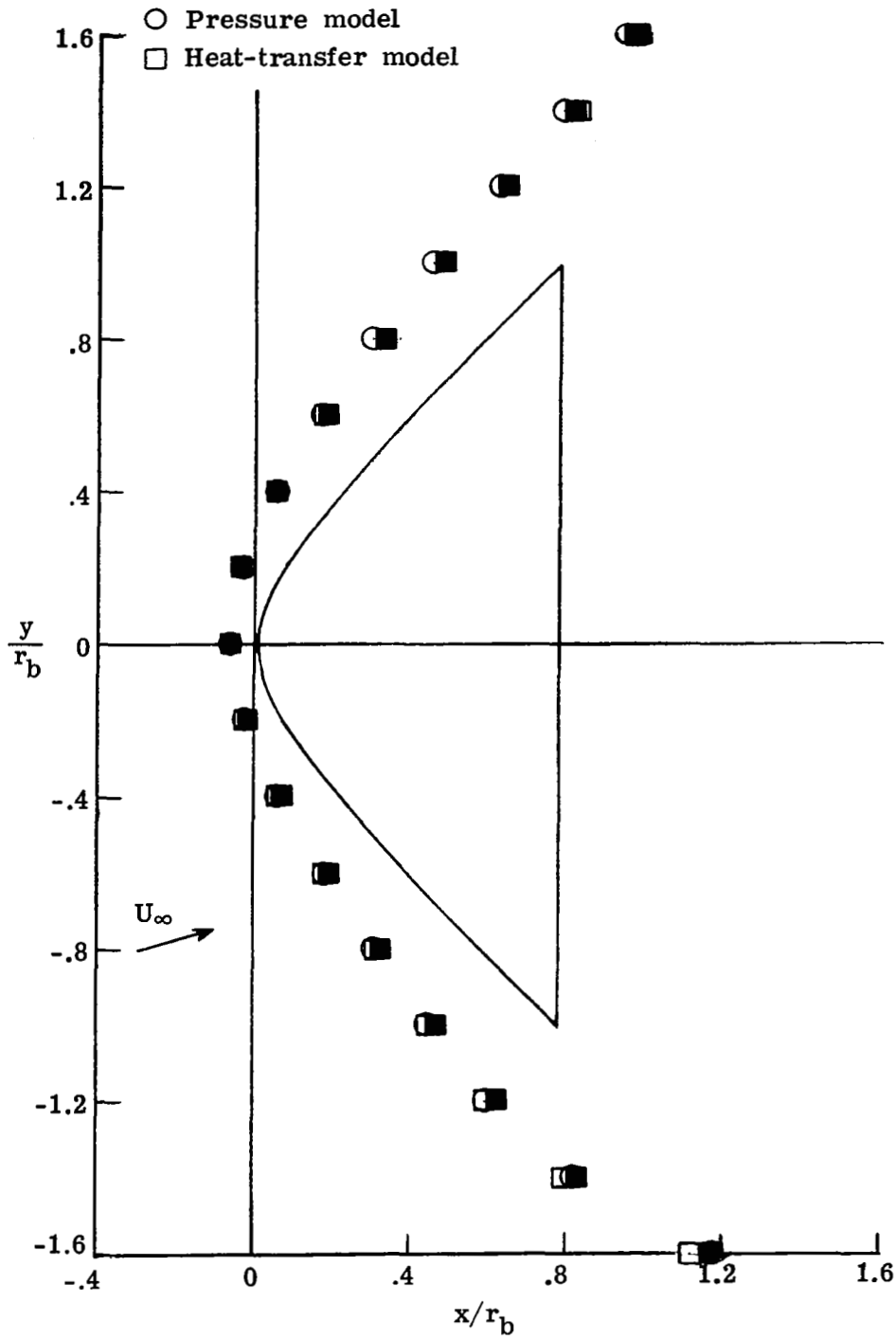

(a) Hyperboloid (model 1). $\alpha = 16°$; $M_\infty = 5.73$.

Figure 8.- Shock shapes measured on the pressure and heat-transfer hyperboloid and paraboloid (models 1 and 3, series 1) in Mach 6 air. Open symbols denote readings from prints; closed symbols denote readings made with an enlarger.

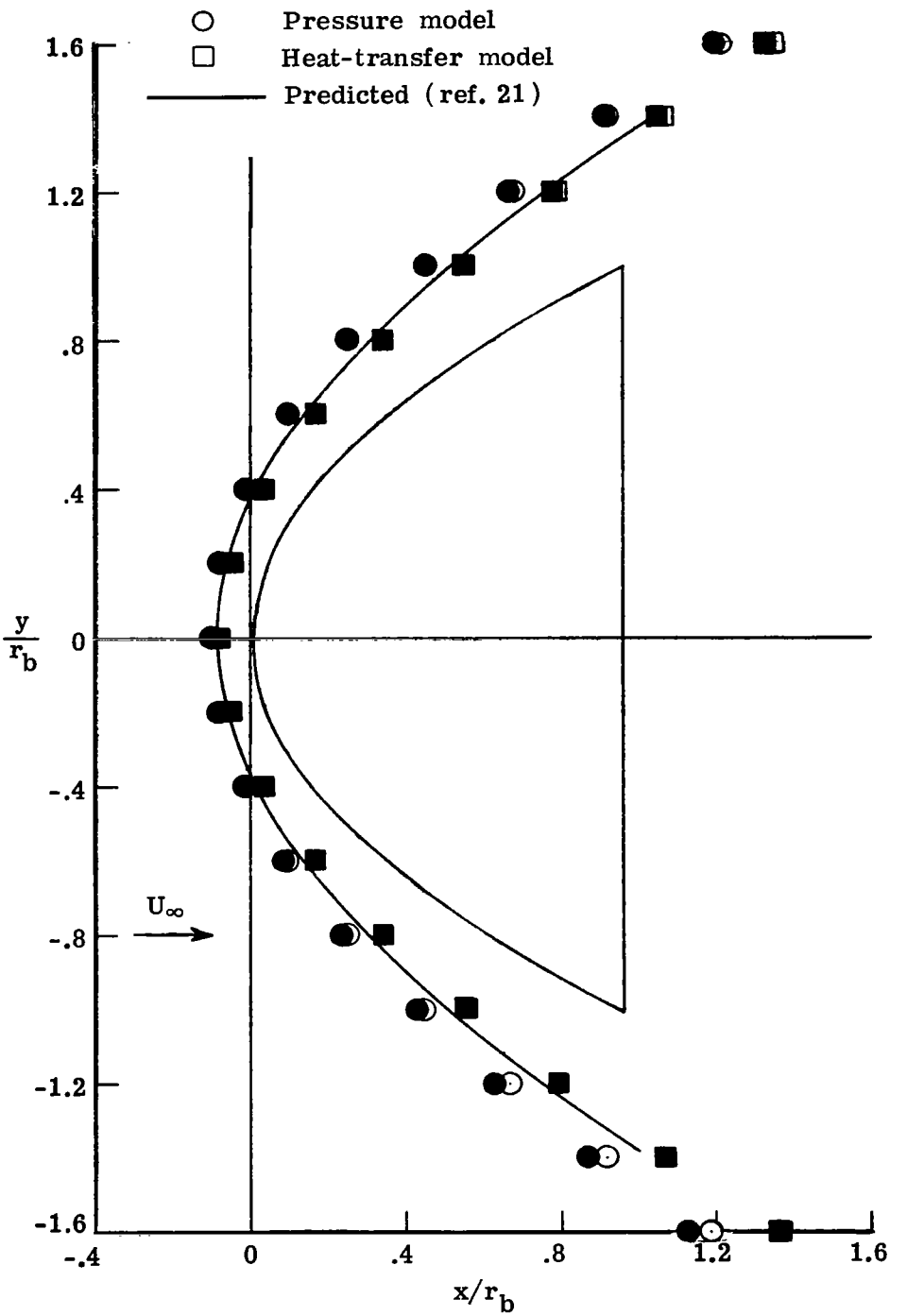

(b) Paraboloid (model 3). $\alpha = 0°$; $M_\infty = 5.73$.

Figure 8.- Continued.

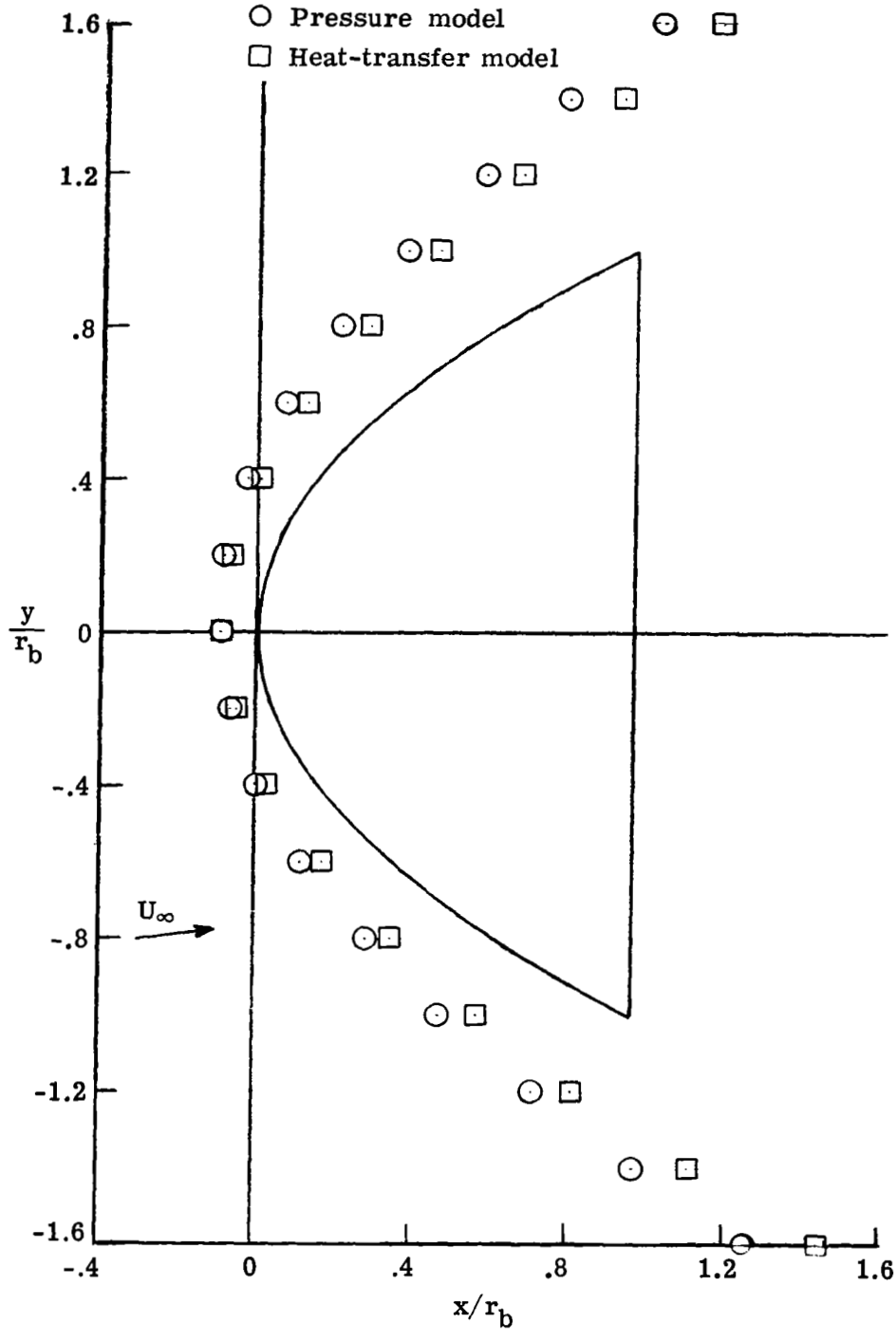

(c) Paraboloid (model 3). $\alpha = 8°$; $M_\infty = 5.73$.

Figure 8.- Concluded.

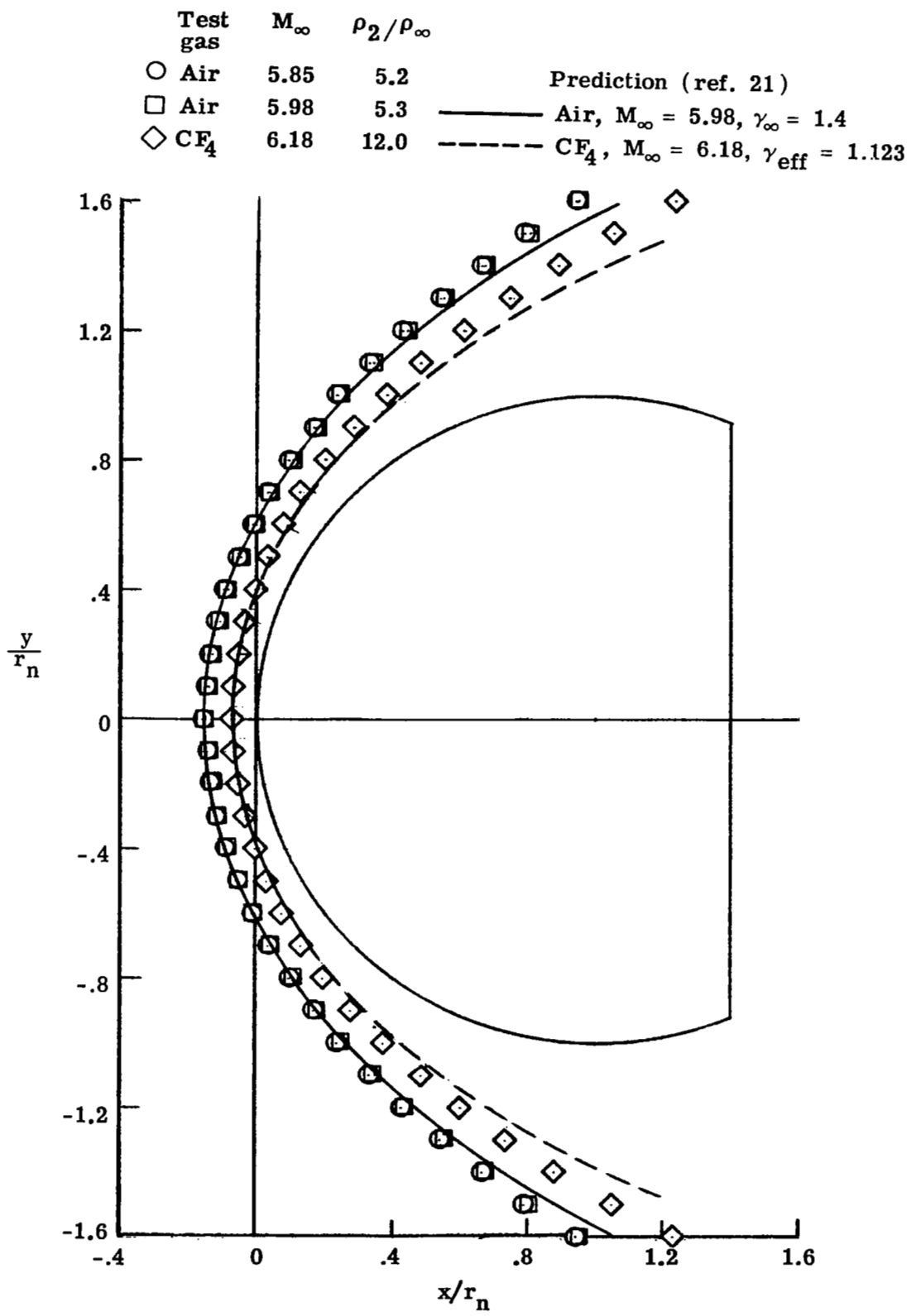

Figure 9.- Shock shapes measured on a 10.16-cm-diameter sphere in Mach 6 air and CF_4.

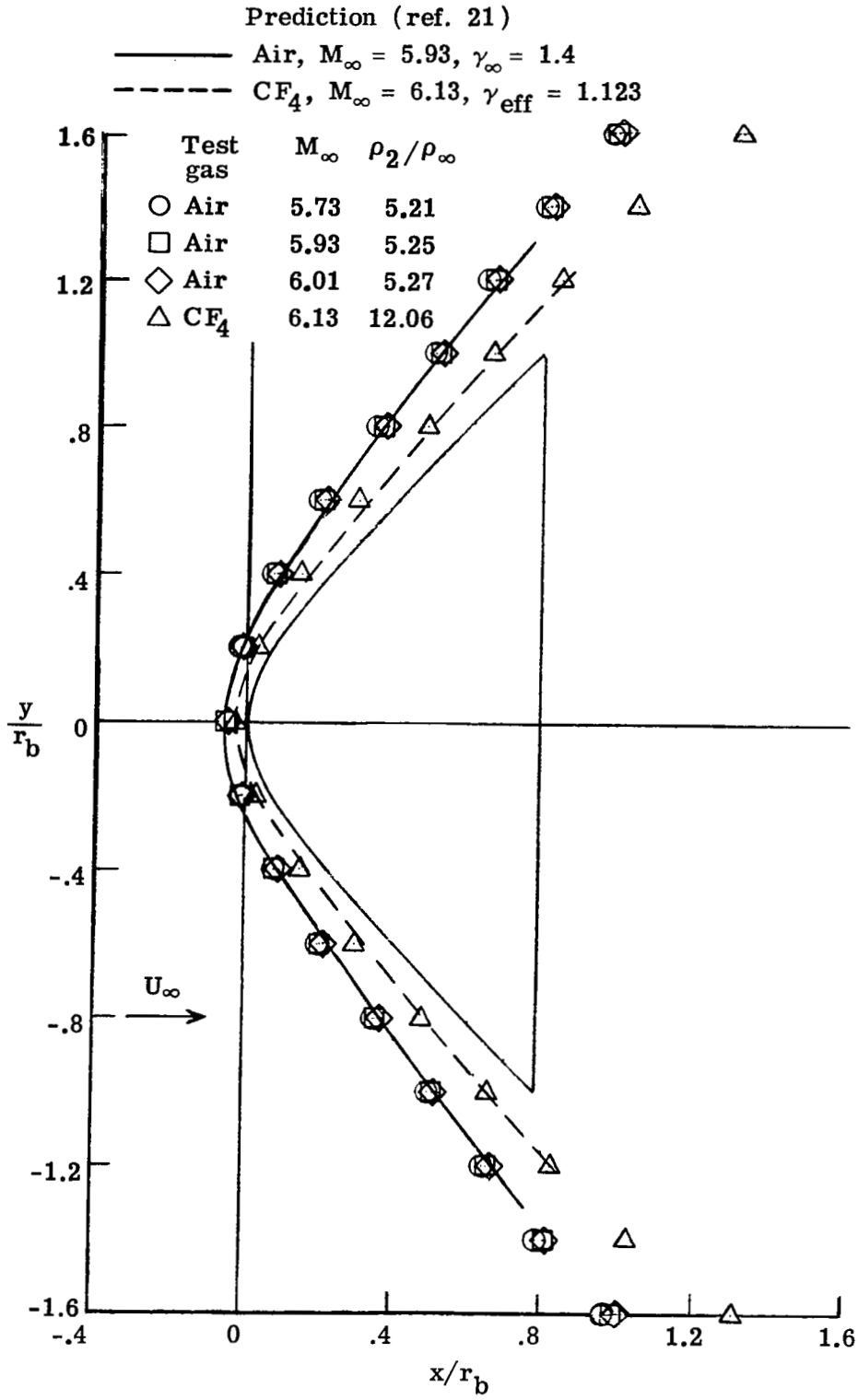

(a) $\alpha = 0°$.

Figure 10.- Shock shapes measured on the hyperboloid pressure model (model 1, series 1) in Mach 6 air and CF_4.

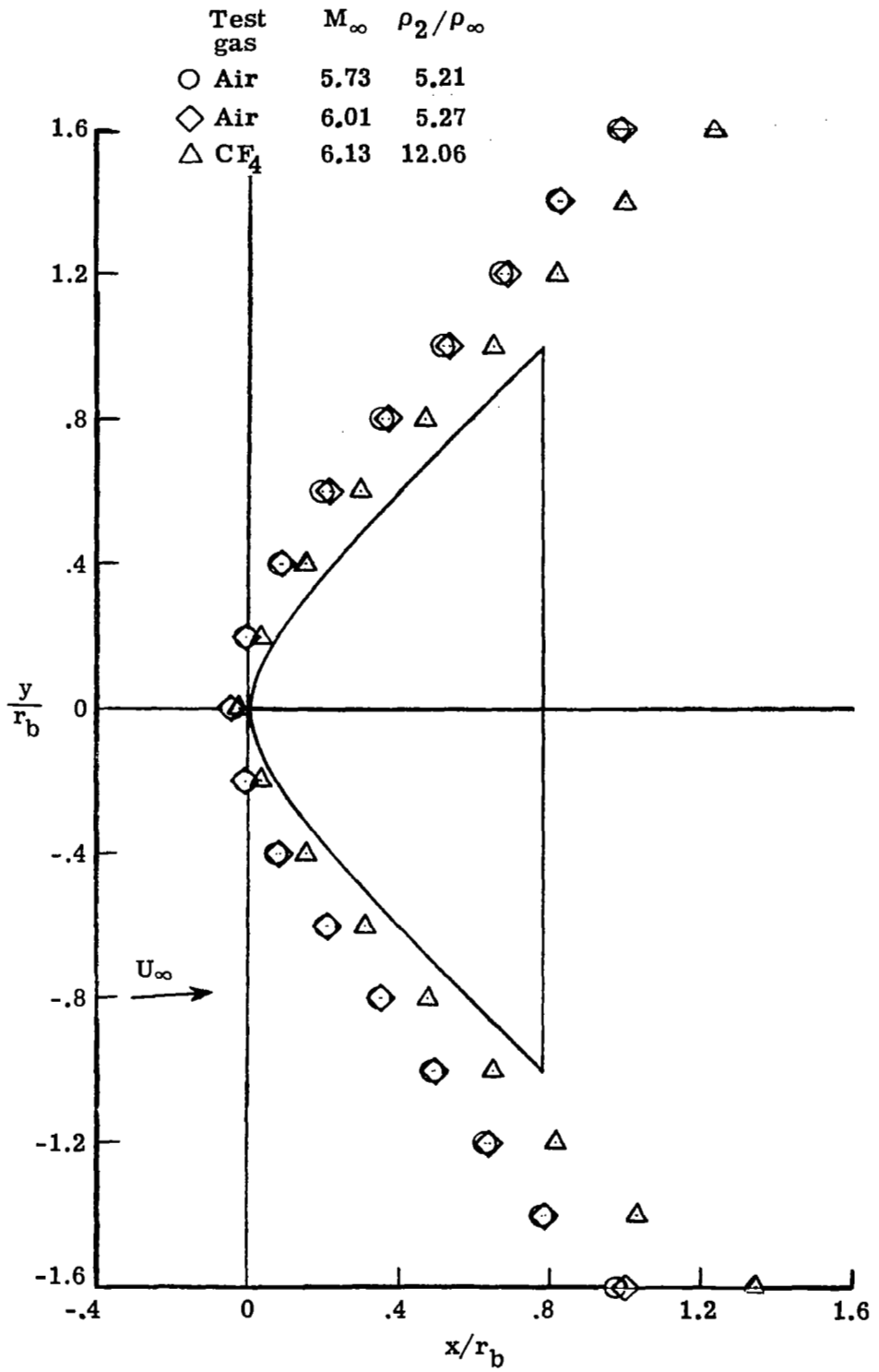

(b) $\alpha = 4°$.

Figure 10.- Continued.

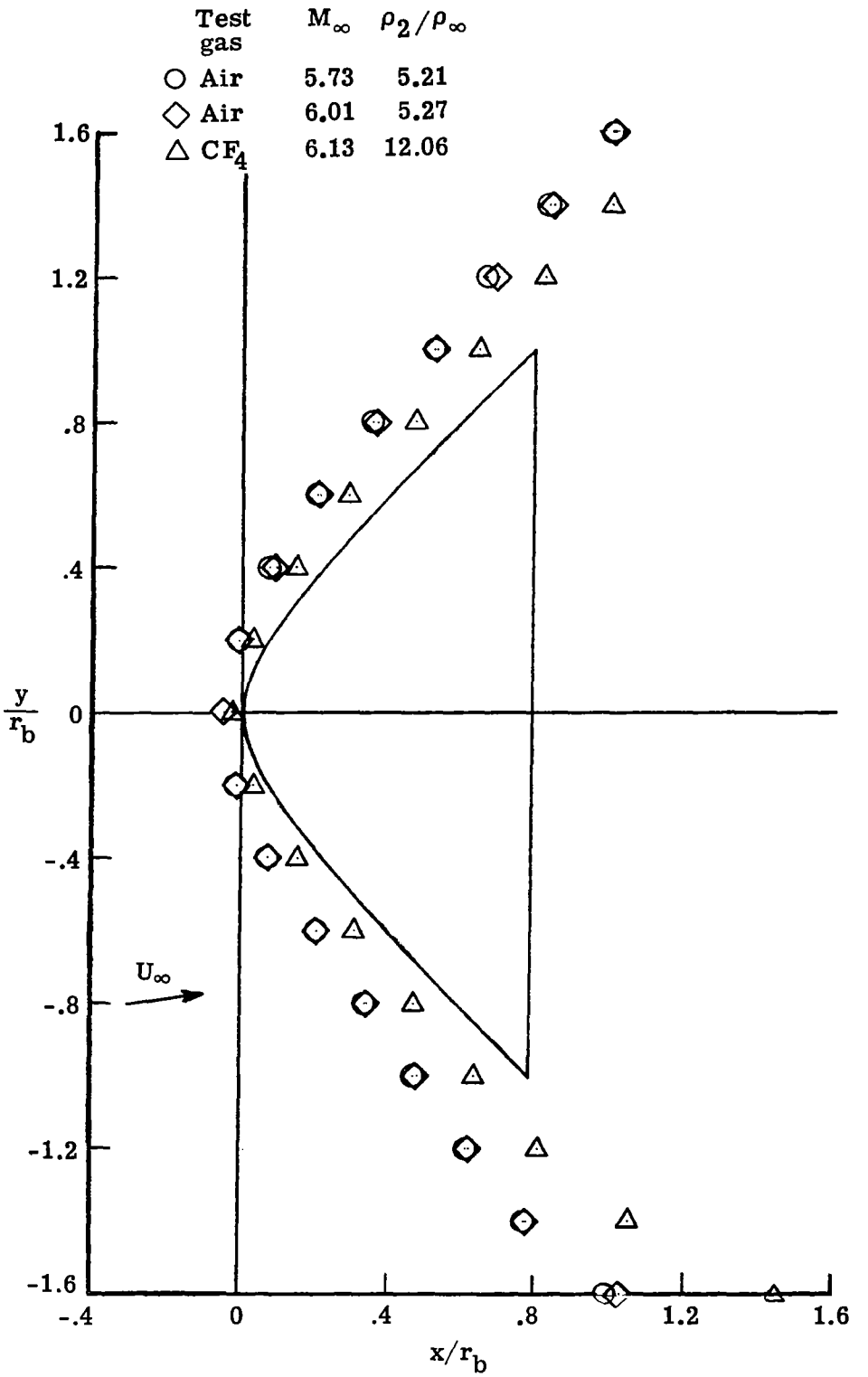

(c) $\alpha = 8°$.

Figure 10.- Continued.

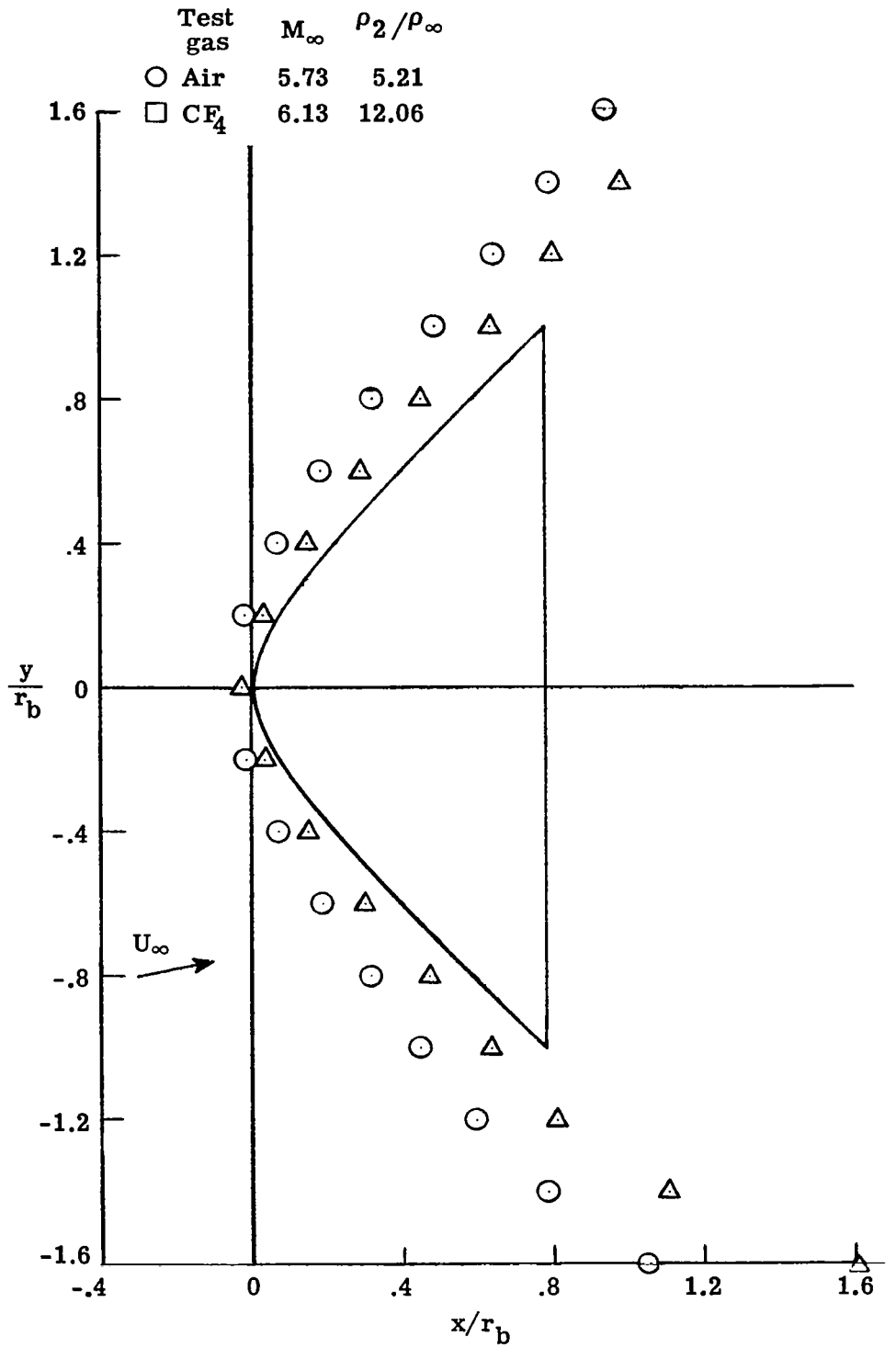

(d) $\alpha = 12°$.

Figure 10.- Continued.

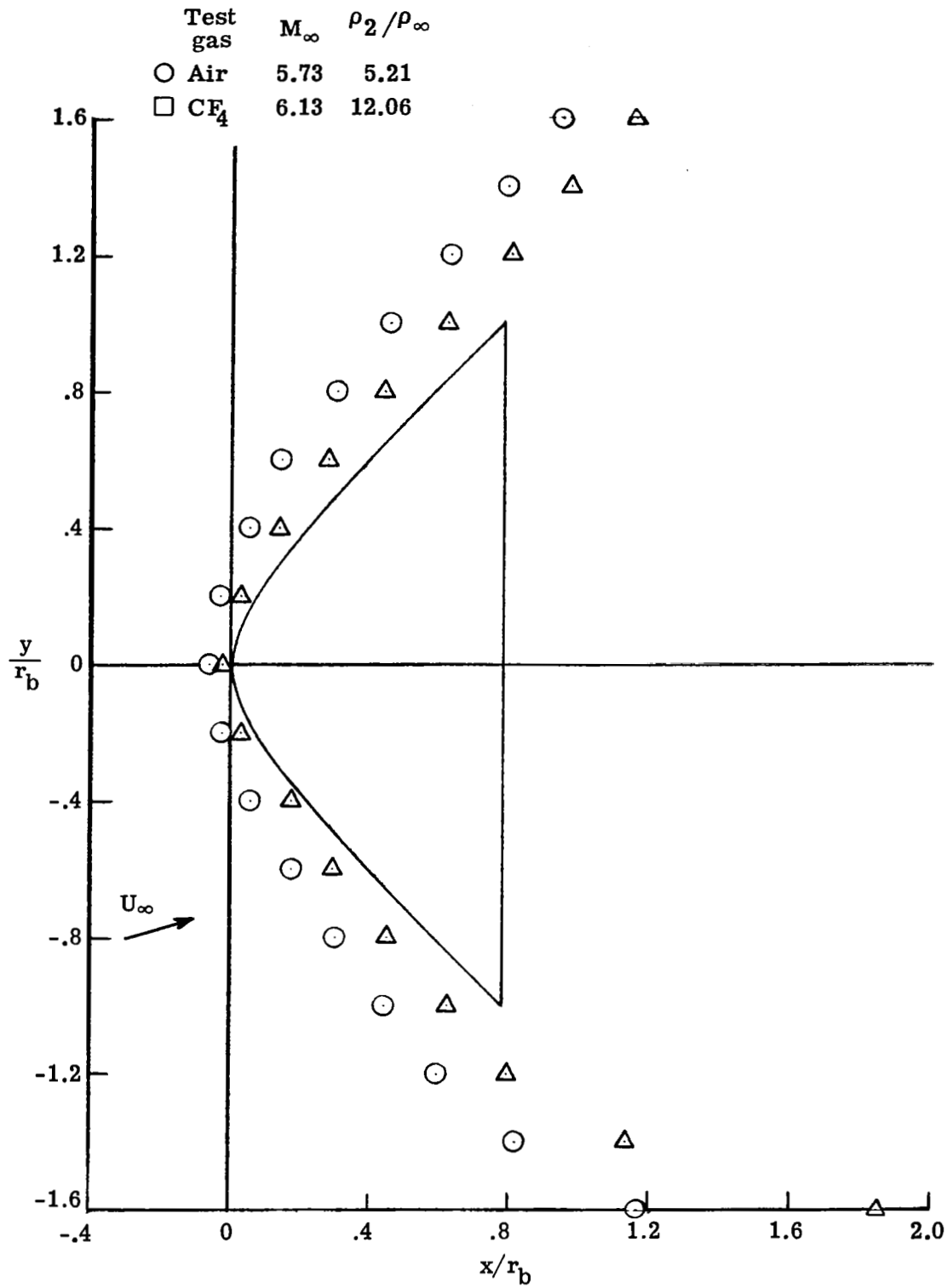

(e) $\alpha = 16°$.

Figure 10.- Continued.

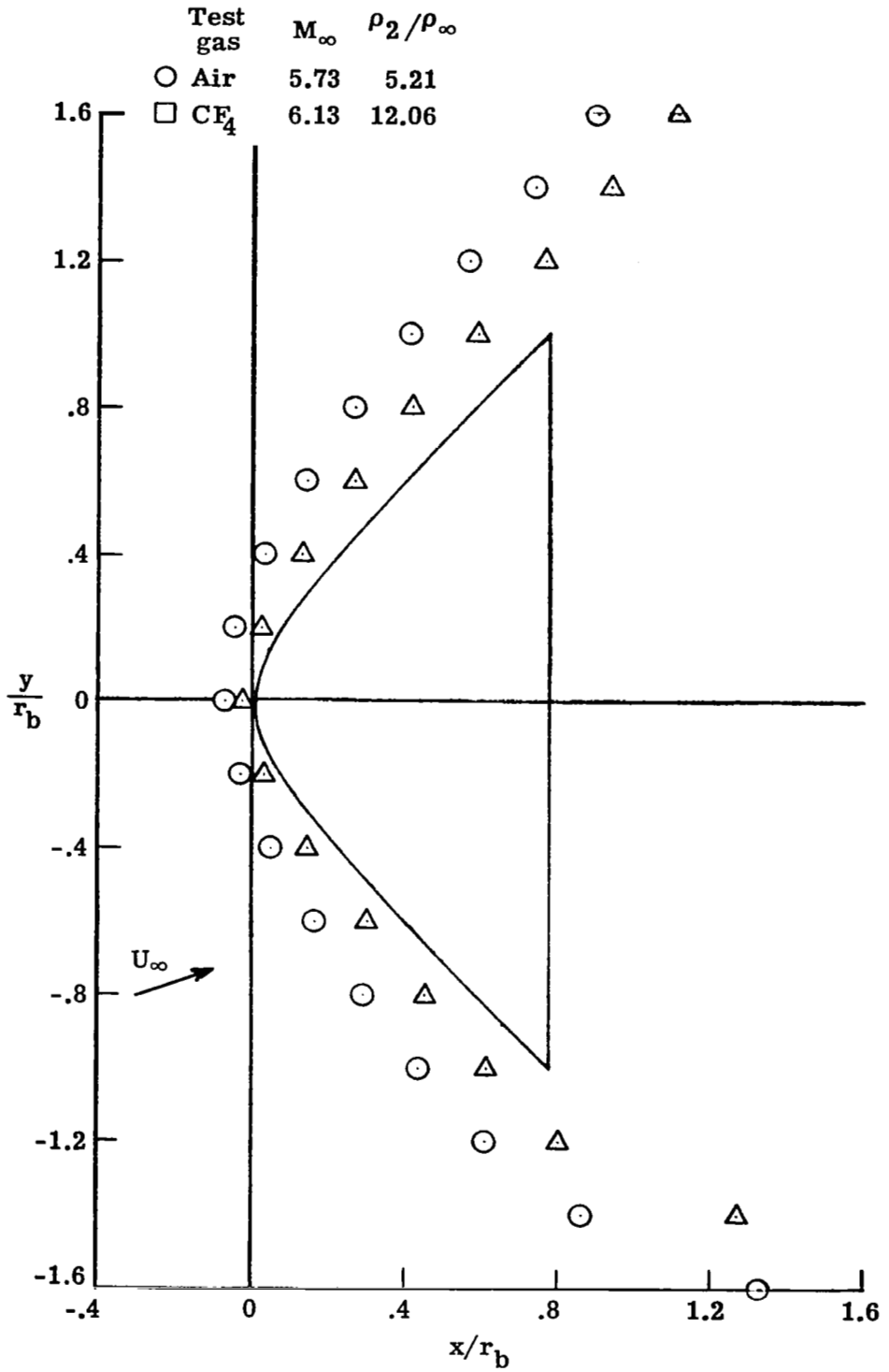

(f) $\alpha = 20°$.

Figure 10.- Concluded.

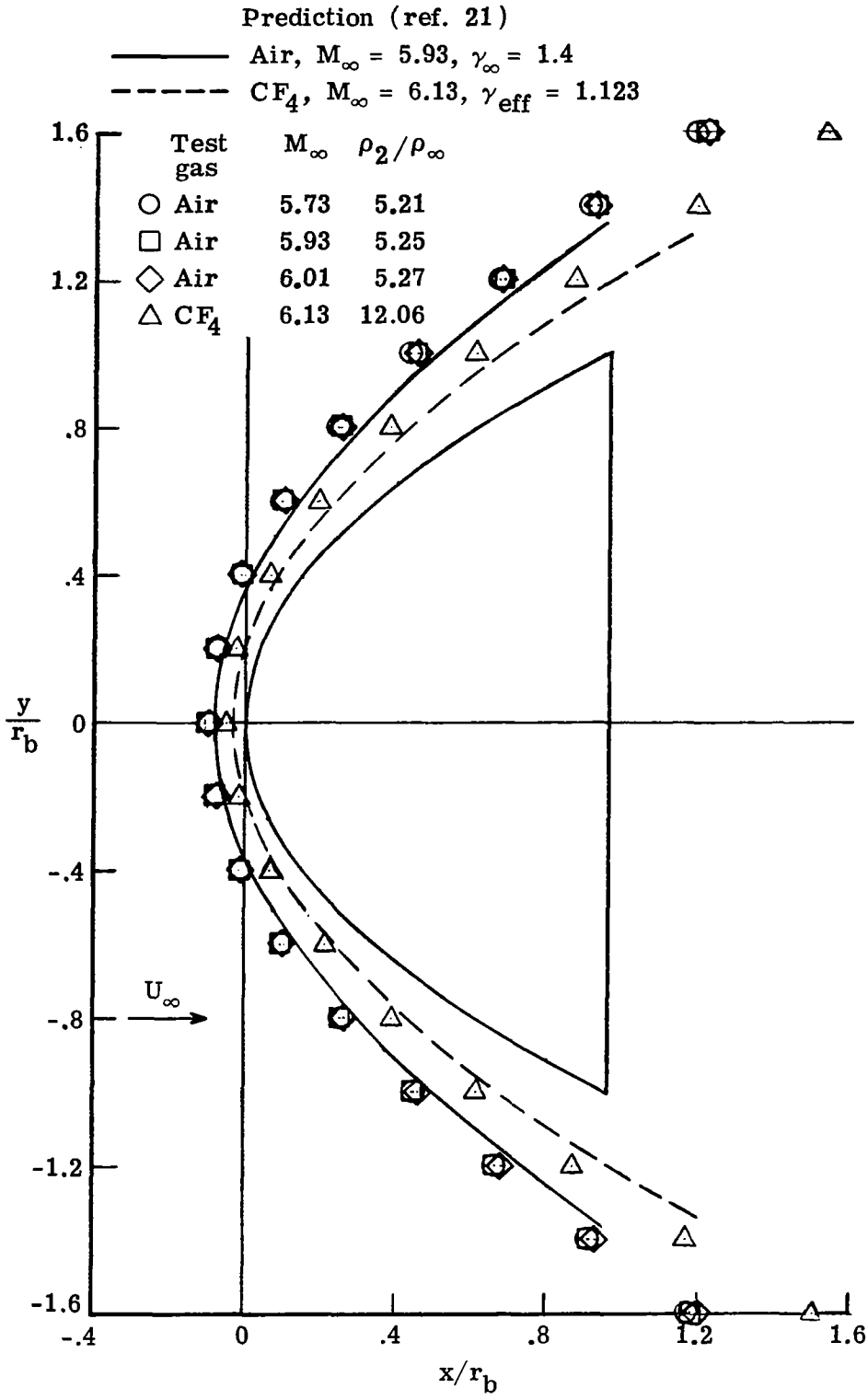

(a) $\alpha = 0°$.

Figure 11.- Shock shapes measured on the paraboloid pressure model (model 3, series 1) in Mach 6 air and CF_4.

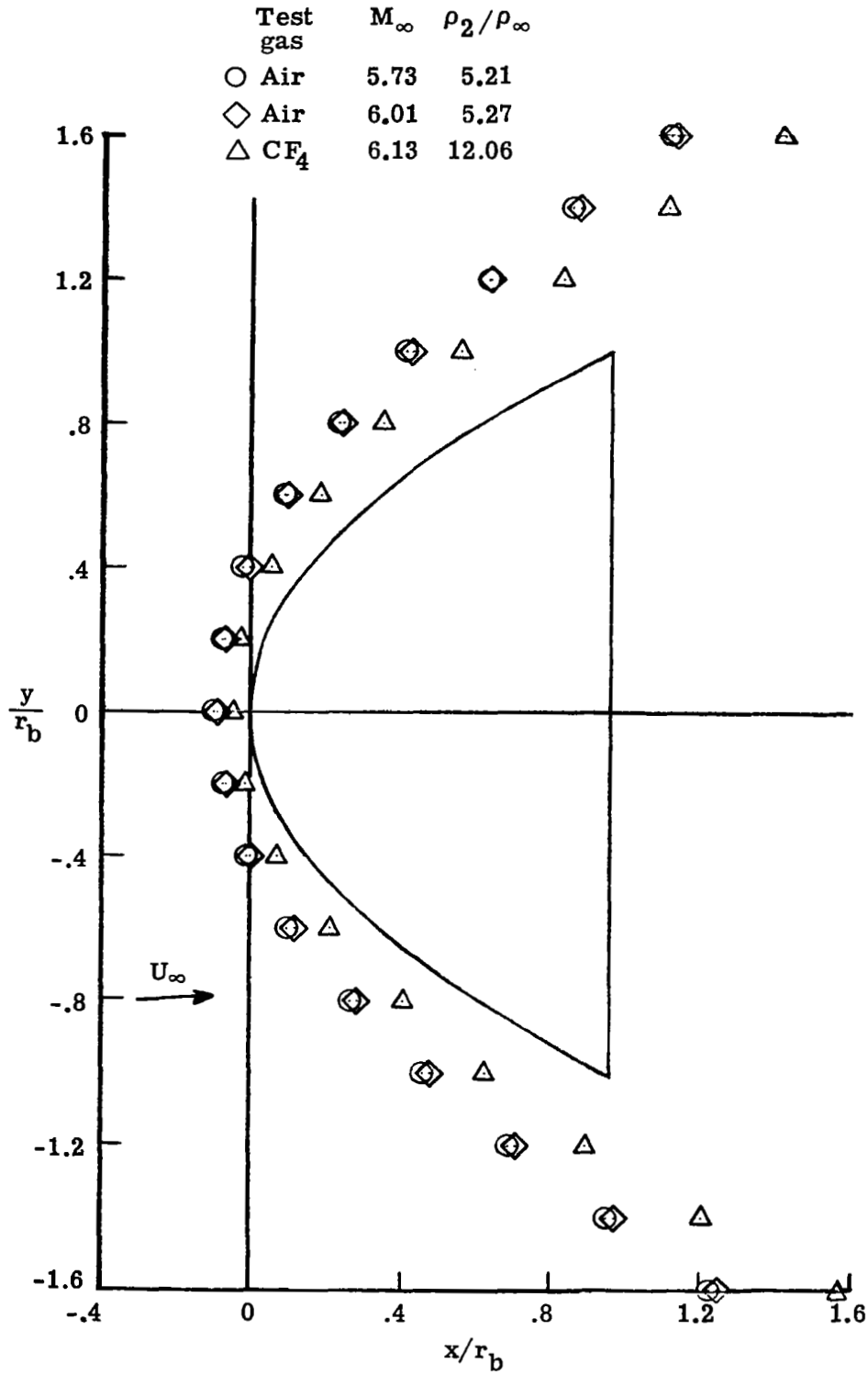

(b) $\alpha = 4°$.

Figure 11.- Continued.

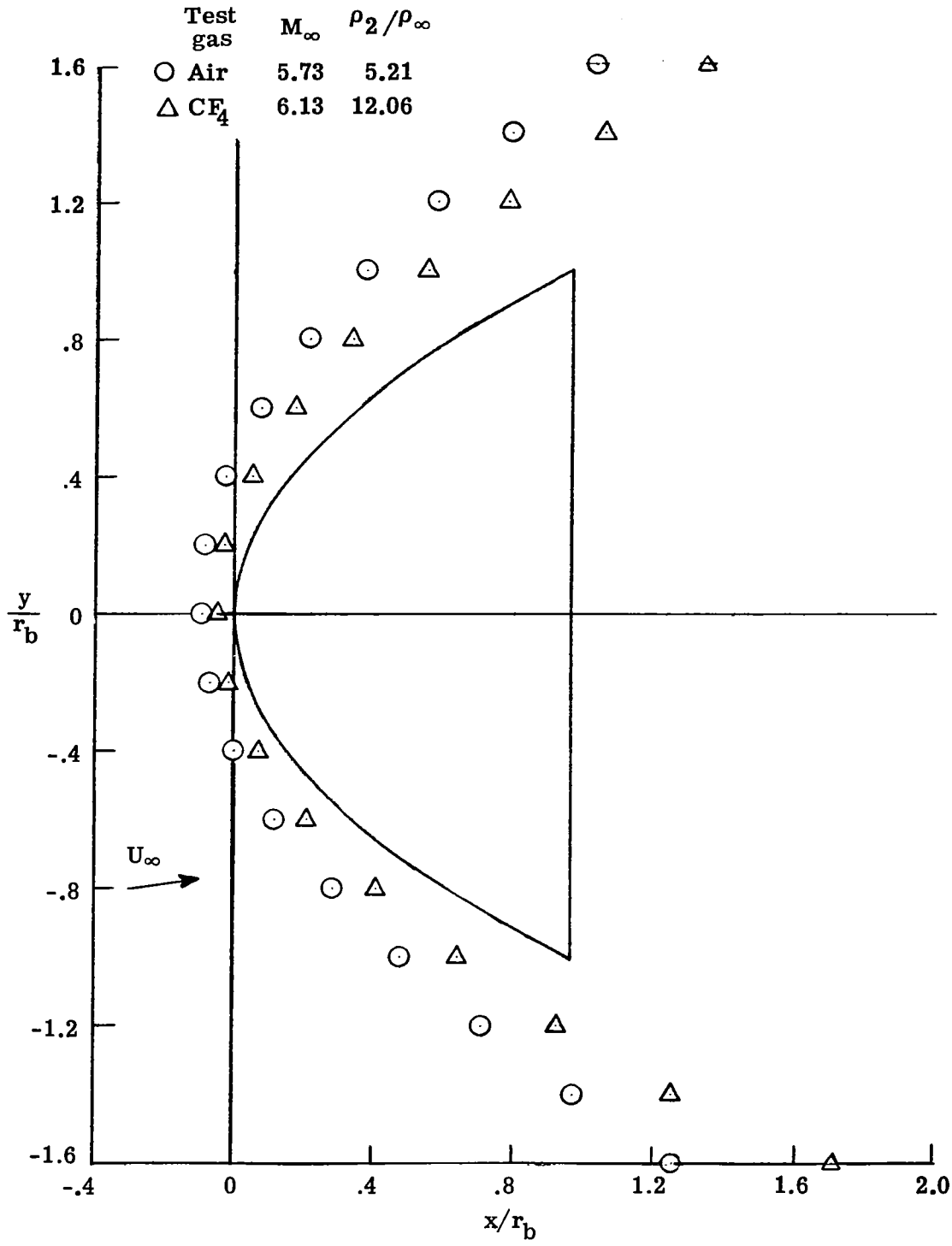

(c) $\alpha = 8°$.

Figure 11.- Continued.

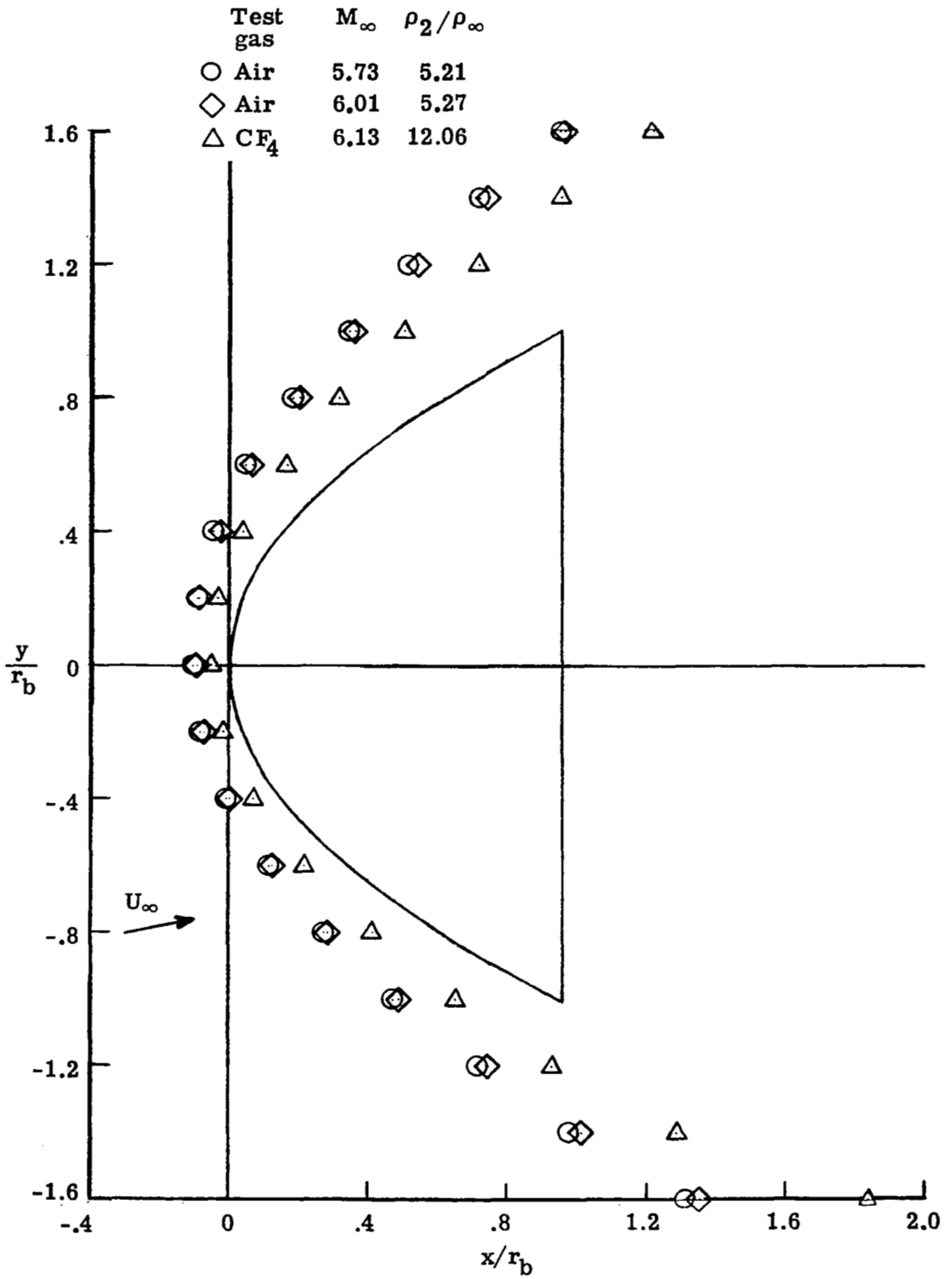

(d) $\alpha = 12°$.

Figure 11.- Continued.

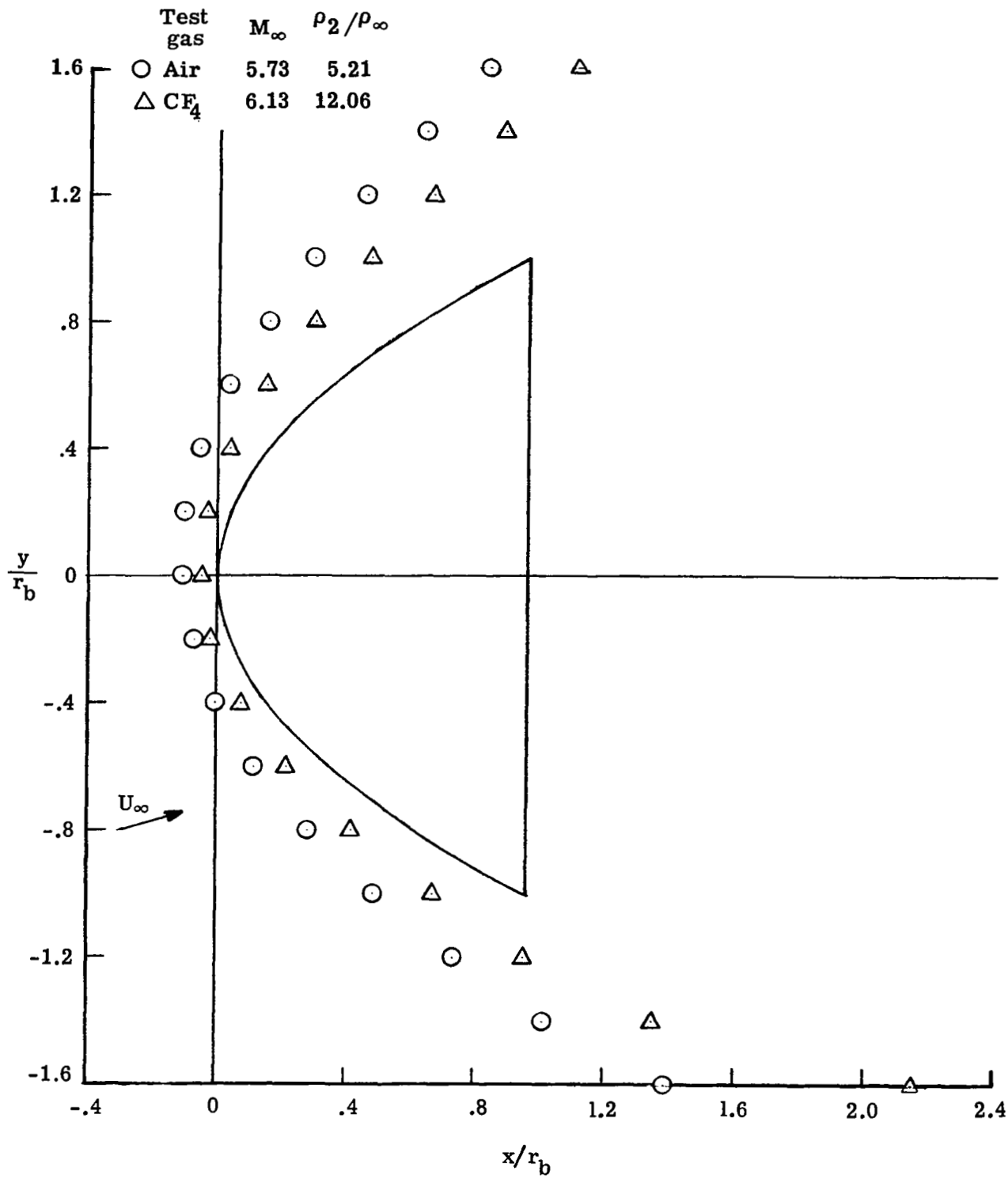

(e) $\alpha = 16°$.

Figure 11.- Continued.

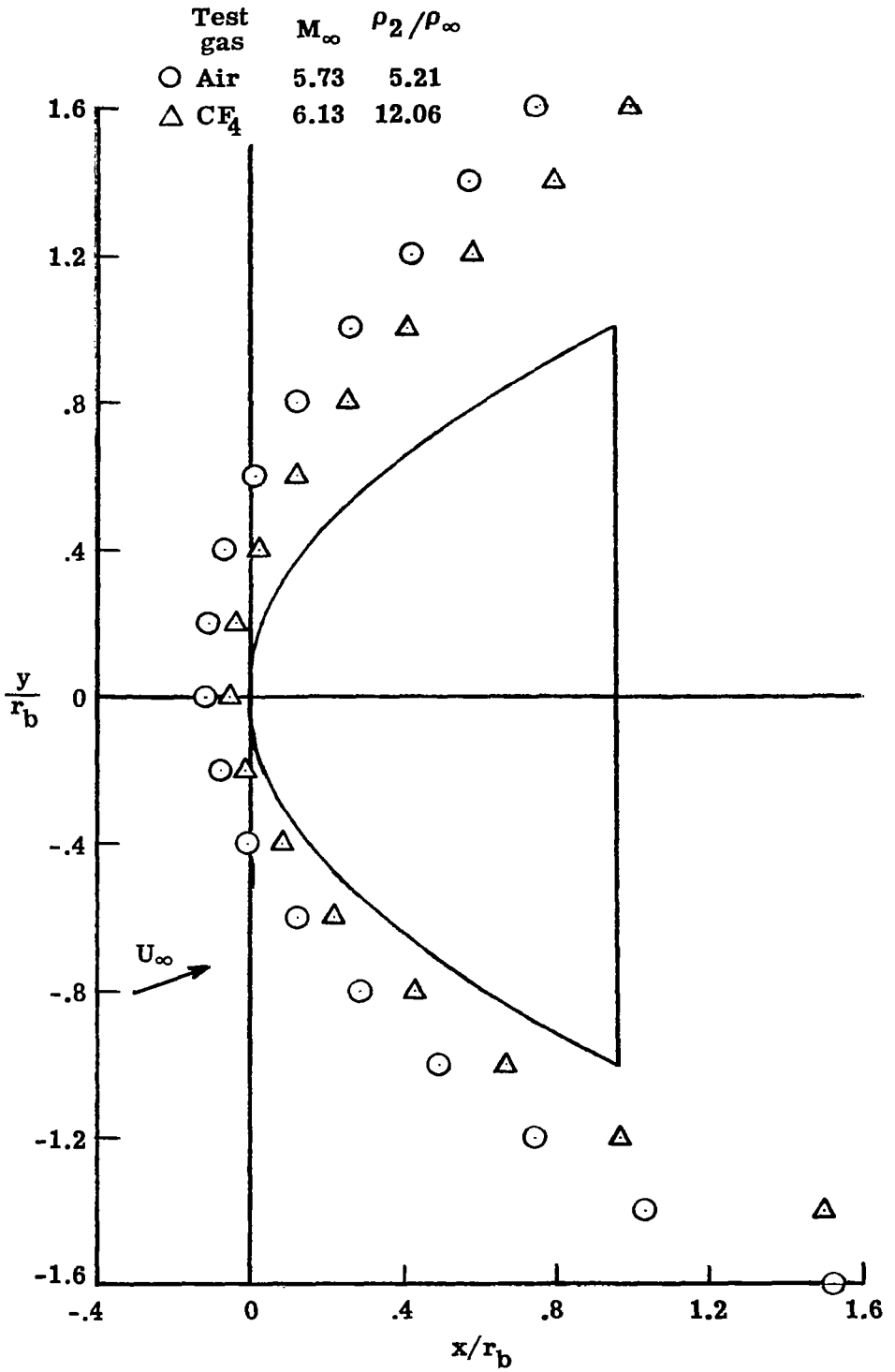

(f) $\alpha = 20°$.

Figure 11.- Concluded.

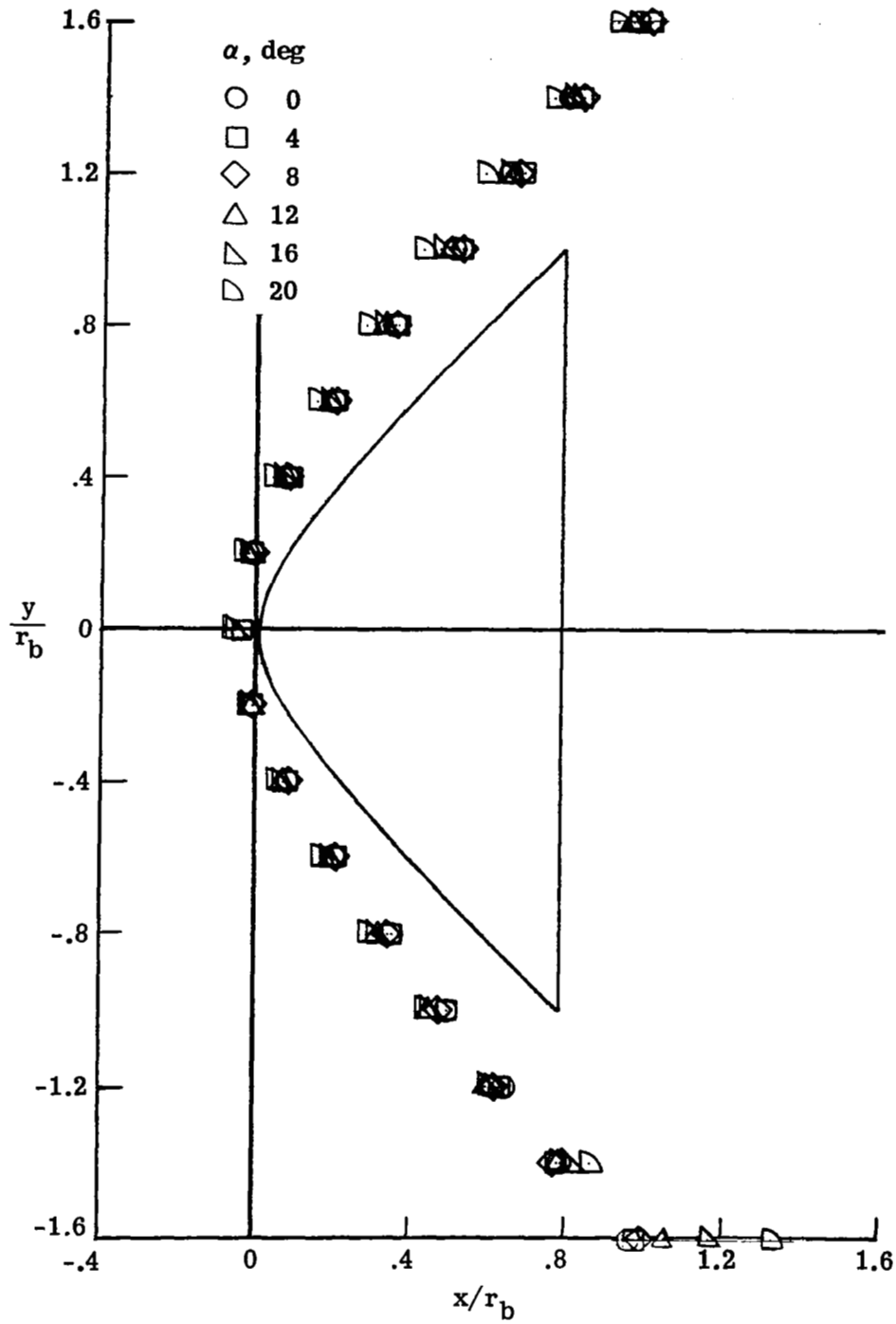

(a) Air; $M_\infty = 5.73$; $\rho_2/\rho_\infty = 5.21$.

Figure 12.- Effect of angle of attack on shock shape measured on the hyperboloid pressure model (model 1, series 1) in Mach 6 air and CF_4.

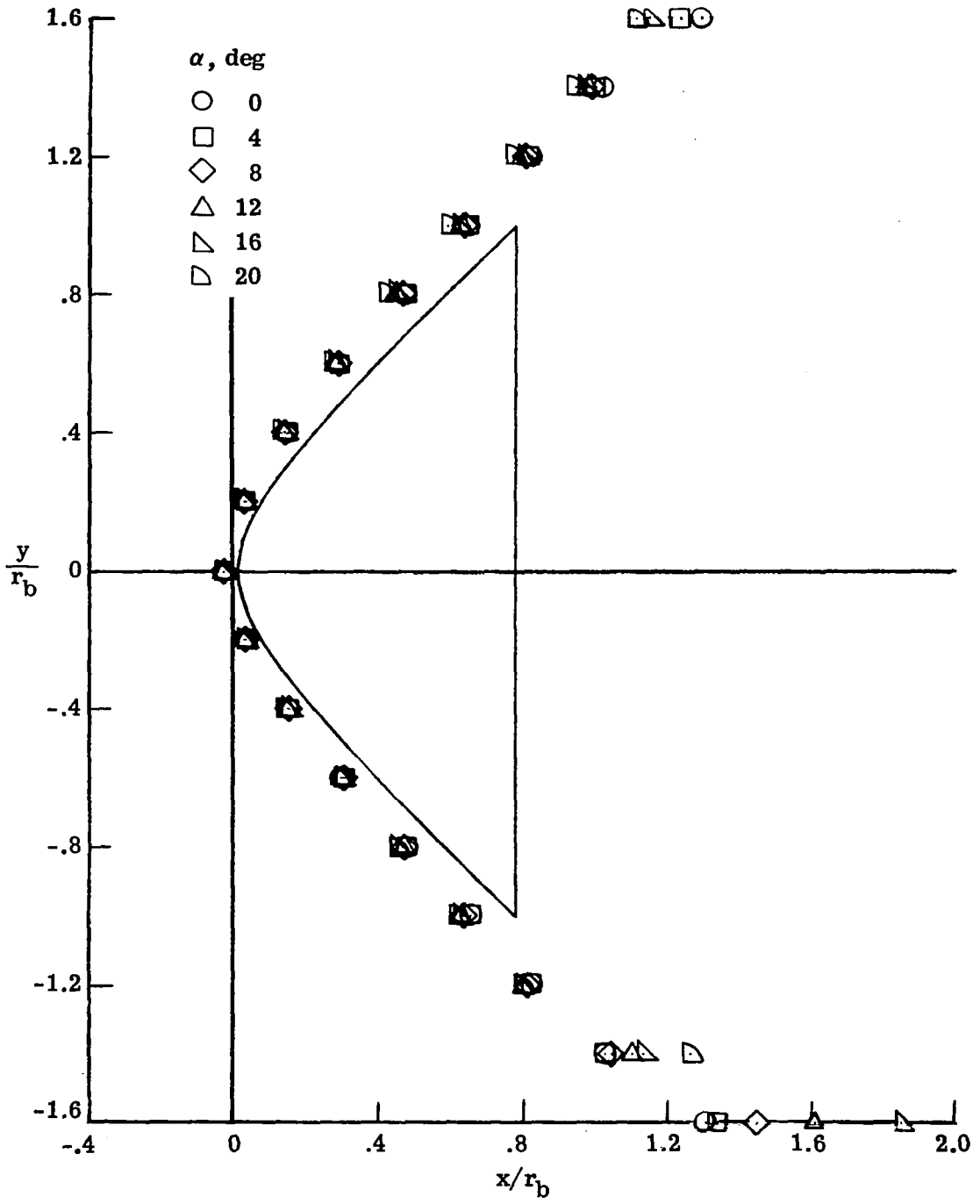

(b) CF_4; $M_\infty = 6.13$; $\rho_2/\rho_\infty = 12.06$.

Figure 12.- Concluded.

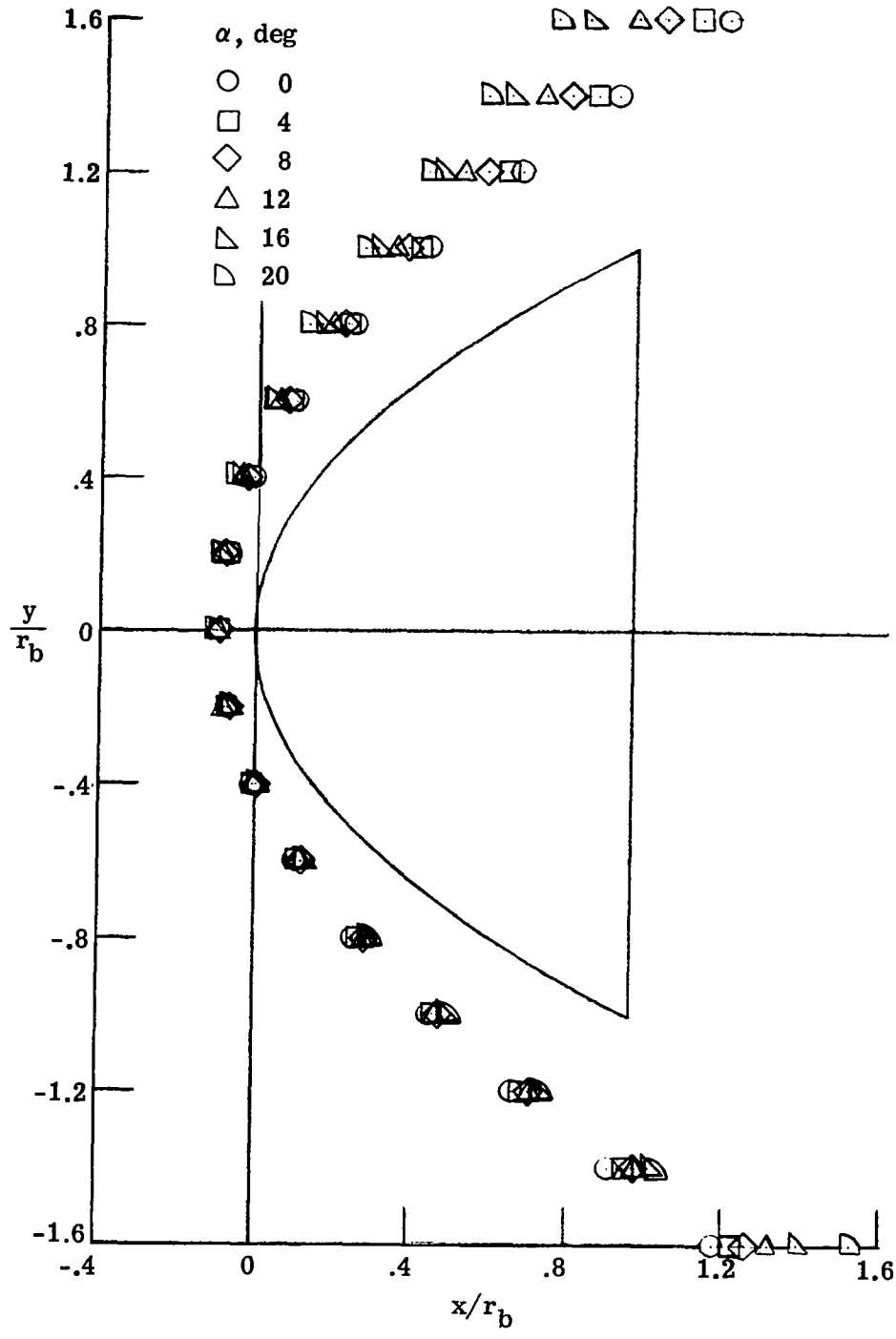

(a) Air; $M_\infty = 5.73$; $\rho_2/\rho_\infty = 5.21$.

Figure 13.- Effect of angle of attack on shock shape measured on the paraboloid pressure model (model 3, series 1) in Mach 6 air and CF_4.

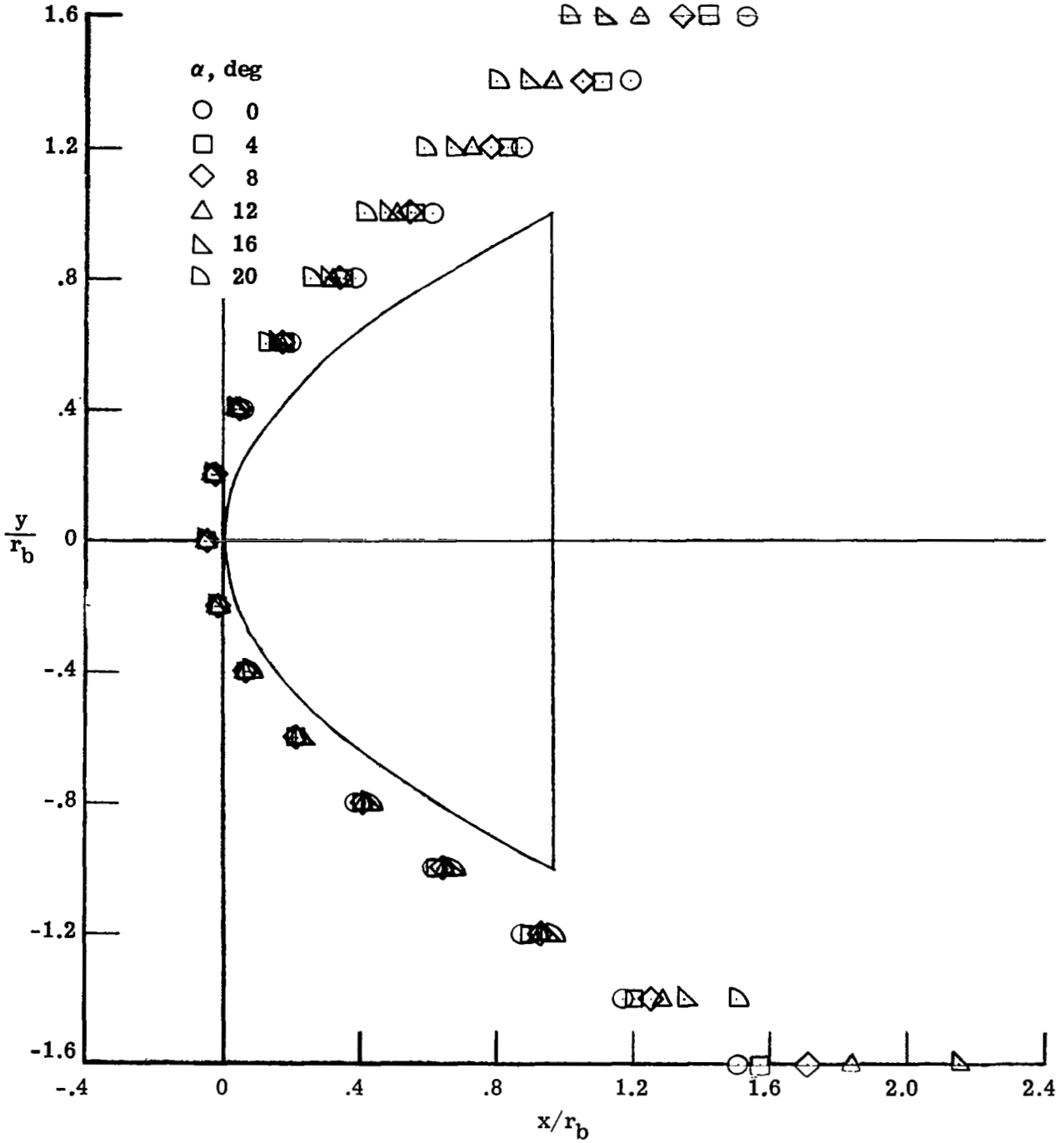

(b) CF_4; $M_\infty = 6.13$; $\rho_2/\rho_\infty = 12.06$.

Figure 13.- Concluded.

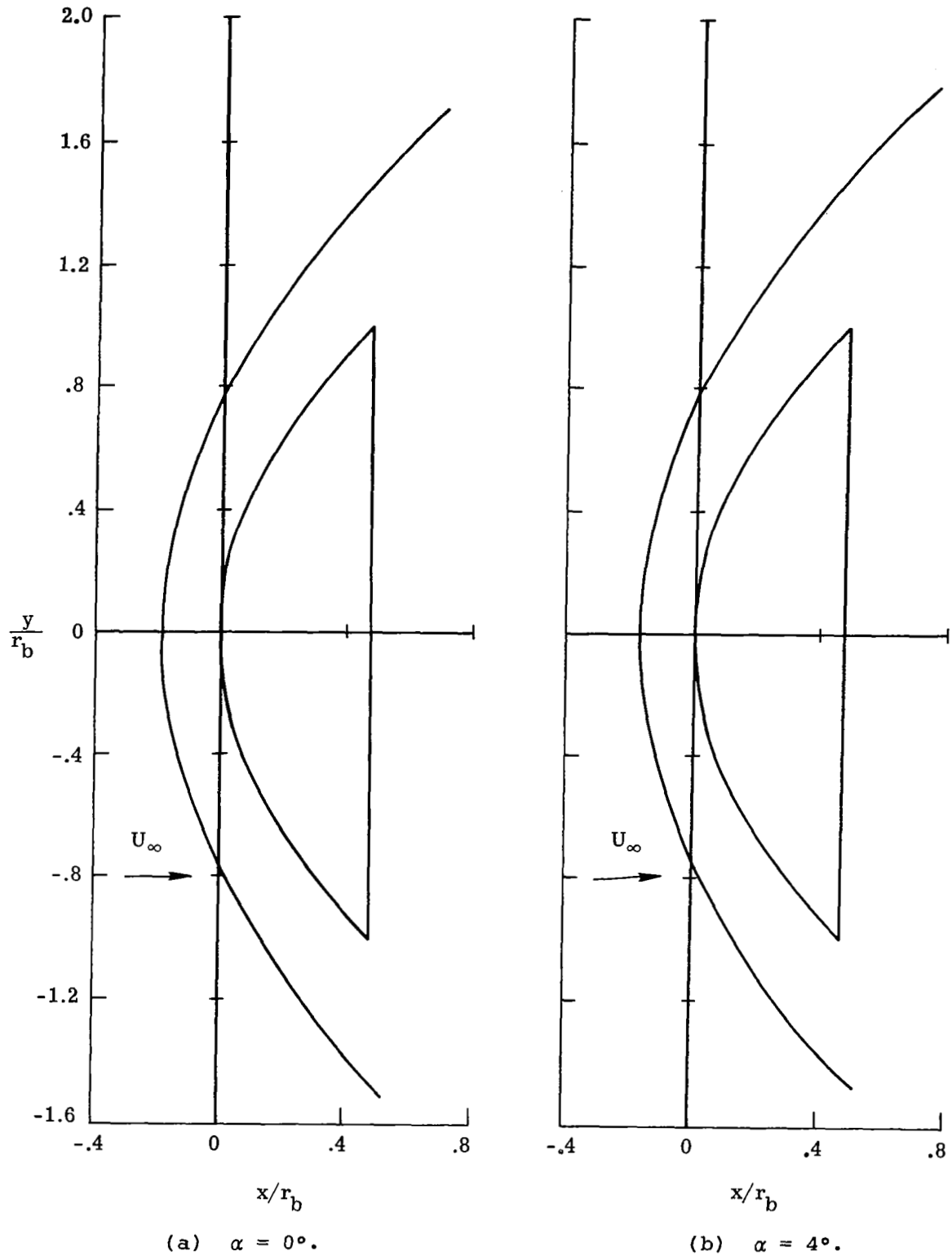

Figure 14.- Shock shapes measured on the sonic-corner paraboloid (model 2) in air. $M_\infty = 5.915$.

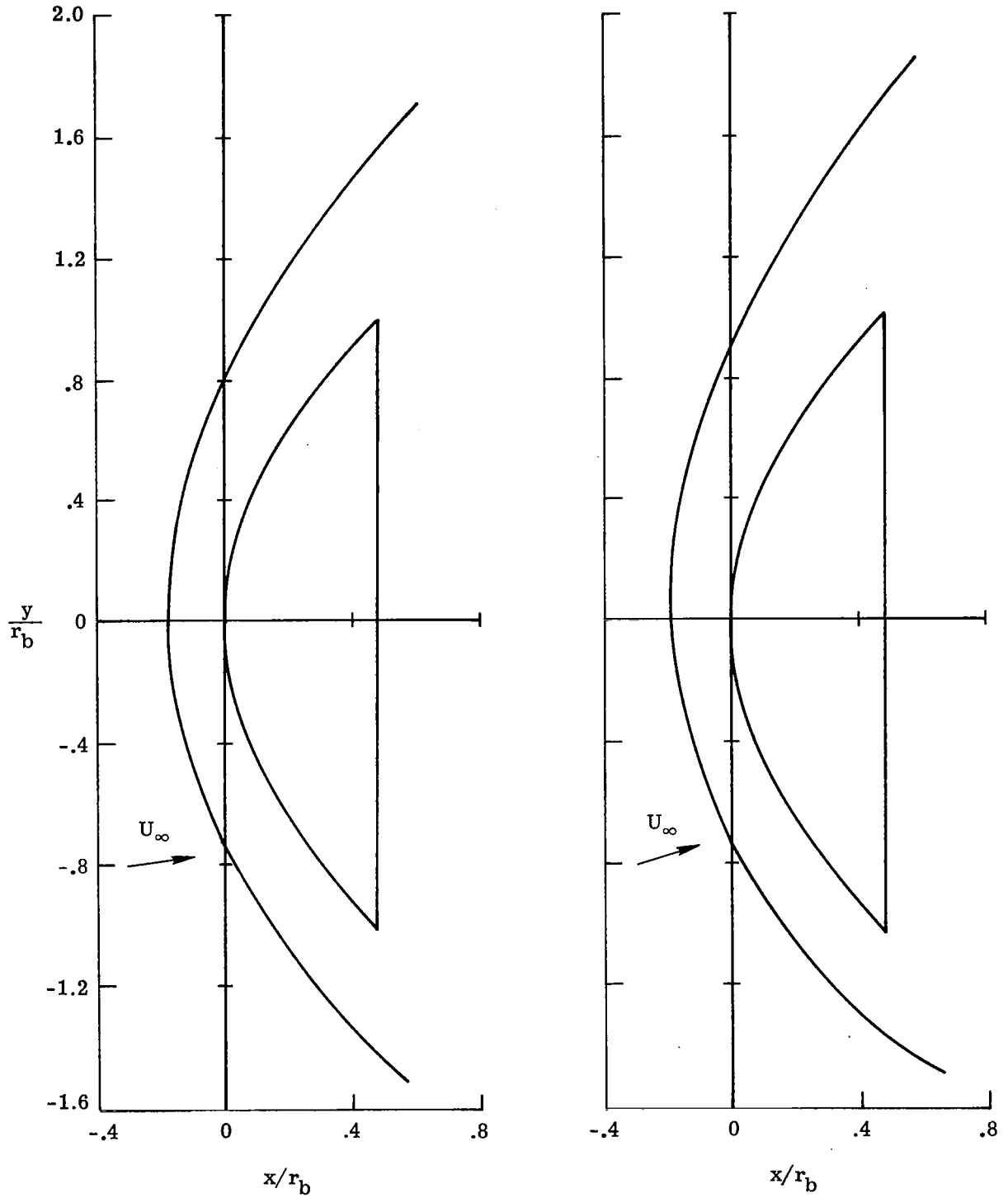

(c) $\alpha = 8°$.

(d) $\alpha = 16°$.

Figure 14.- Concluded.

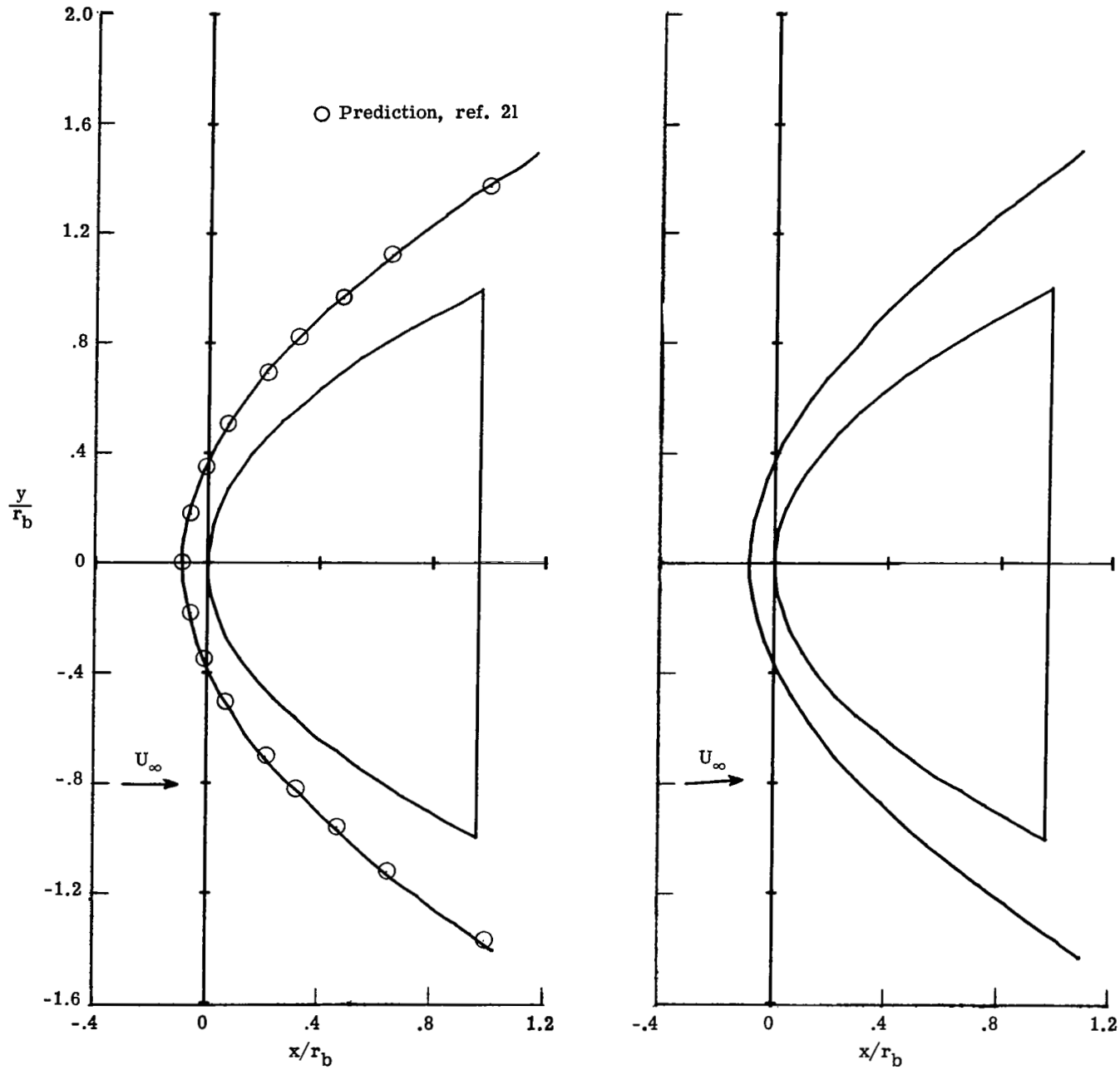

Figure 15.- Shock shapes measured on the paraboloid (model 3, series 2) in air. $M_\infty = 5.915$.

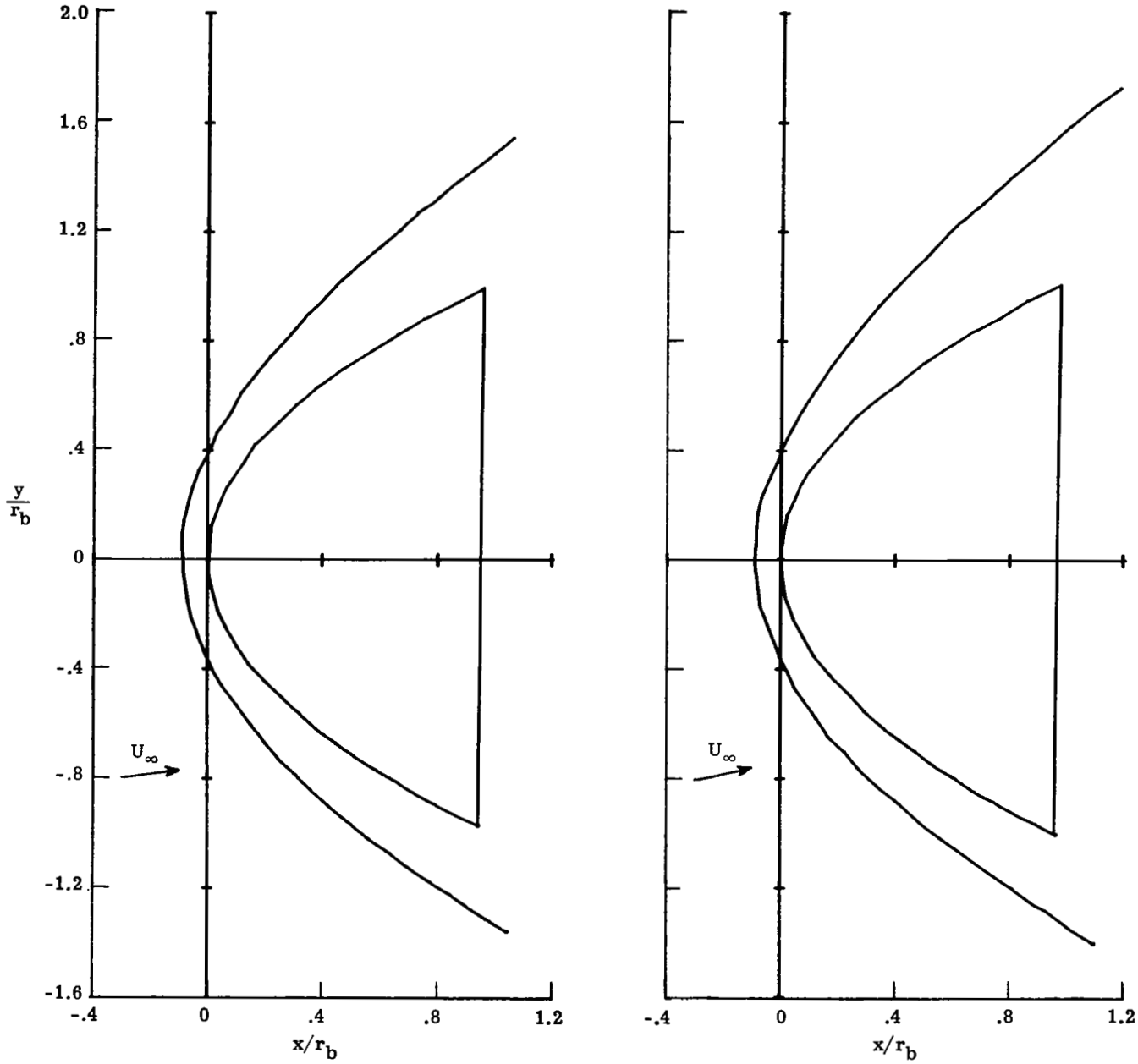

(c) $\alpha = 8°$.

(d) $\alpha = 12°$

Figure 15.- Continued.

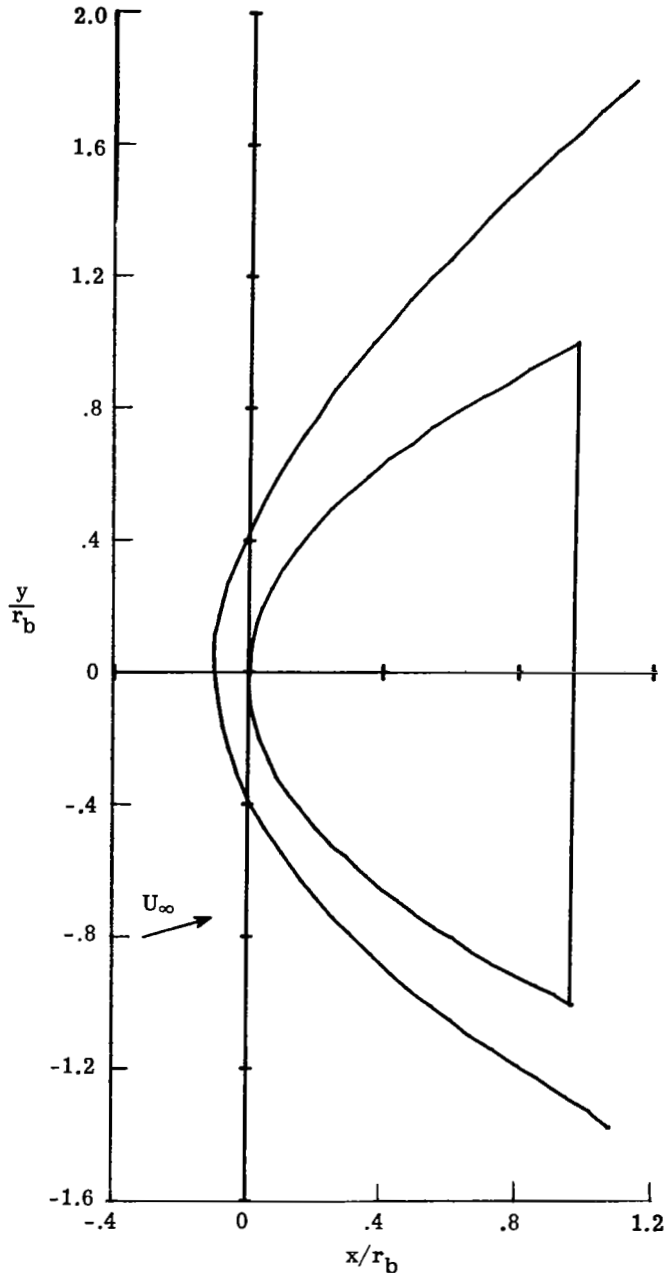

(e) $\alpha = 16°$.

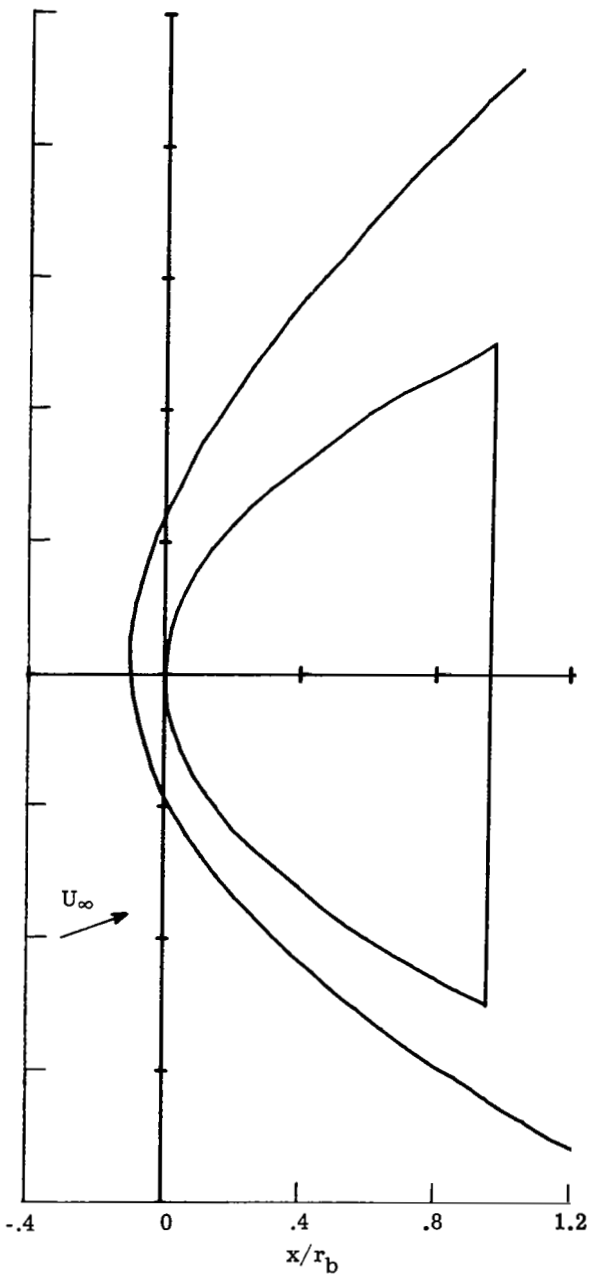

(f) $\alpha = 20°$.

Figure 15.- Concluded.

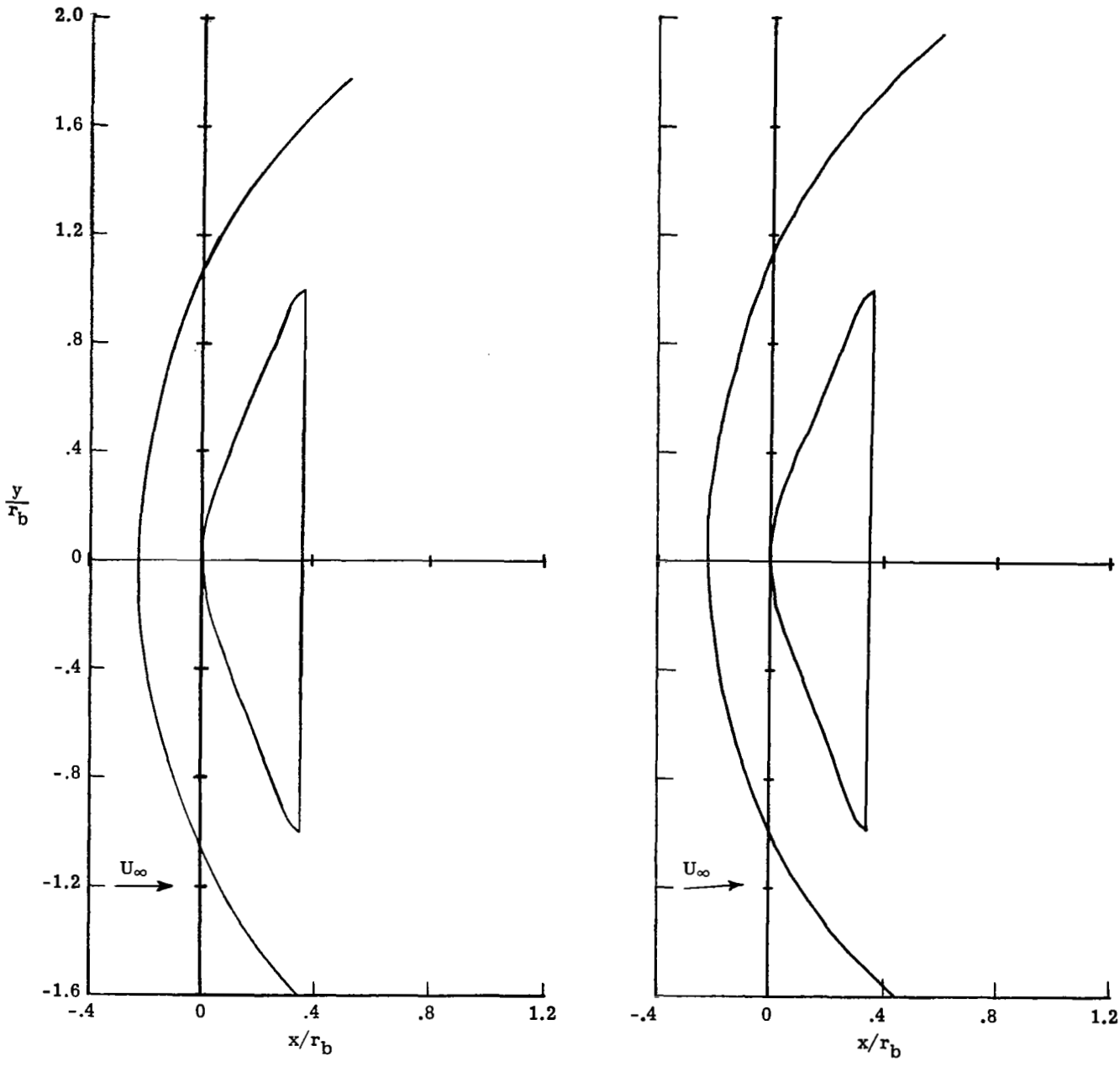

Figure 16.- Shock shapes measured on the Viking aeroshell (model 4) in air. $M_\infty = 5.915$.

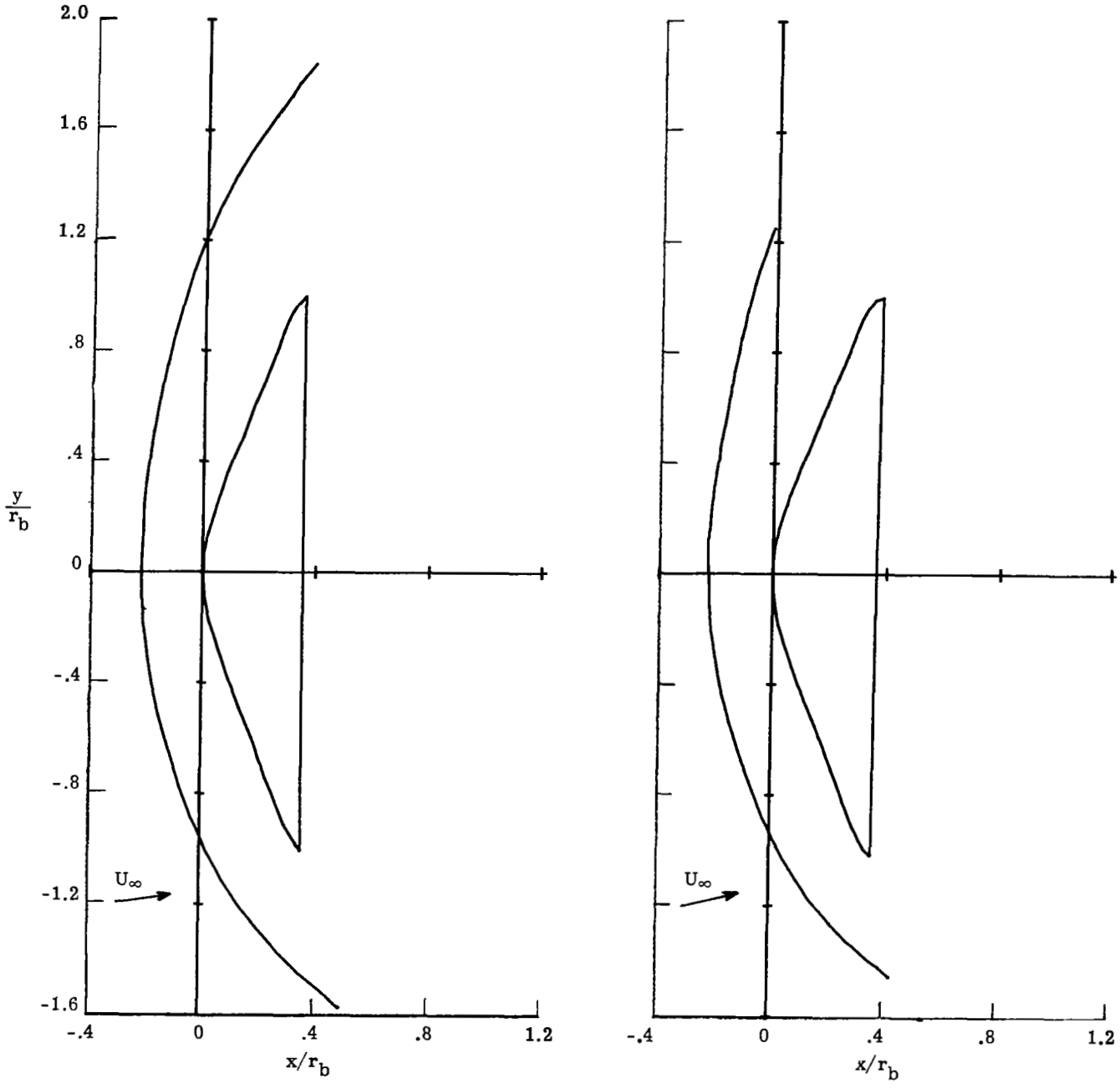

(c) $\alpha = 8°$.

(d) $\alpha = 12°$.

Figure 16.- Continued.

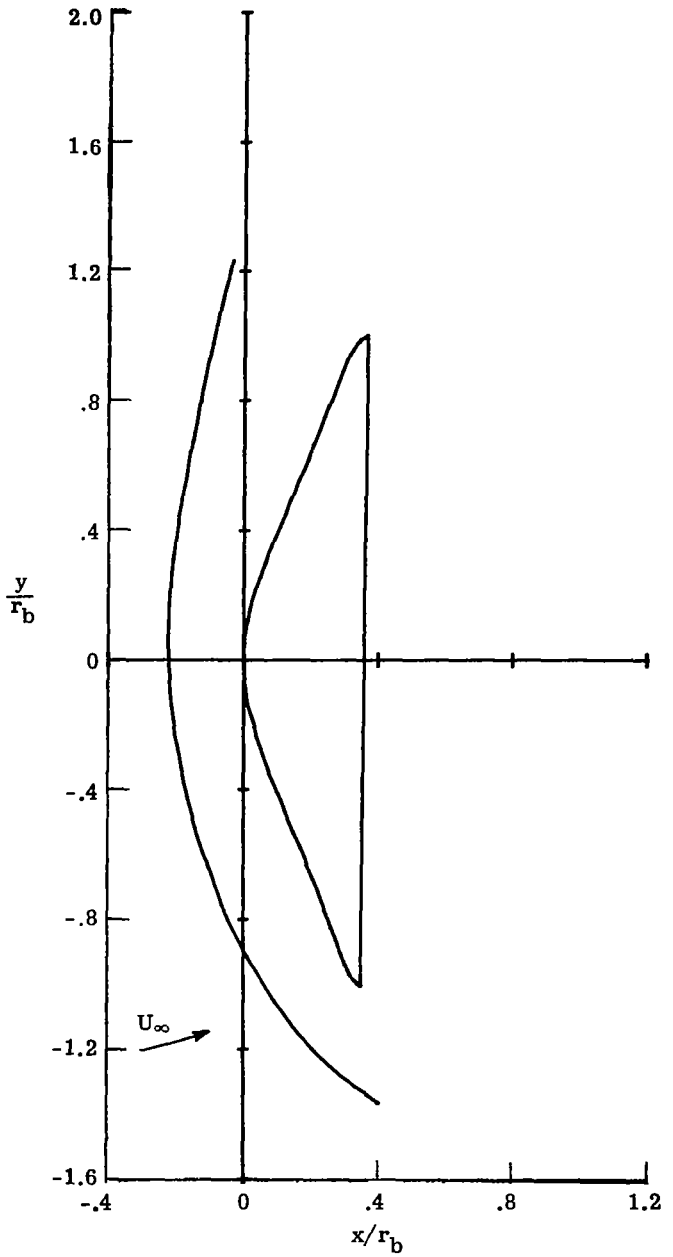

(e) $\alpha = 16°$.

Figure 16.- Concluded.

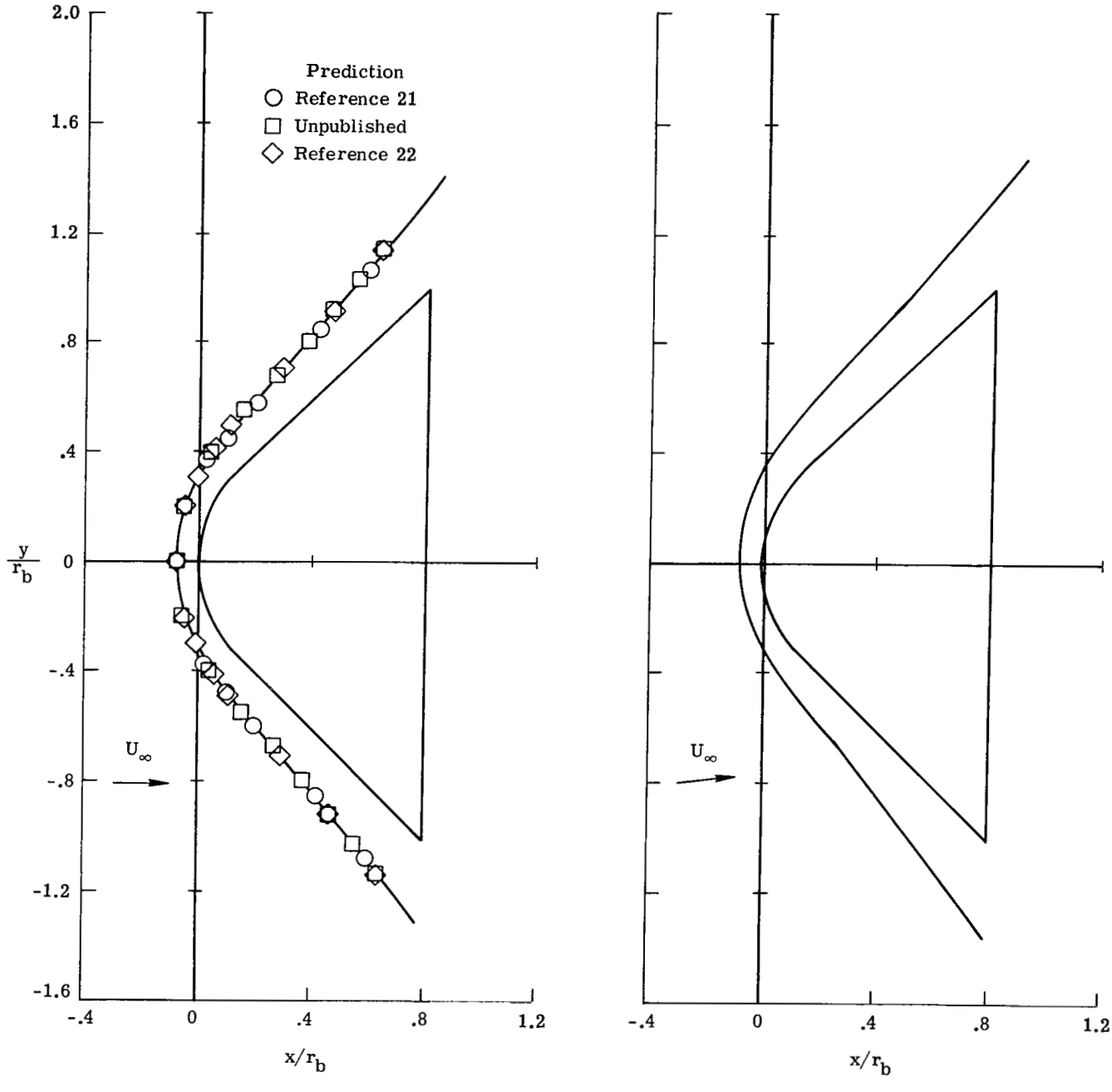

Figure 17.- Shock shapes measured on the spherical-nose cone (model 5) in air. $M_\infty = 5.915$.

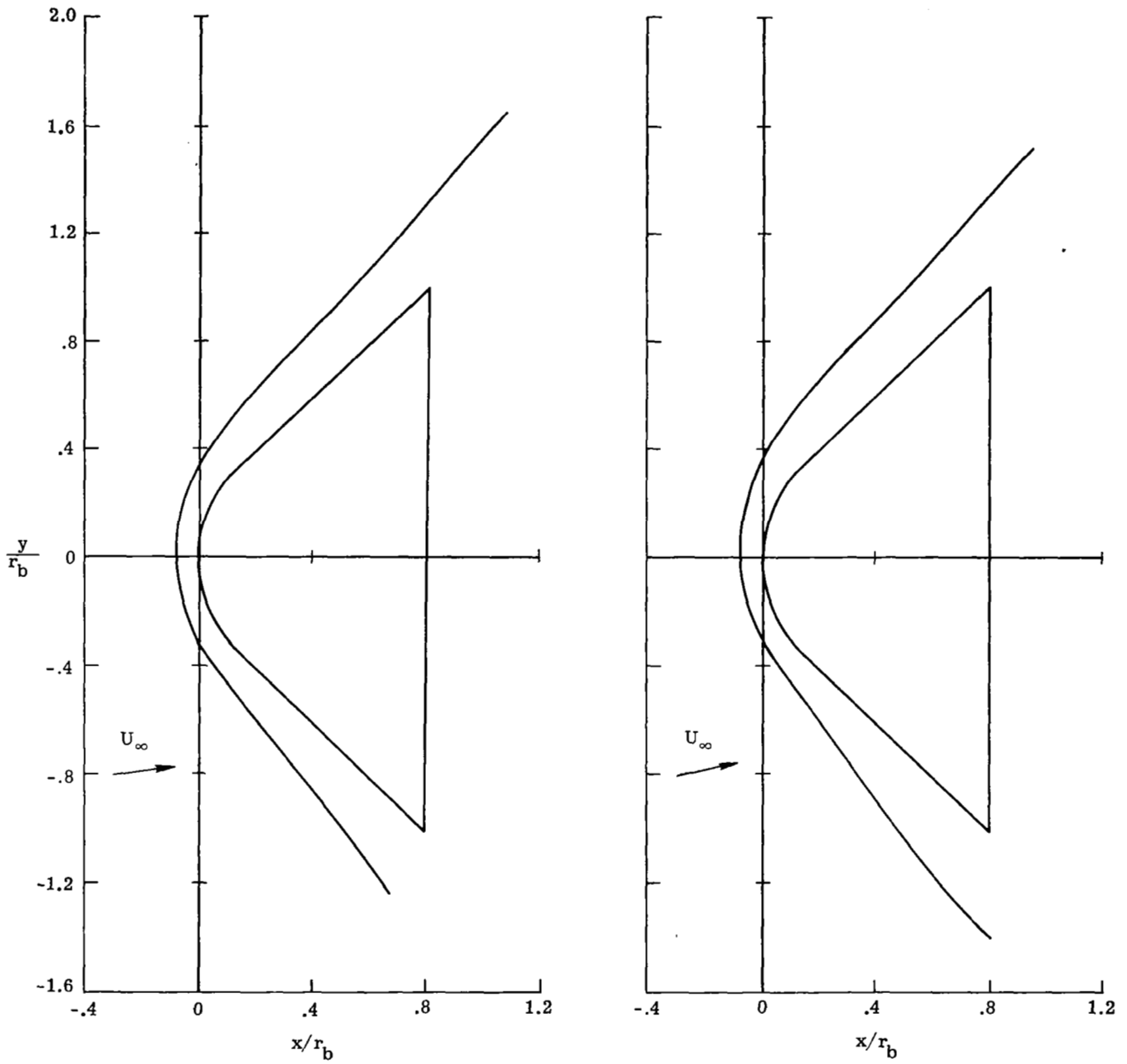

(c) $\alpha = 8°$.

(d) $\alpha = 12°$.

Figure 17.- Continued.

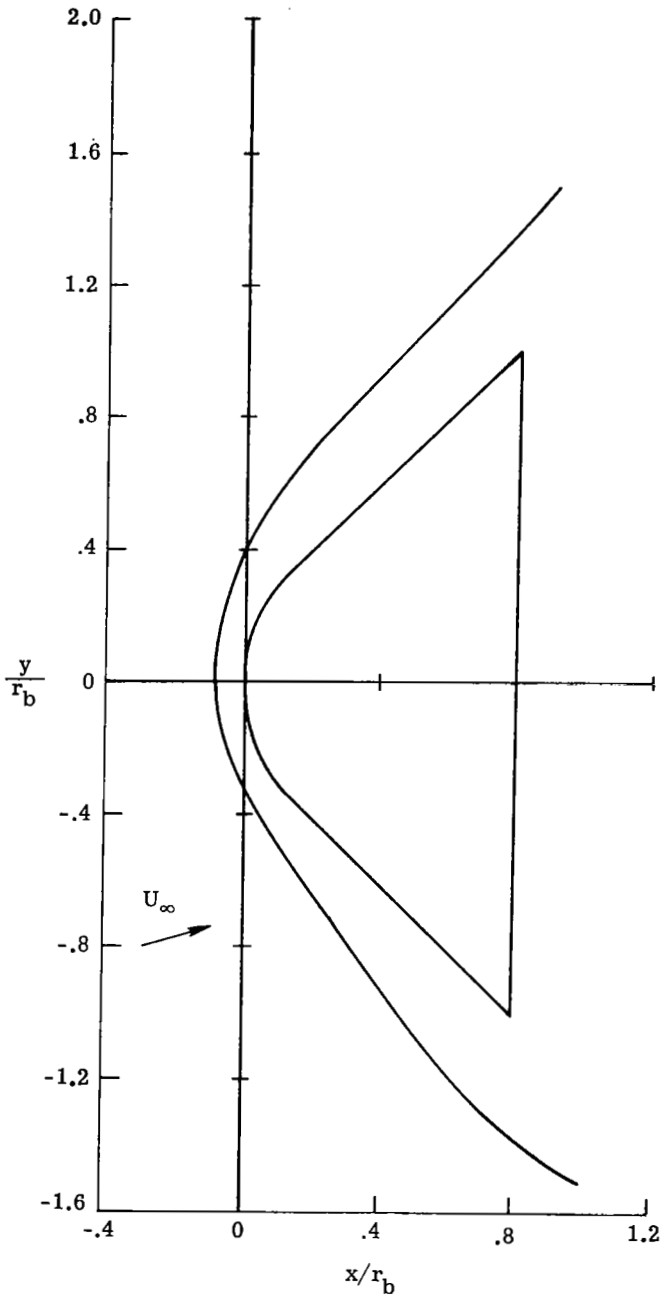

(e) $\alpha = 16°$.

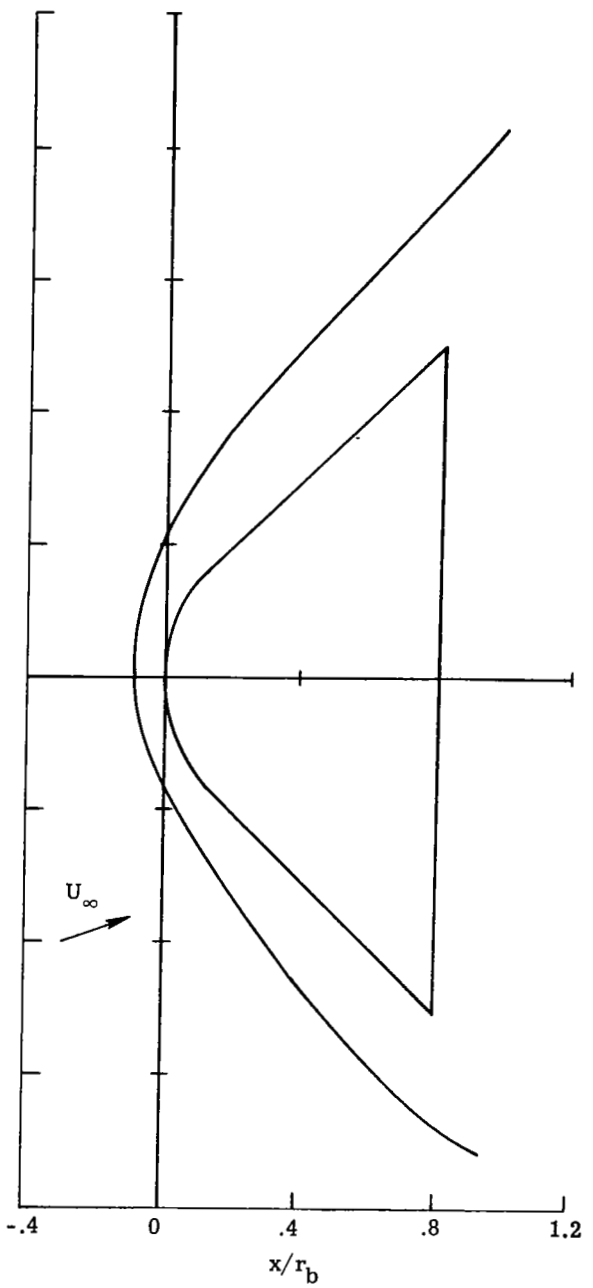

(f) $\alpha = 20°$.

Figure 17.- Concluded.

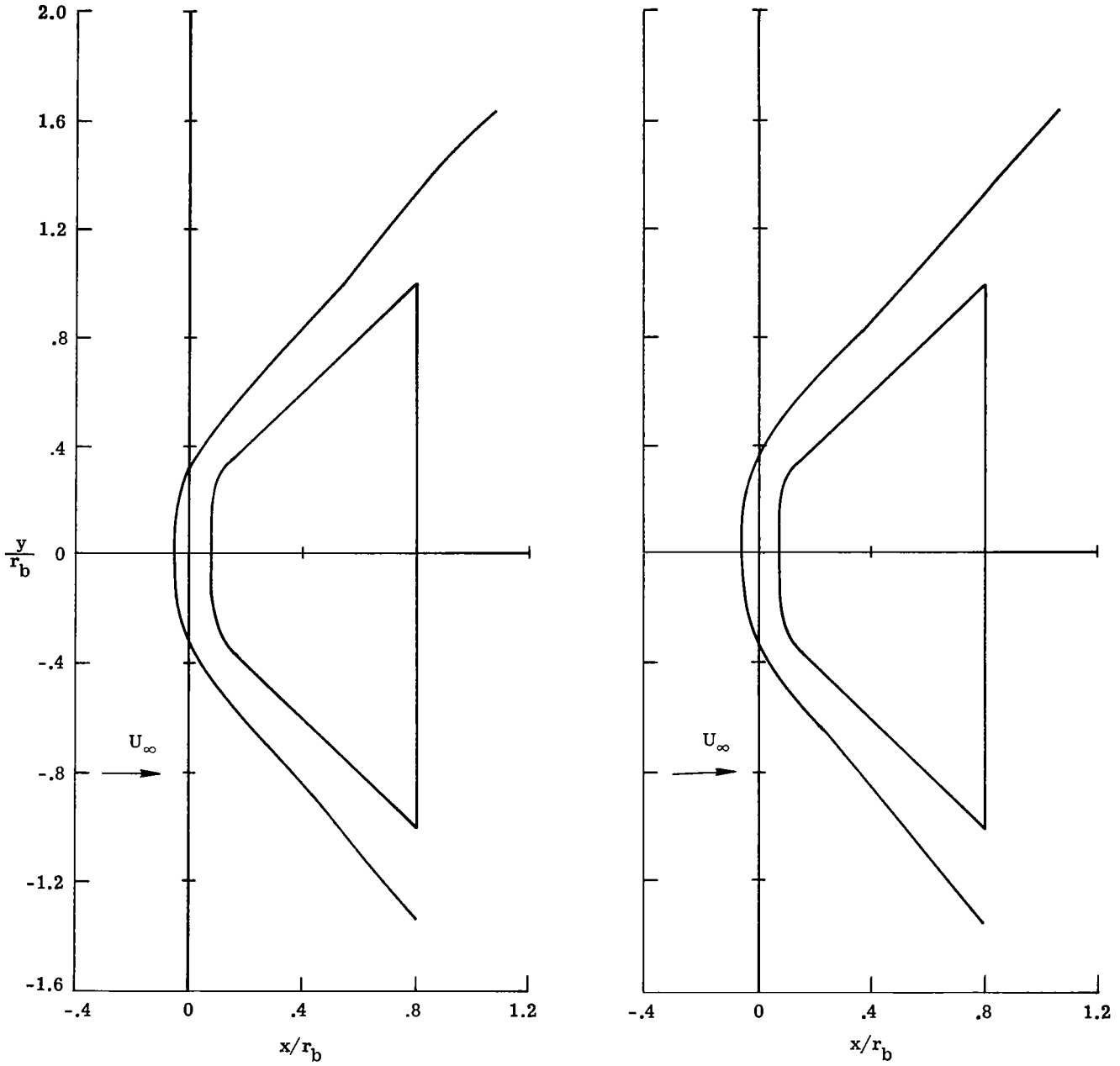

Figure 18.- Shock shapes measured on the flattened-nose cone (model 6) in air. $M_\infty = 5.915$.

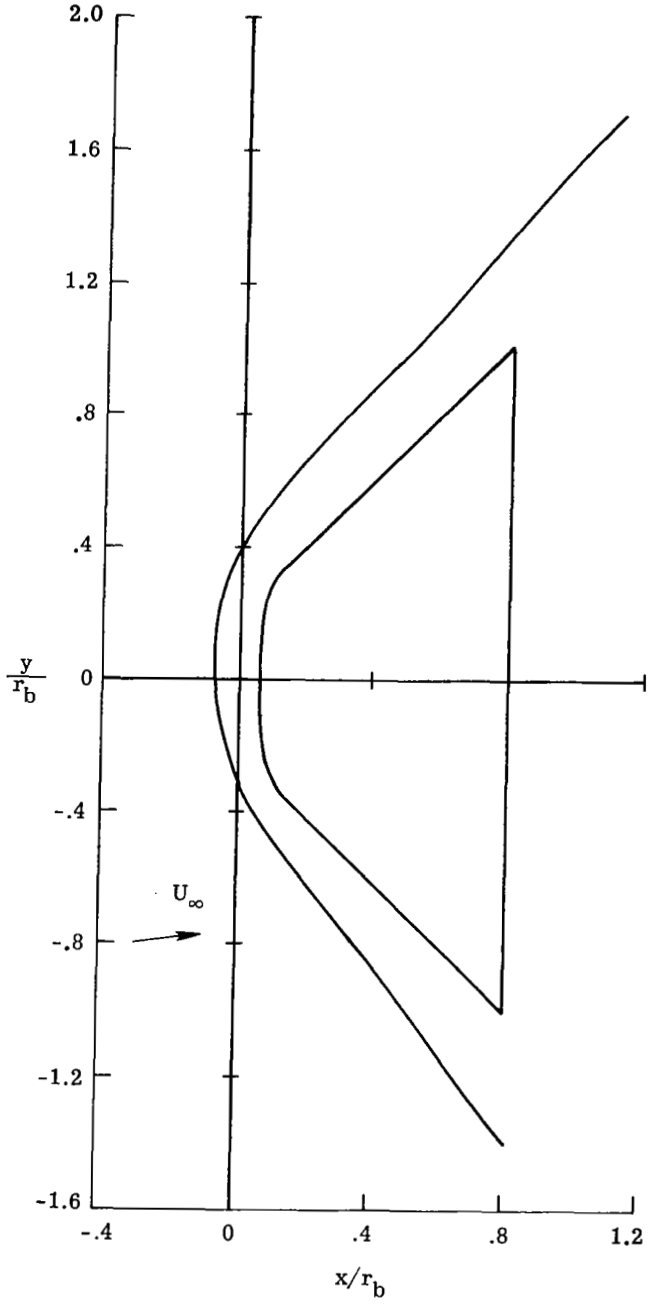

(c) $\alpha = 8°$.

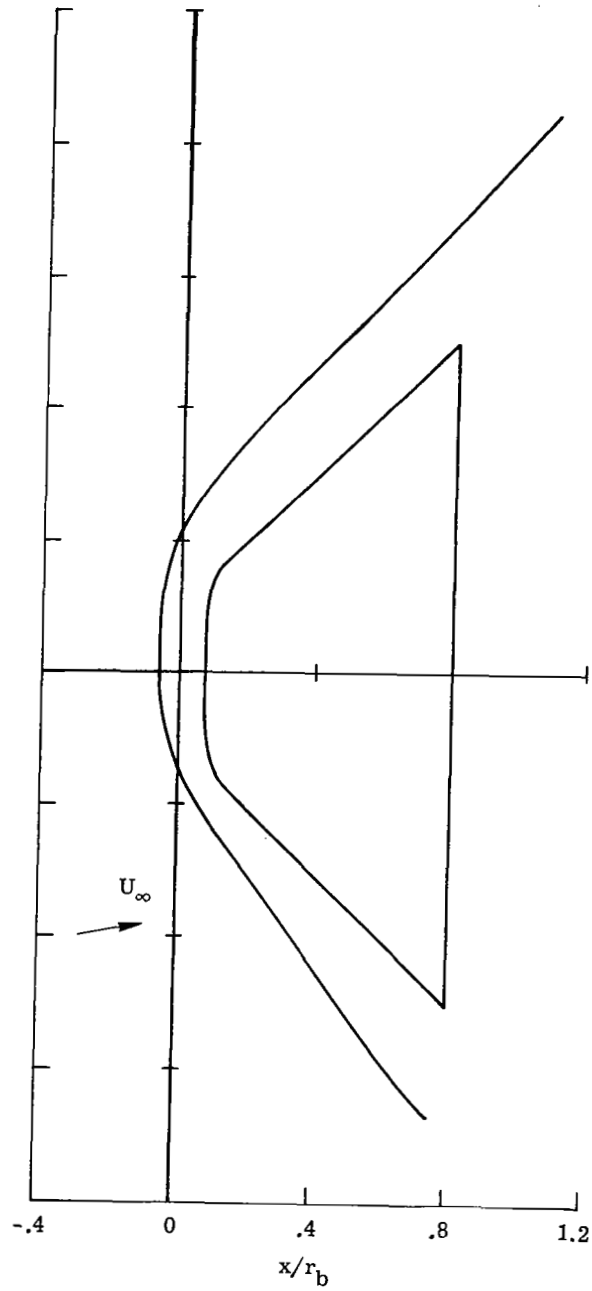

(d) $\alpha = 12°$.

Figure 18.- Continued.

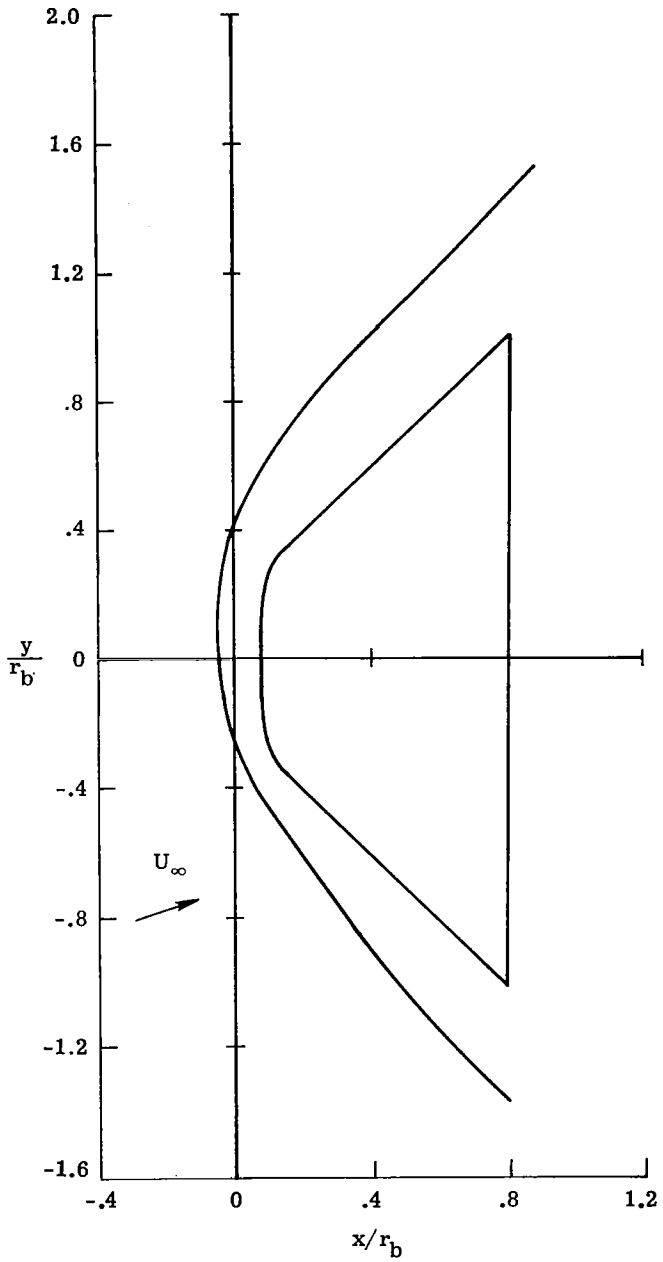

(e) $\alpha = 16°$.

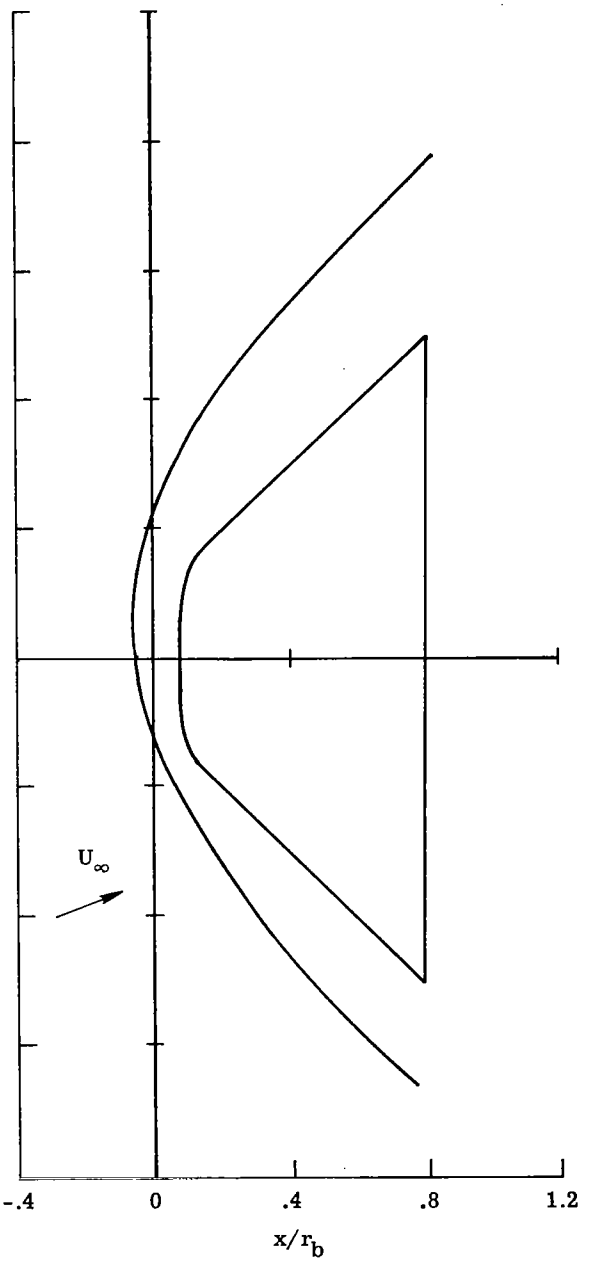

(f) $\alpha = 20°$.

Figure 18.- Concluded.

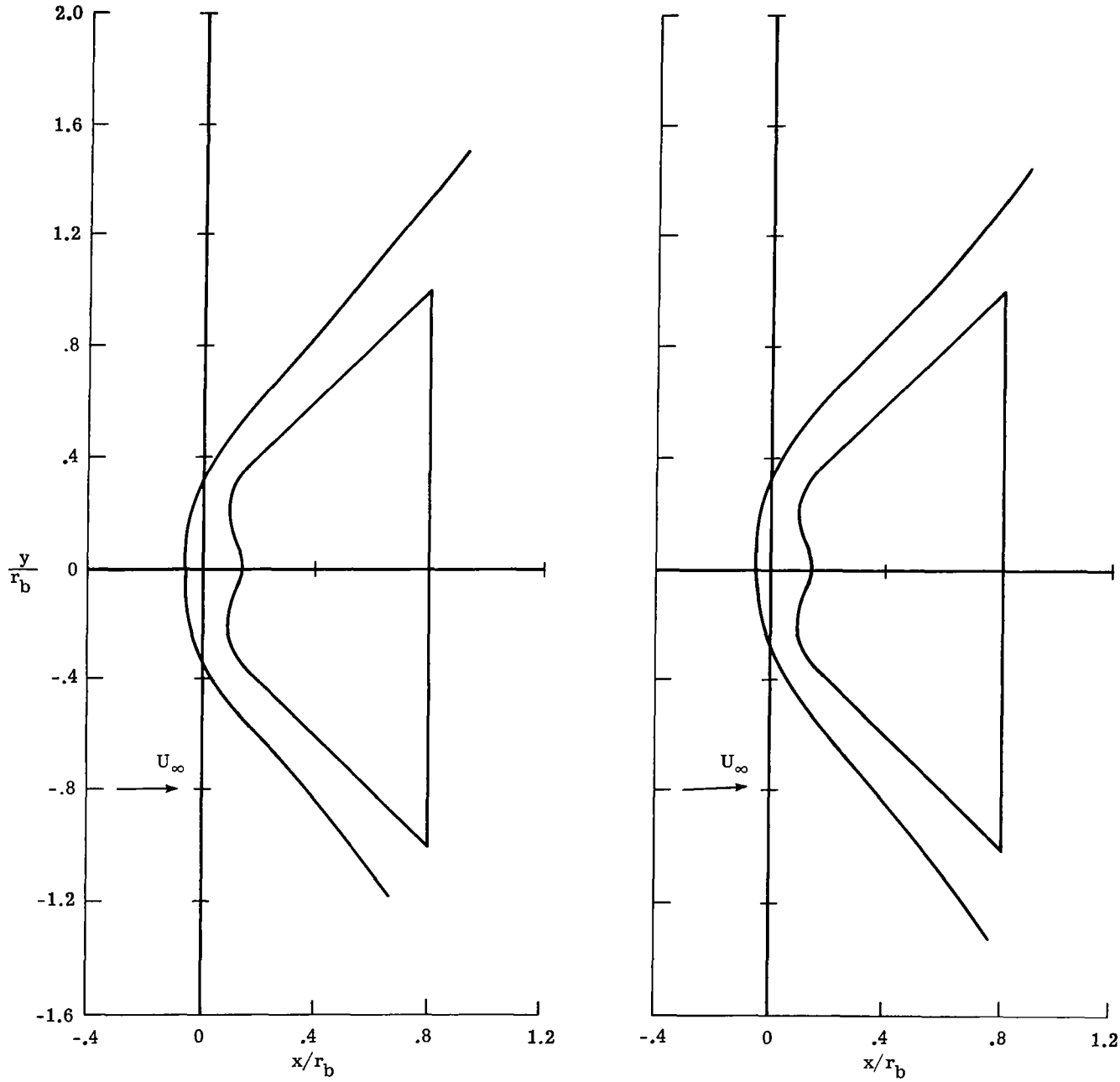

Figure 19.- Shock shapes measured on the concave-nose cone (model 7) in air. $M_\infty = 5.915$.

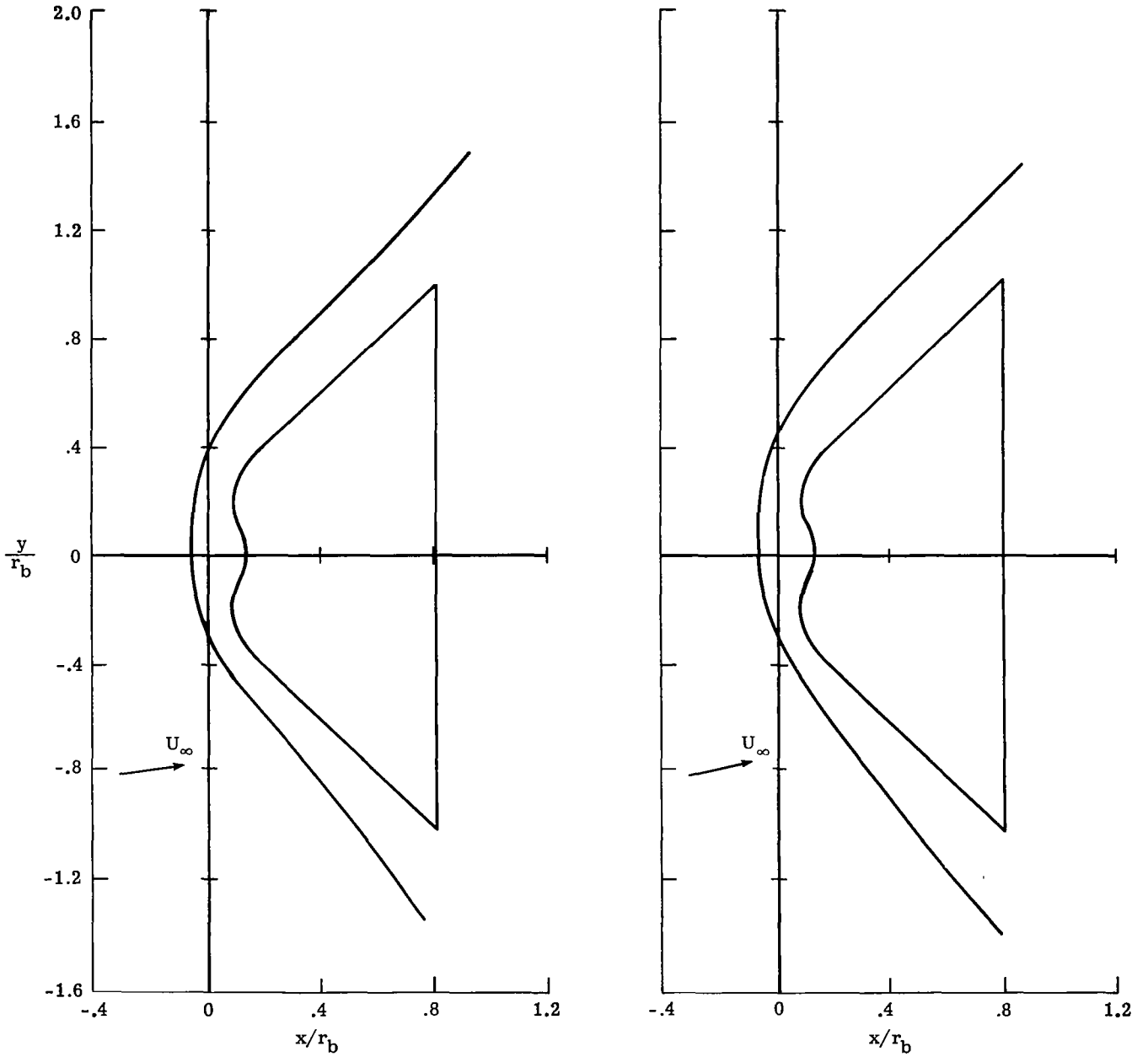

(c) $\alpha = 8°$.

(d) $\alpha = 12°$.

Figure 19.- Continued.

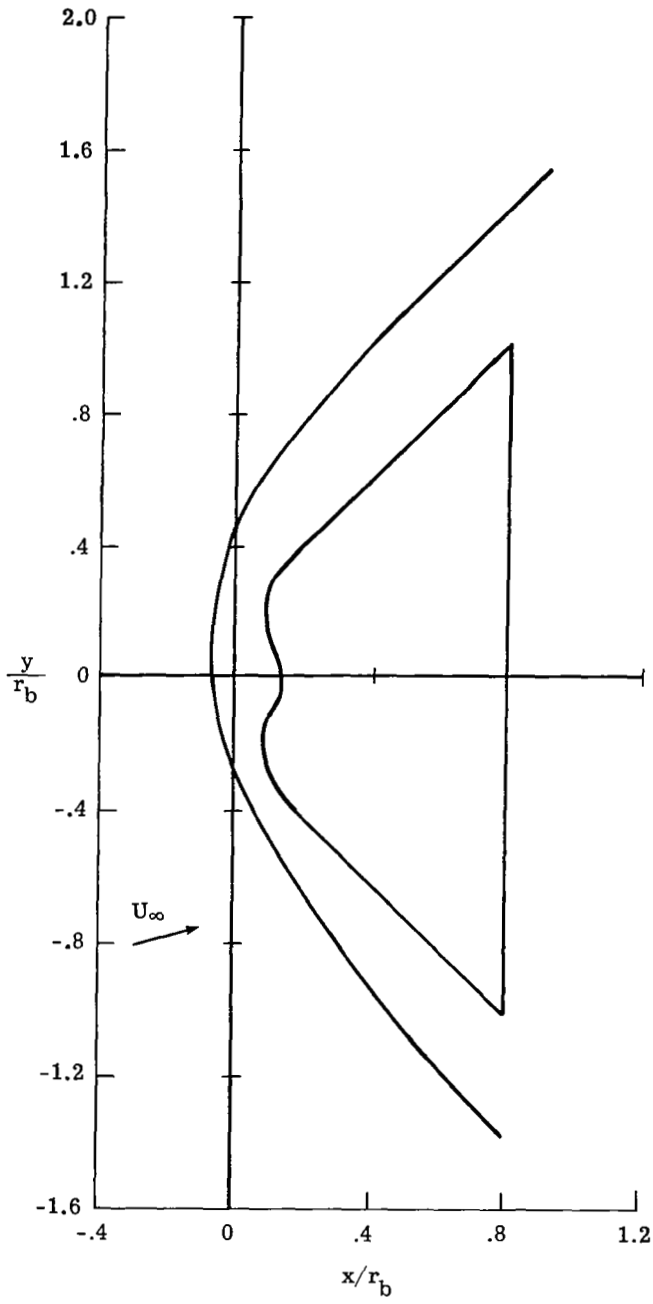

(e) $\alpha = 16°$.

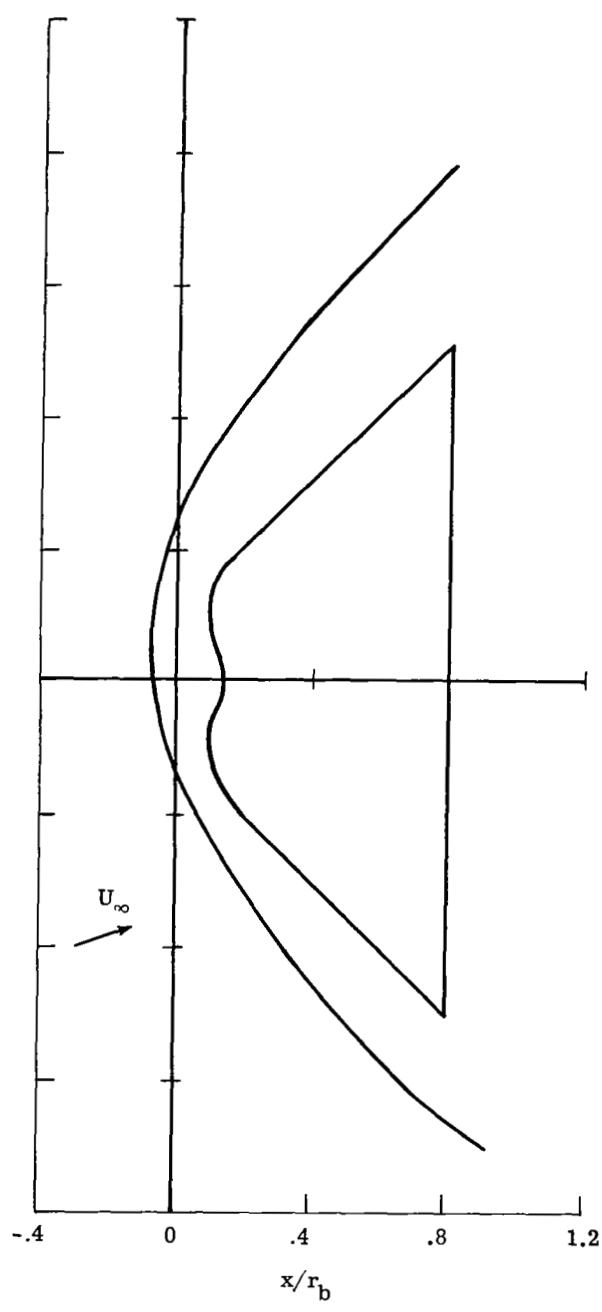

(f) $\alpha = 20°$.

Figure 19.- Concluded.

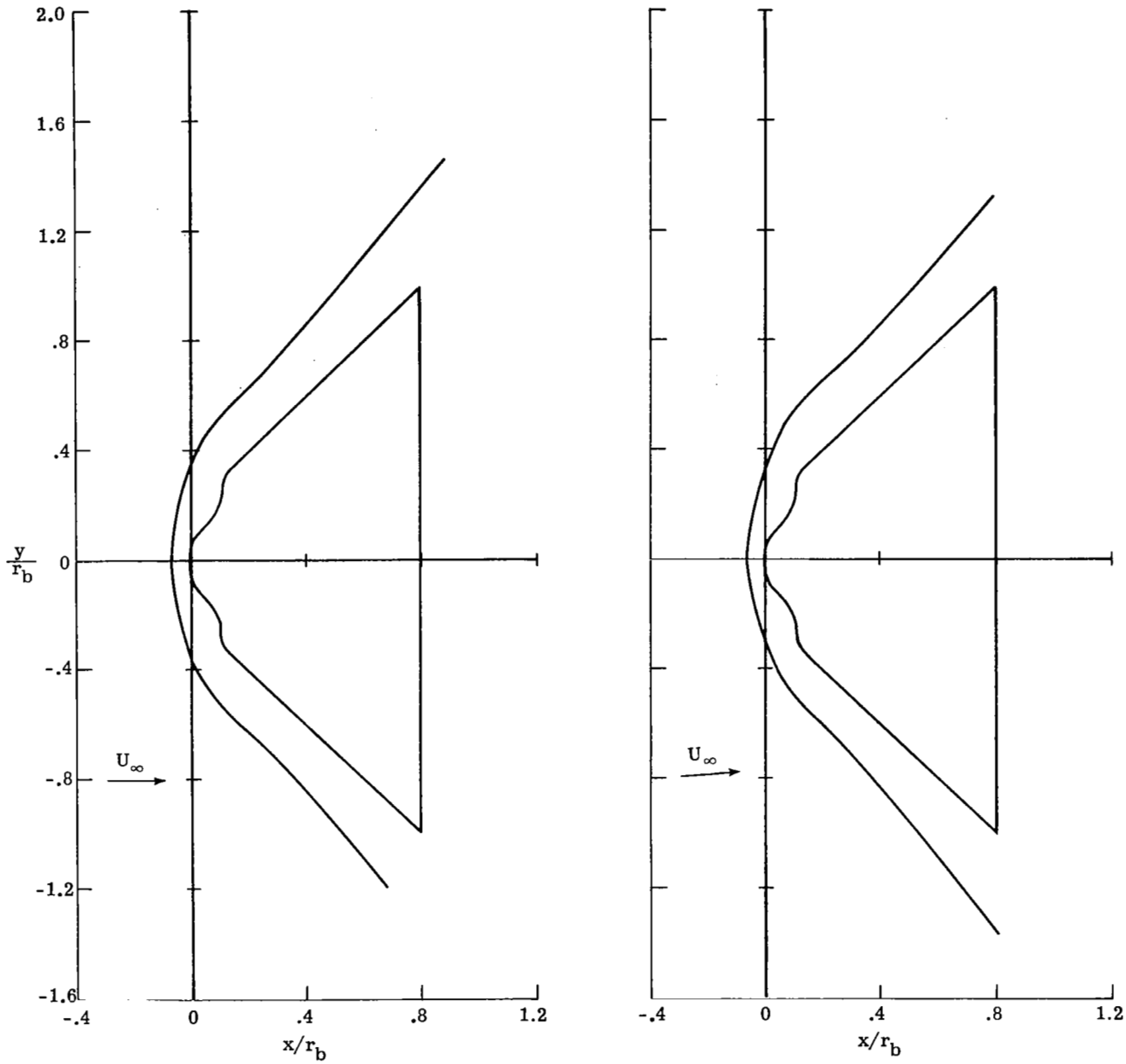

(a) $\alpha = 0°$.

(b) $\alpha = 4°$.

Figure 20.- Shock shapes measured on the cusp-nose cone (model 8) in air. $M_\infty = 5.915$.

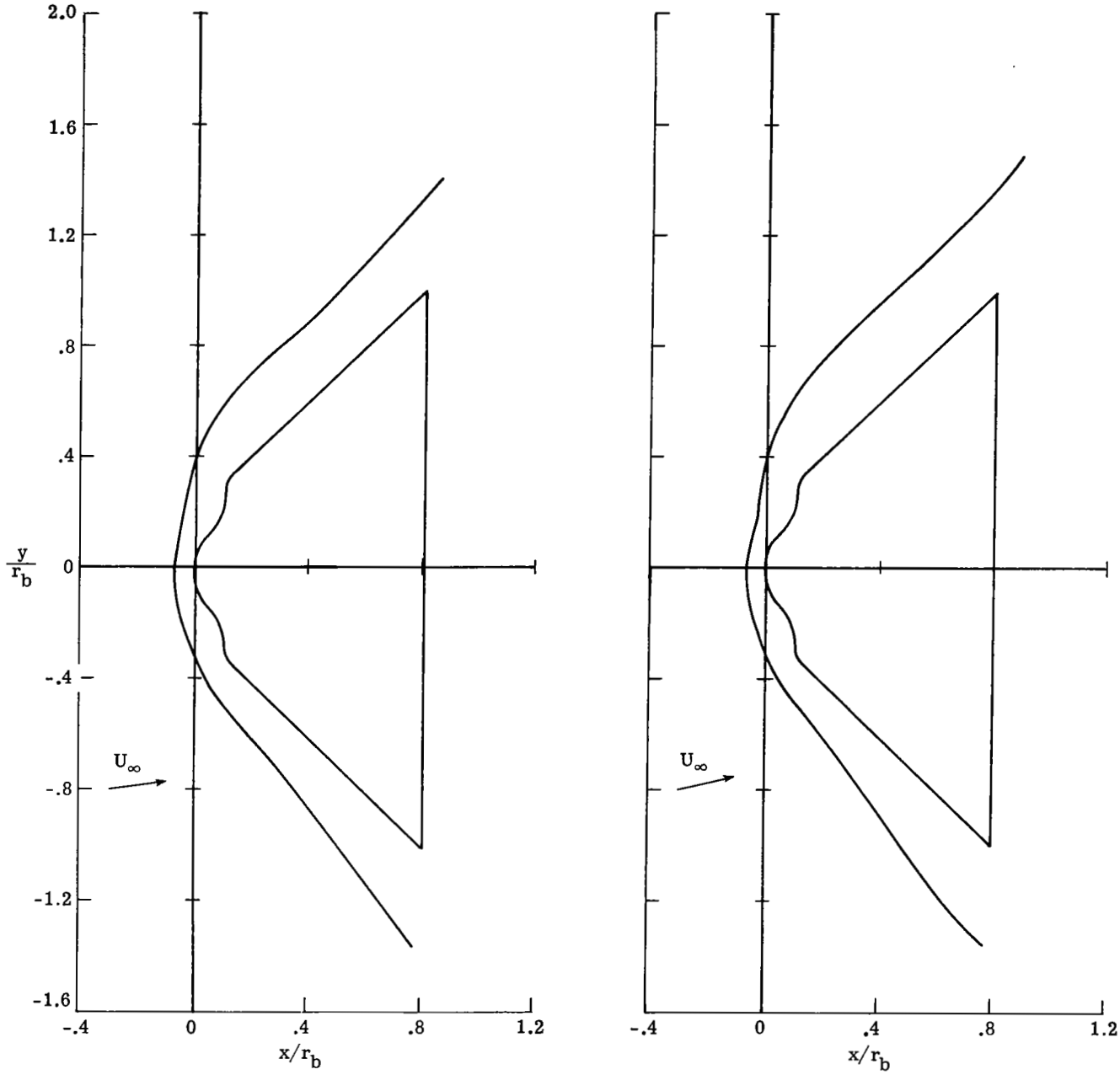

(c) $\alpha = 8°$.

(d) $\alpha = 12°$.

Figure 20.- Continued.

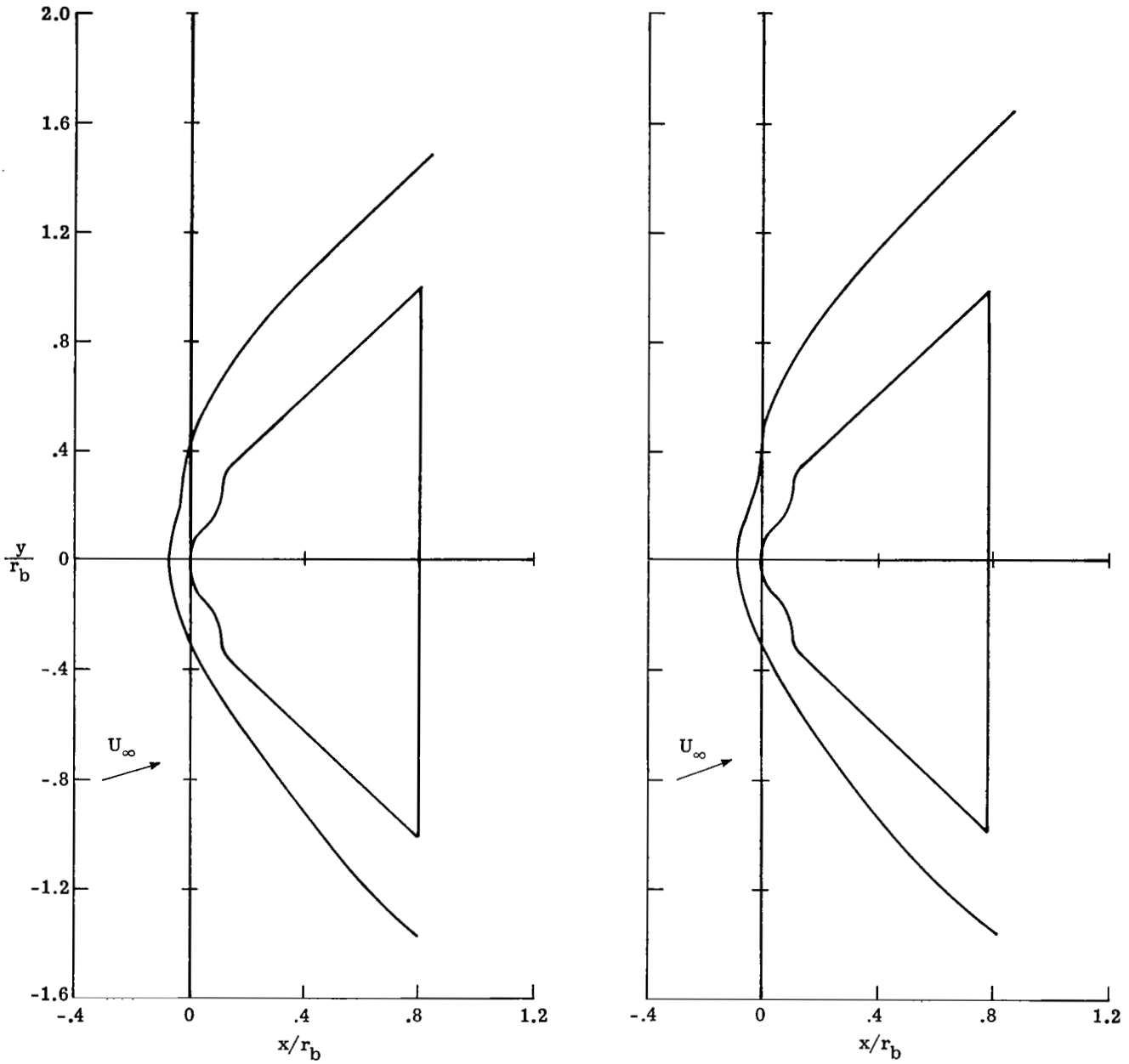

(e) $\alpha = 16°$.

(f) $\alpha = 20°$.

Figure 20.- Concluded.

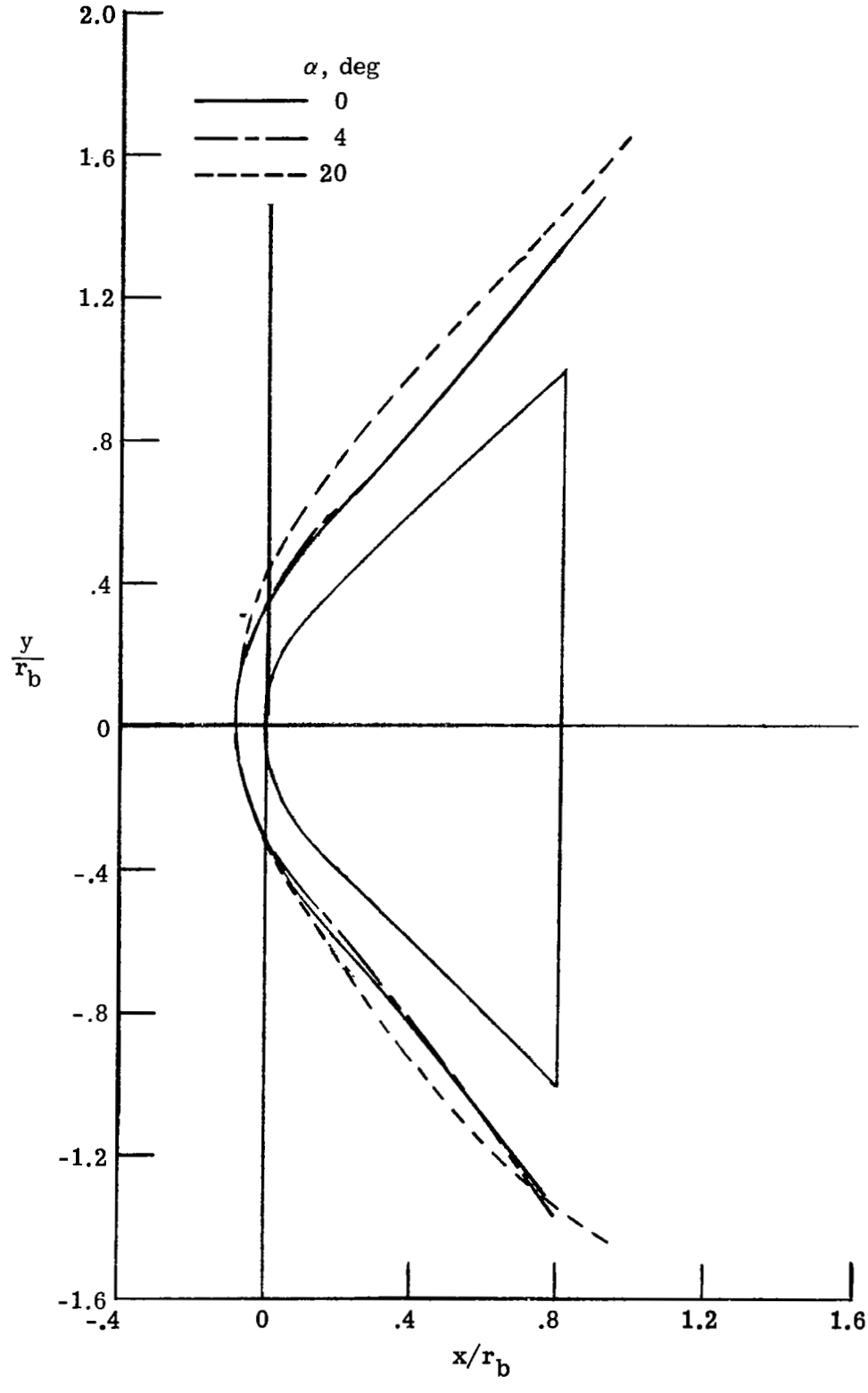

(a) Spherical-nose cone (model 5).

Figure 21.- Effect of angle of attack on shock shapes measured on the cones (models 5 to 8) in air. $M_\infty = 5.915$.

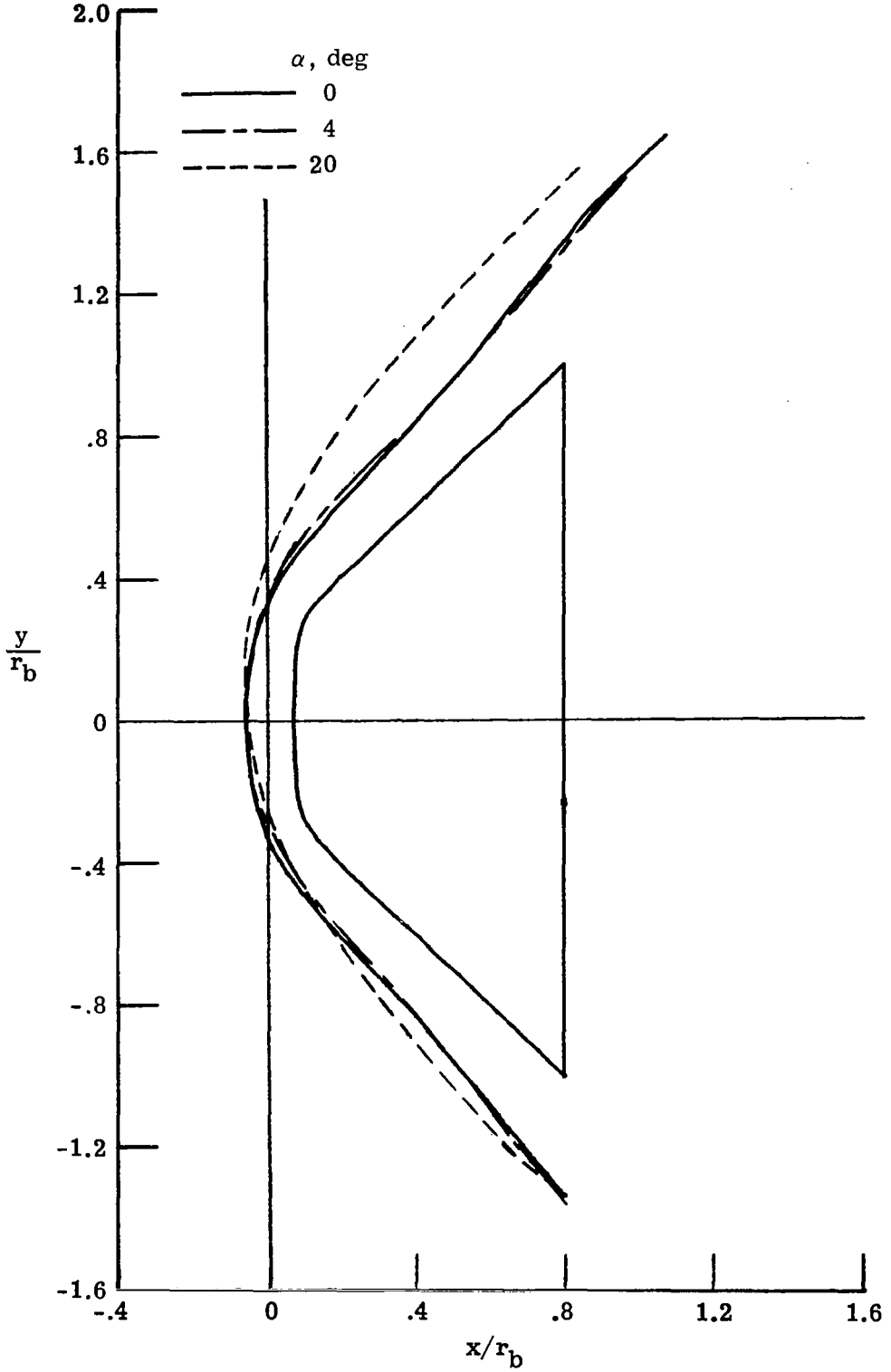

(b) Flattened-nose cone (model 6).

Figure 21.- Continued.

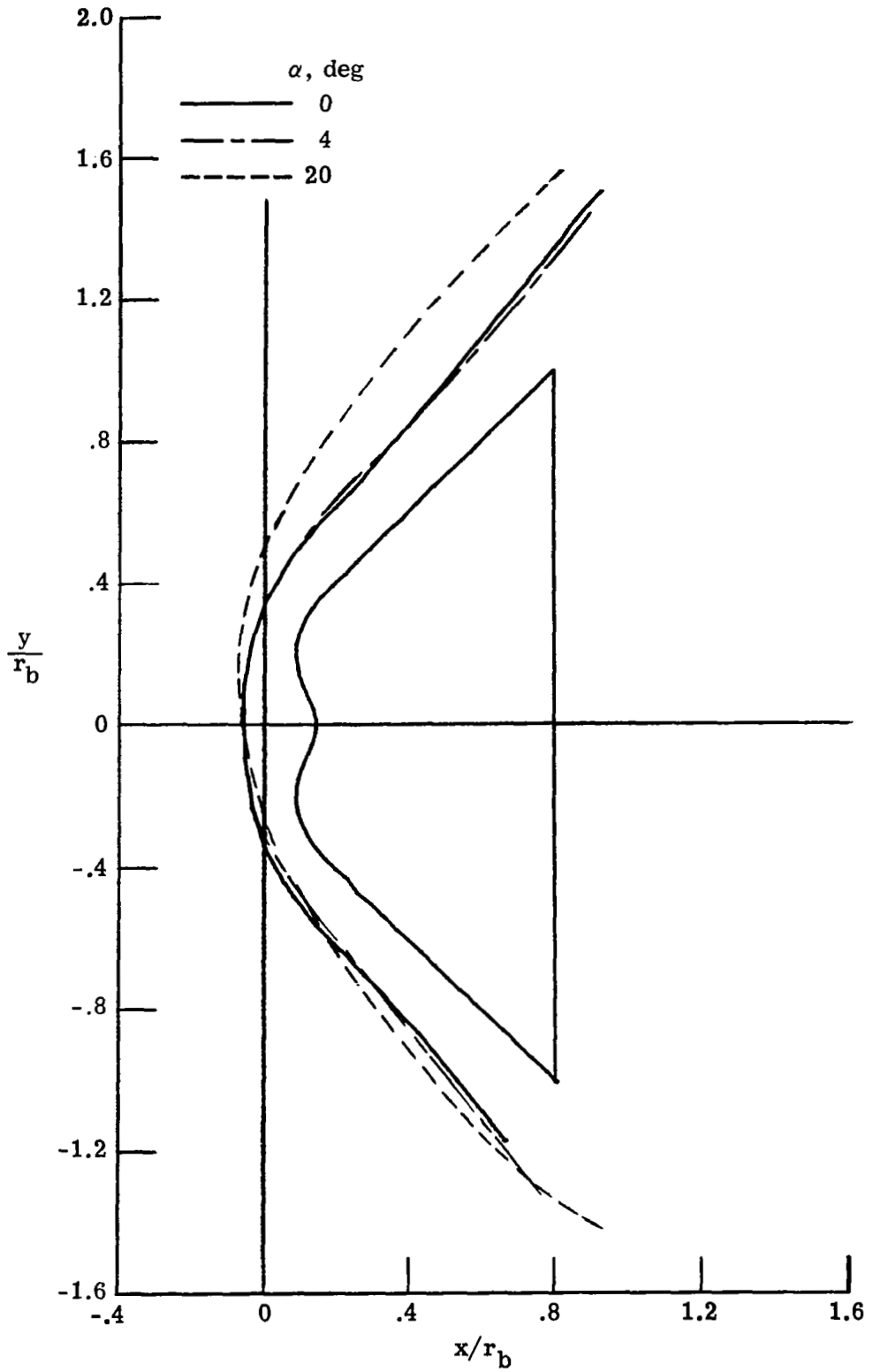

(c) Concave-nose cone (model 7).

Figure 21.- Continued.

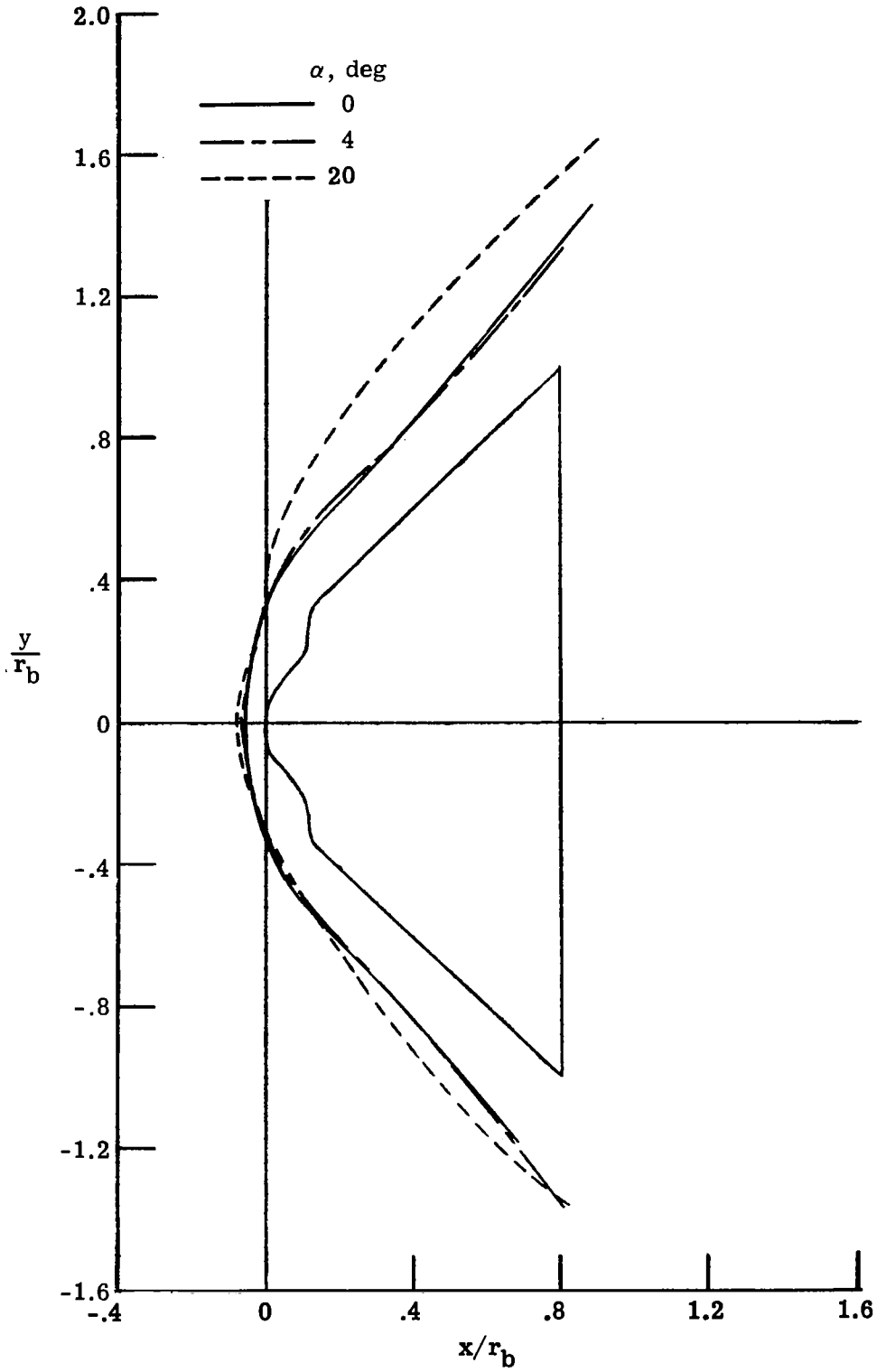

(d) Cusp-nose cone (model 8).

Figure 21.- Concluded.

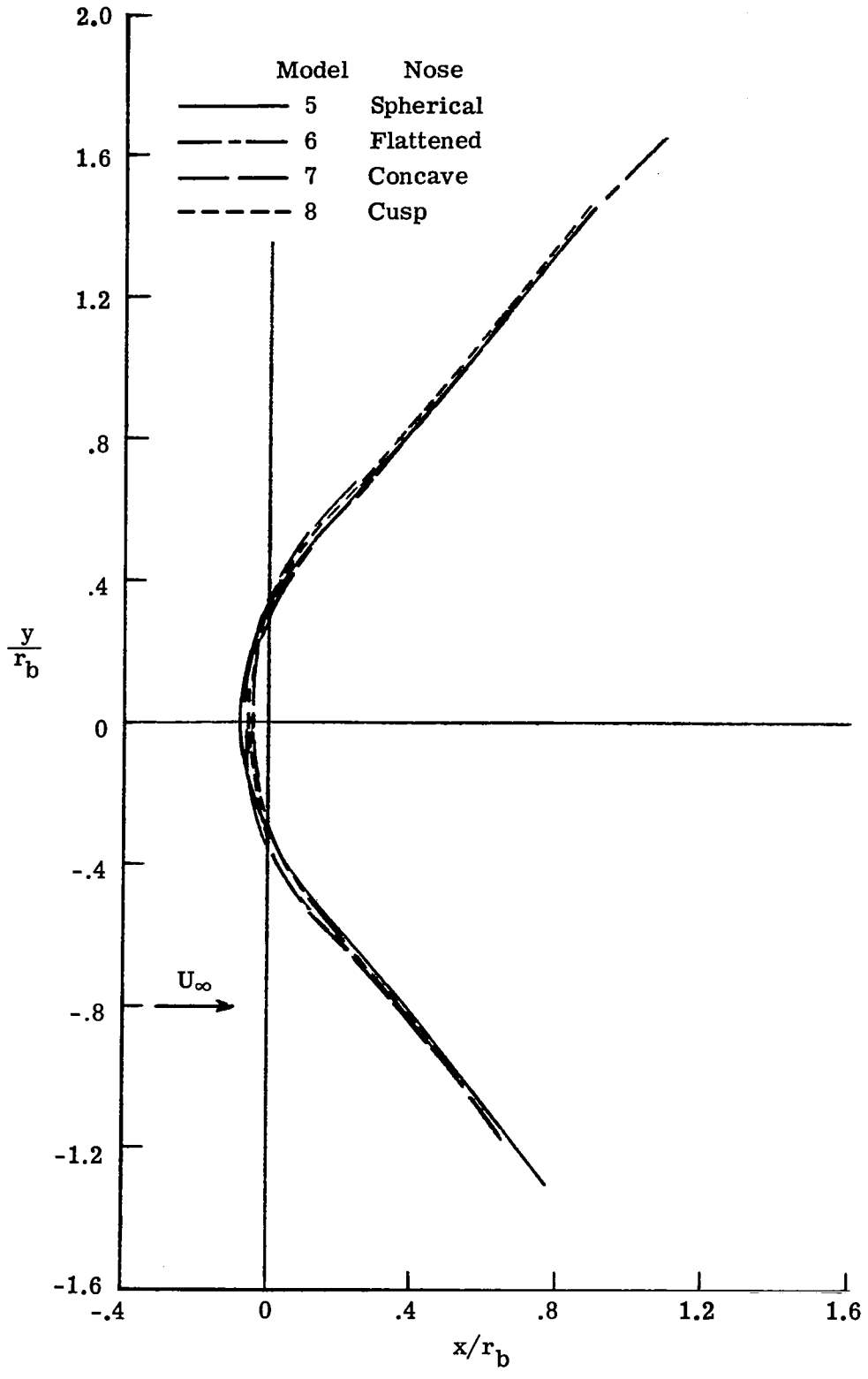

(a) $\alpha = 0°$.

Figure 22.- Effect of nose shape (models 5 to 8) on measured shock shape in air. $M_\infty = 5.915$.

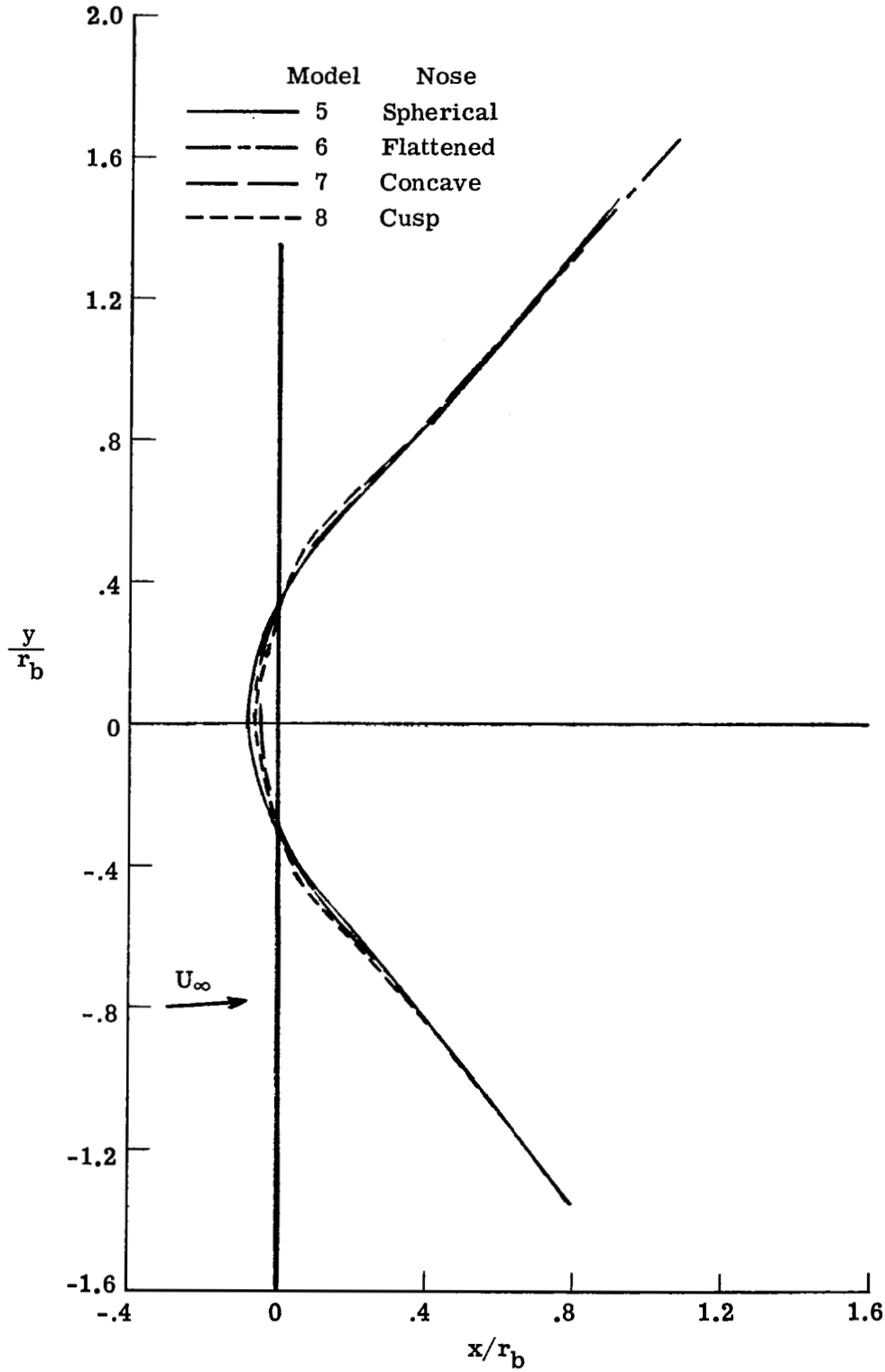

(b) $\alpha = 4°$.

Figure 22.- Continued.

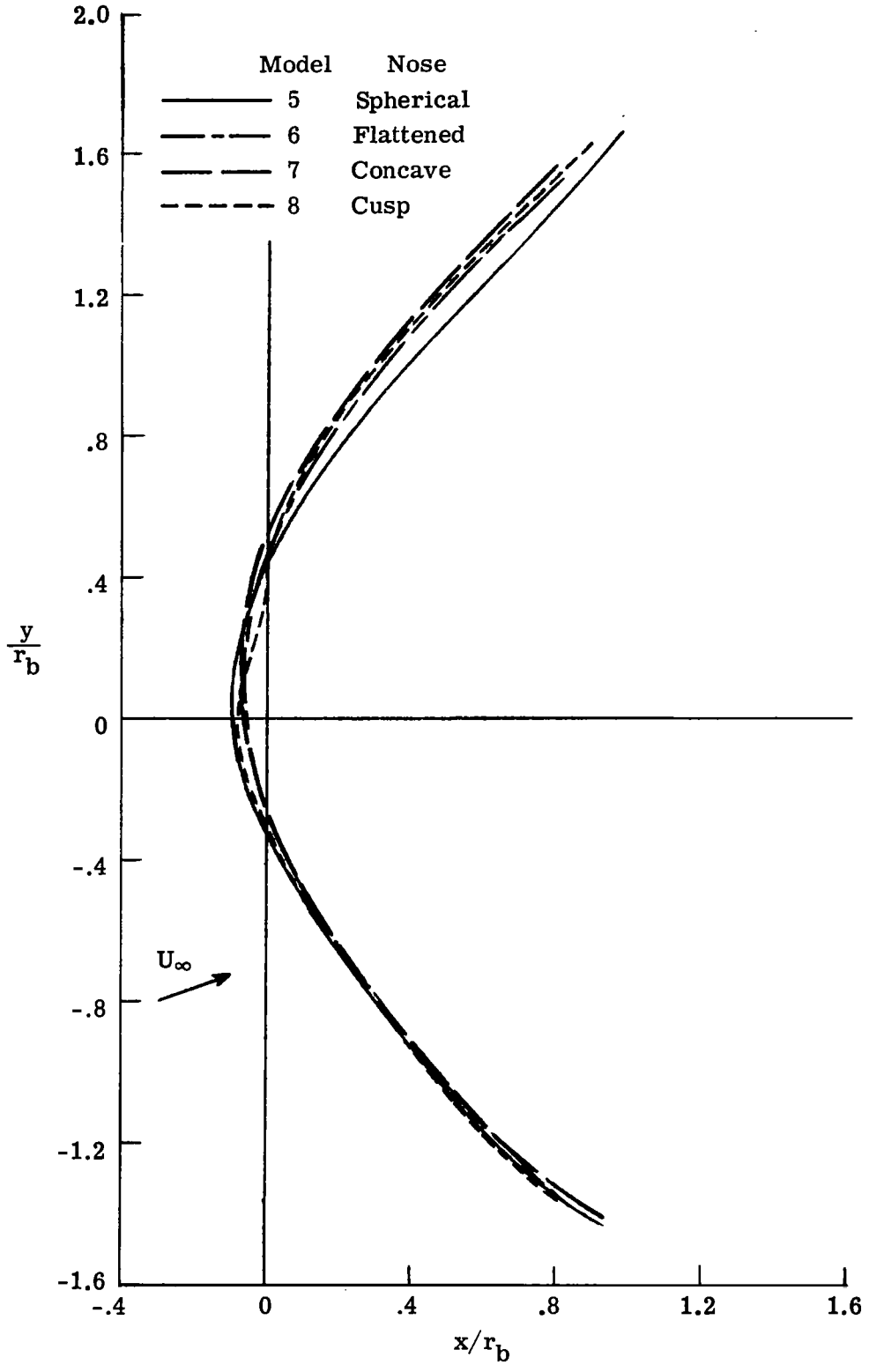

(c) $\alpha = 20°$.

Figure 22.- Concluded.

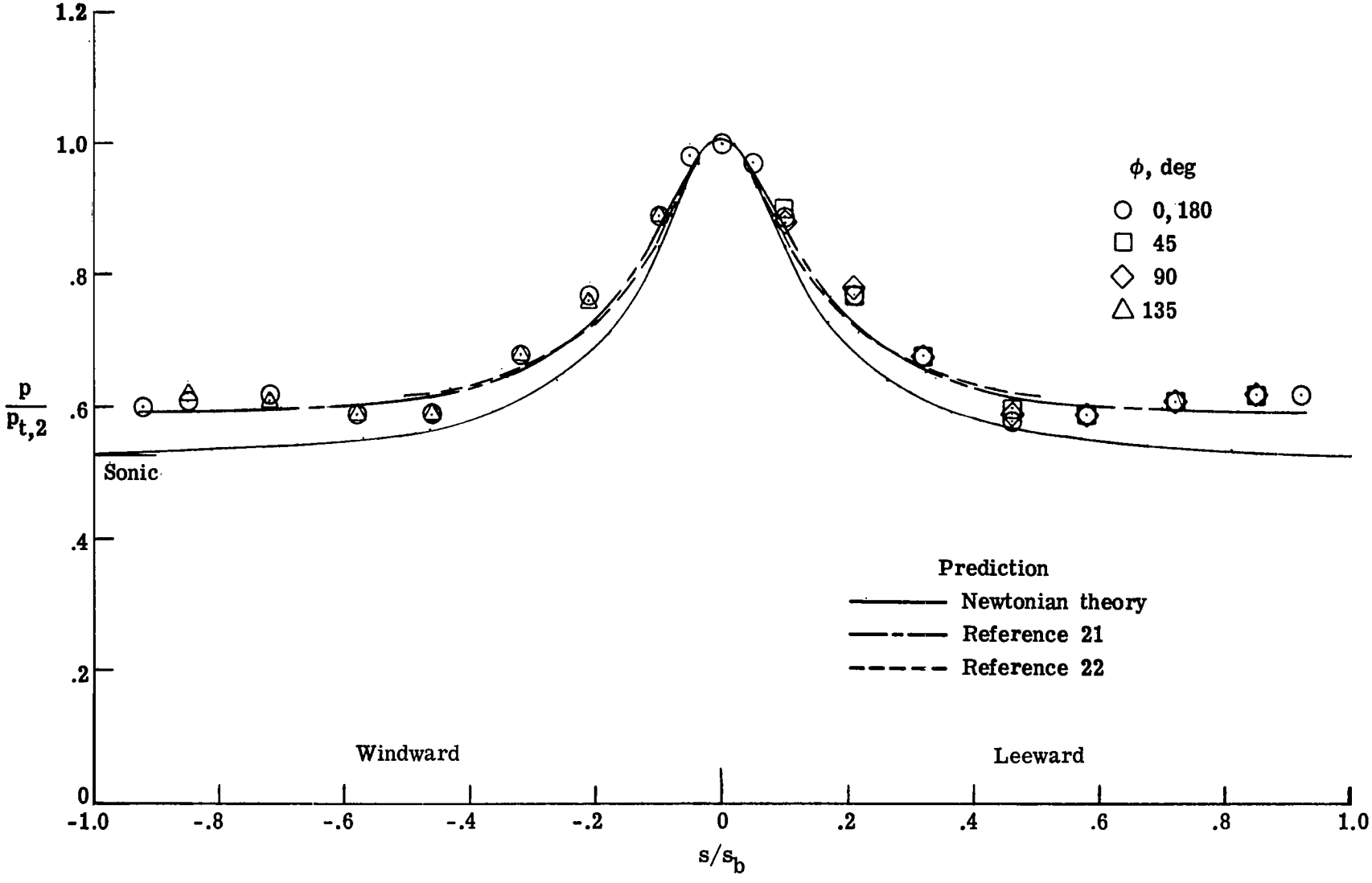

(a) $\alpha = 0°$.

Figure 23.- Pressure distributions measured on the hyperboloid (model $1_{,5}$ series 1) in Mach 5.93 air at various angles of attack. $N_{Re,\infty,d_b} = 7 \times 10^5$.

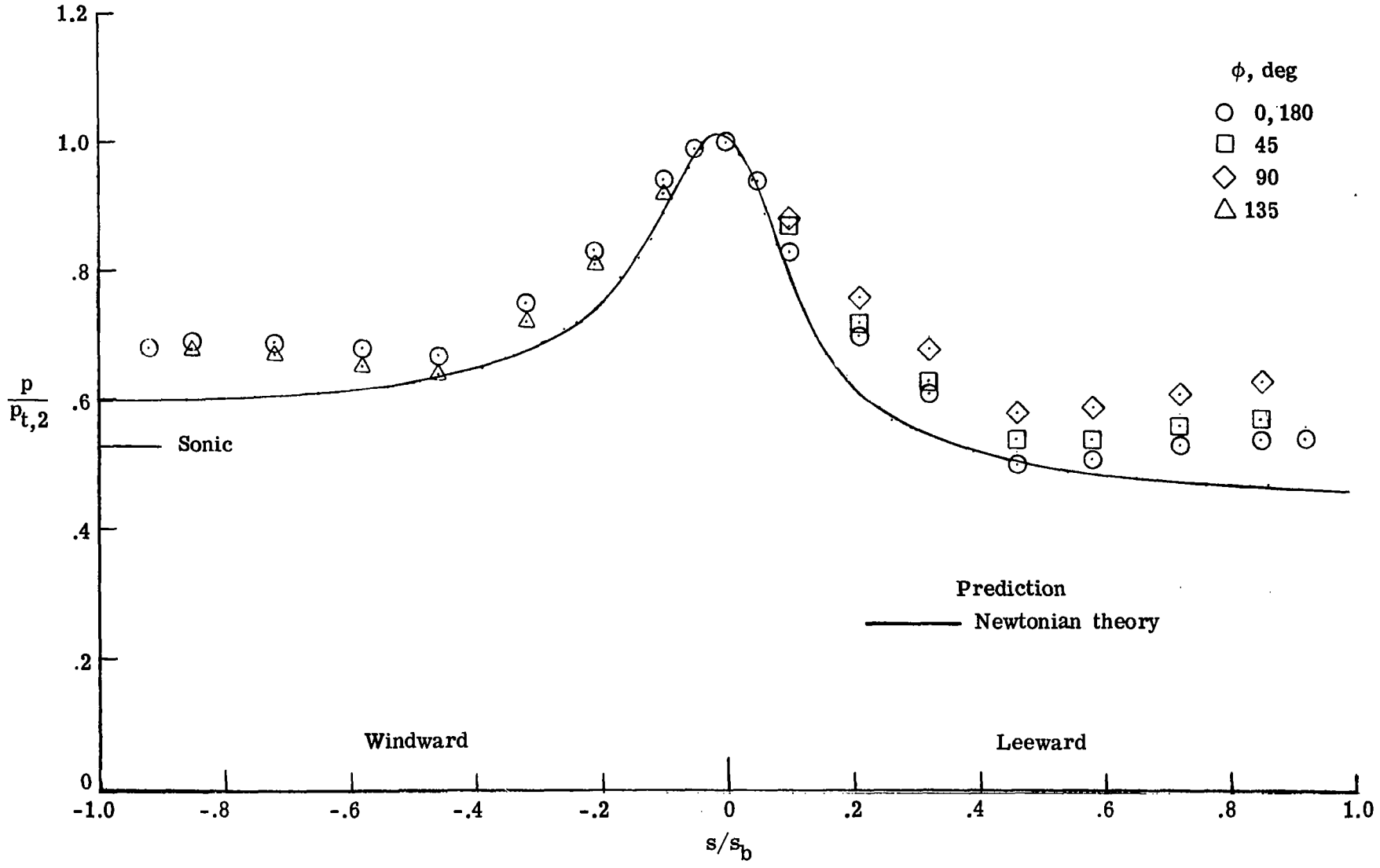

(b) $\alpha = 4°$.

Figure 23.- Continued.

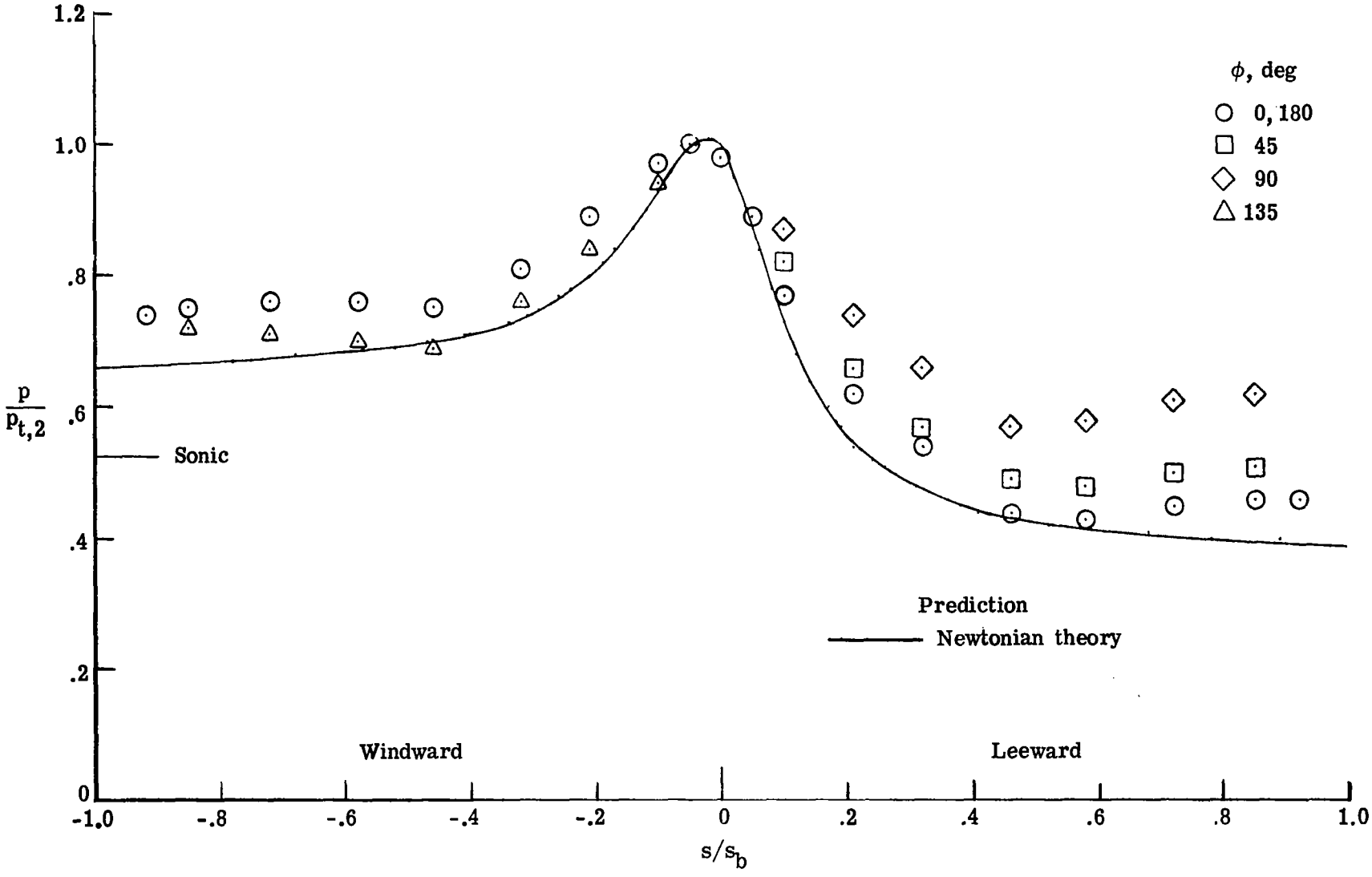

(c) $\alpha = 8°$.

Figure 23.- Continued.

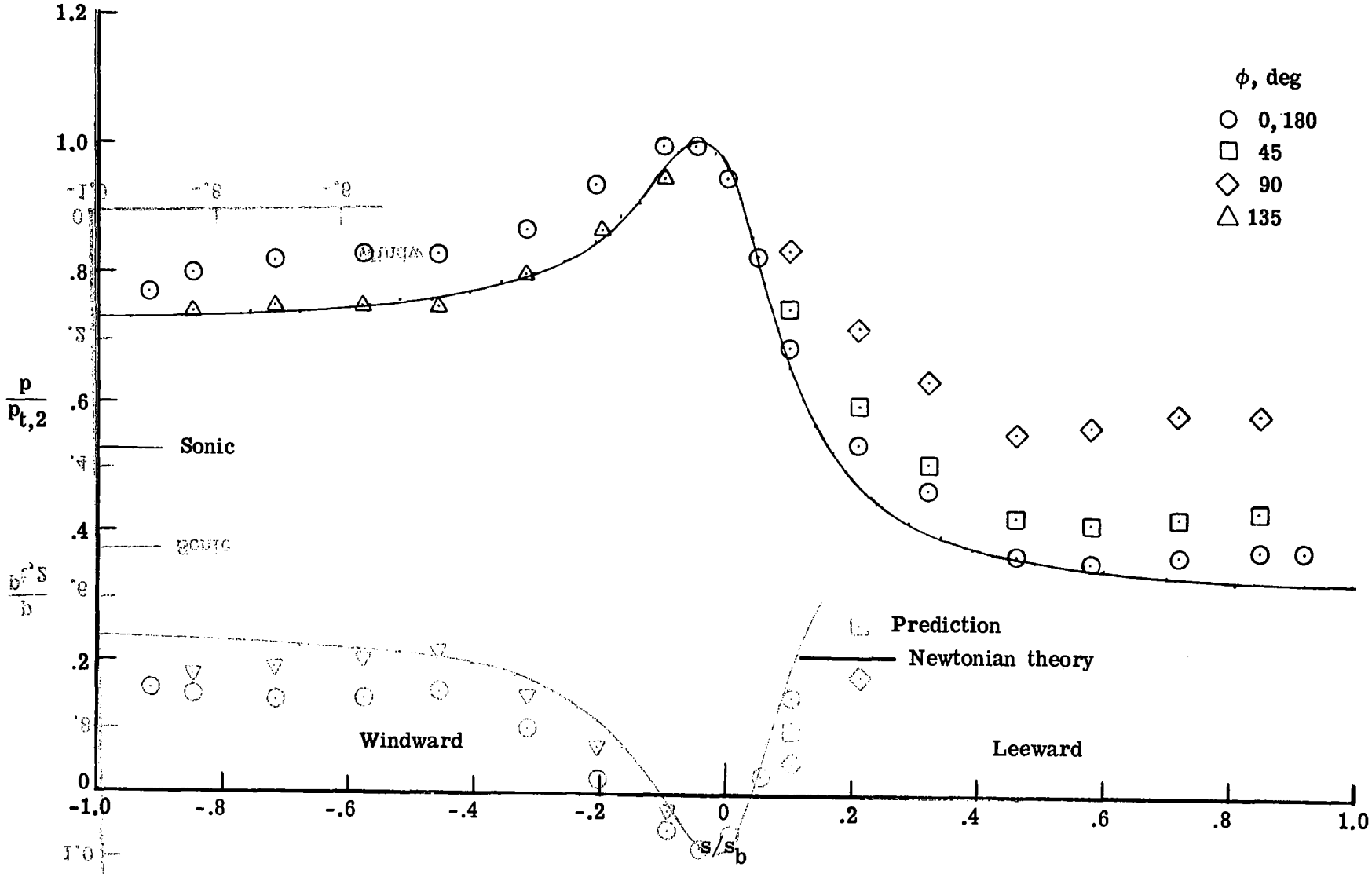

(d) $\alpha = 12°$.

Figure 23.- Continued.

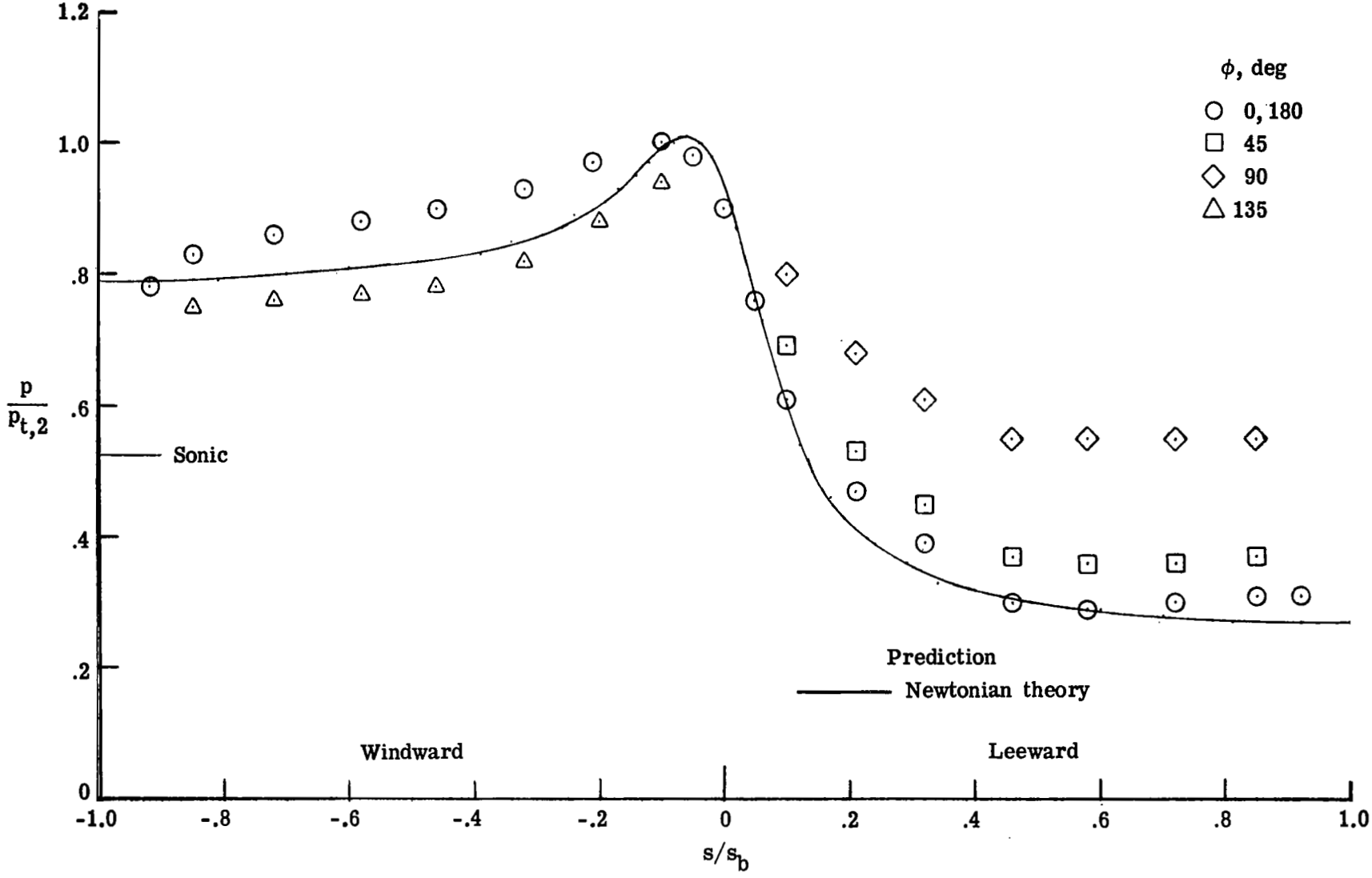

(e) $\alpha = 16°$.

Figure 23.- Continued.

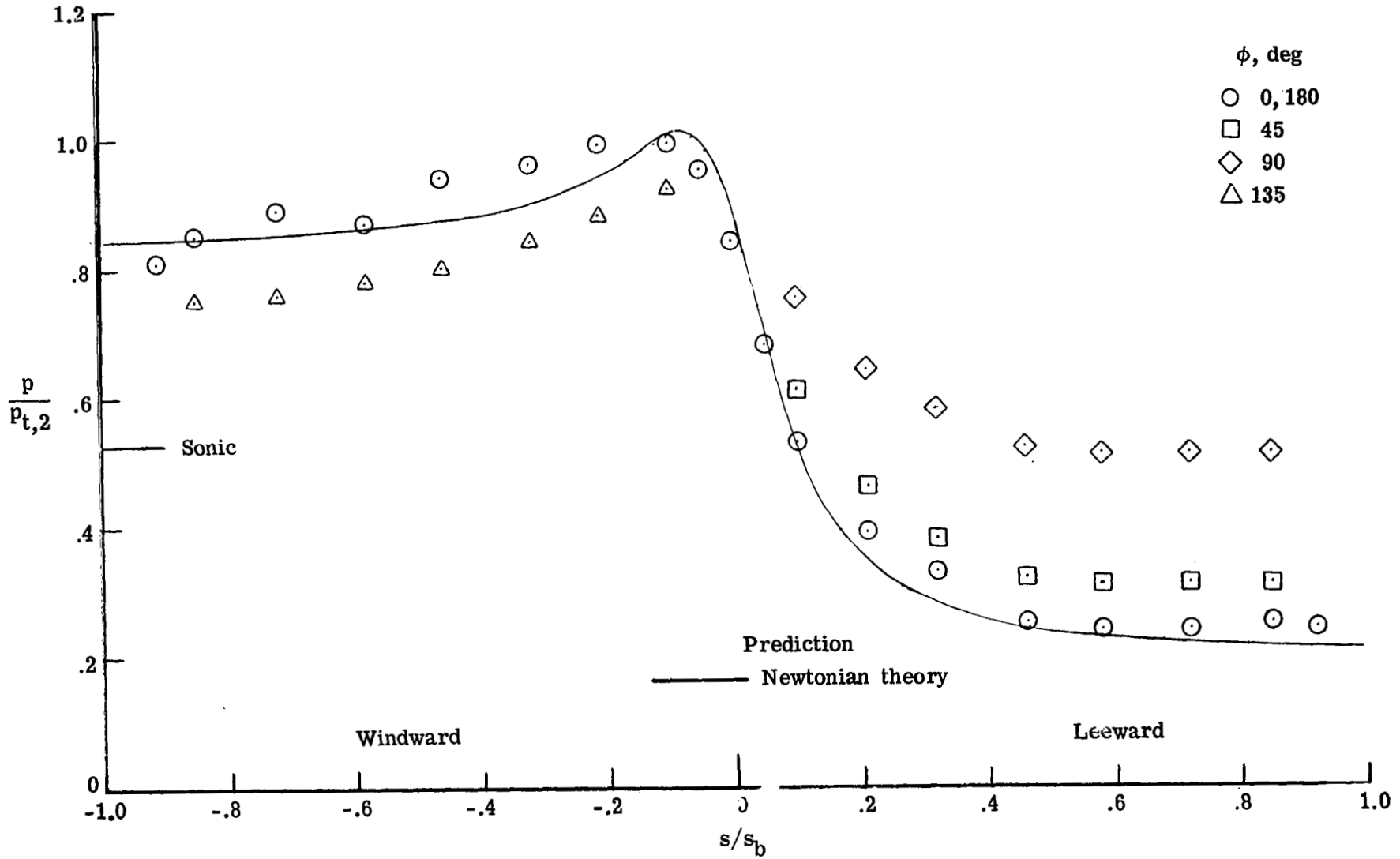

(f) $\alpha = 20°$.

Figure 23.- Concluded.

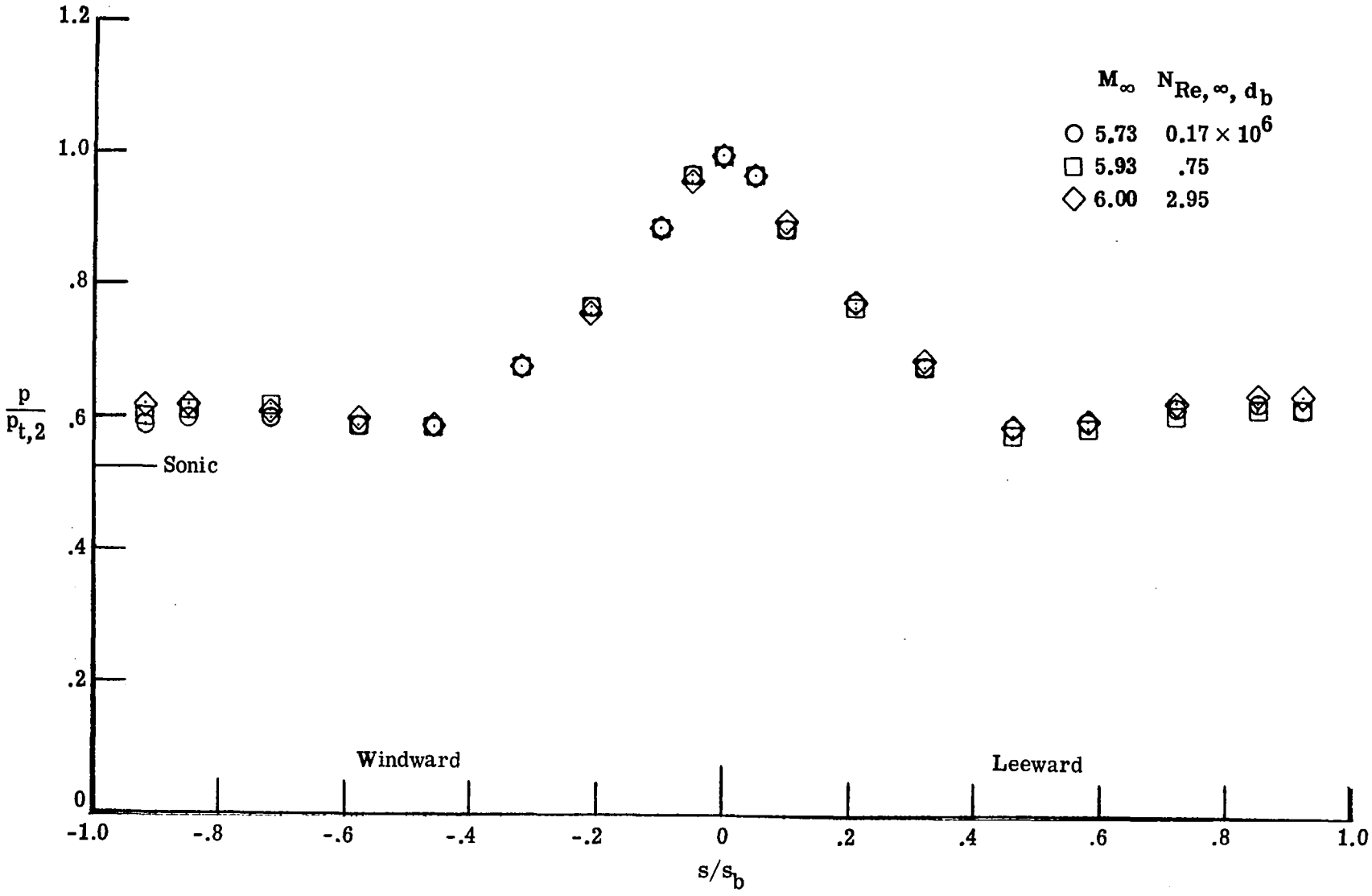

(a) $\alpha = 0°$.

Figure 24.- Effect of free-stream Reynolds number on pressure distributions in air for the most windward and leeward rays of the hyperboloid (model 1, series 1).

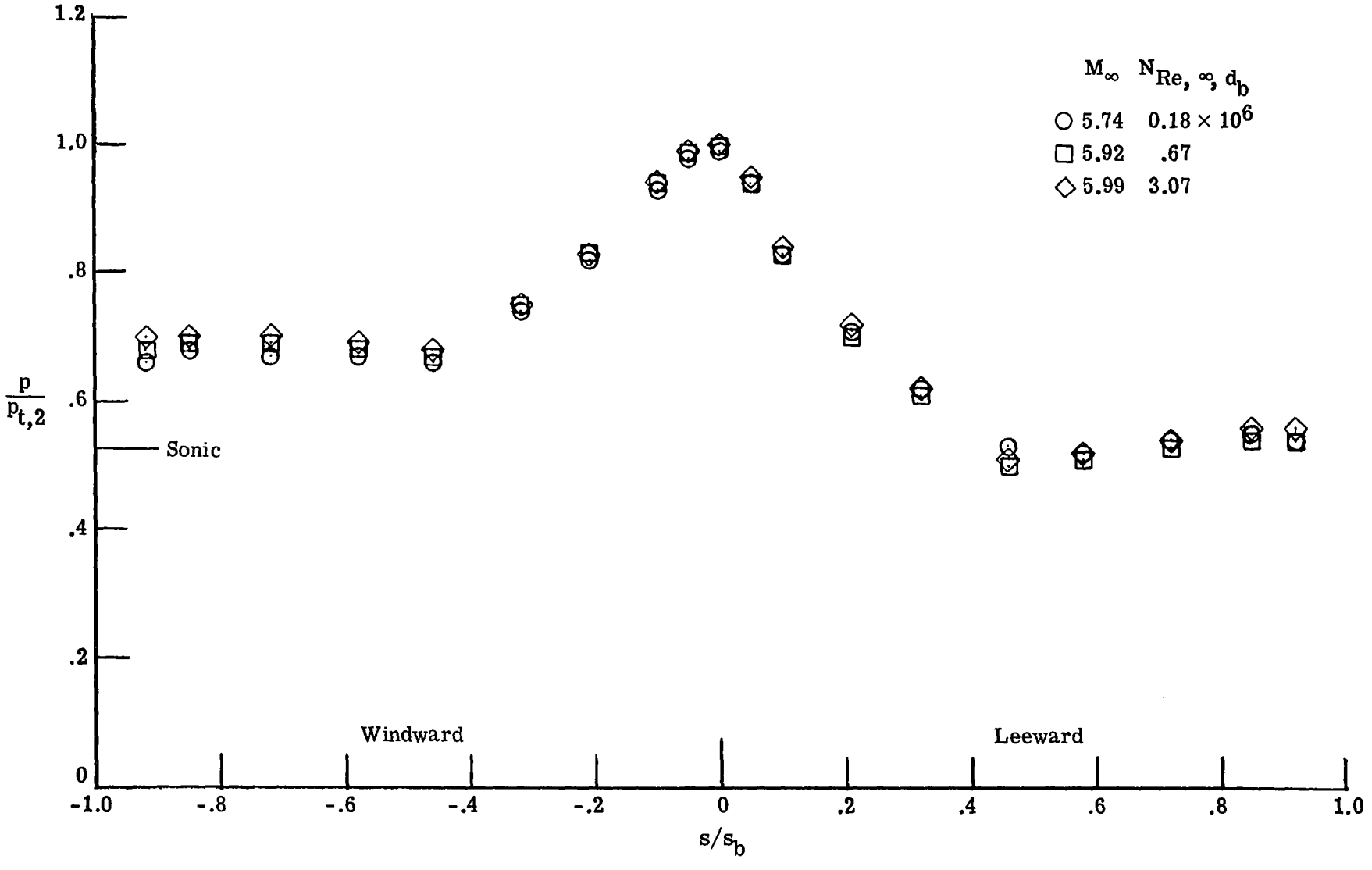

(b) $\alpha = 4°$.

Figure 24.- Continued.

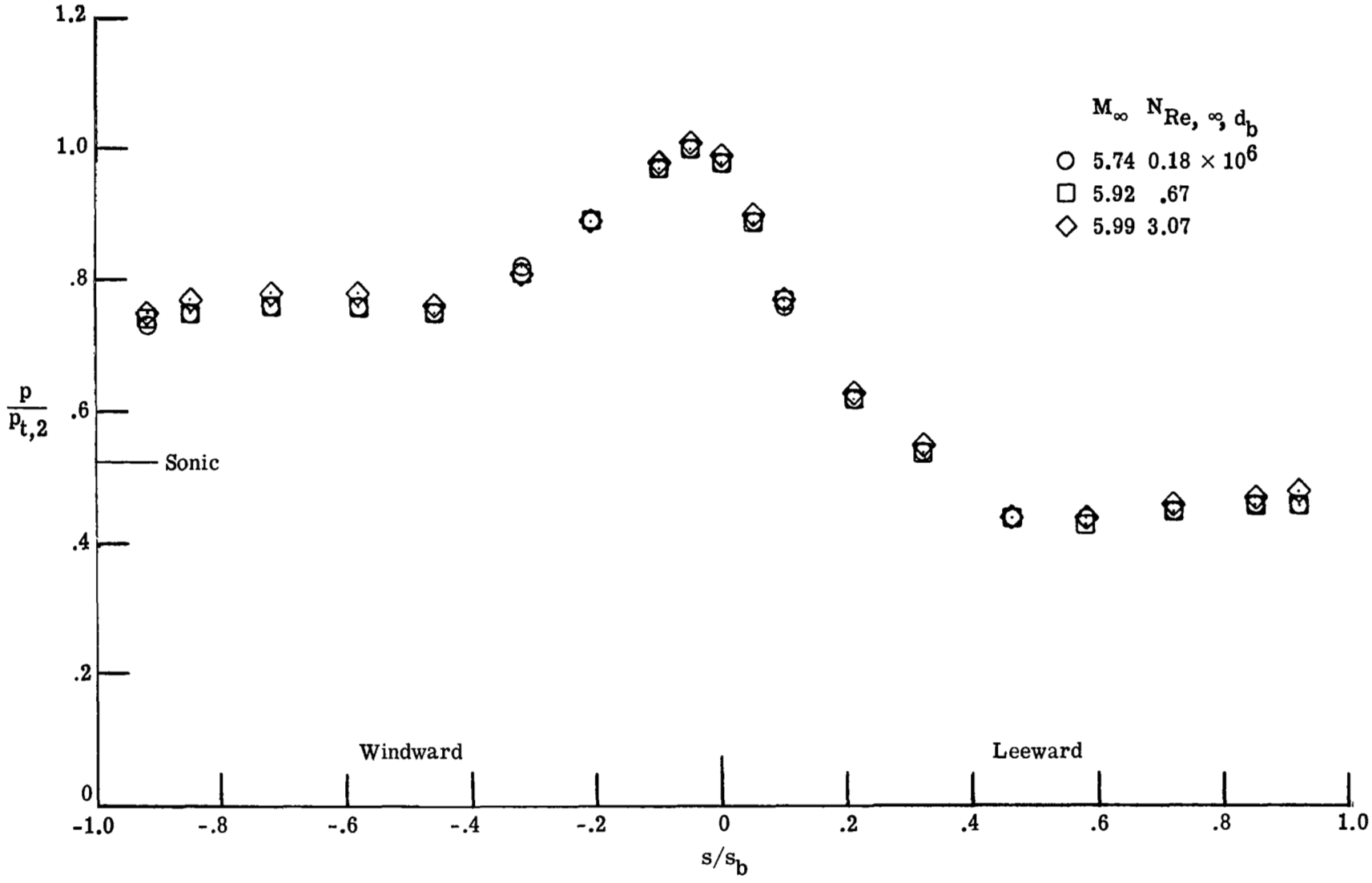

(c) $\alpha = 8°$.

Figure 24.- Continued.

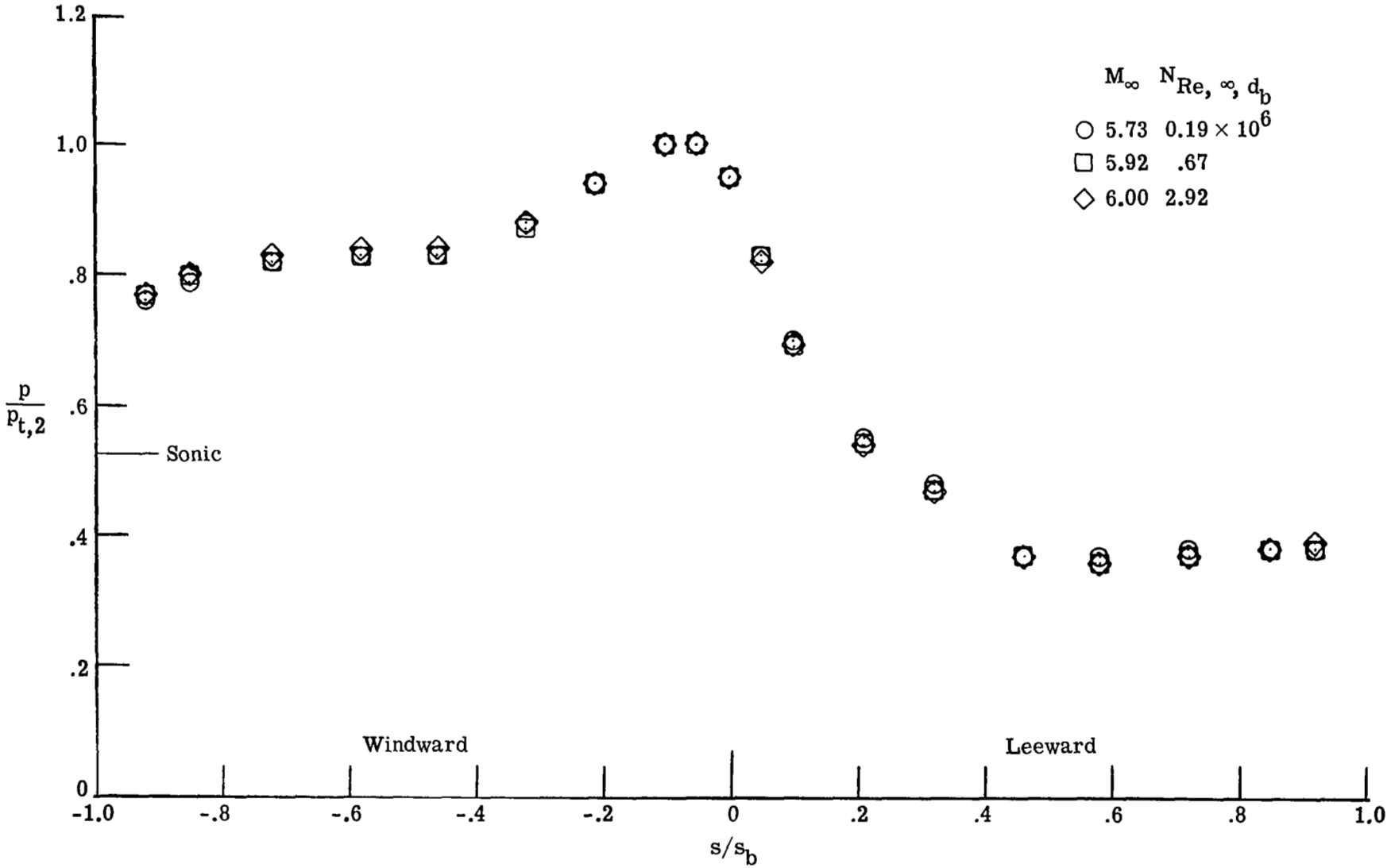

(d) $\alpha = 12°$.

Figure 24.- Continued.

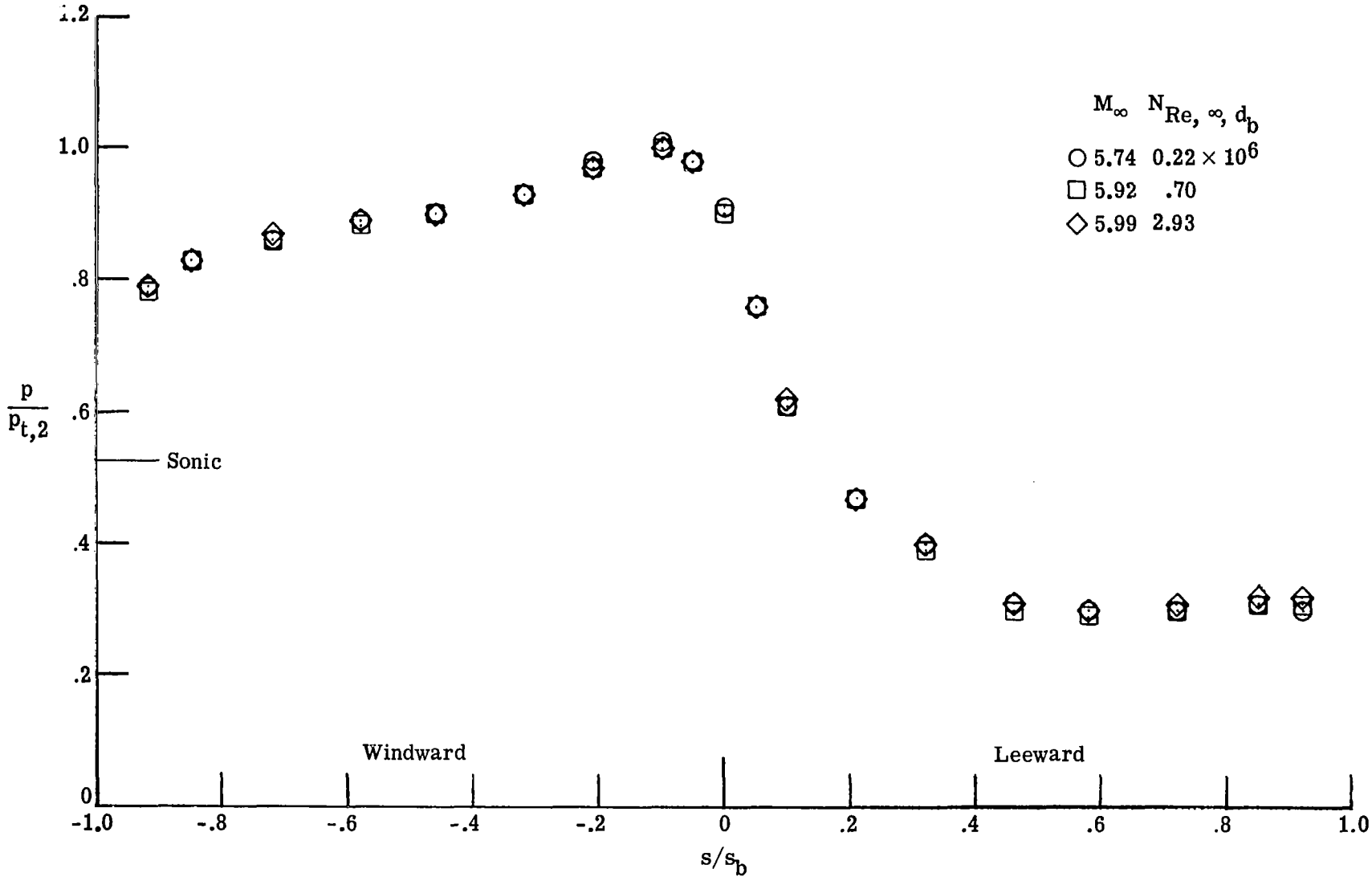

(e) $\alpha = 16°$.

Figure 24.- Continued.

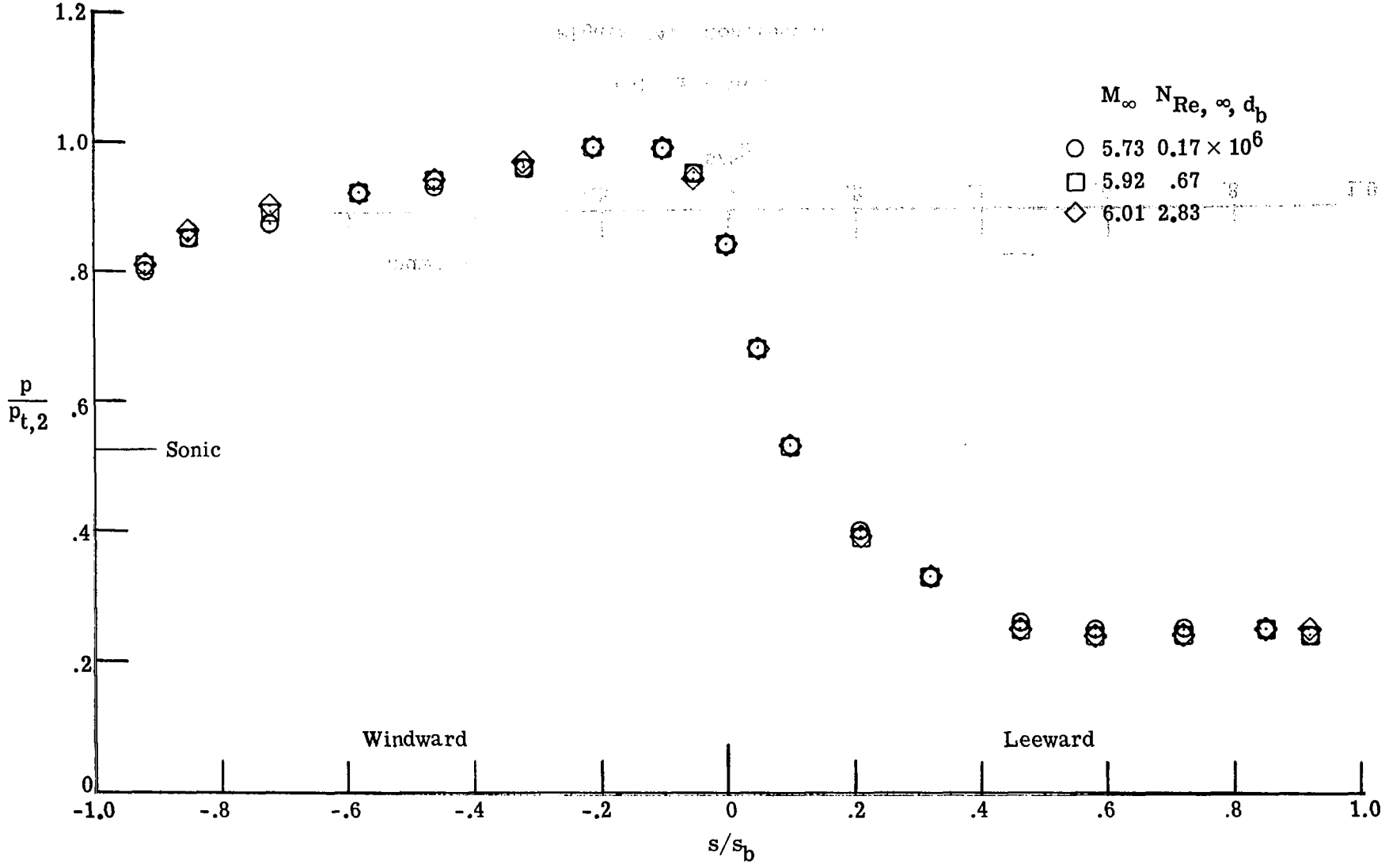

(f) $\alpha = 20°$.

Figure 24.- Concluded.

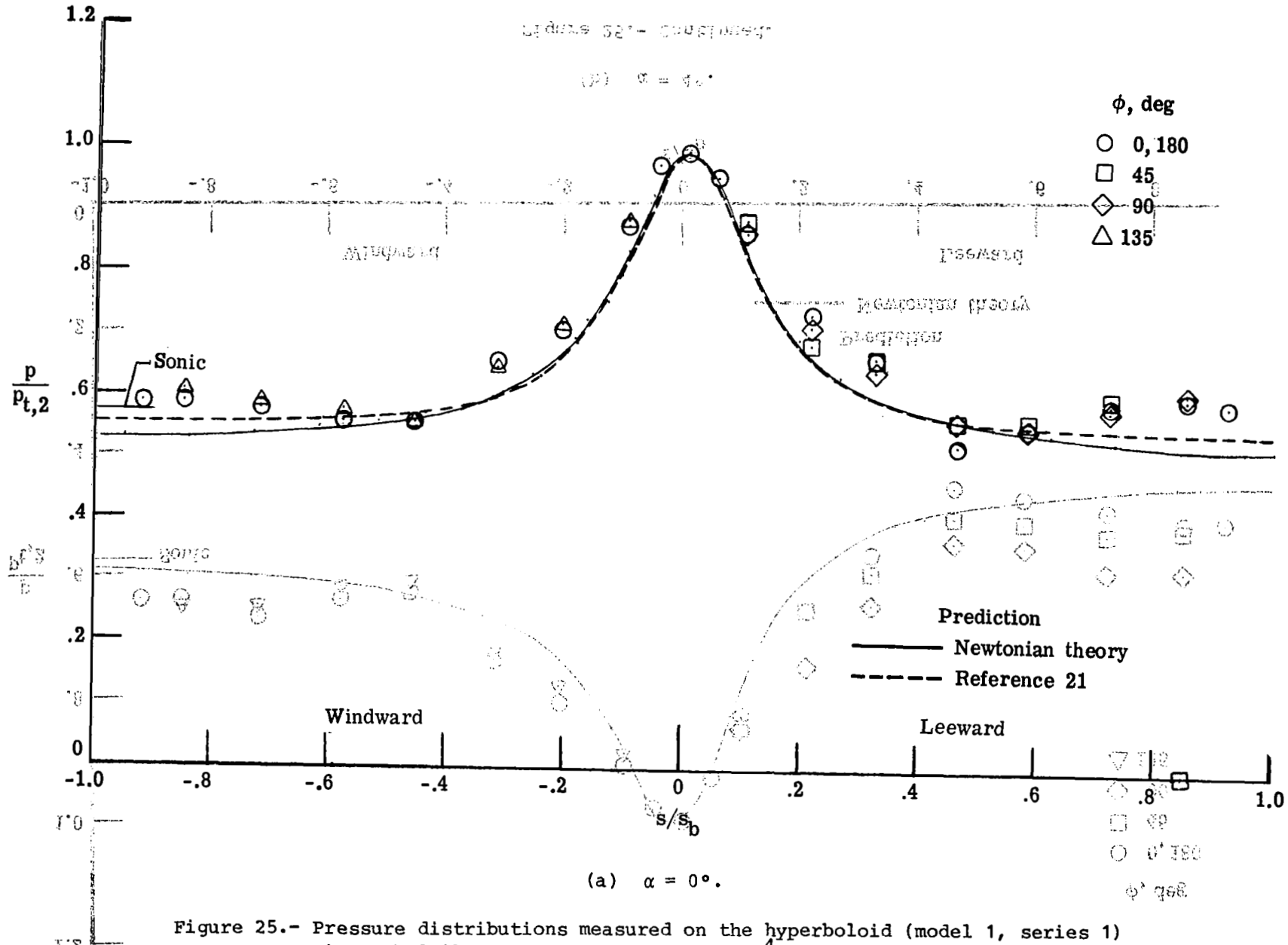

(a) $\alpha = 0°$.

Figure 25.- Pressure distributions measured on the hyperboloid (model 1, series 1) in Mach 6.13 CF_4. $N_{Re,\infty,d_b} = 7.8 \times 10^4$; $\rho_2/\rho_\infty = 12.06$.

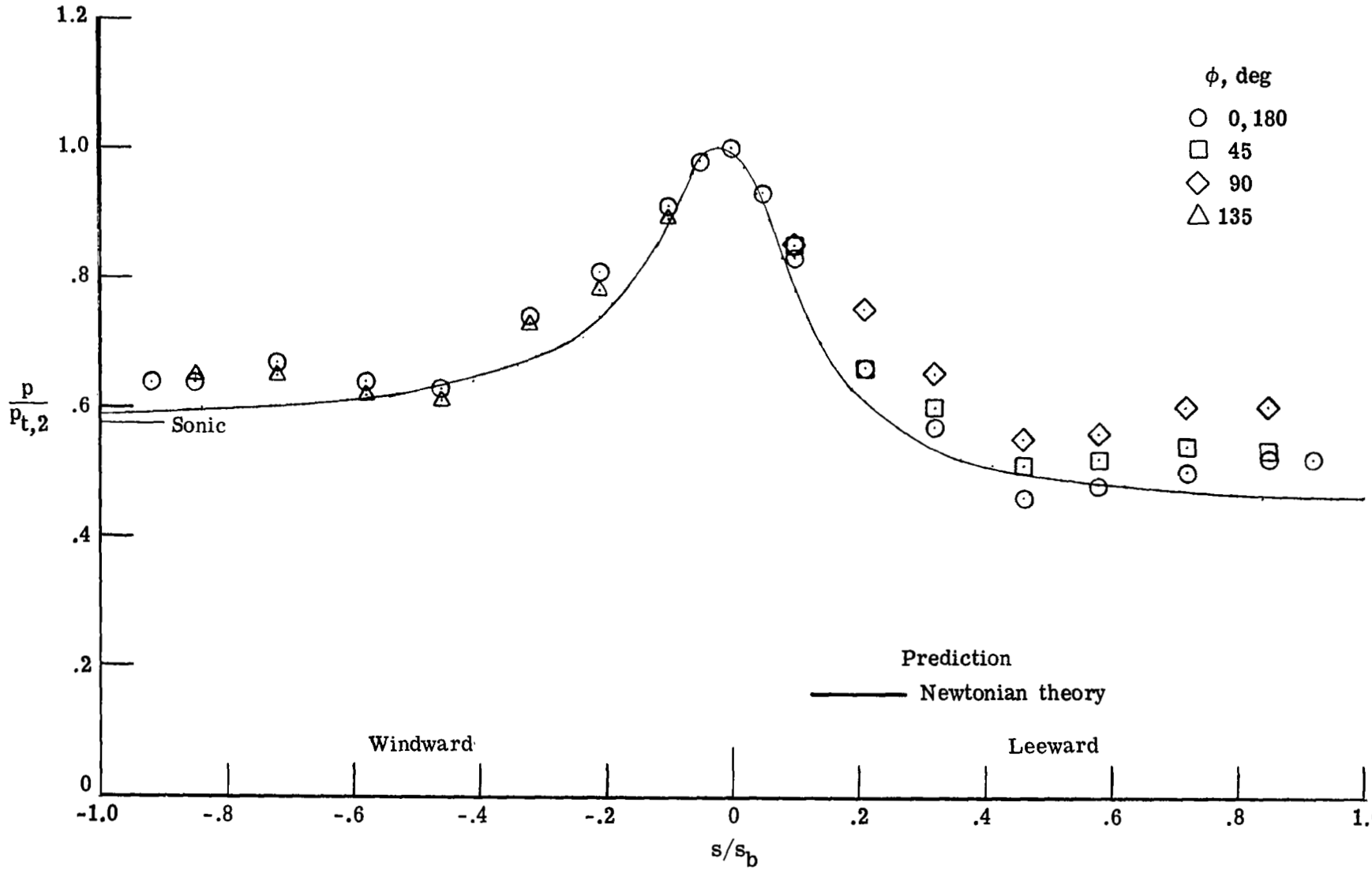

(b) $\alpha = 4°$.

Figure 25.- Continued.

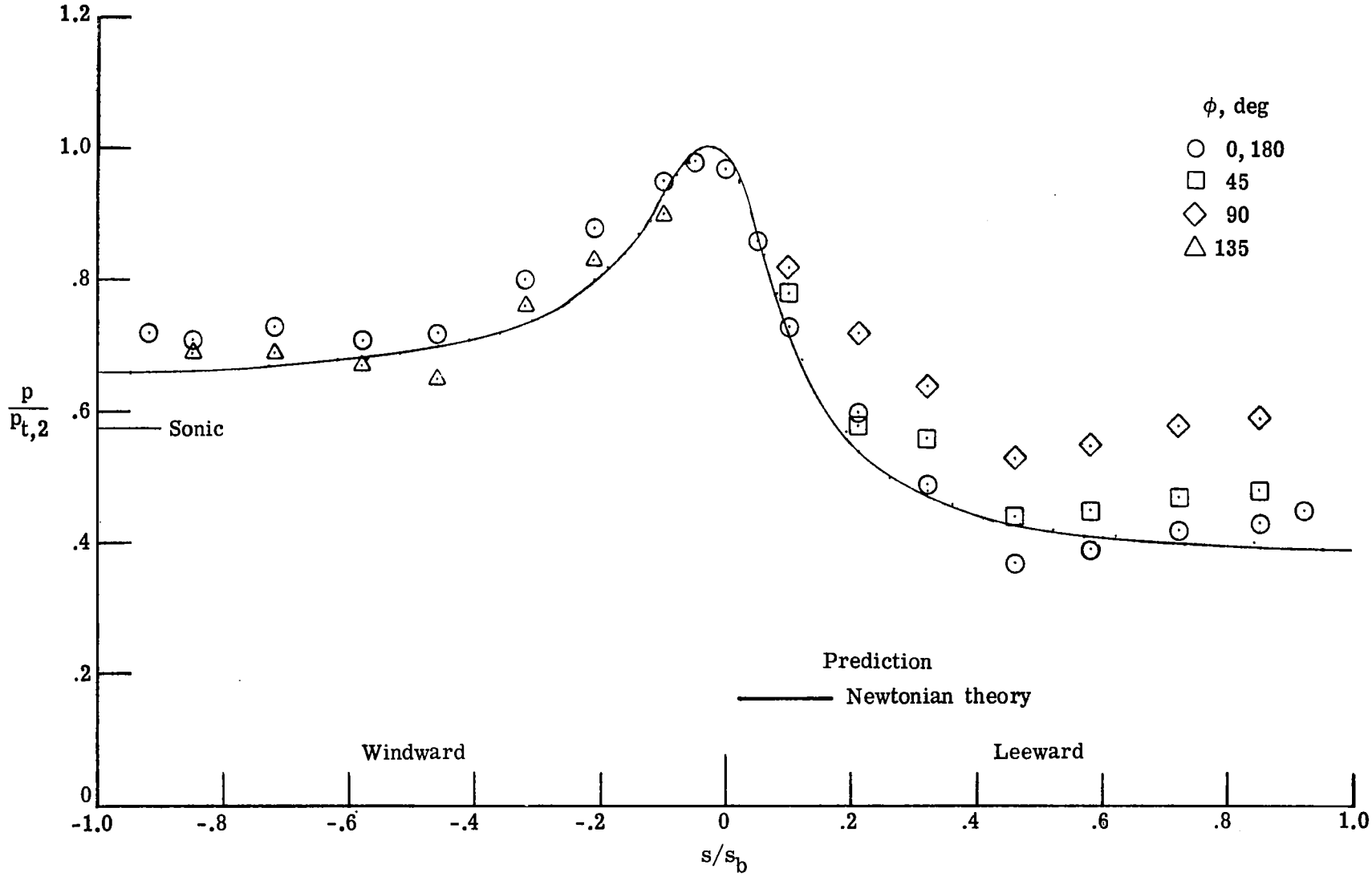

(c) $\alpha = 8°$.

Figure 25.- Continued.

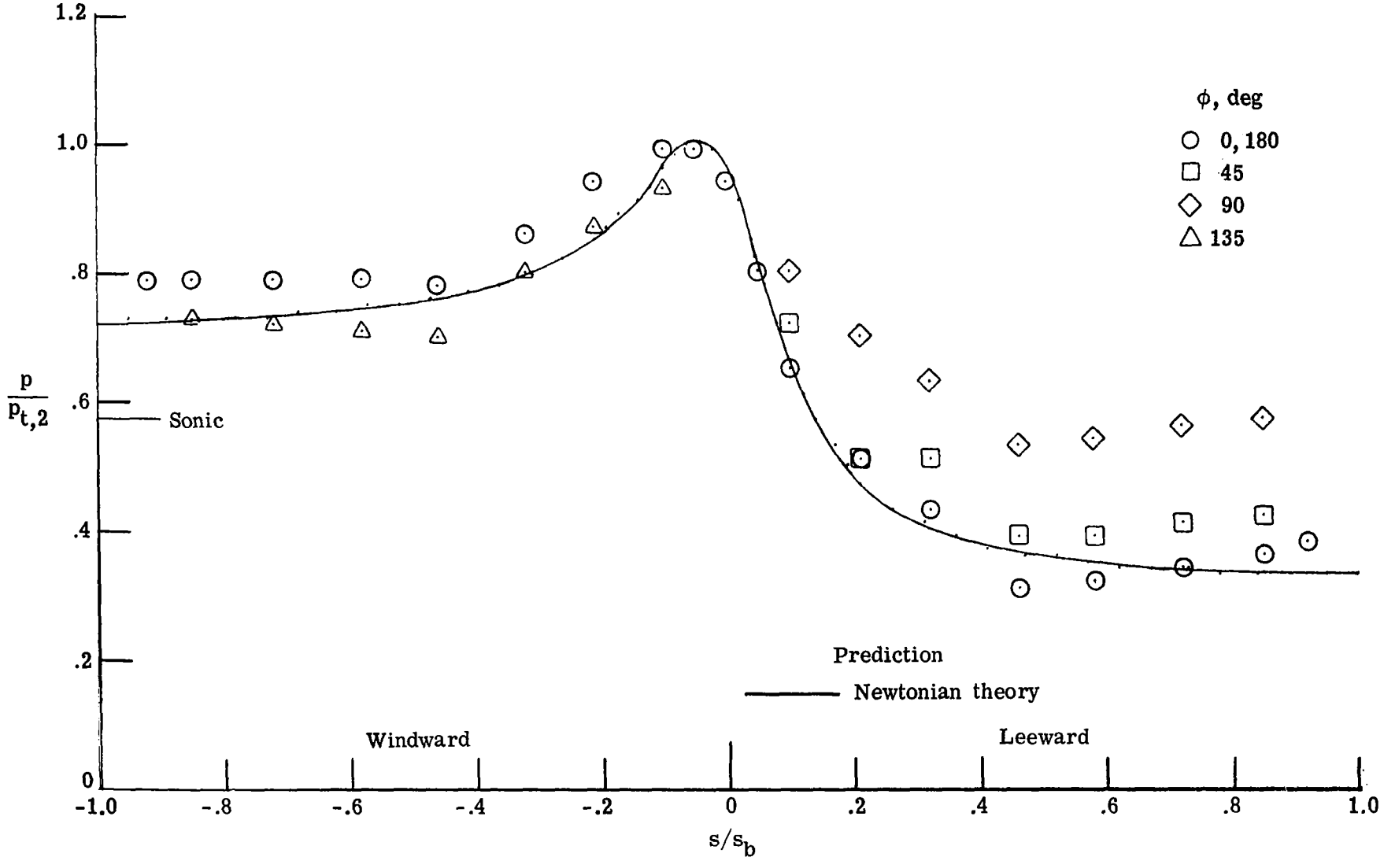

(d) $\alpha = 12°$.

Figure 25.- Continued.

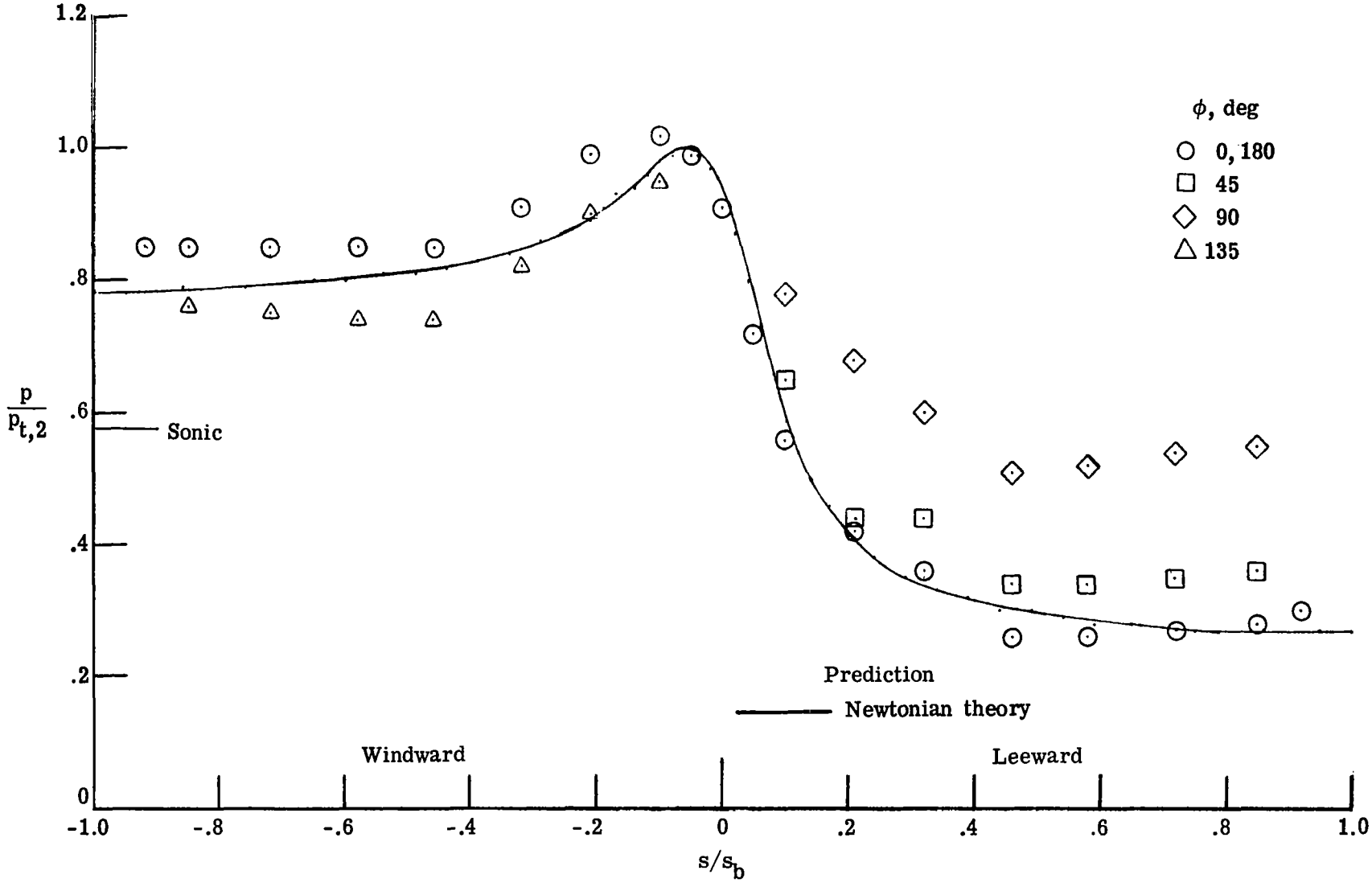

(e) $\alpha = 16°$.

Figure 25.- Continued.

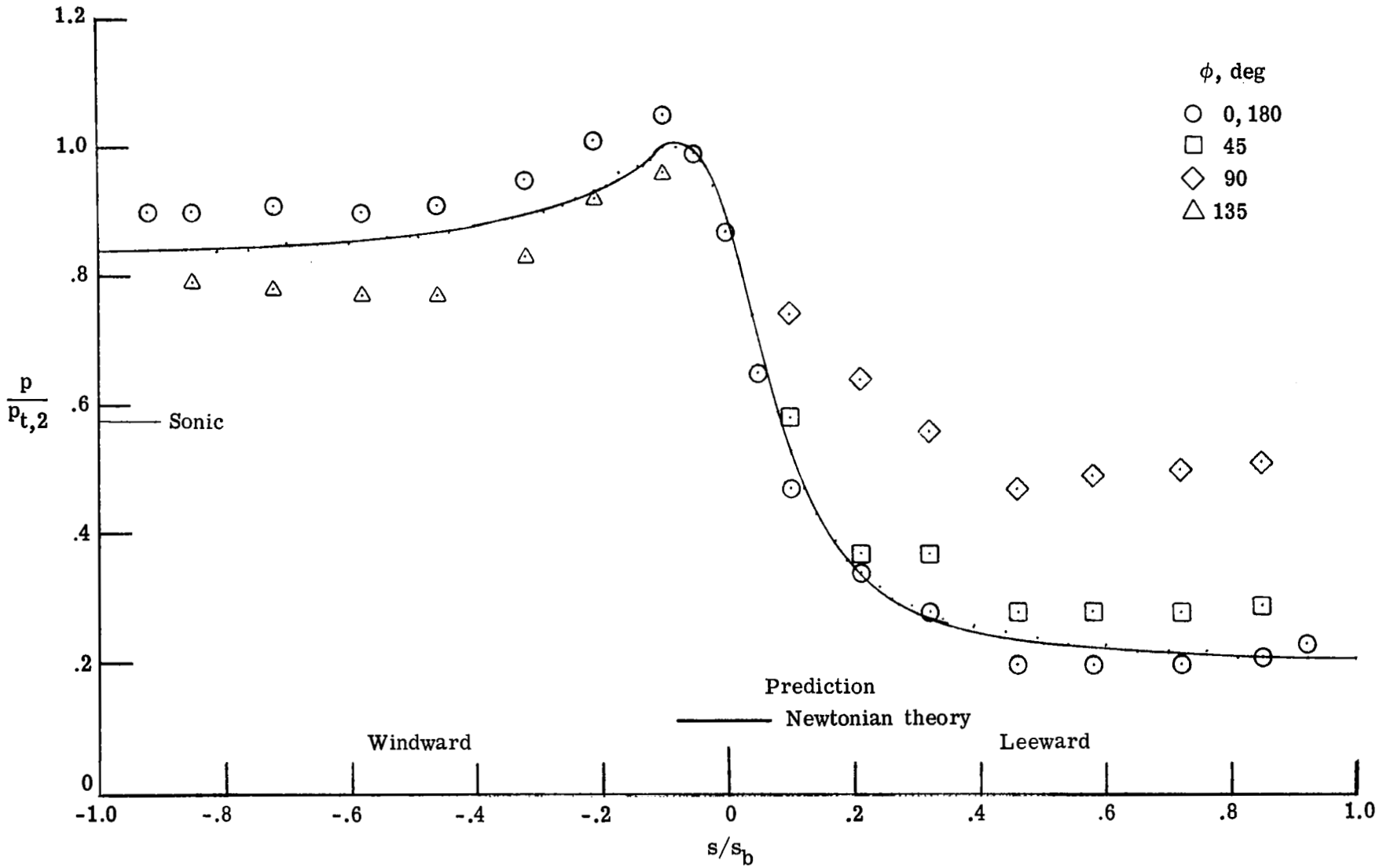

(f) $\alpha = 20°$.

Figure 25.- Concluded.

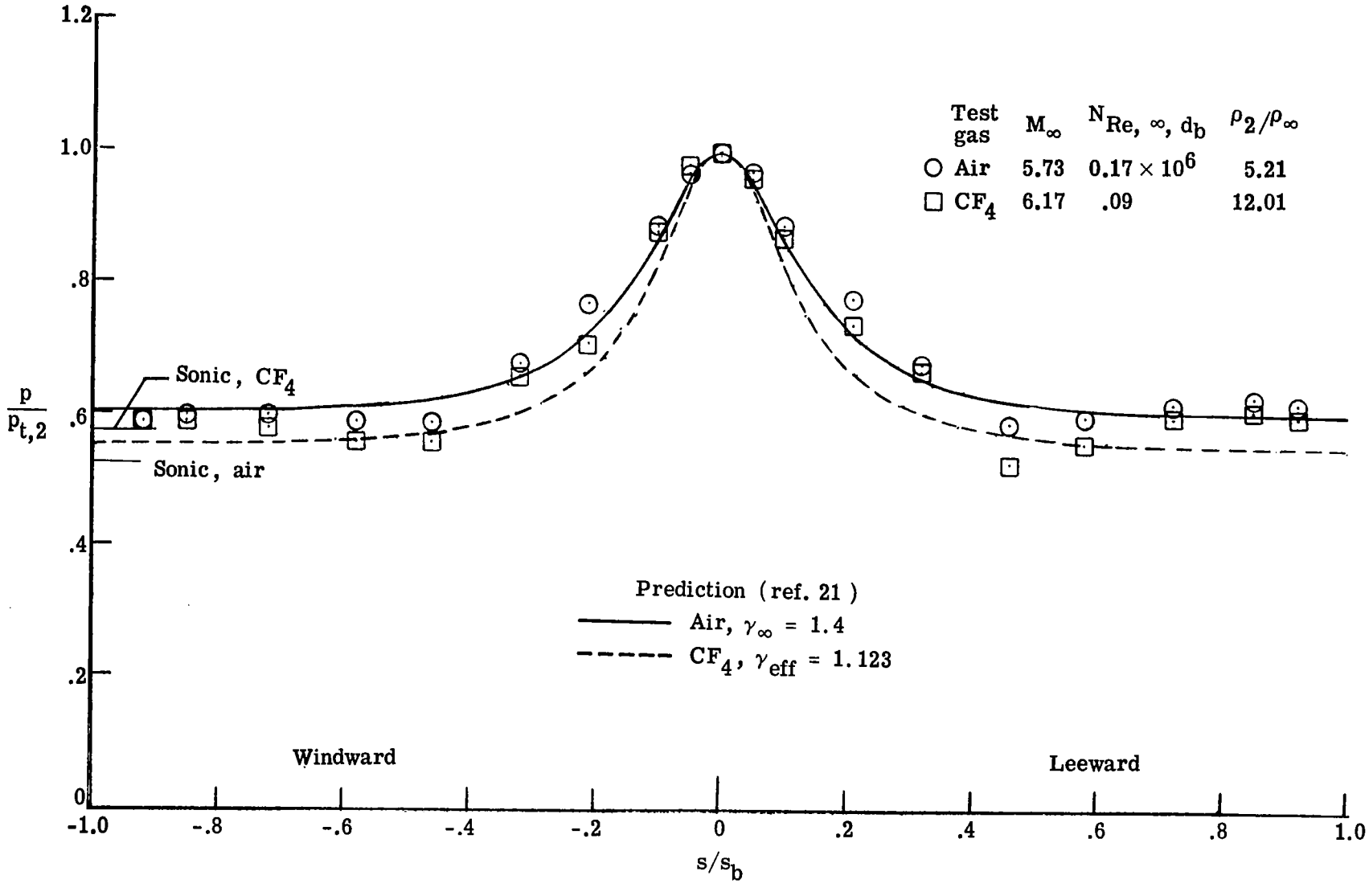

(a) $\alpha = 0°$.

Figure 26.- Effect of normal-shock density ratio on pressure distributions along the most windward and leeward rays of the hyperboloid (model 1, series 1).

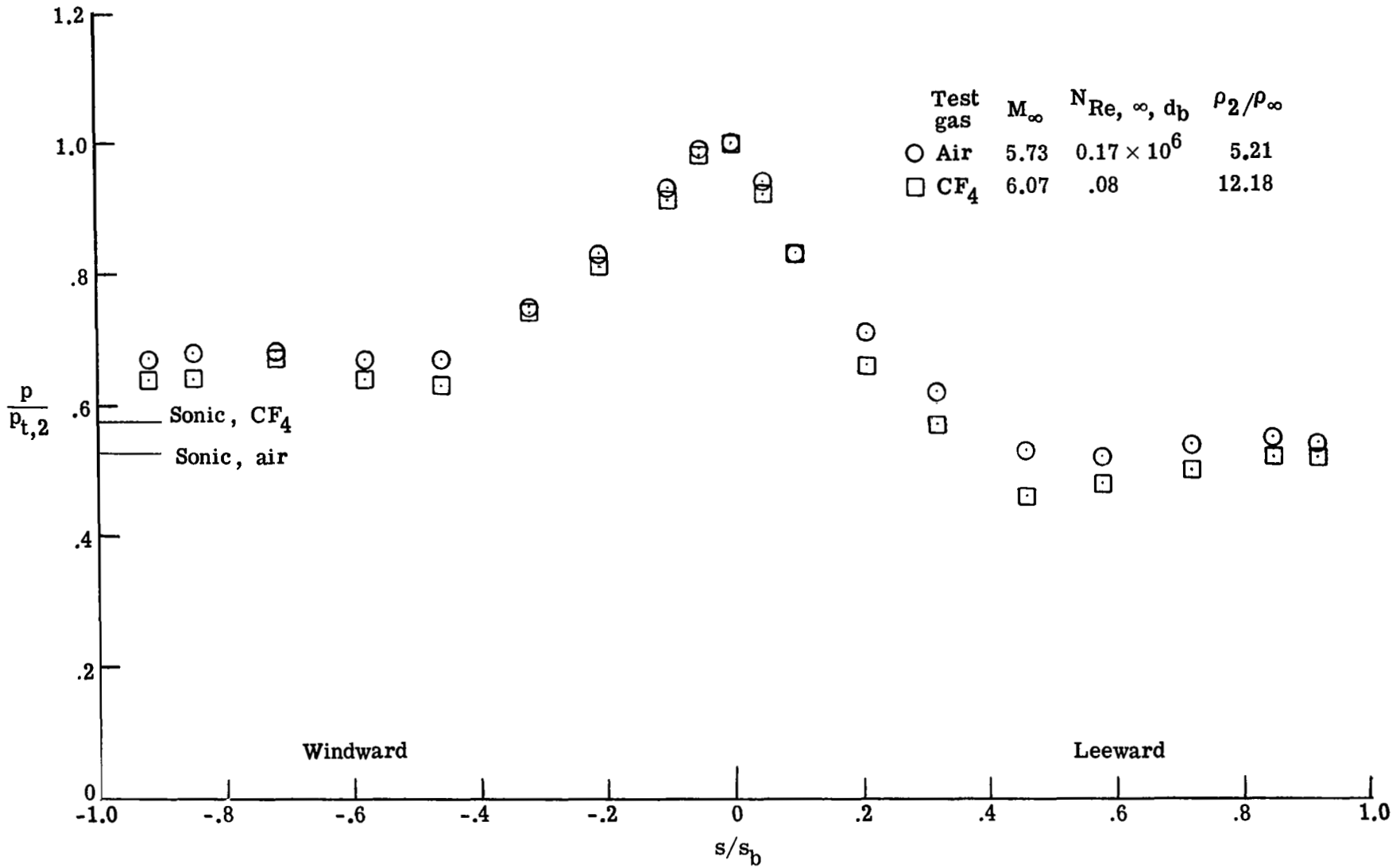

(b) $\alpha = 4°$.

Figure 26.- Continued.

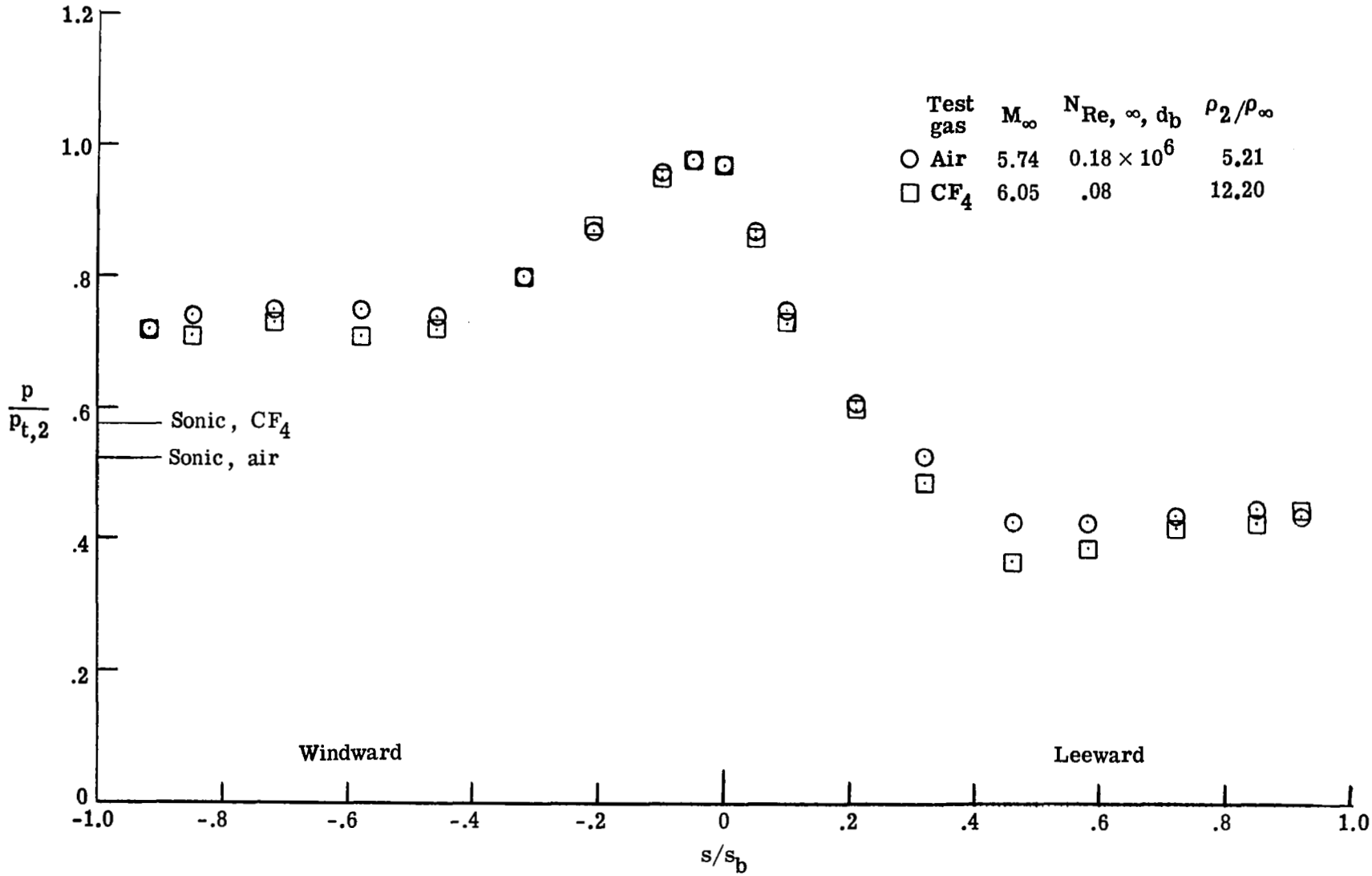

(c) $\alpha = 8°$.

Figure 26.- Continued.

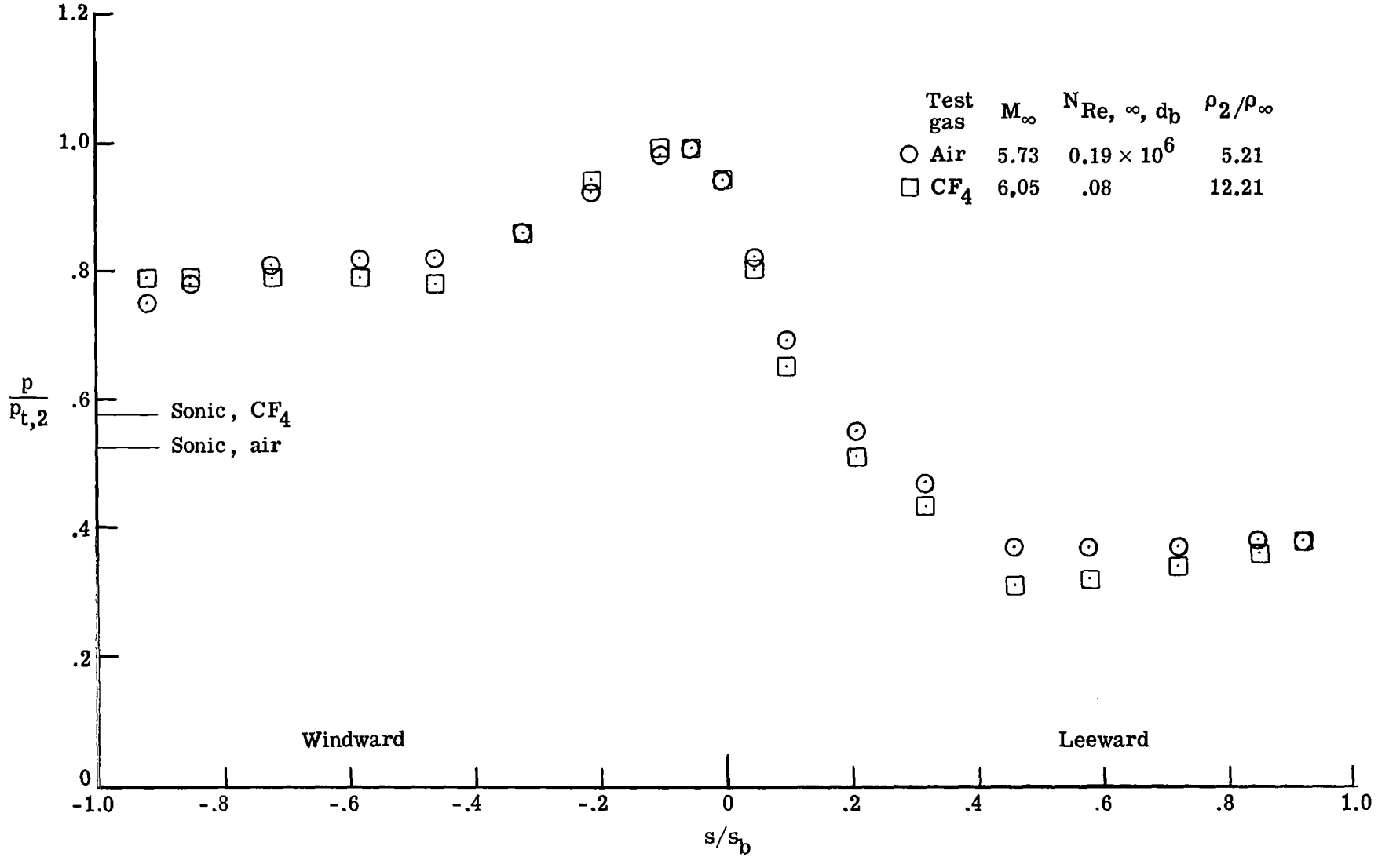

(d) $\alpha = 12°$.

Figure 26.- Continued.

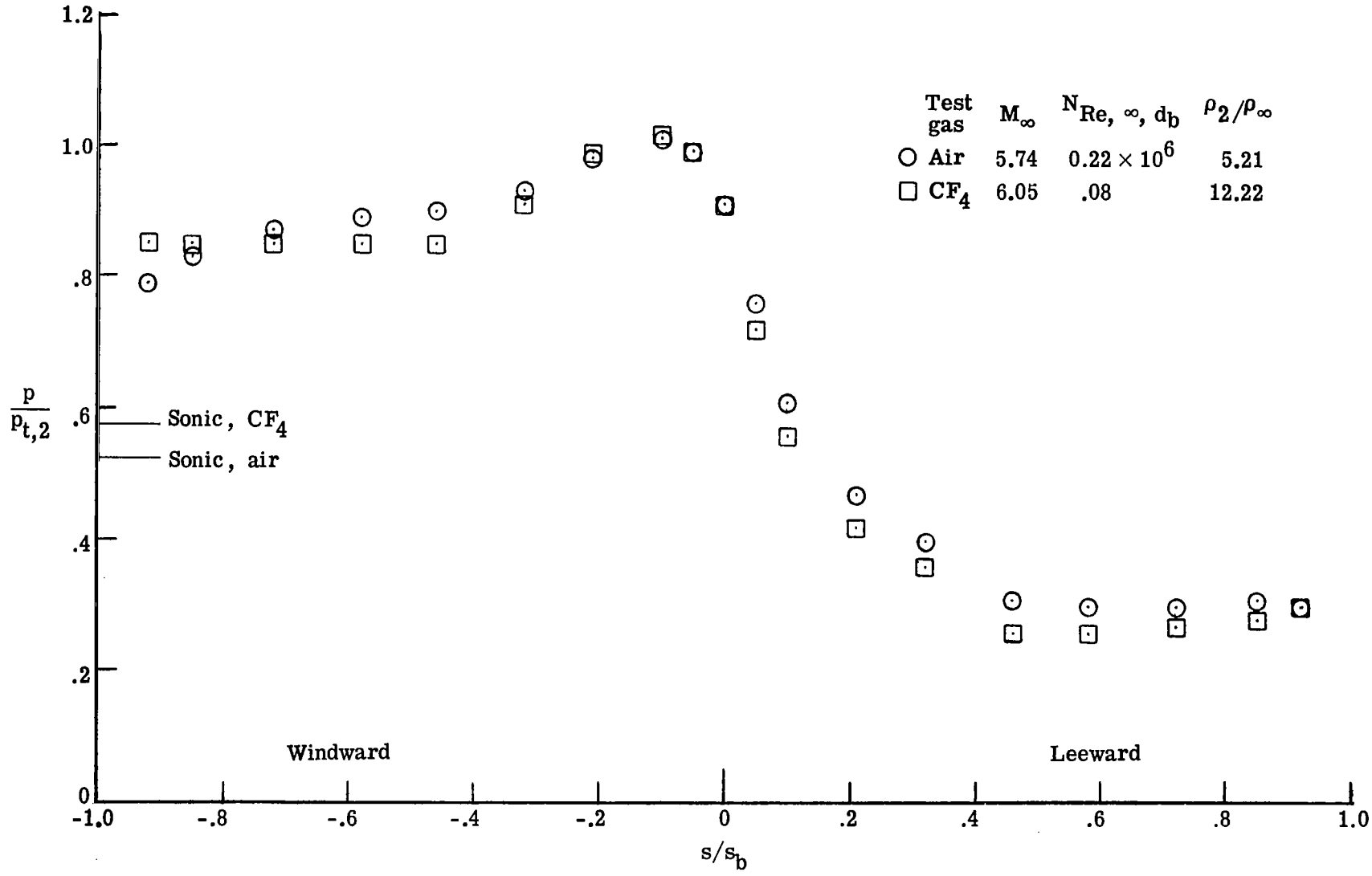

(e) $\alpha = 16°$.

Figure 26.- Continued.

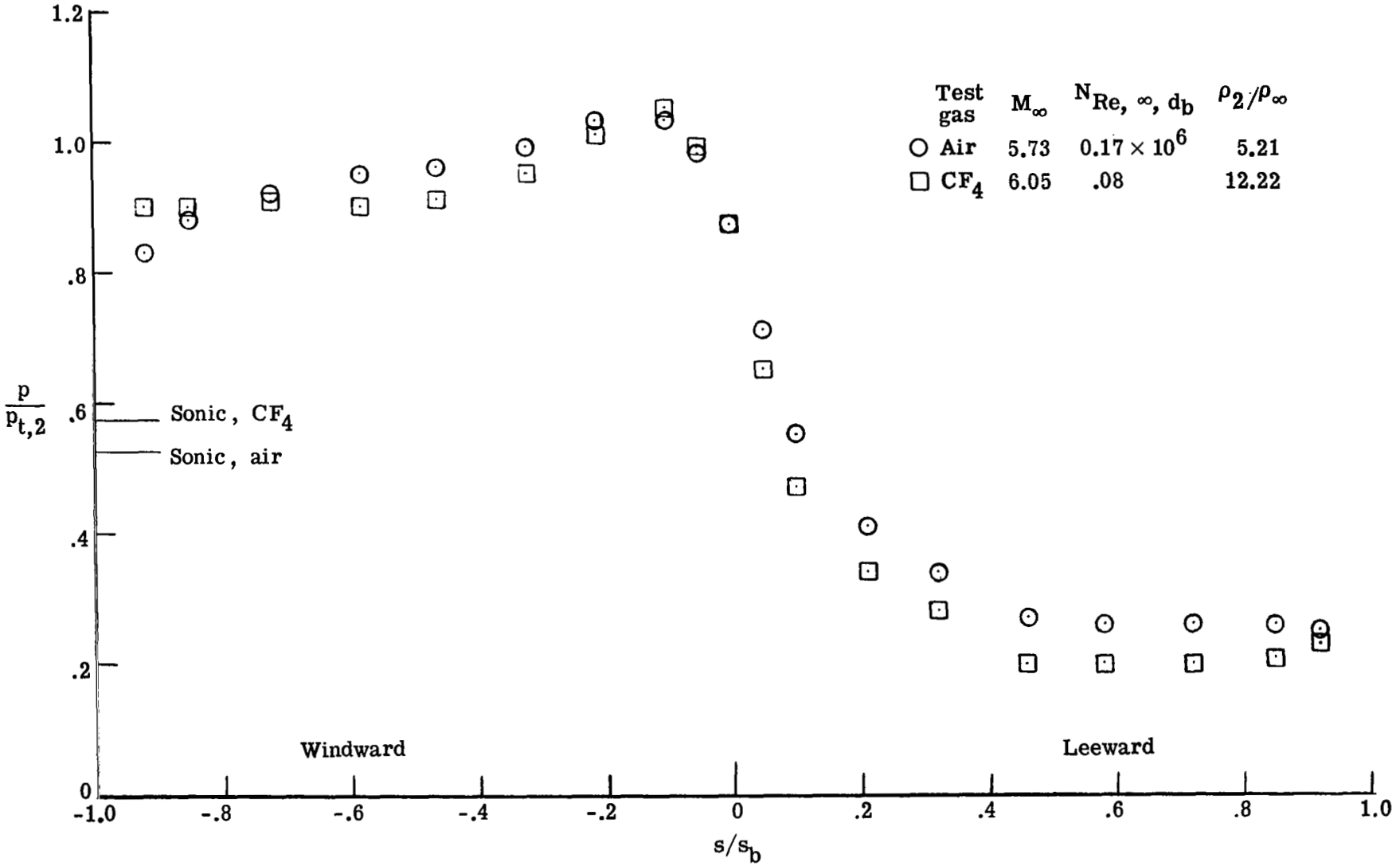

(f) $\alpha = 20°$.

Figure 26.- Concluded.

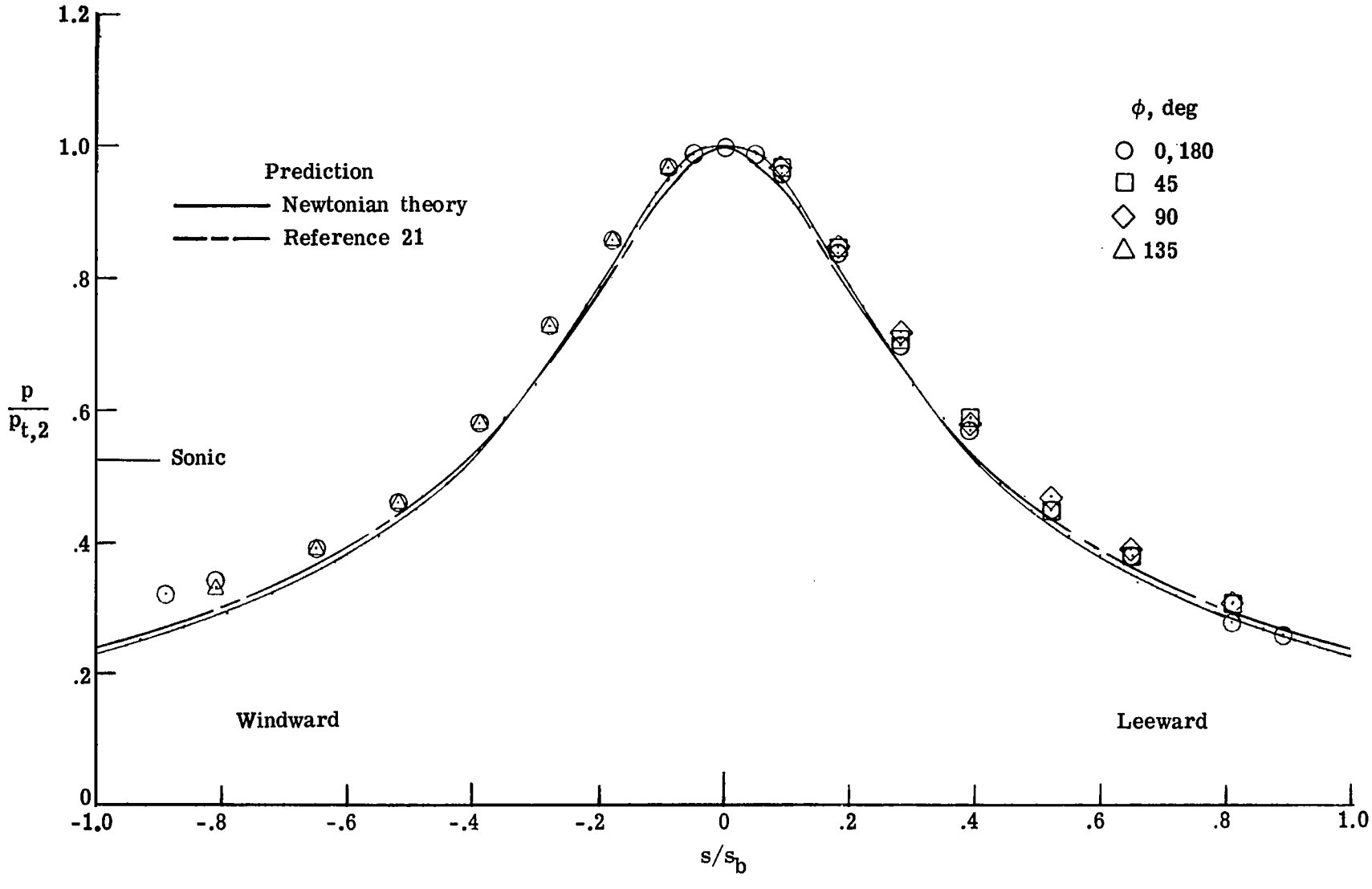

(a) $\alpha = 0°$.

Figure 27.- Pressure distributions measured on the paraboloid (model 3, series 1) in Mach 5.93 air. $N_{Re,\infty,d_b} = 7 \times 10^5$.

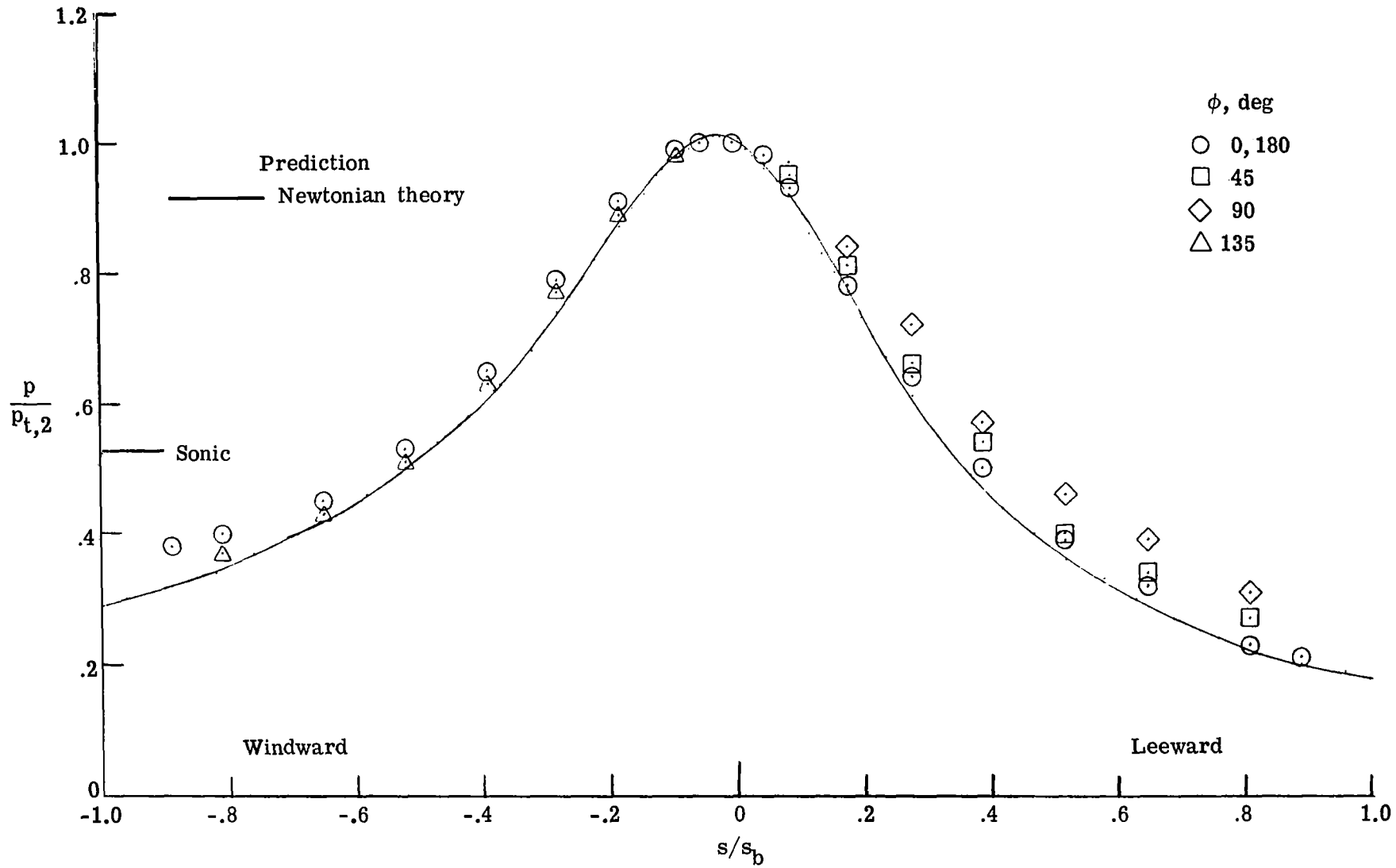

(b) $\alpha = 4°$.

Figure 27.- Continued.

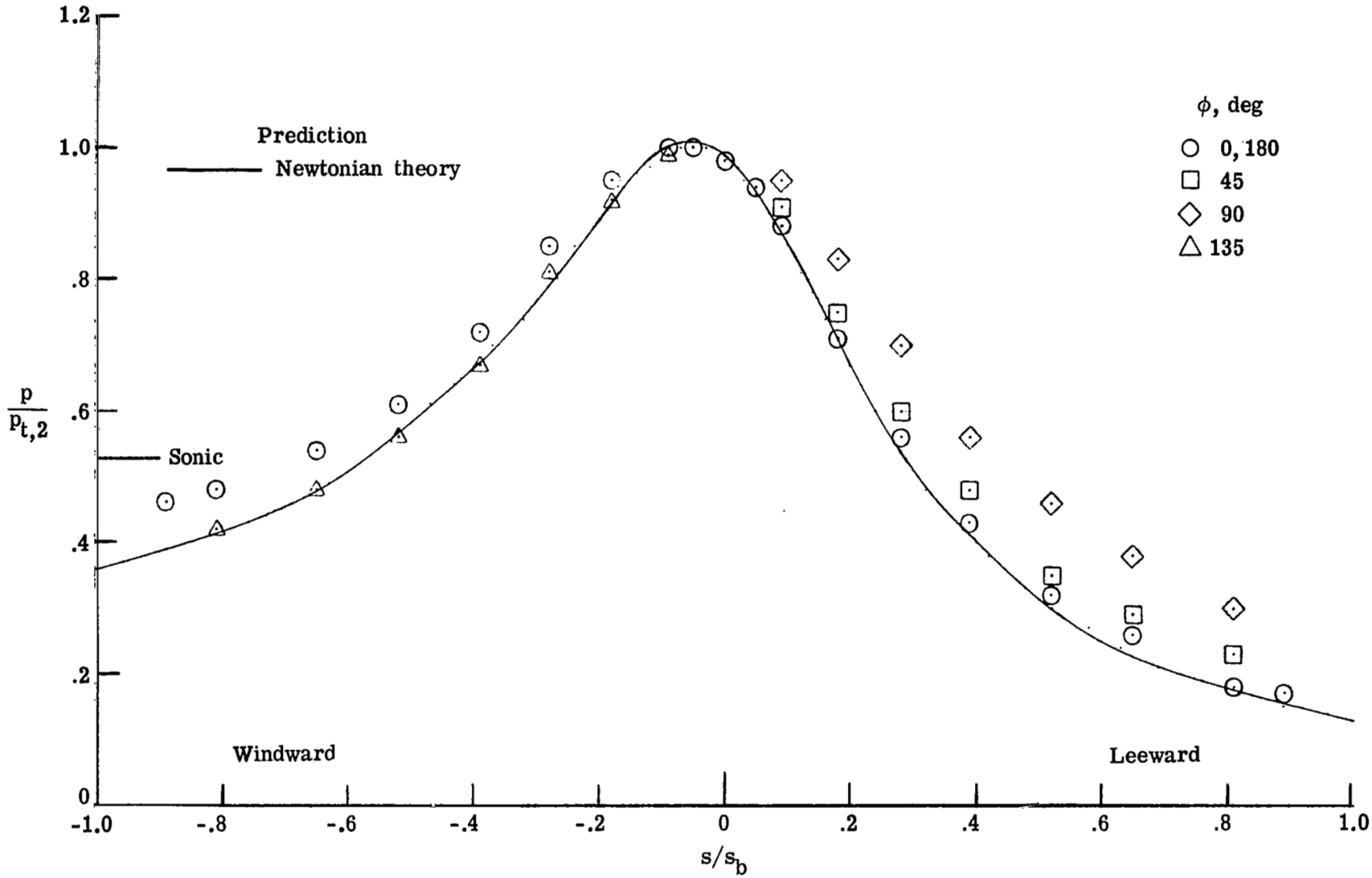

(c) $\alpha = 8°$.

Figure 27.- Continued.

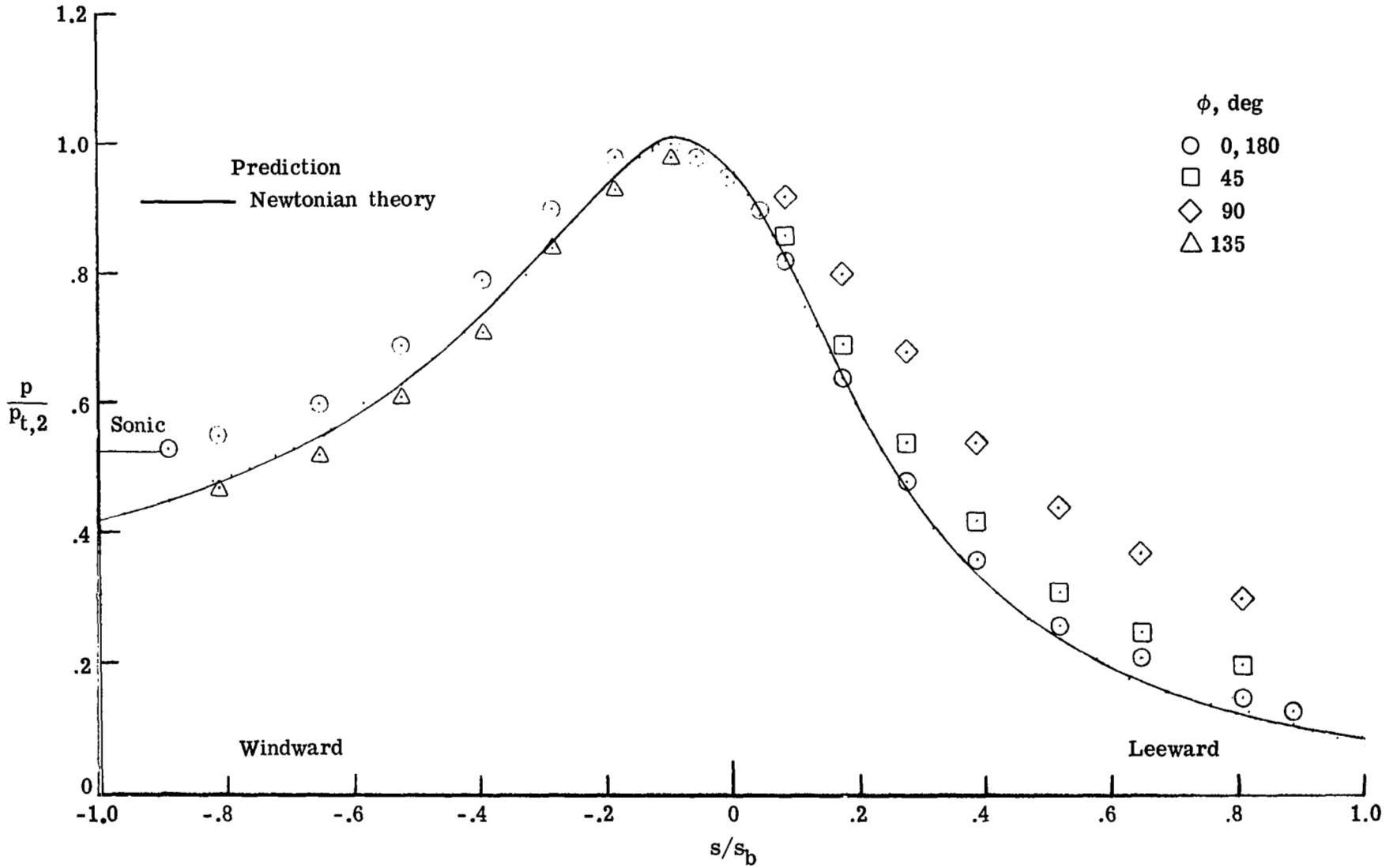

(d) $\alpha = 12°$.

Figure 27.- Continued.

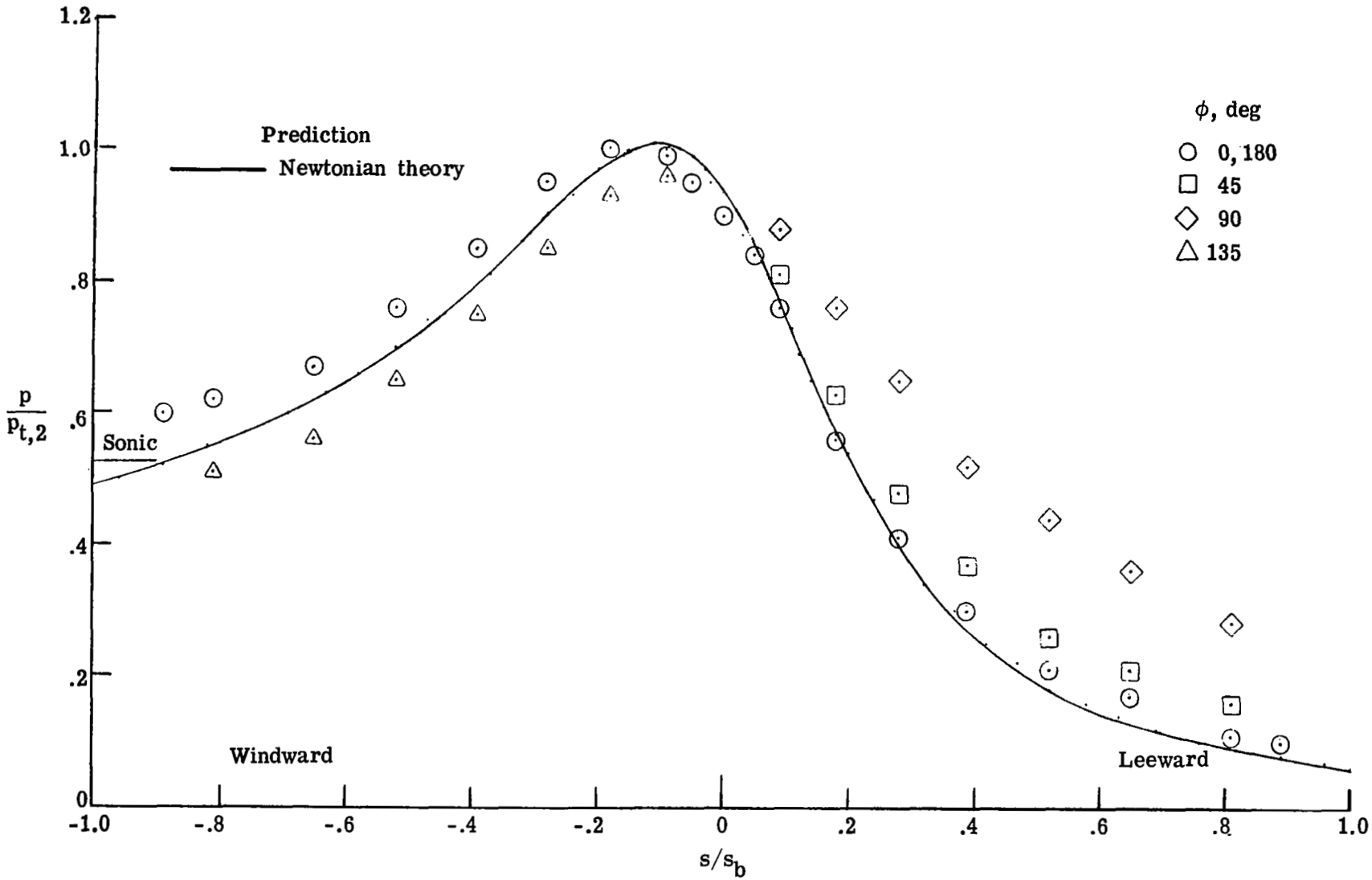

(e) $\alpha = 16°$.

Figure 27.- Continued.

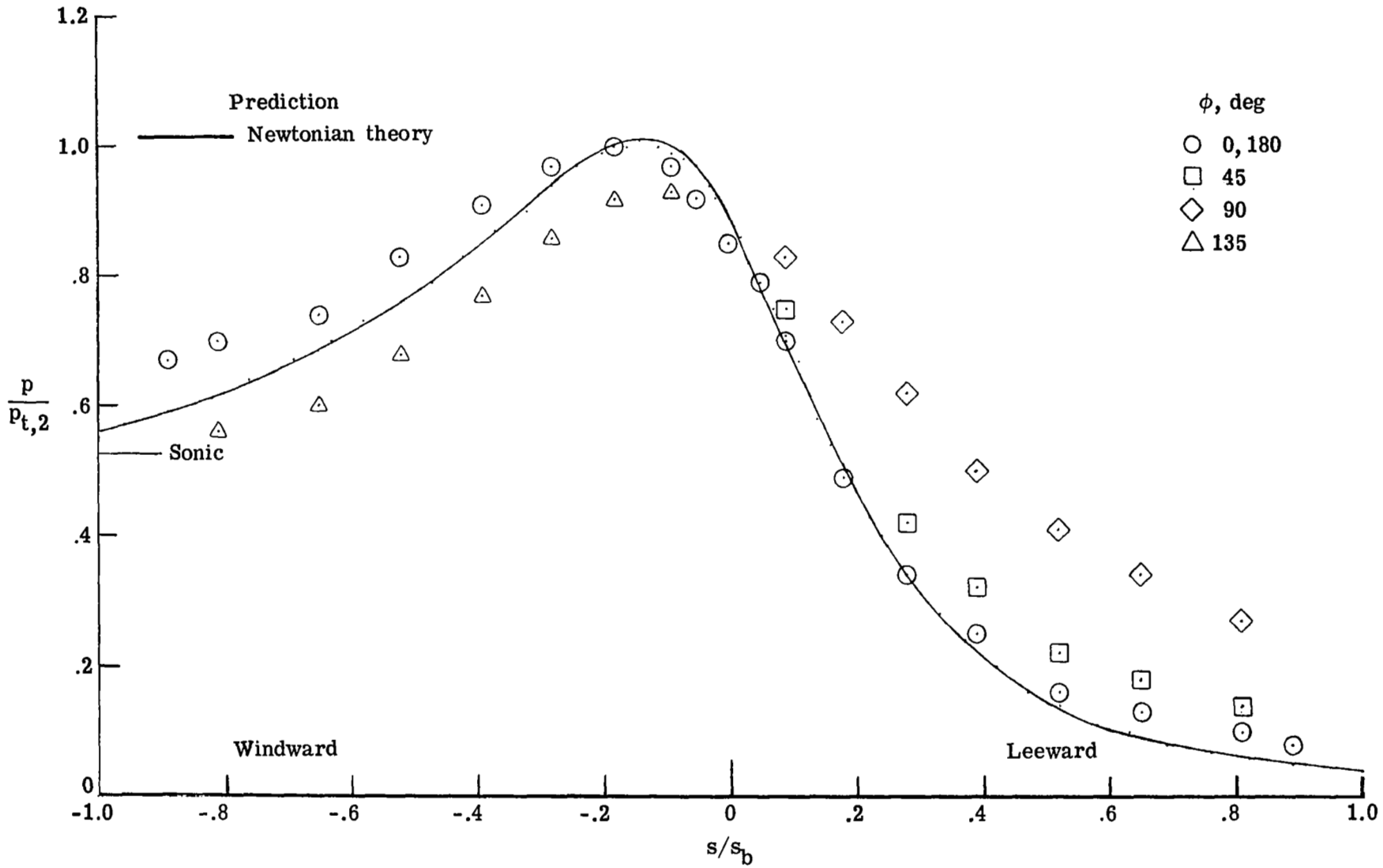

(f) $\alpha = 20°$.

Figure 27.- Concluded.

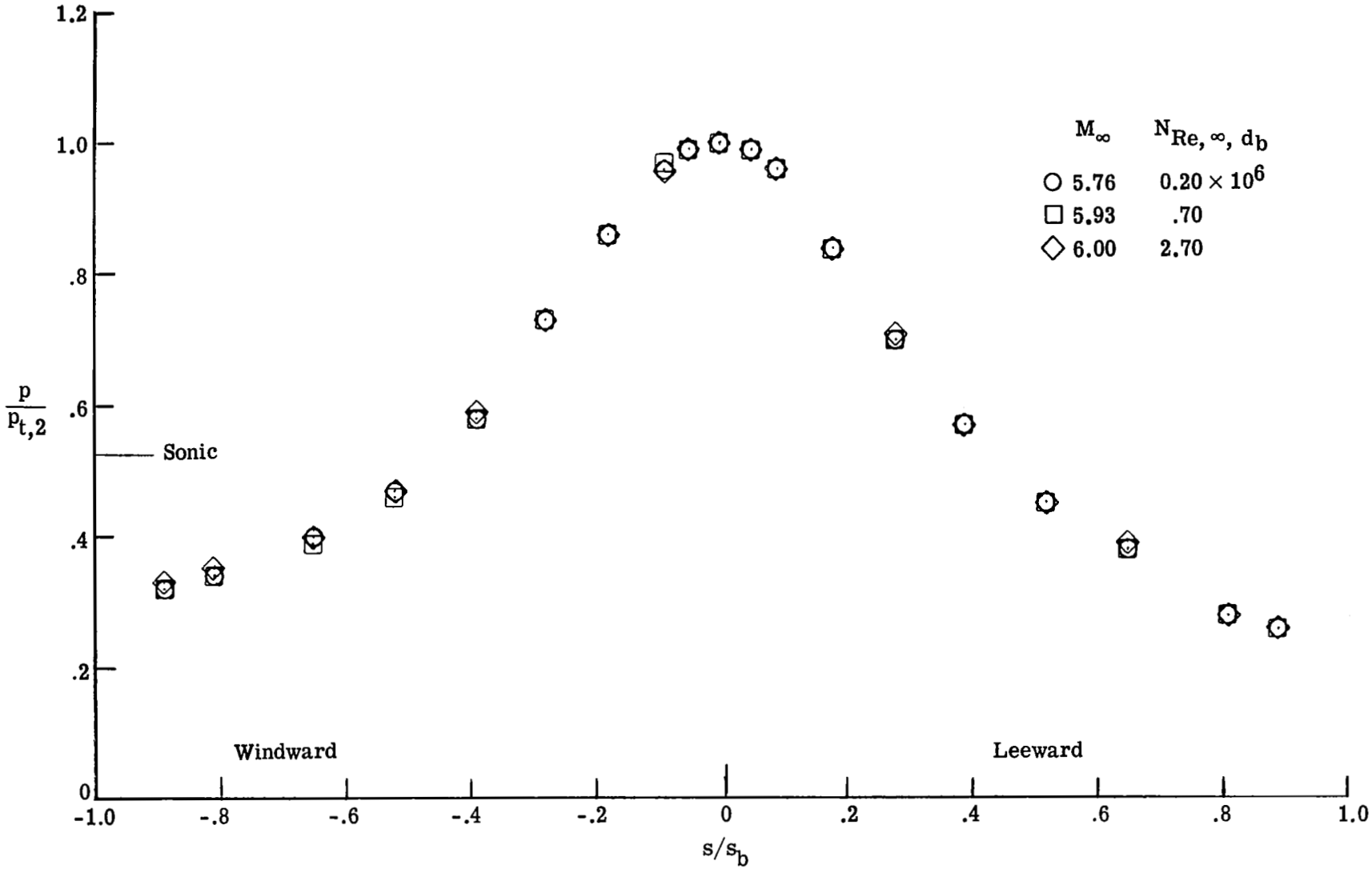

(a) $\alpha = 0°$.

Figure 28.- Effect of free-stream Reynolds number on pressure distributions in air along the most windward and leeward rays of the paraboloid (model 3, series 1).

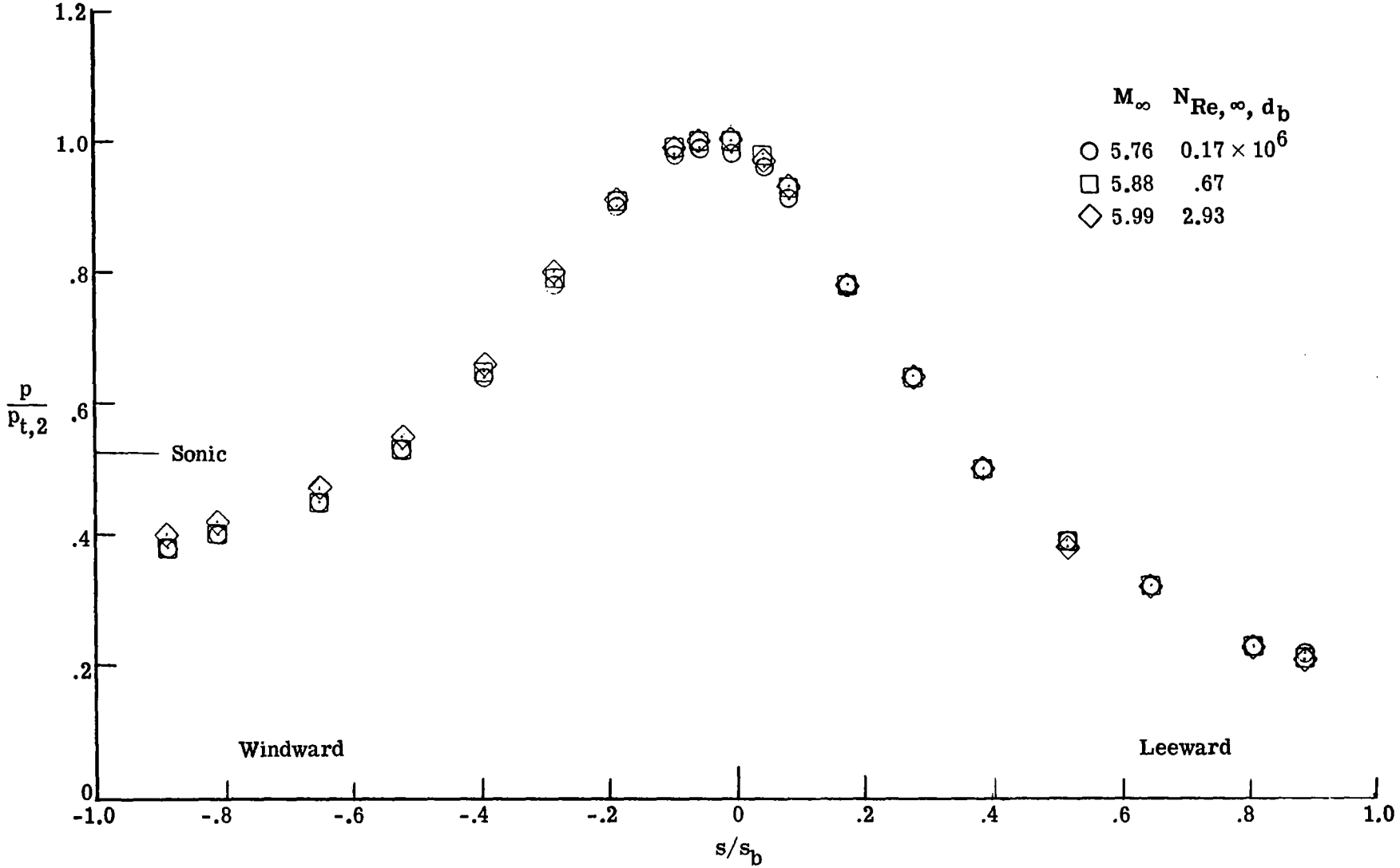

(b) $\alpha = 4°$.

Figure 28.- Continued.

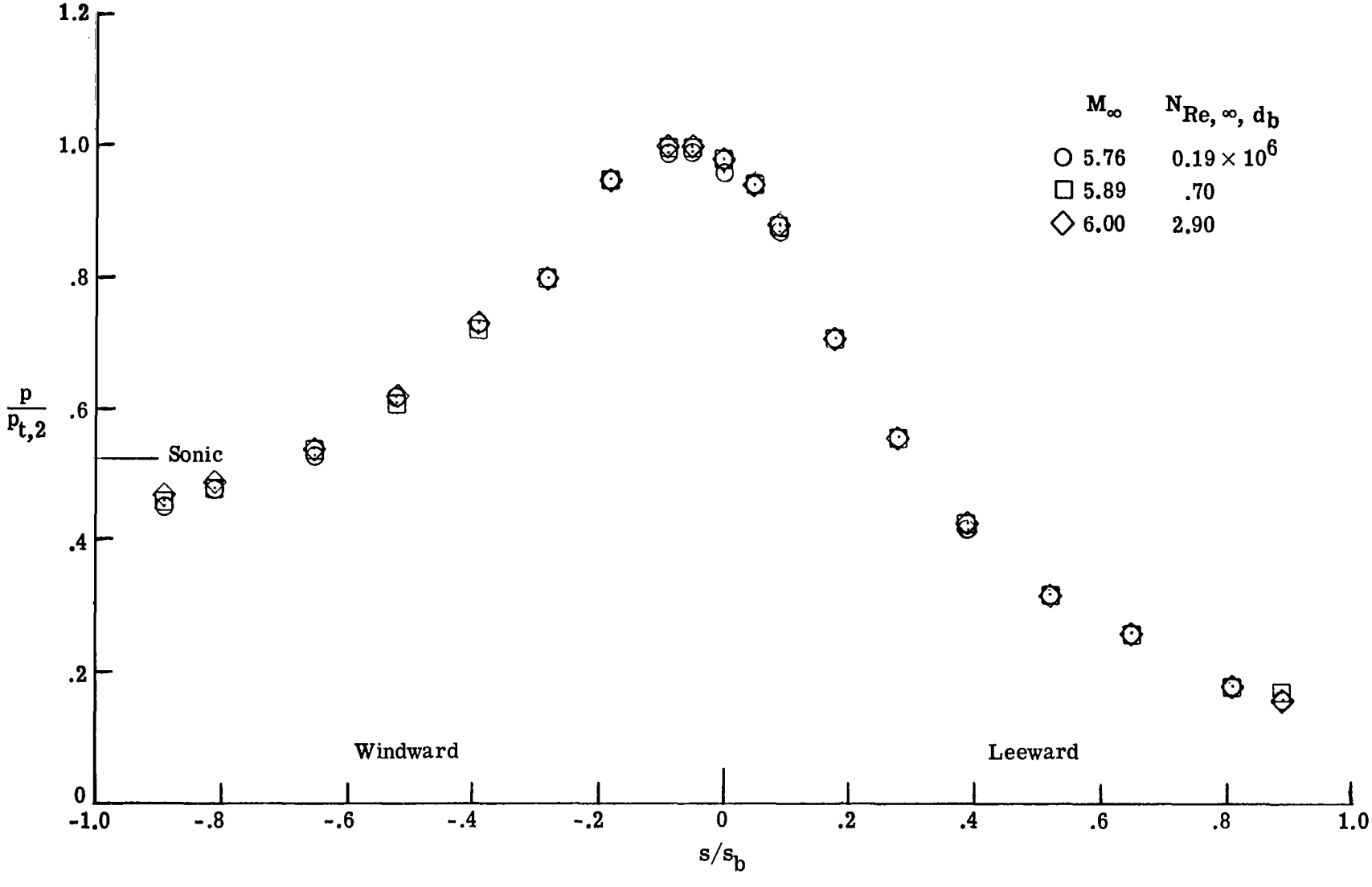

(c) $\alpha = 8°$.

Figure 28.- Continued.

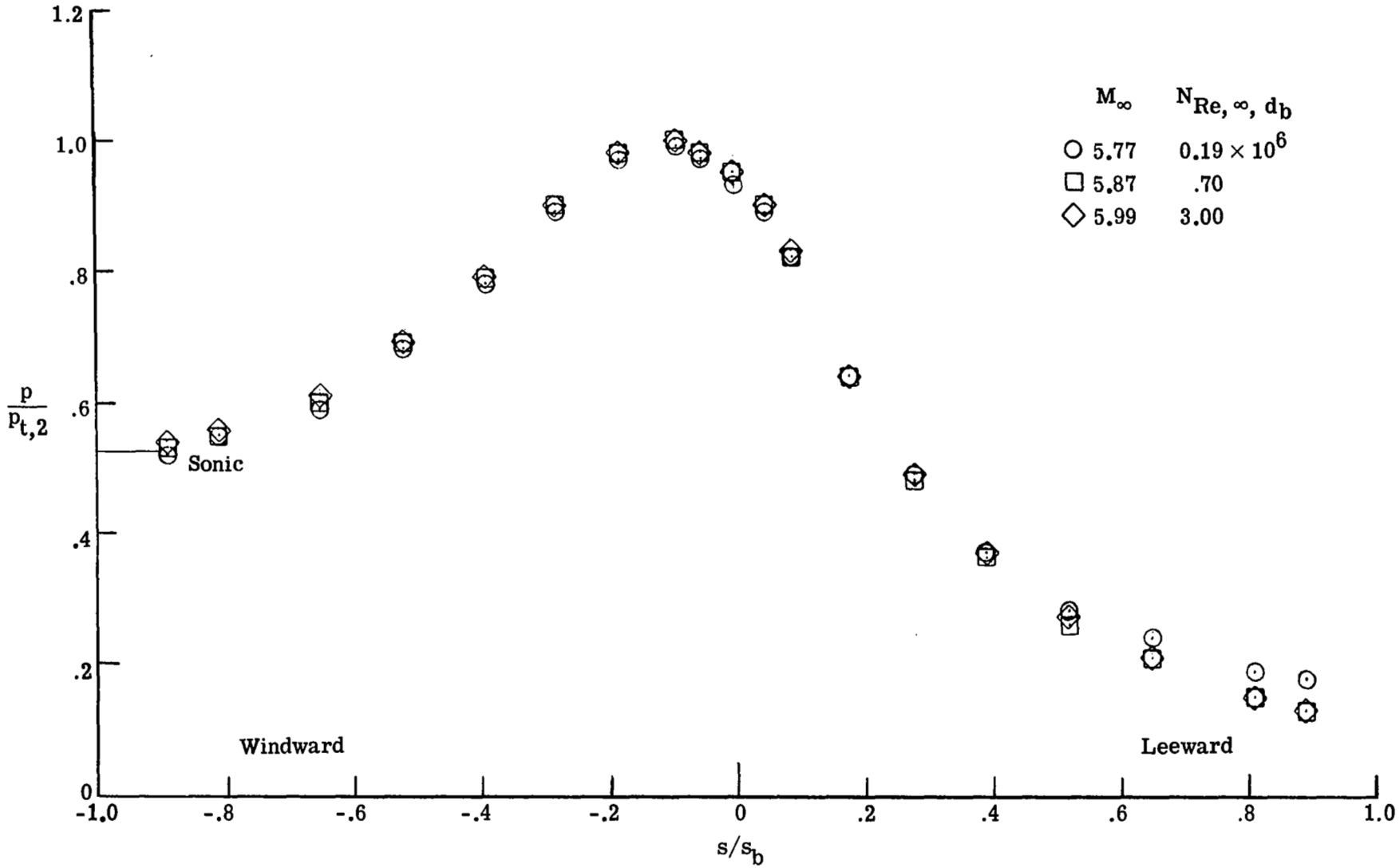

(d) $\alpha = 12°$.

Figure 28.- Continued.

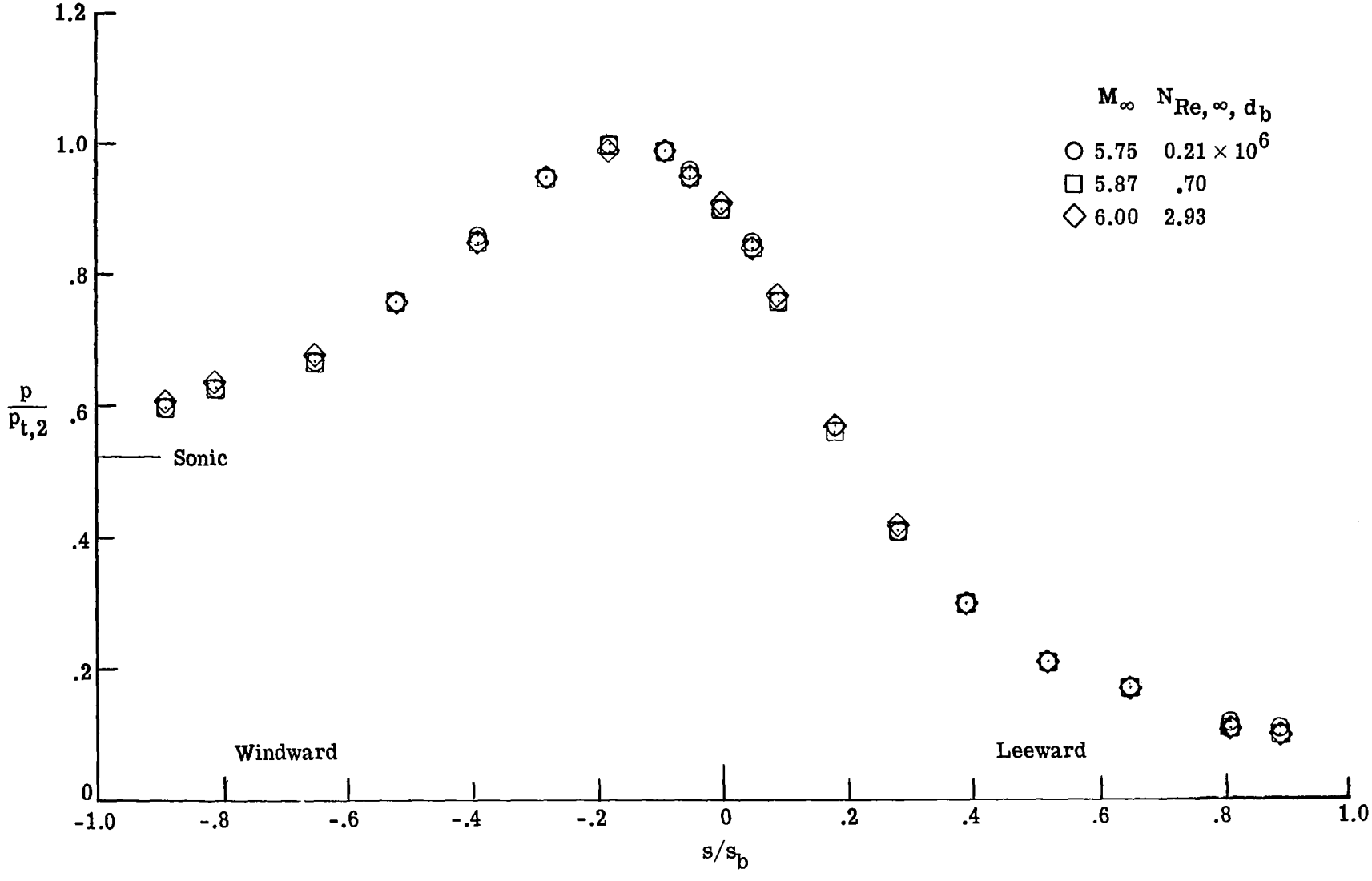

(e) $\alpha = 16°$.

Figure 28.- Continued.

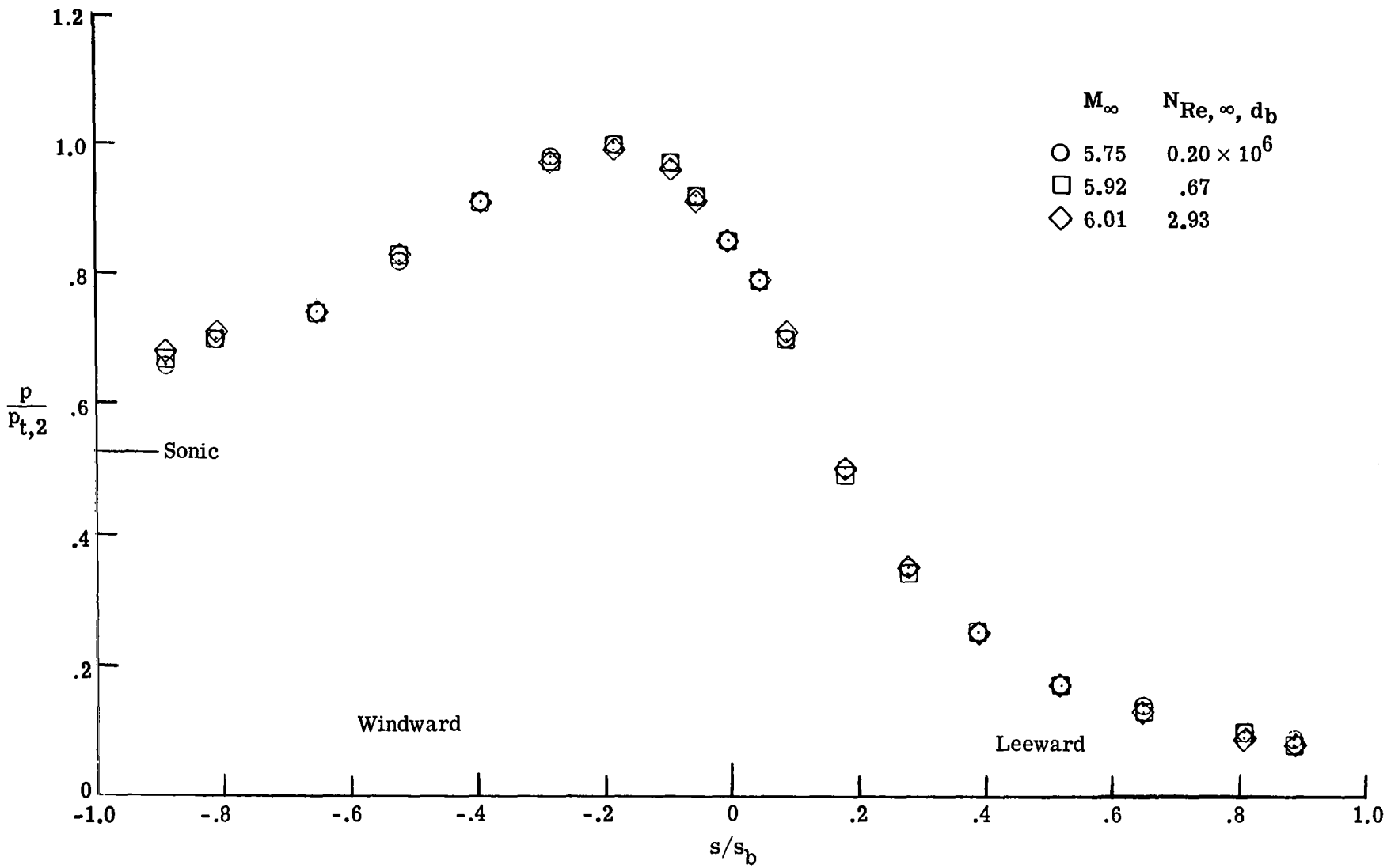

(f) $\alpha = 20°$.

Figure 28.- Concluded.

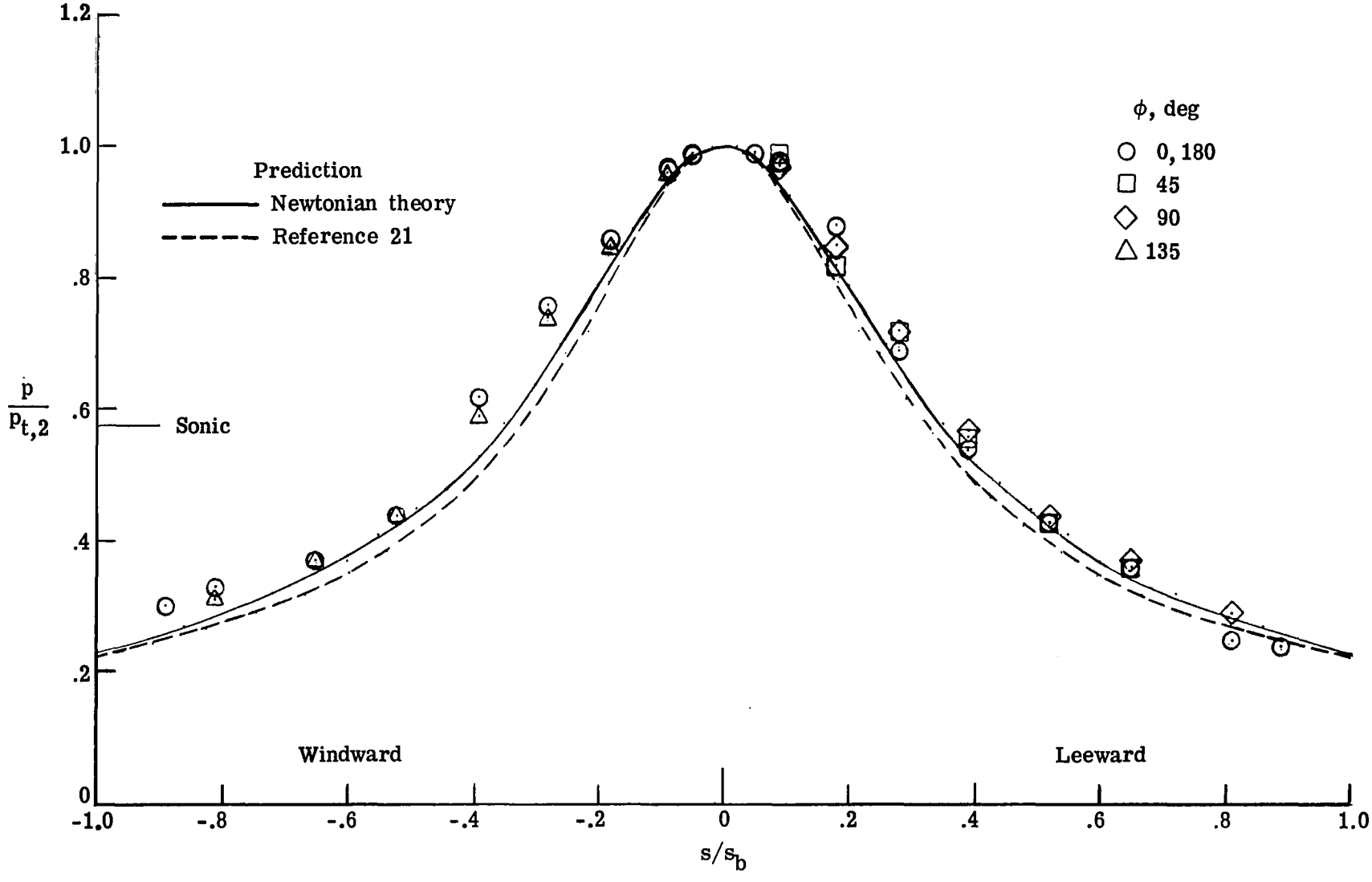

(a) $\alpha = 0°$.

Figure 29.- Pressure distributions measured on the paraboloid (model 3, series 1) in Mach 6.13 CF_4. $N_{Re,\infty,d_b} = 7.8 \times 10^4$; $\rho_2/\rho_\infty = 12.06$.

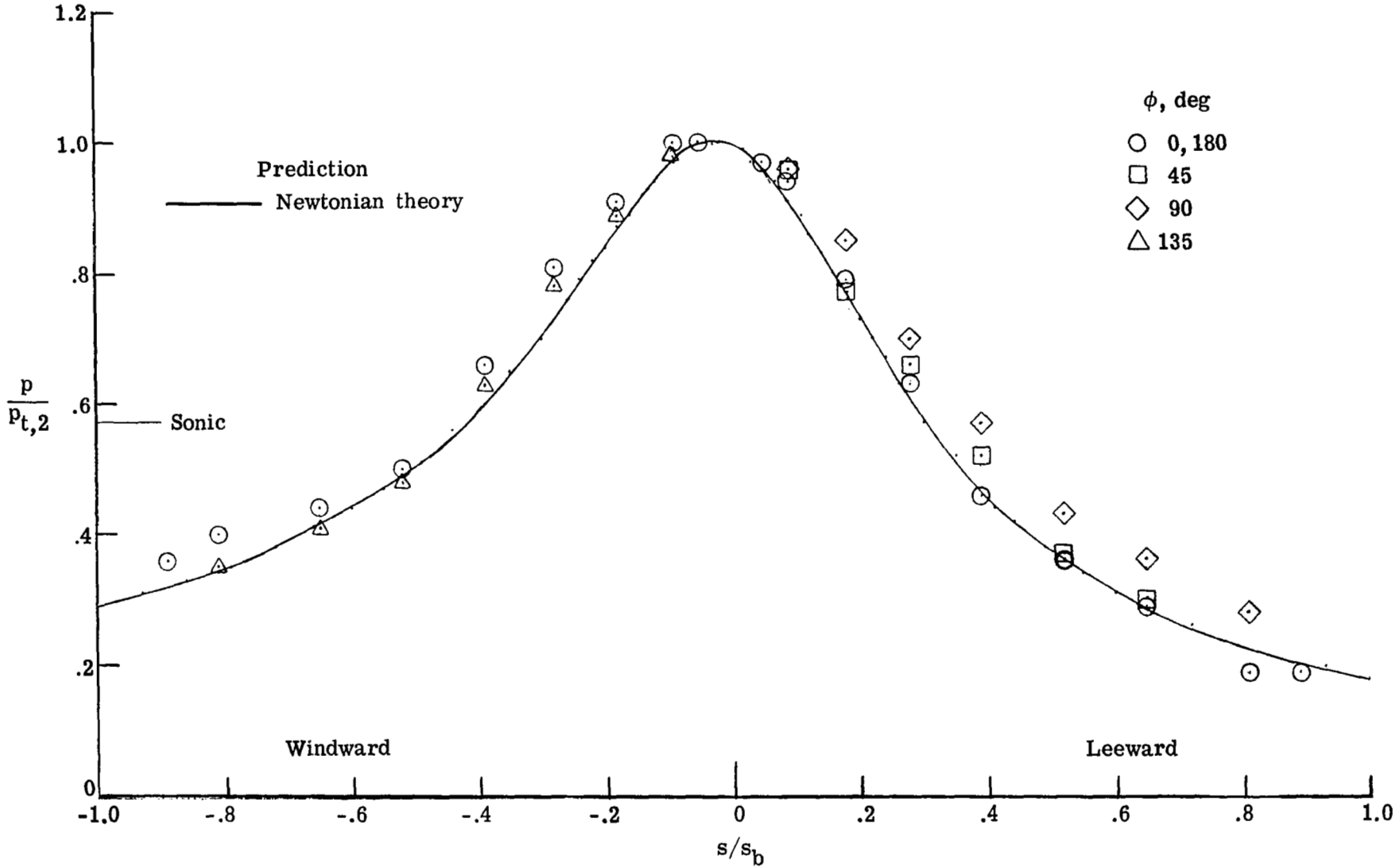

(b) $\alpha = 4°$.

Figure 29.- Continued.

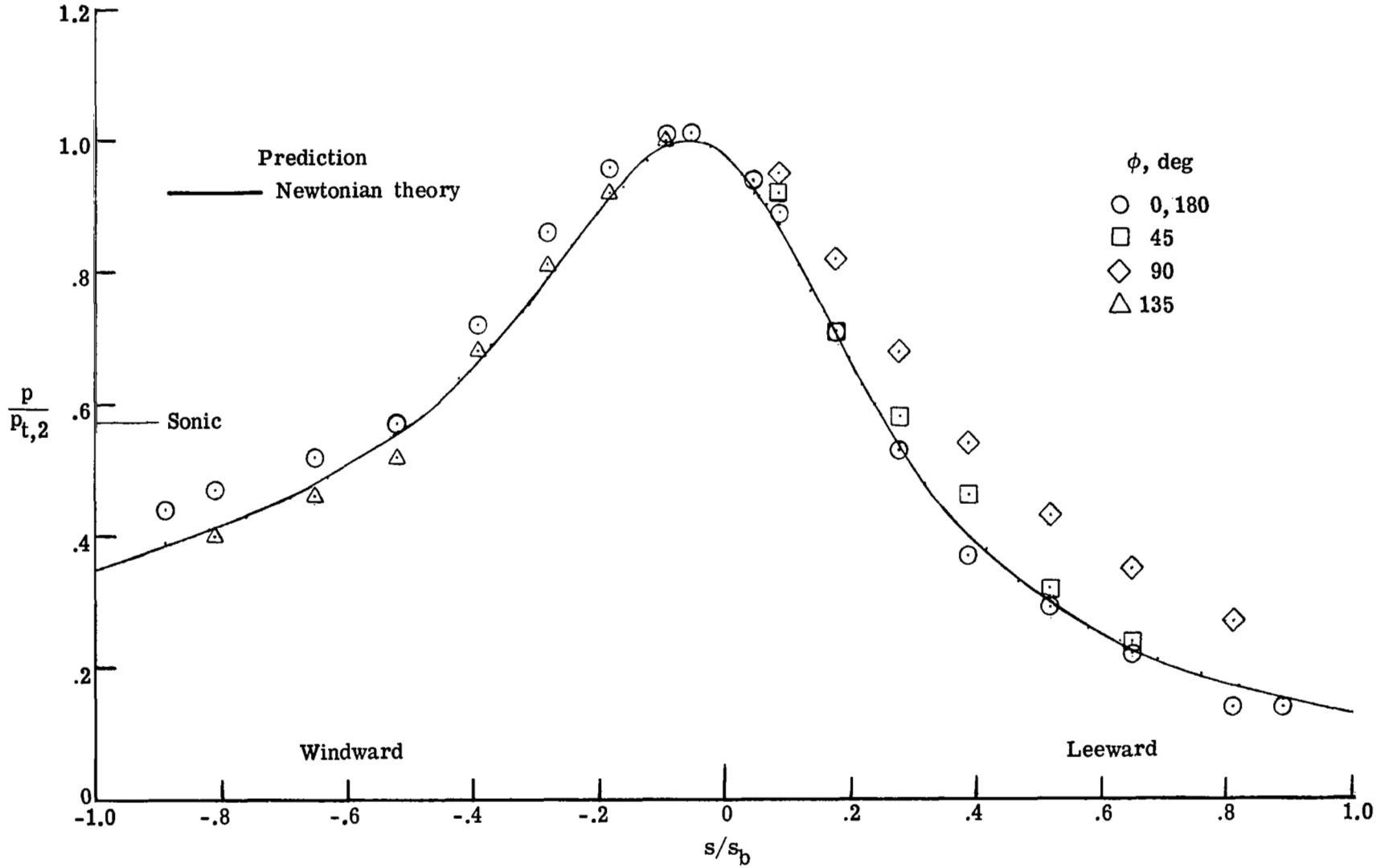

(c) $\alpha = 8°$.

Figure 29.- Continued.

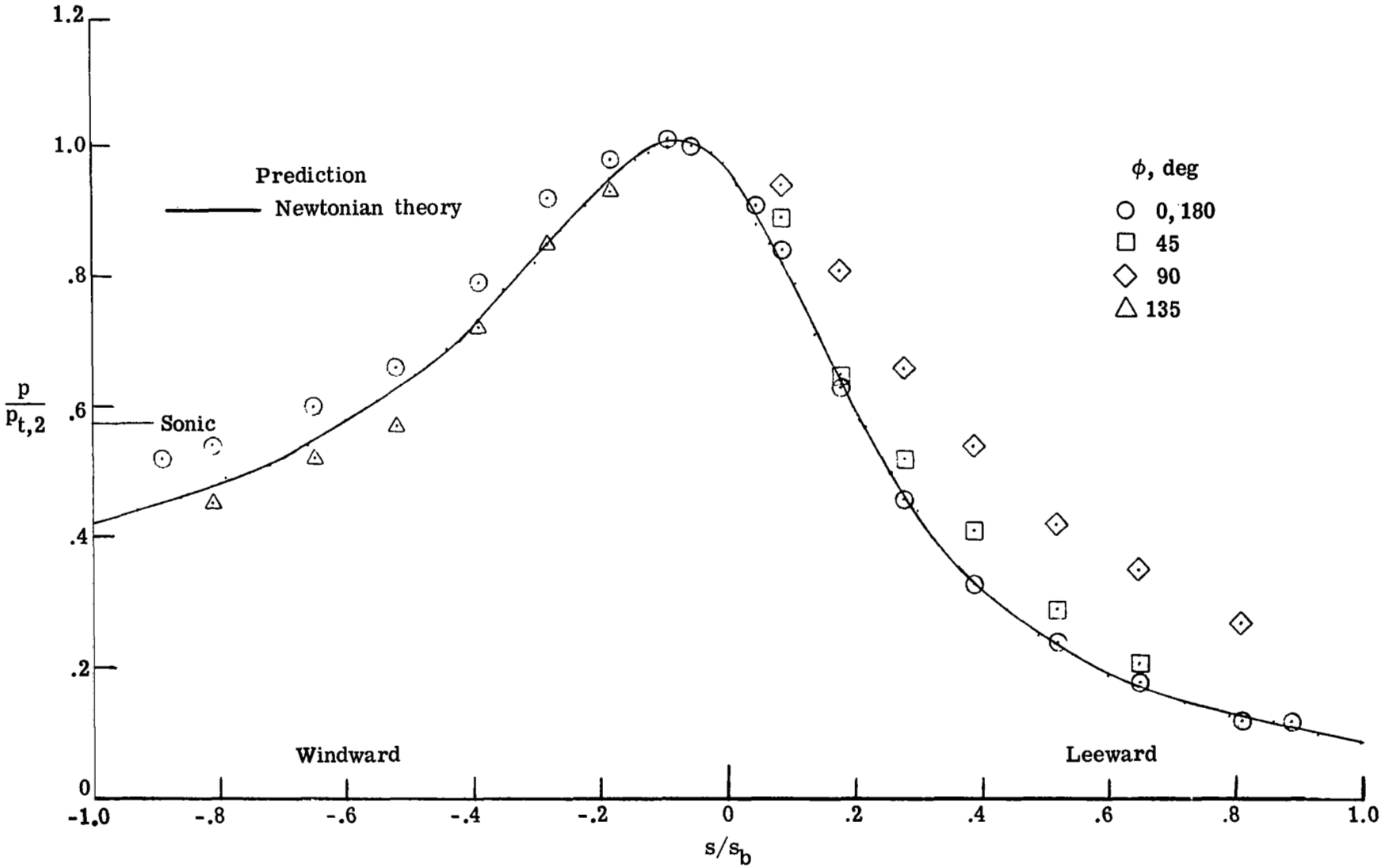

(d) $\alpha = 12°$.

Figure 29.- Continued.

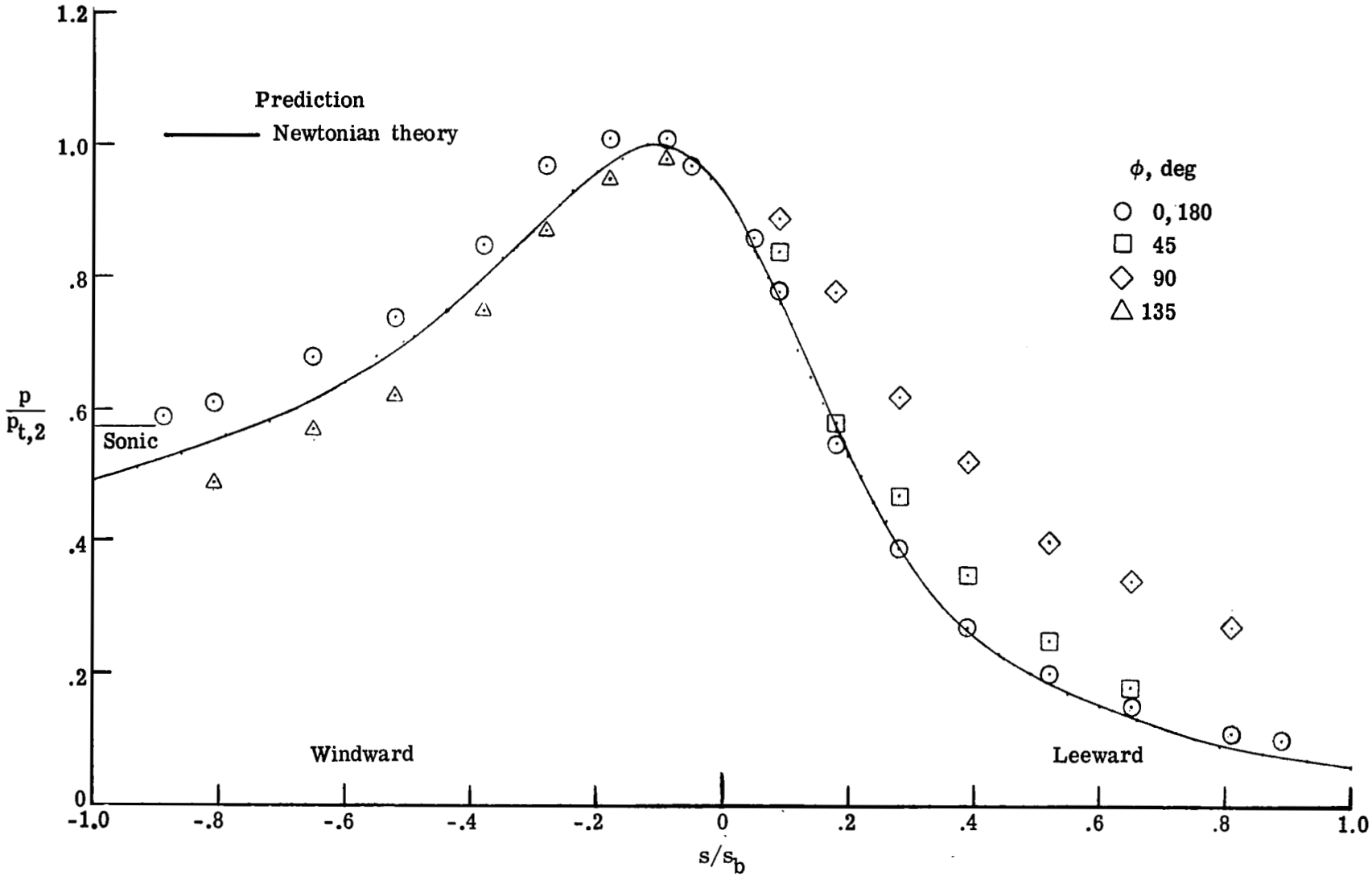

(e) $\alpha = 16°$.

Figure 29.- Continued.

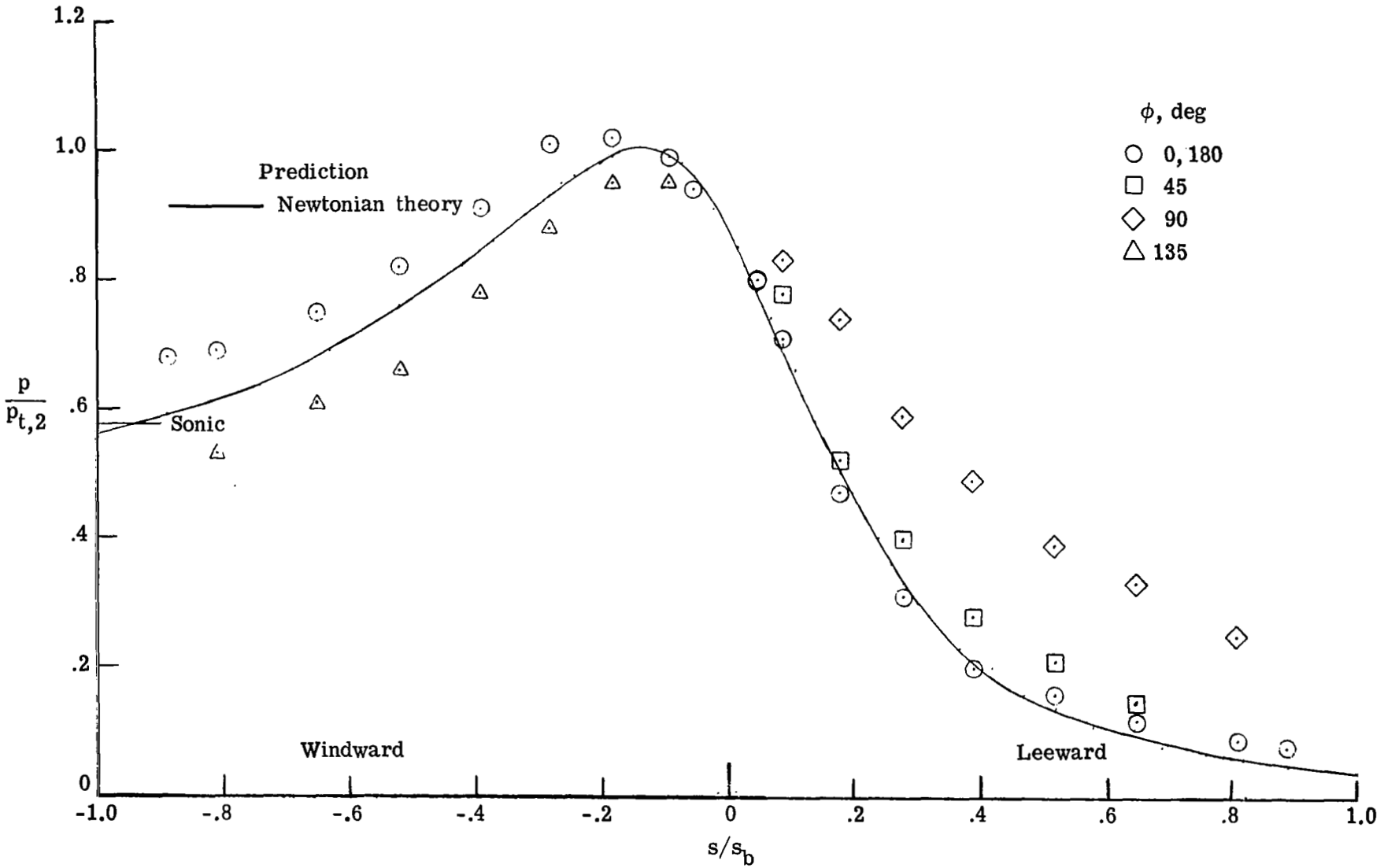

(f) $\alpha = 20°$.

Figure 29.- Concluded.

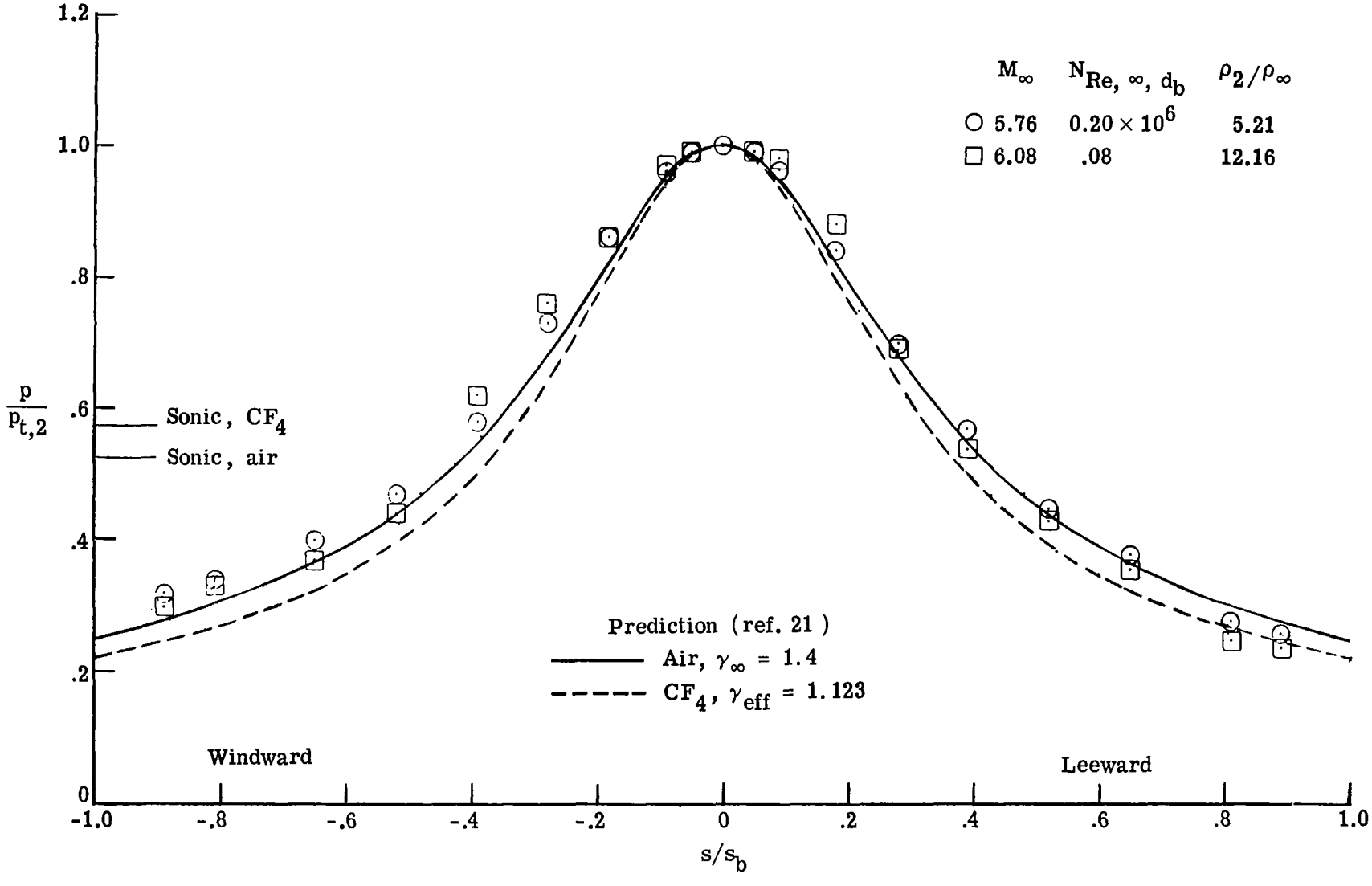

(a) $\alpha = 0°$.

Figure 30.- Effect of normal-shock density ratio on pressure distributions along the most windward and leeward rays of the paraboloid (model 3, series 1).

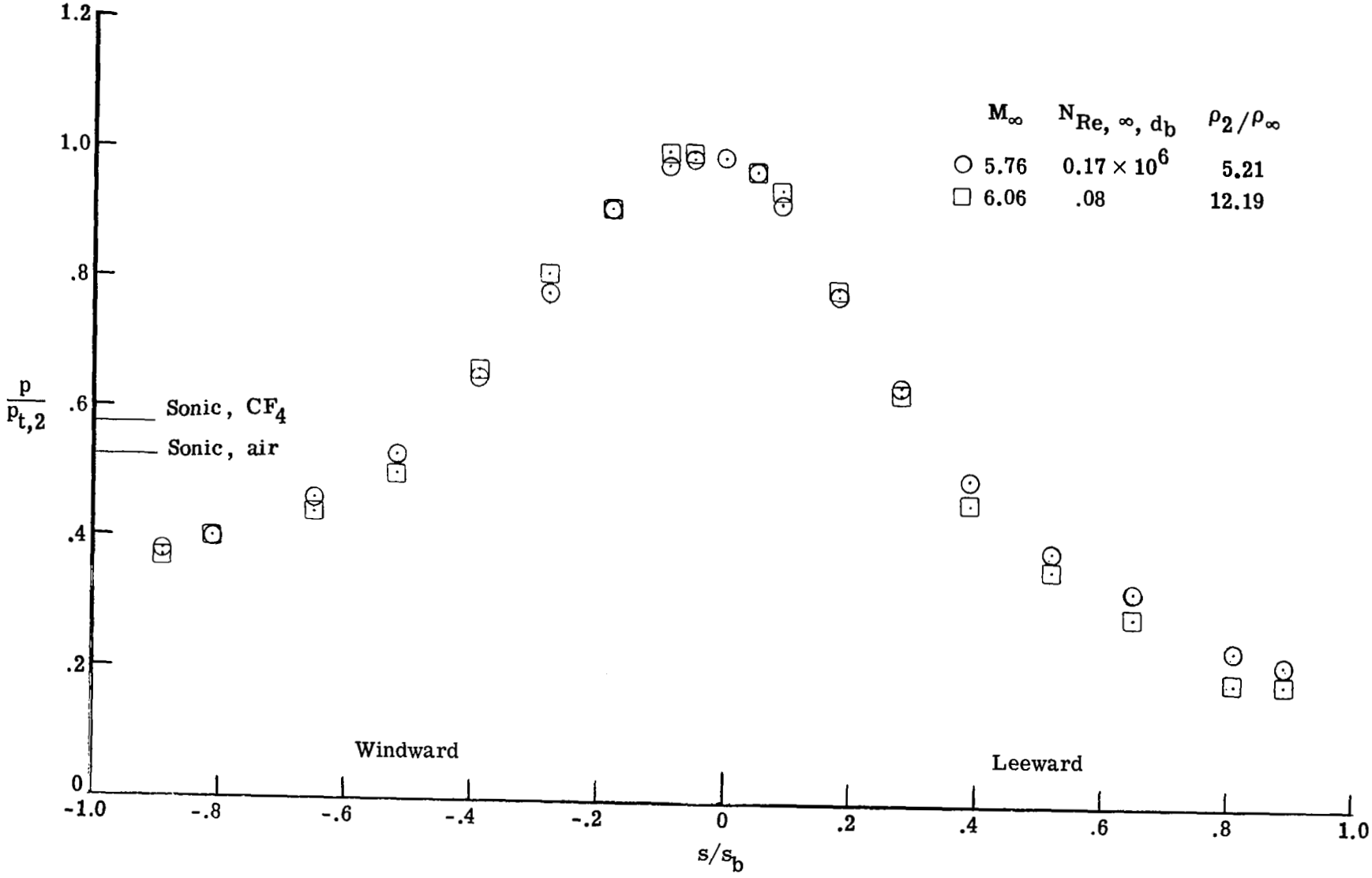

(b) $\alpha = 4°$.

Figure 30.- Continued.

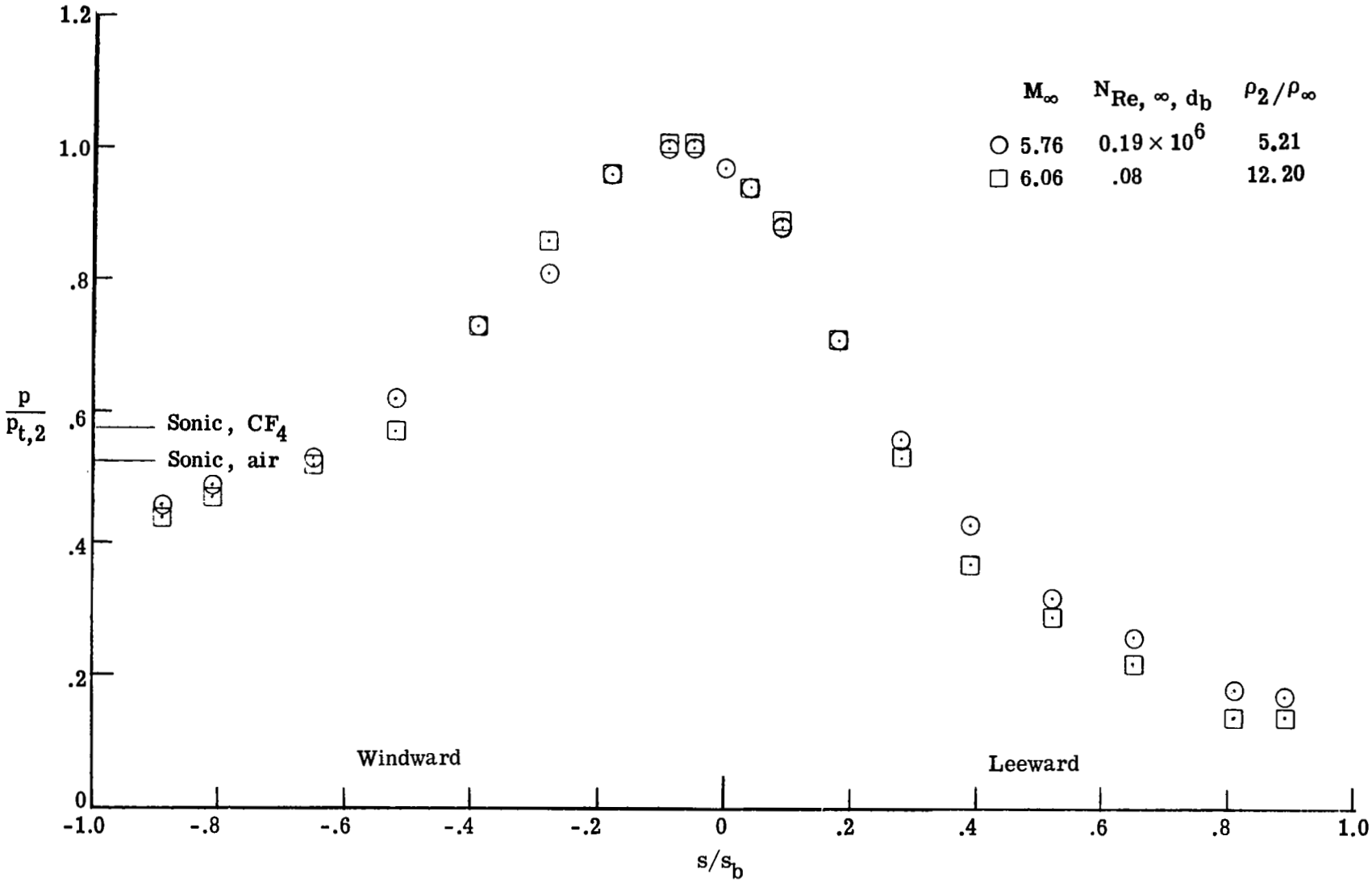

(c) $\alpha = 8°$.

Figure 30.- Continued.

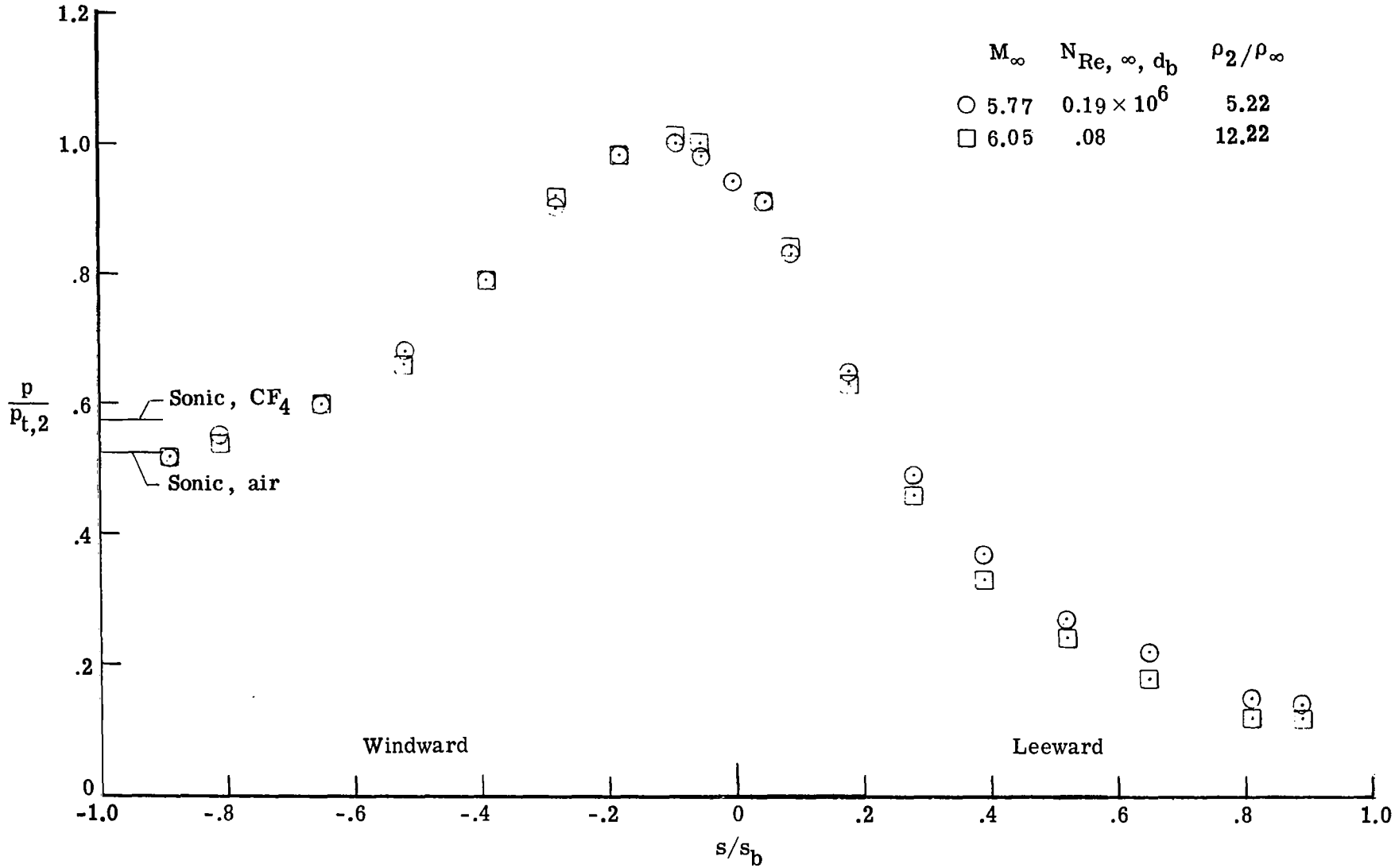

(d) $\alpha = 12°$.

Figure 30.- Continued.

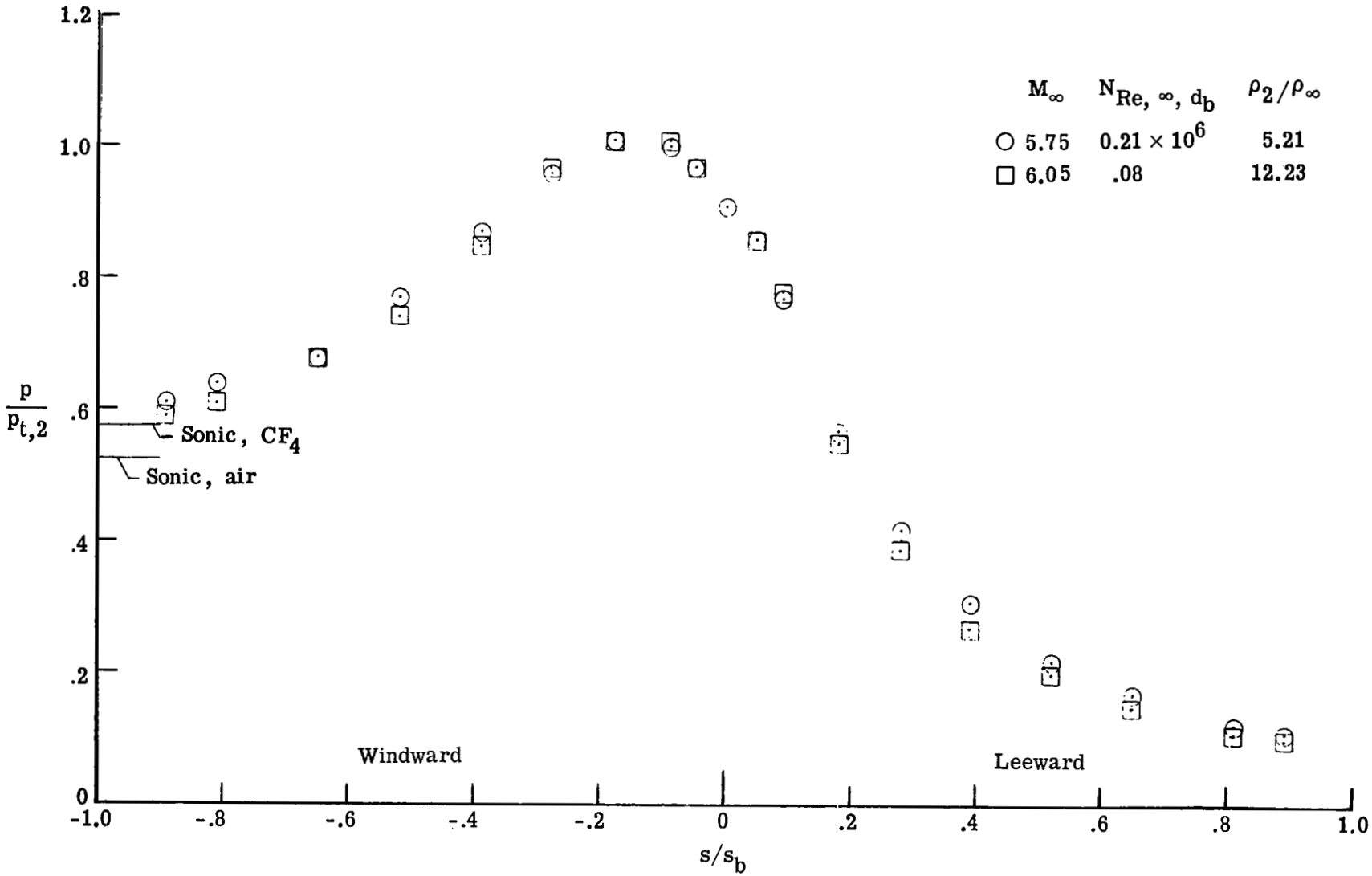

(e) $\alpha = 16°$.

Figure 30.- Continued.

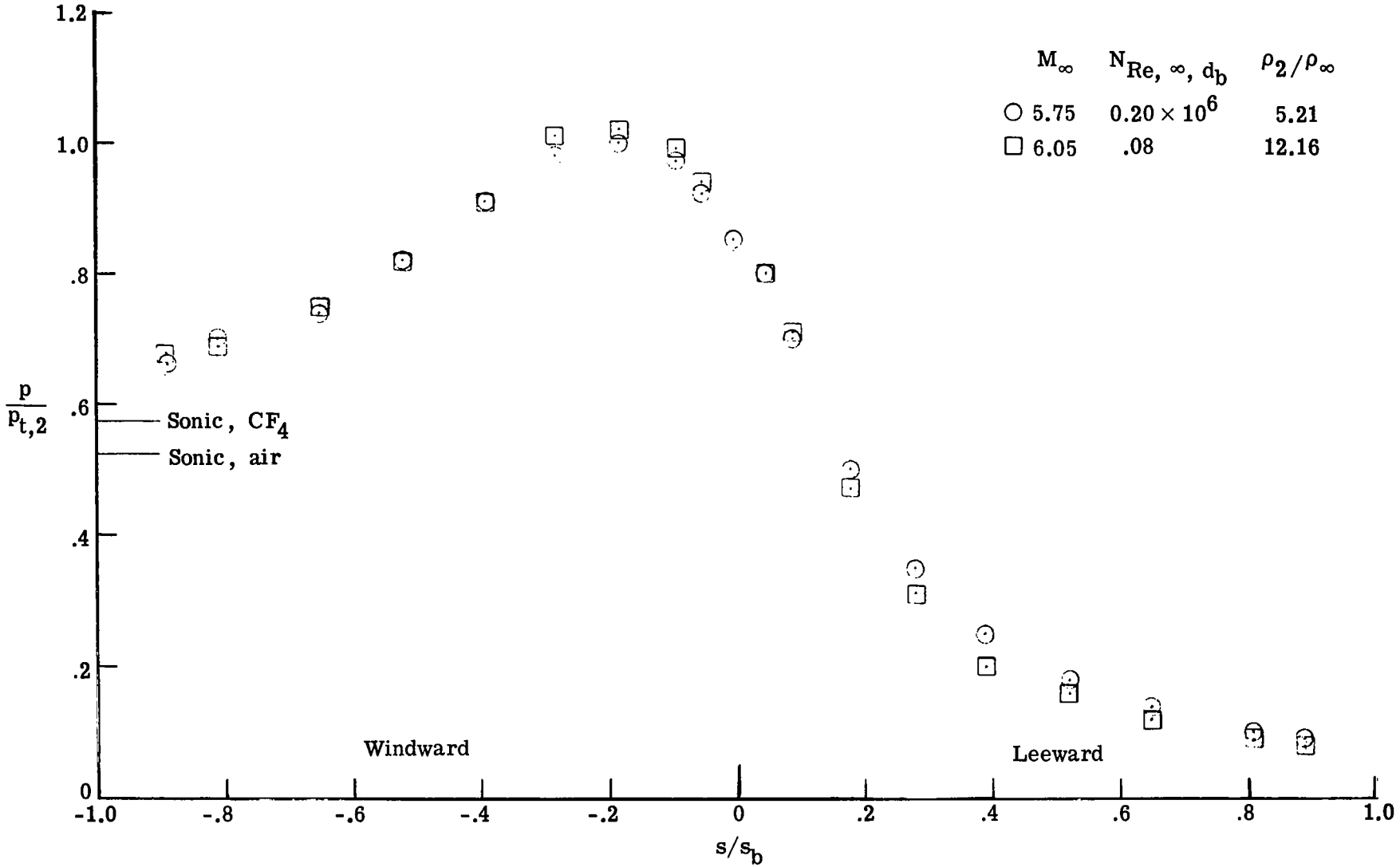

(f) $\alpha = 20°$.

Figure 30.- Concluded.

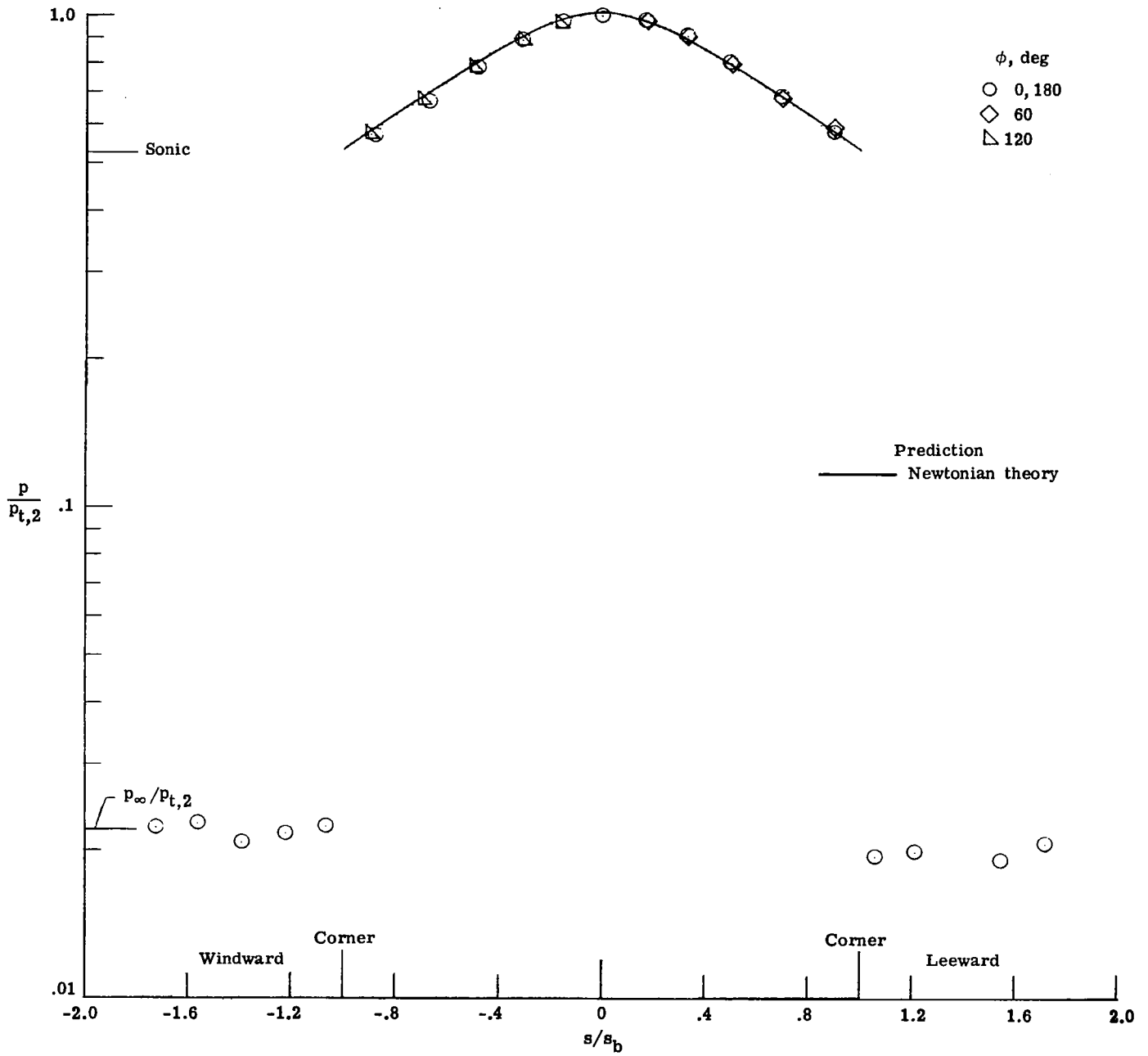

(a) $\alpha = 0°$.

Figure 31.- Pressure distributions measured on the sonic-corner paraboloid (model 2) in Mach 5.9 air.

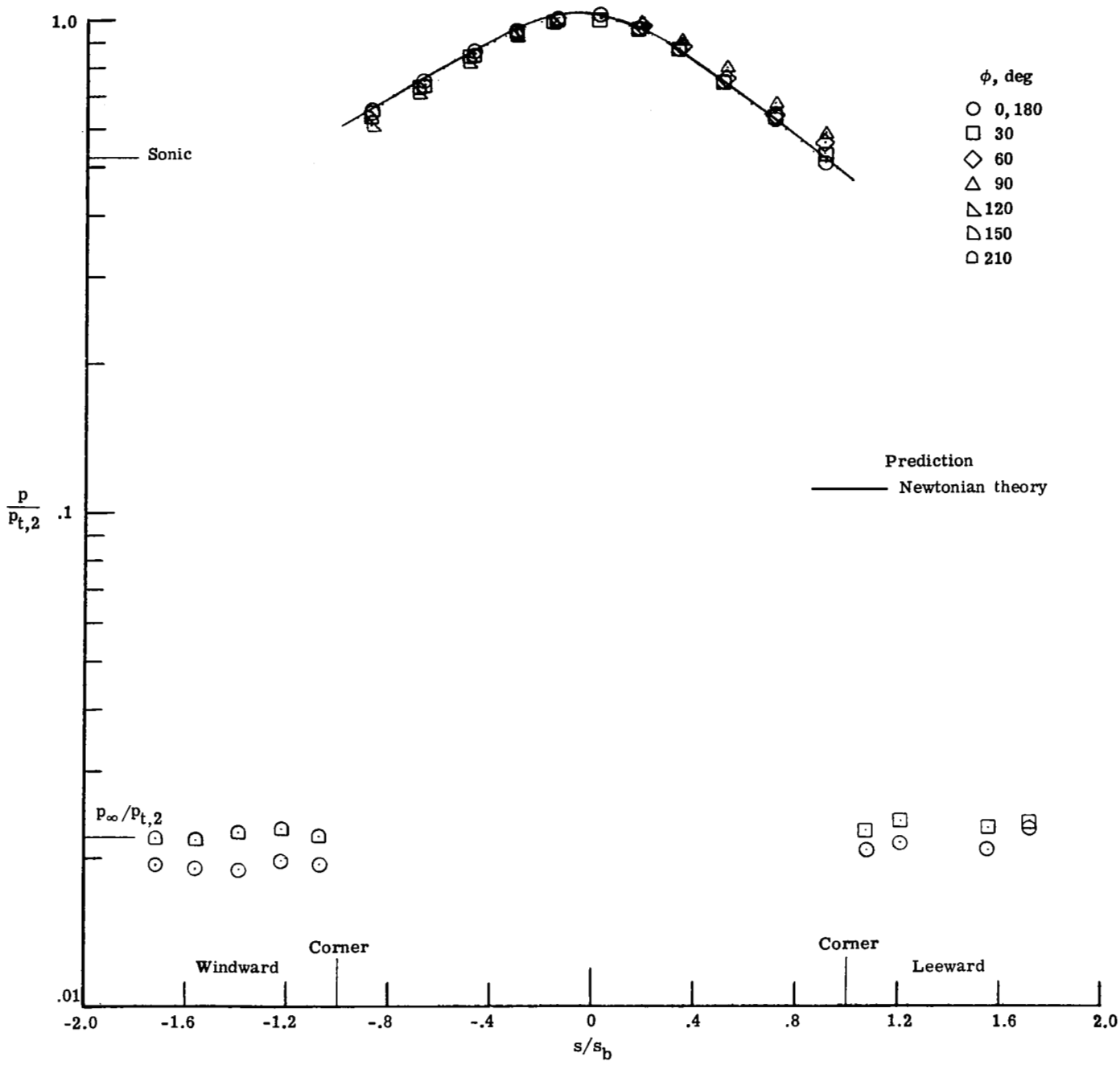

(b) $\alpha = 4°$.

Figure 31.- Continued.

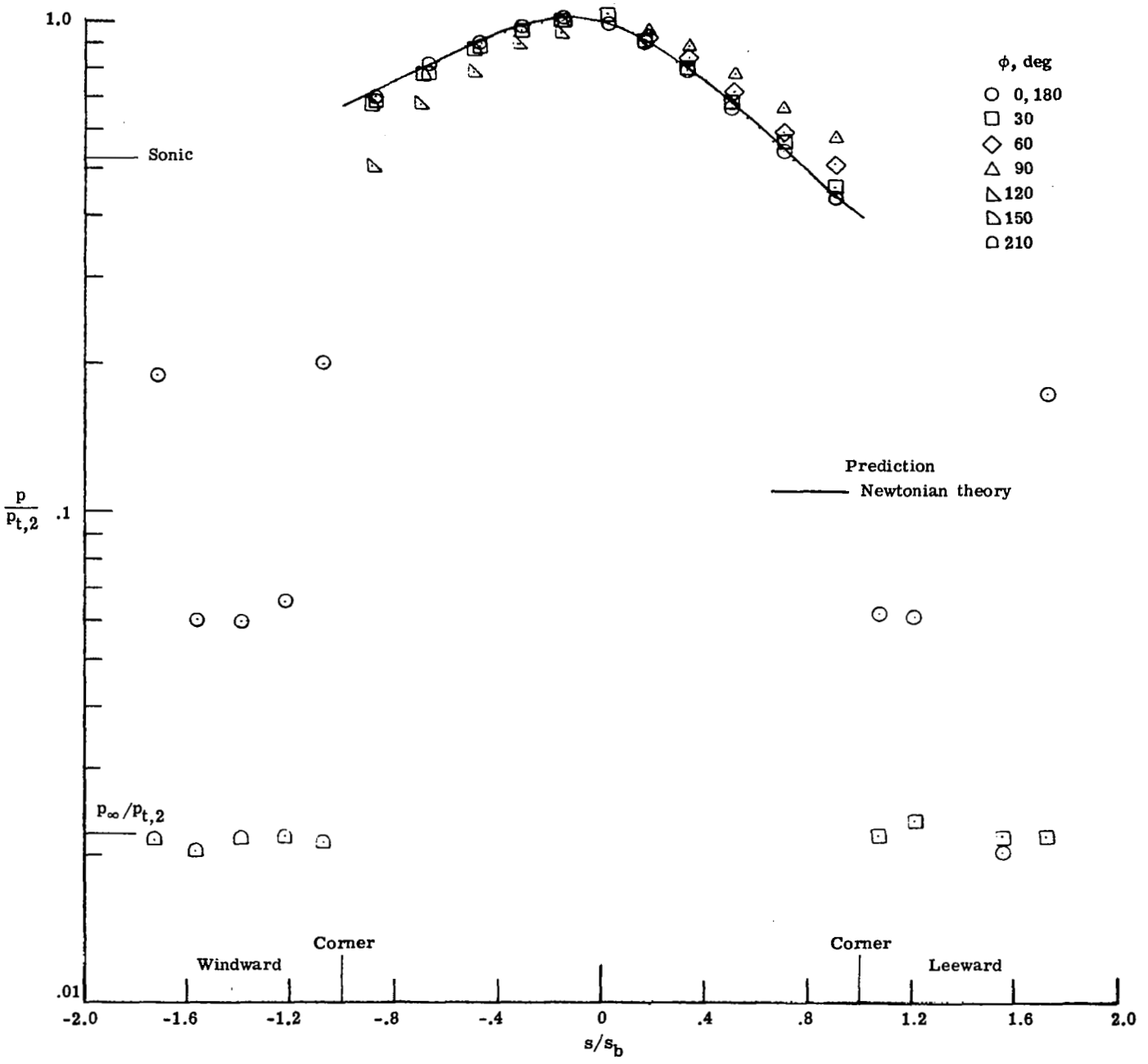

(c) $\alpha = 8°$.

Figure 31.- Continued.

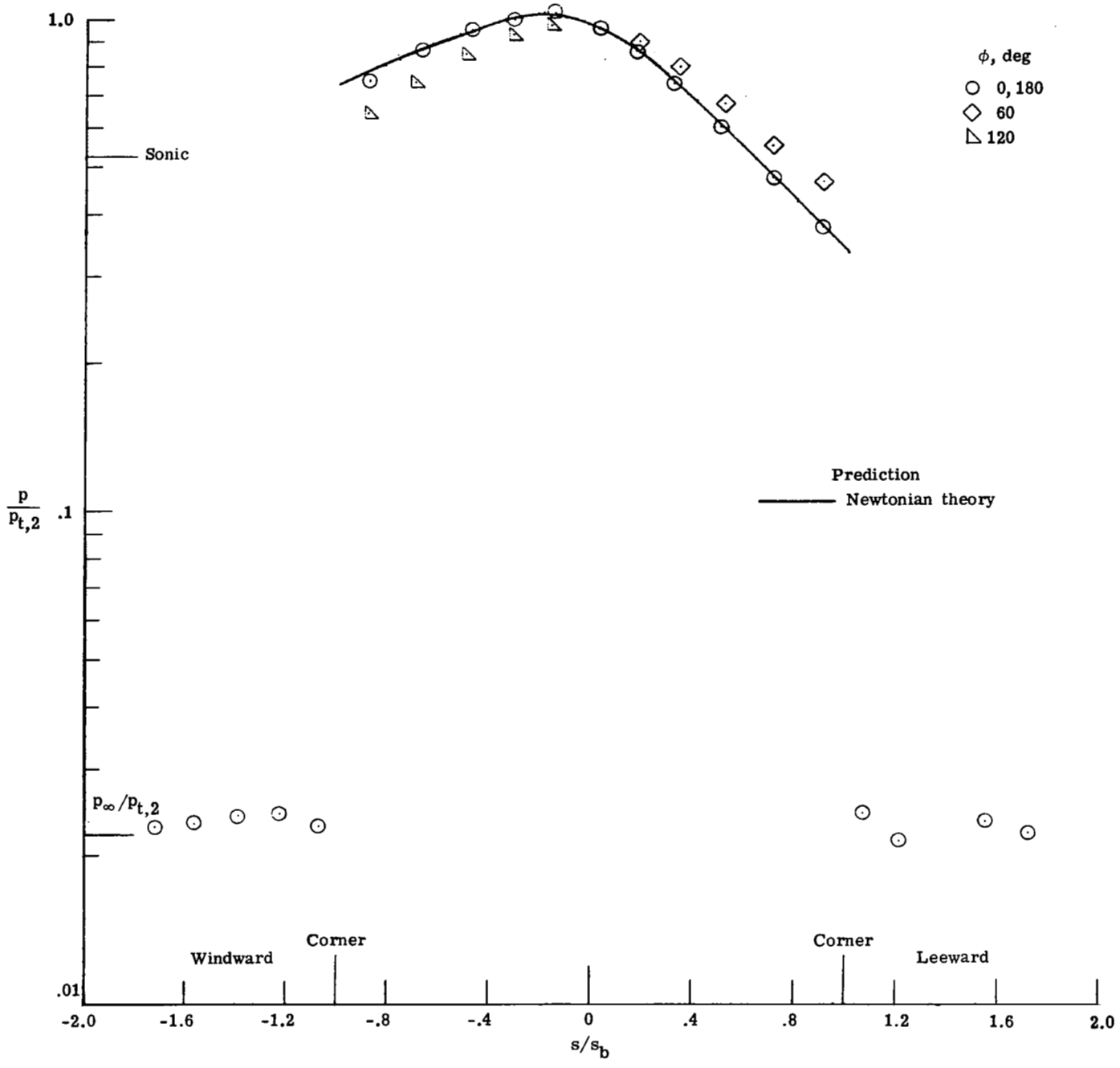

(d) $\alpha = 12°$.

Figure 31.- Continued.

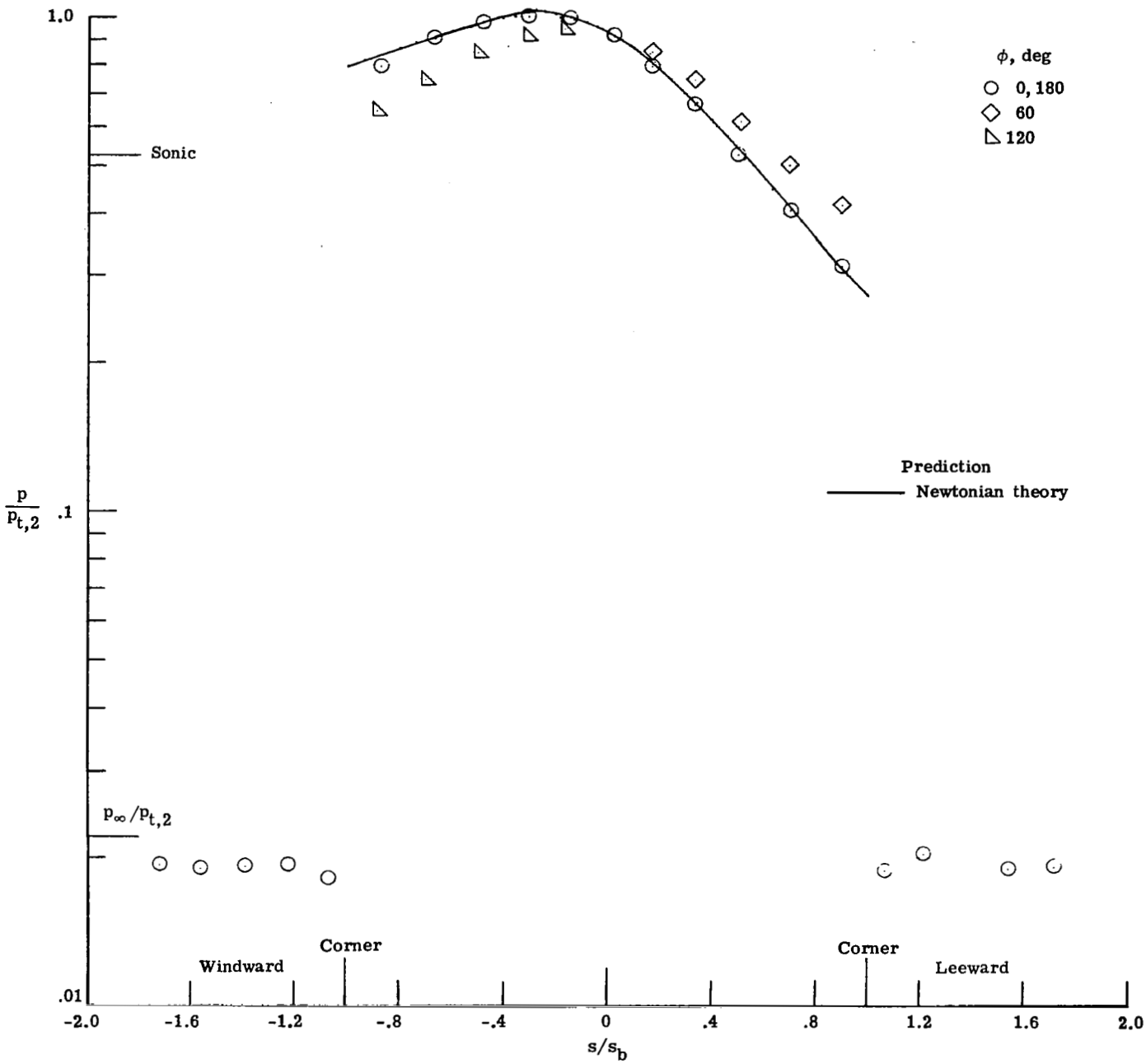

(e) $\alpha = 16°$.

Figure 31.- Concluded.

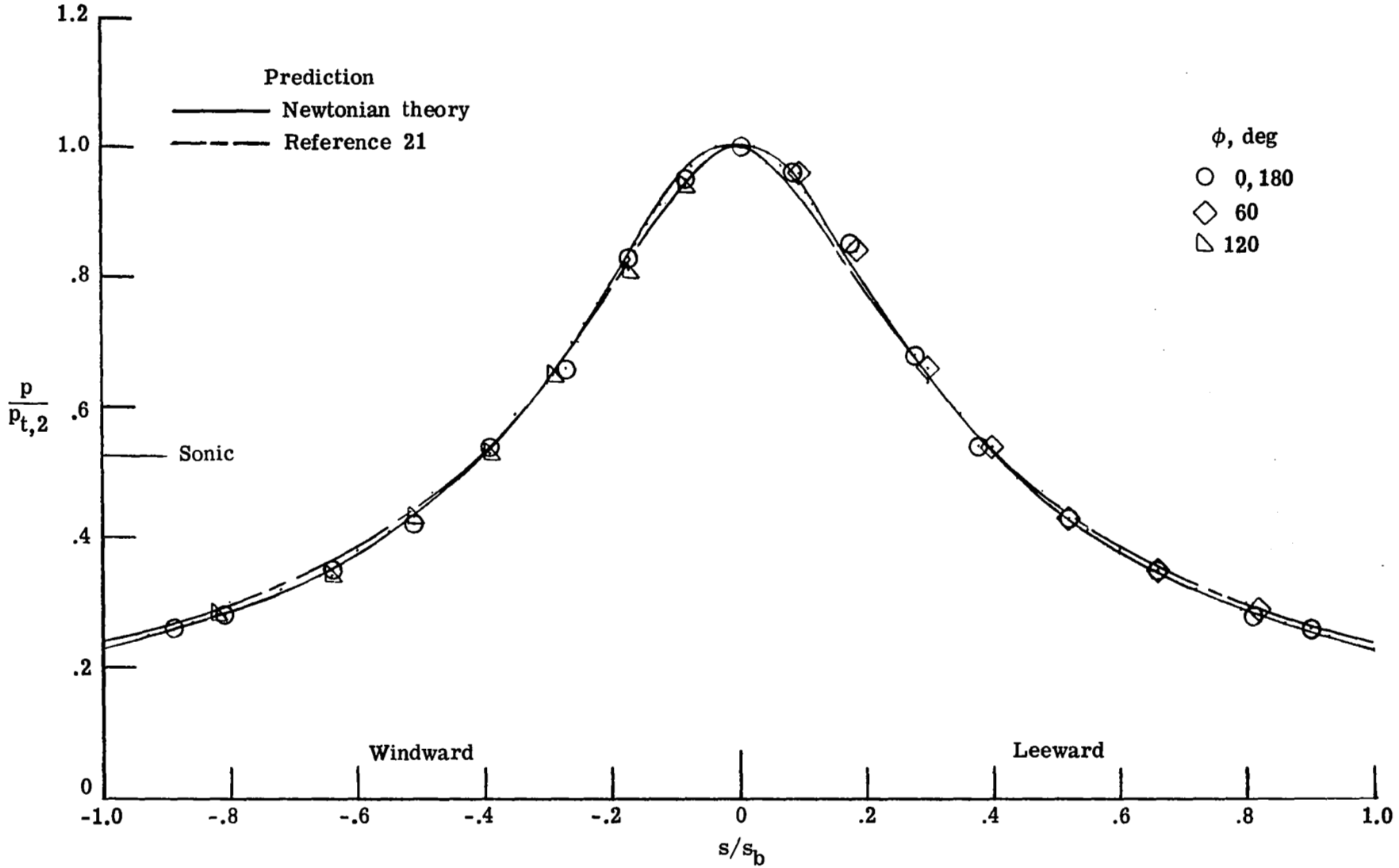

(a) $\alpha = 0°$.

Figure 32.- Pressure distributions measured on the paraboloid (model 3, series 2) in Mach 5.9 air.

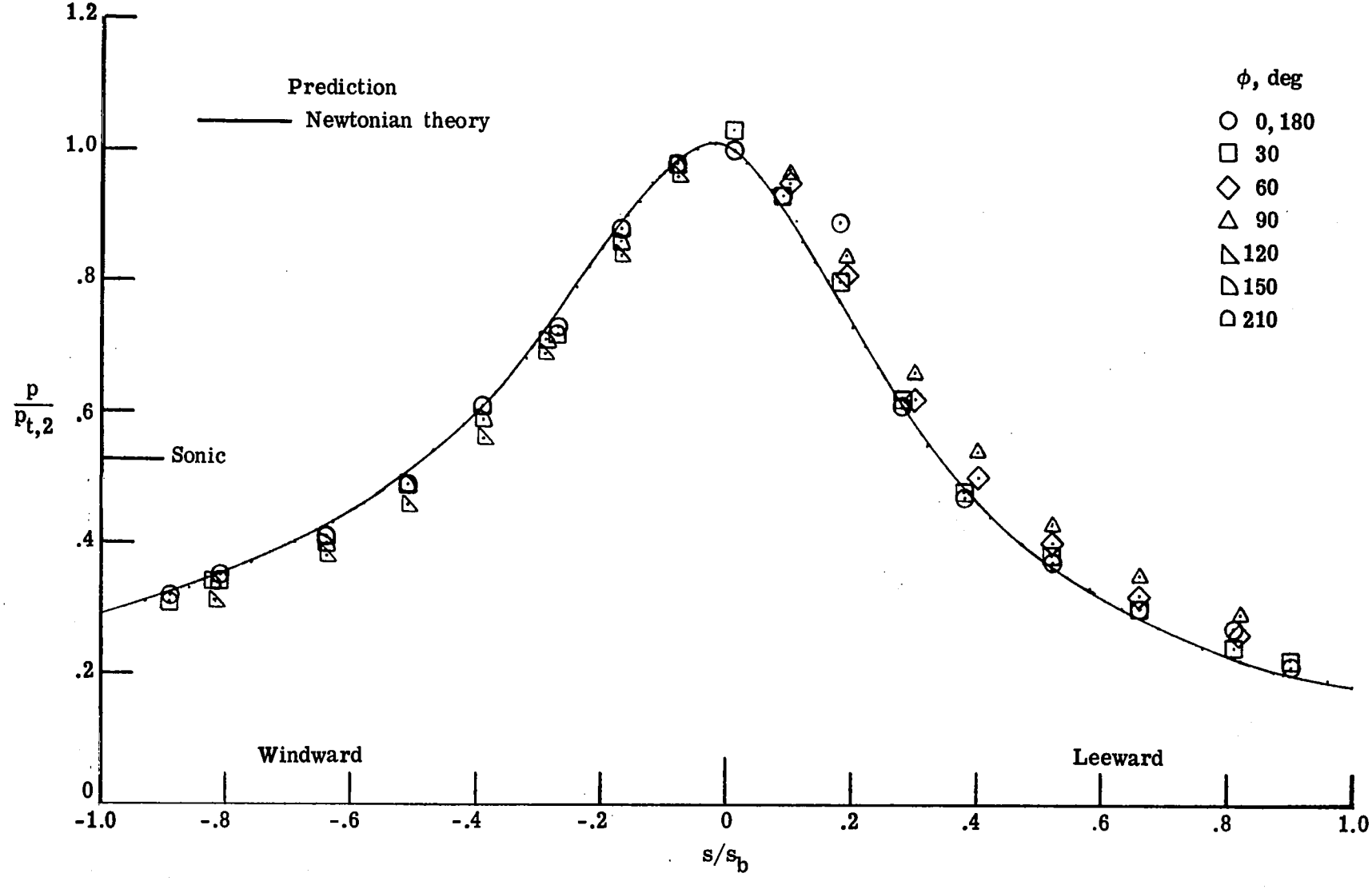

(b) $\alpha = 4°$.

Figure 32.- Continued.

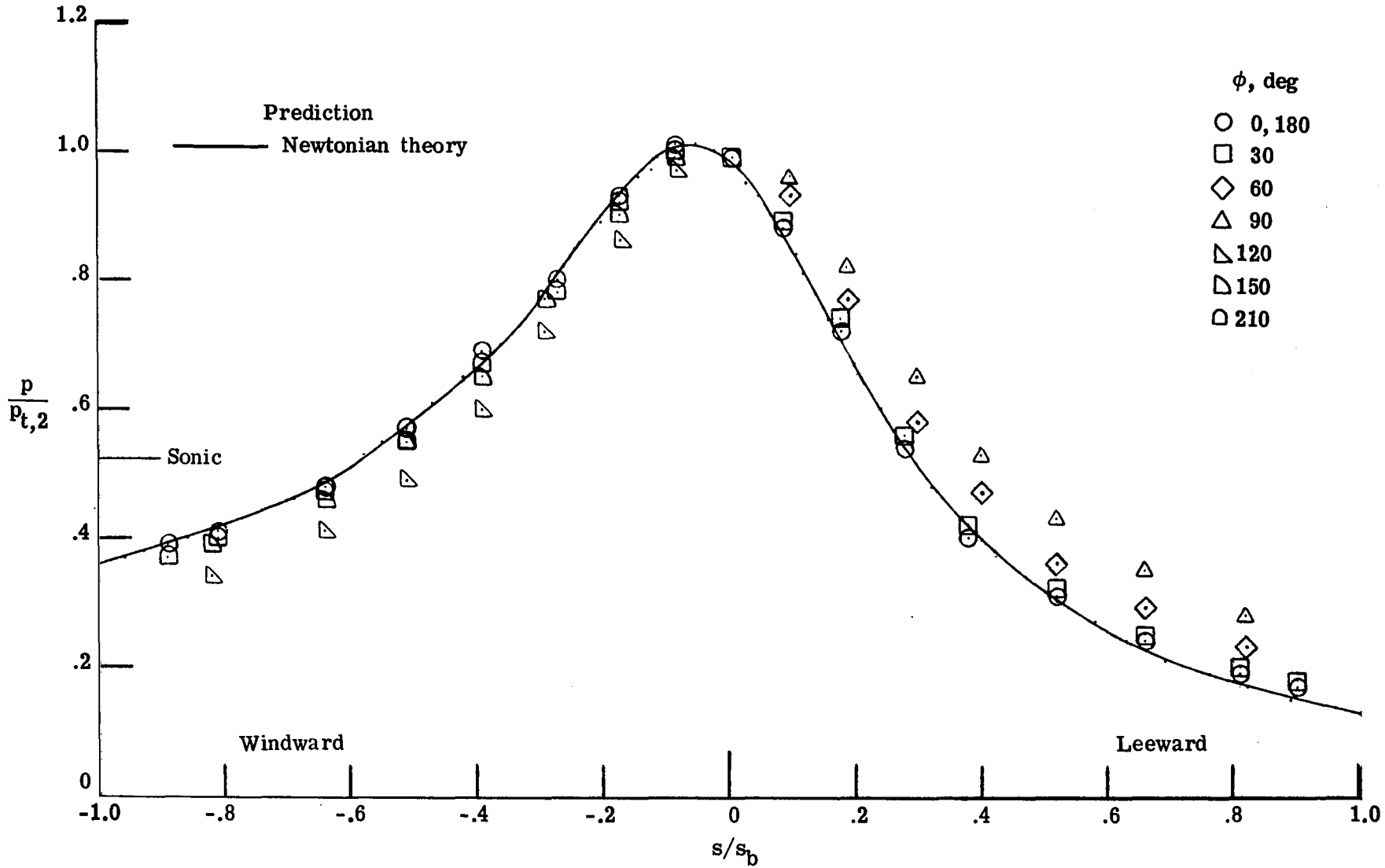

(c) $\alpha = 8°$.

Figure 32.- Continued.

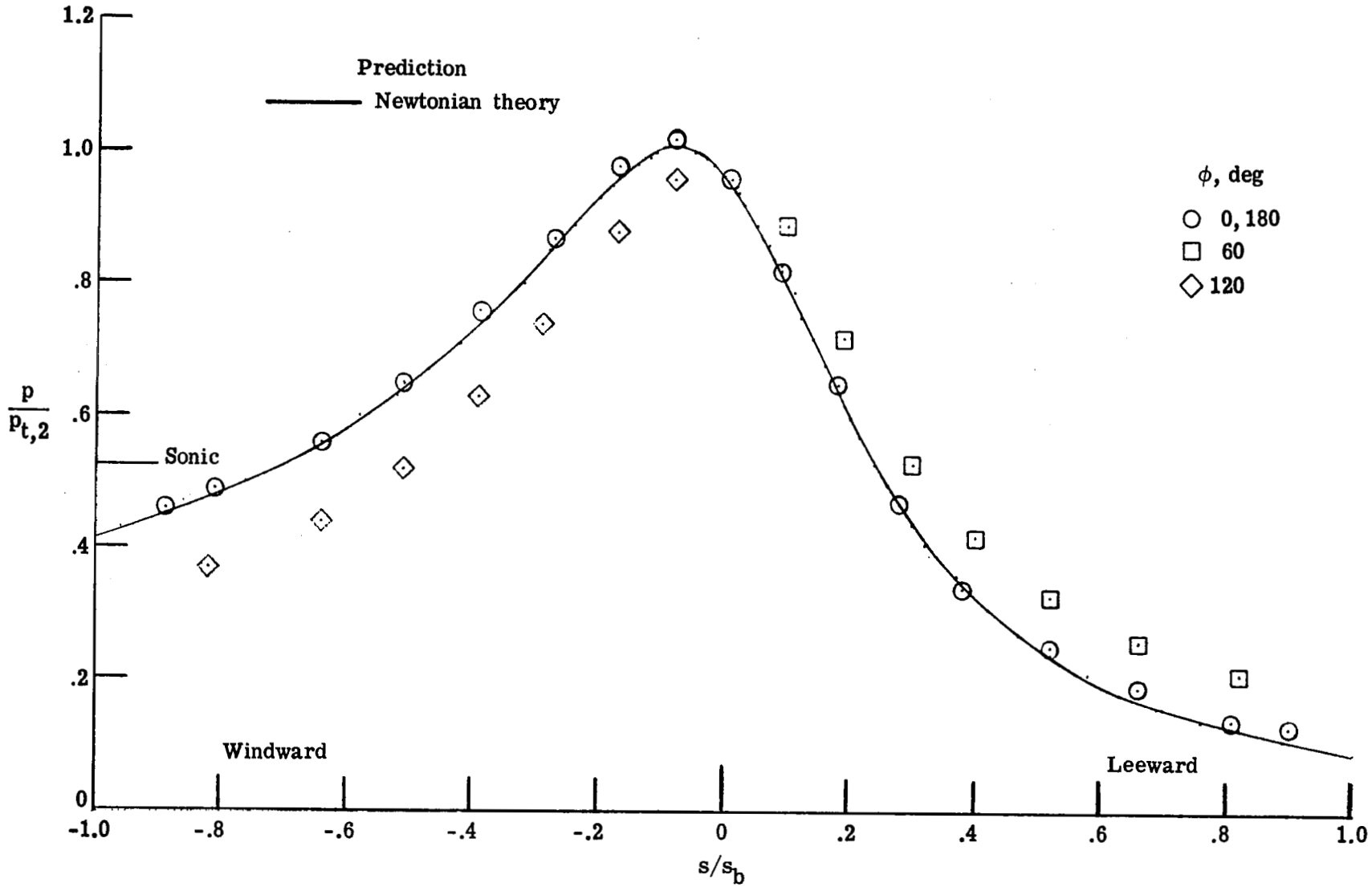

(d) $\alpha = 12°$.

Figure 32.- Continued.

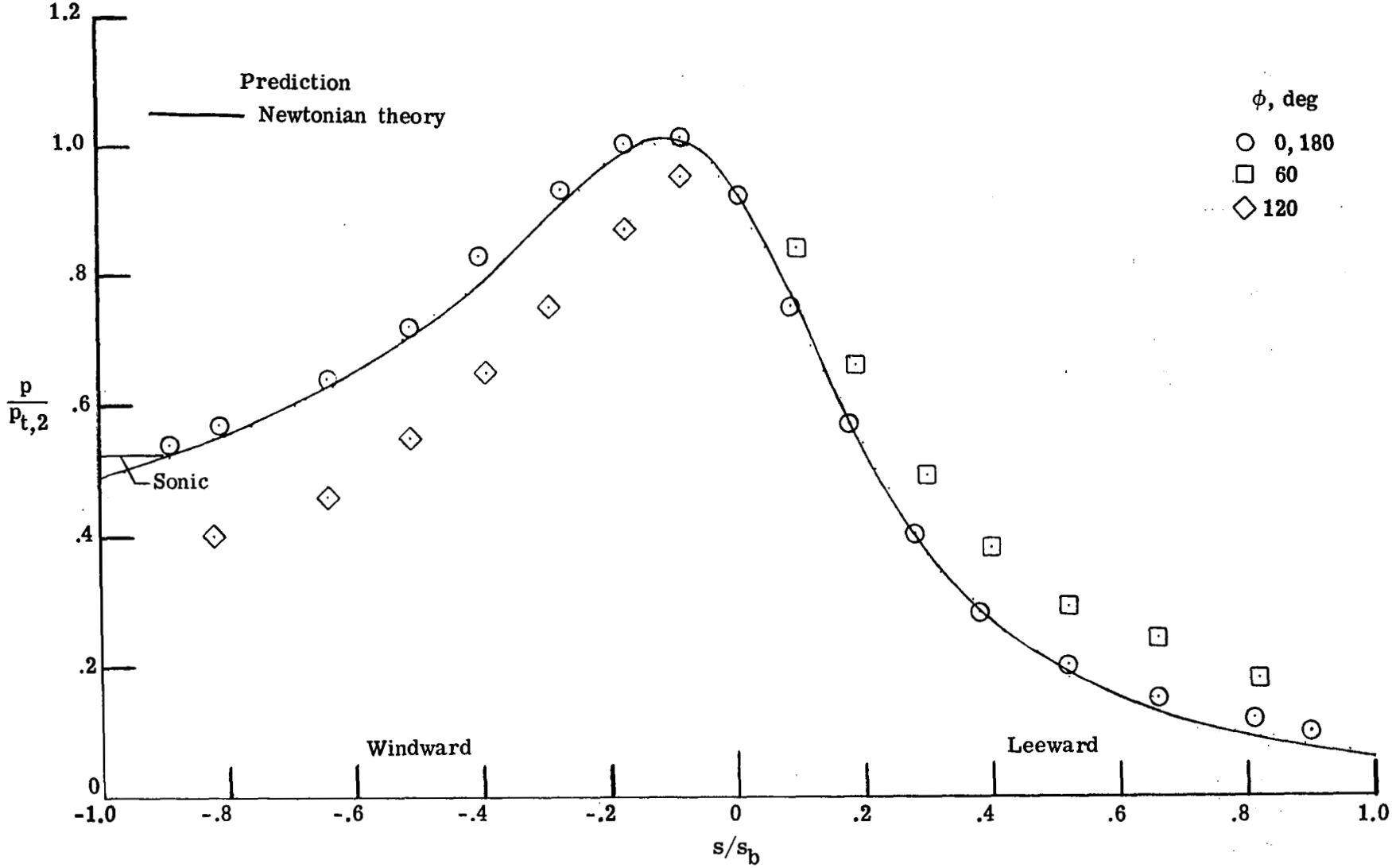

(e) $\alpha = 16°$.

Figure 32.- Continued.

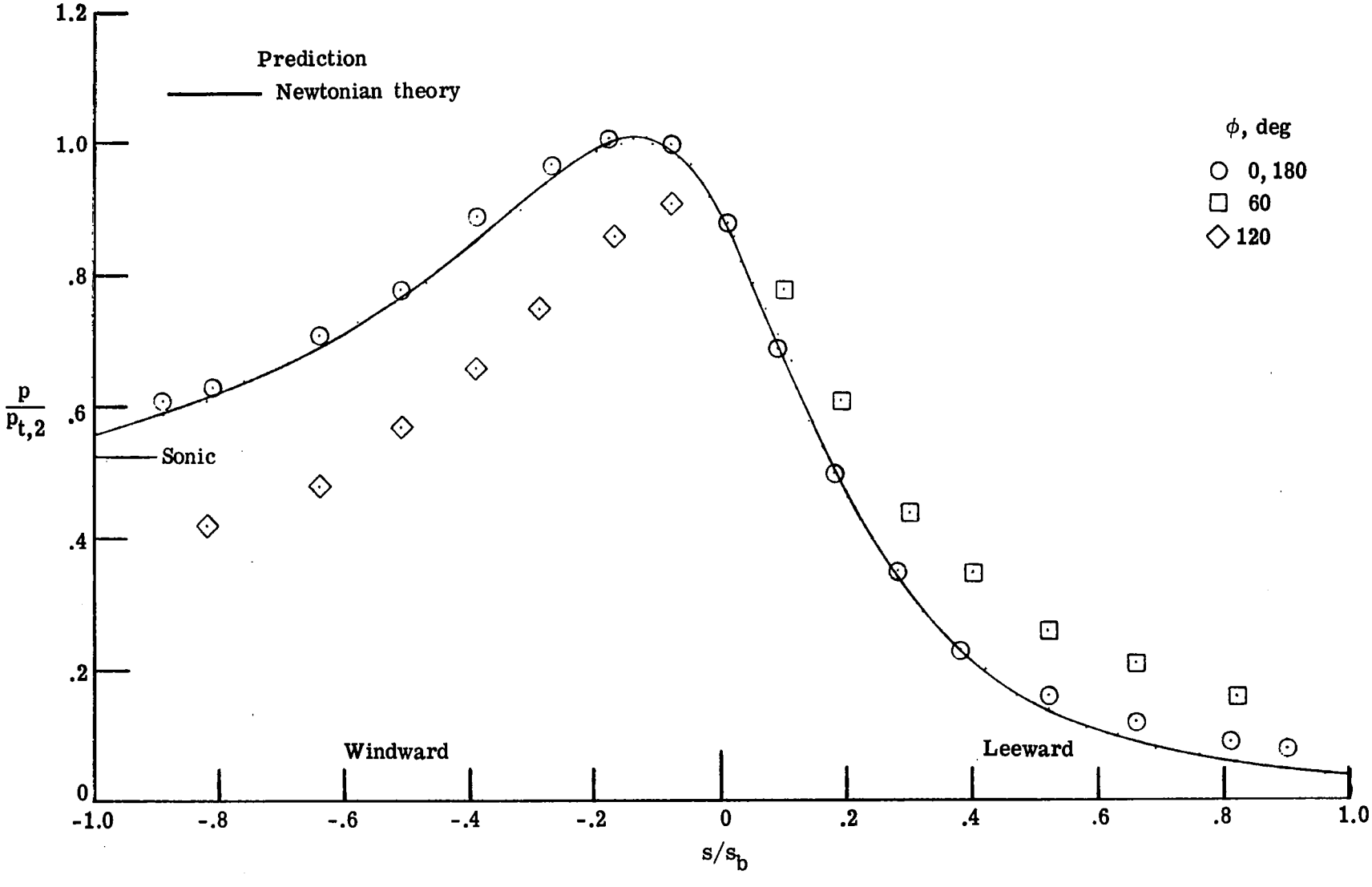

(f) $\alpha = 20°$.

Figure 32.- Concluded.

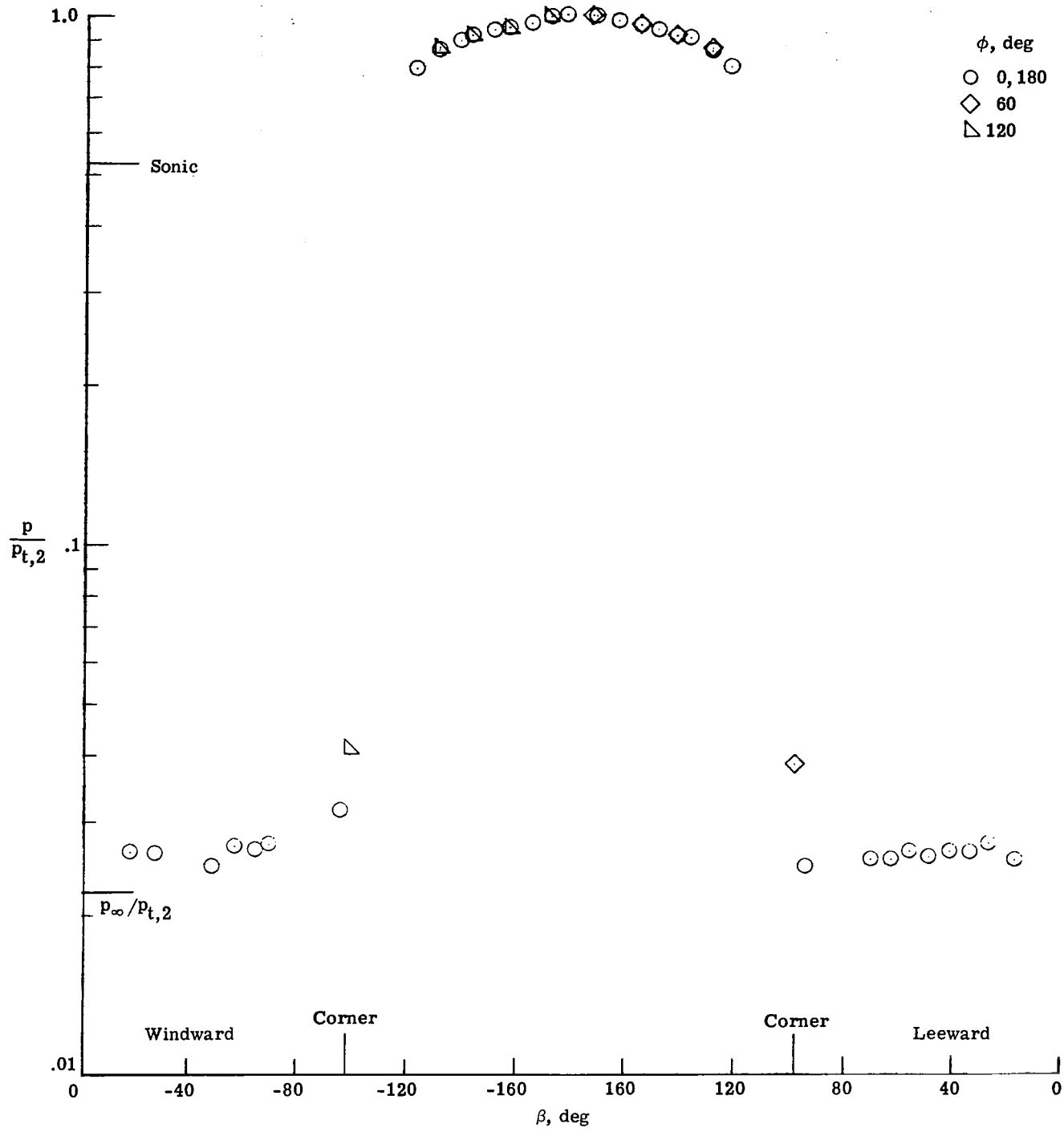

(a) $\alpha = 0°$.

Figure 33.- Pressure distributions measured on the Viking aeroshell (model 4) in Mach 5.9 air.

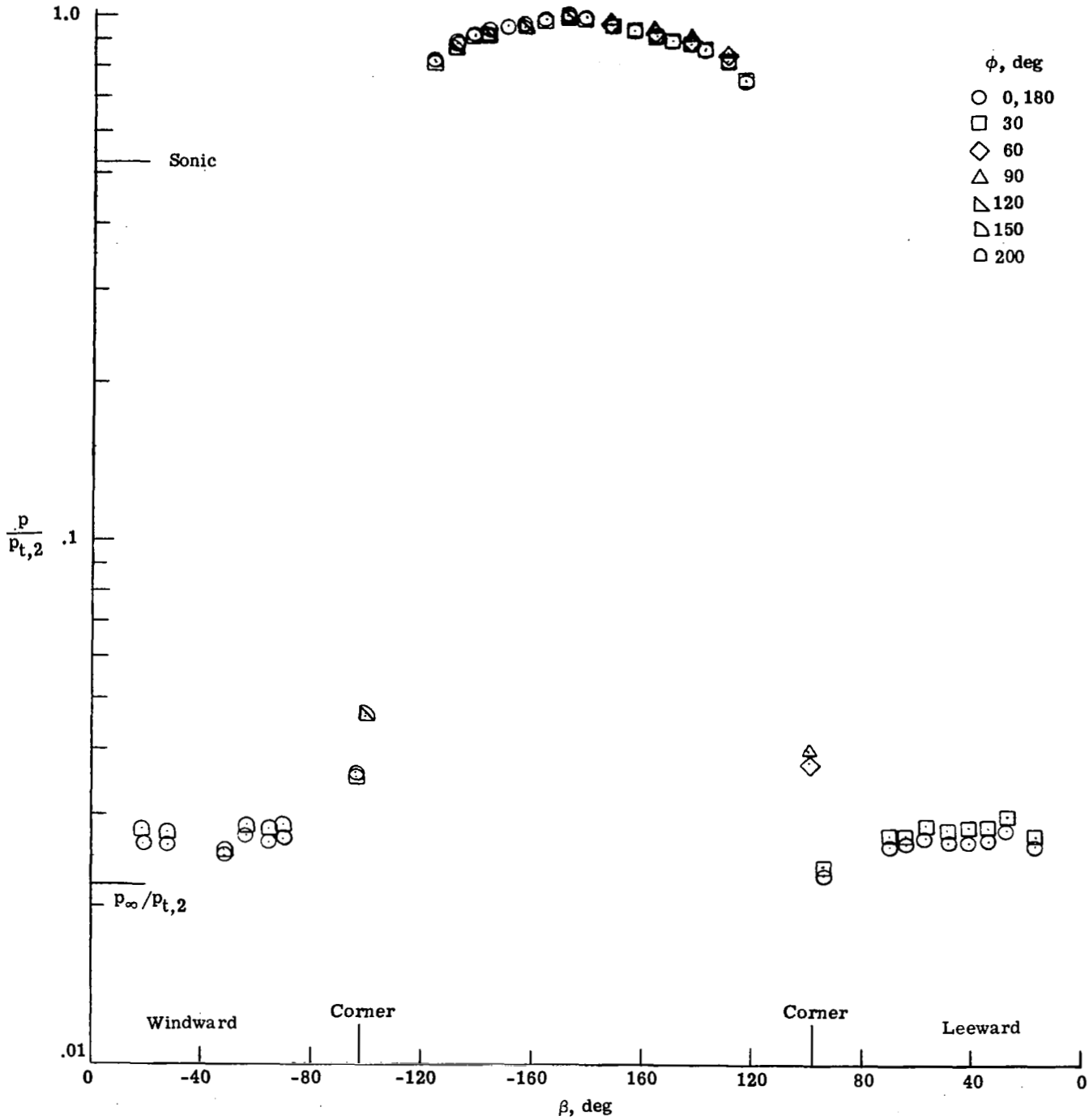

(b) $\alpha = 4°$.

Figure 33.- Continued.

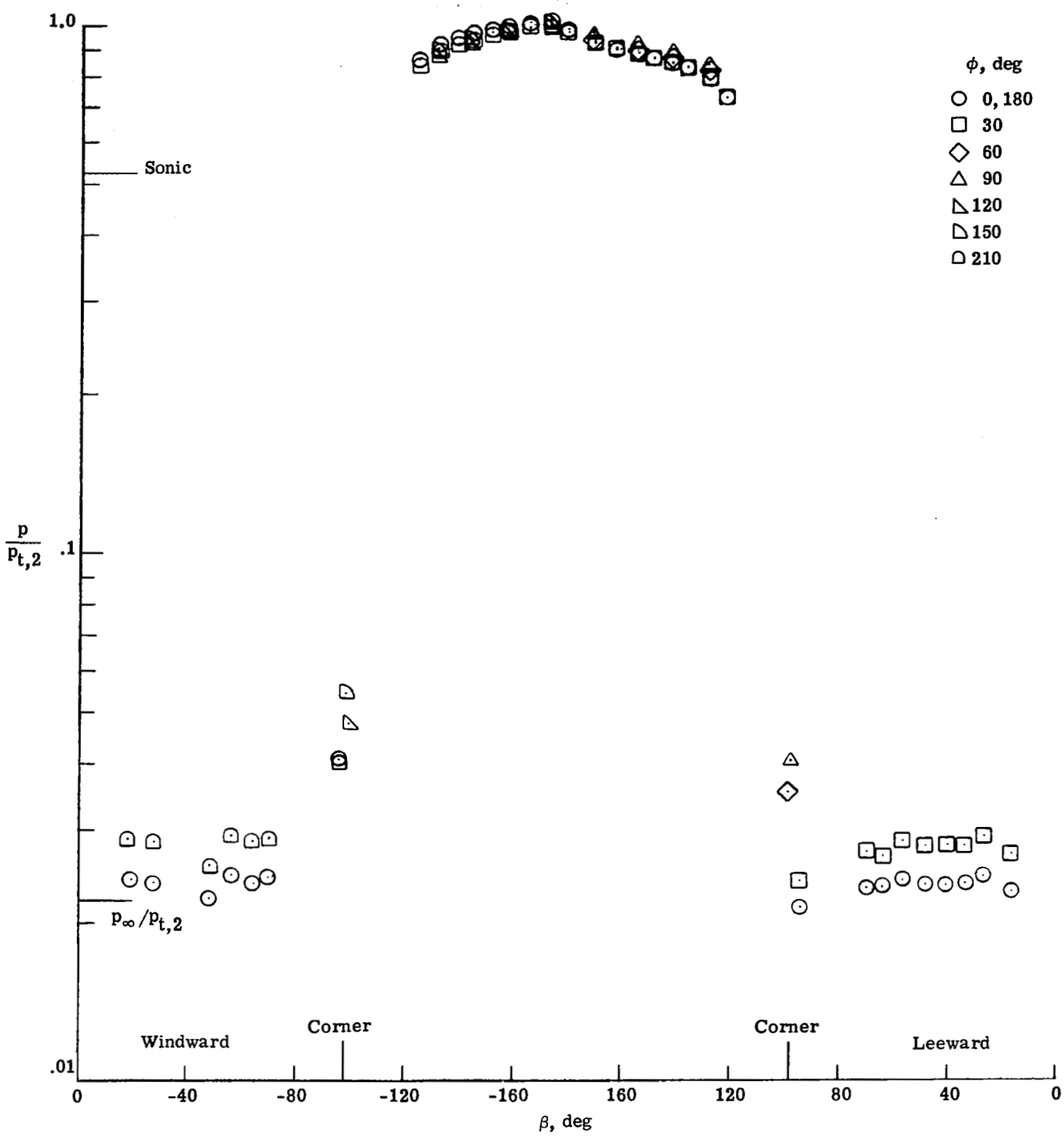

(c) $\alpha = 8°$.

Figure 33.- Continued.

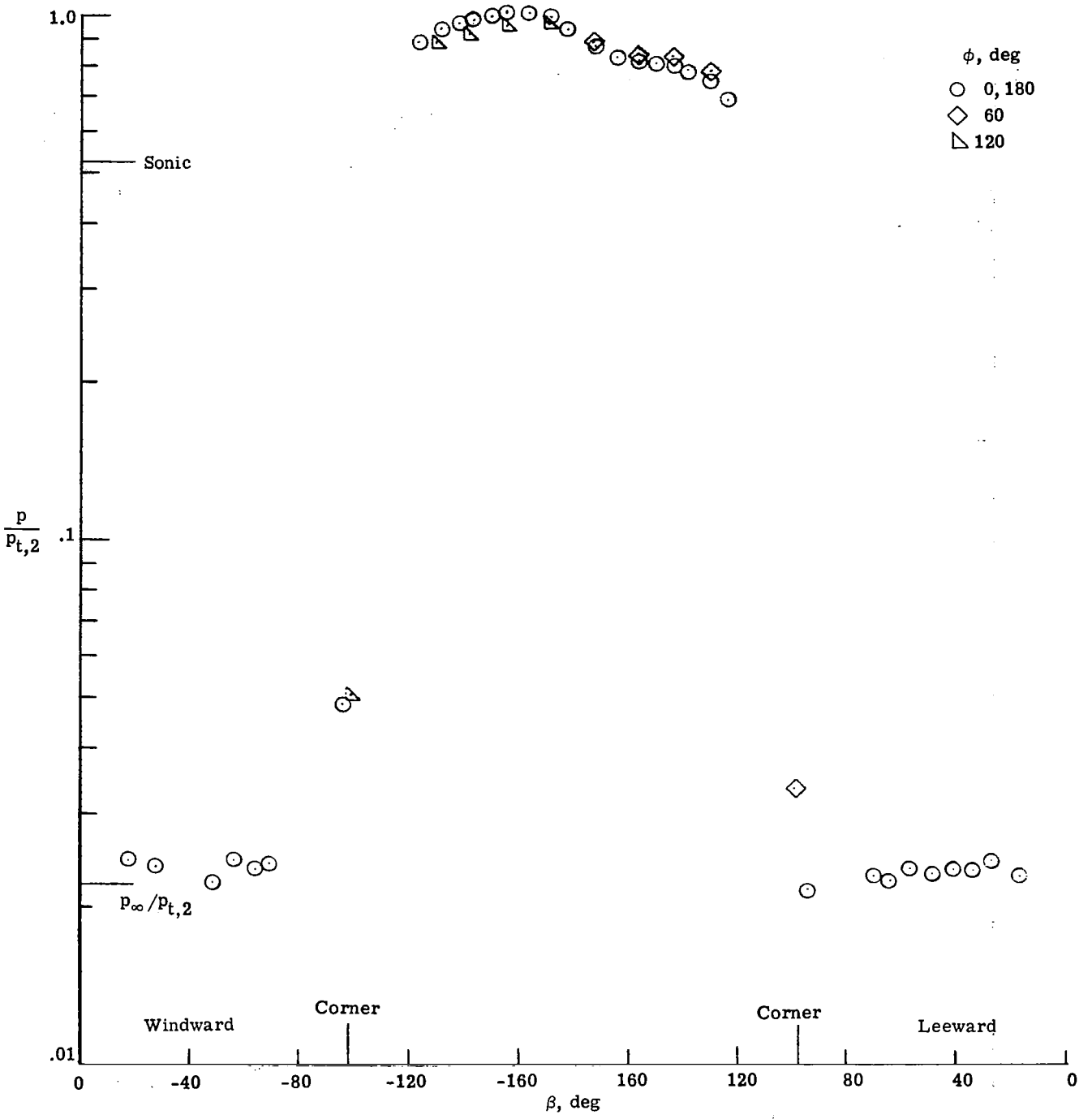

(d) $\alpha = 12°$.

Figure 33.- Continued.

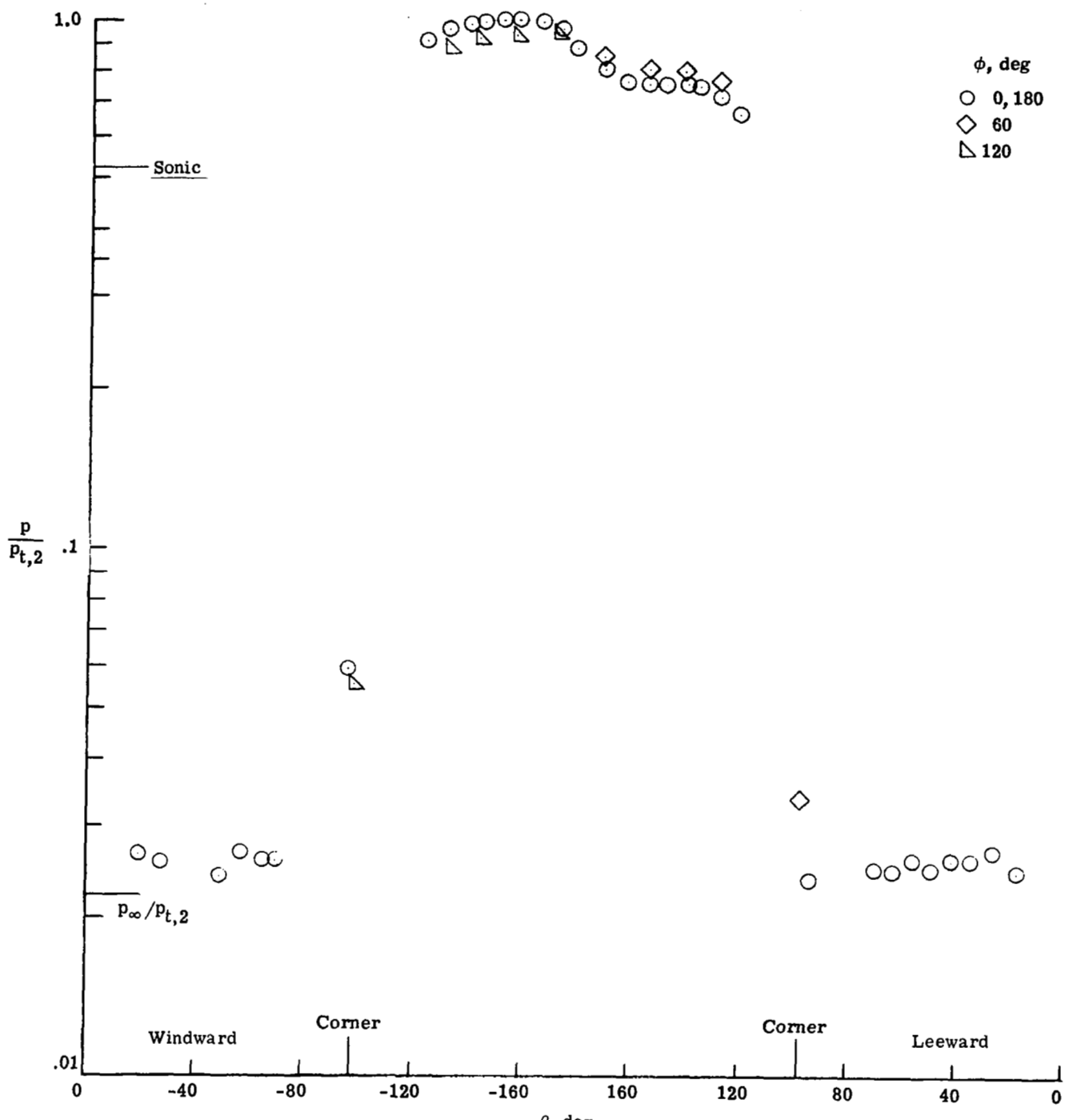

(e) $\alpha = 16°$.

Figure 33.- Concluded.

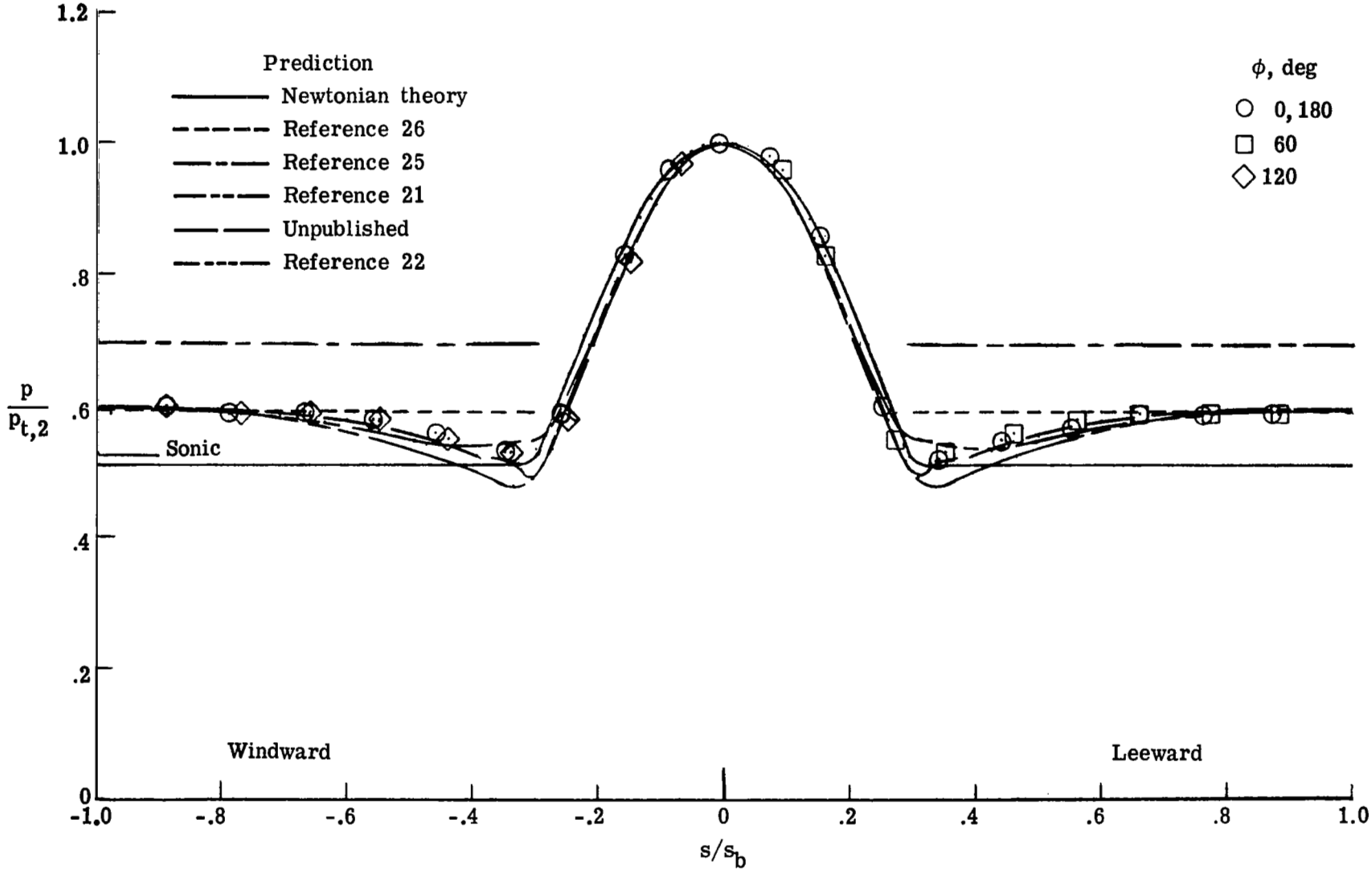

(a) $\alpha = 0°$.

Figure 34.- Pressure distributions measured on the spherical-nose cone (model 5) in Mach 5.9 air.

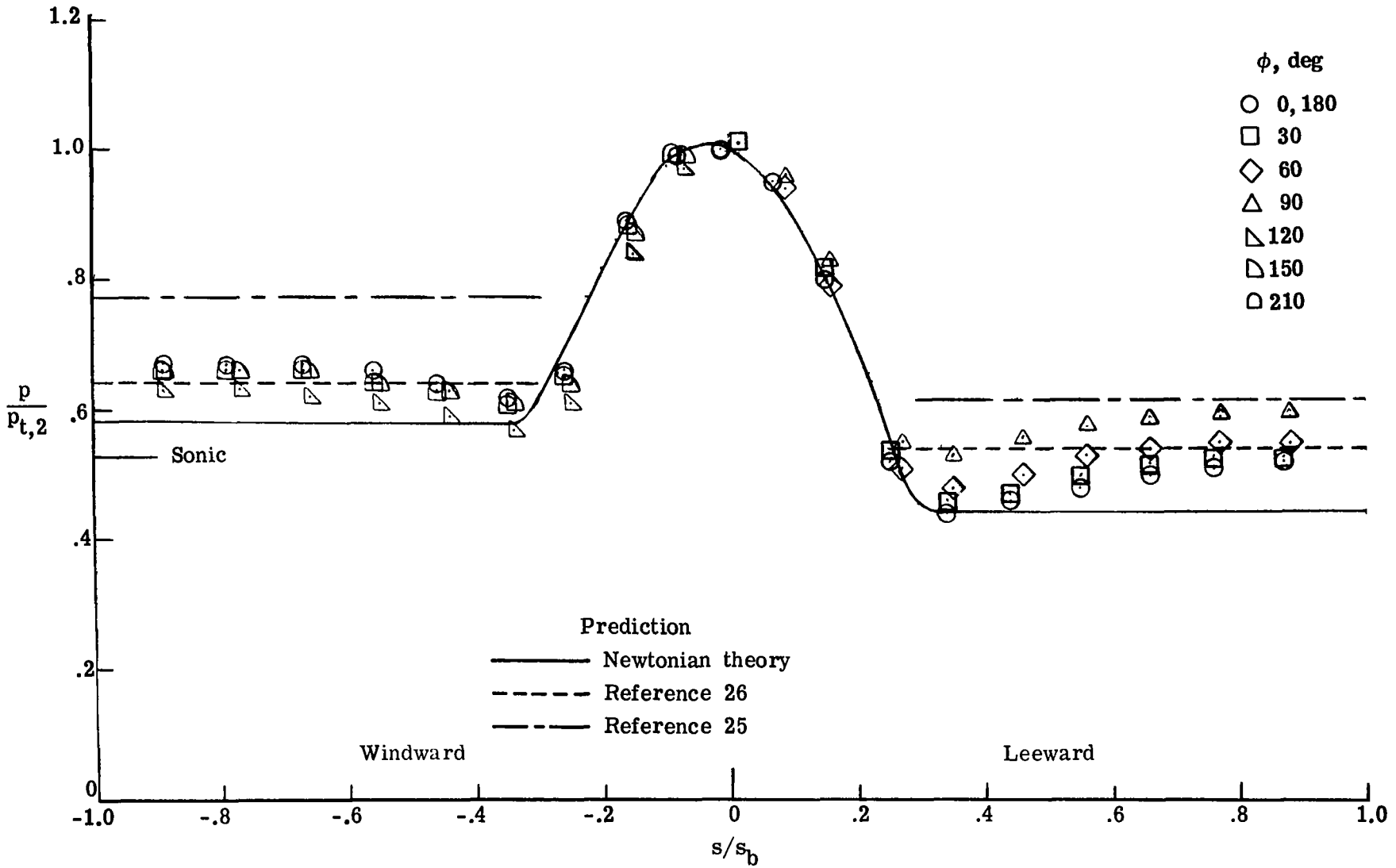

(b) $\alpha = 4°$.

Figure 34.- Continued.

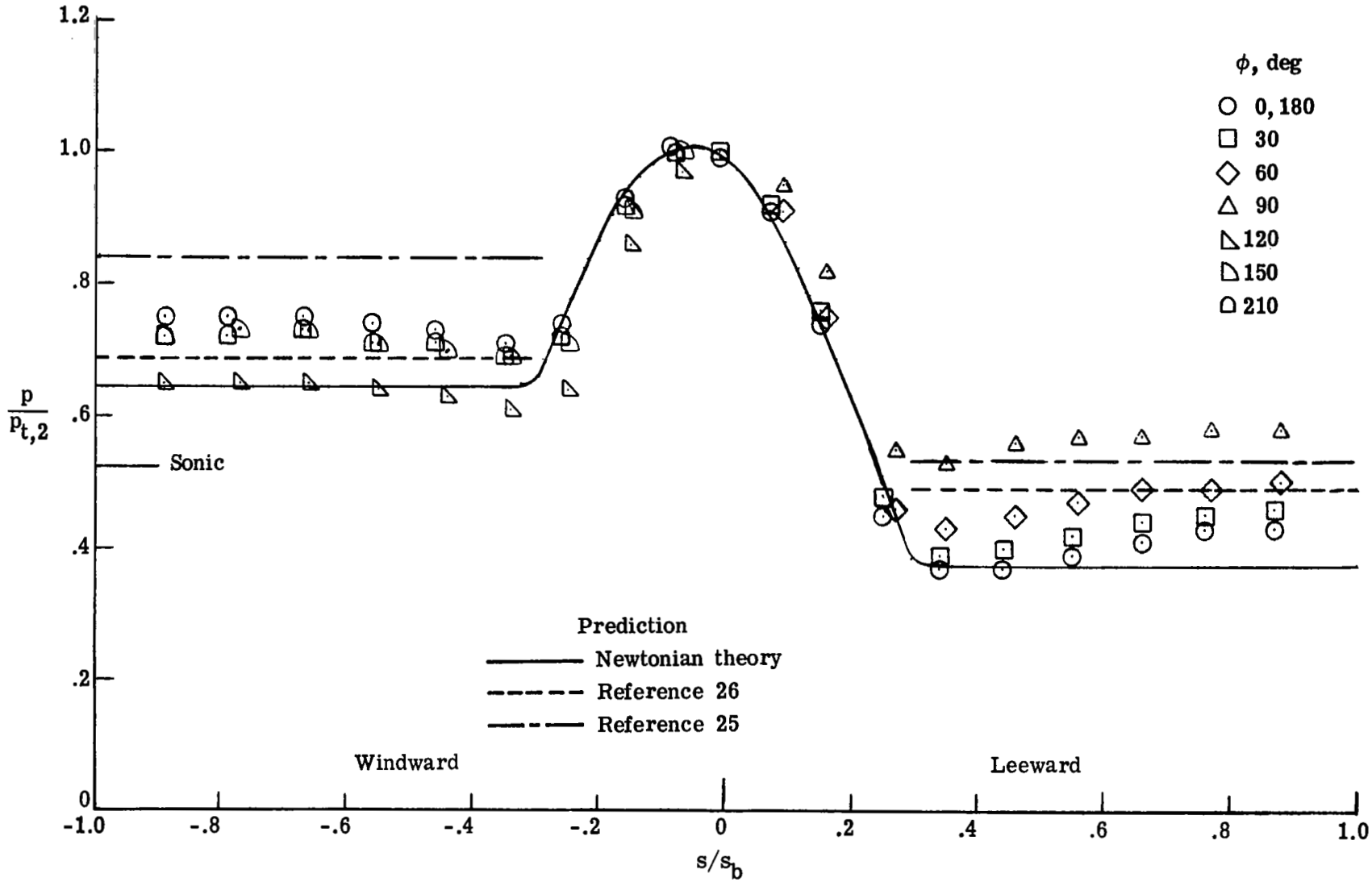

(c) $\alpha = 8°$.

Figure 34.- Continued.

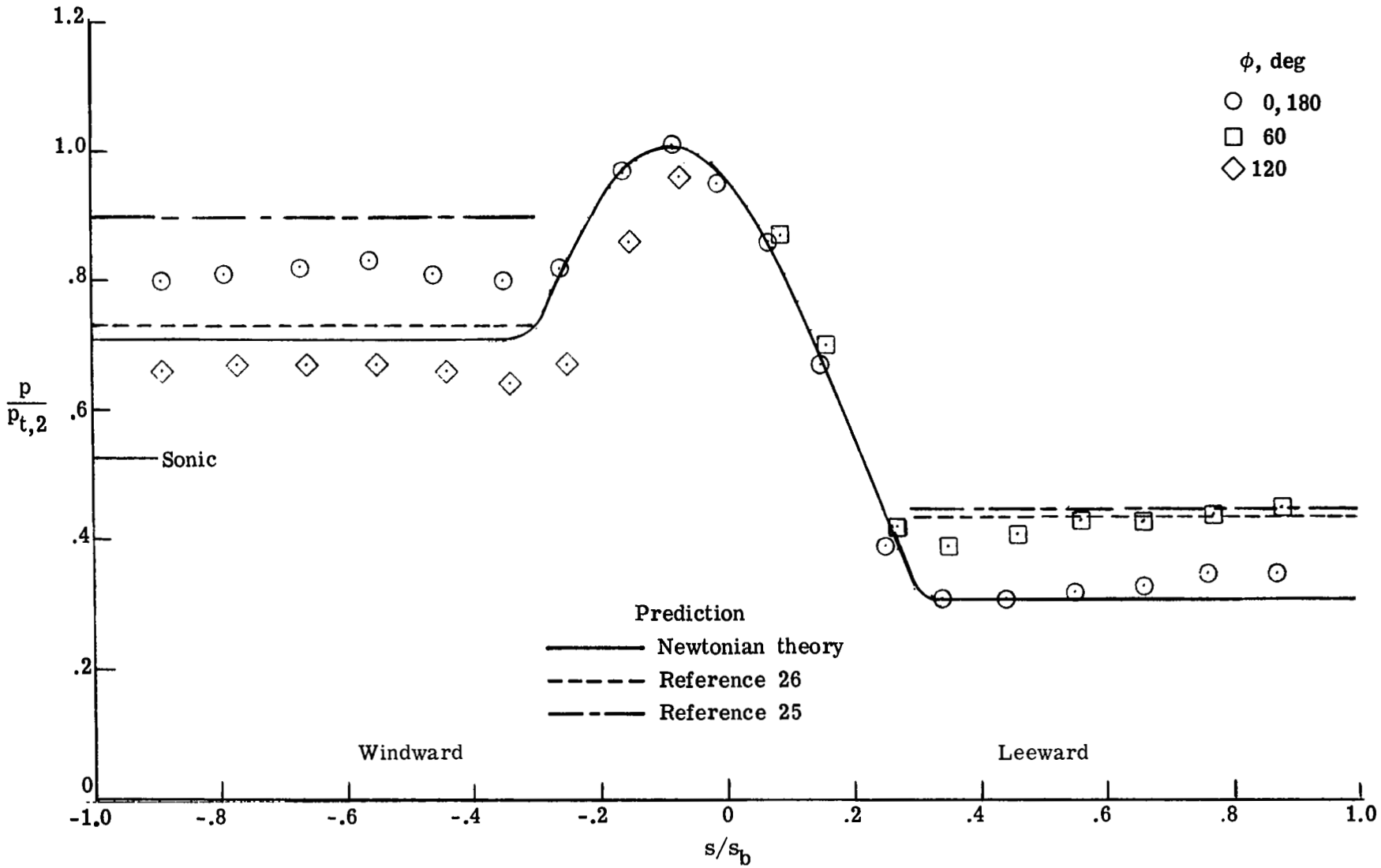

(d) $\alpha = 12°$.

Figure 34.- Continued.

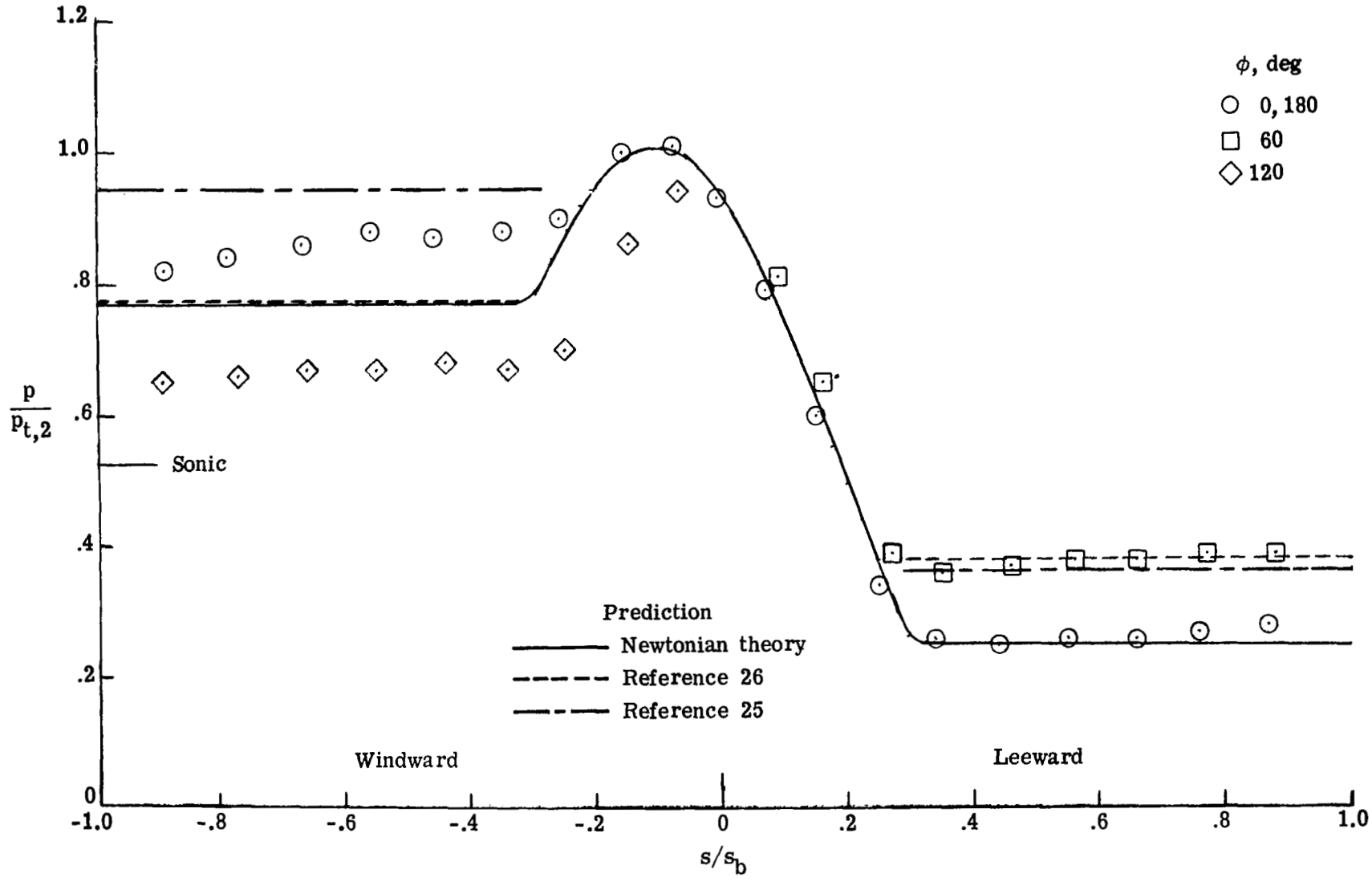

(e) $\alpha = 16°$.

Figure 34.- Continued.

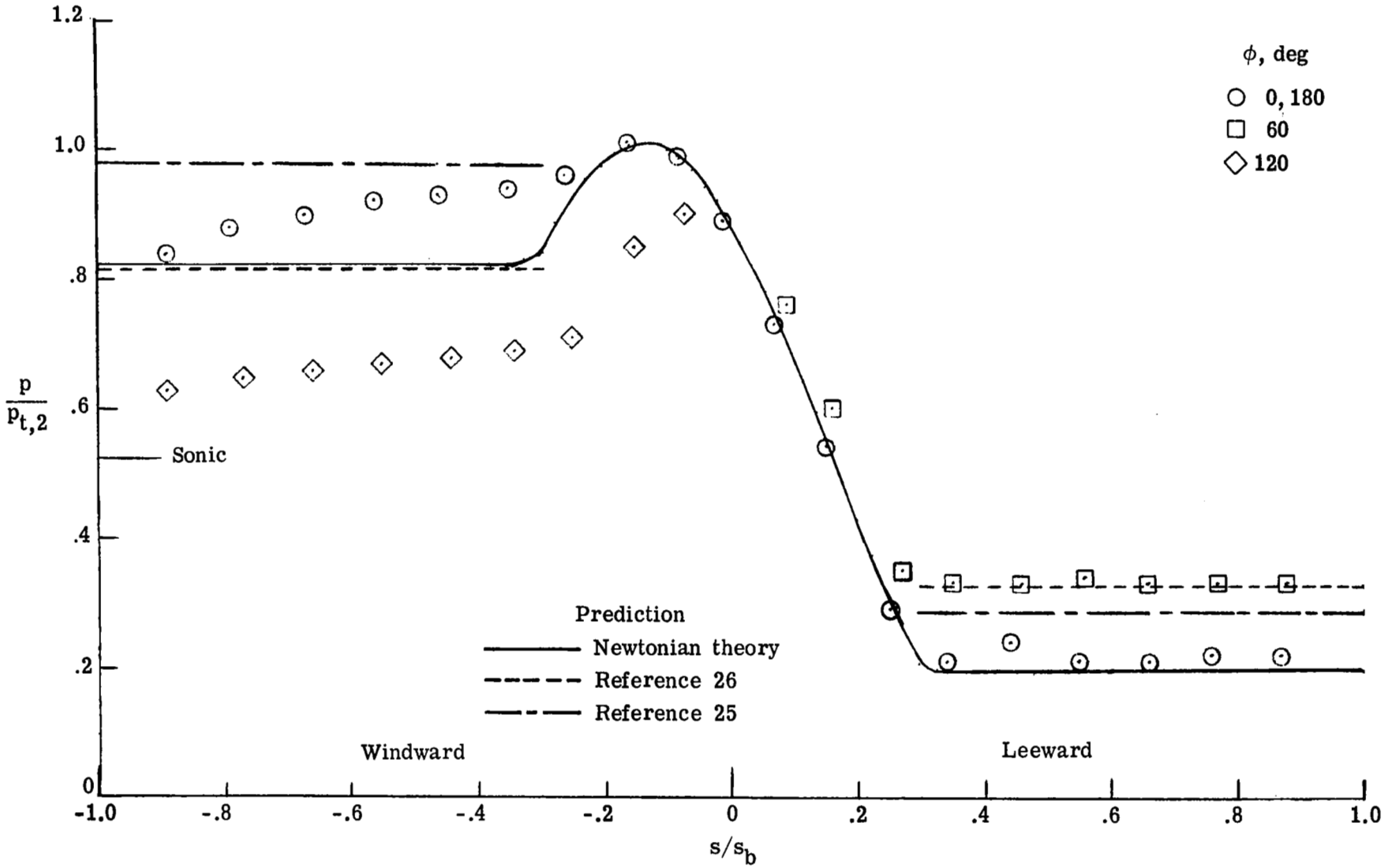

(f) $\alpha = 20°$.

Figure 34.- Concluded.

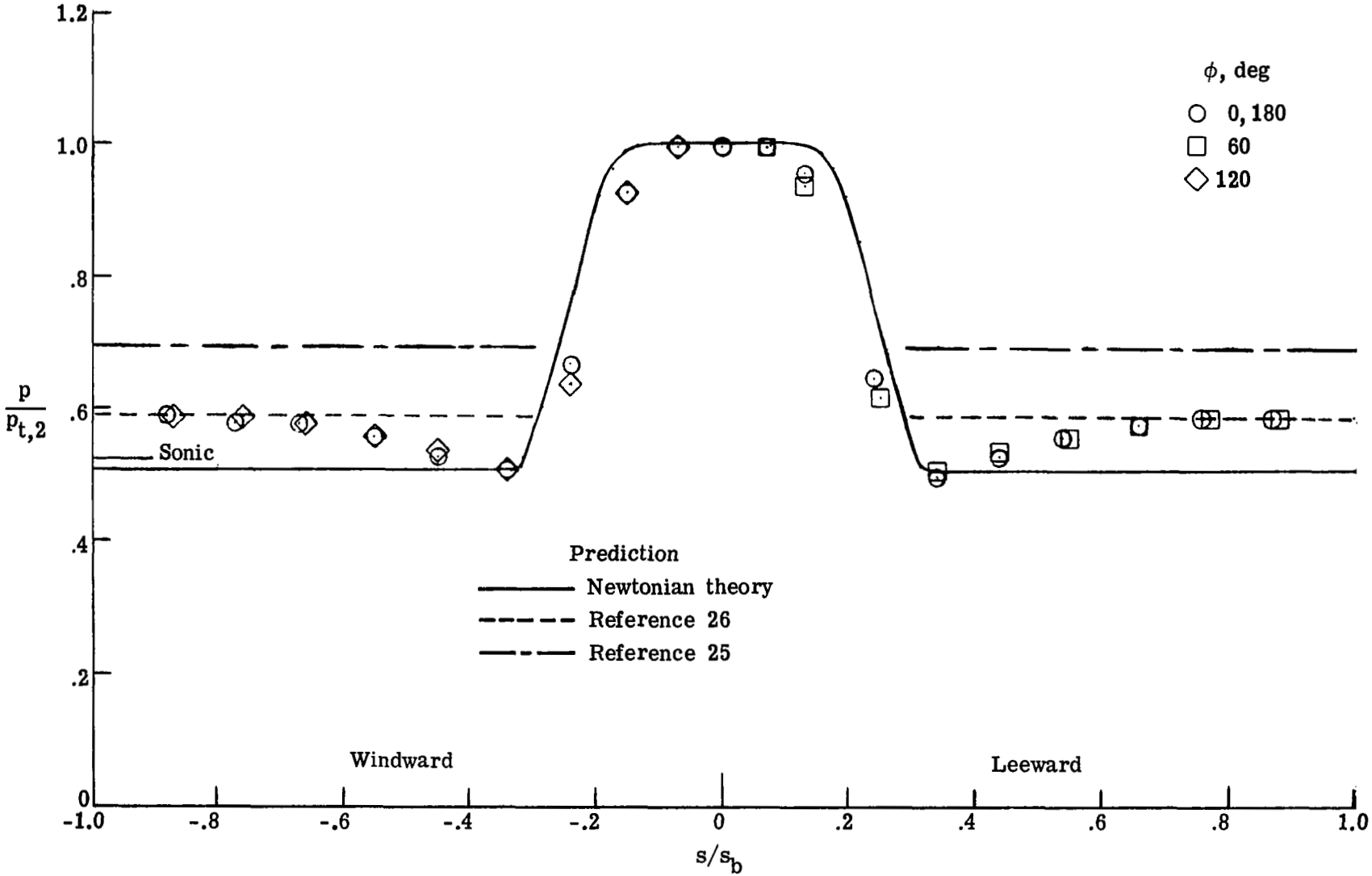

(a) $\alpha = 0°$.

Figure 35.- Pressure distributions measured on the flattened-nose cone (model 6) in Mach 5.9 air.

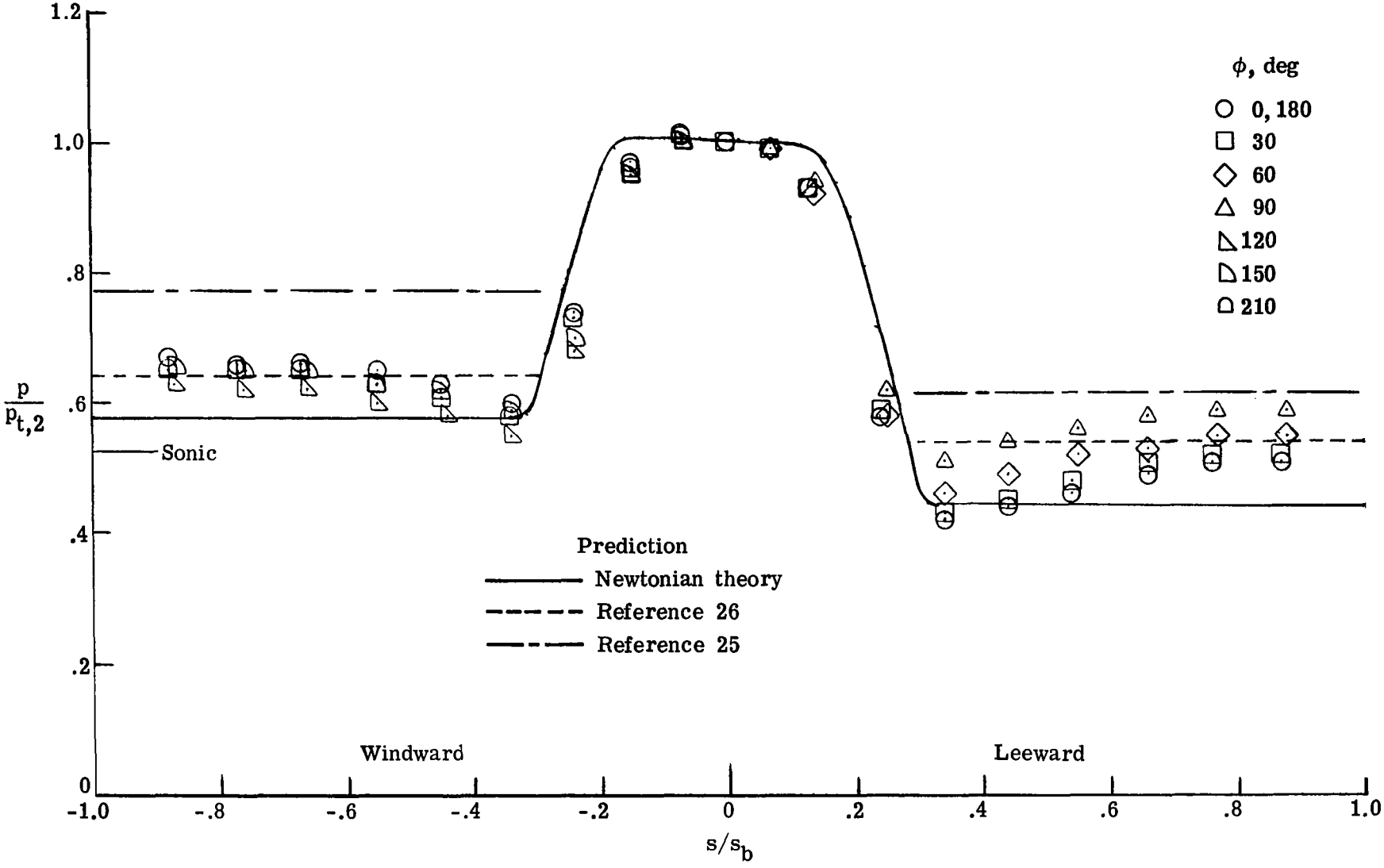

(b) $\alpha = 4°$.

Figure 35.- Continued.

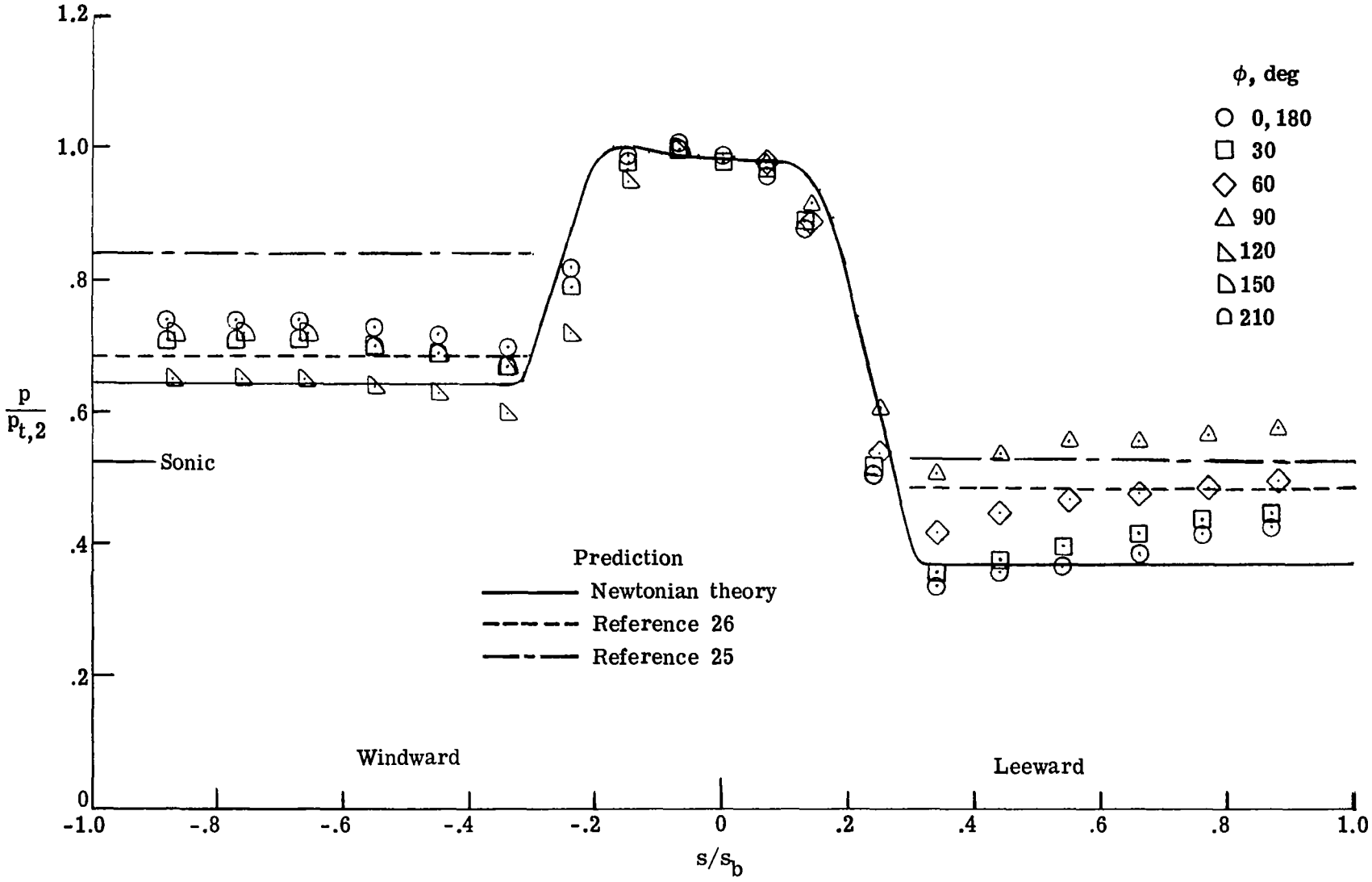

(c) $\alpha = 8°$.

Figure 35.- Continued.

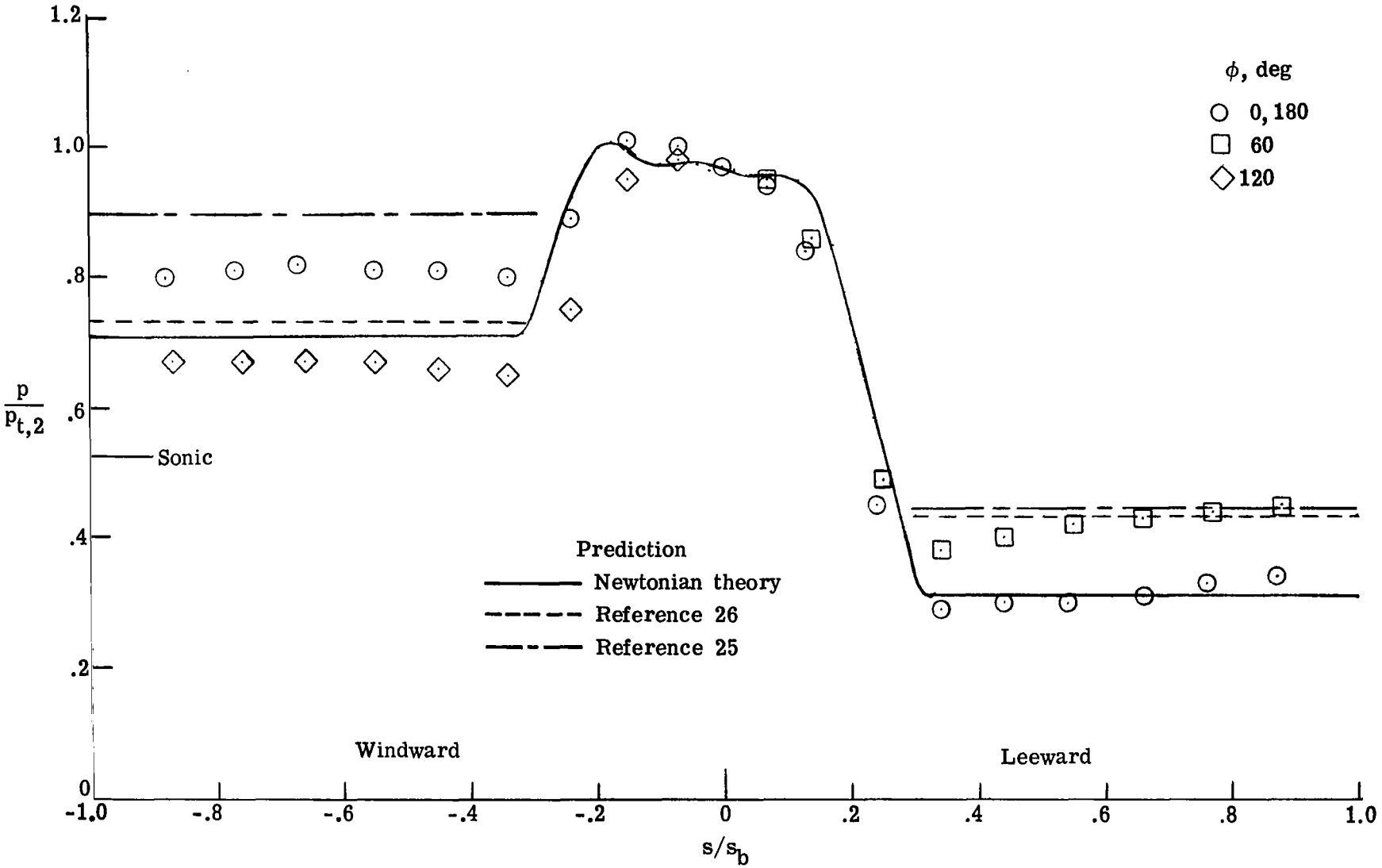

(d) $\alpha = 12°$.

Figure 35.- Continued.

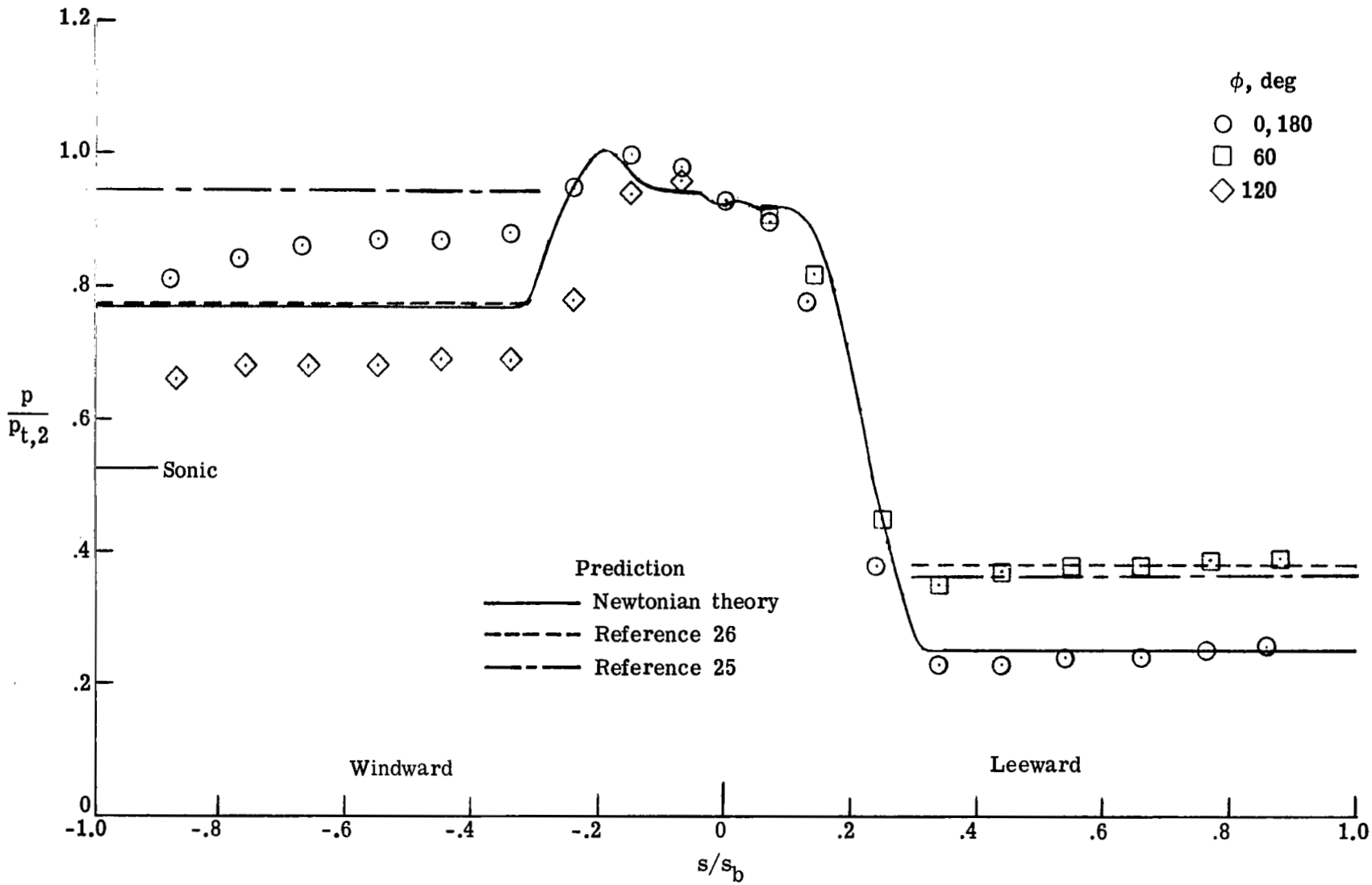

(e) $\alpha = 16°$.

Figure 35.- Continued.

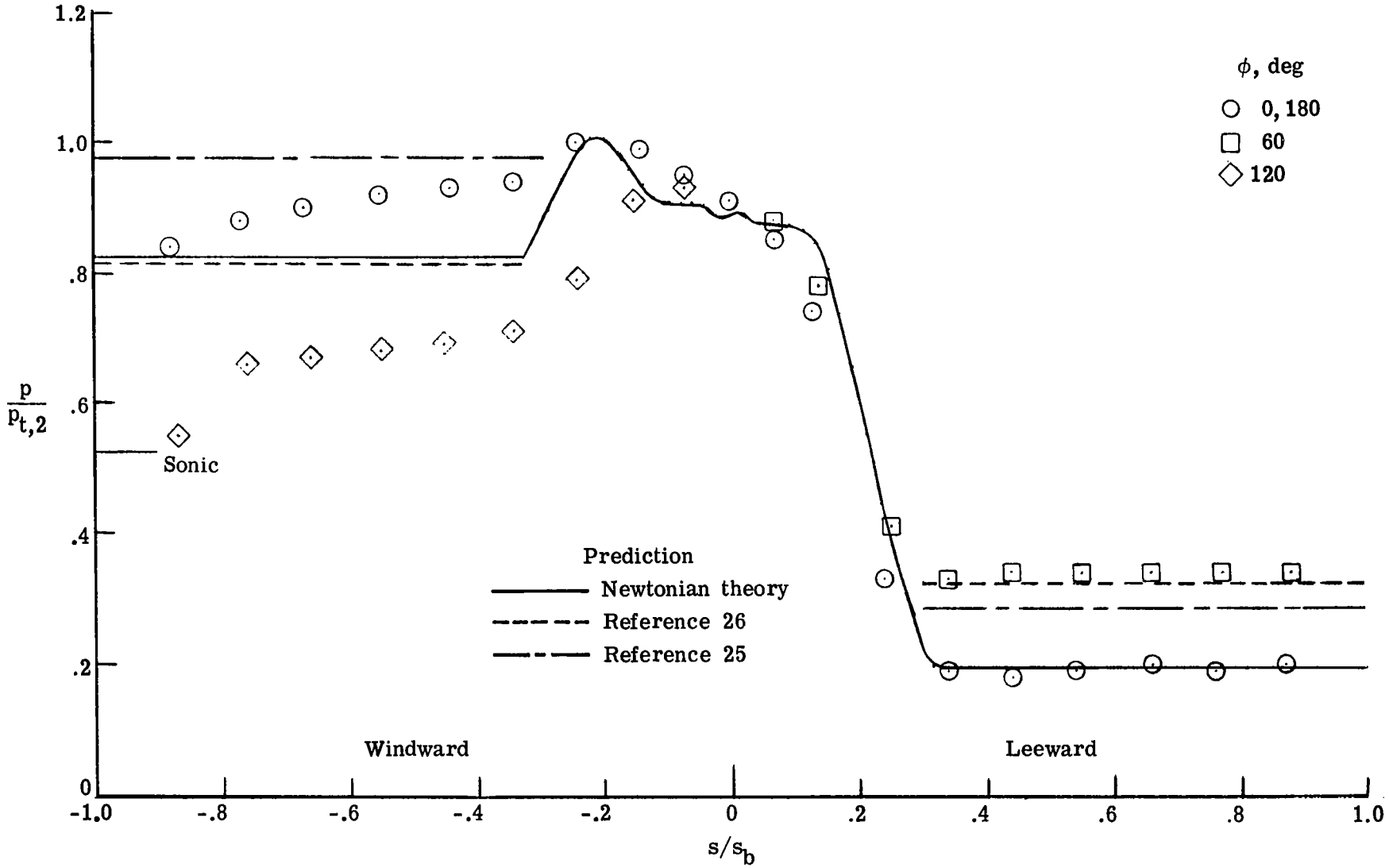

(f) $\alpha = 20°$.

Figure 35.- Concluded.

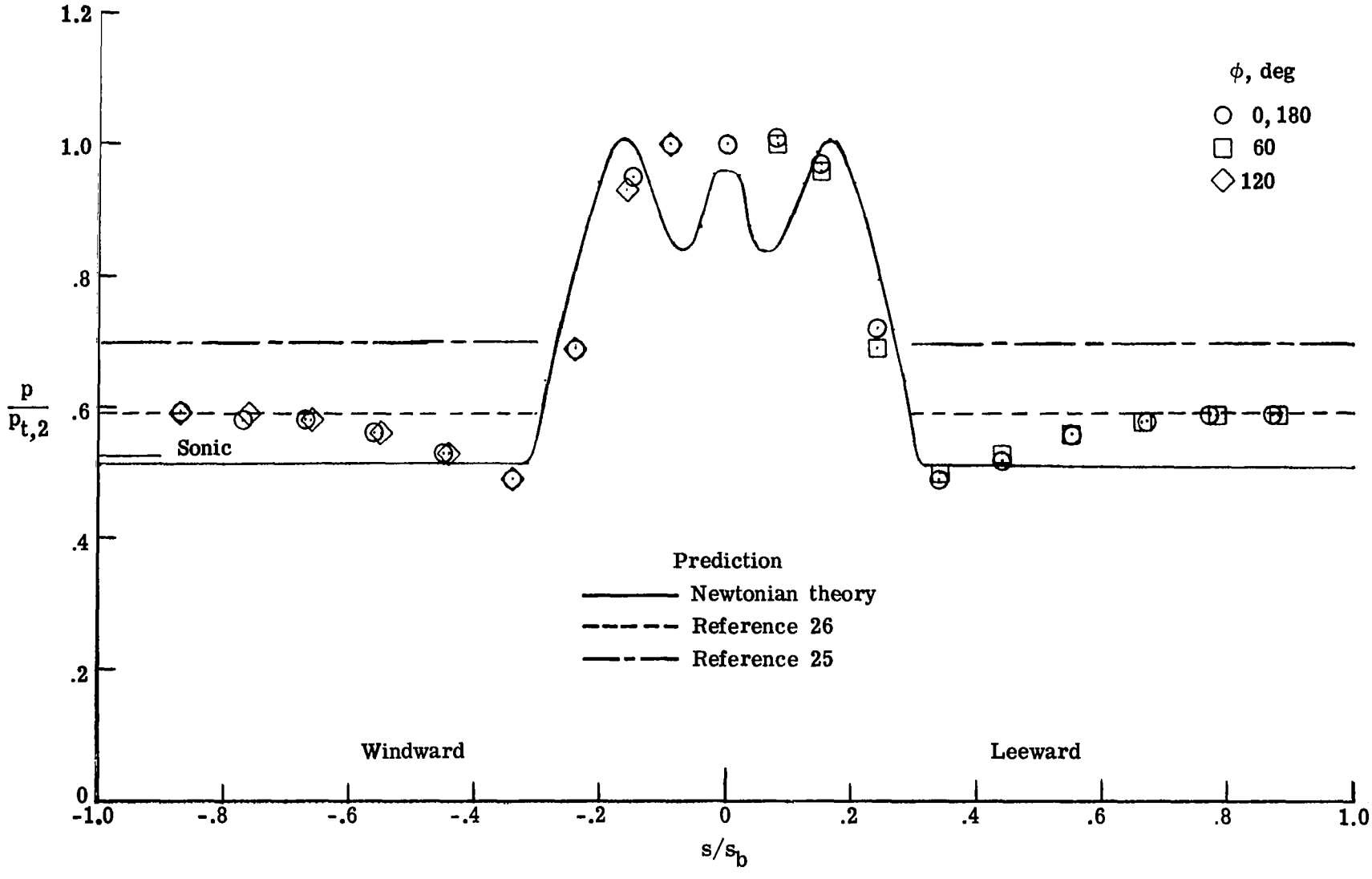

(a) $\alpha = 0°$.

Figure 36.- Pressure distributions measured on the concave-nose cone (model 7) in Mach 5.9 air.

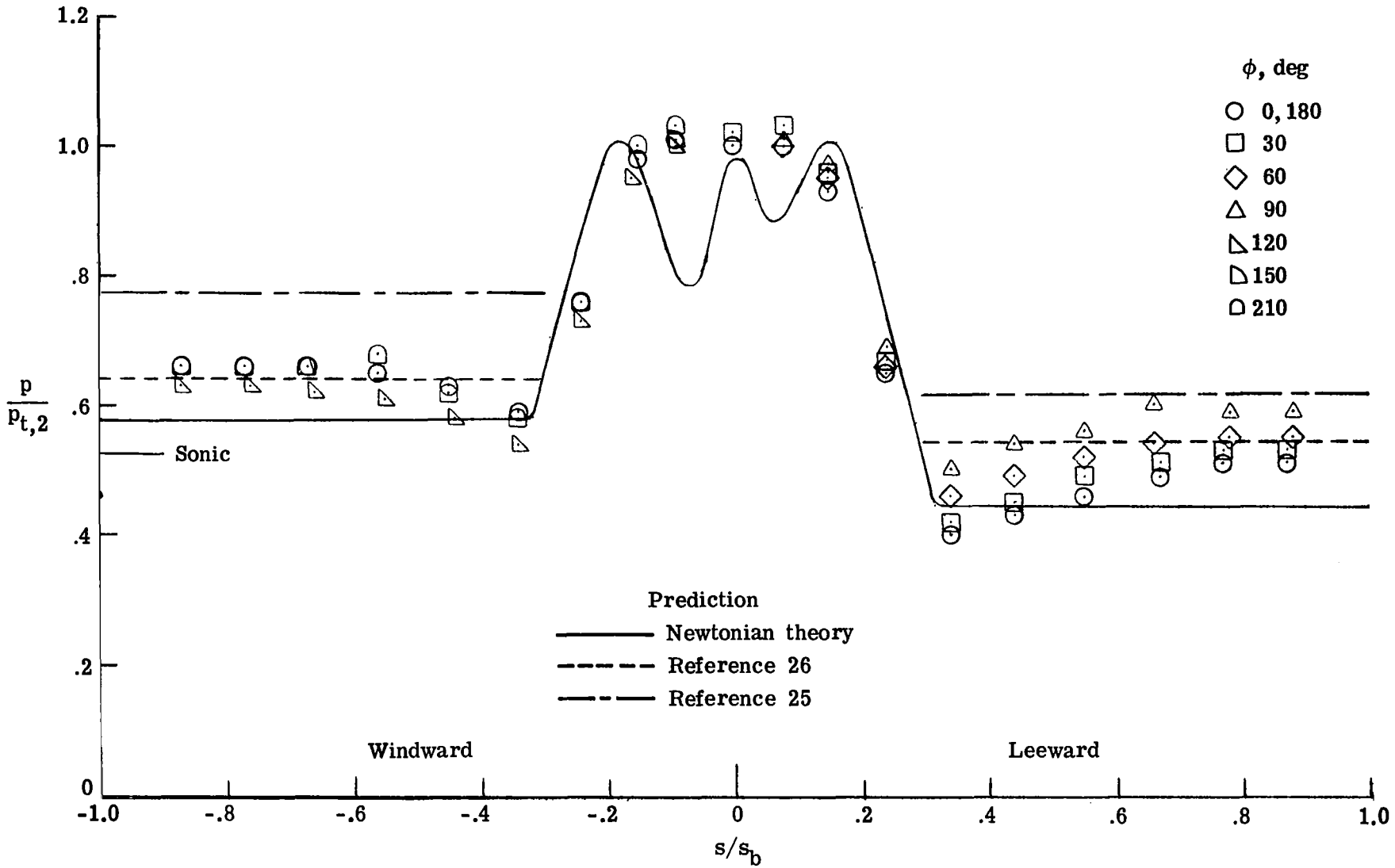

(b) $\alpha = 4°$.

Figure 36.- Continued.

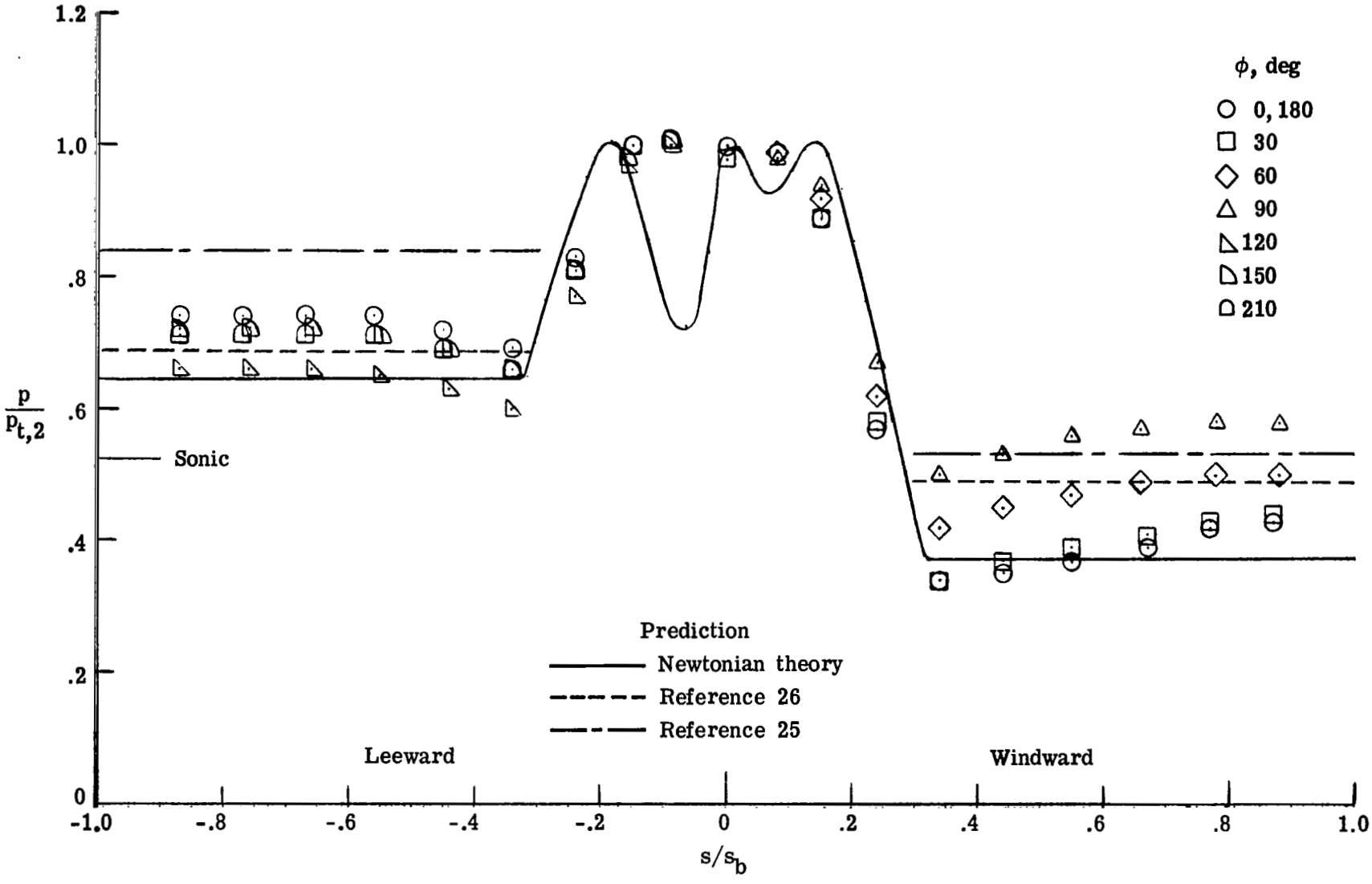

(c) $\alpha = 8°$.

Figure 36.- Continued.

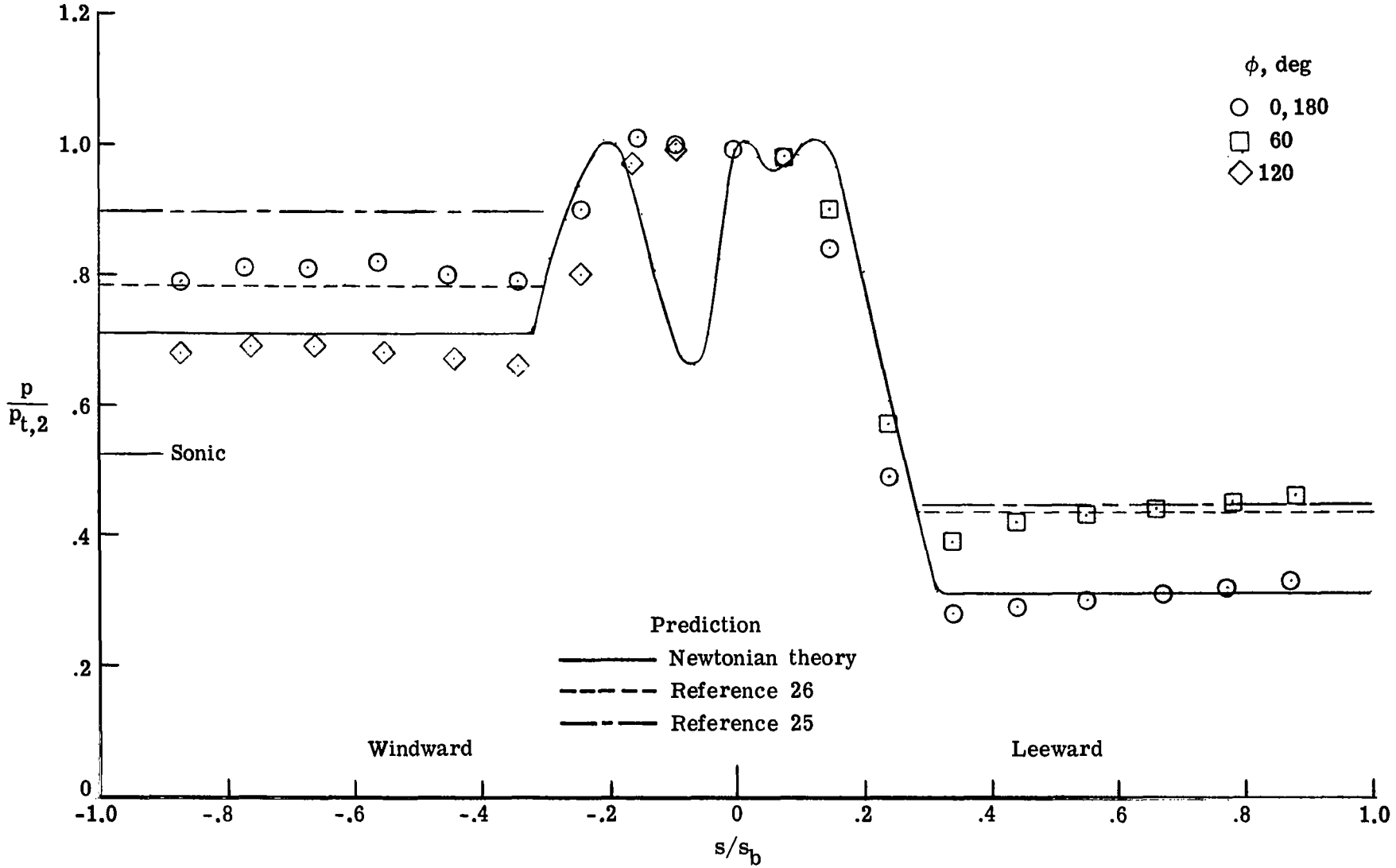

(d) $\alpha = 12°$.

Figure 36.- Continued.

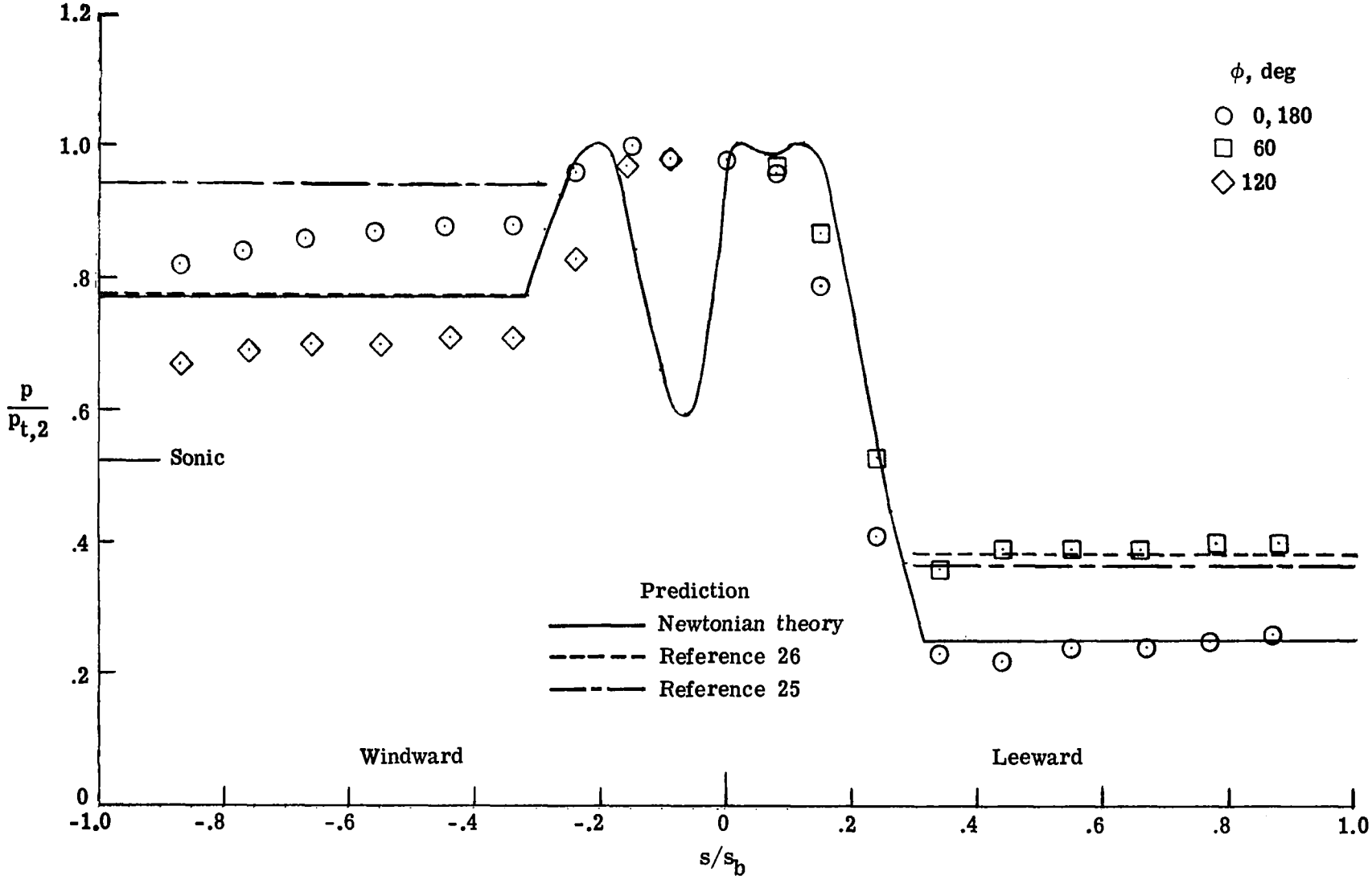

(e) $\alpha = 16°$.

Figure 36.- Continued.

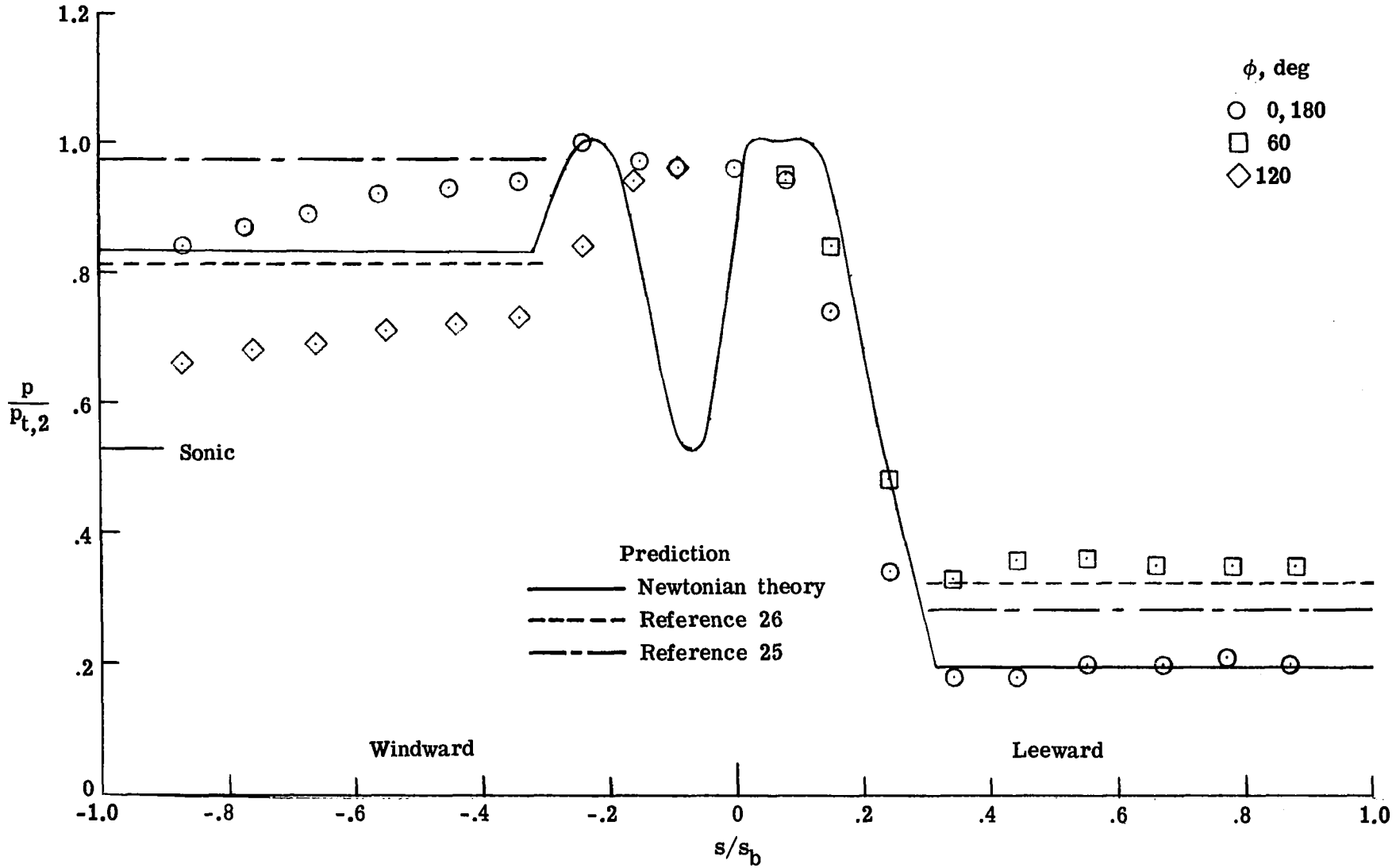

(f) $\alpha = 20°$.

Figure 36.- Concluded.

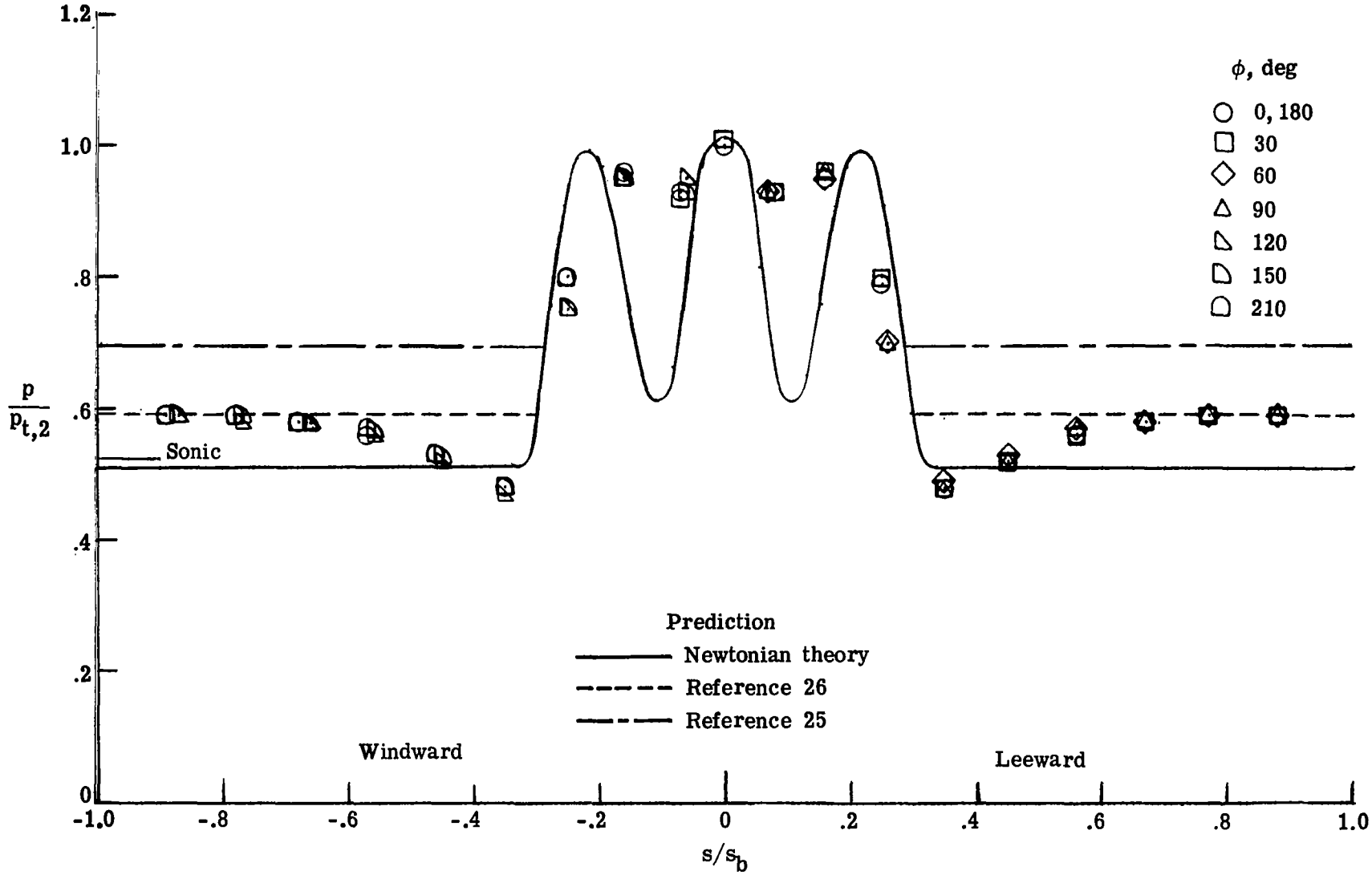

(a) $\alpha = 0°$.

Figure 37.- Pressure distributions measured on the cusp-nose cone (model 8) in Mach 5.9 air.

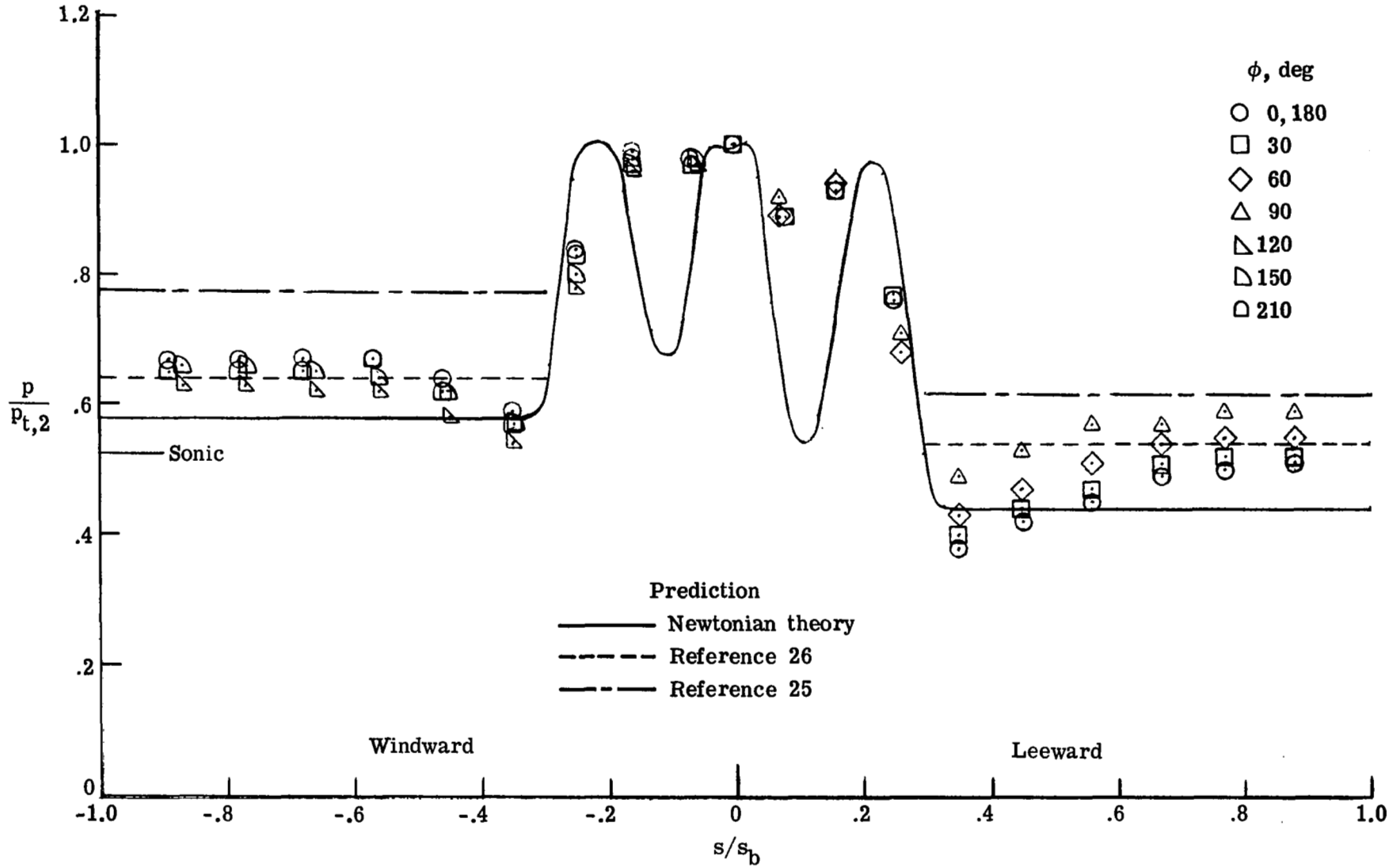

(b) $\alpha = 4°$.

Figure 37.- Continued.

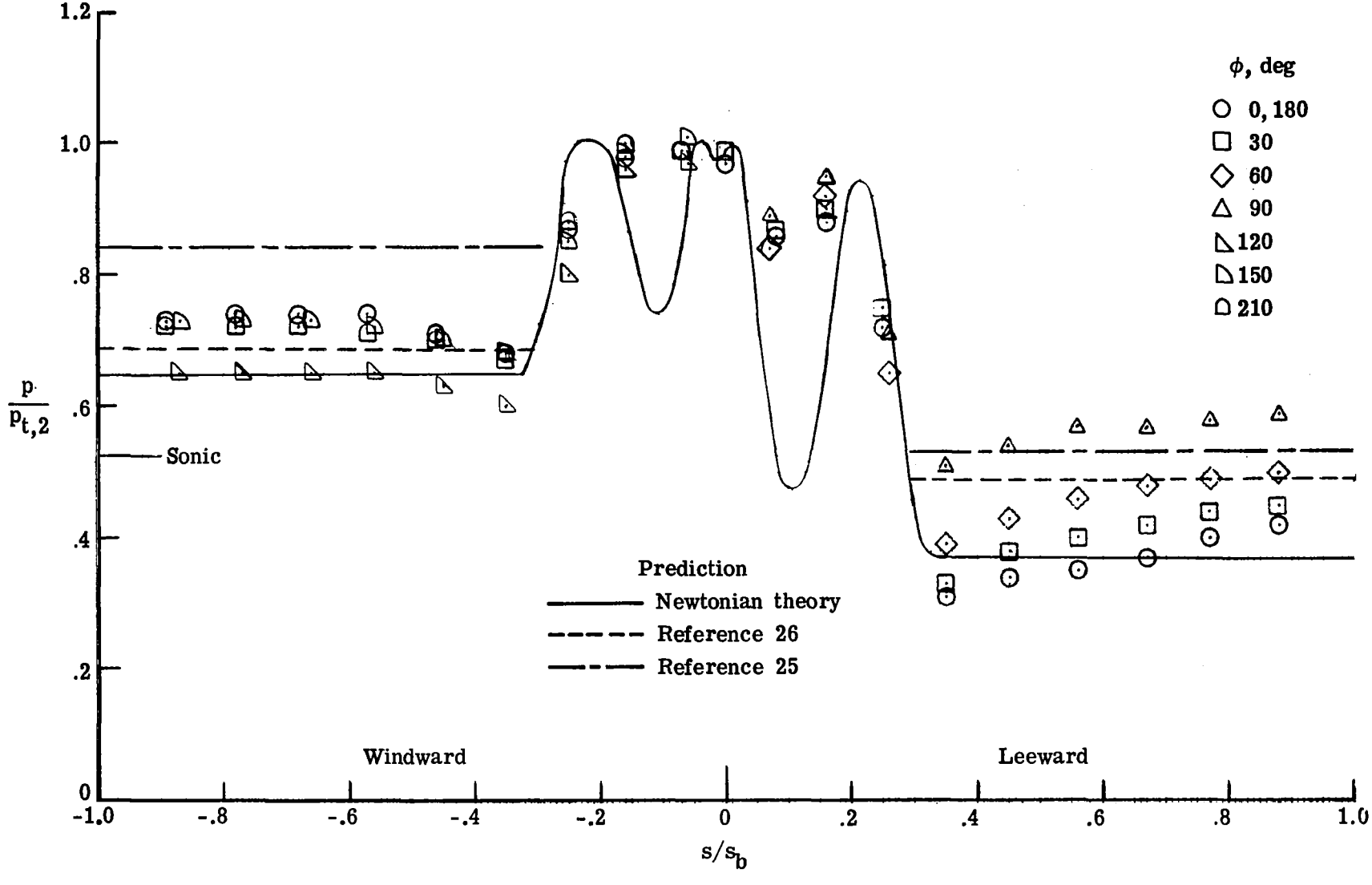

(c) $\alpha = 8°$.

Figure 37.- Continued.

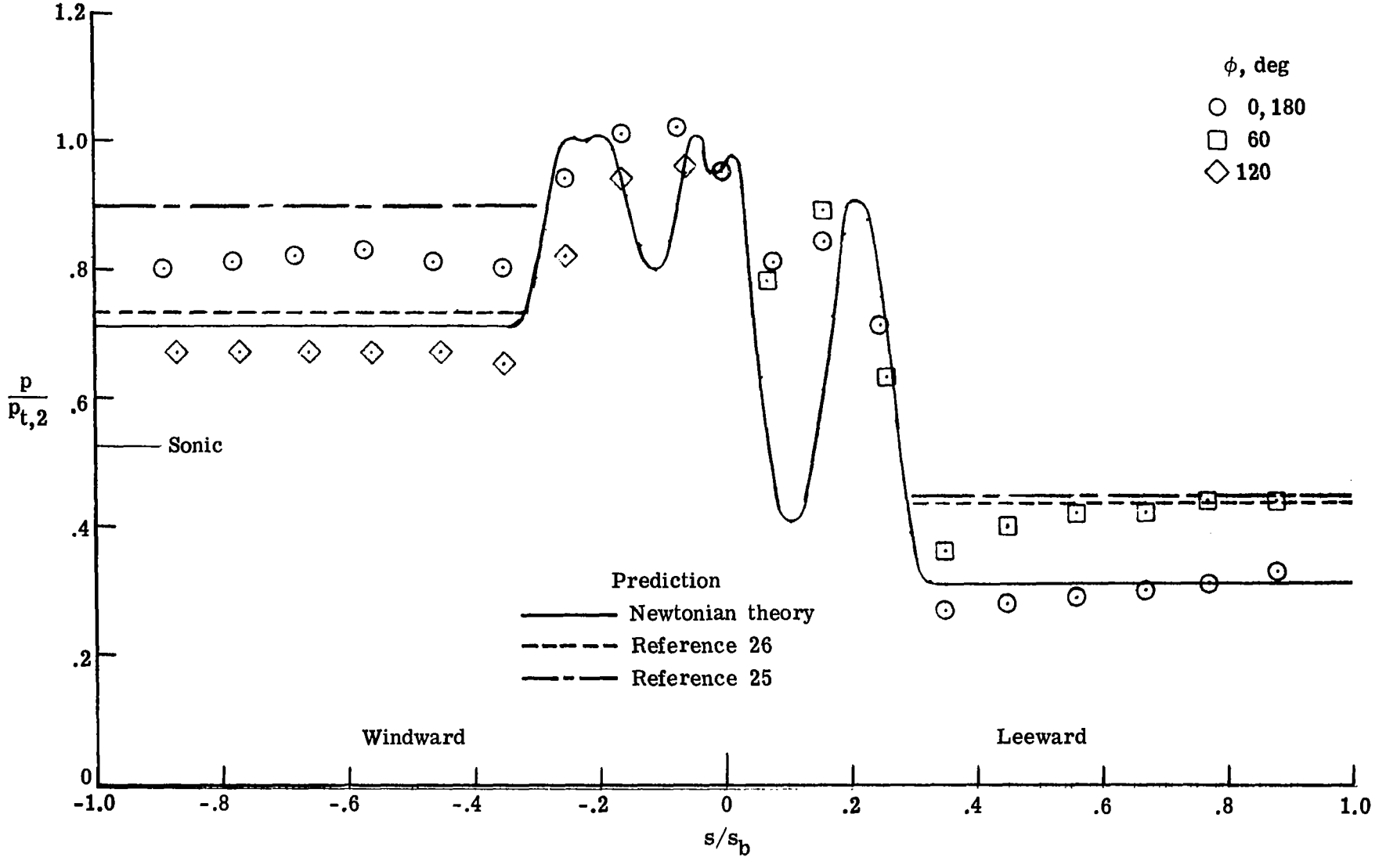

(d) $\alpha = 12°$.

Figure 37.- Continued.

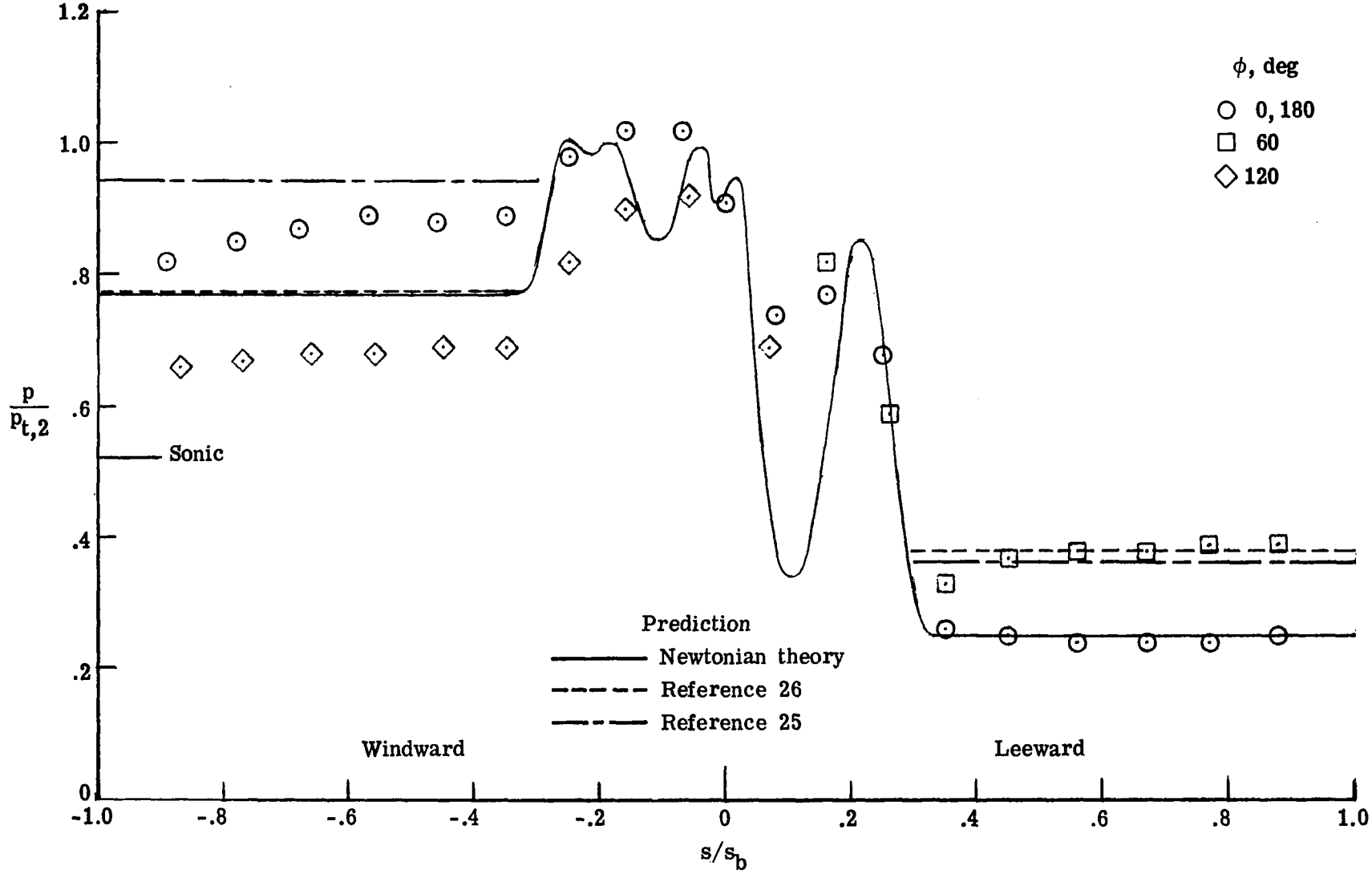

(e) $\alpha = 16°$.

Figure 37.- Continued.

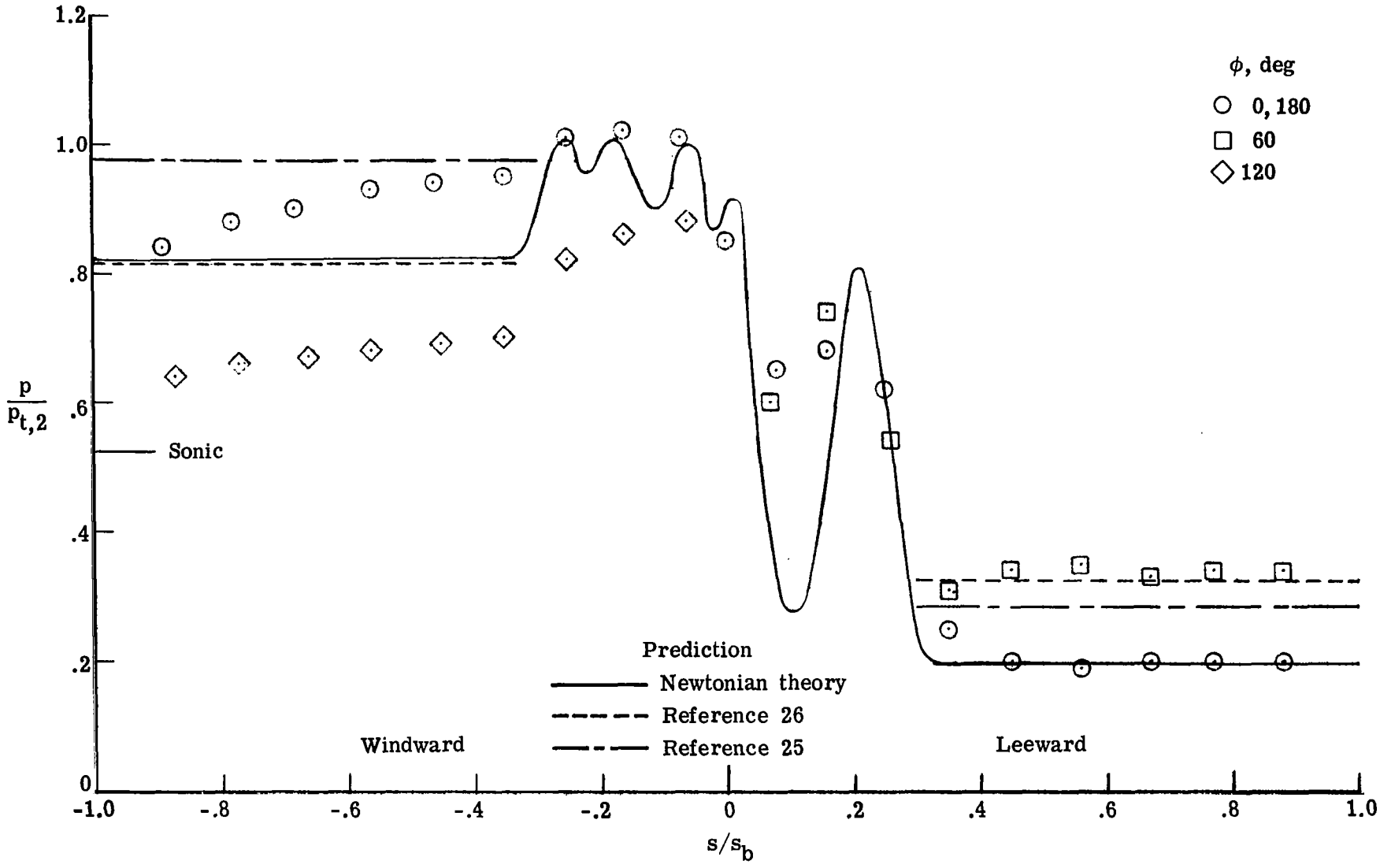

(f) $\alpha = 20°$.

Figure 37.- Concluded.

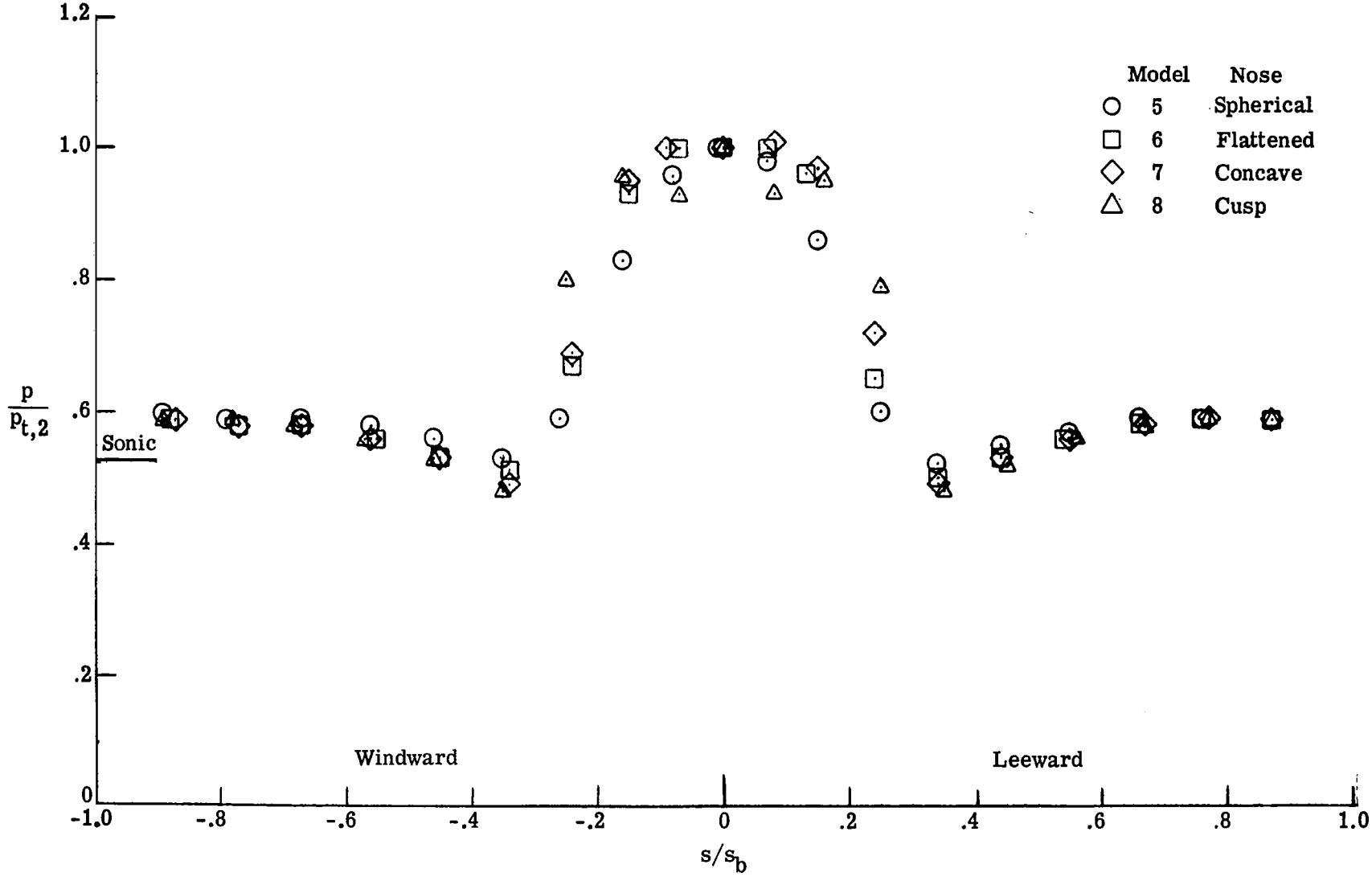

(a) $\alpha = 0°$.

Figure 38.- Effect of nose shape of the cones (models 5 to 8) on pressure distributions along the most windward ($\phi = 180°$) and leeward ($\phi = 0°$) rays in Mach 5.9 air.

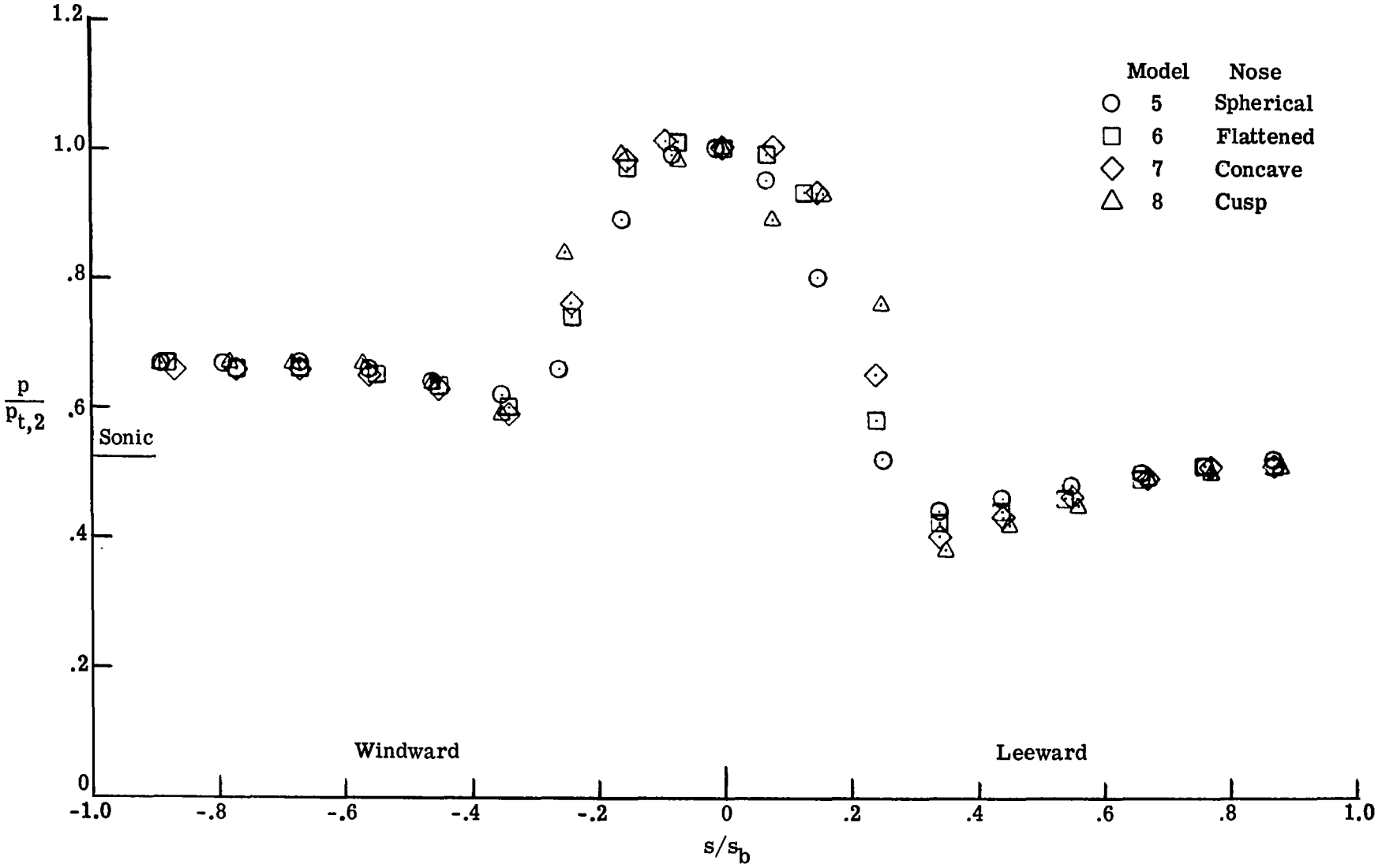

(b) $\alpha = 4°$.

Figure 38.- Continued.

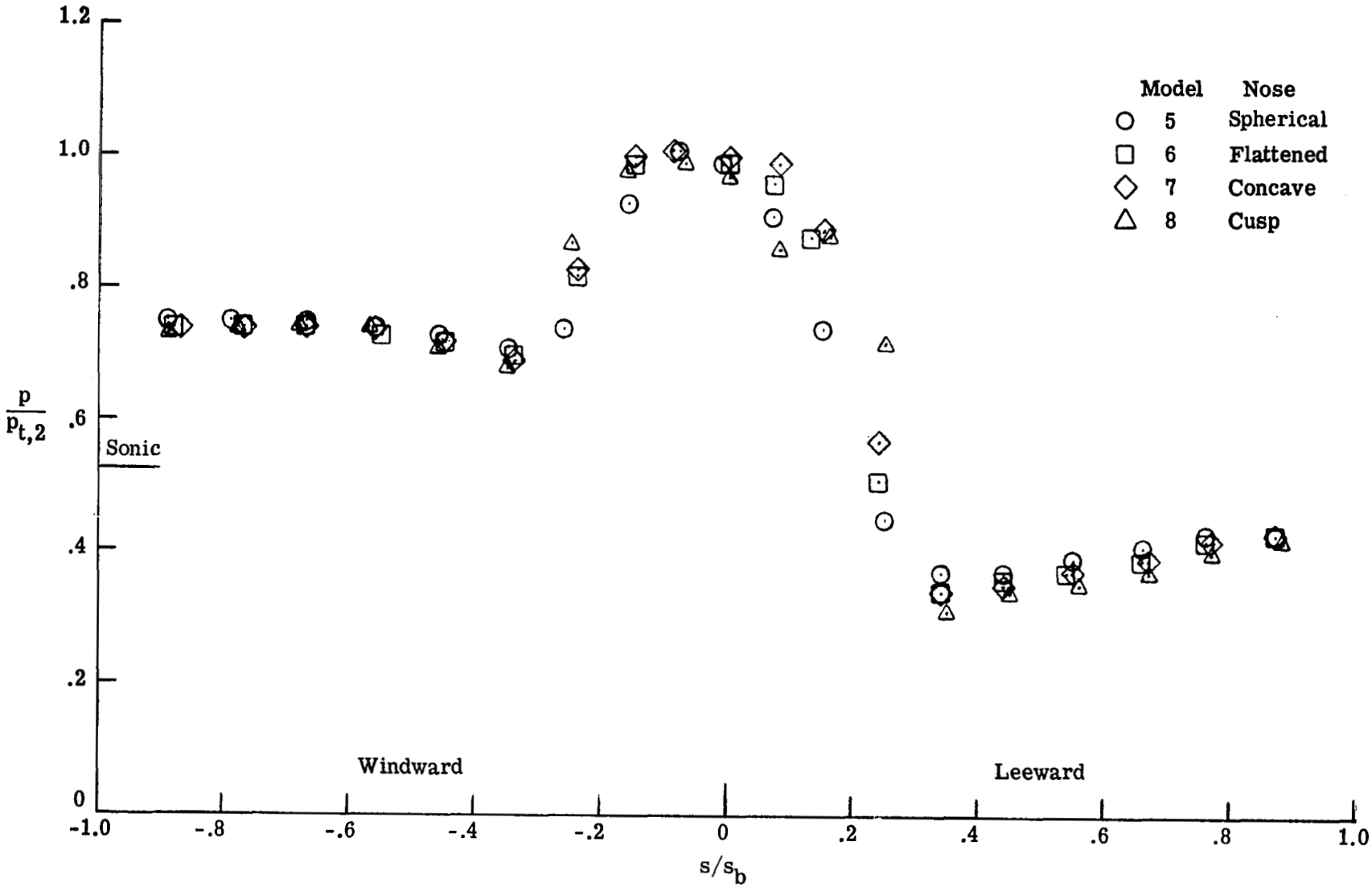

(c) $\alpha = 8°$.

Figure 38.- Continued.

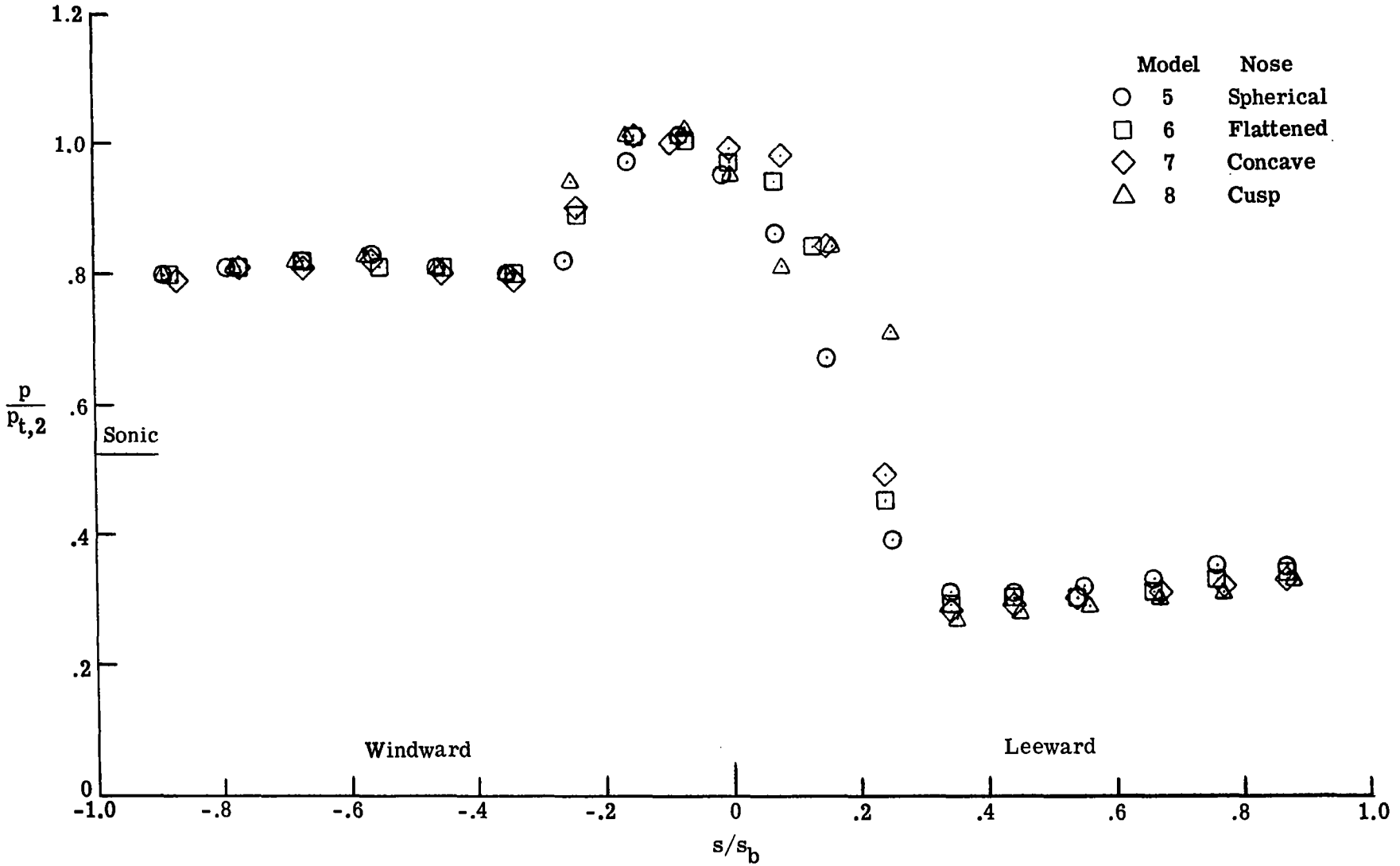

(d) $\alpha = 12°$.

Figure 38.- Continued.

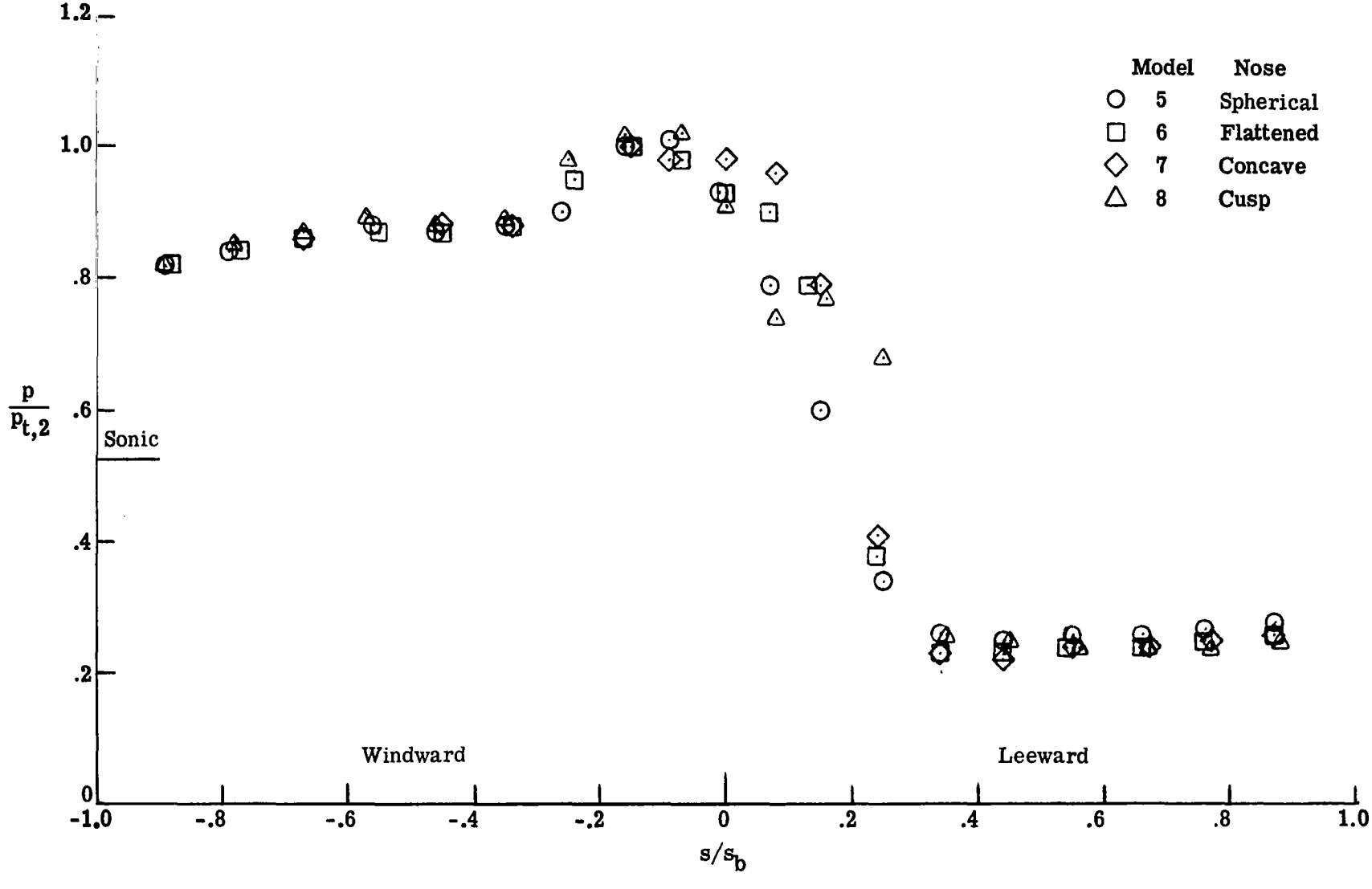

(e) $\alpha = 16°$.

Figure 38.- Continued.

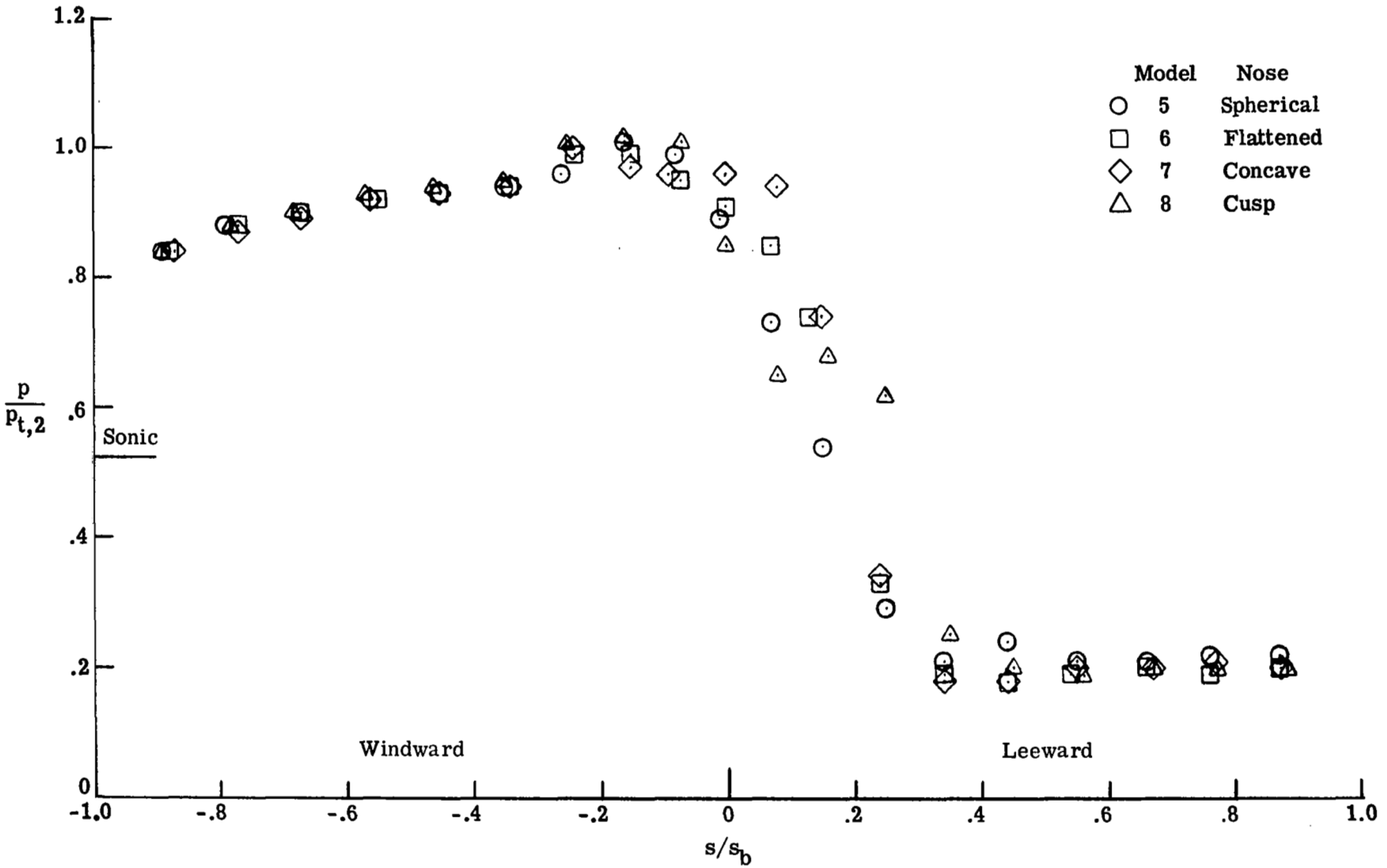

(f) $\alpha = 20°$.

Figure 38.- Concluded.

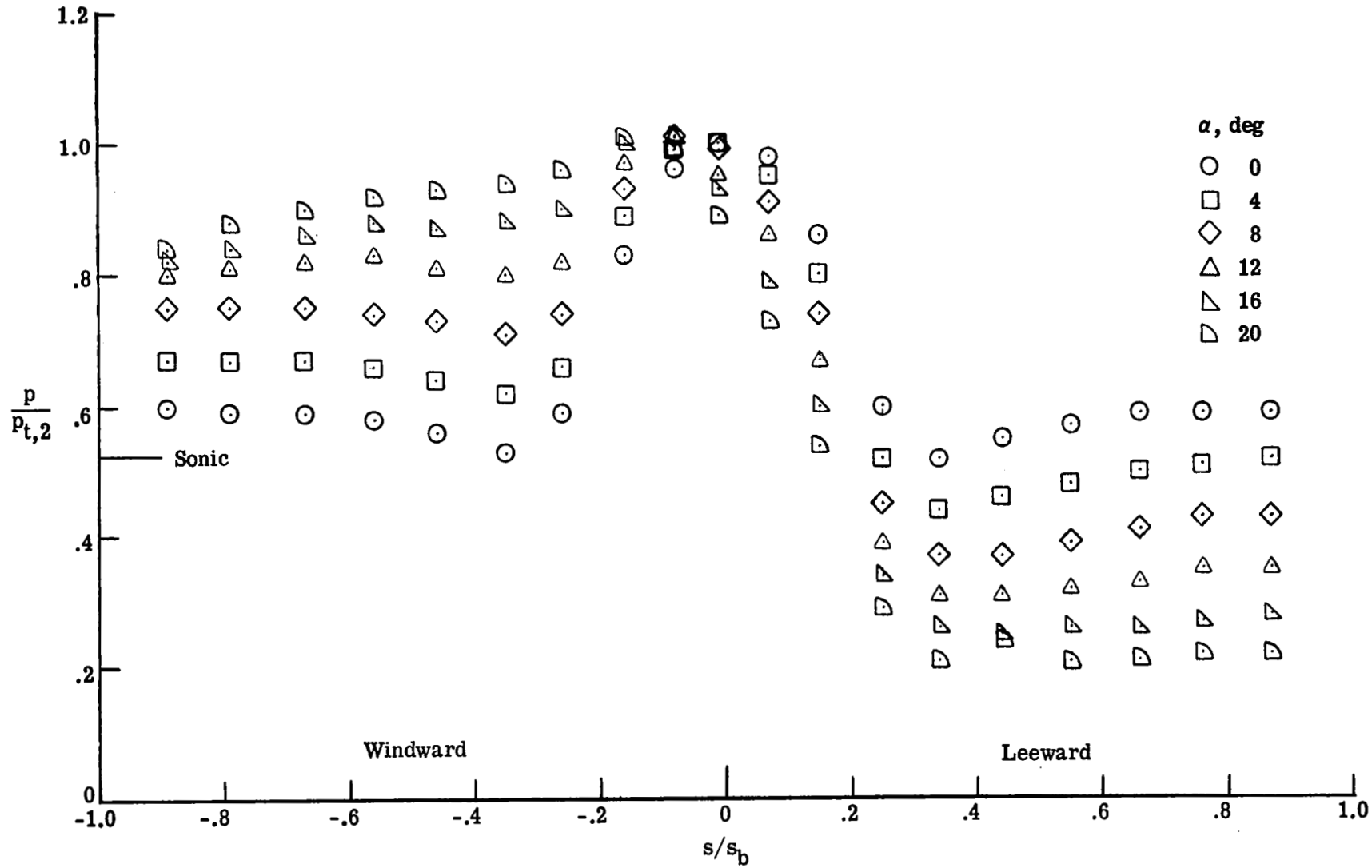

(a) Spherical-nose cone (model 5).

Figure 39.- Effect of angle of attack on pressure distributions along the most windward (ϕ = 180°) and leeward (ϕ = 0°) rays of the cones (models 5 to 8) with various nose shapes in Mach 5.9 air.

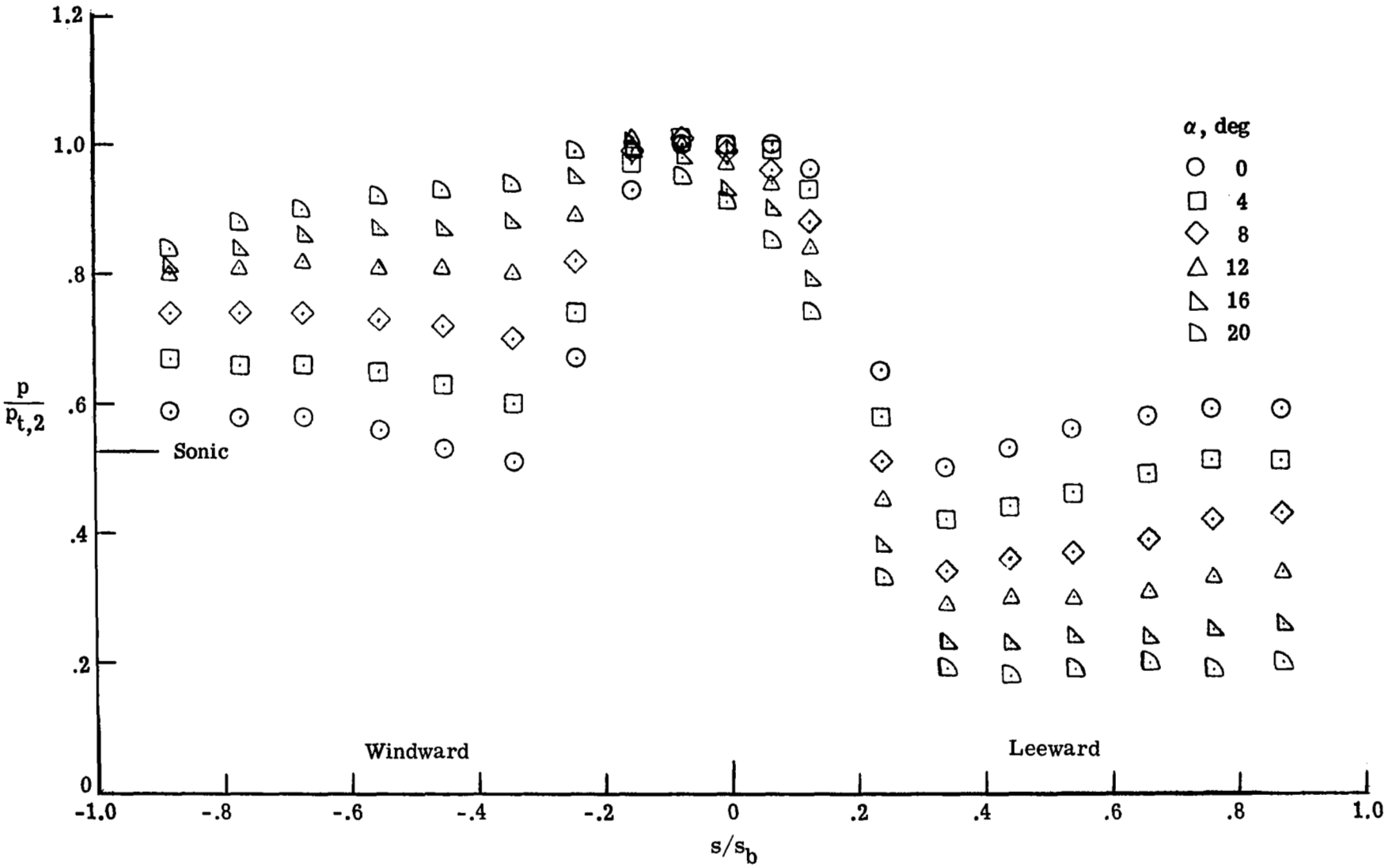

(b) Flattened-nose cone (model 6).

Figure 39.- Continued.

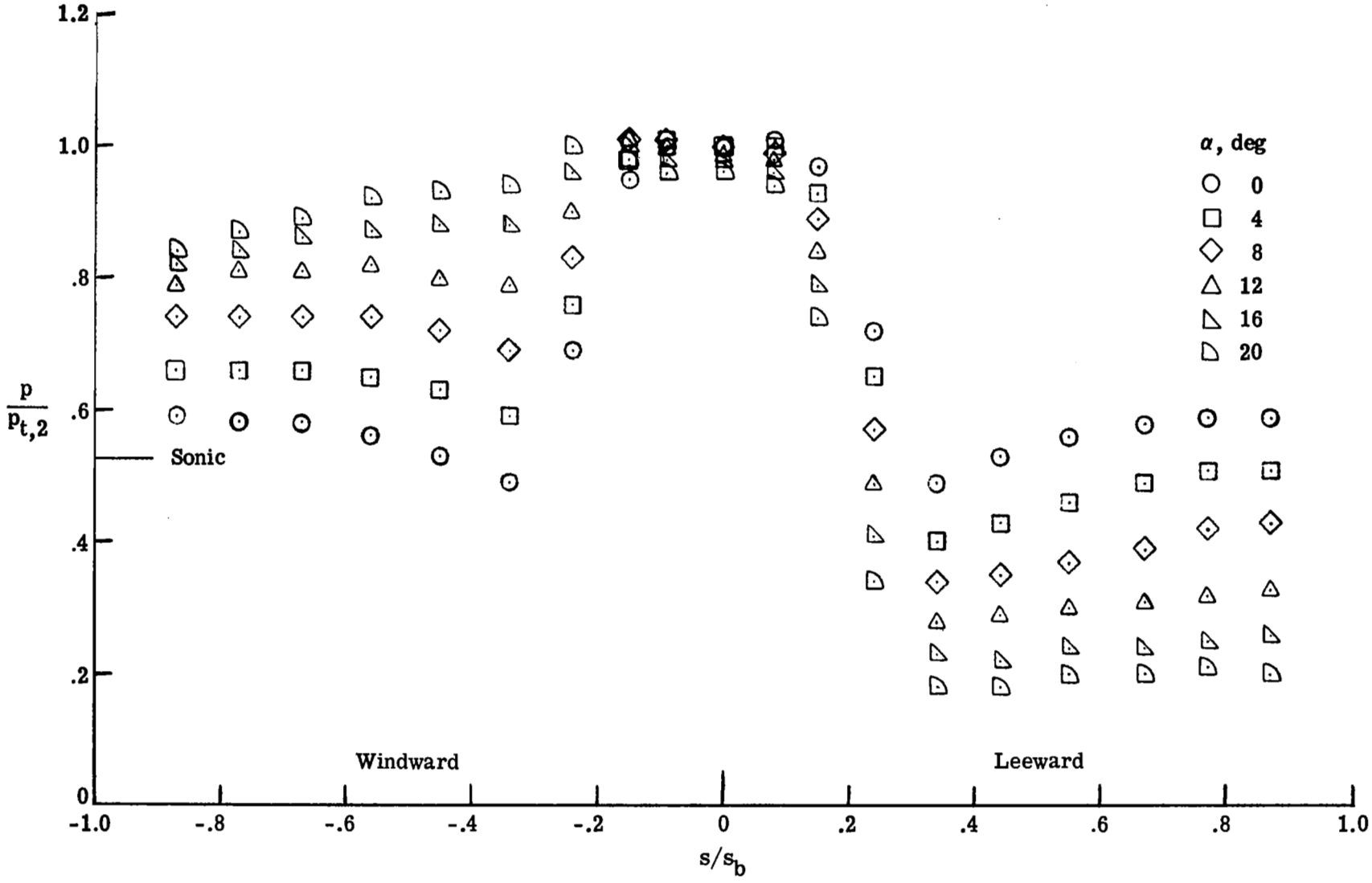

(c) Concave-nose cone (model 7).

Figure 39.- Continued.

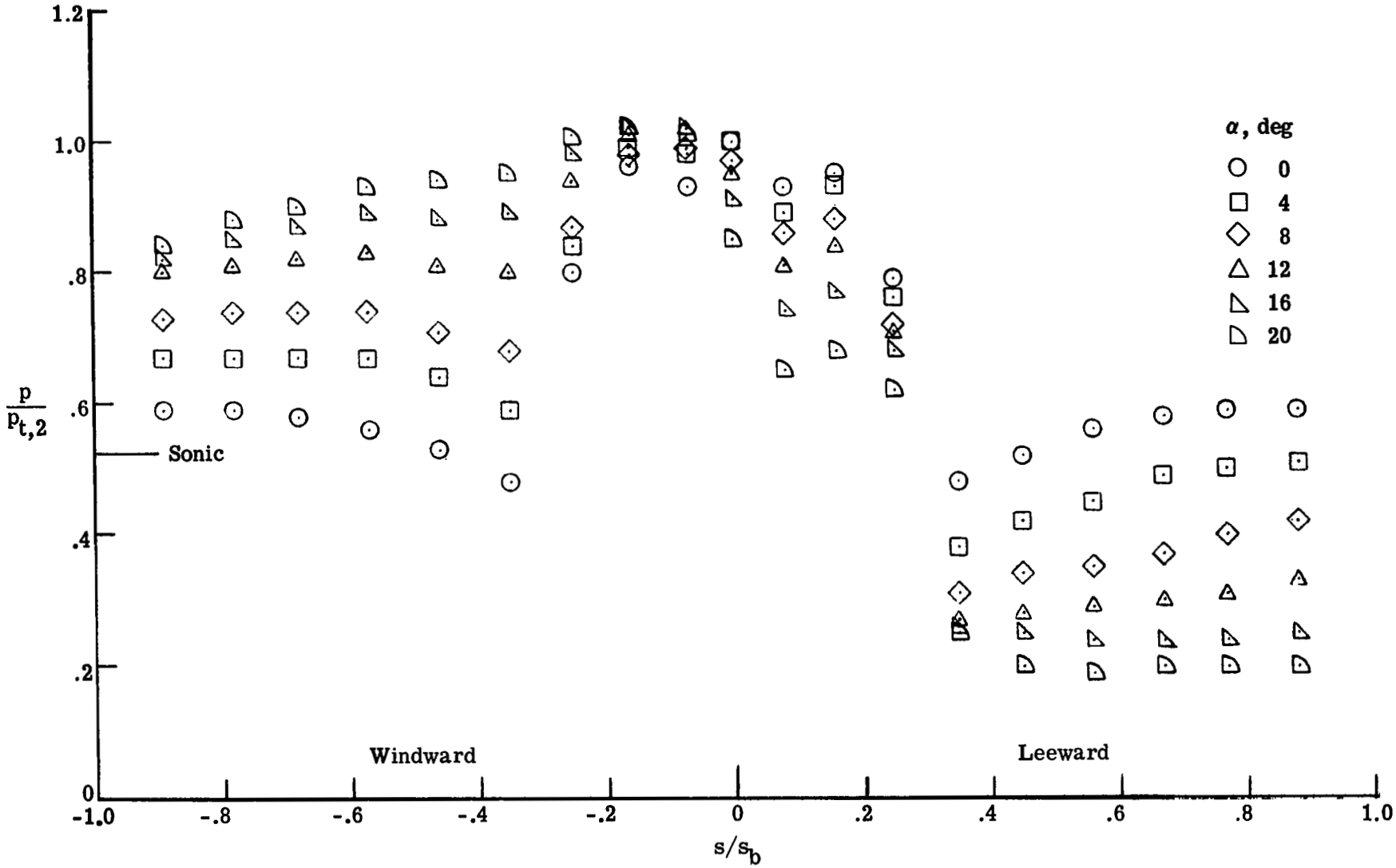

(d) Cusp-nose cone (model 8).

Figure 39.- Concluded.

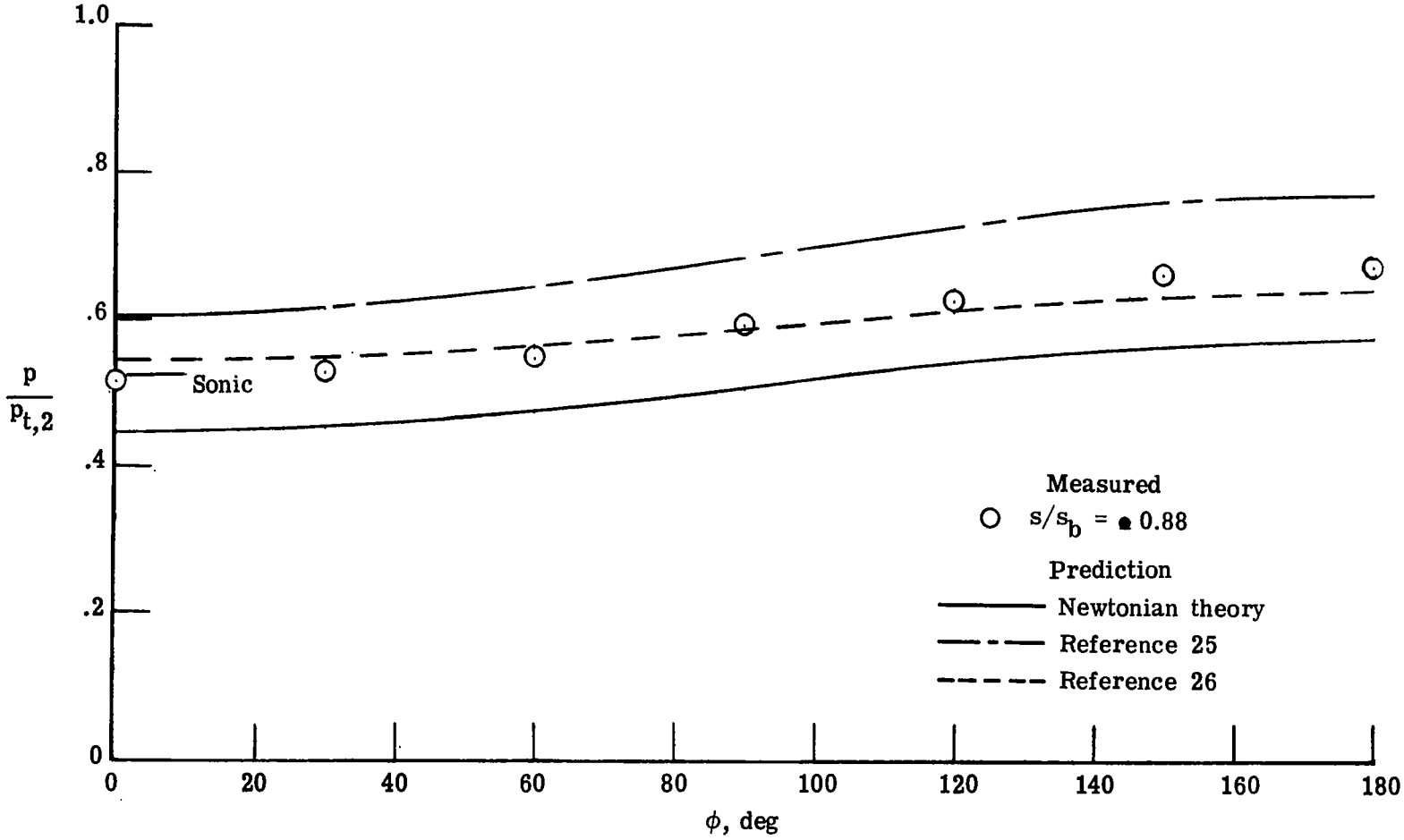

(a) $\alpha = 4°$.

Figure 40.- Circumferential pressure distributions on cone section of the spherical-nose cone (model 5) in Mach 5.9 air.

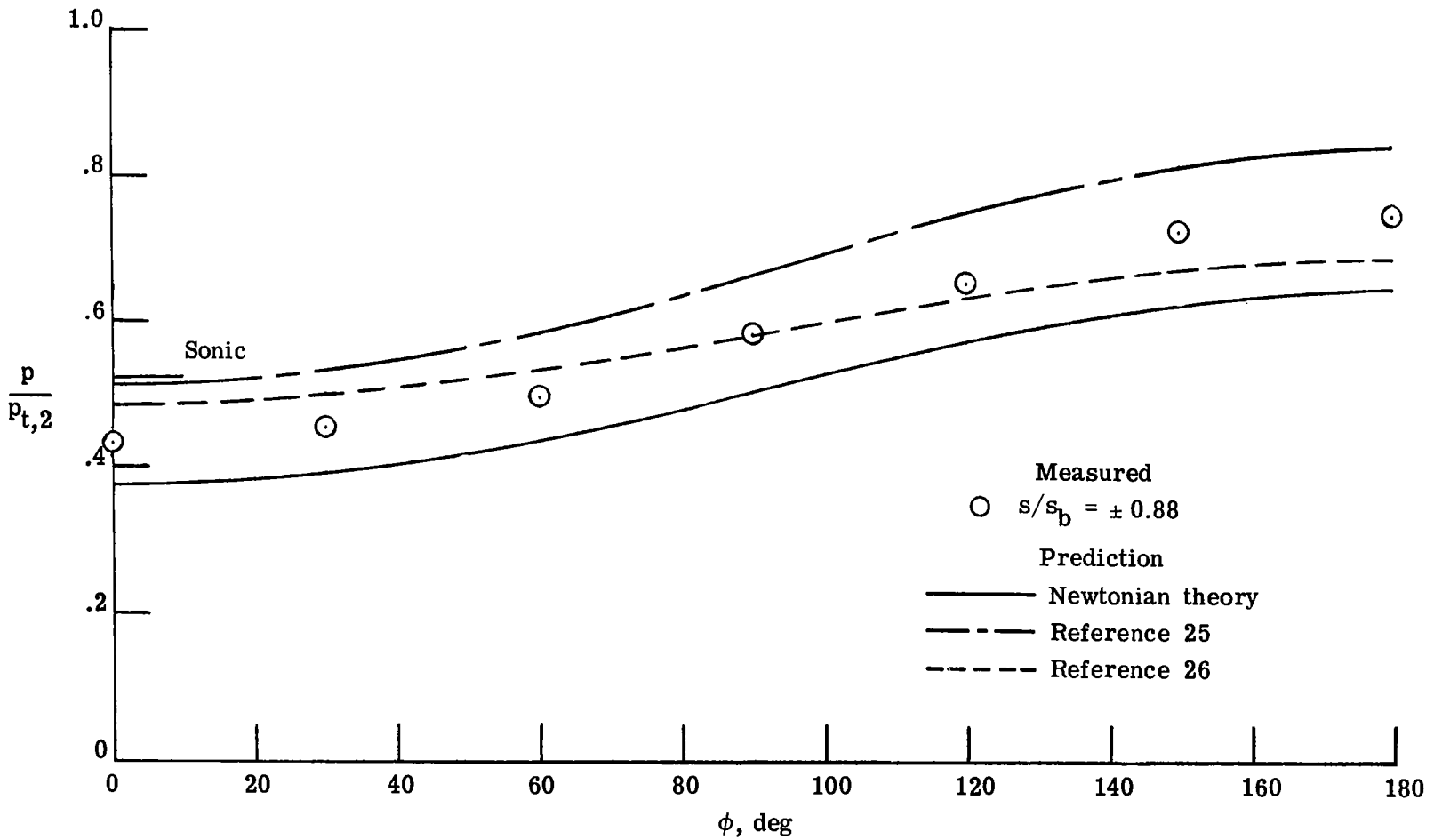

(b) $\alpha = 8°$.

Figure 40.- Continued.

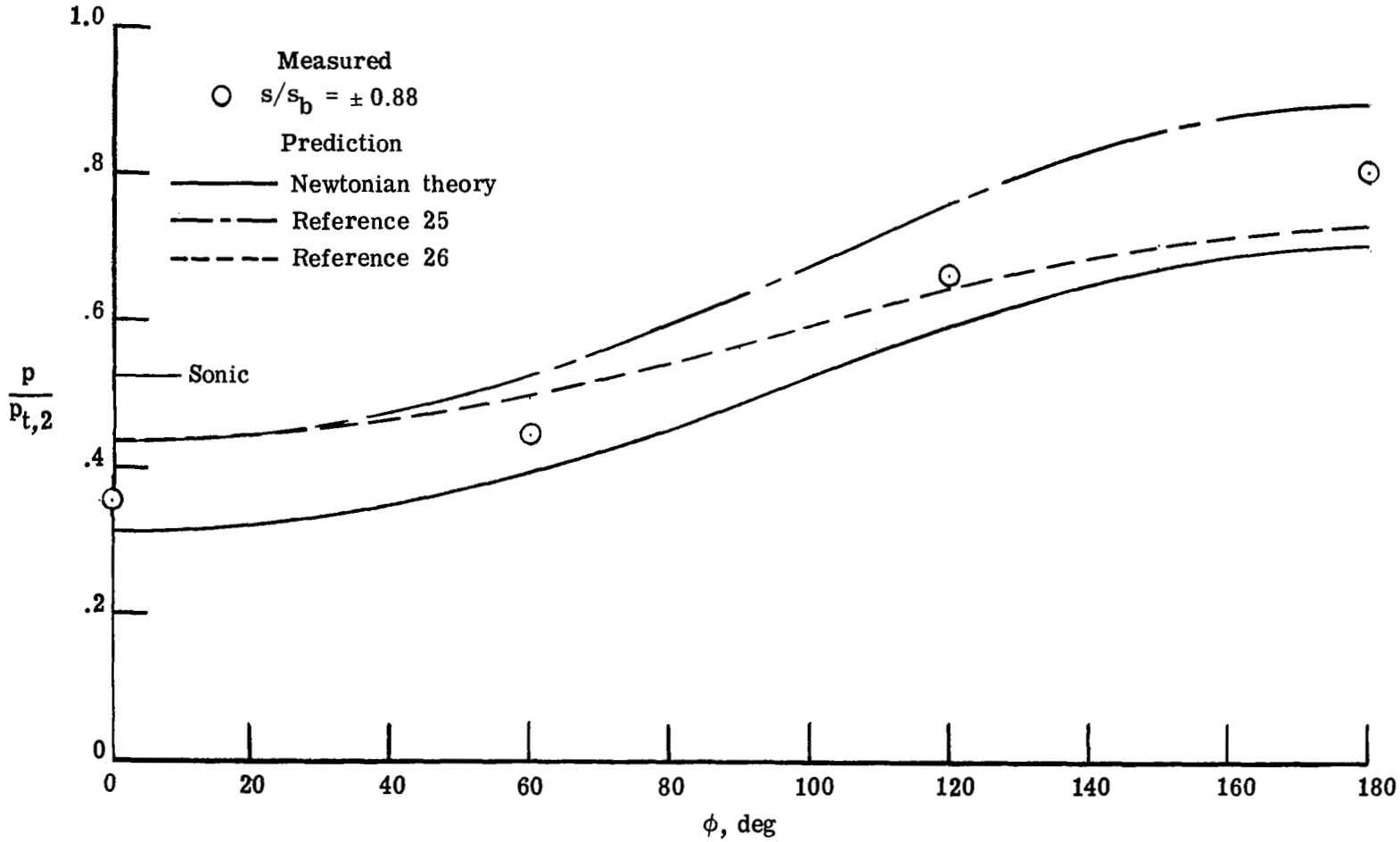

(c) $\alpha = 12°$.

Figure 40.- Continued.

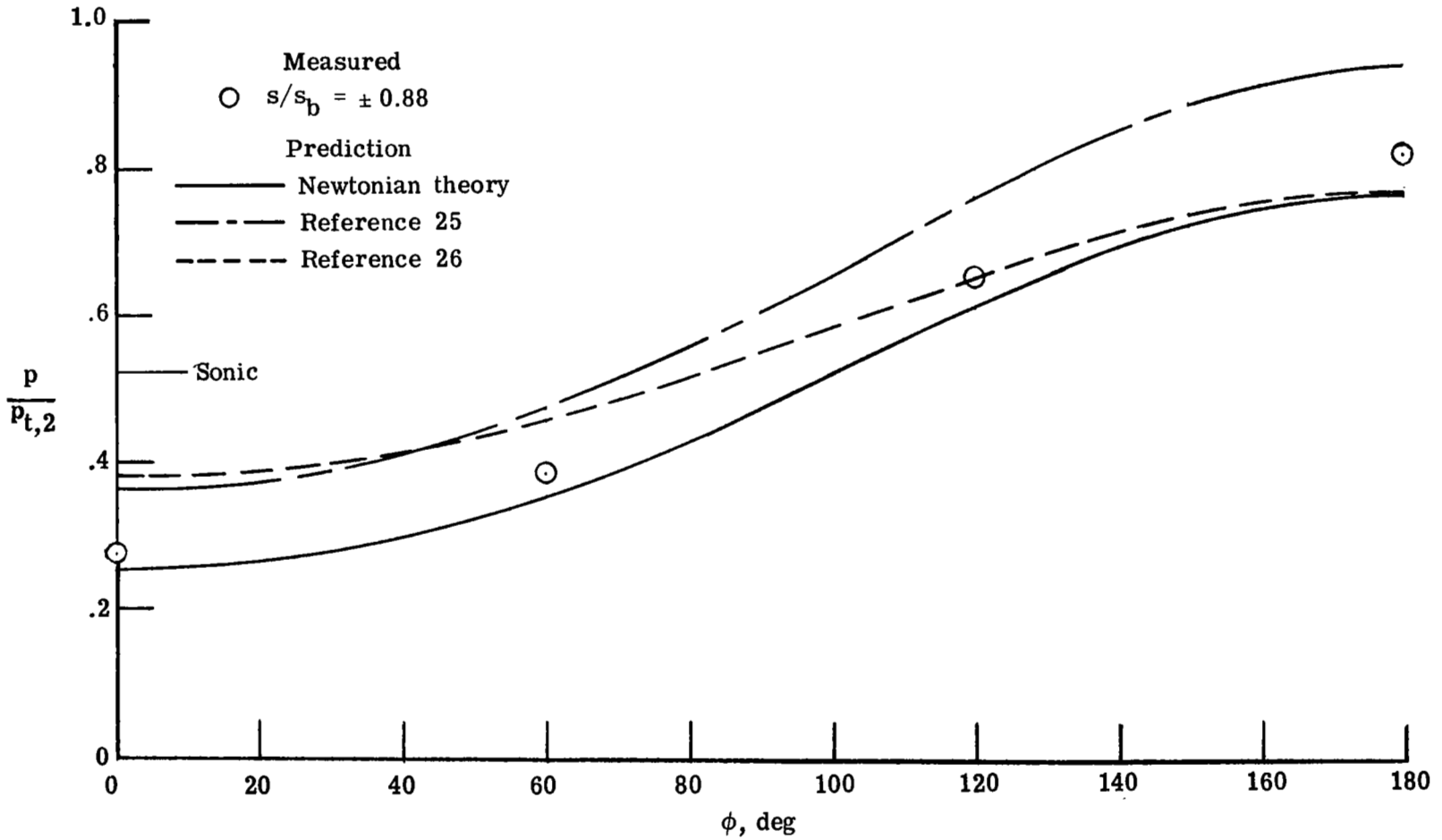

(d) $\alpha = 16°$.

Figure 40.- Continued.

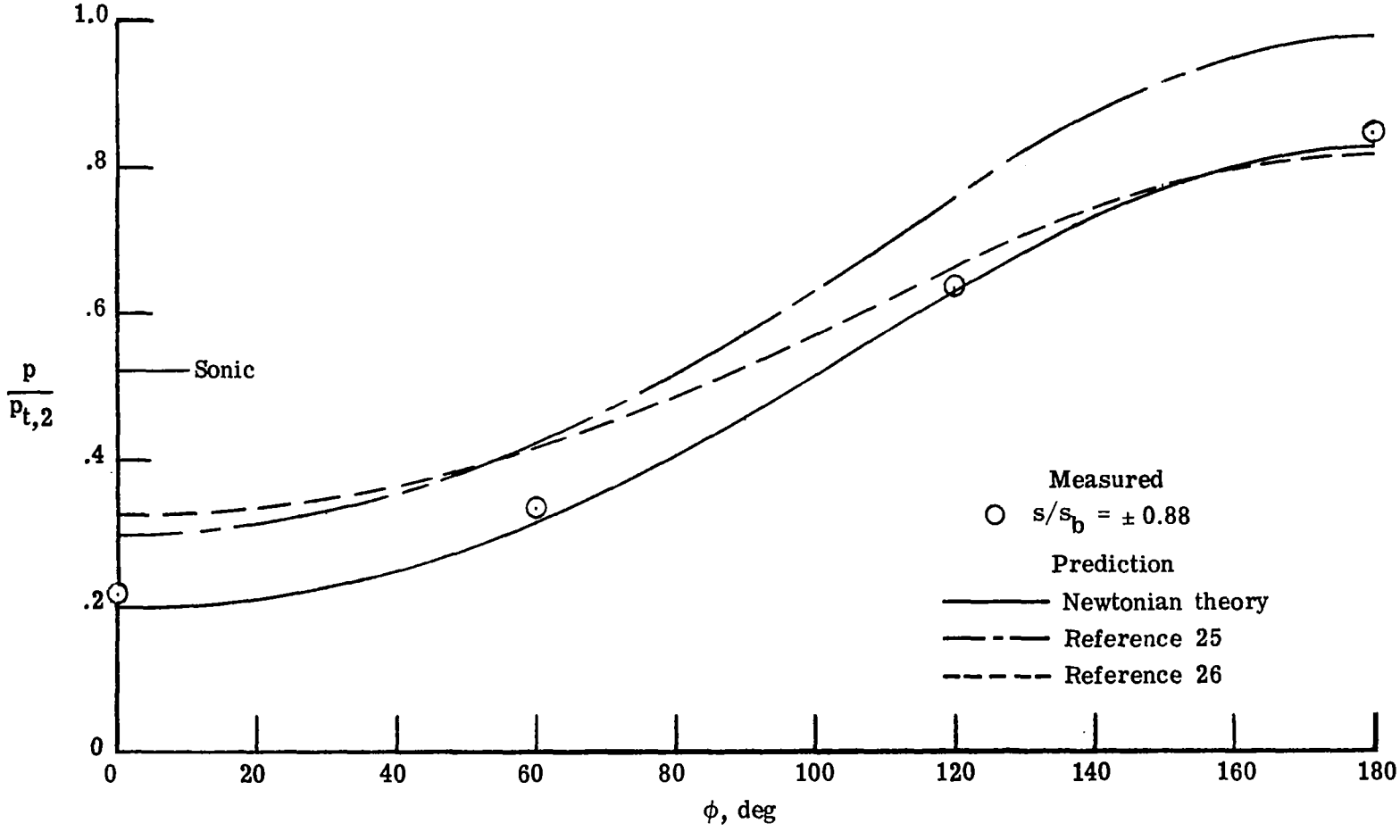

(e) $\alpha = 20°$.

Figure 40.- Concluded.

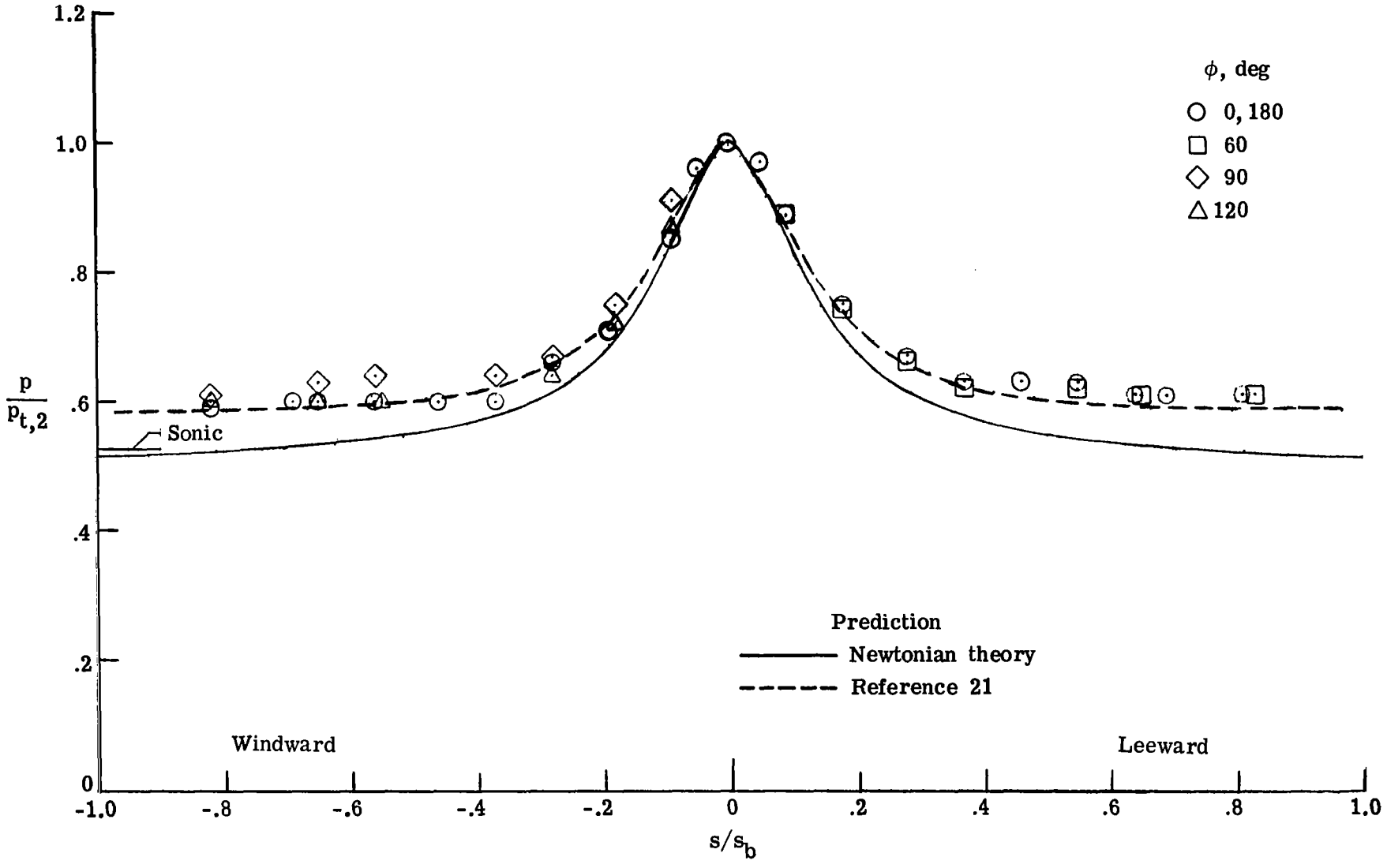

(a) $\alpha = 0°$.

Figure 41.- Pressure distributions measured on the hyperboloid (model 1, series 2) in Mach 10.0 air. $N_{Re,\infty,d_b} = 3.65 \times 10^5$.

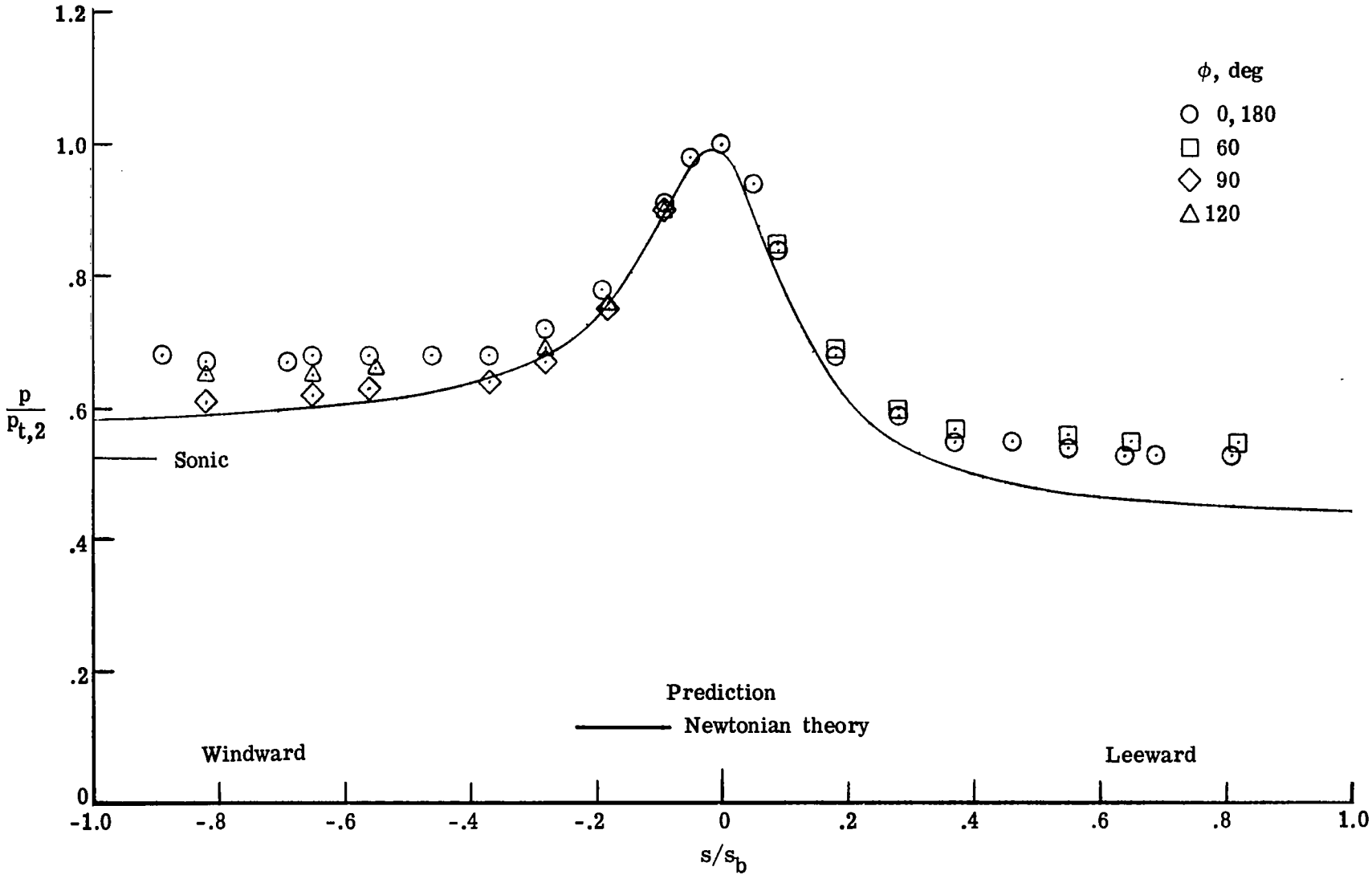

(b) $\alpha = 4°$.

Figure 41.- Continued.

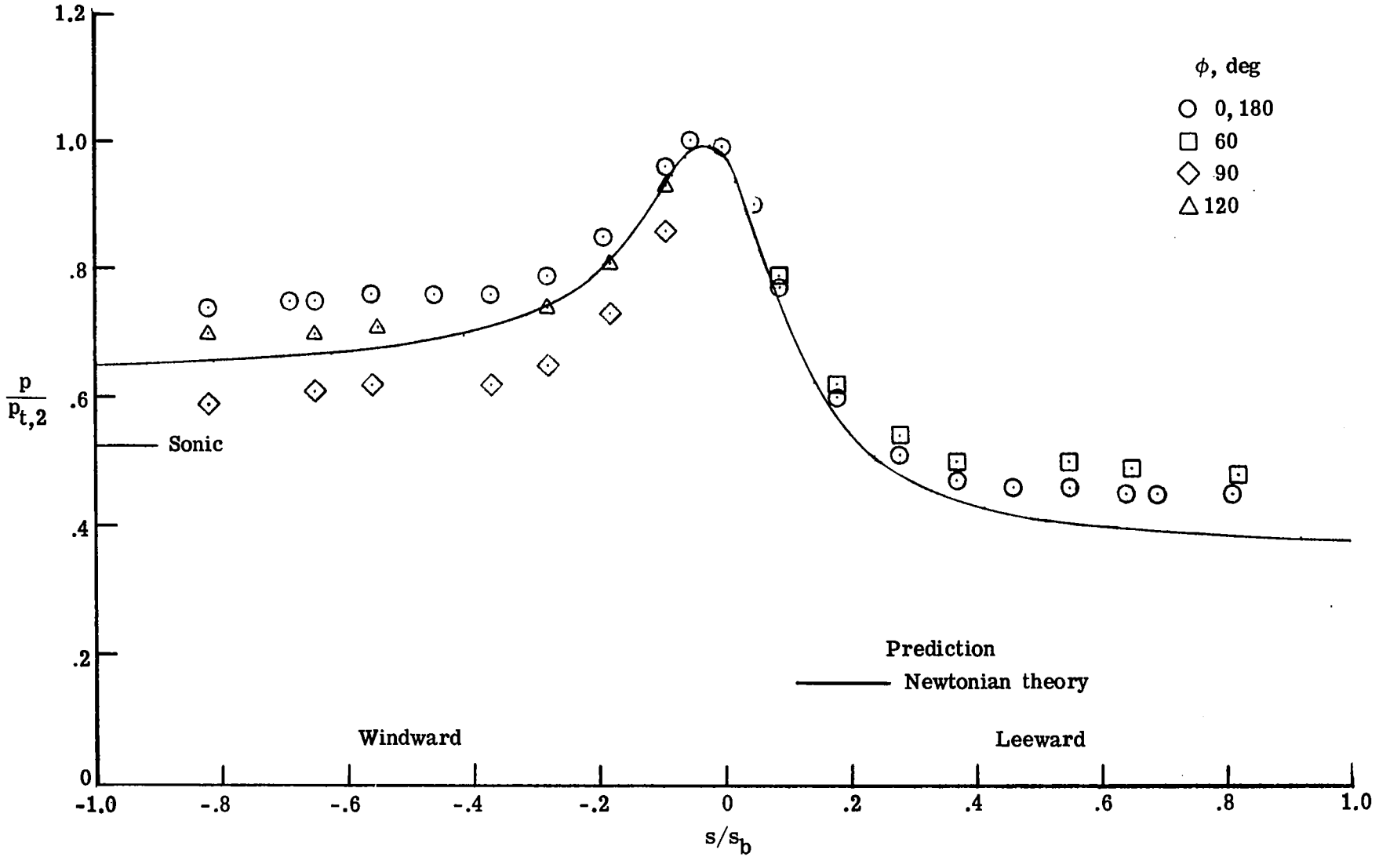

(c) $\alpha = 8°$.

Figure 41.- Continued.

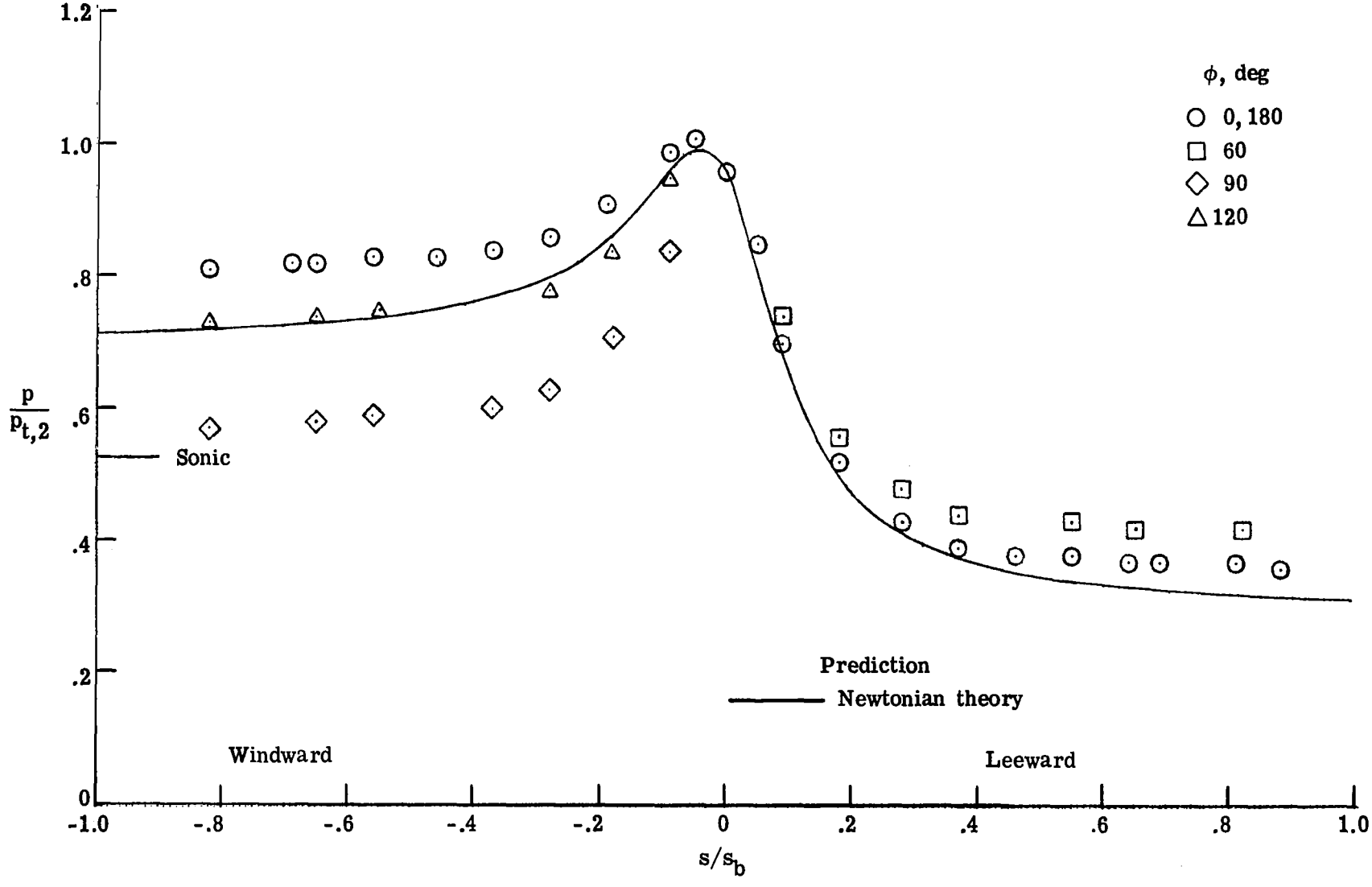

(d) $\alpha = 12°$.

Figure 41.- Continued.

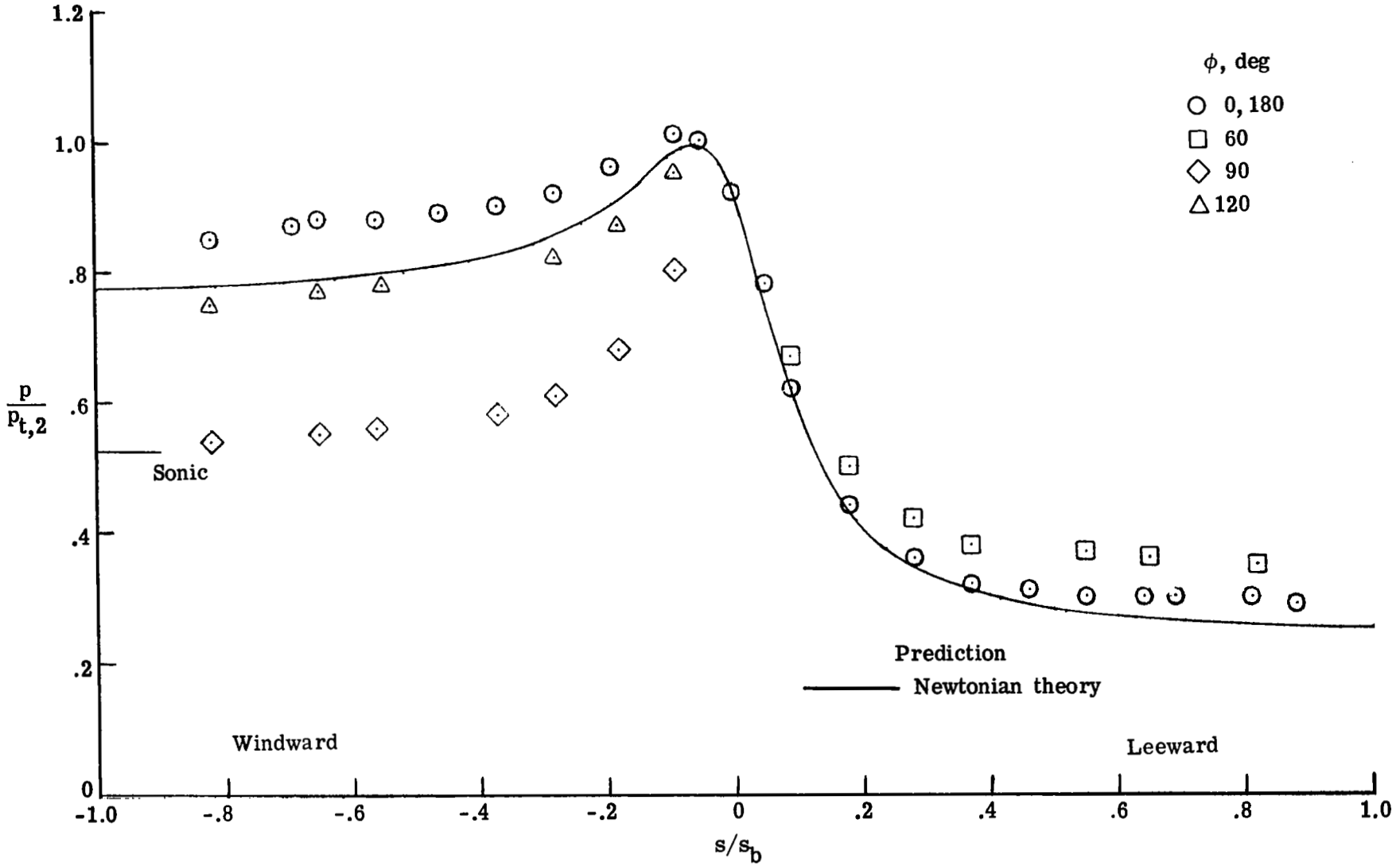

(e) $\alpha = 16°$.

Figure 41.- Concluded.

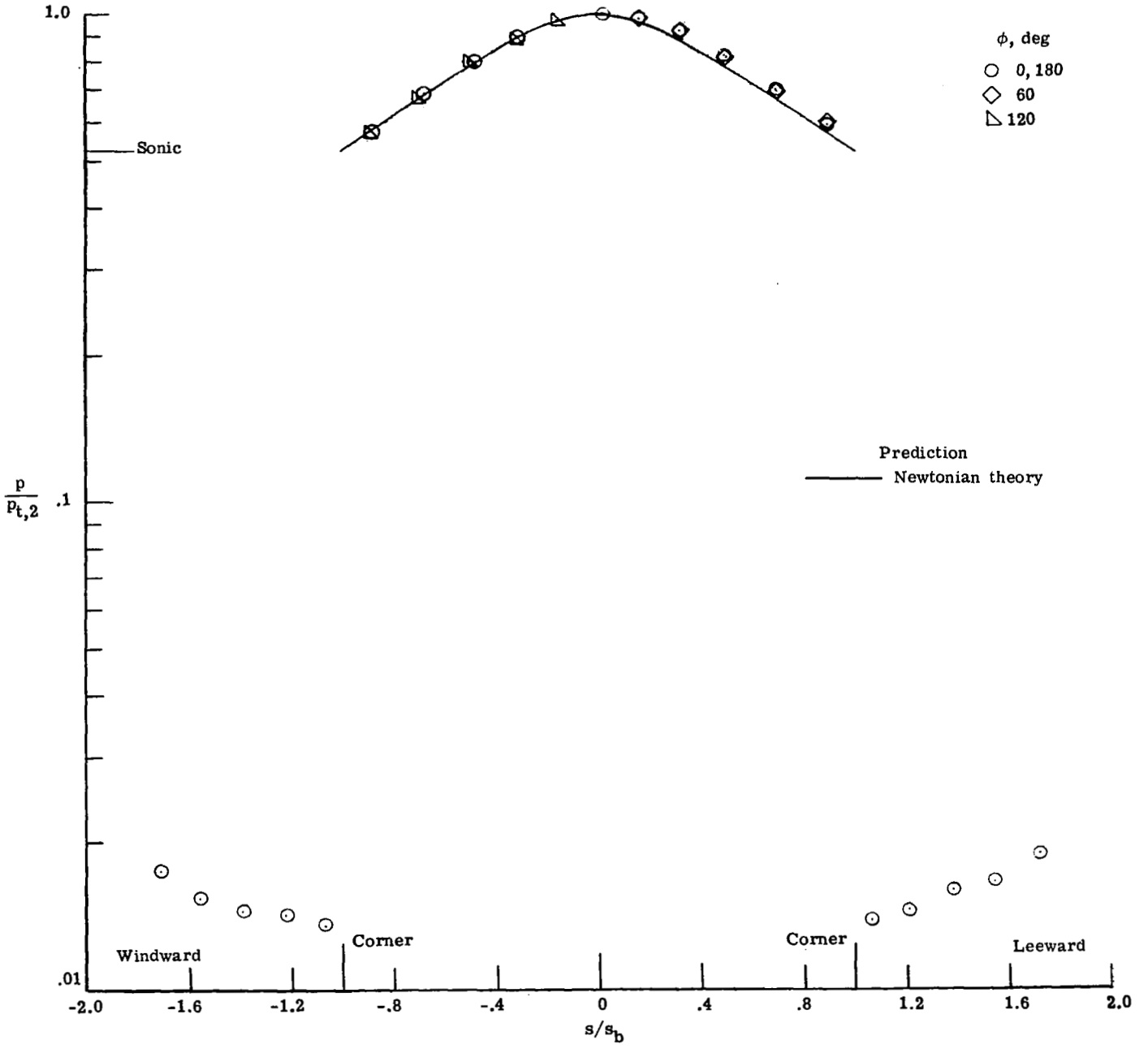

(a) $\alpha = 0°$.

Figure 42.- Pressure distributions measured on the sonic-corner paraboloid (model 2) in Mach 10.0 air. $N_{Re,\infty,d_b} = 3.8 \times 10^5$.

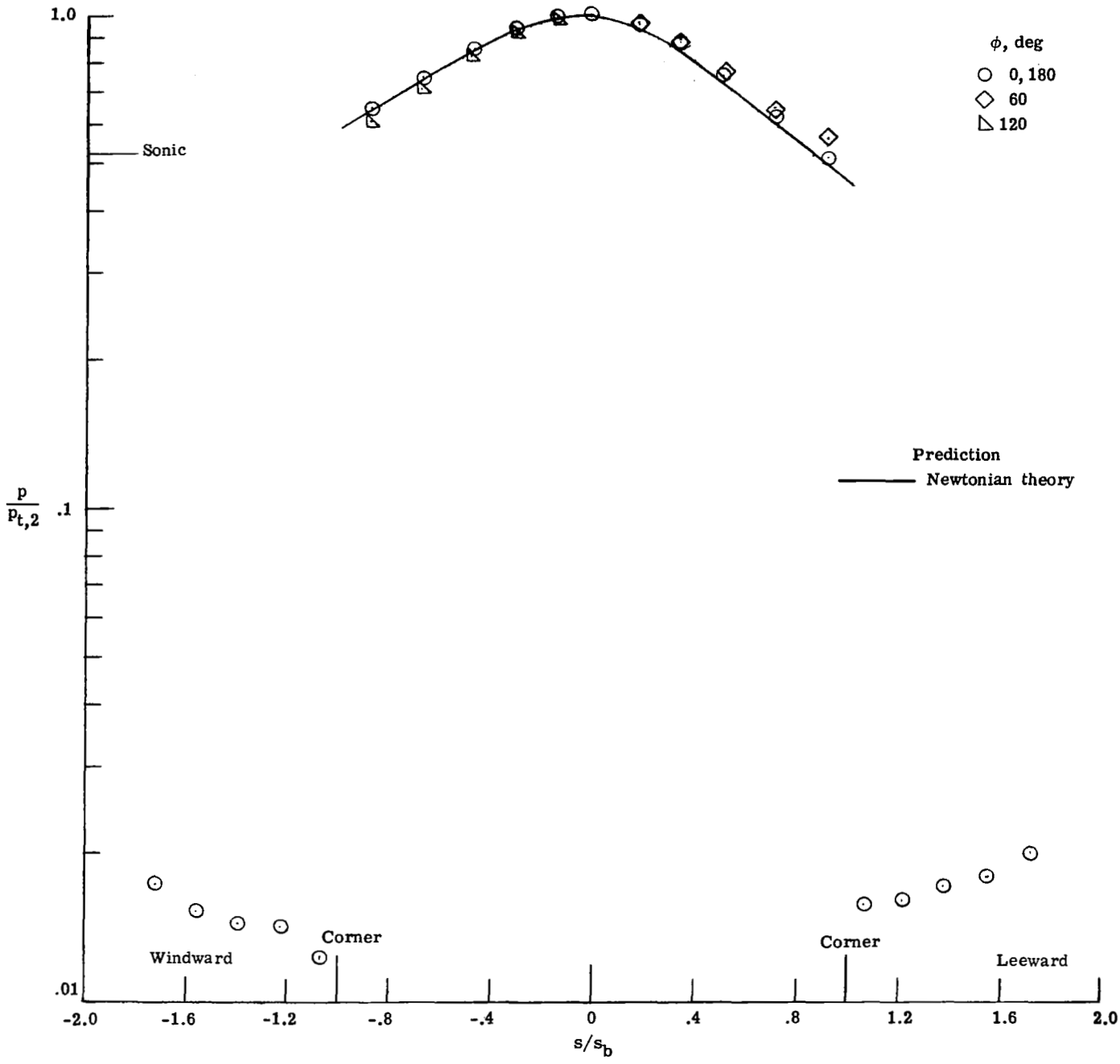

(b) $\alpha = 4°$.

Figure 42.- Continued.

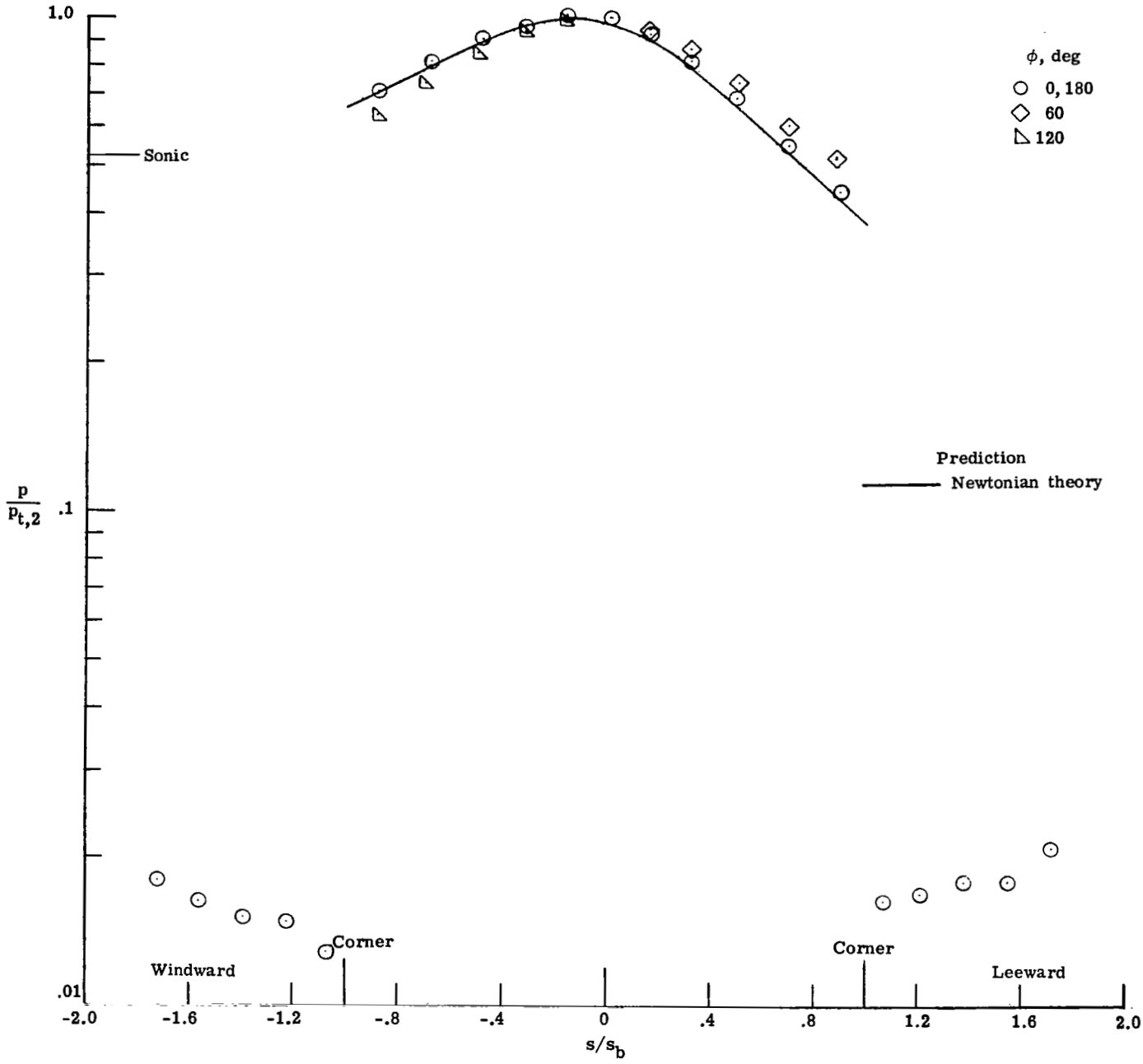

(c) $\alpha = 8°$.

Figure 42.- Continued.

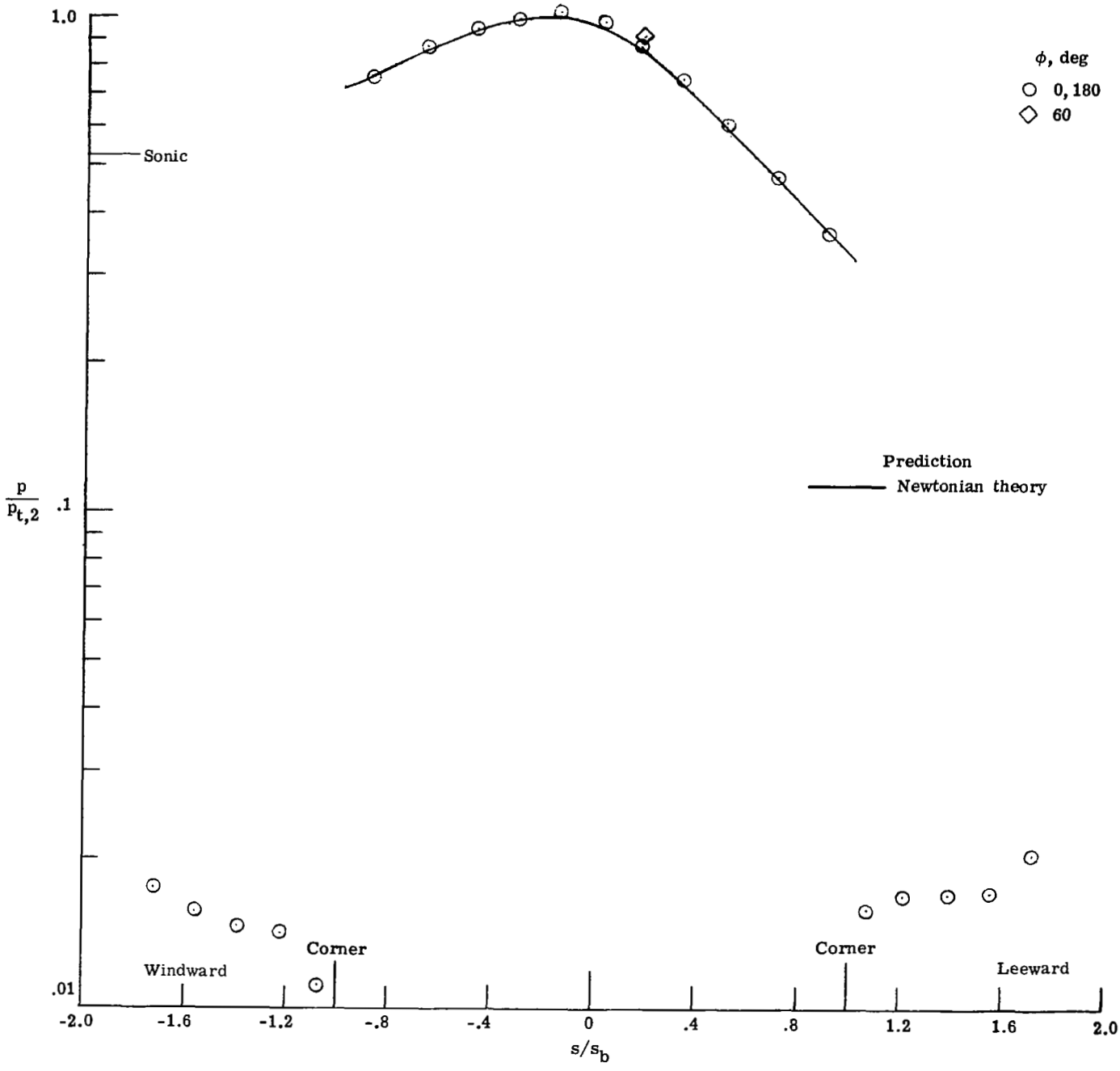

(d) $\alpha = 12°$.

Figure 42.- Continued.

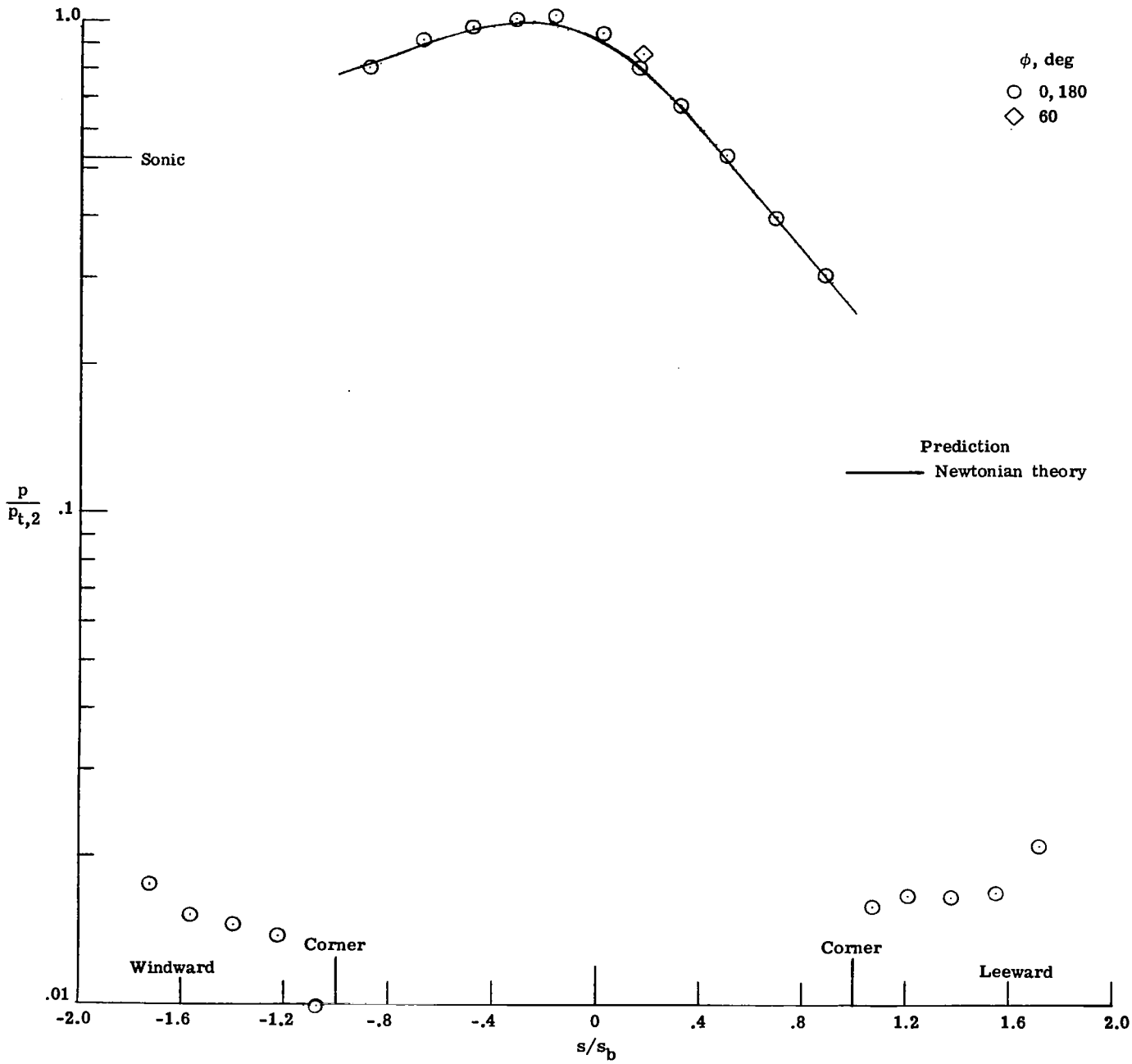

(e) $\alpha = 16°$.

Figure 42.- Concluded.

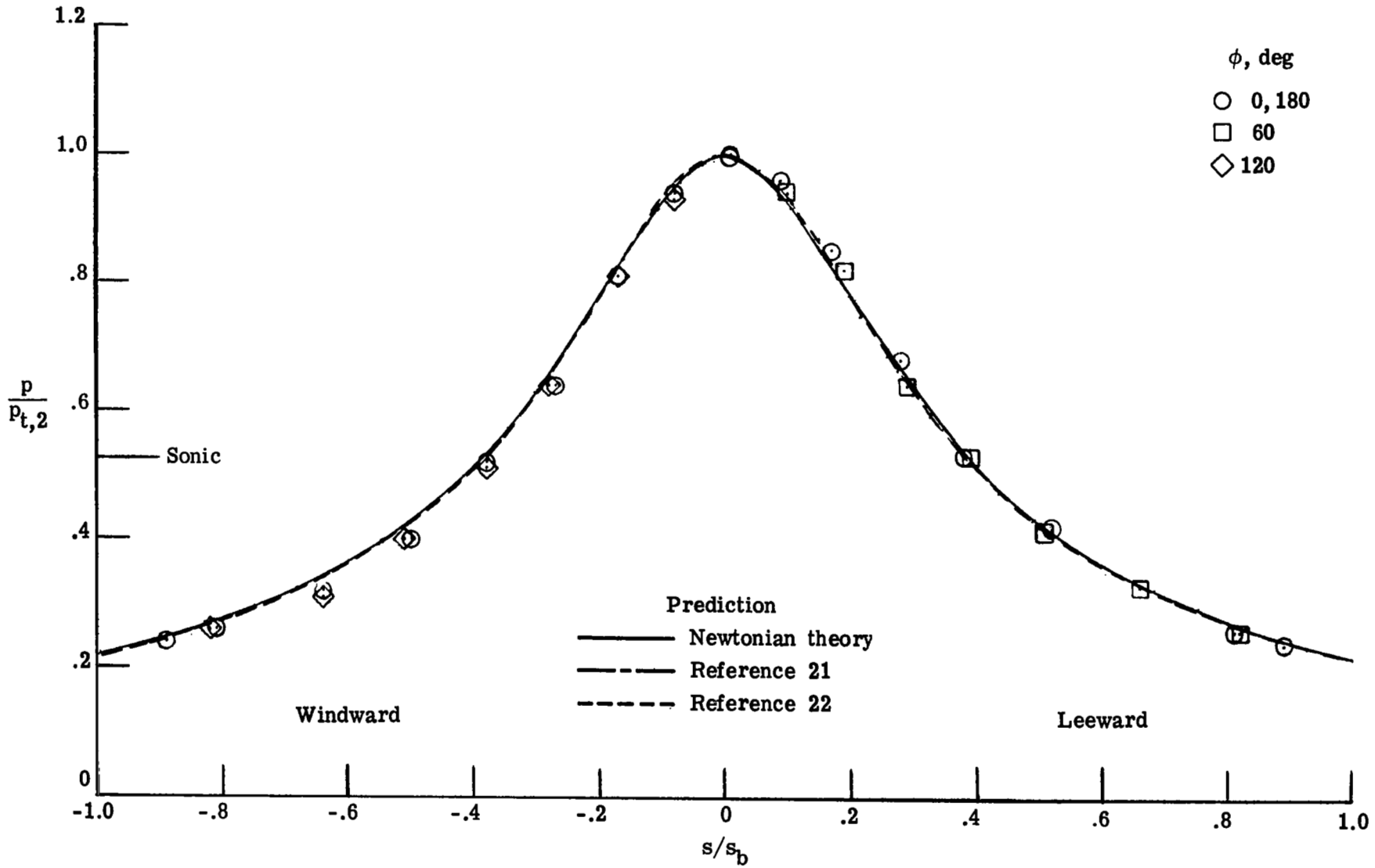

(a) $\alpha = 0°$.

Figure 43.- Pressure distributions measured on the paraboloid (model 3, series 2) in Mach 9.9 air. $N_{Re,\infty,d_b} = 1.9 \times 10^5$.

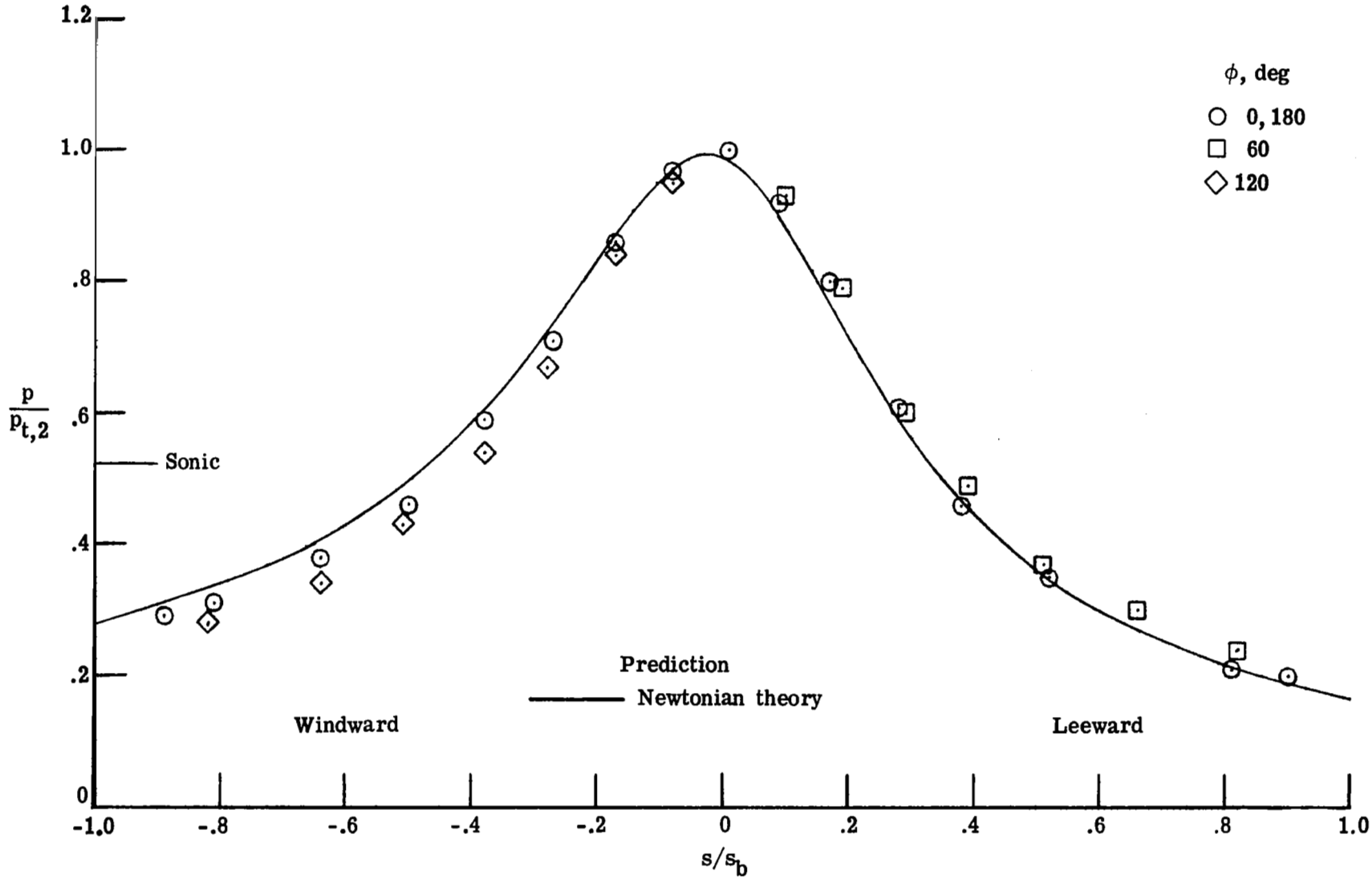

(b) $\alpha = 4°$.

Figure 43.- Continued.

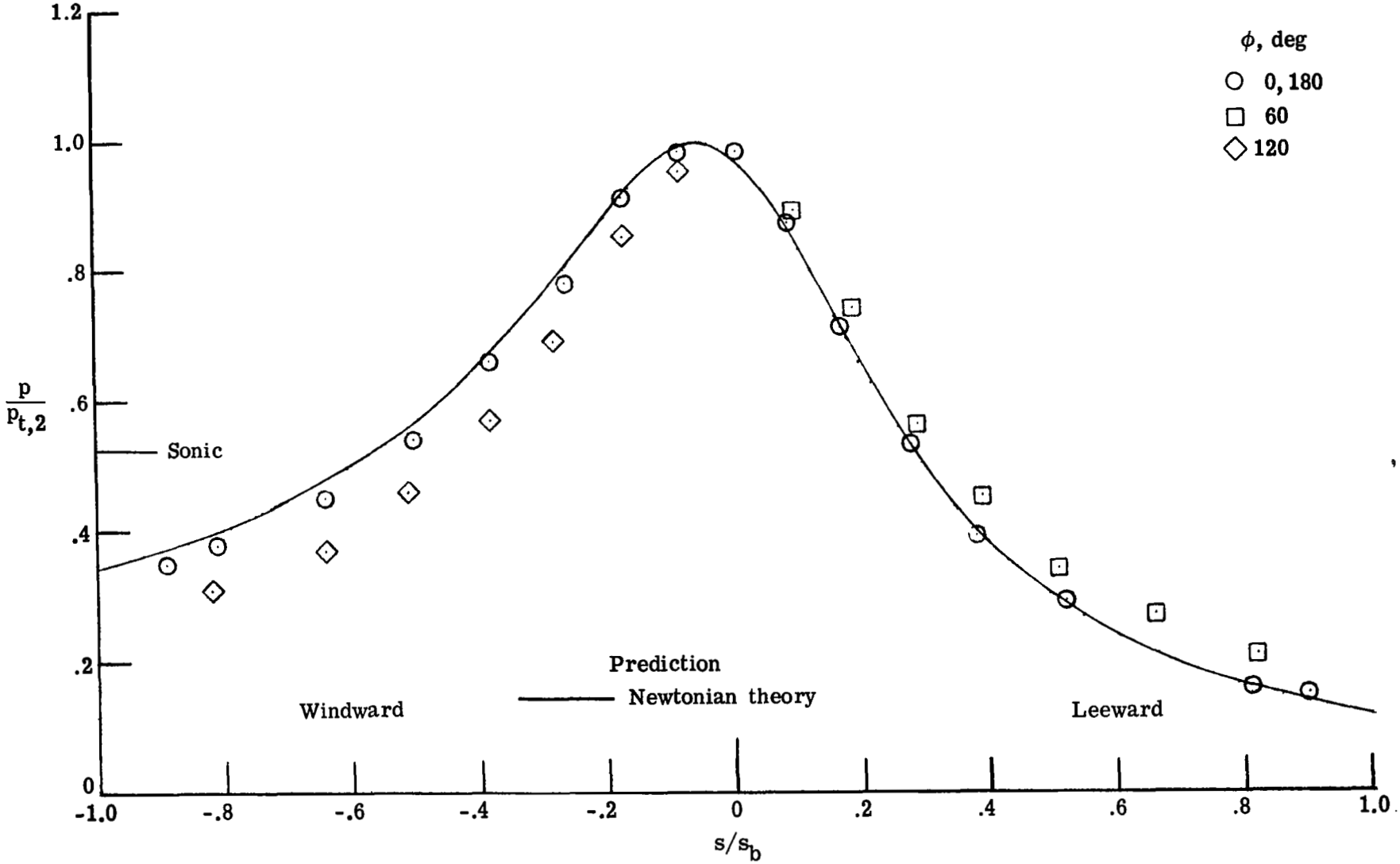

(c) $\alpha = 8°$.

Figure 43.- Continued.

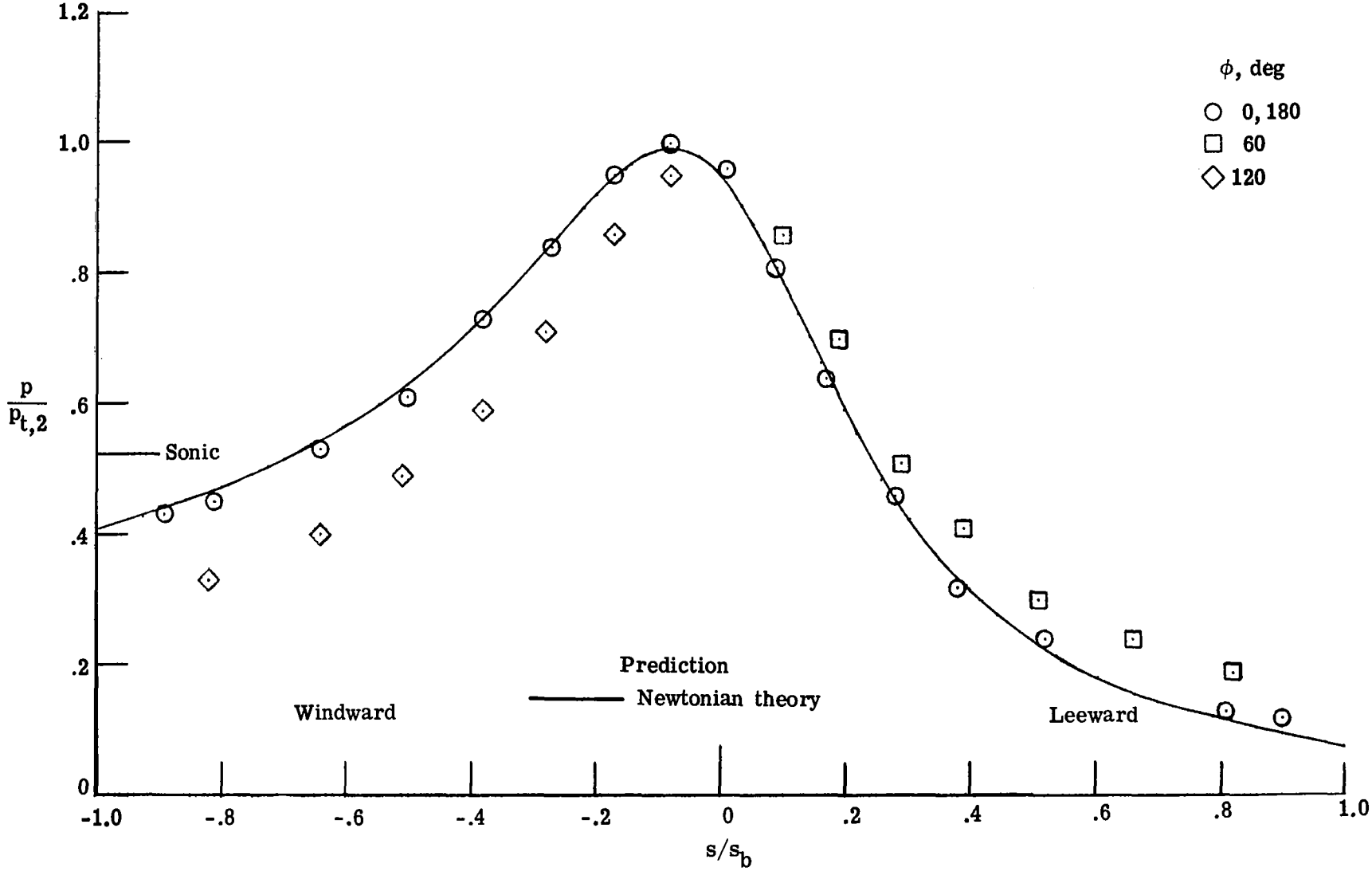

(d) $\alpha = 12°$.

Figure 43.- Continued.

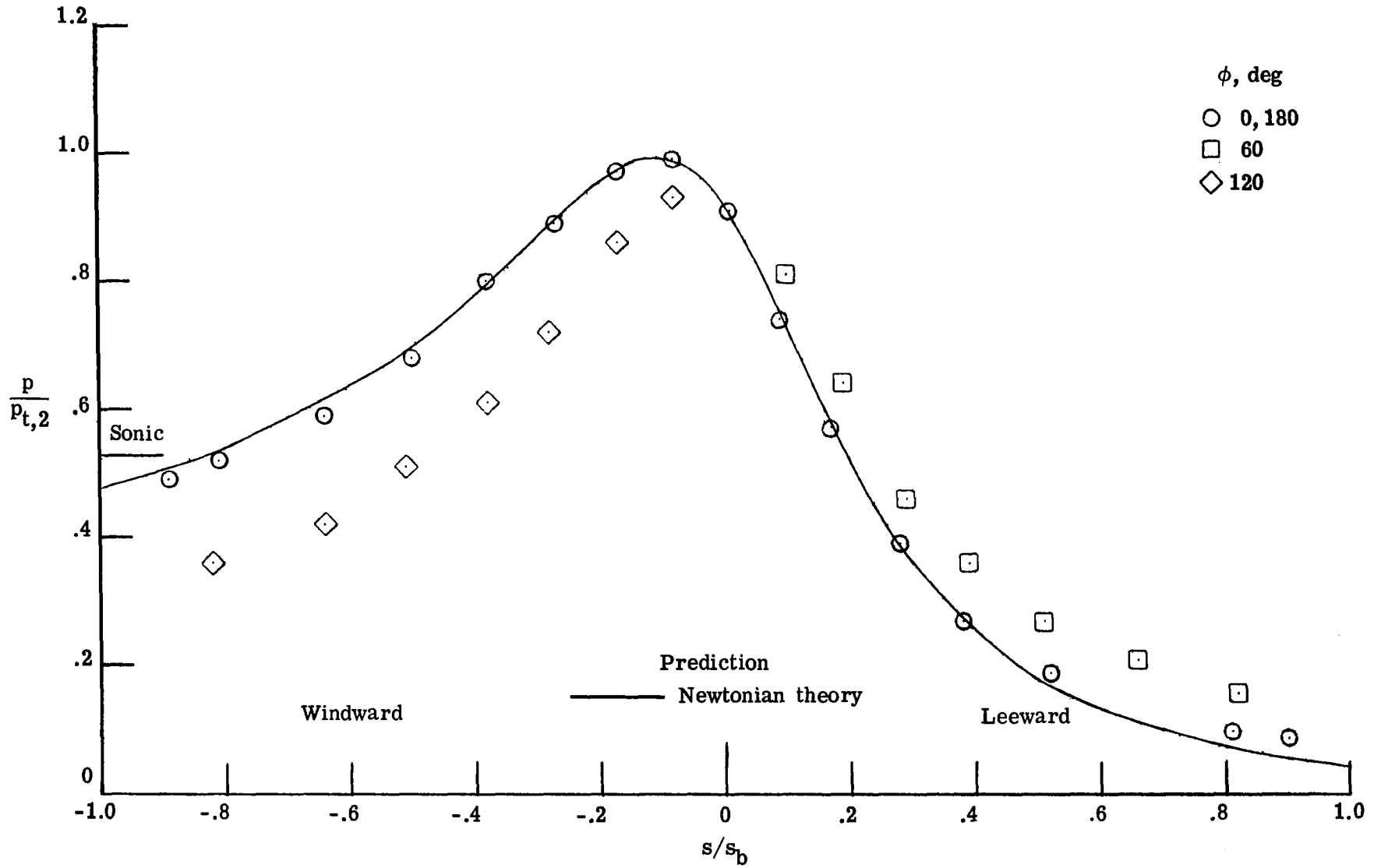

(e) $\alpha = 16°$.

Figure 43.- Concluded.

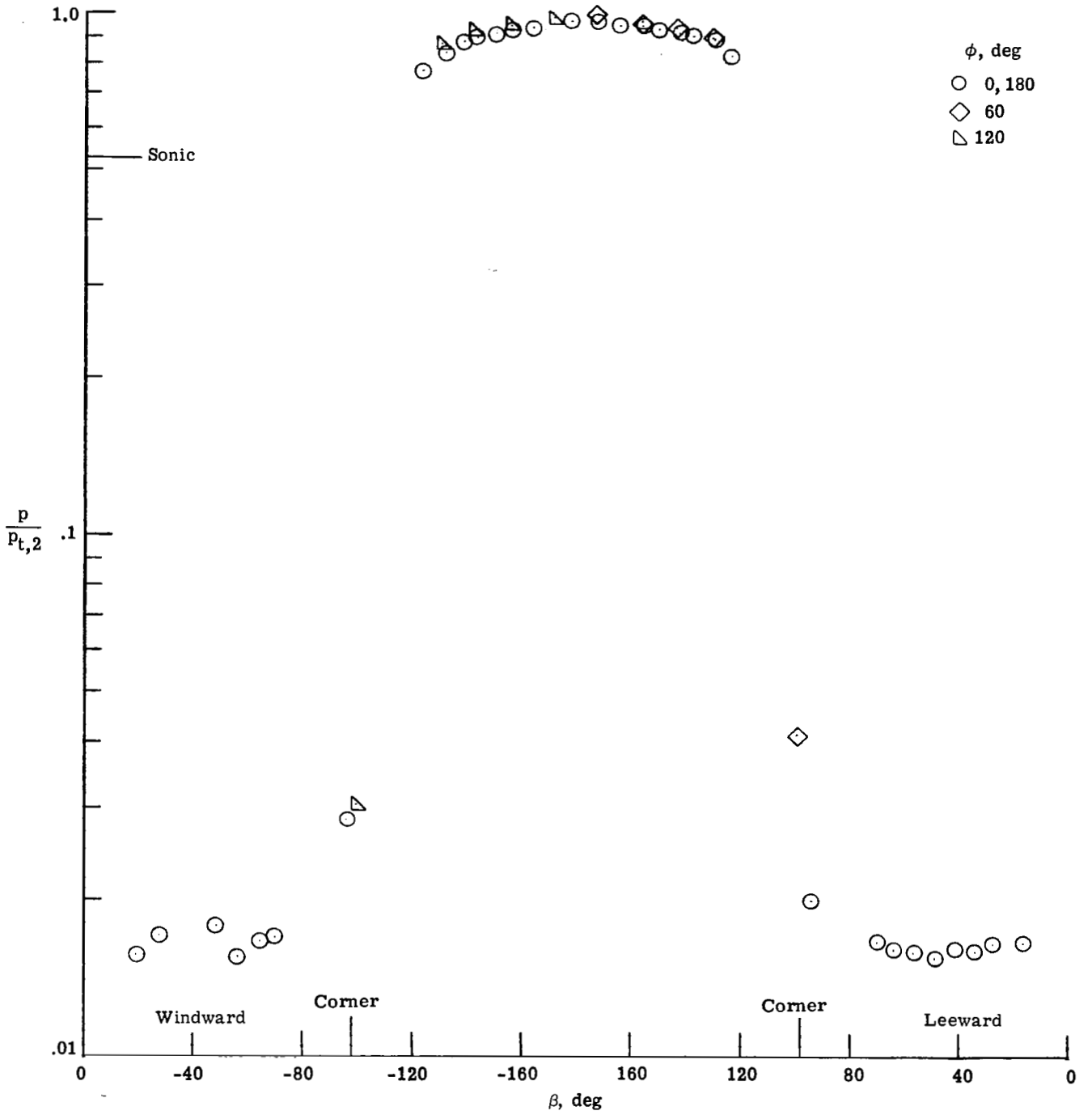

(a) $\alpha = 0°$.

Figure 44.- Pressure distributions measured on the Viking aeroshell (model 4) in Mach 9.9 air. $N_{Re,\infty,d_b} = 1.9 \times 10^5$.

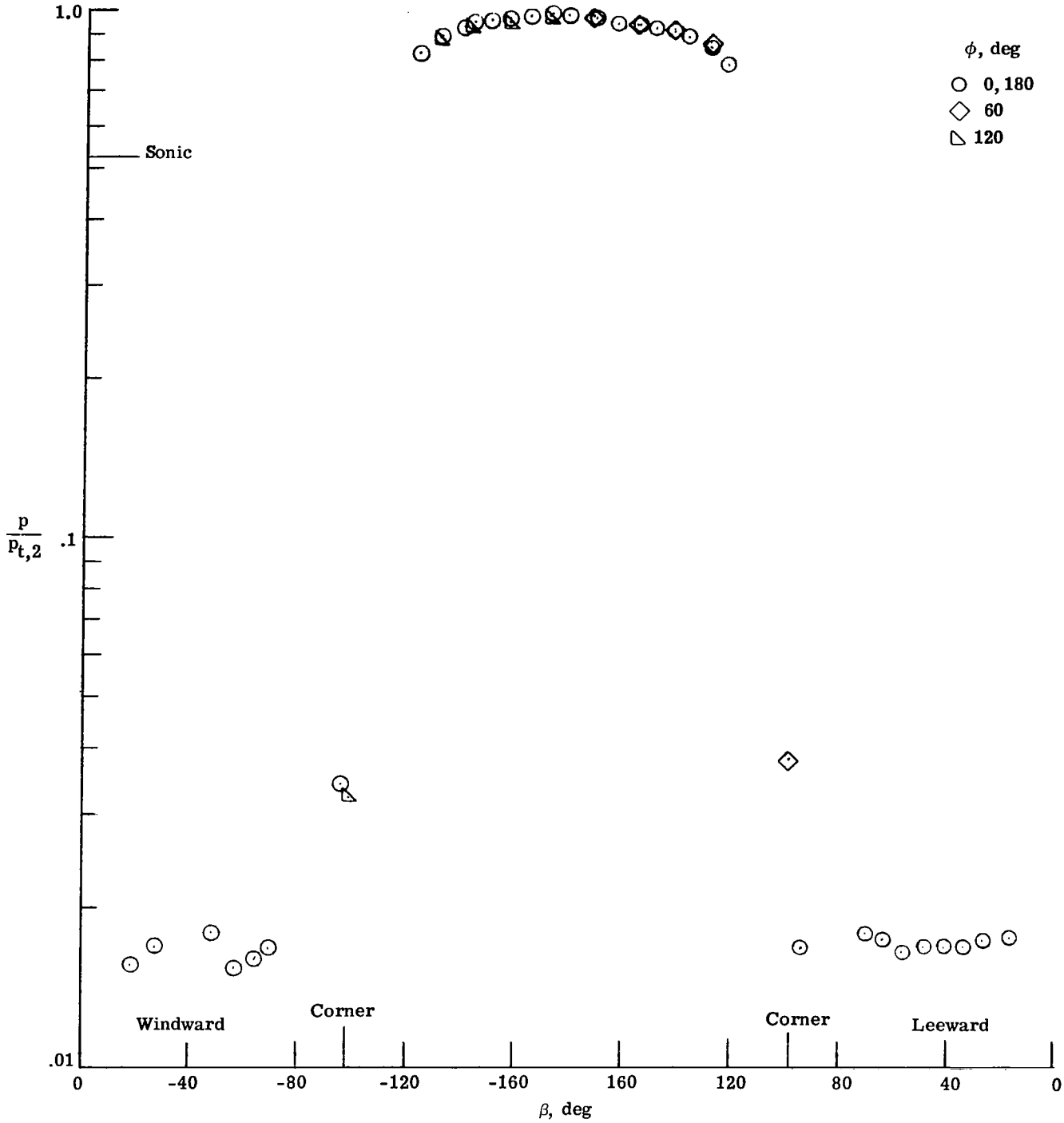

(b) $\alpha = 4°$.

Figure 44.- Continued.

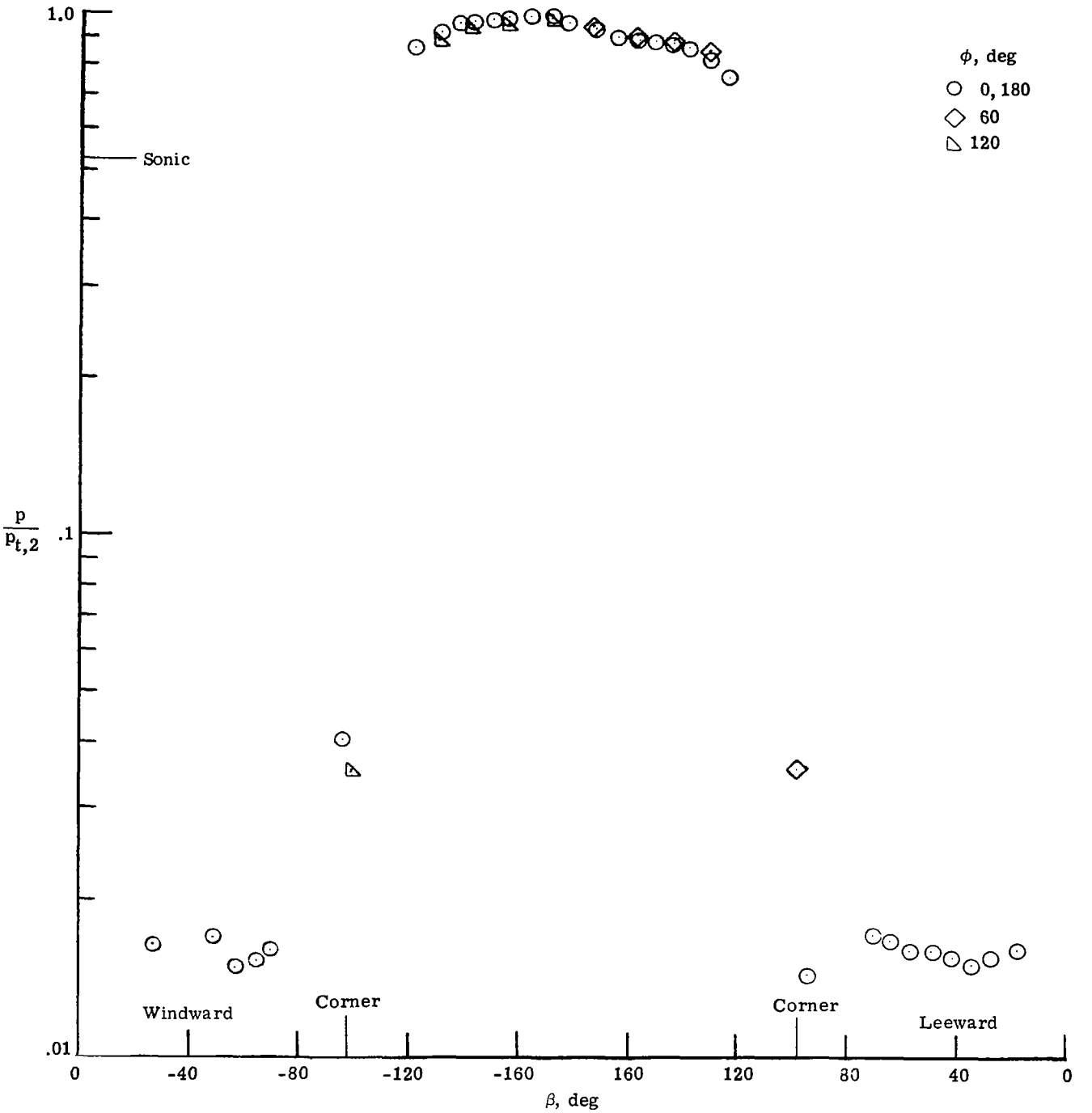

(c) $\alpha = 8°$.

Figure 44.- Continued.

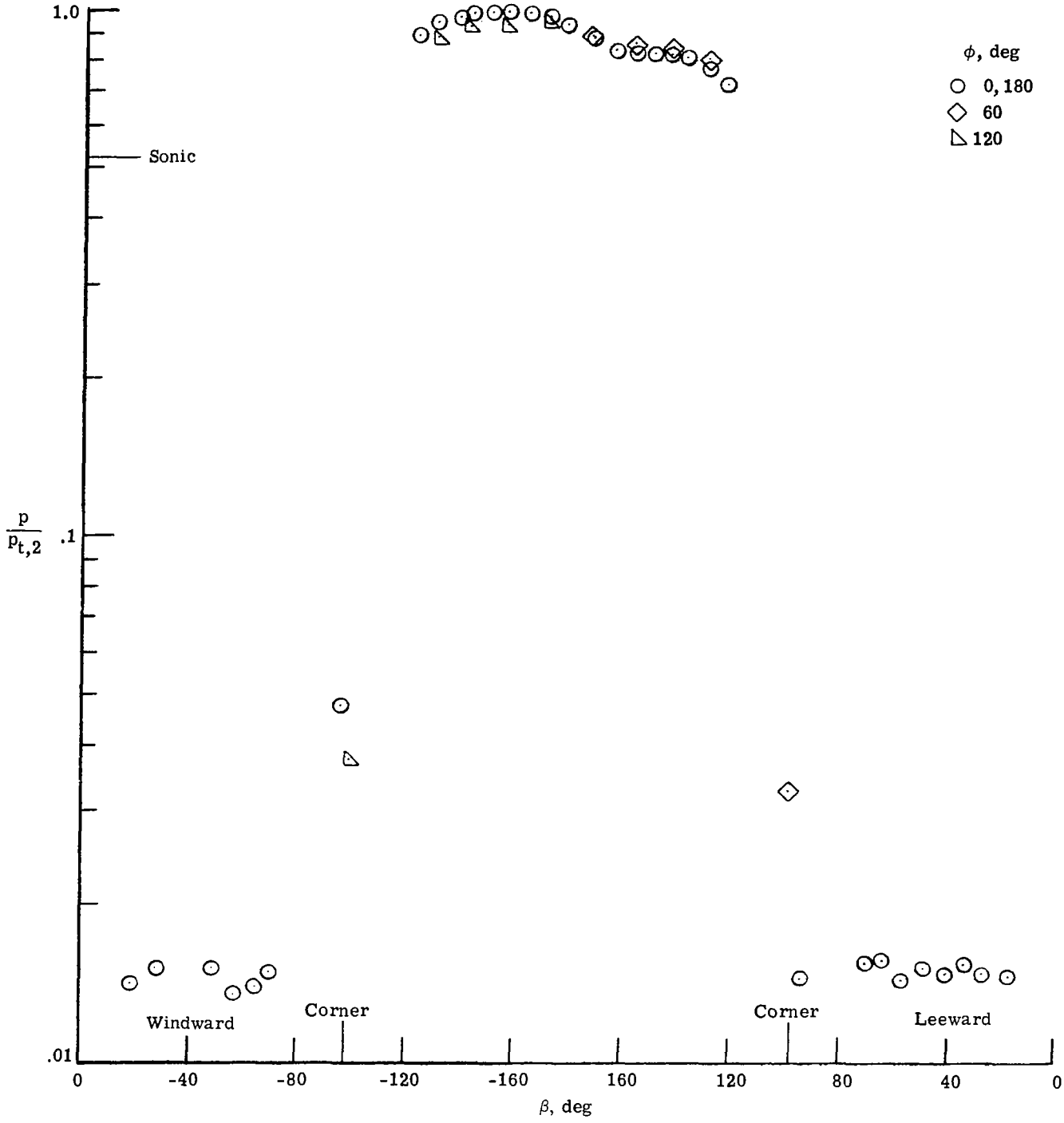

(d) $\alpha = 12°$.

Figure 44.- Continued.

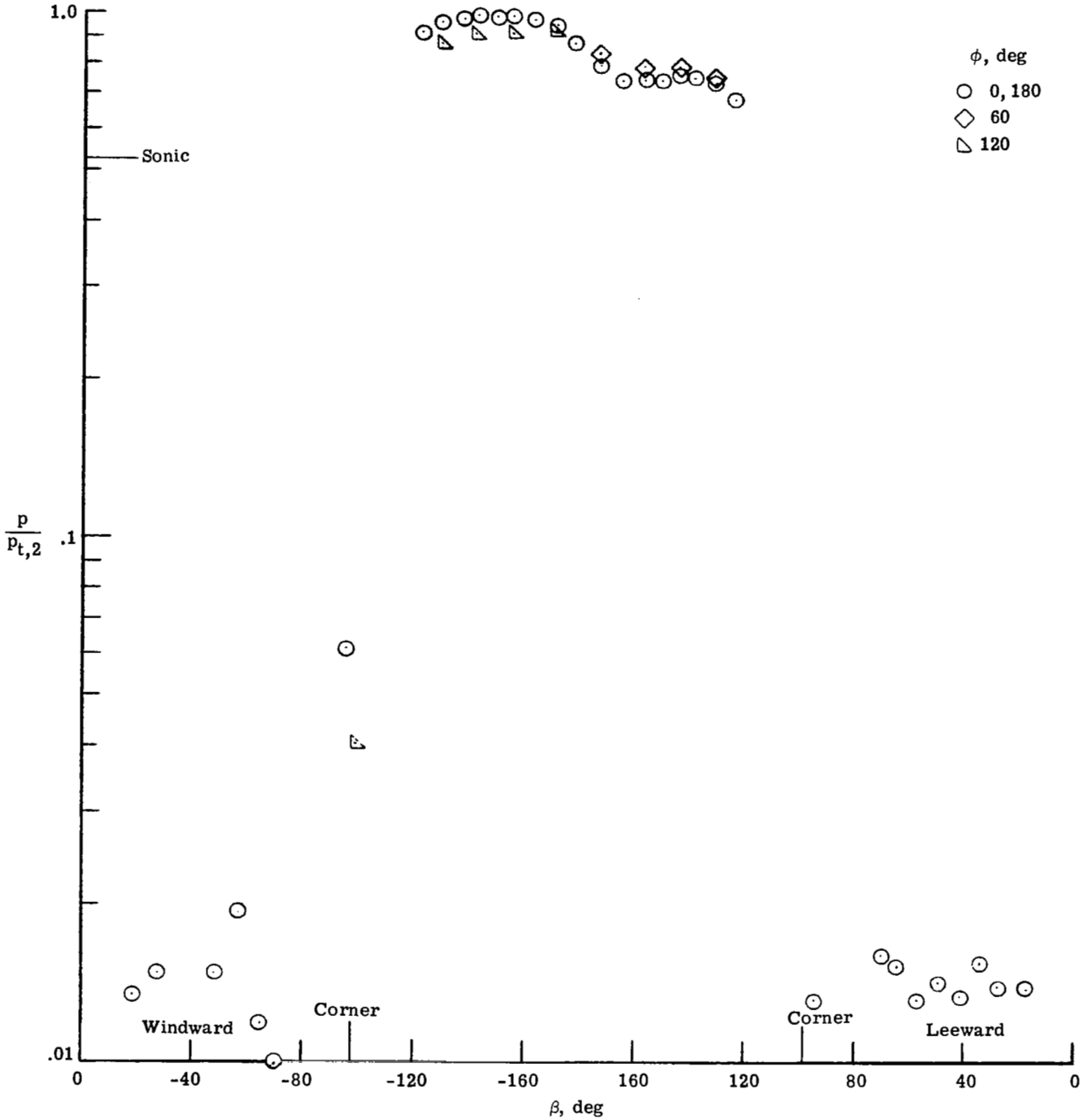

(e) $\alpha = 16°$.

Figure 44.- Concluded.

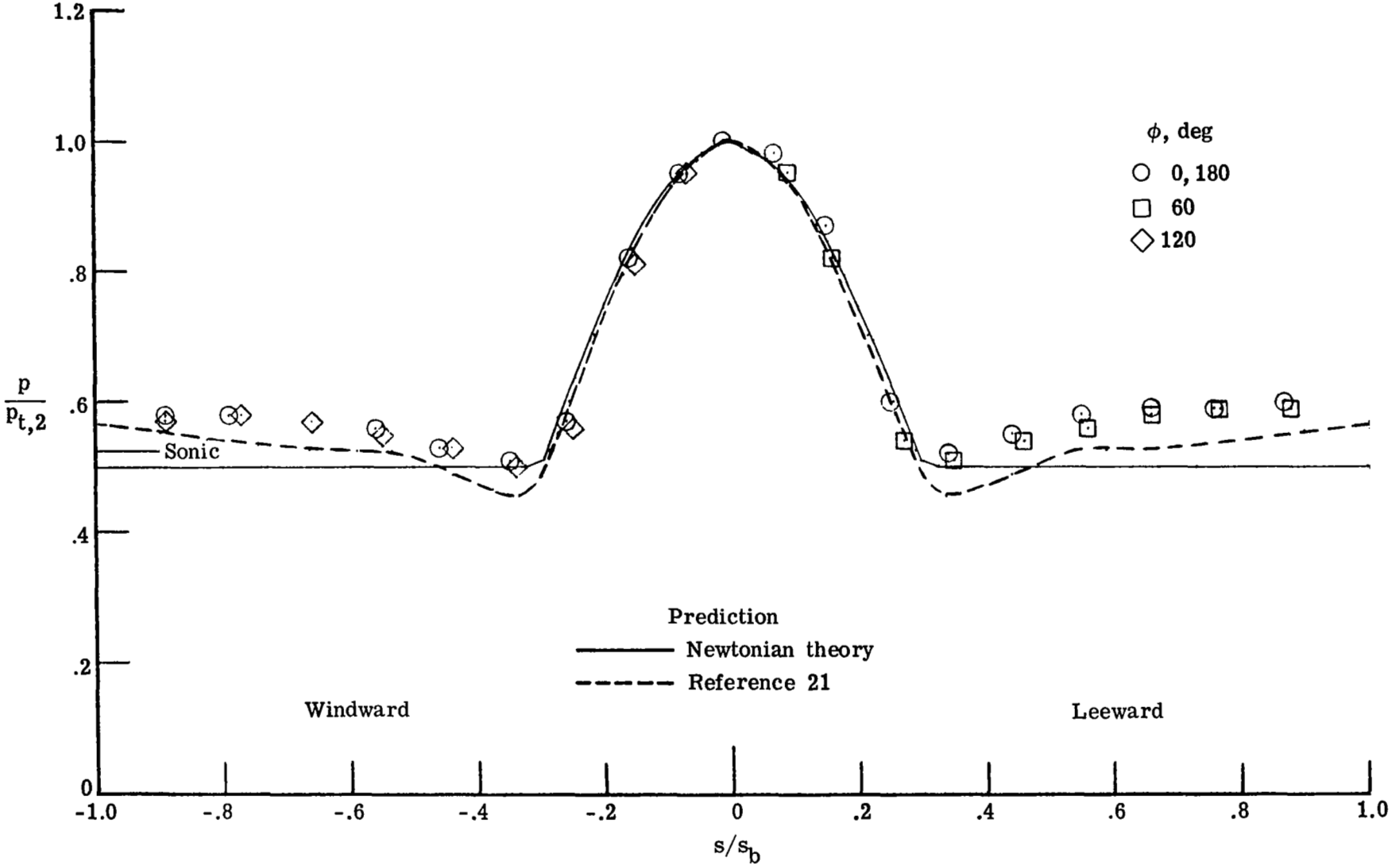

(a) $\alpha = 0°$.

Figure 45.- Pressure distributions measured on the spherical-nose cone (model 5) in Mach 10.0 air. $N_{Re,\infty,d_b} = 3.65 \times 10^5$.

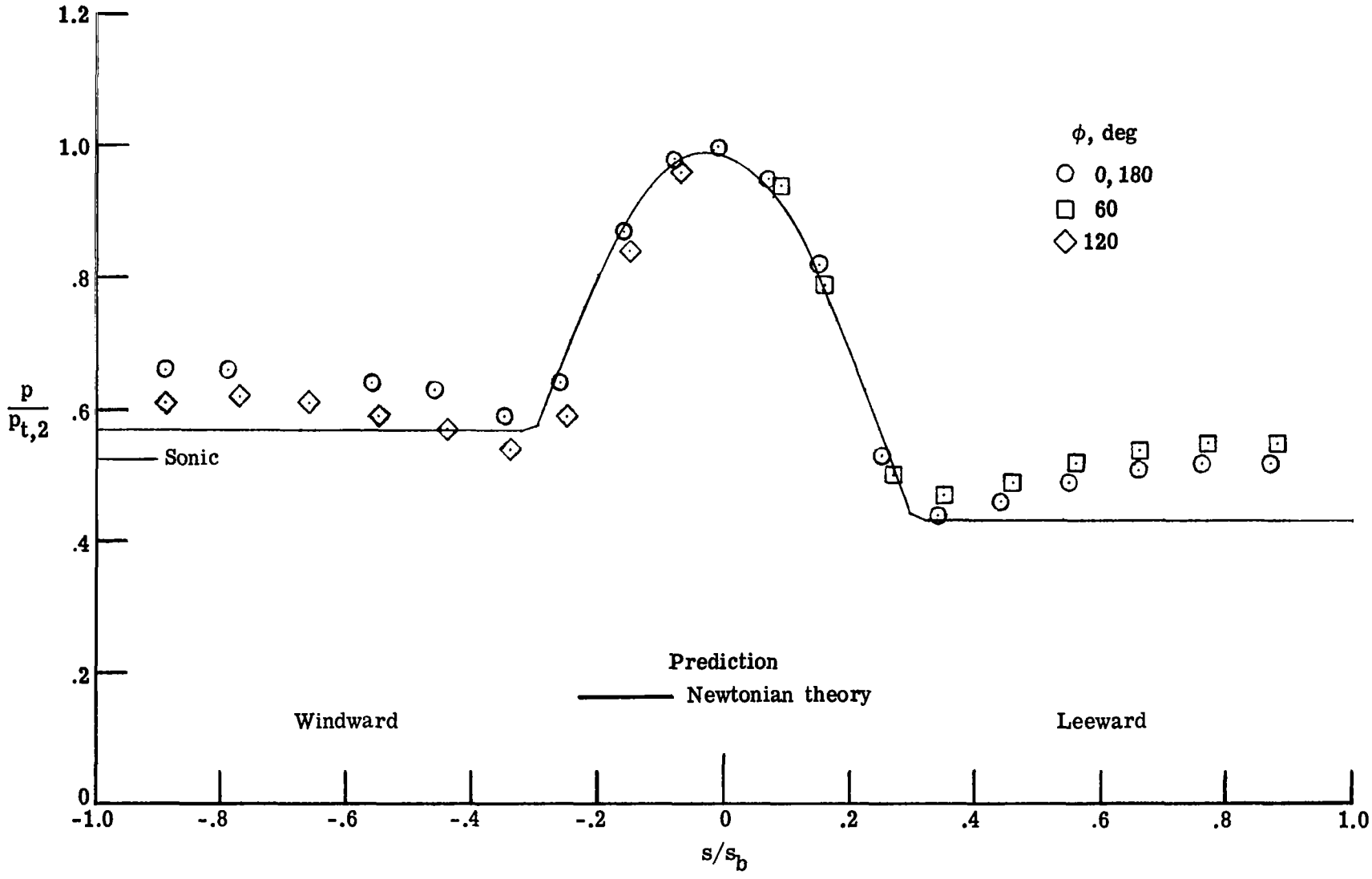

(b) $\alpha = 4°$.

Figure 45.- Continued.

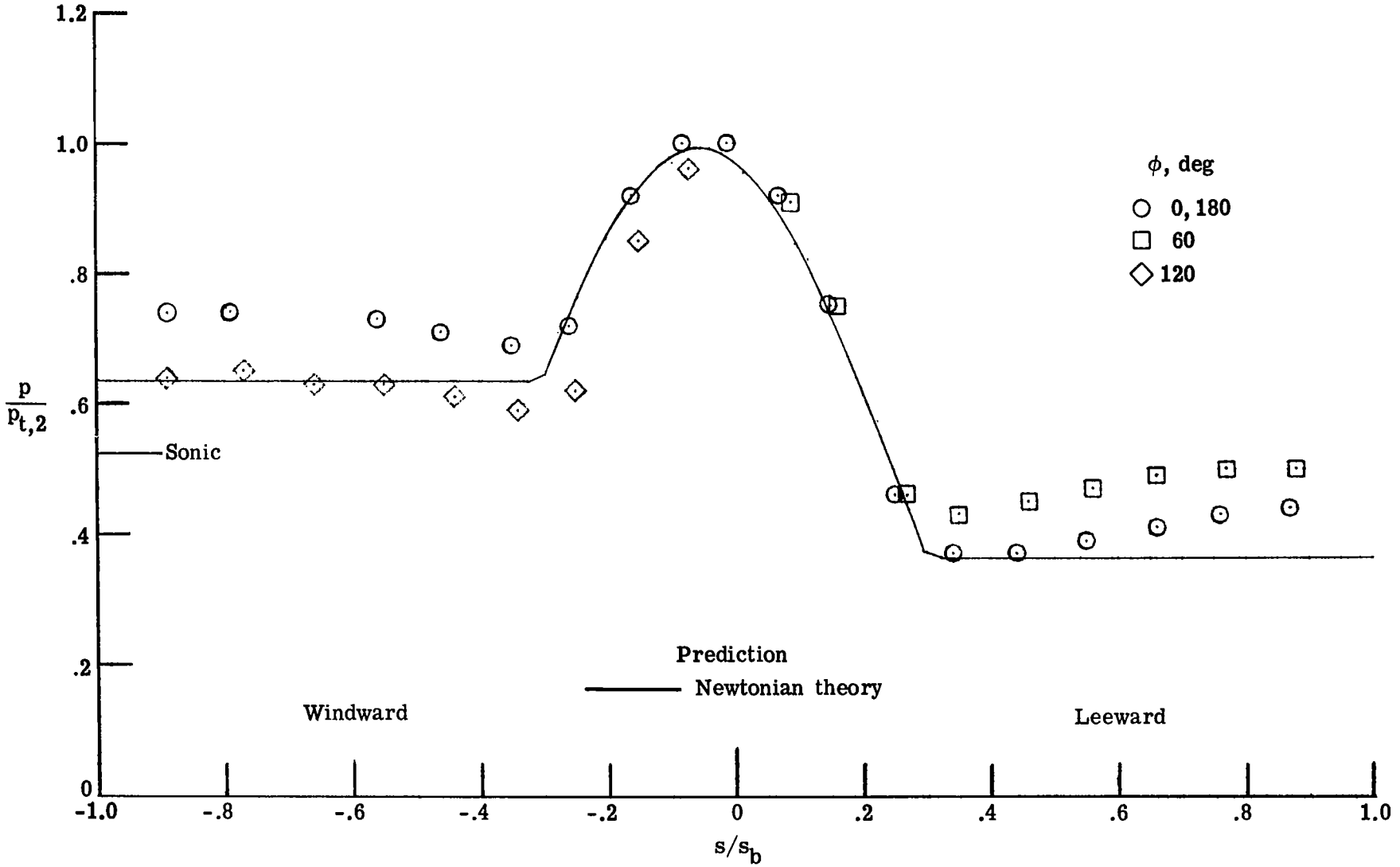

(c) $\alpha = 8°$.

Figure 45.- Continued.

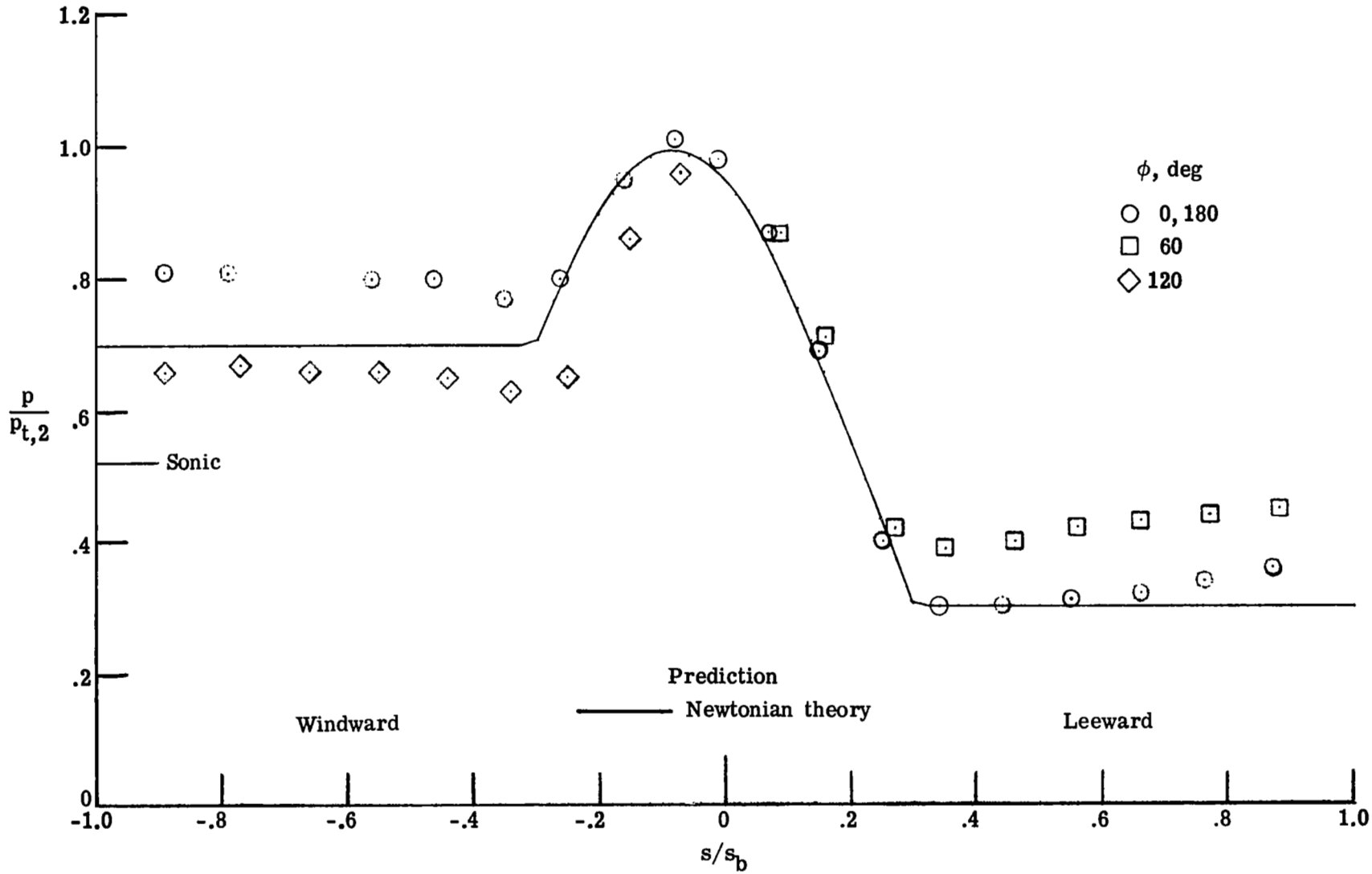

(d) $\alpha = 12°$.

Figure 45.- Continued.

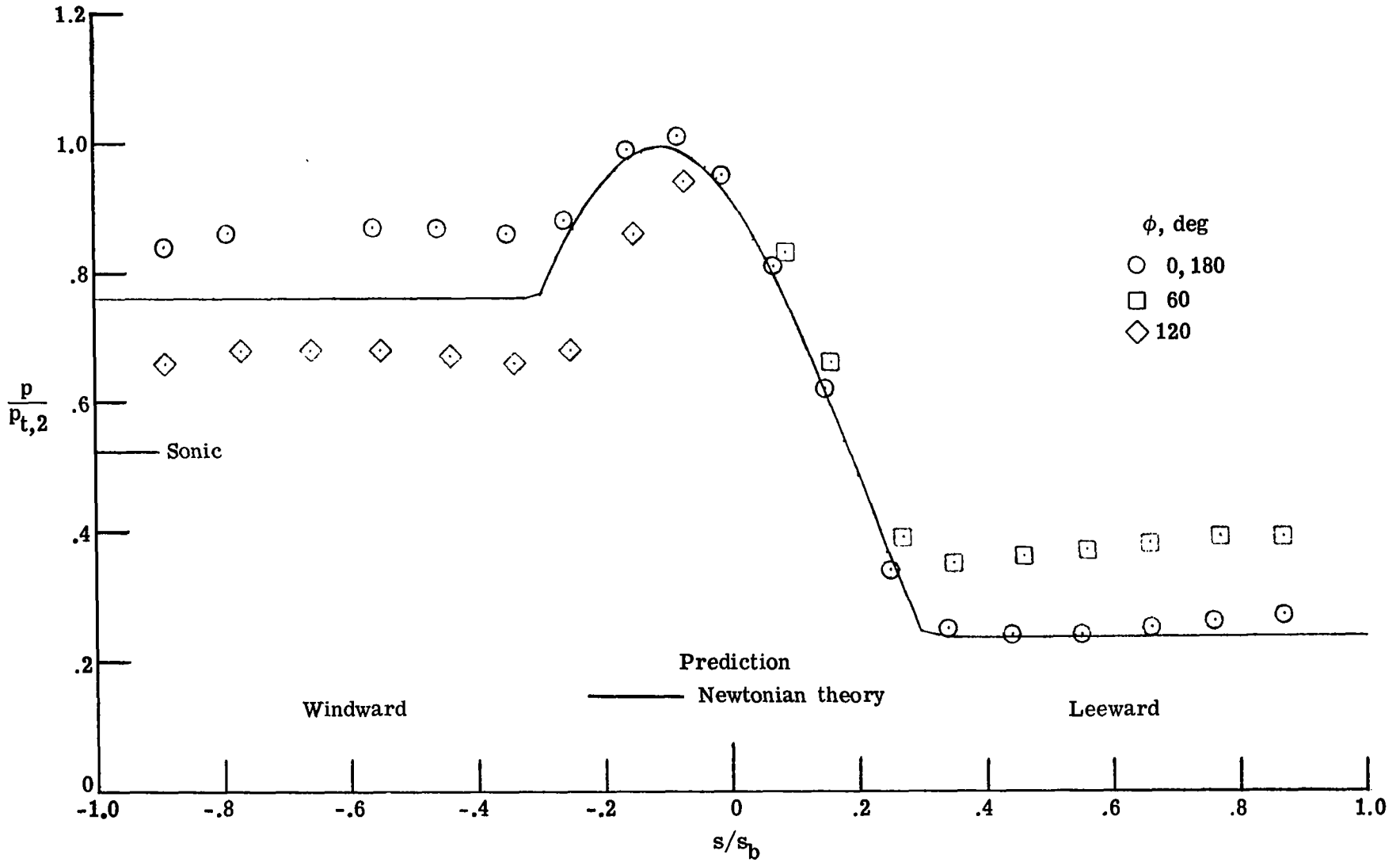

(e) $\alpha = 16°$.

Figure 45.- Concluded.

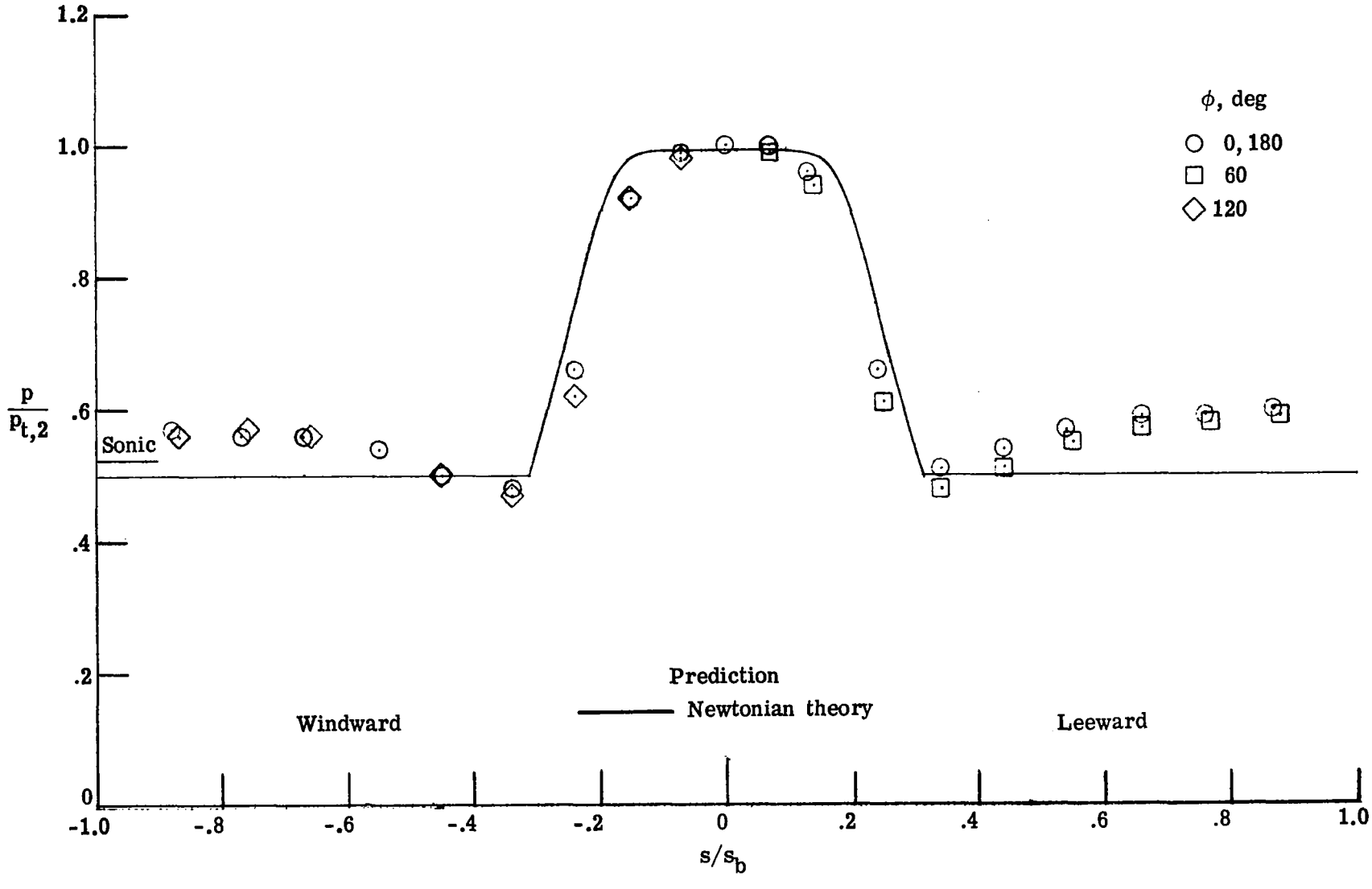

(a) $\alpha = 0°$.

Figure 46.- Pressure distributions measured on the flattened-nose cone (model 6) in Mach 10.0 air. $N_{Re,\infty,d_b} = 3.65 \times 10^5$.

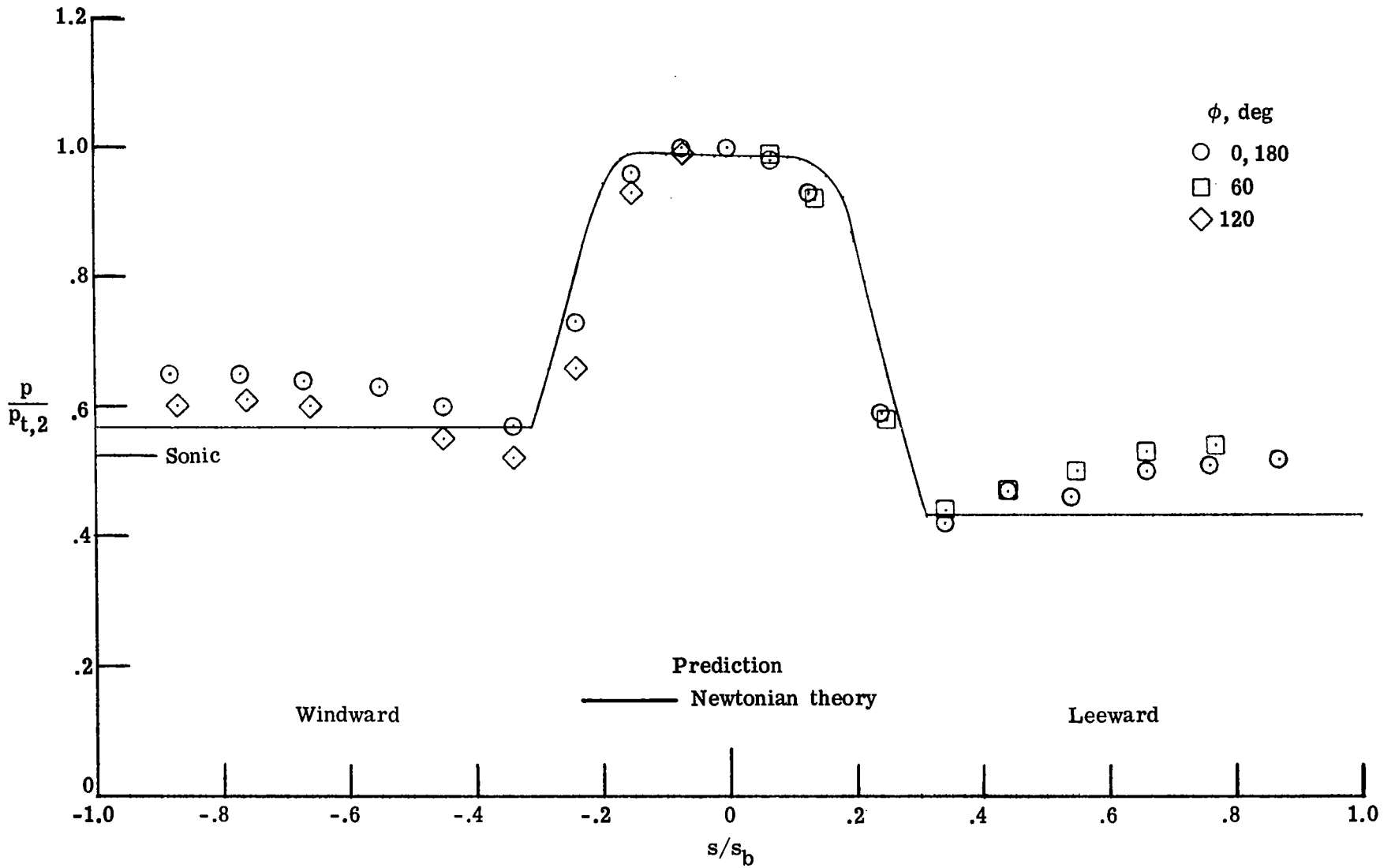

(b) $\alpha = 4°$.

Figure 46.- Continued.

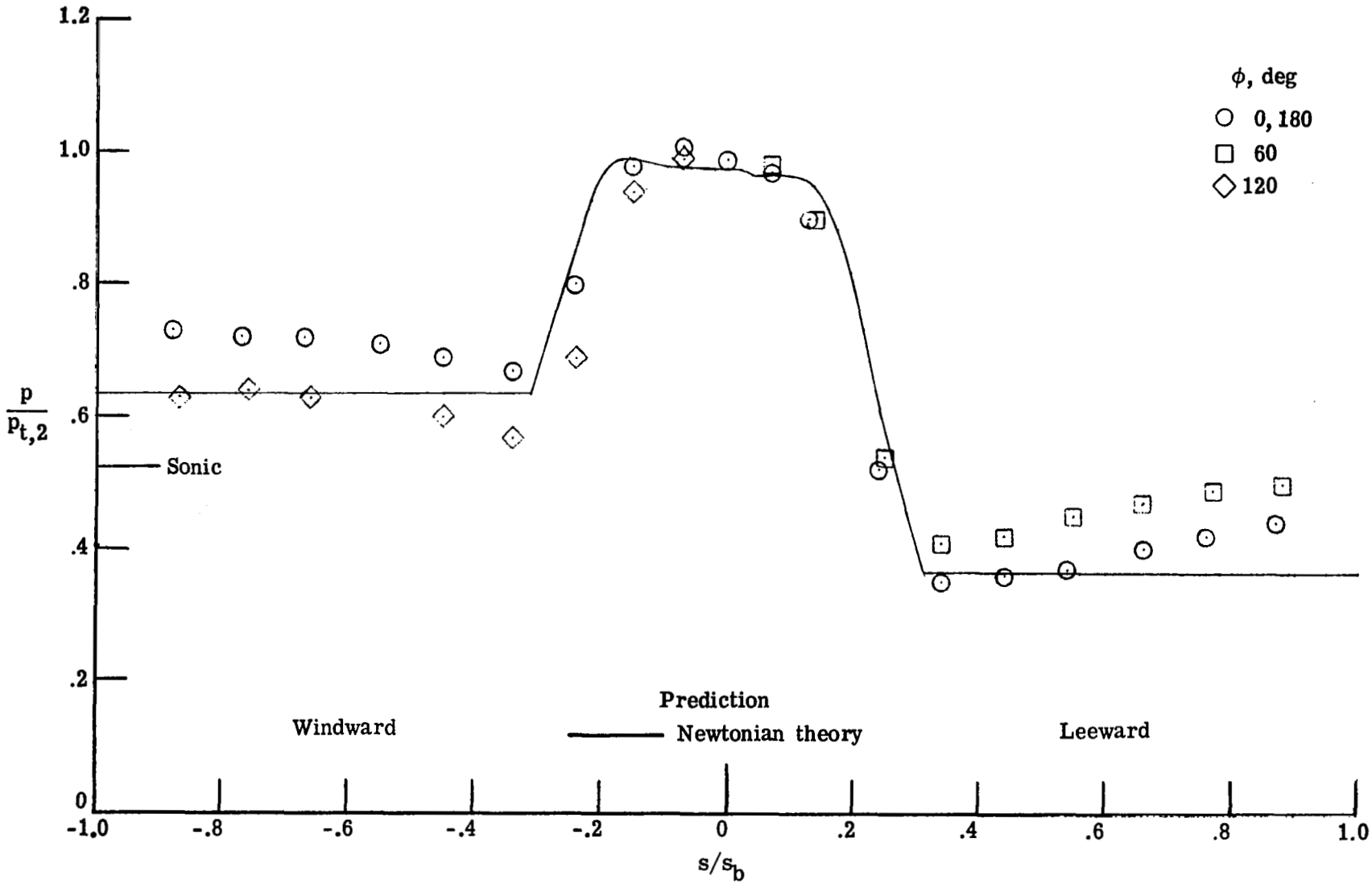

(c) $\alpha = 8°$.

Figure 46.- Continued.

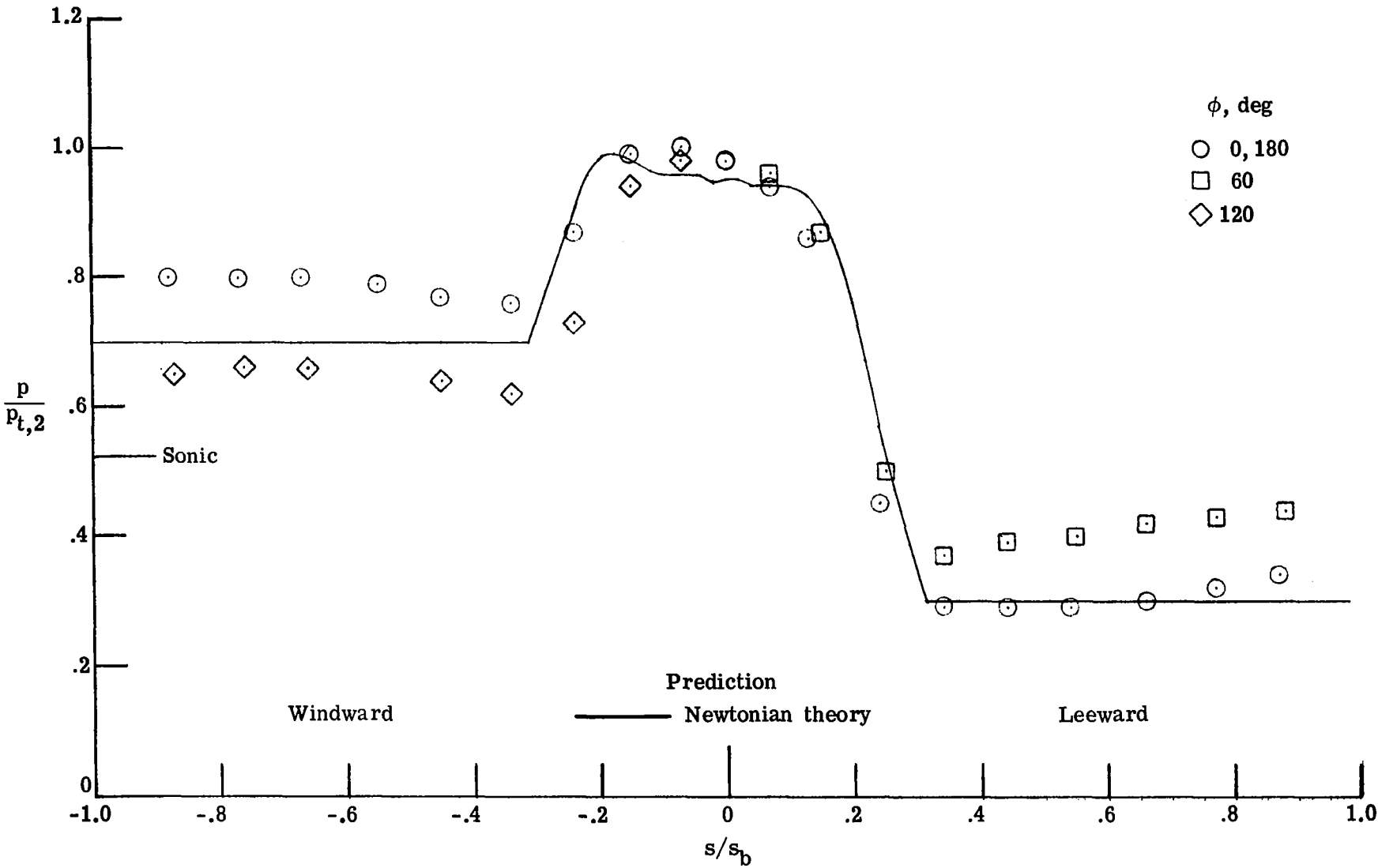

(d) $\alpha = 12°$.

Figure 46.- Continued.

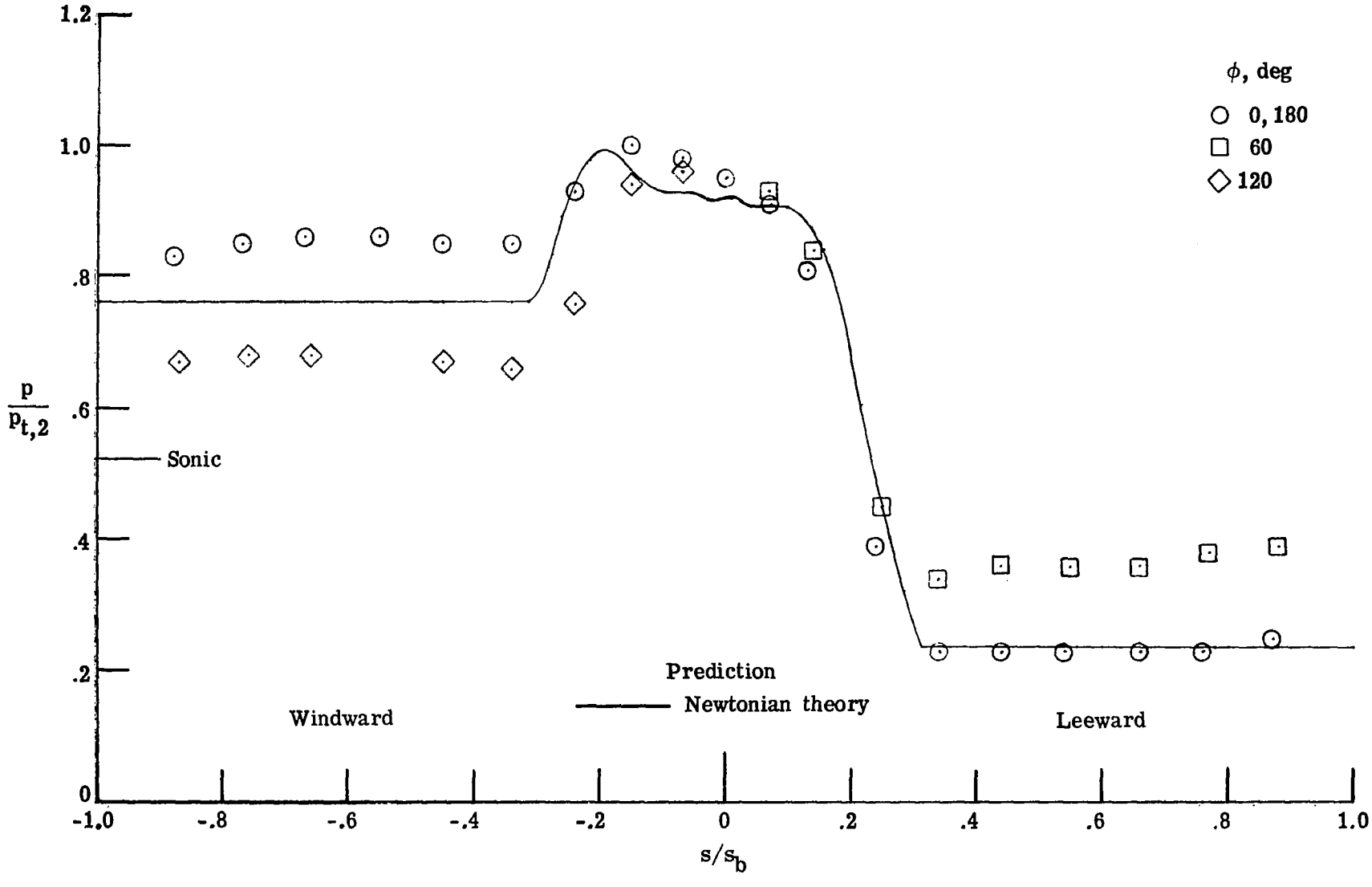

(e) $\alpha = 16°$.

Figure 46.- Concluded.

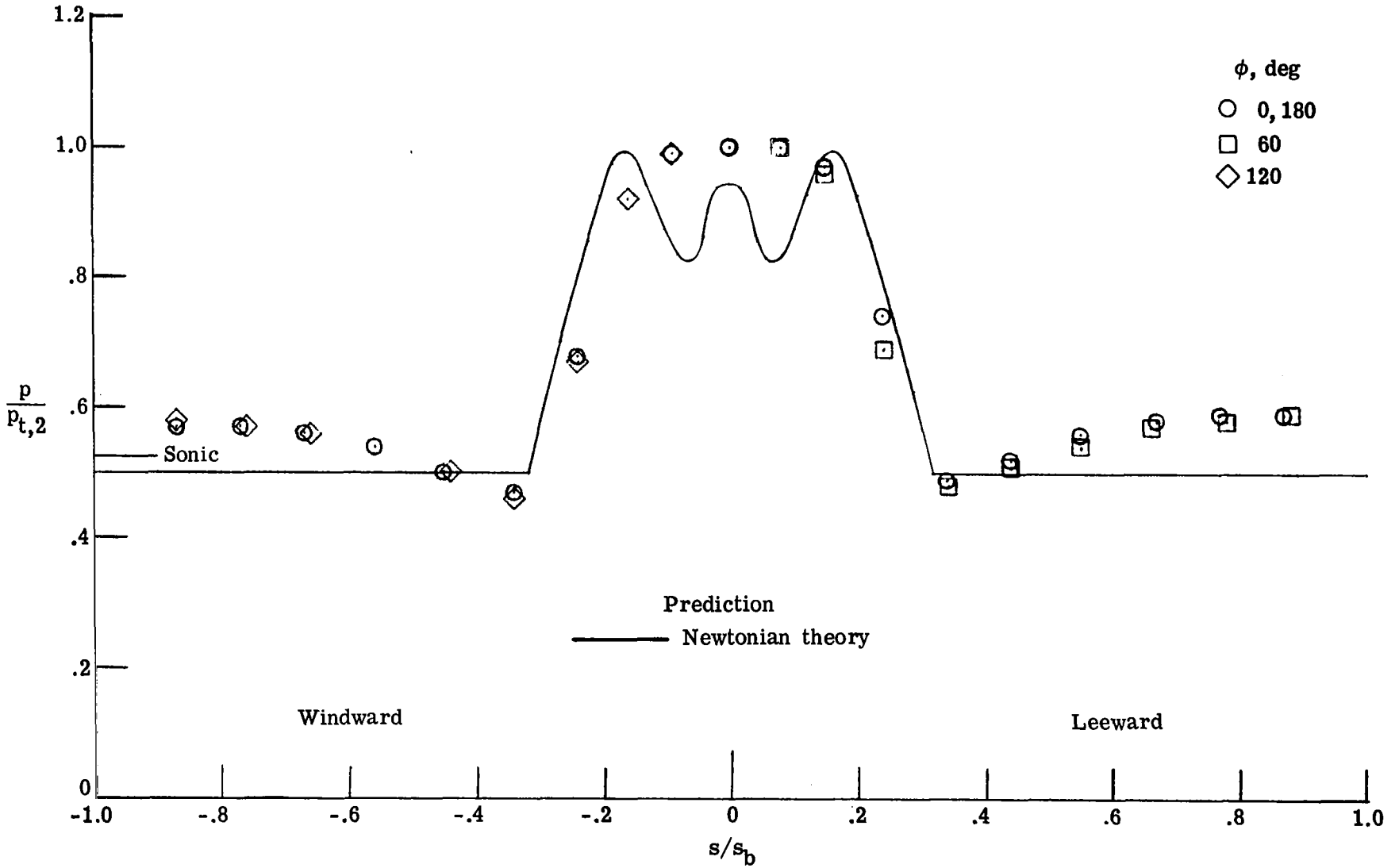

(a) $\alpha = 0°$.

Figure 47.- Pressure distributions measured on the concave-nose cone (model 7) in Mach 10.0 air. $N_{Re,\infty,d_b} = 3.65 \times 10^5$.

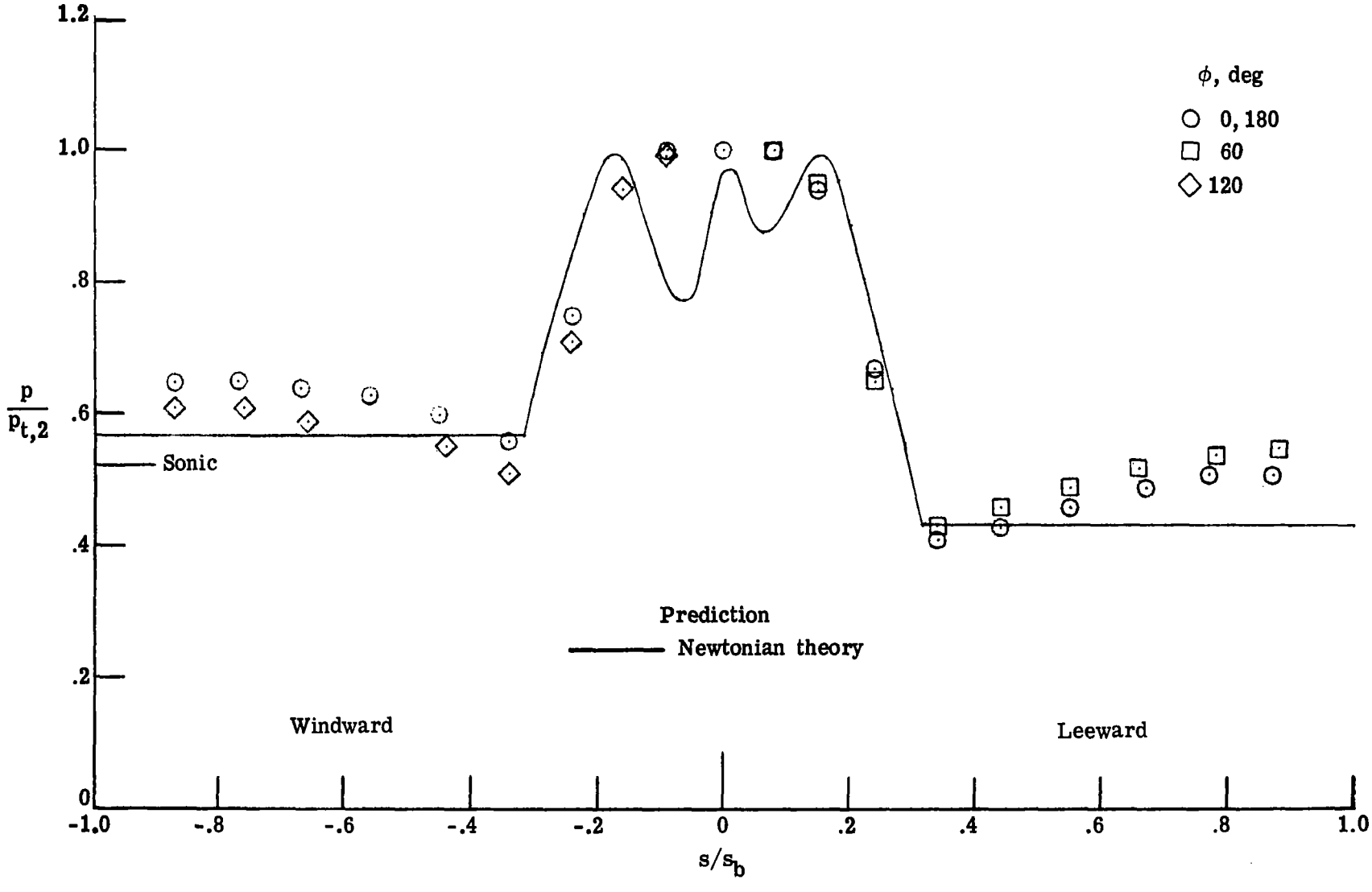

(b) $\alpha = 4°$.

Figure 47.- Continued.

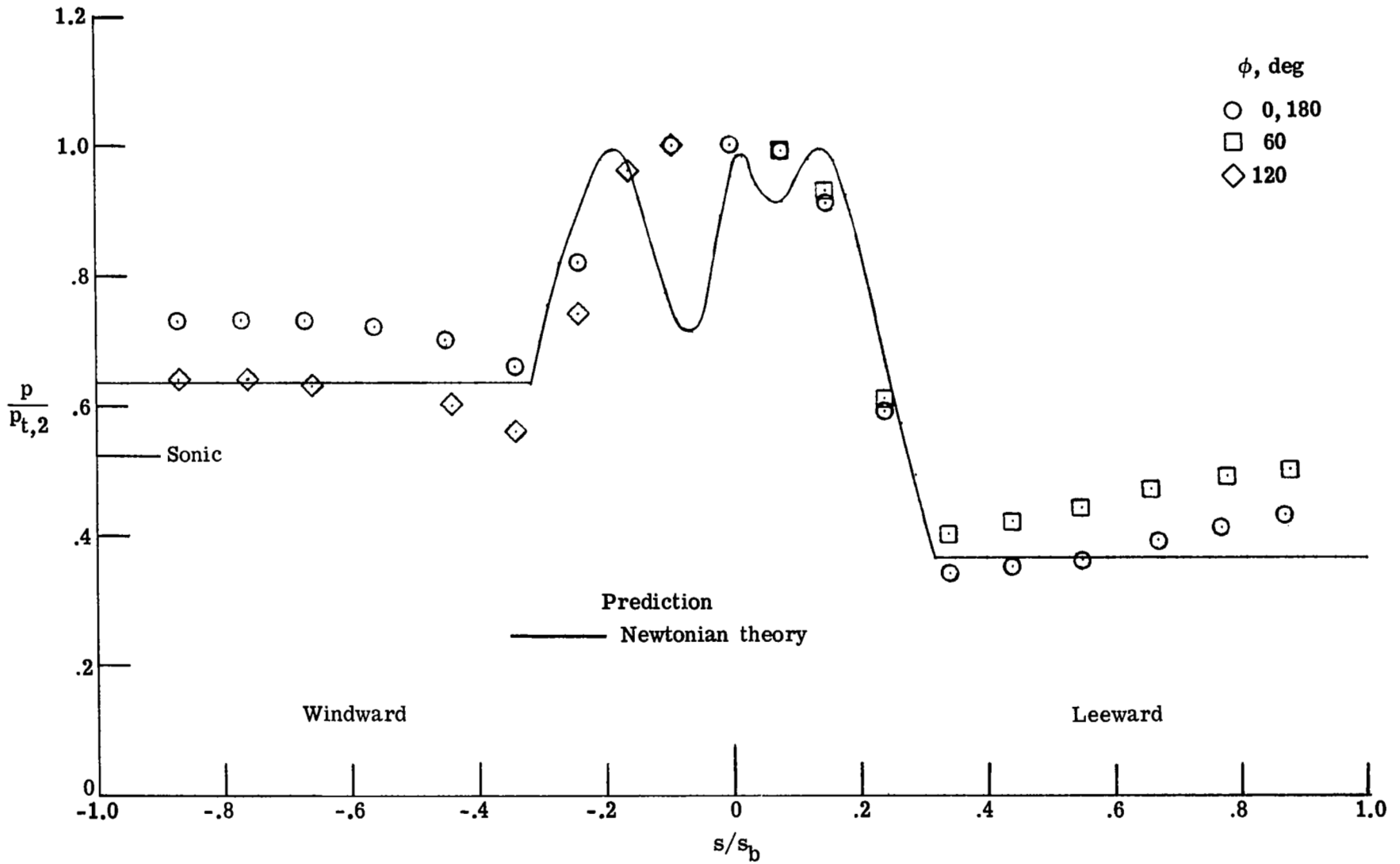

(c) $\alpha = 8°$.

Figure 47.- Continued.

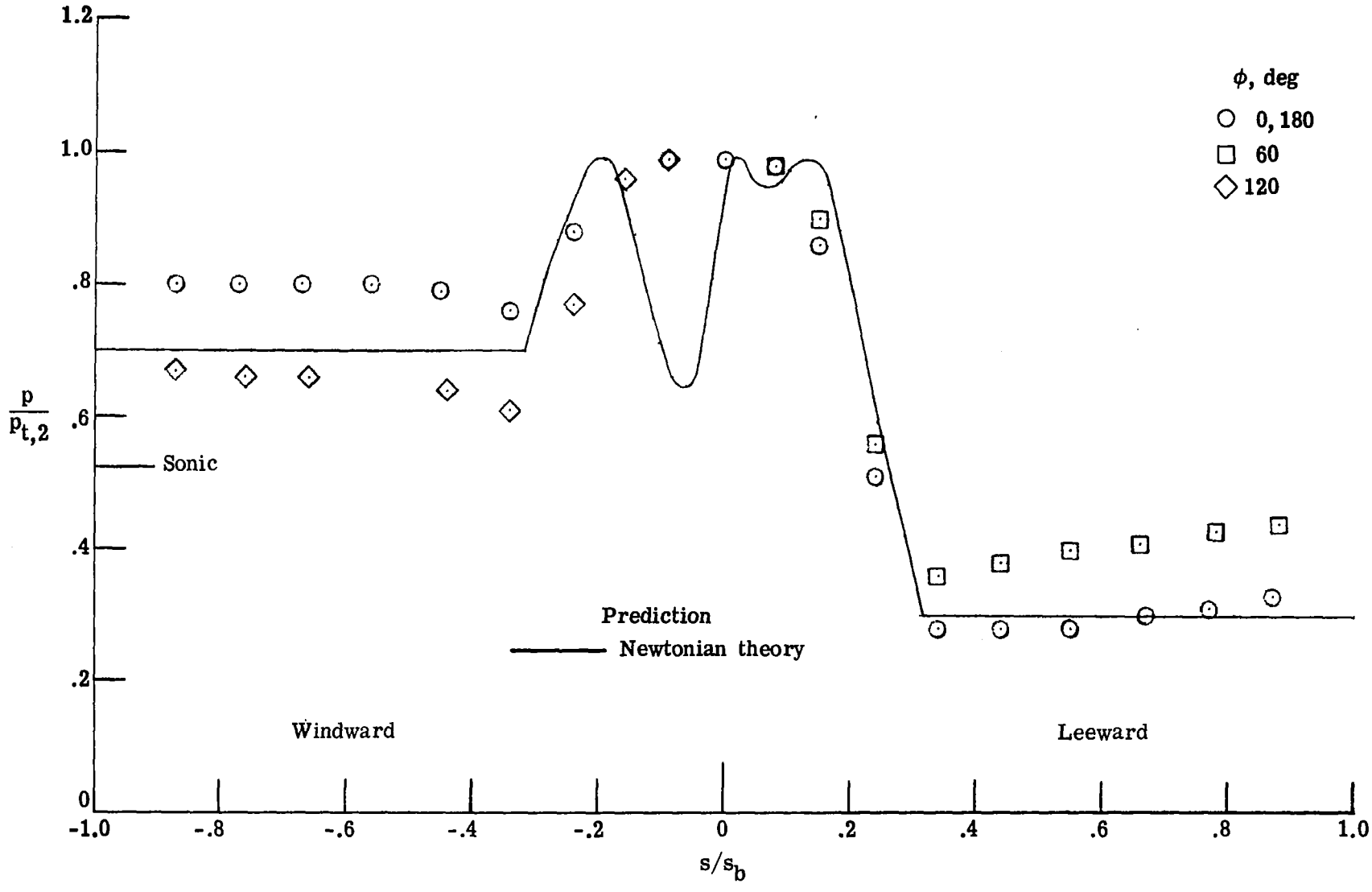

(d) $\alpha = 12°$.

Figure 47.- Continued.

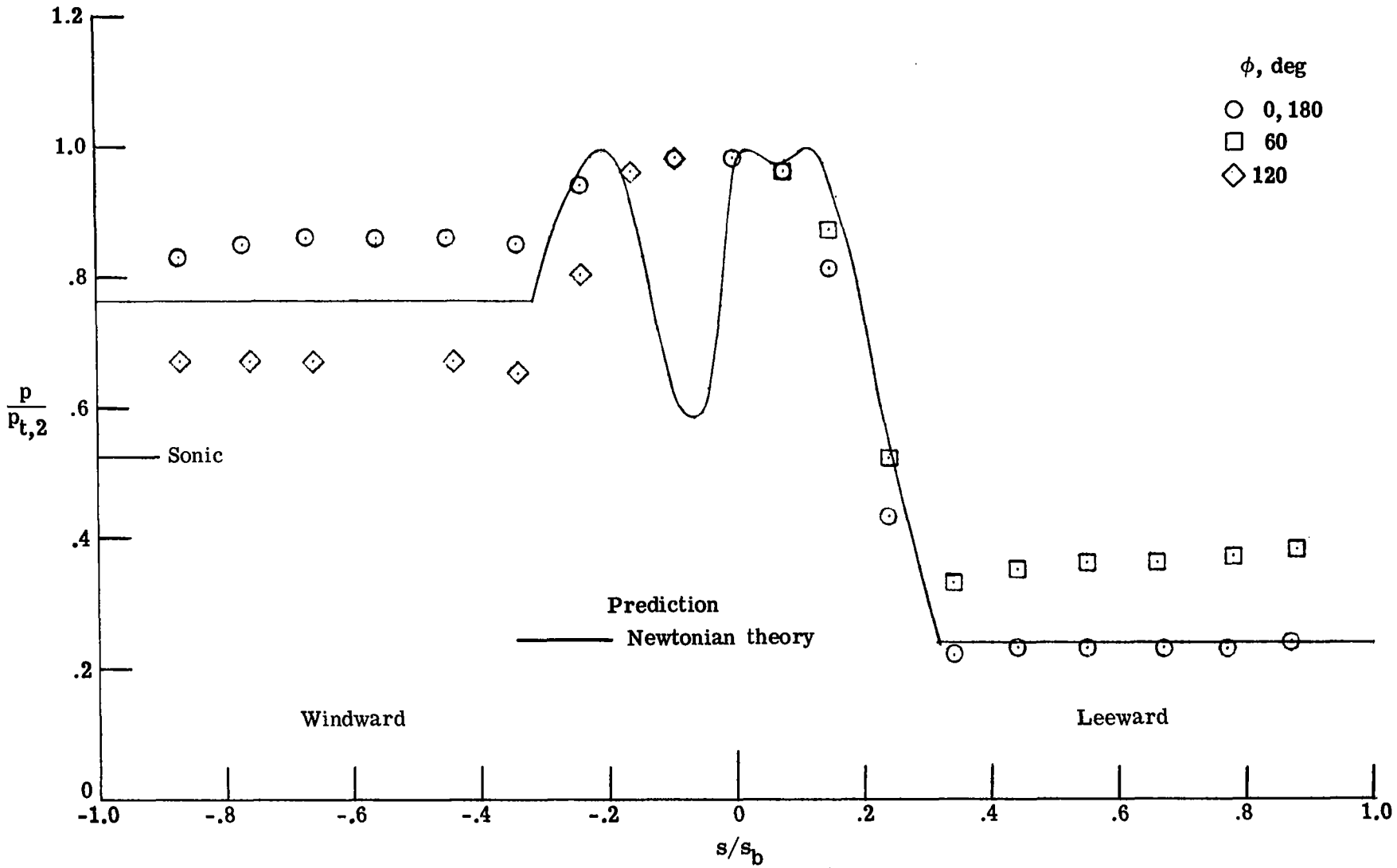

(e) $\alpha = 16°$.

Figure 47.- Concluded.

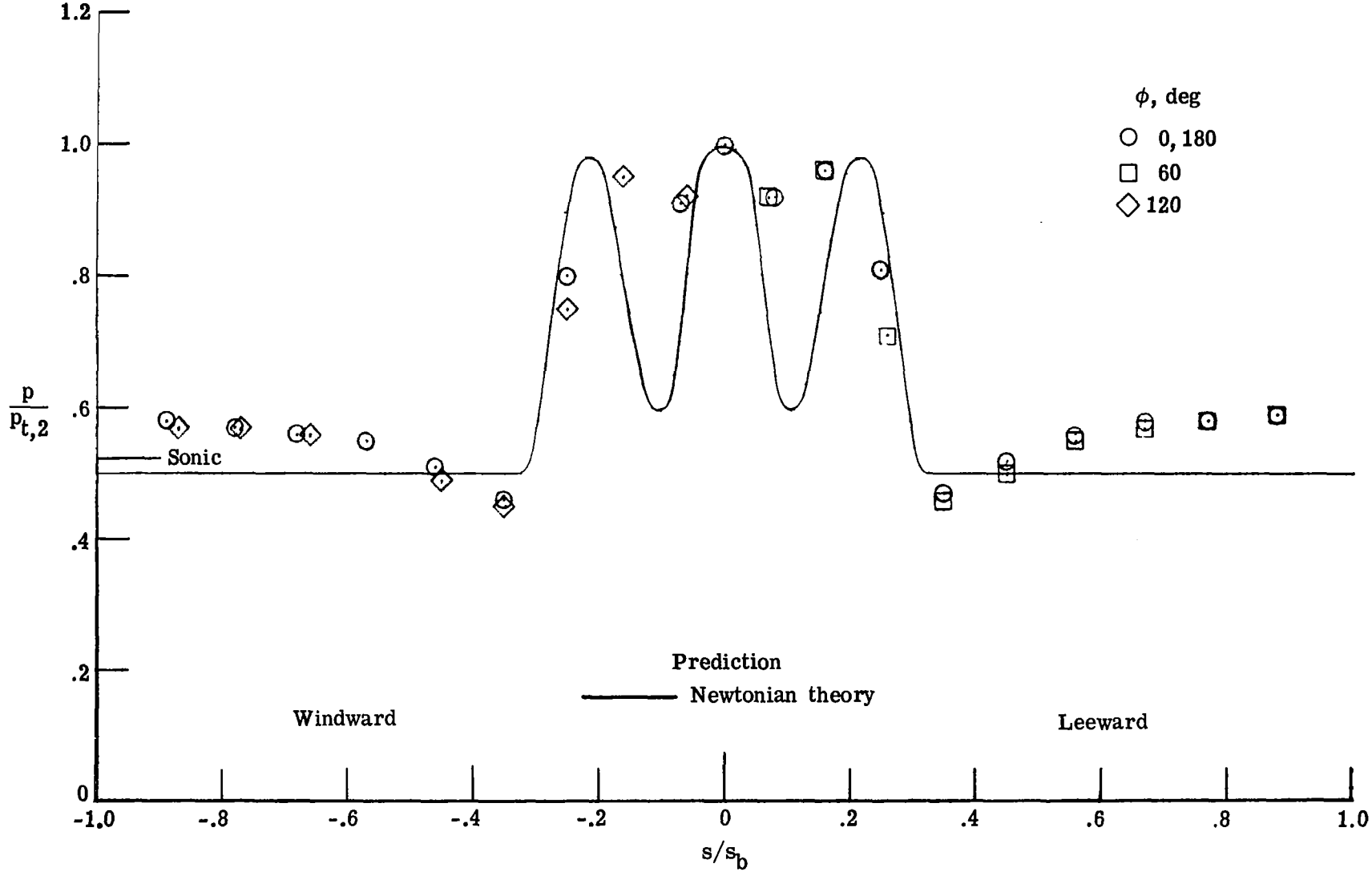

(a) $\alpha = 0°$.

Figure 48.- Pressure distributions measured on the cusp-nose cone (model 8) in Mach 10.0 air. $N_{Re,\infty,d_b} = 3.65 \times 10^5$.

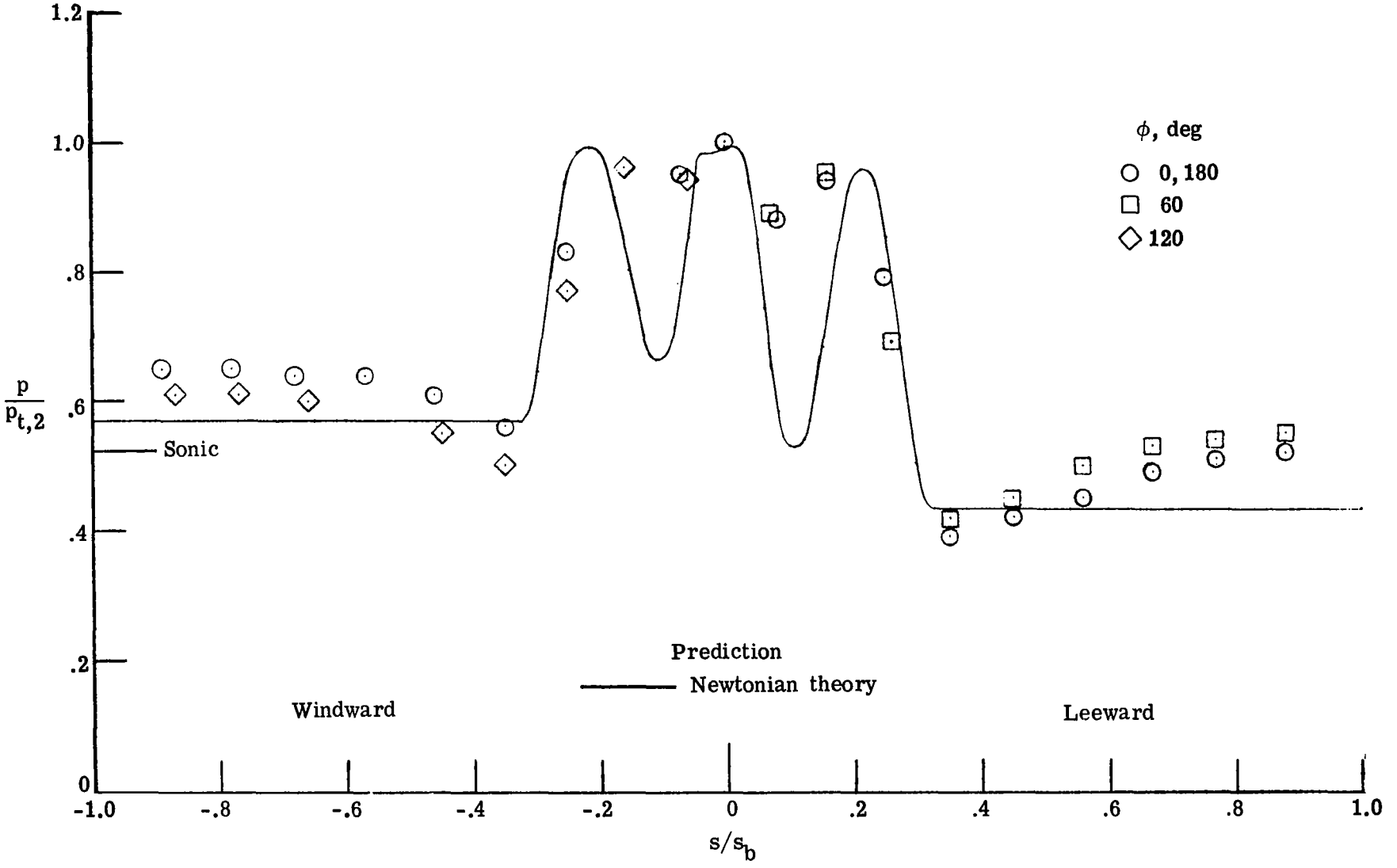

(b) $\alpha = 4°$.

Figure 48.- Continued.

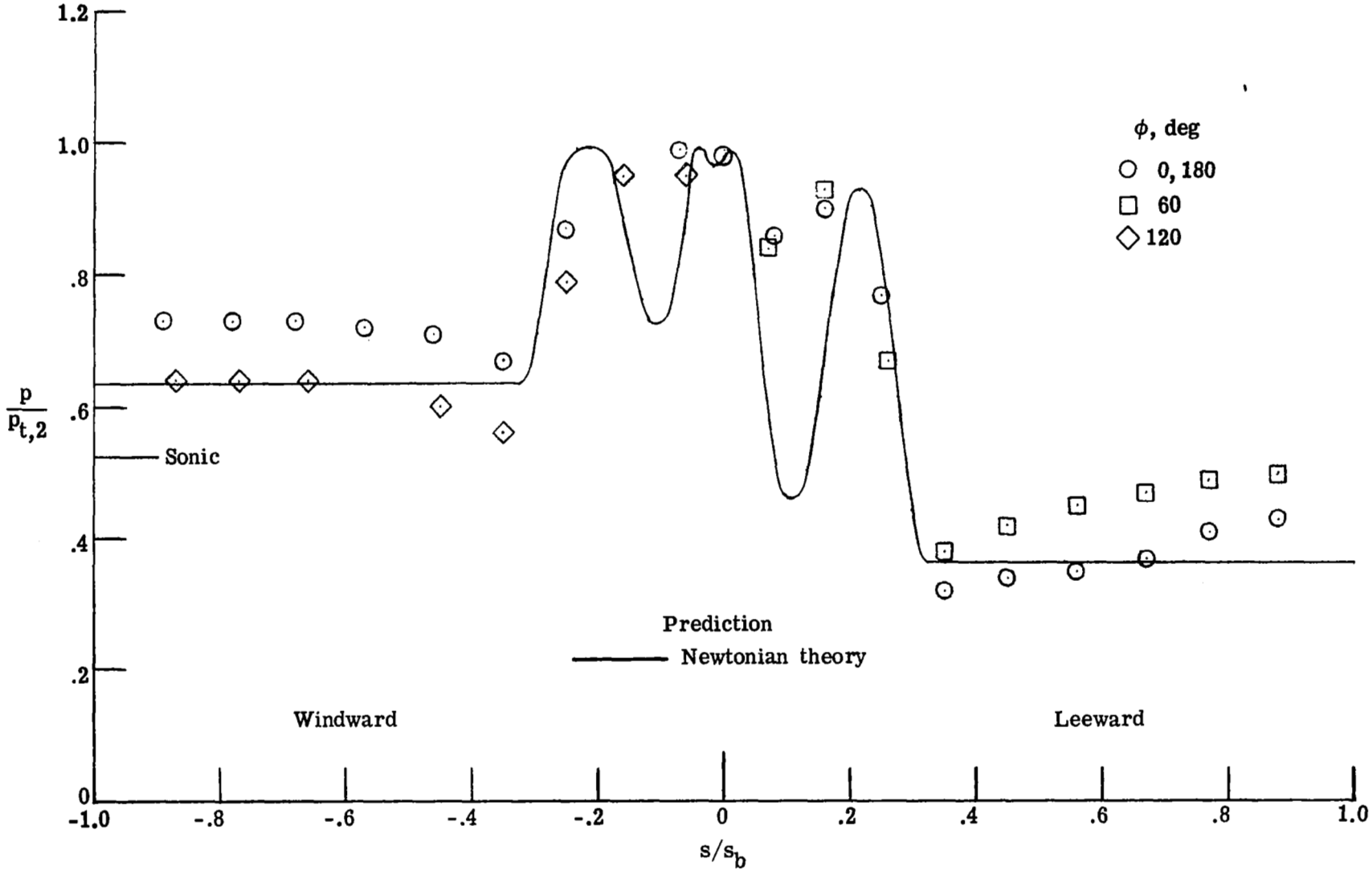

(c) $\alpha = 8°$.

Figure 48.- Continued.

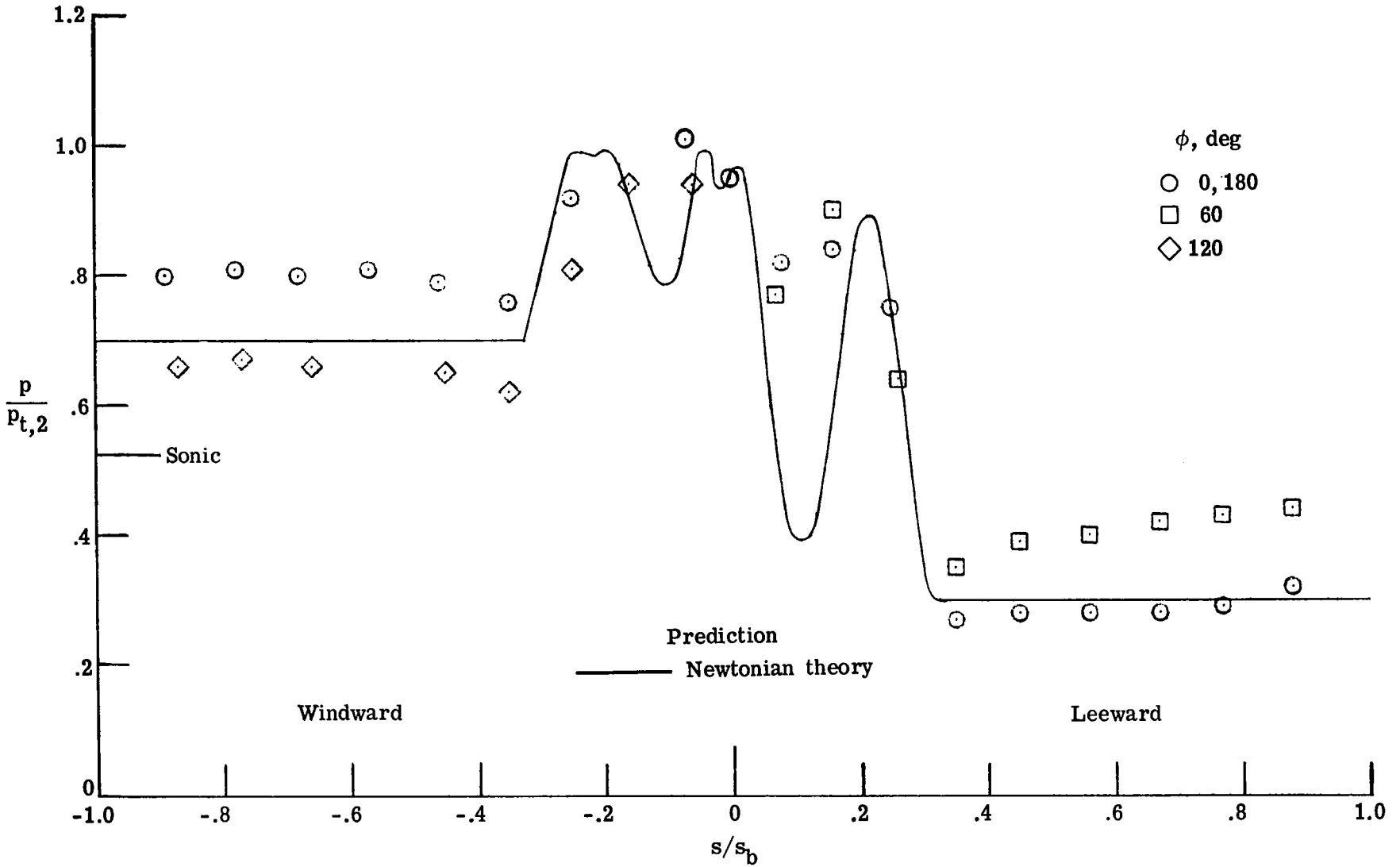

(d) $\alpha = 12°$.

Figure 48.- Continued.

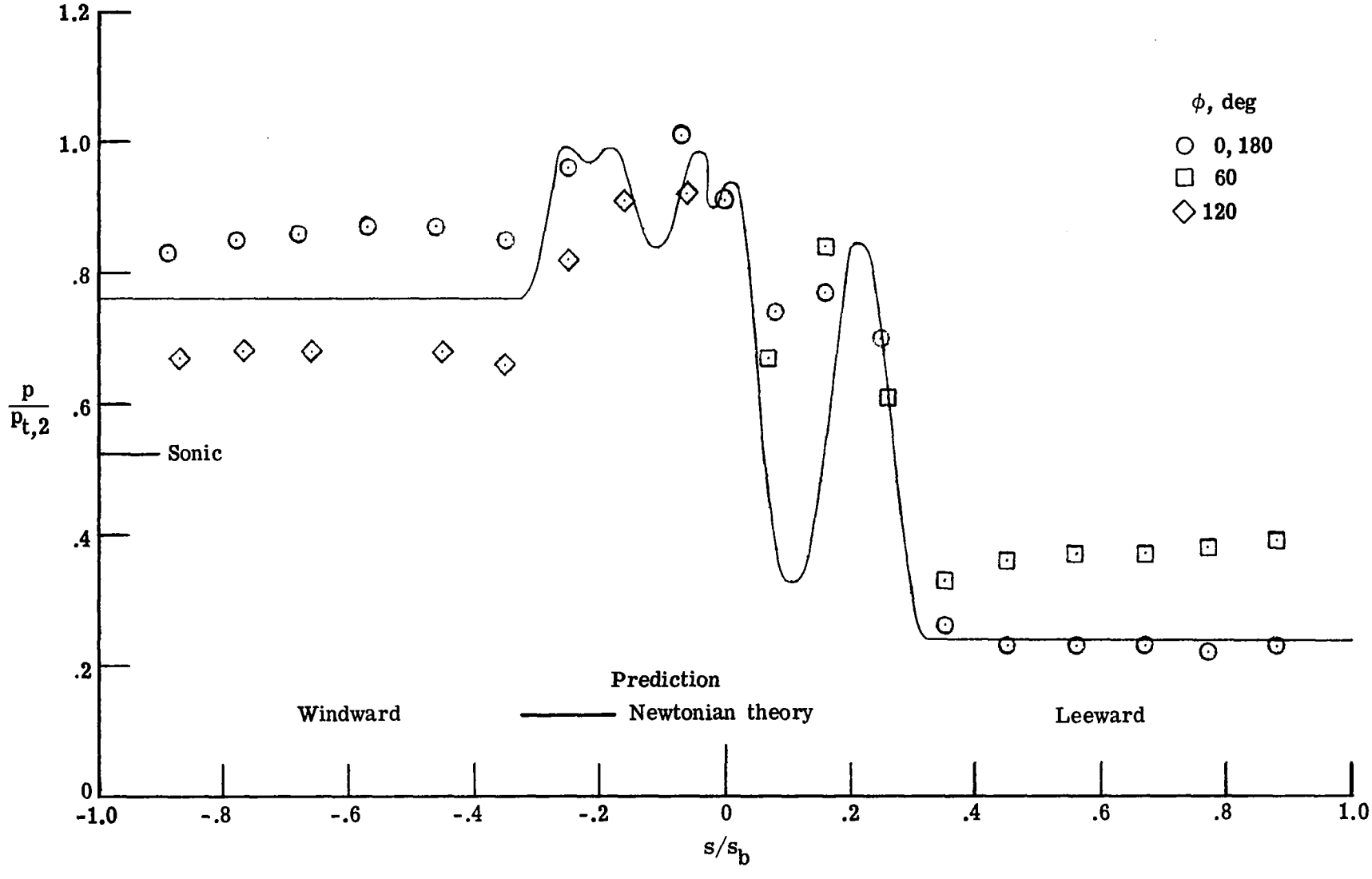

(e) $\alpha = 16°$.

Figure 48.- Concluded.

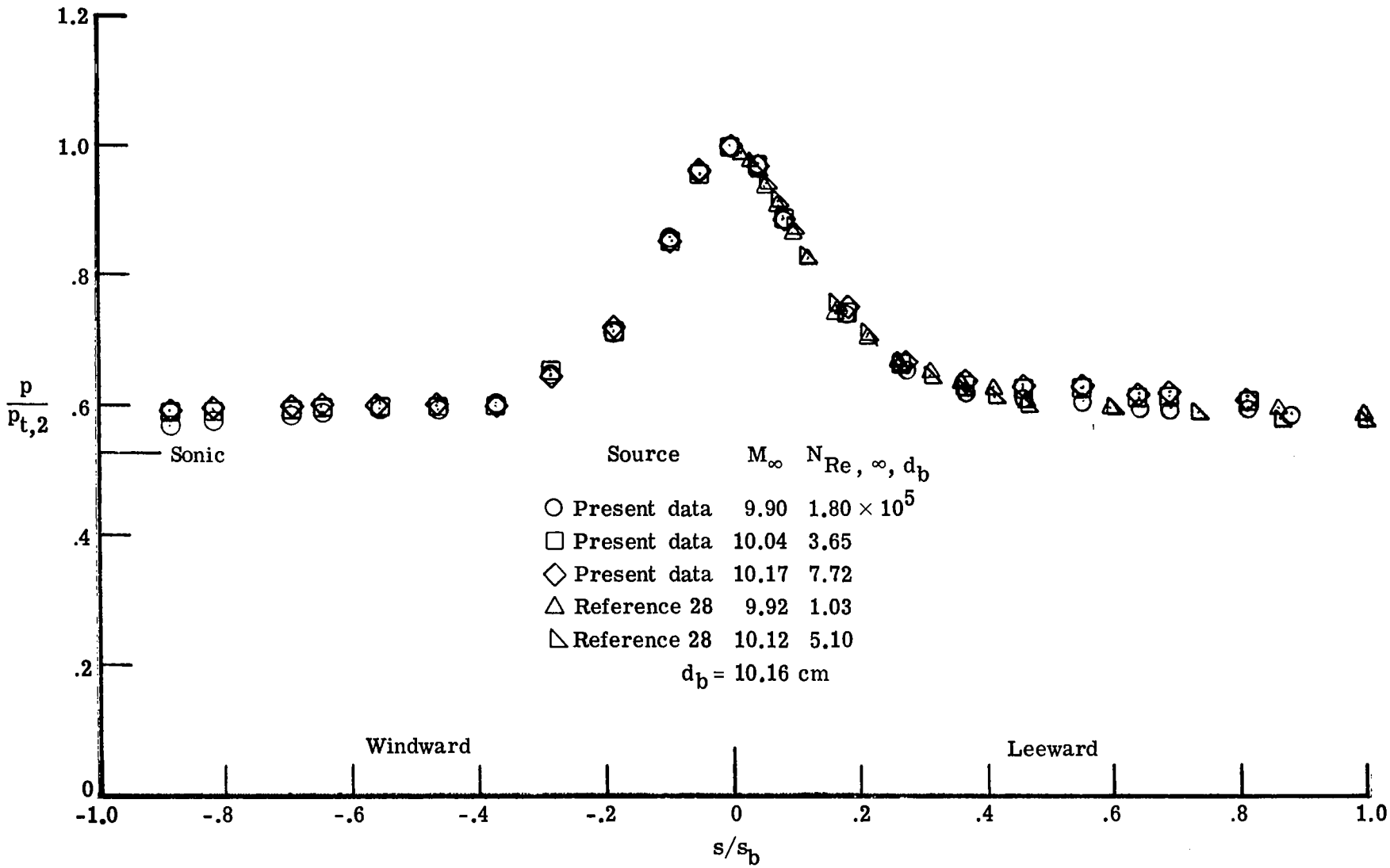

Figure 49.- Effect of free-stream Reynolds number on the pressure distributions along the most windward (ϕ = 180°) and leeward (ϕ = 0°) rays of the hyperboloid (model 1, series 2) in Mach 10 air. α = 0°.

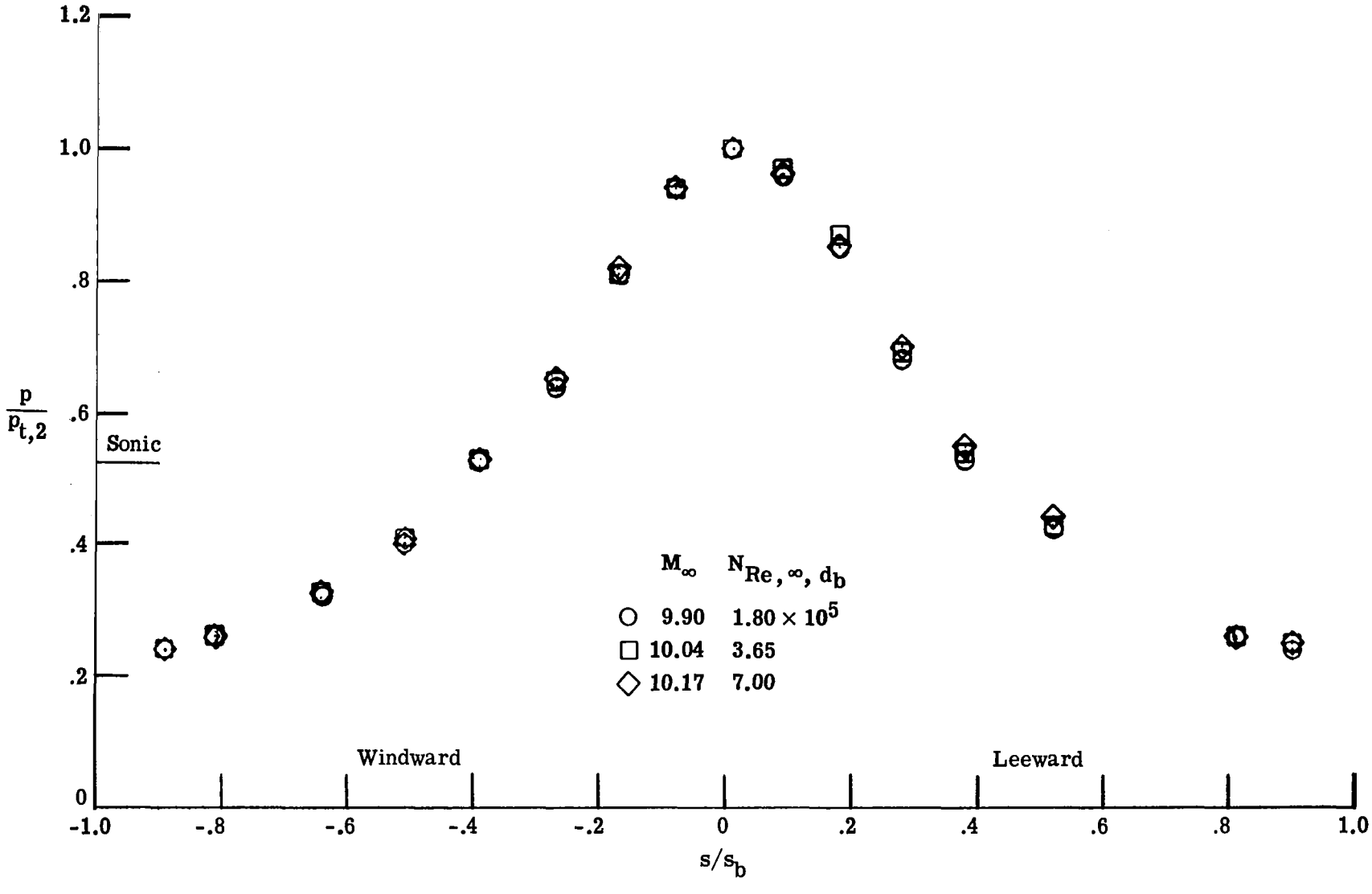

Figure 50.- Effect of free-stream Reynolds number on the pressure distributions along the most windward (ϕ = 180°) and leeward (ϕ = 0°) rays of the paraboloid (model 3, series 2) in Mach 10 air. α = 0°.

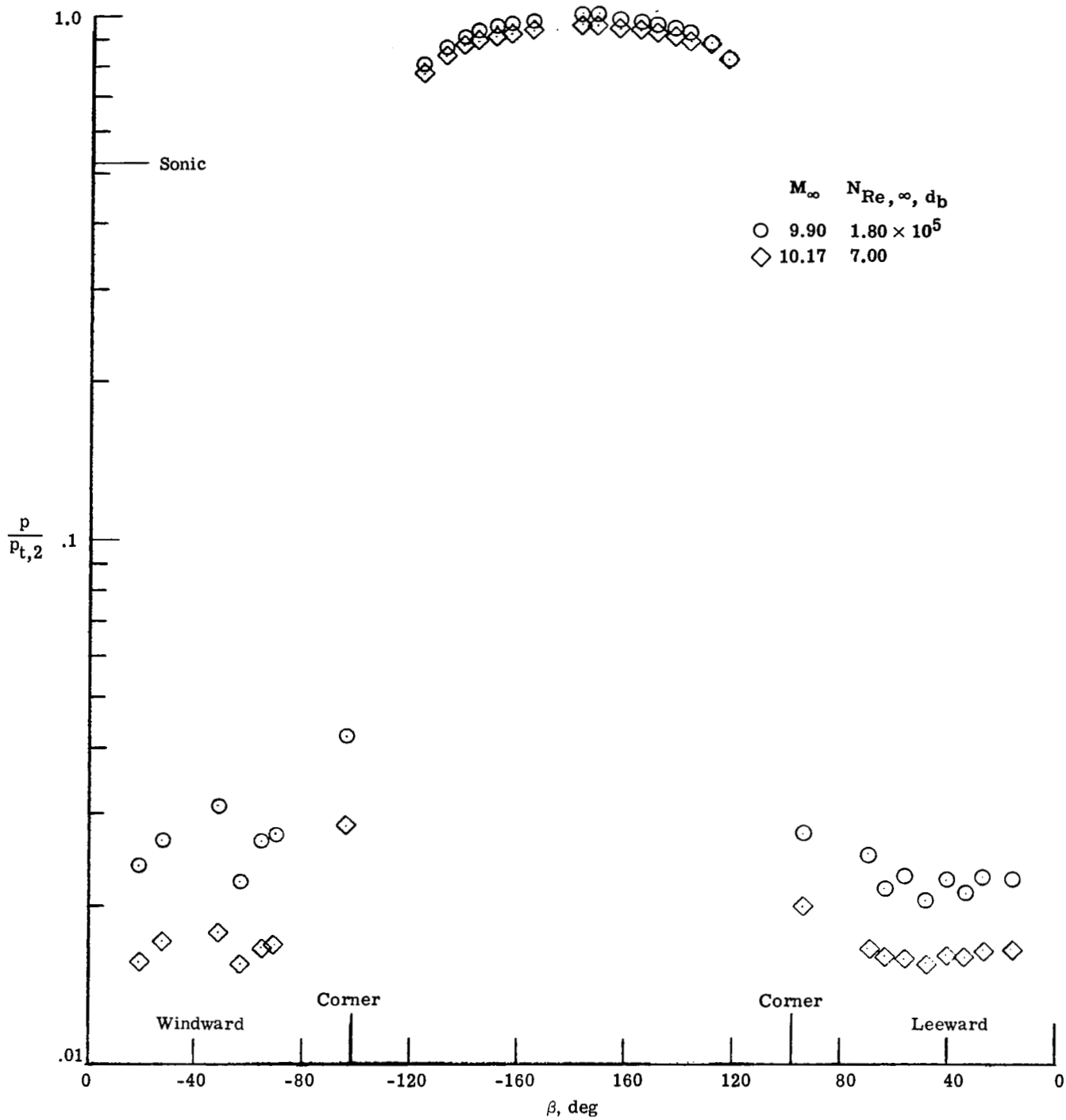

(a) $\alpha = 0°$.

Figure 51.- Effect of free-stream Reynolds number on the pressure distributions along the most windward ($\phi = 180°$) and leeward ($\phi = 0°$) rays of the Viking aeroshell (model 4) in Mach 10 air.

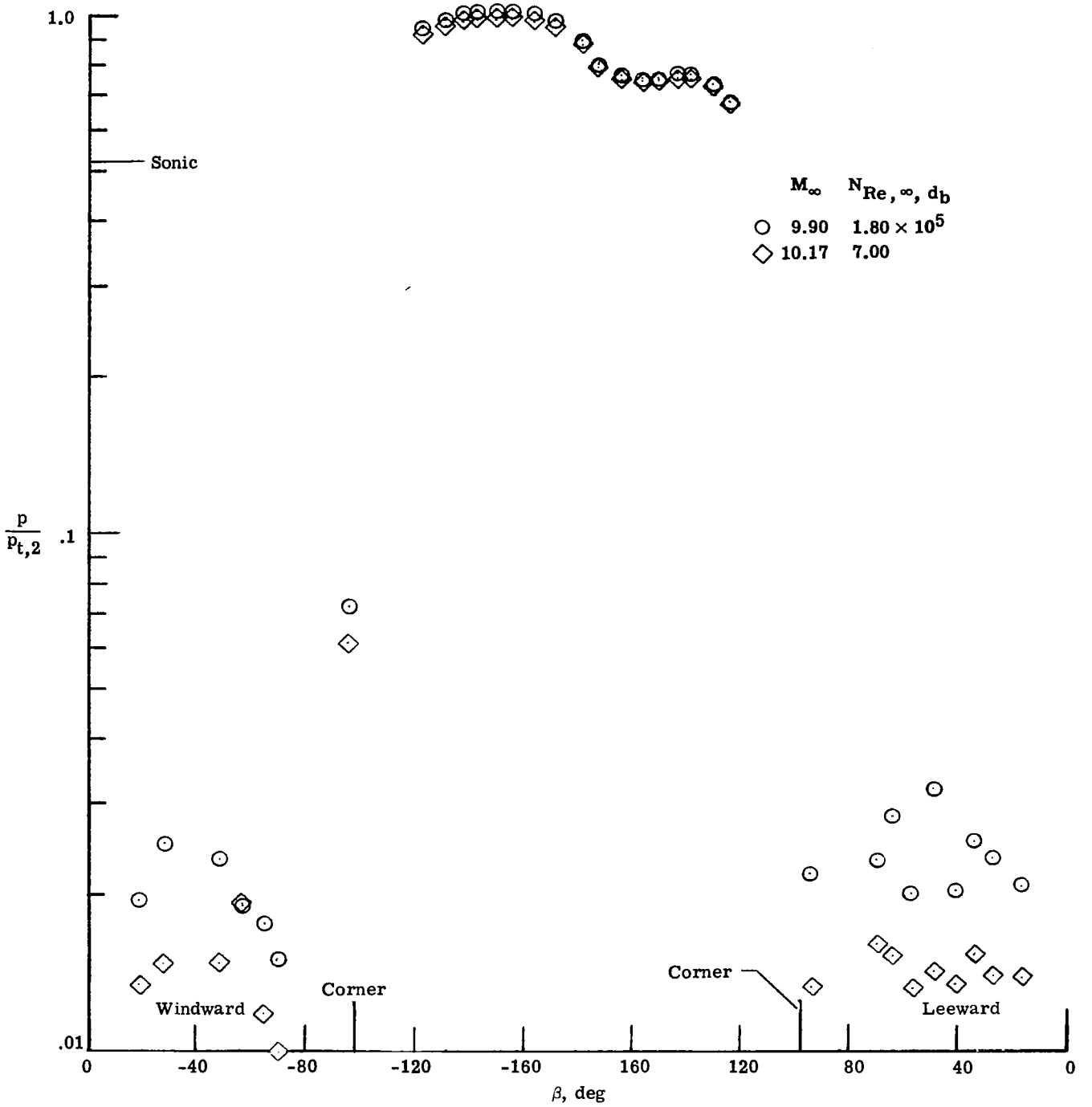

(b) $\alpha = 16°$.

Figure 51.- Concluded.

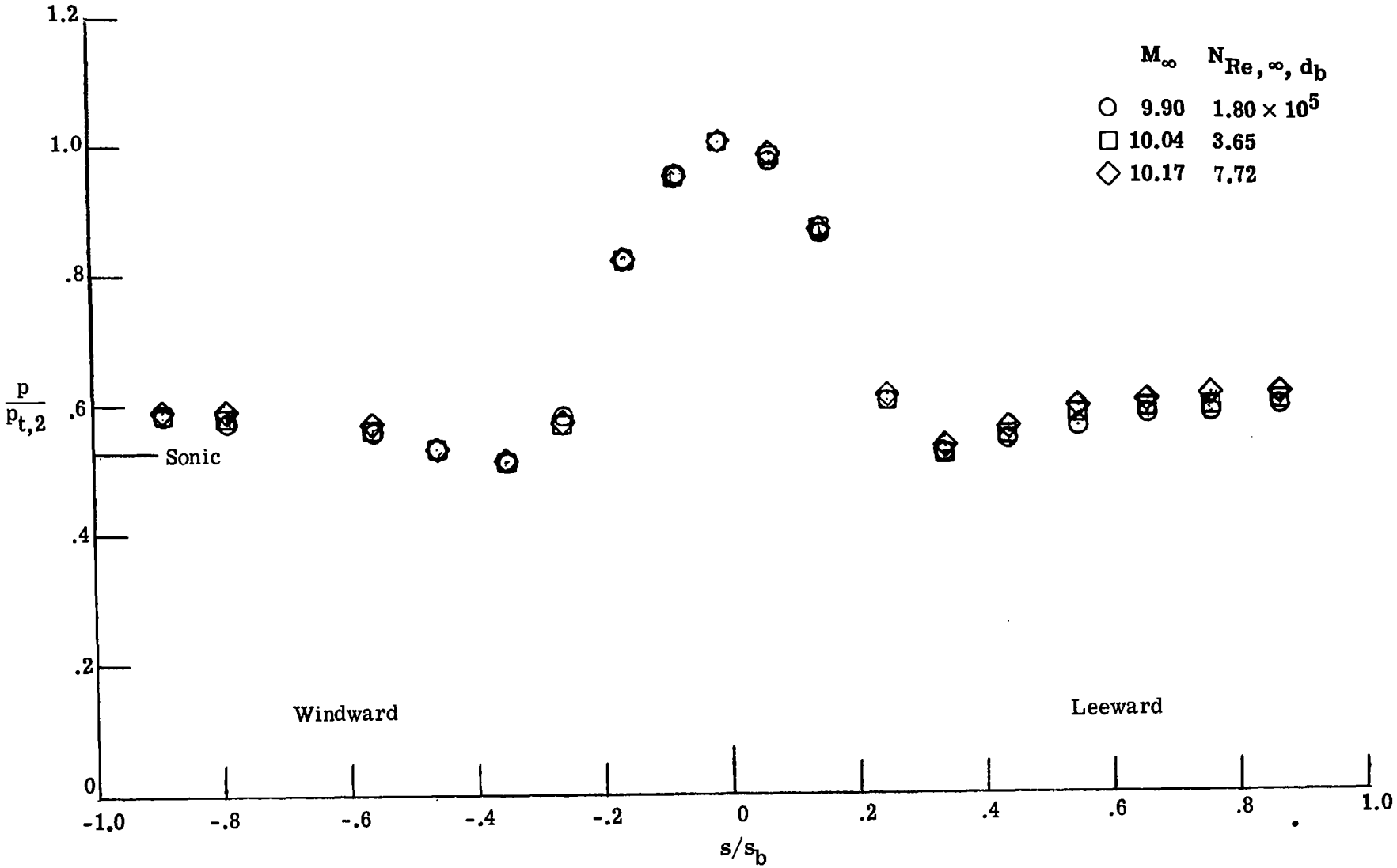

(a) $\alpha = 0°$.

Figure 52.- Effect of free-stream Reynolds number on the pressure distributions along the most windward ($\phi = 180°$) and leeward ($\phi = 0°$) rays for the spherical-nose cone (model 5) in Mach 10 air.

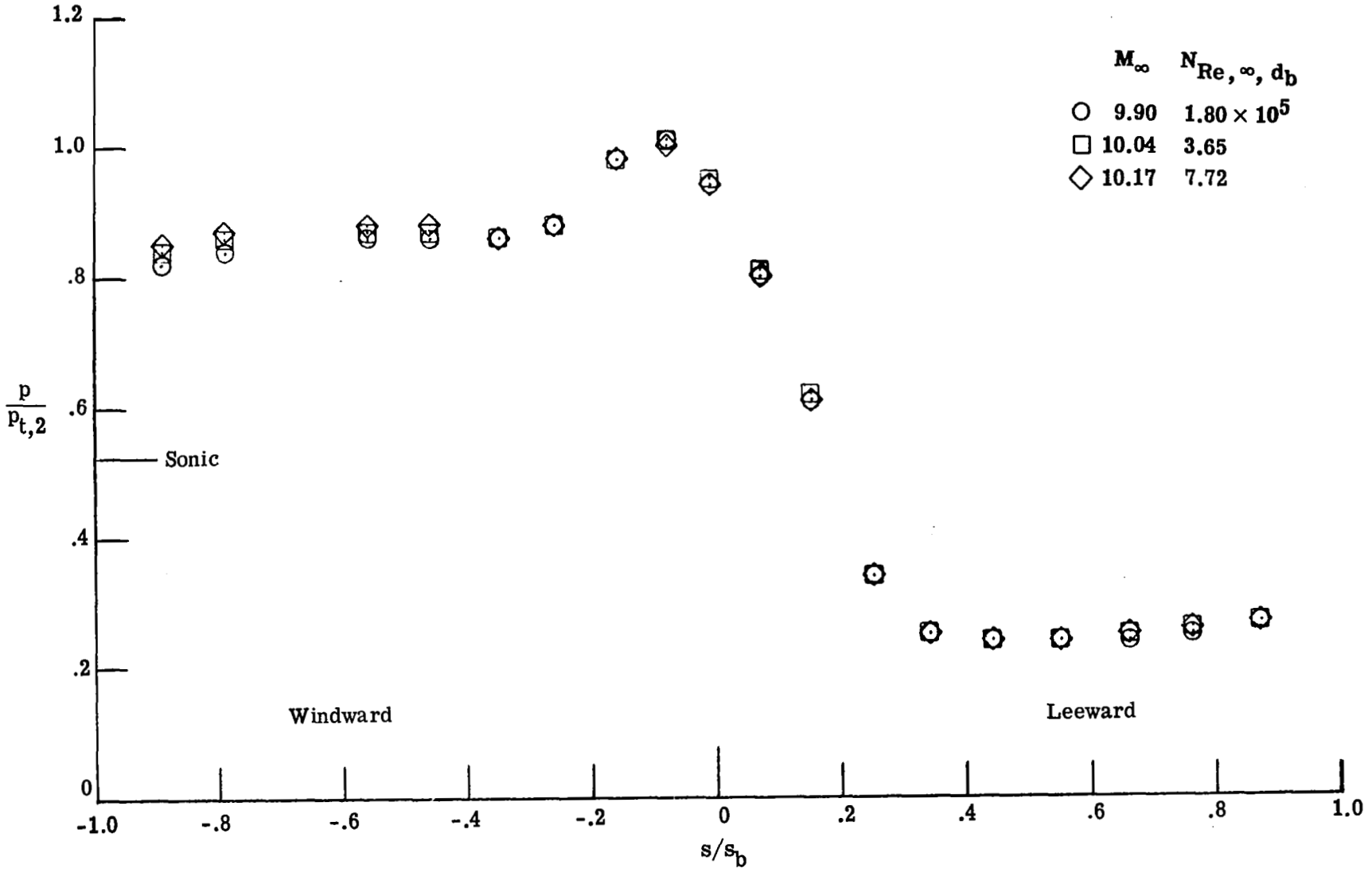

(b) $\alpha = 16°$.

Figure 52.- Concluded.

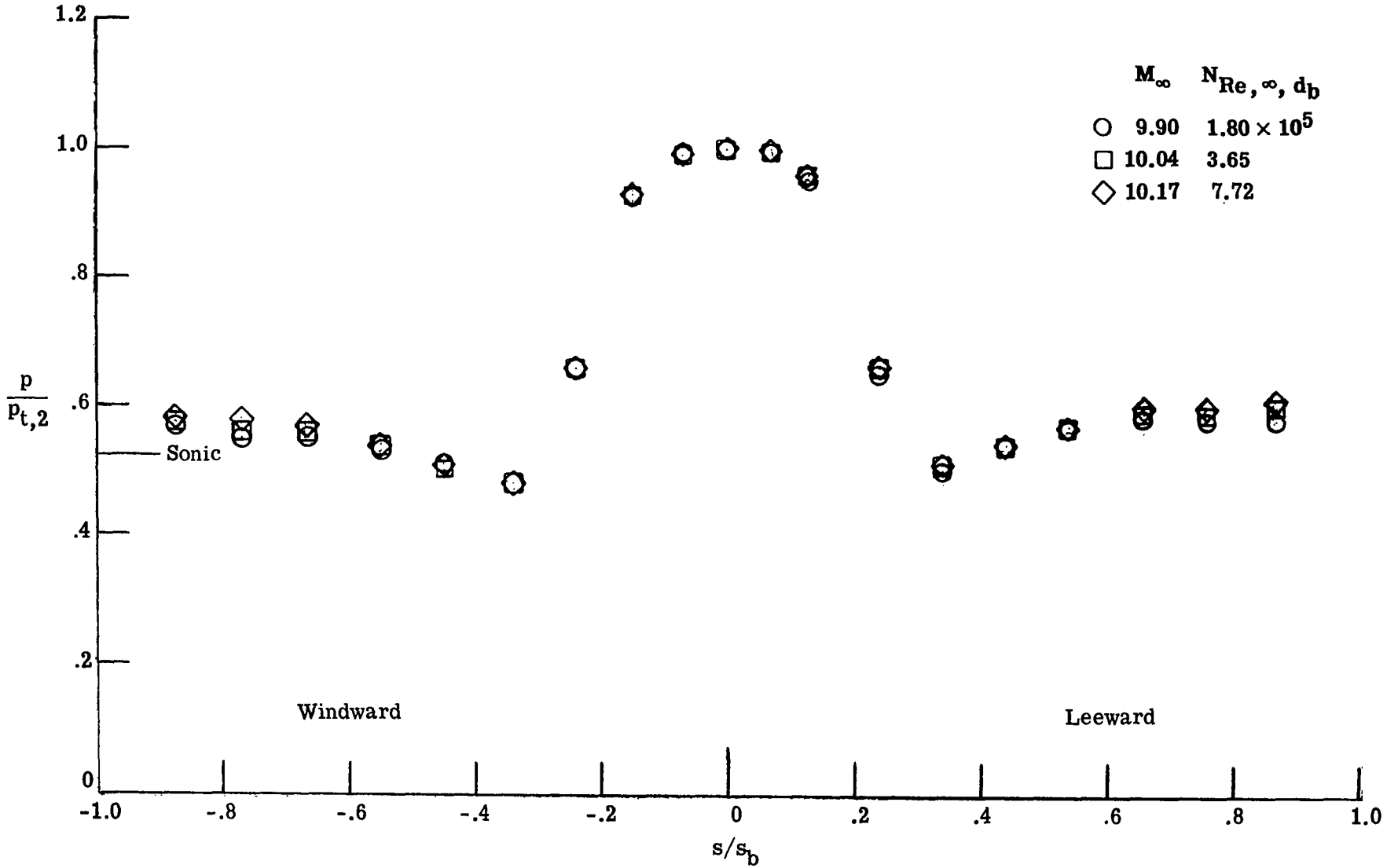

(a) $\alpha = 0°$.

Figure 53.- Effect of free-stream Reynolds number on the pressure distributions along the most windward ($\phi = 180°$) and leeward ($\phi = 0°$) rays of the flattened-nose cone (model 6) in Mach 10 air.

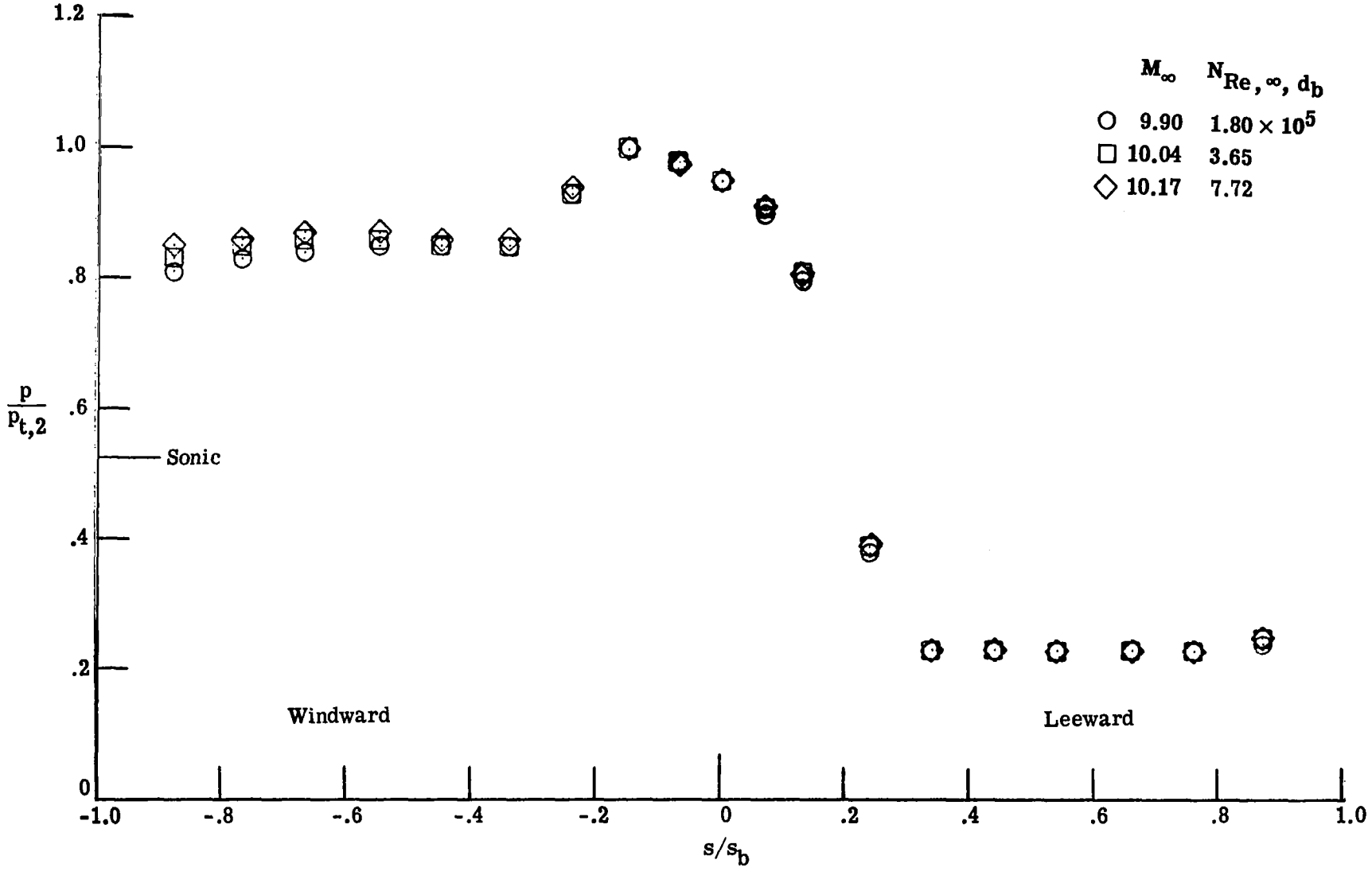

(b) $\alpha = 16°$.

Figure 53.- Concluded.

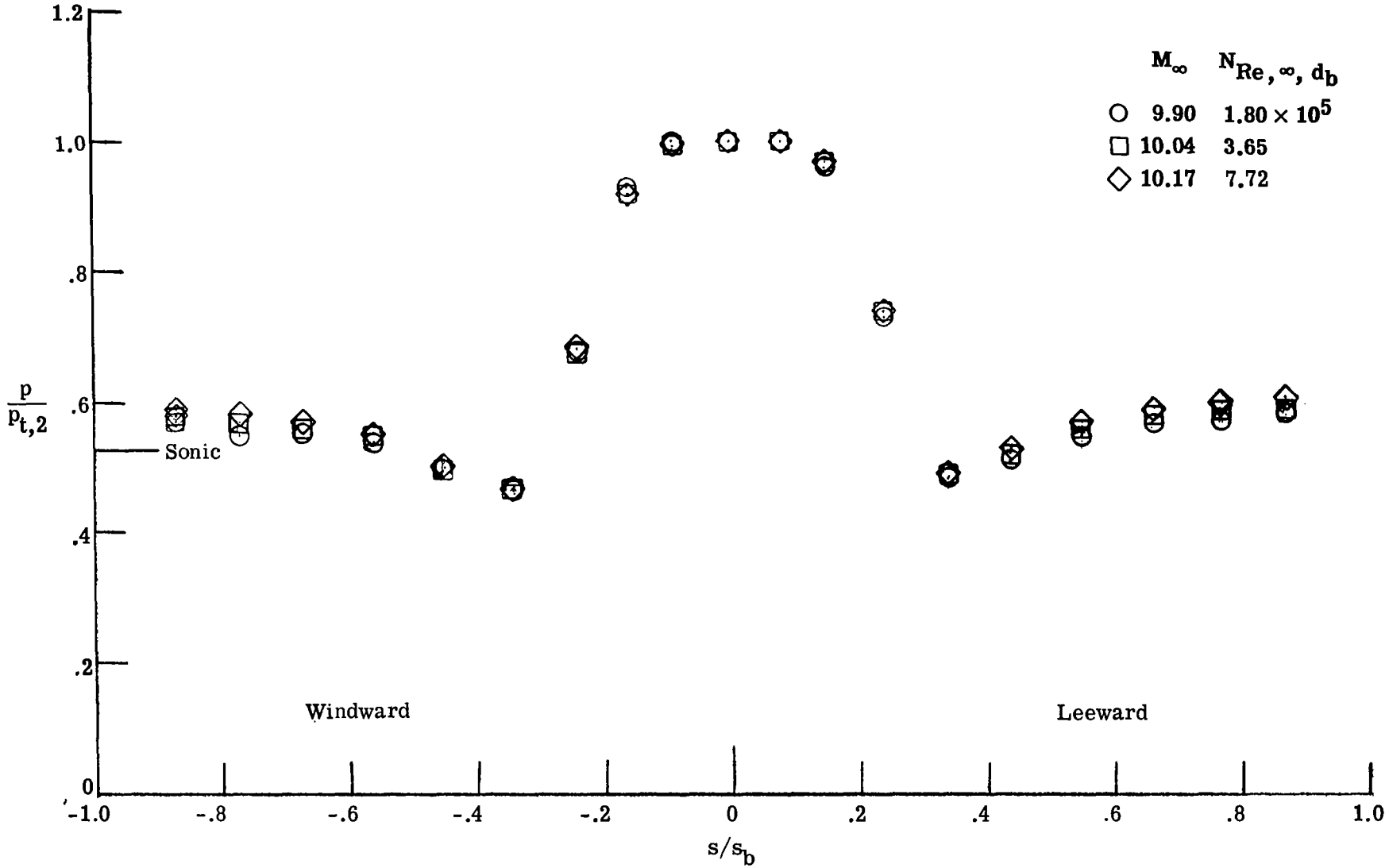

(a) $\alpha = 0°$.

Figure 54.- Effect of free-stream Reynolds number on the pressure distributions along the most windward ($\phi = 180°$) and leeward ($\phi = 0°$) rays of the concave-nose cone (model 7) in Mach 10 air.

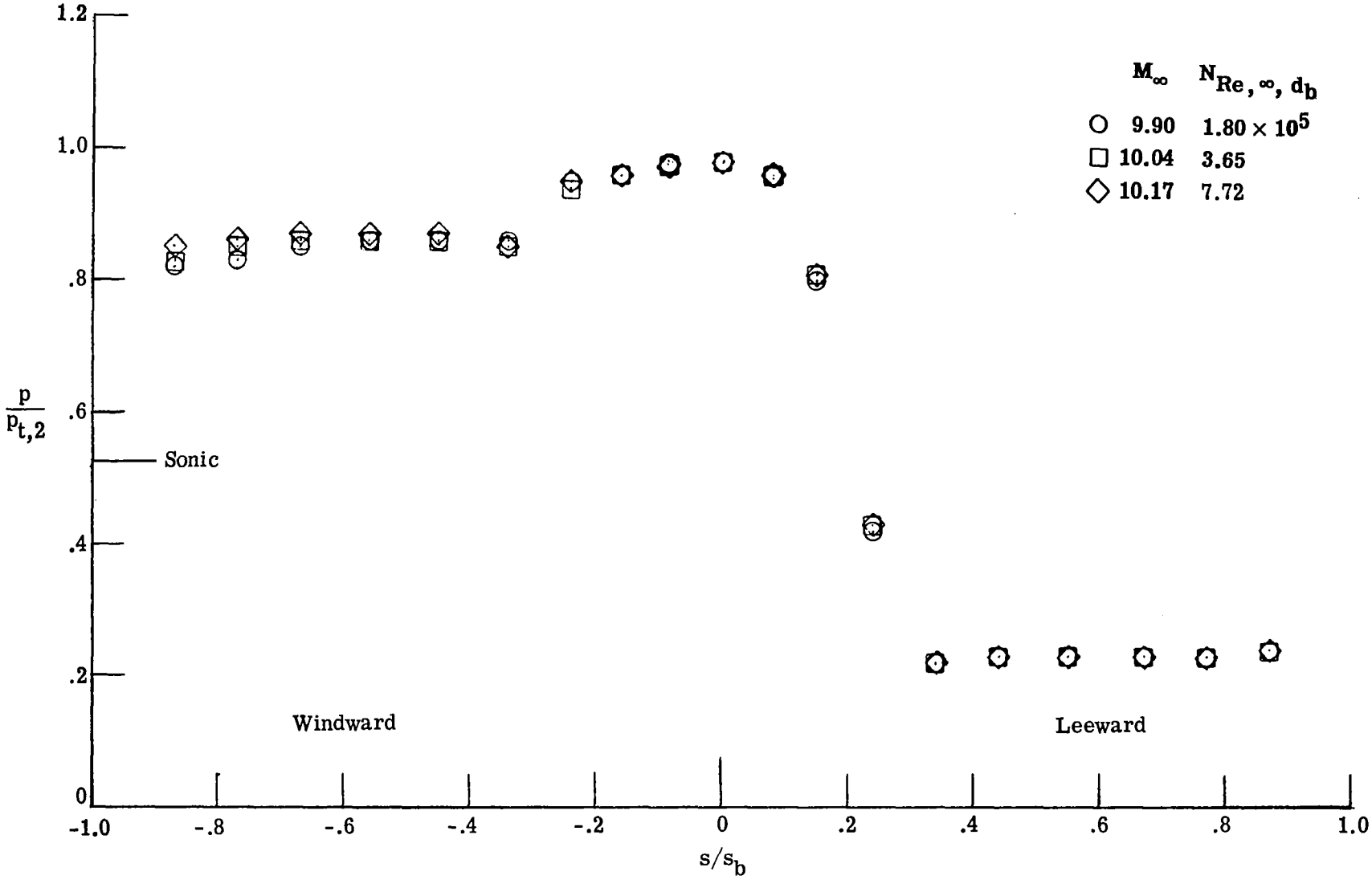

(b) $\alpha = 16°$.

Figure 54.- Concluded.

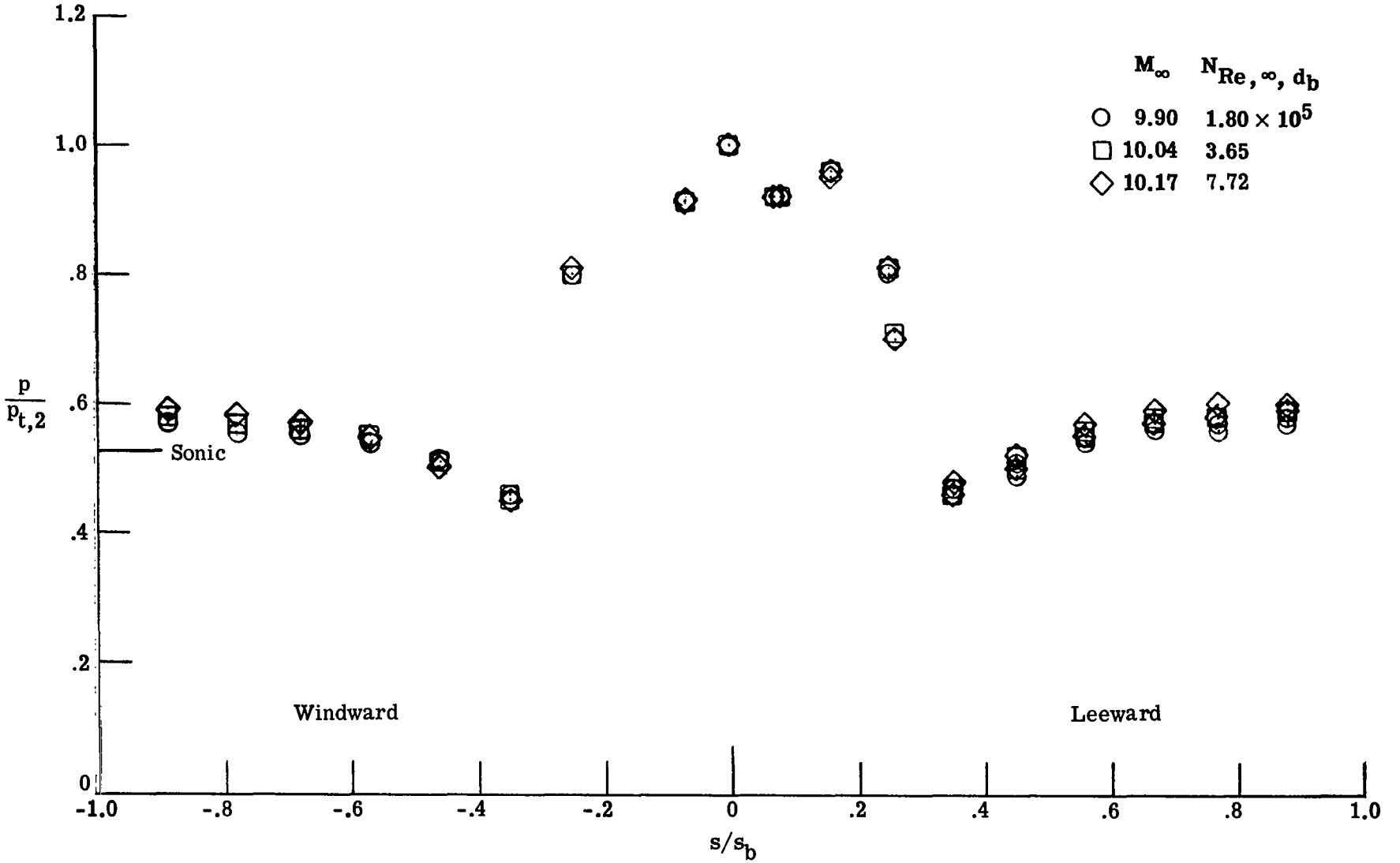

(a) $\alpha = 0°$.

Figure 55.- Effect of free-stream Reynolds number on the pressure distributions along the most windward ($\phi = 180°$) and leeward ($\phi = 0°$) rays of the cusp-nose cone (model 8) in Mach 10 air.

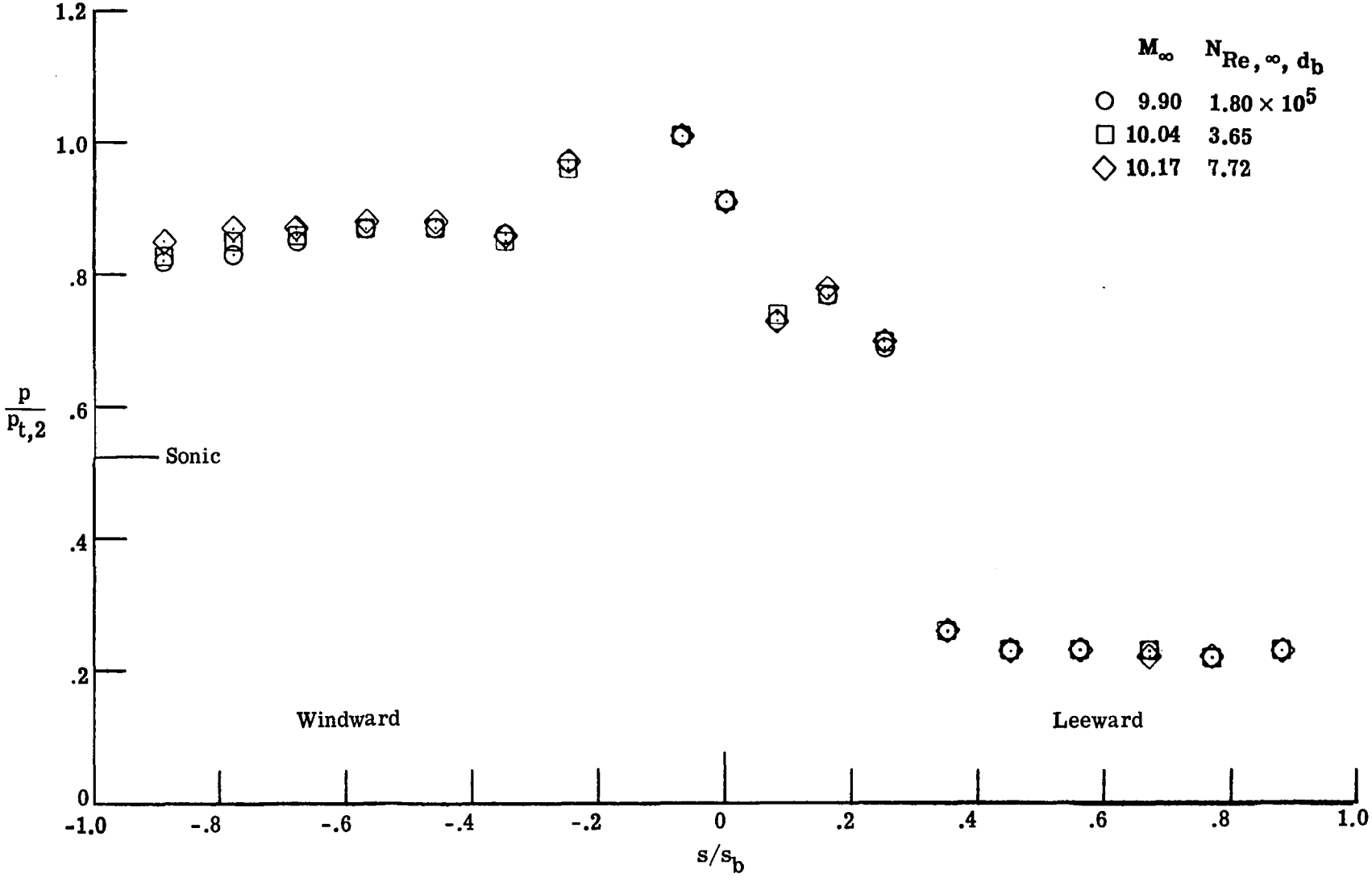

(b) $\alpha = 16°$.

Figure 55.- Concluded.

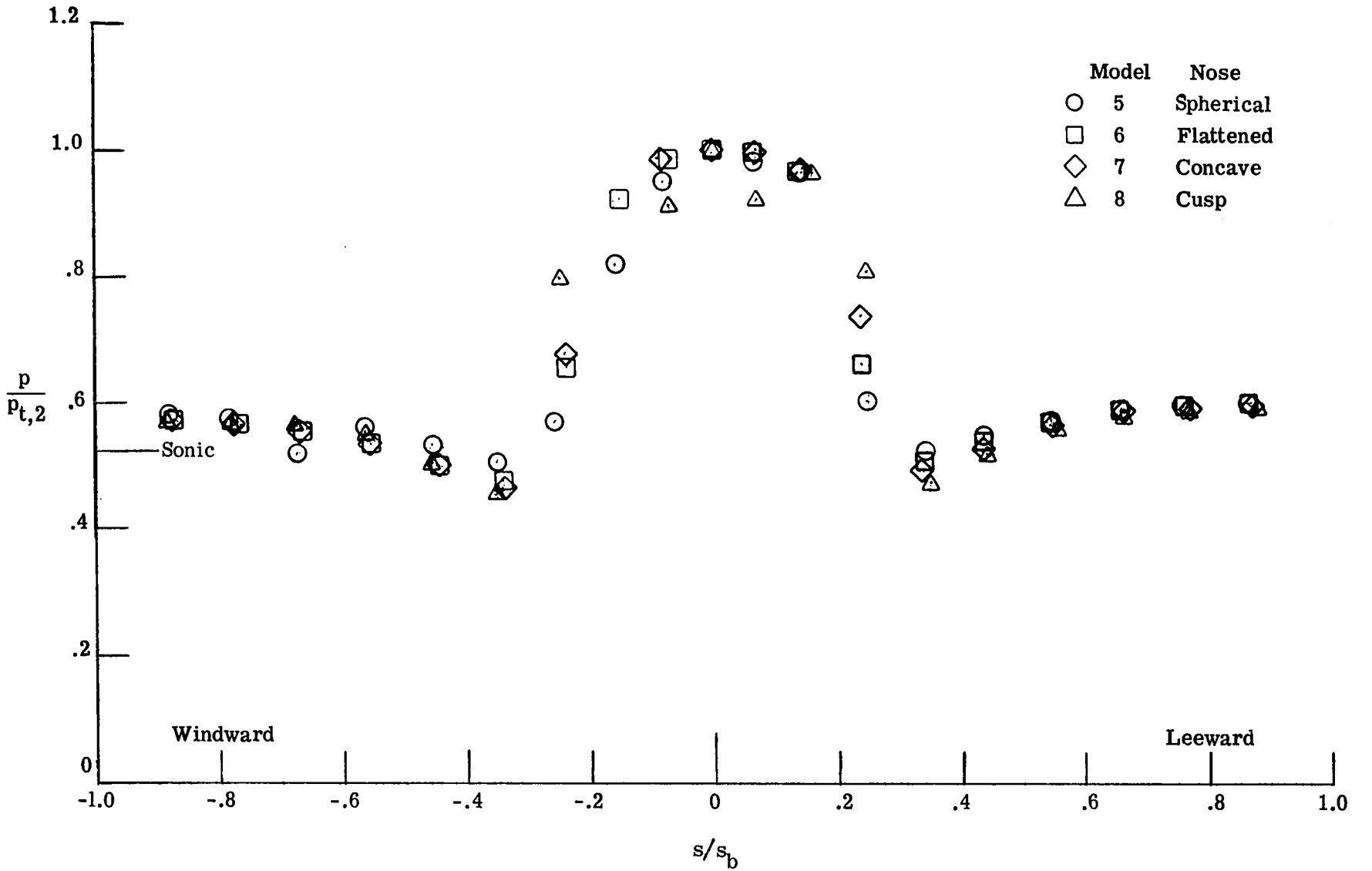

(a) $\alpha = 0°$.

Figure 56.- Effect of nose shape of the cones (models 5 to 8) on the pressure distributions along the most windward ($\phi = 180°$) and leeward ($\phi = 0°$) rays in Mach 10.0 air. $N_{Re,\infty,d_b} = 3.65 \times 10^5$.

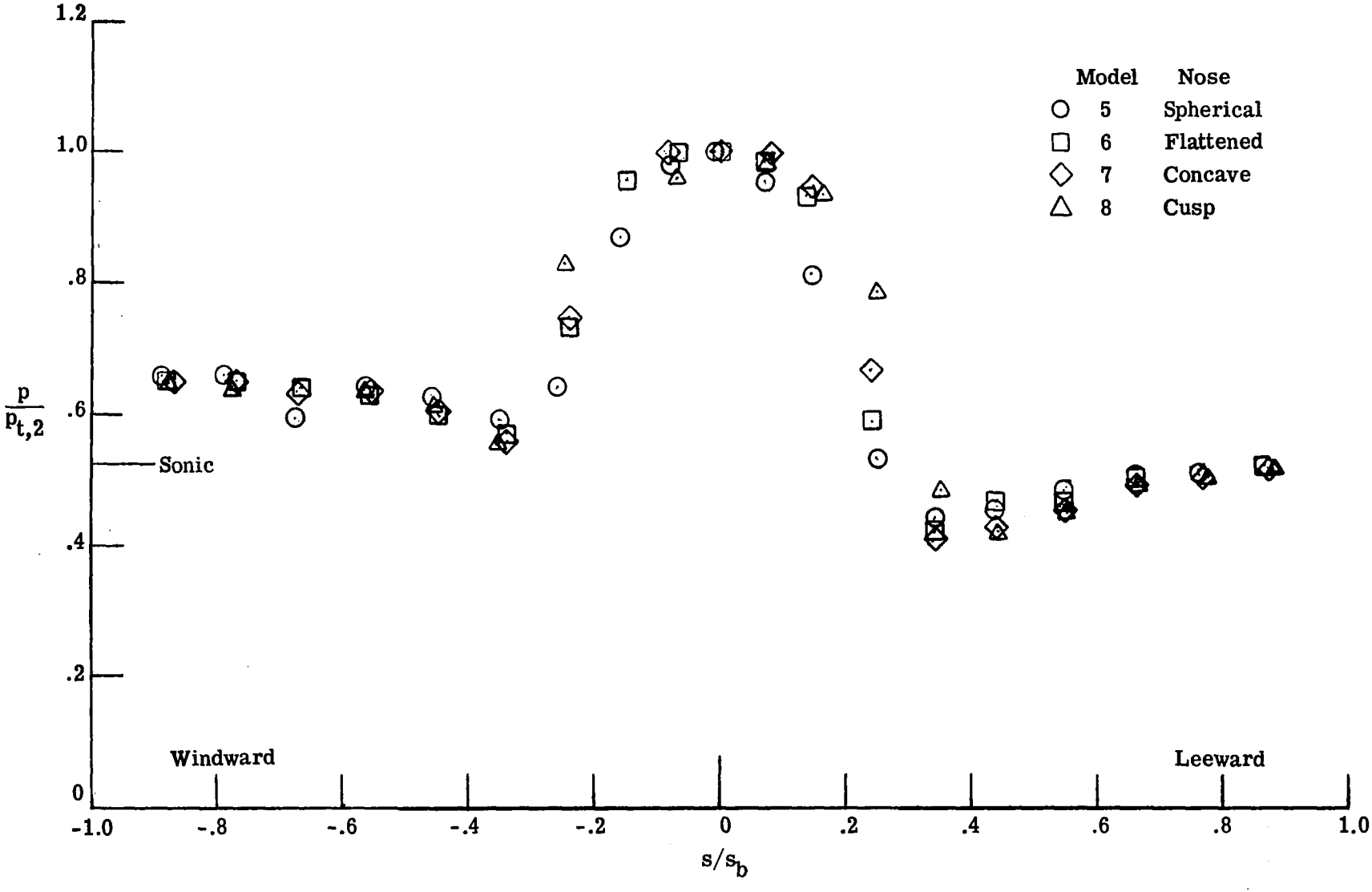

(b) $\alpha = 4°$.

Figure 56.- Continued.

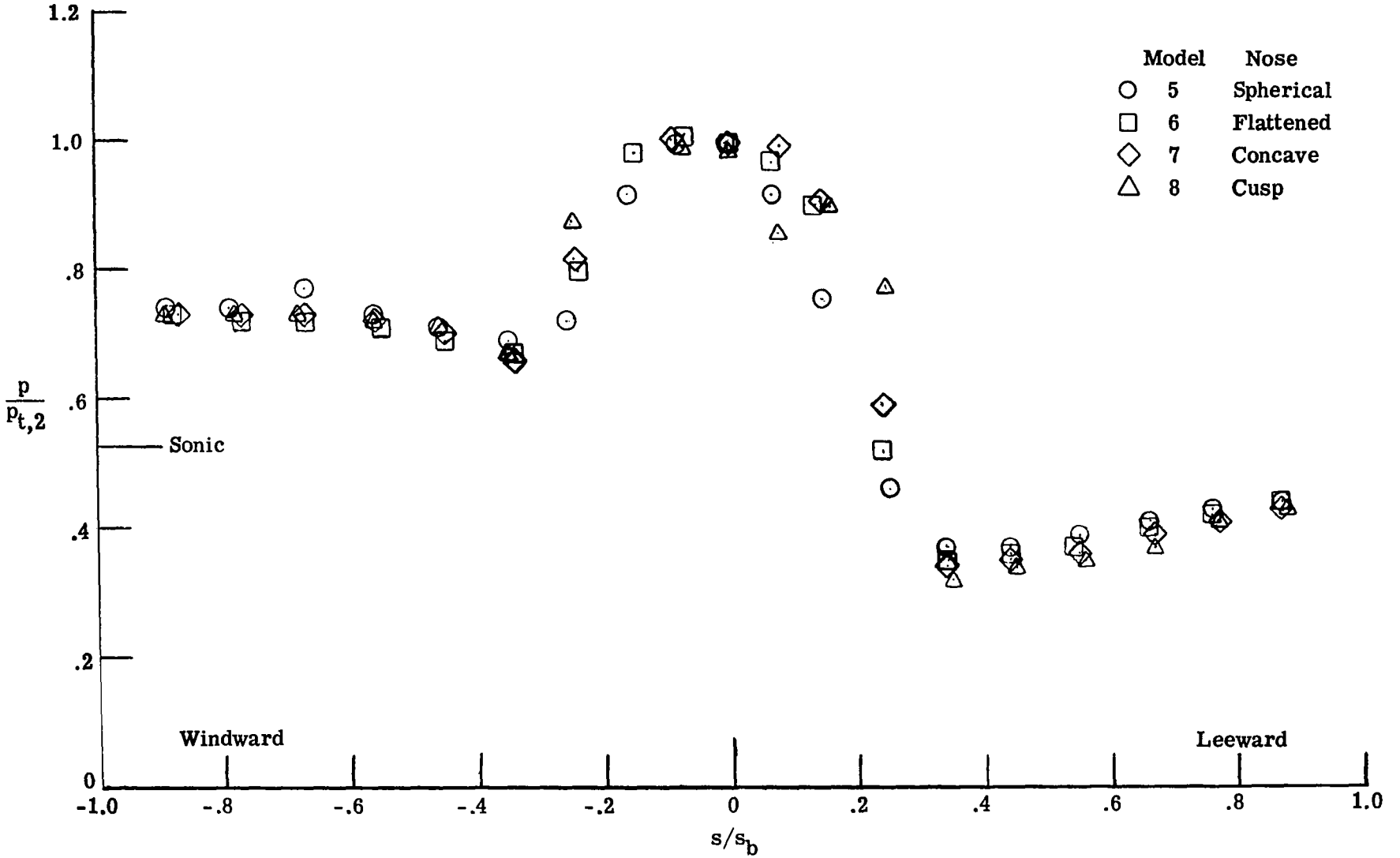

(c) $\alpha = 8°$.

Figure 56.- Continued.

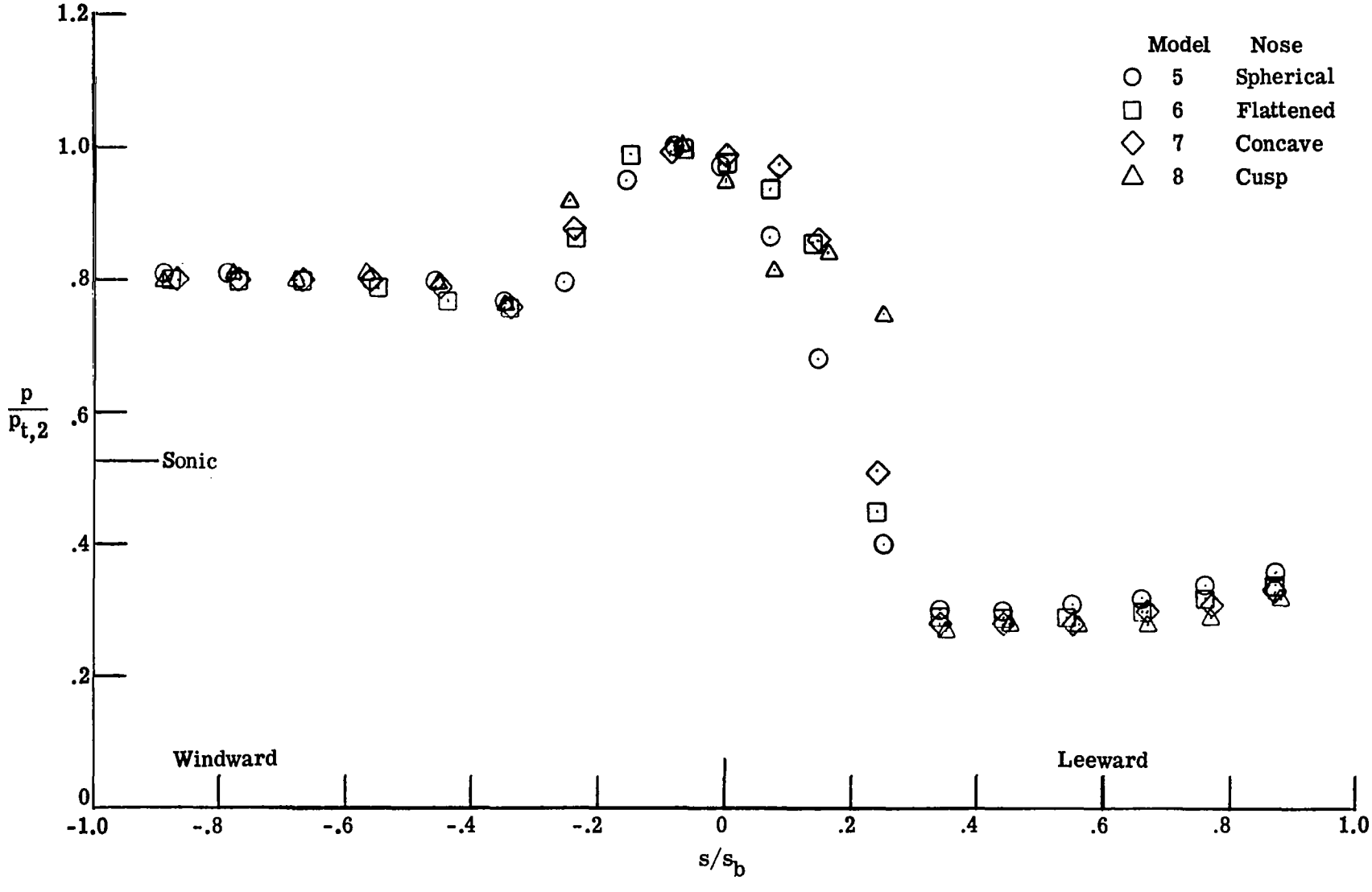

(d) $\alpha = 12°$.

Figure 56.- Continued.

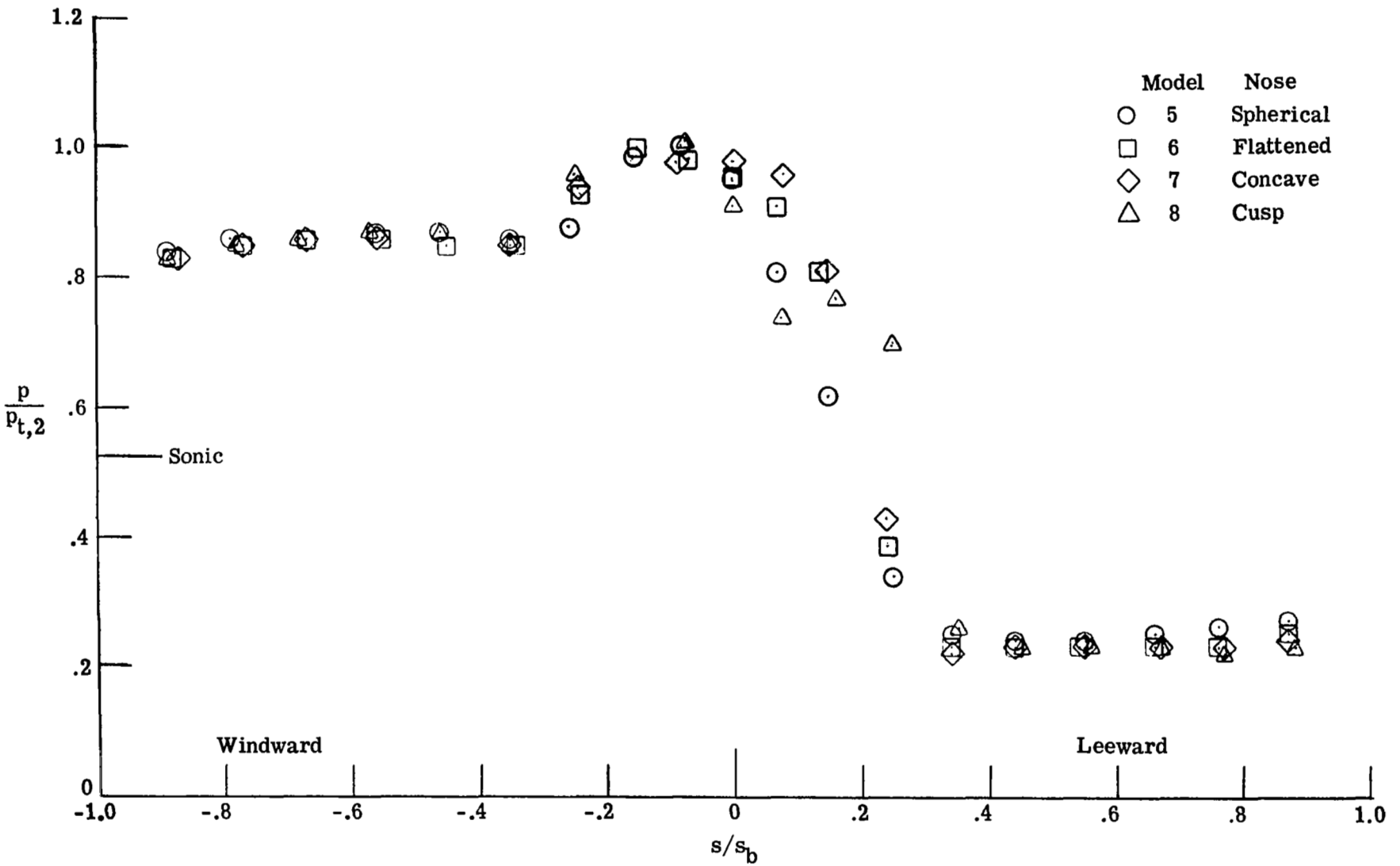

(e) $\alpha = 16°$.

Figure 56.- Concluded.

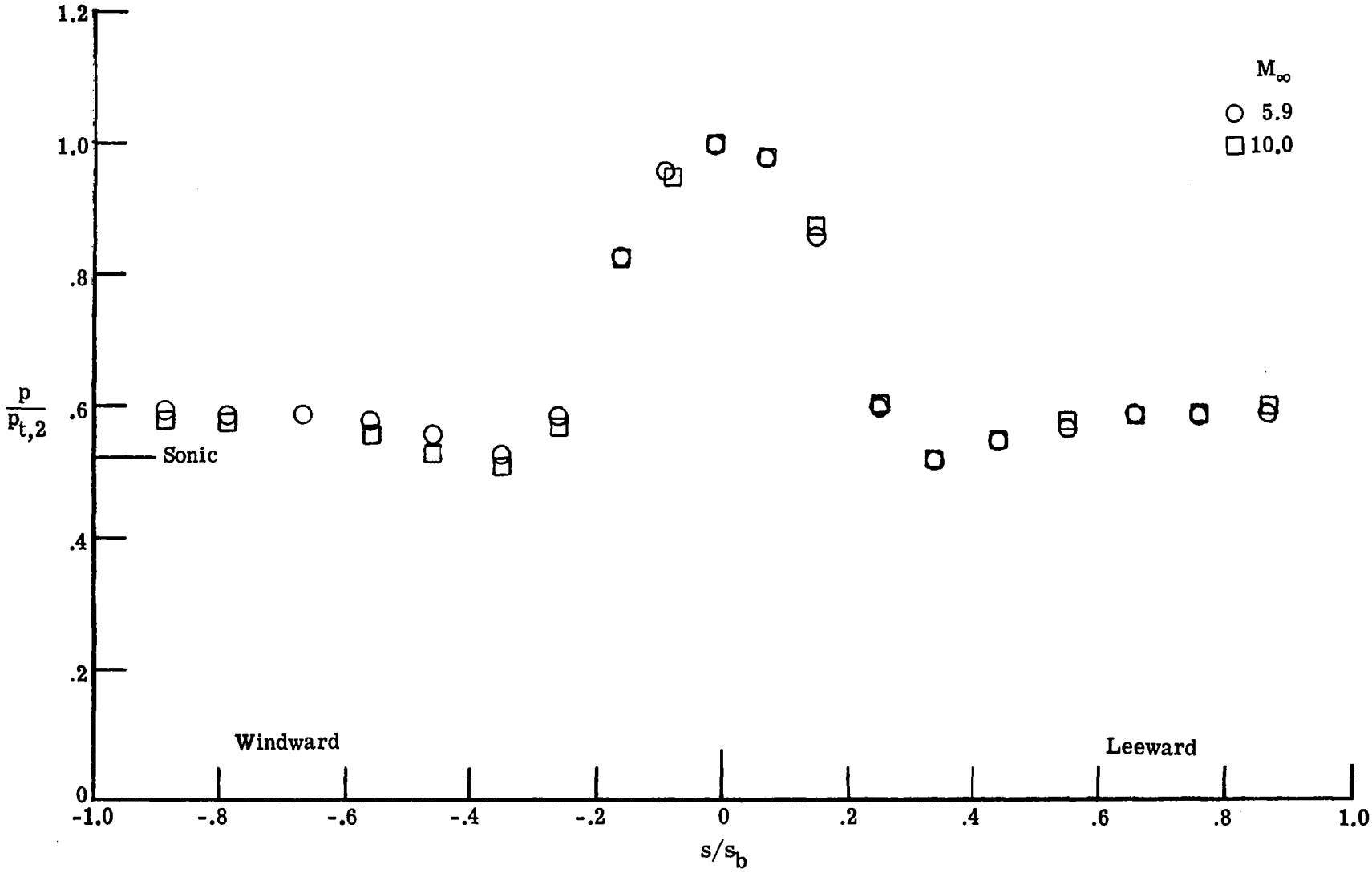

(a) $\alpha = 0°$.

Figure 57.- Effect of Mach number on the pressure distributions along the most windward ($\phi = 180°$) and leeward ($\phi = 0°$) rays of the spherical-nose cone (model 5) in air.

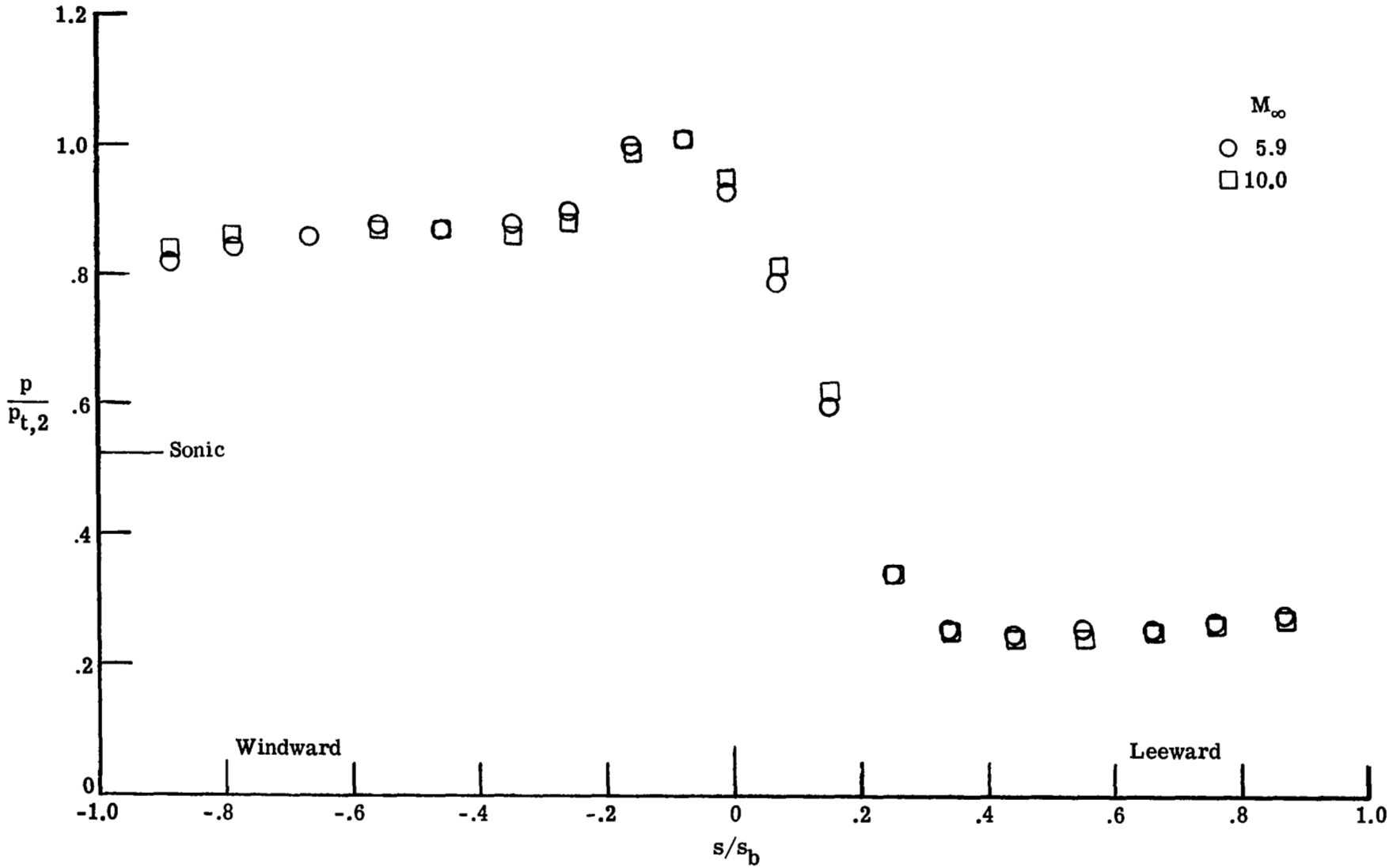

(b) $\alpha = 16°$.

Figure 57.- Concluded.

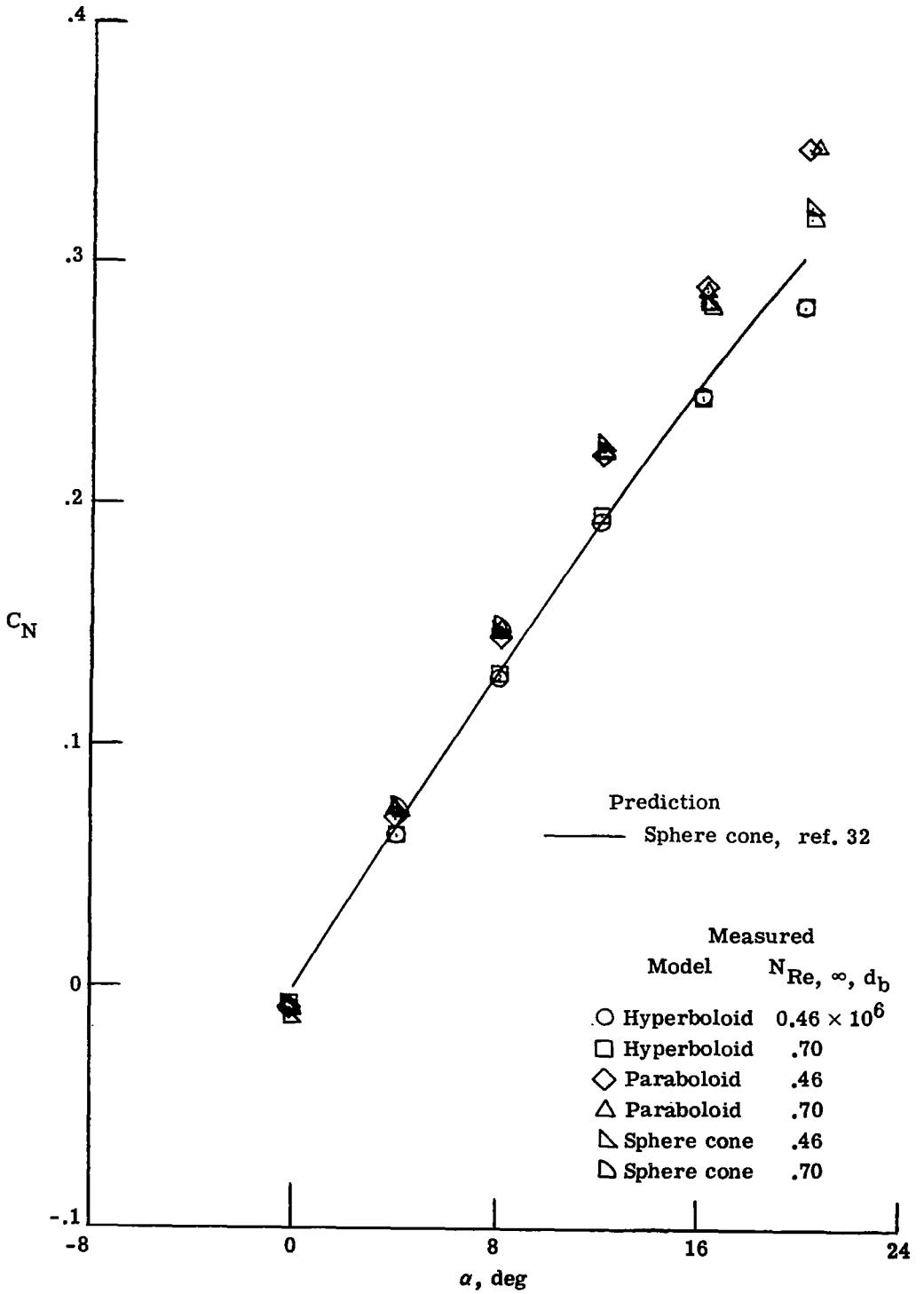

(a) Normal-force coefficient.

Figure 58.- Aerodynamic coefficients measured for the hyperboloid (model 1, series 2), paraboloid (model 3, series 2), and spherical-nose cone (model 5) in Mach 10 air.

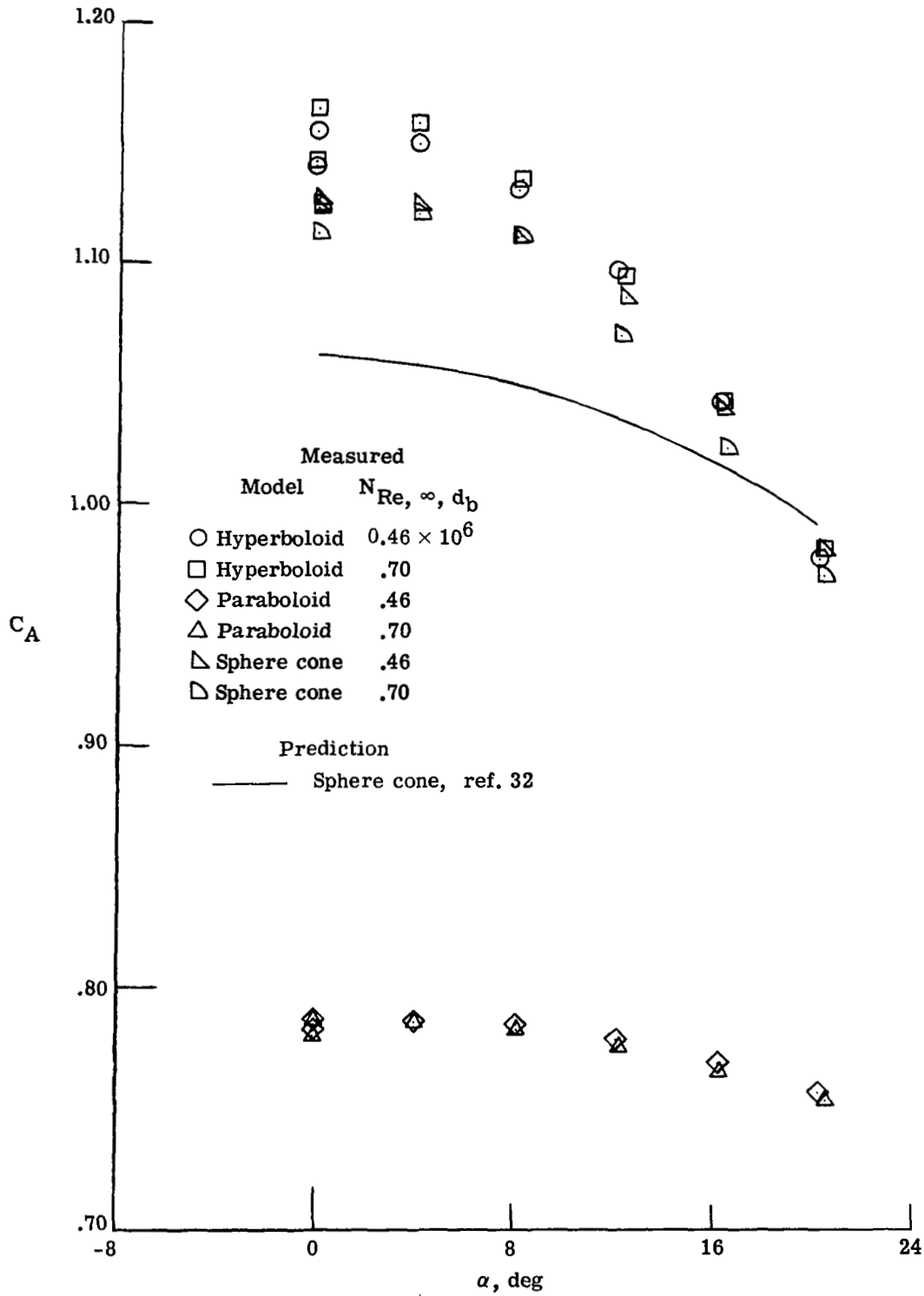

(b) Axial-force coefficient.

Figure 58.- Continued.

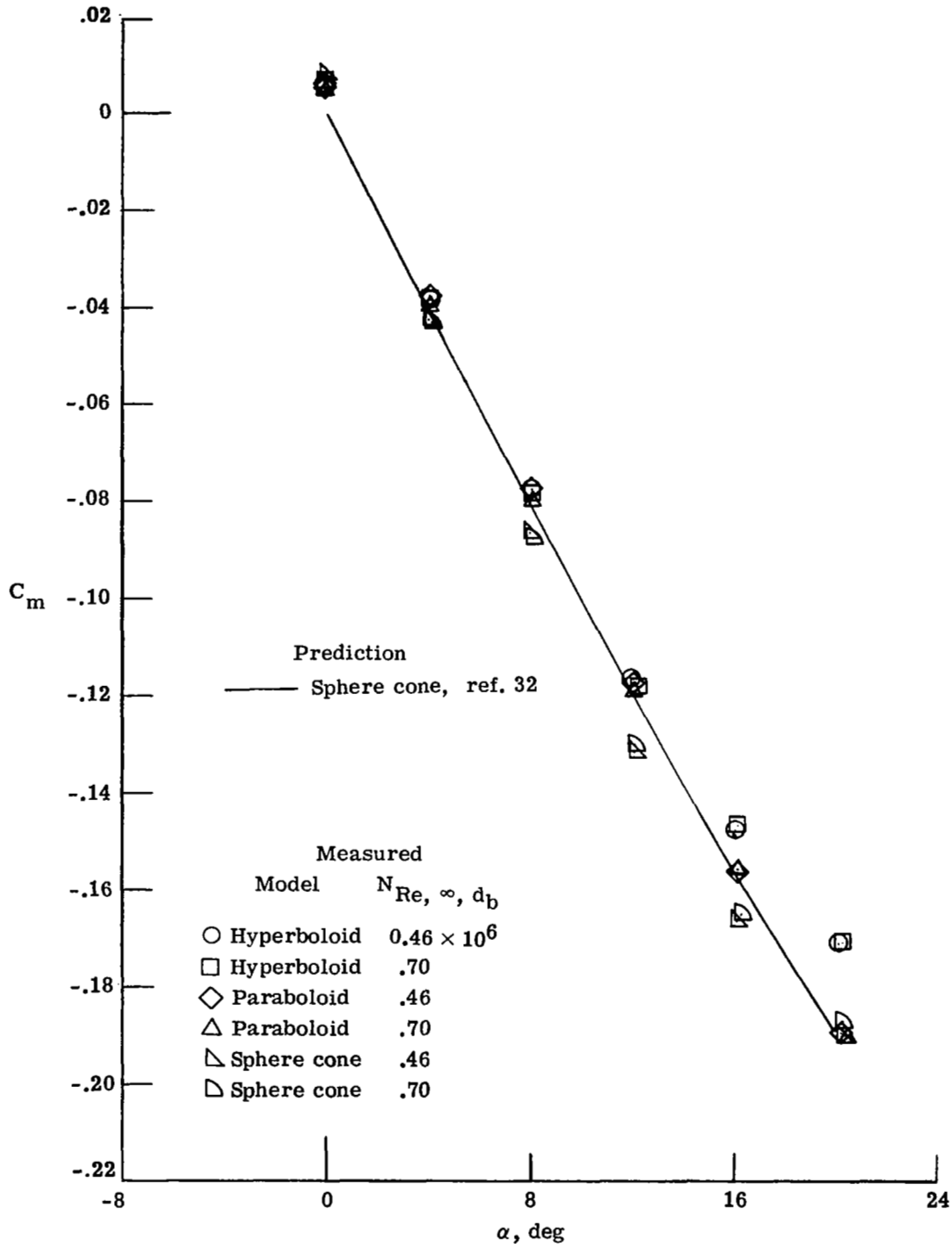

(c) Pitching-moment coefficient.

Figure 58.- Concluded.

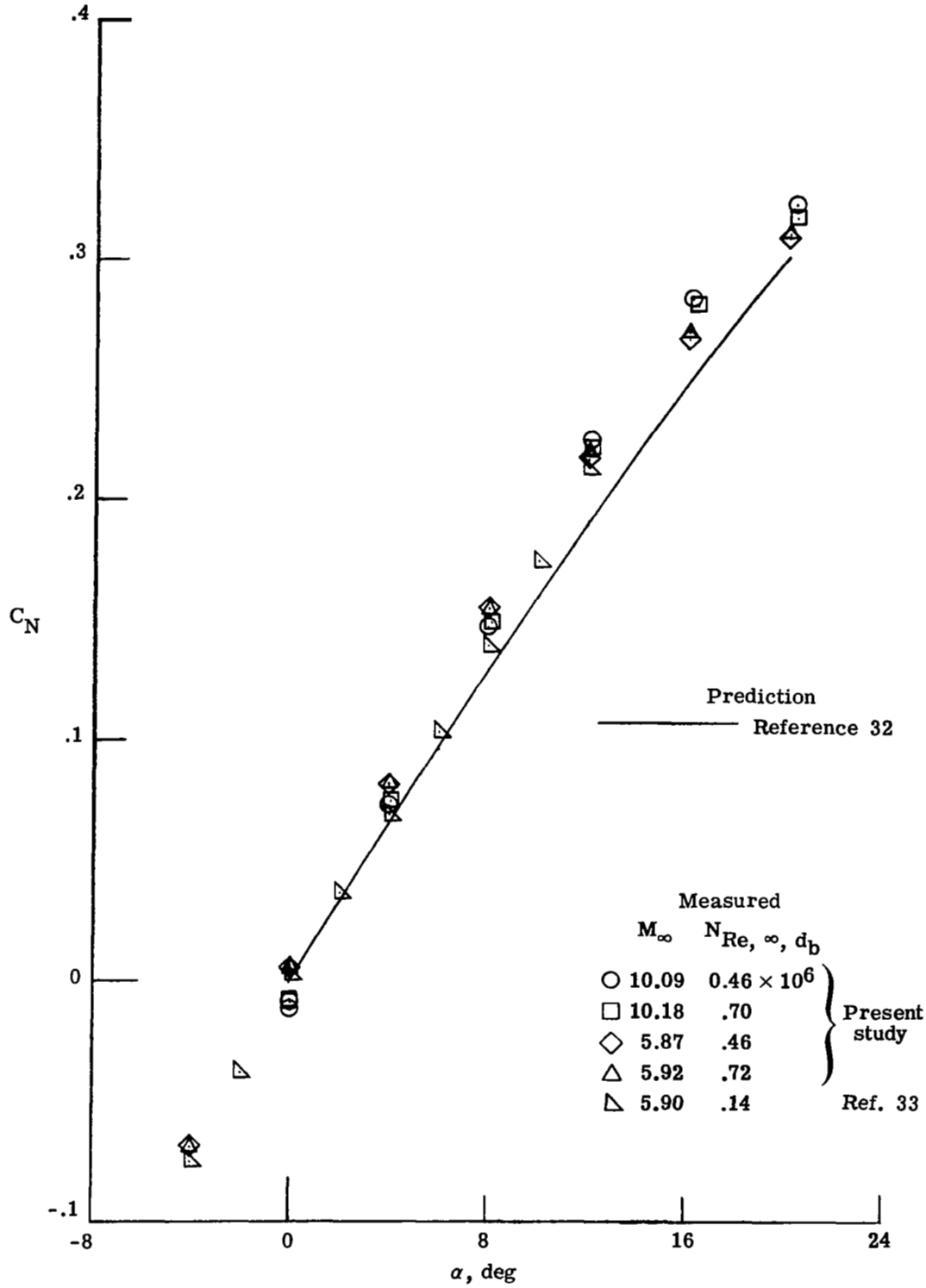

(a) Normal-force coefficient.

Figure 59.- Aerodynamic coefficients measured for the spherical-nose cone (model 5) in Mach 6 and Mach 10 air.

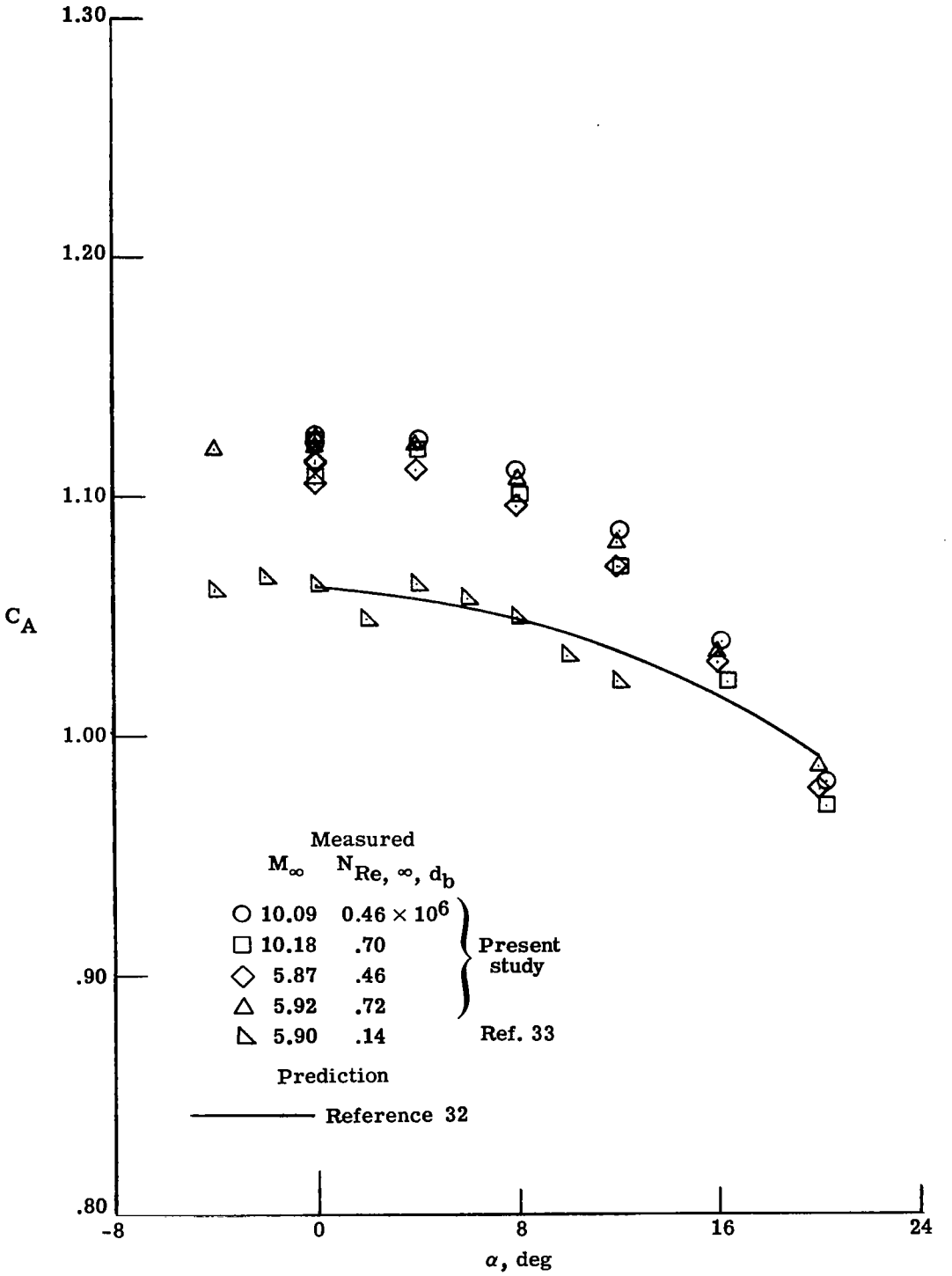

(b) Axial-force coefficient.

Figure 59.- Continued.

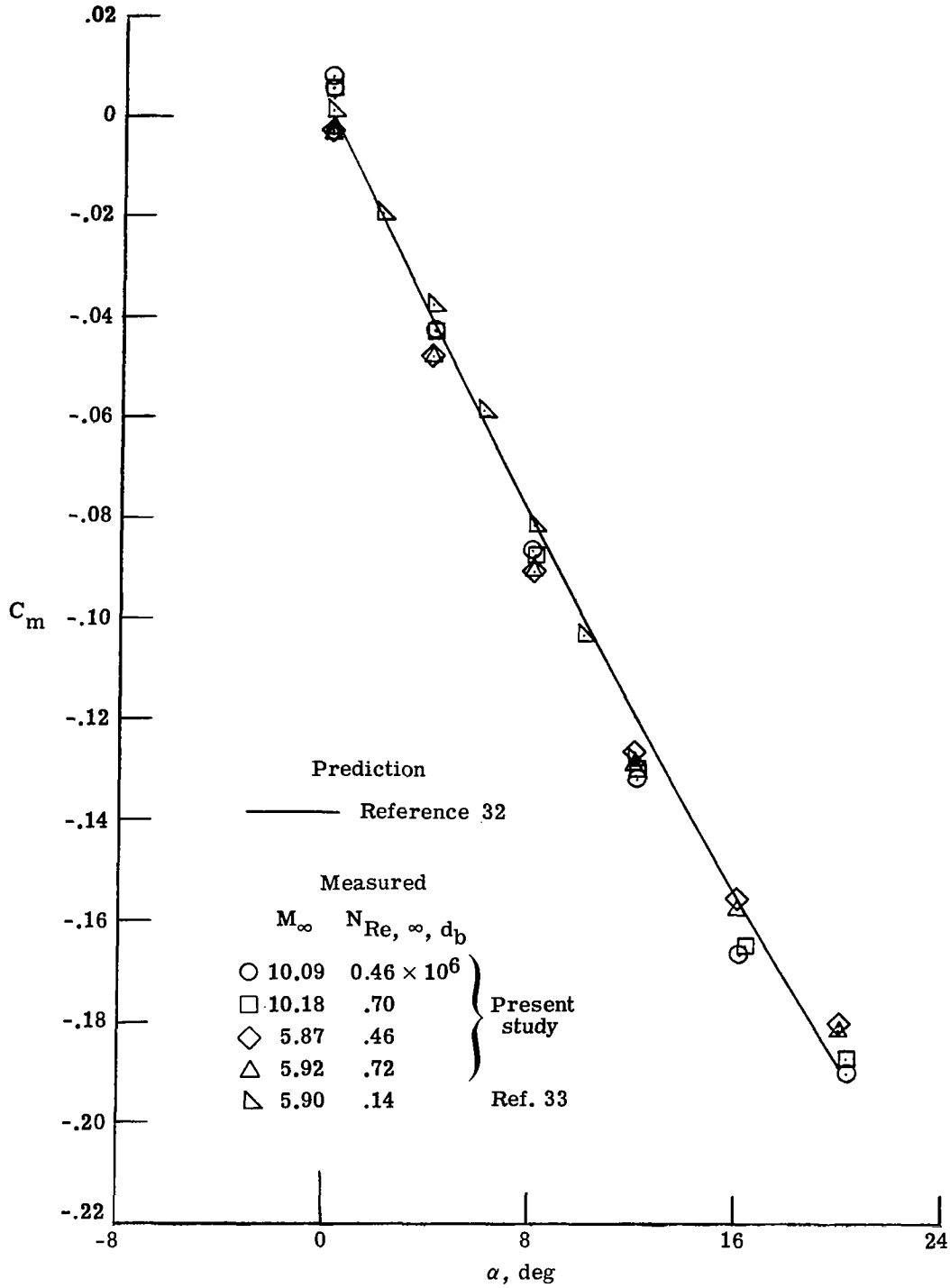

(c) Pitching-moment coefficient.

Figure 59.- Concluded.

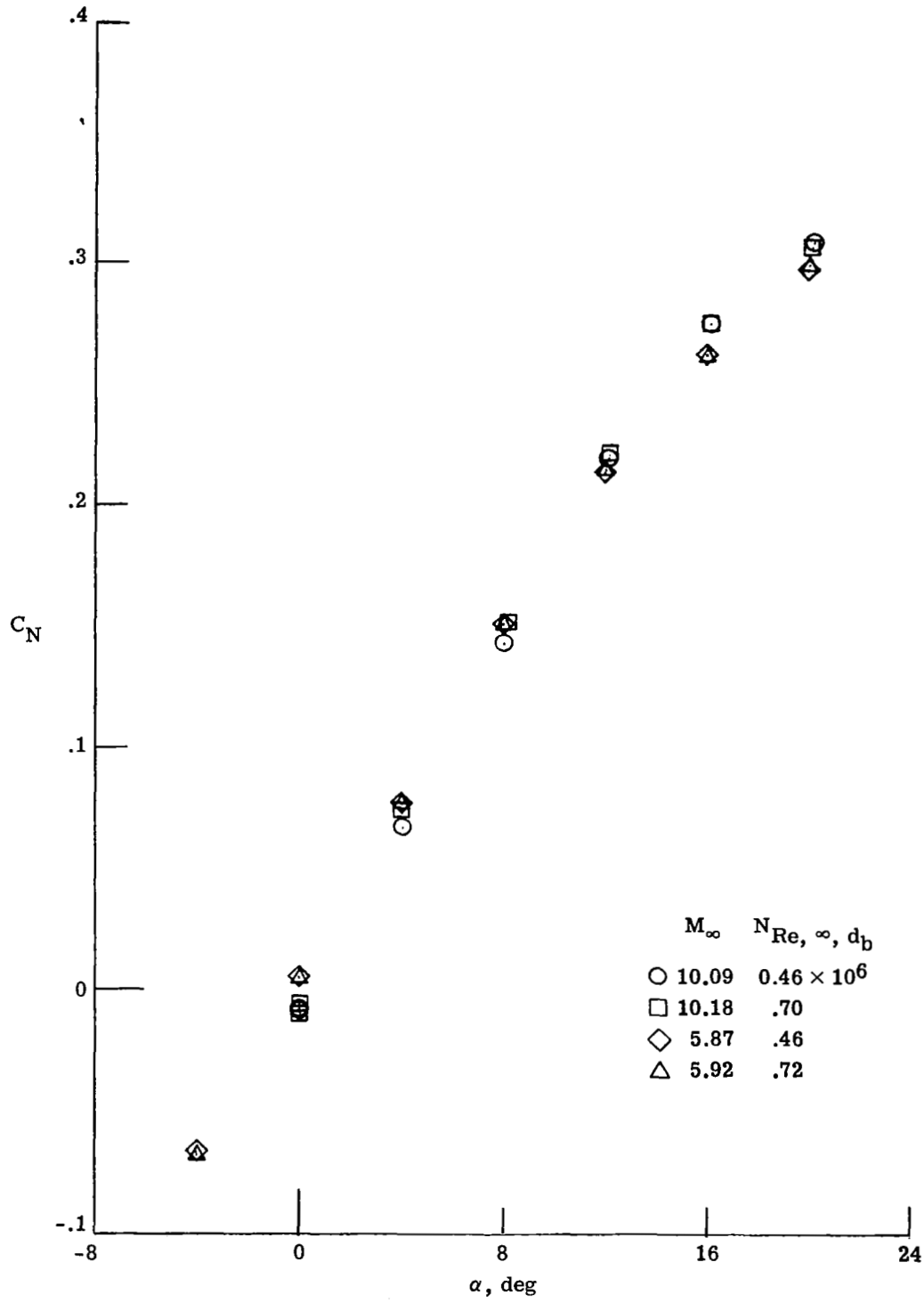

(a) Normal-force coefficient.

Figure 60.- Aerodynamic coefficients measured for the flattened-nose cone (model 6) in Mach 6 and Mach 10 air.

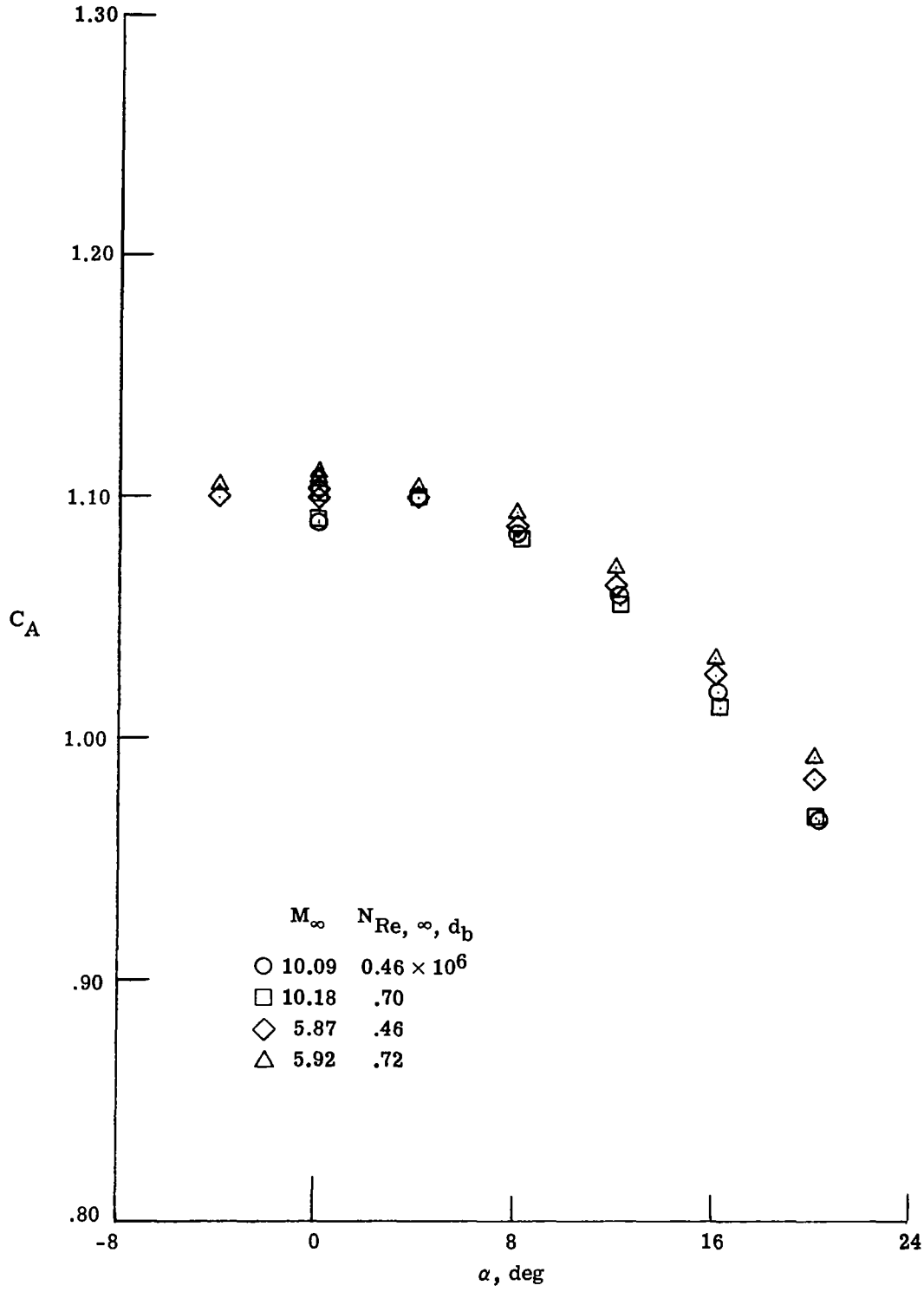

(b) Axial-force coefficient.

Figure 60.- Continued.

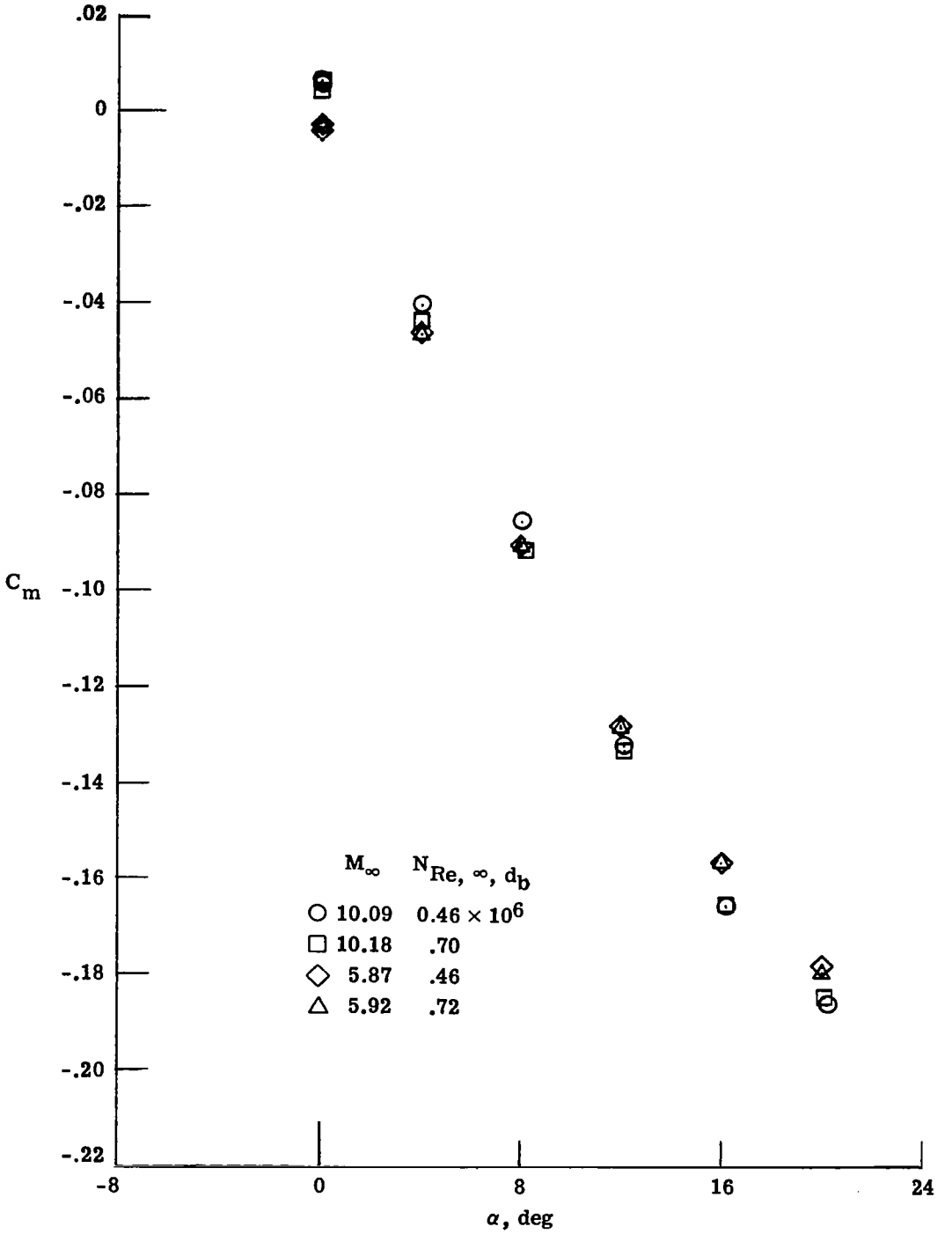

(c) Pitching-moment coefficient.

Figure 60.- Concluded.

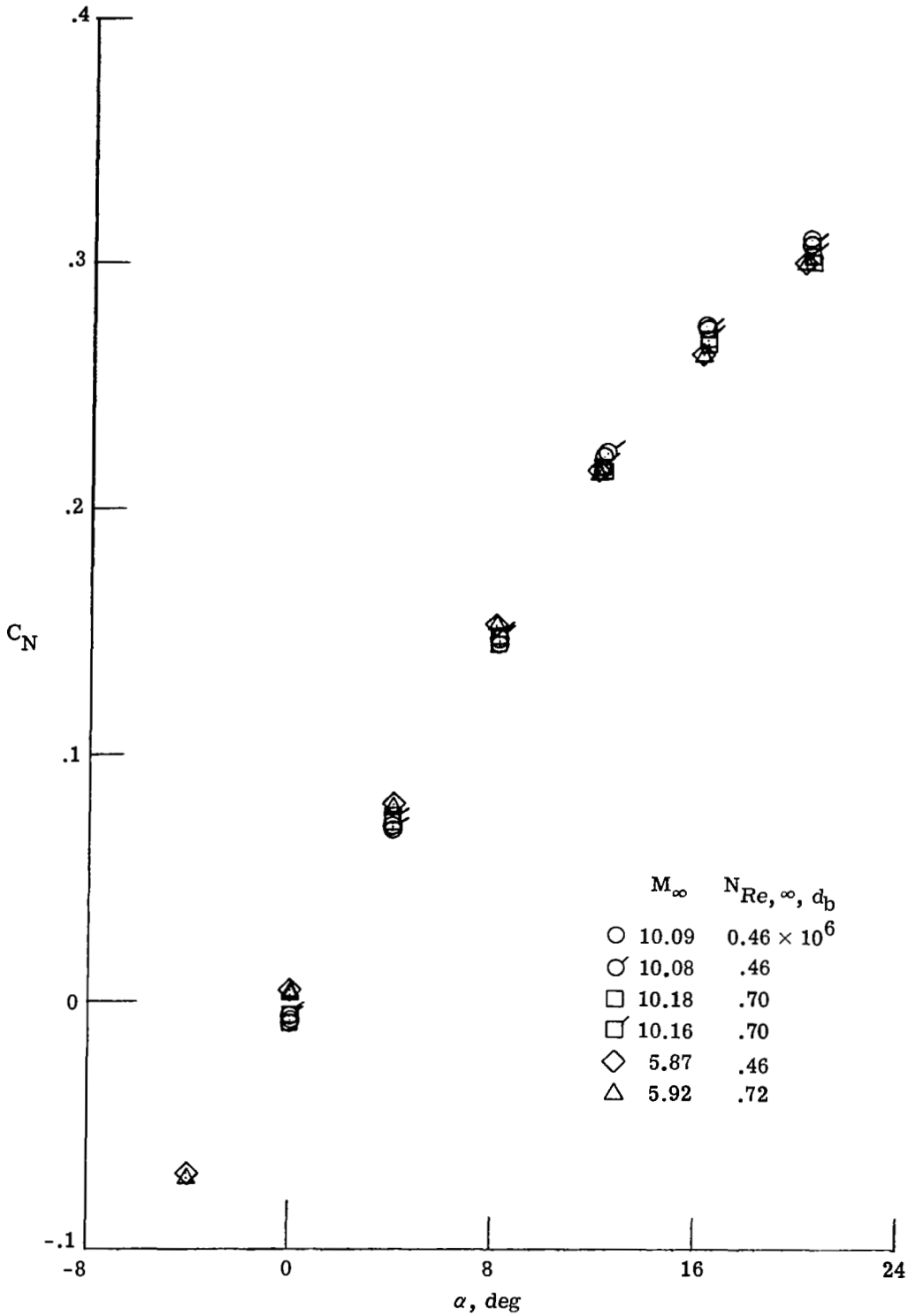

(a) Normal-force coefficient.

Figure 61.- Aerodynamic coefficients measured for the concave-nose cone (model 7) in Mach 6 and Mach 10 air.

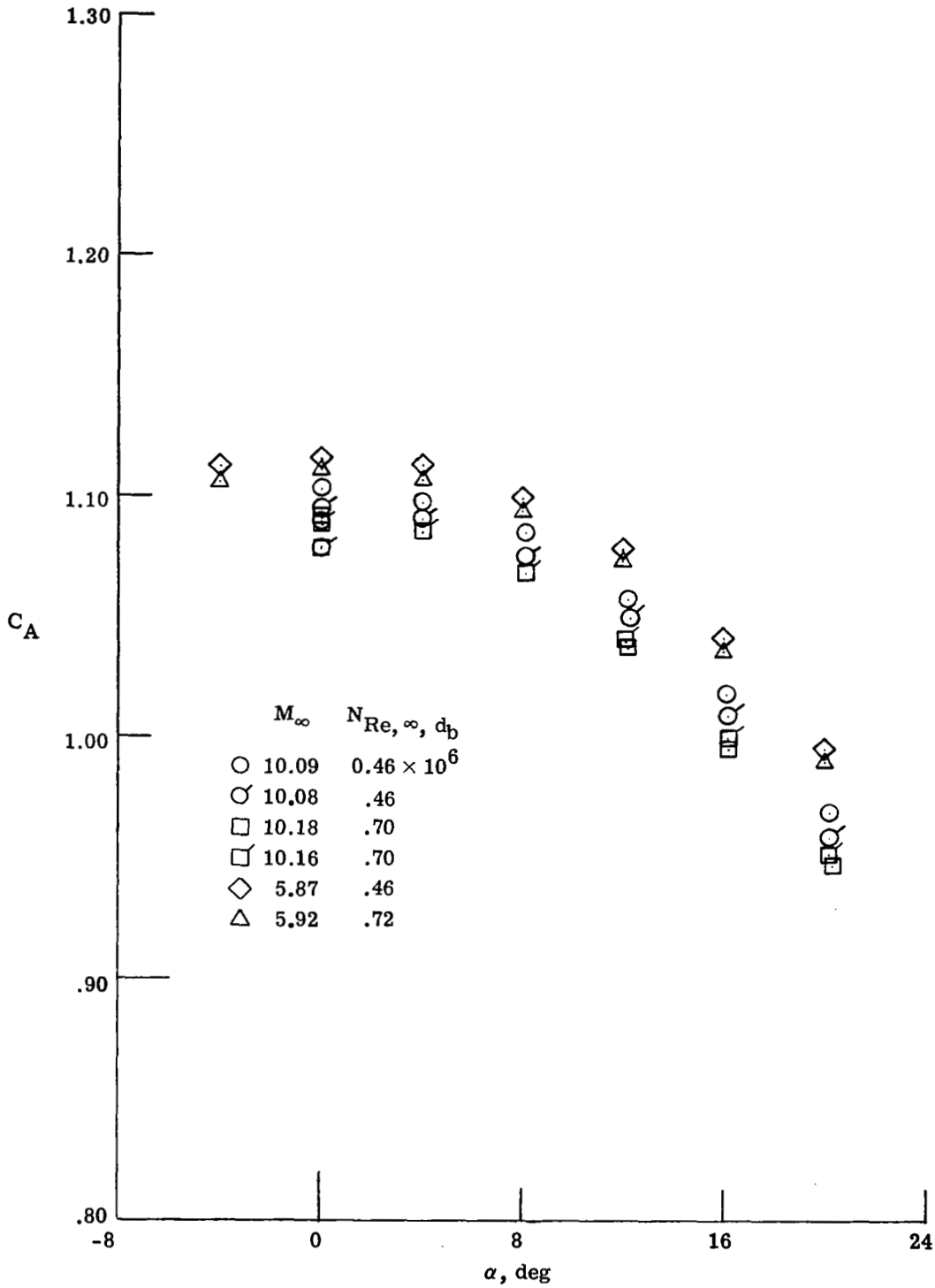

(b) Axial-force coefficient.

Figure 61.- Continued.

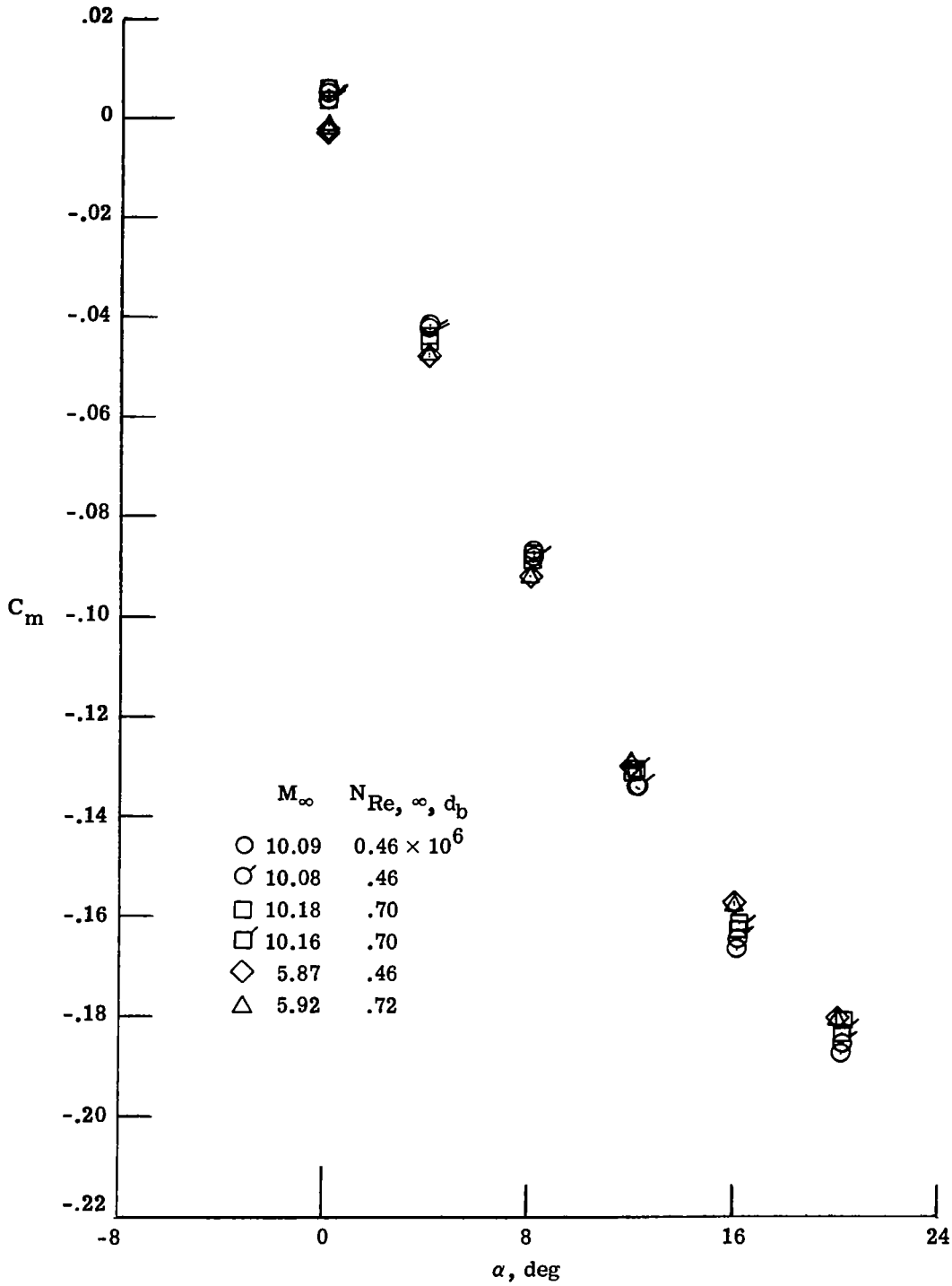

(c) Pitching-moment coefficient.

Figure 61.- Concluded.

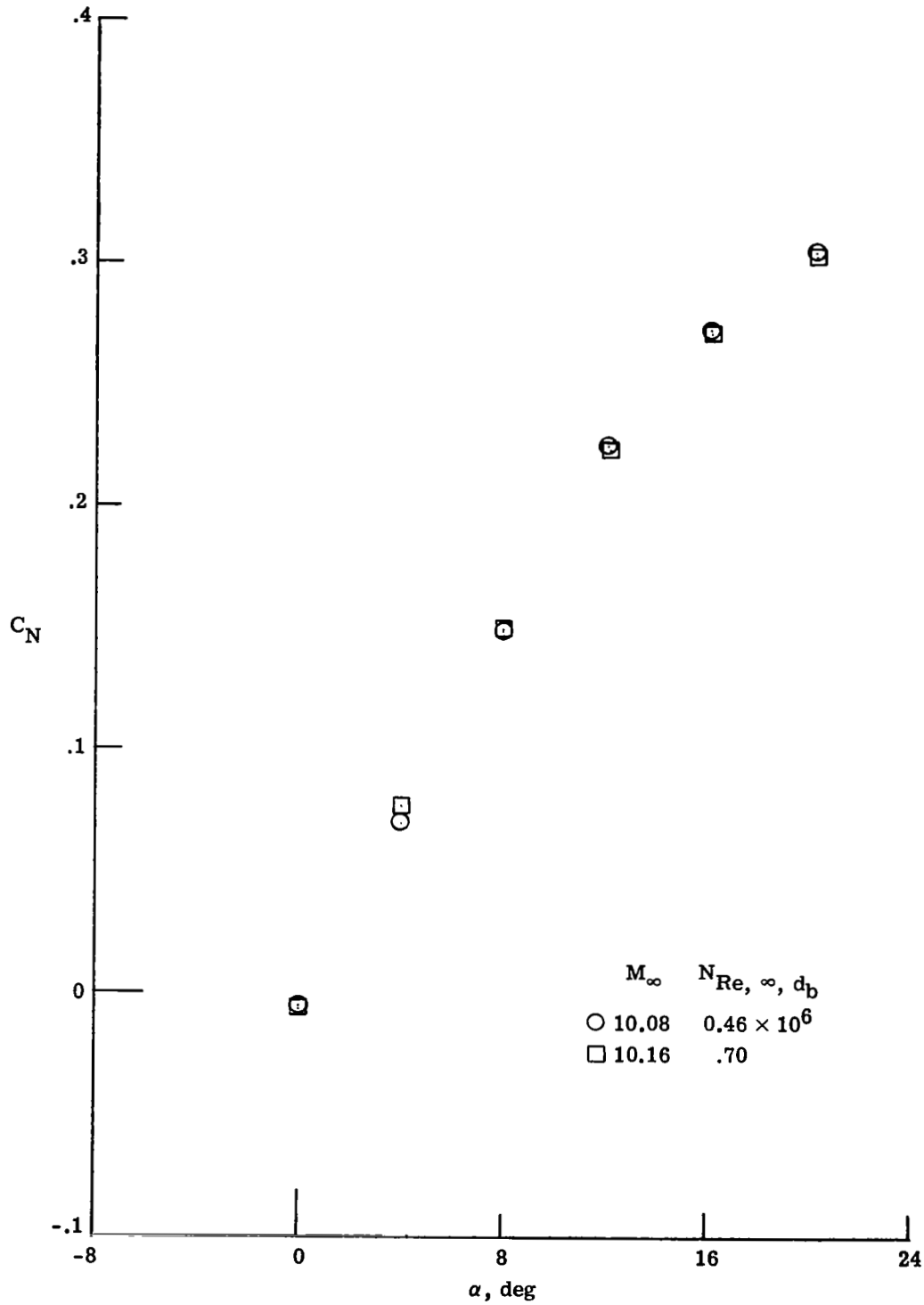

(a) Normal-force coefficient.

Figure 62.- Aerodynamic coefficients measured for the cusp-nose cone (model 8) in Mach 10 air.

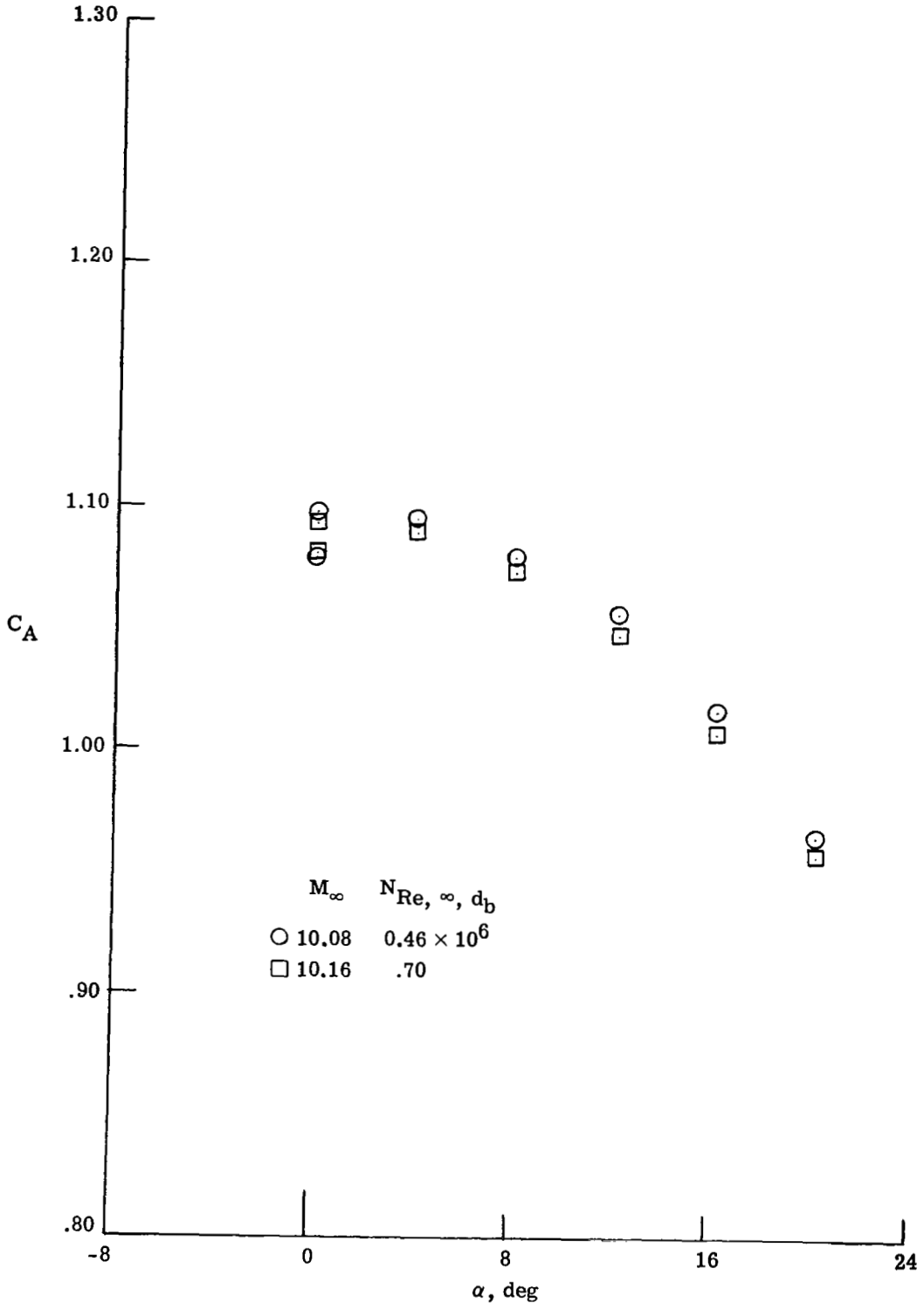

(b) Axial-force coefficient.

Figure 62.- Continued.

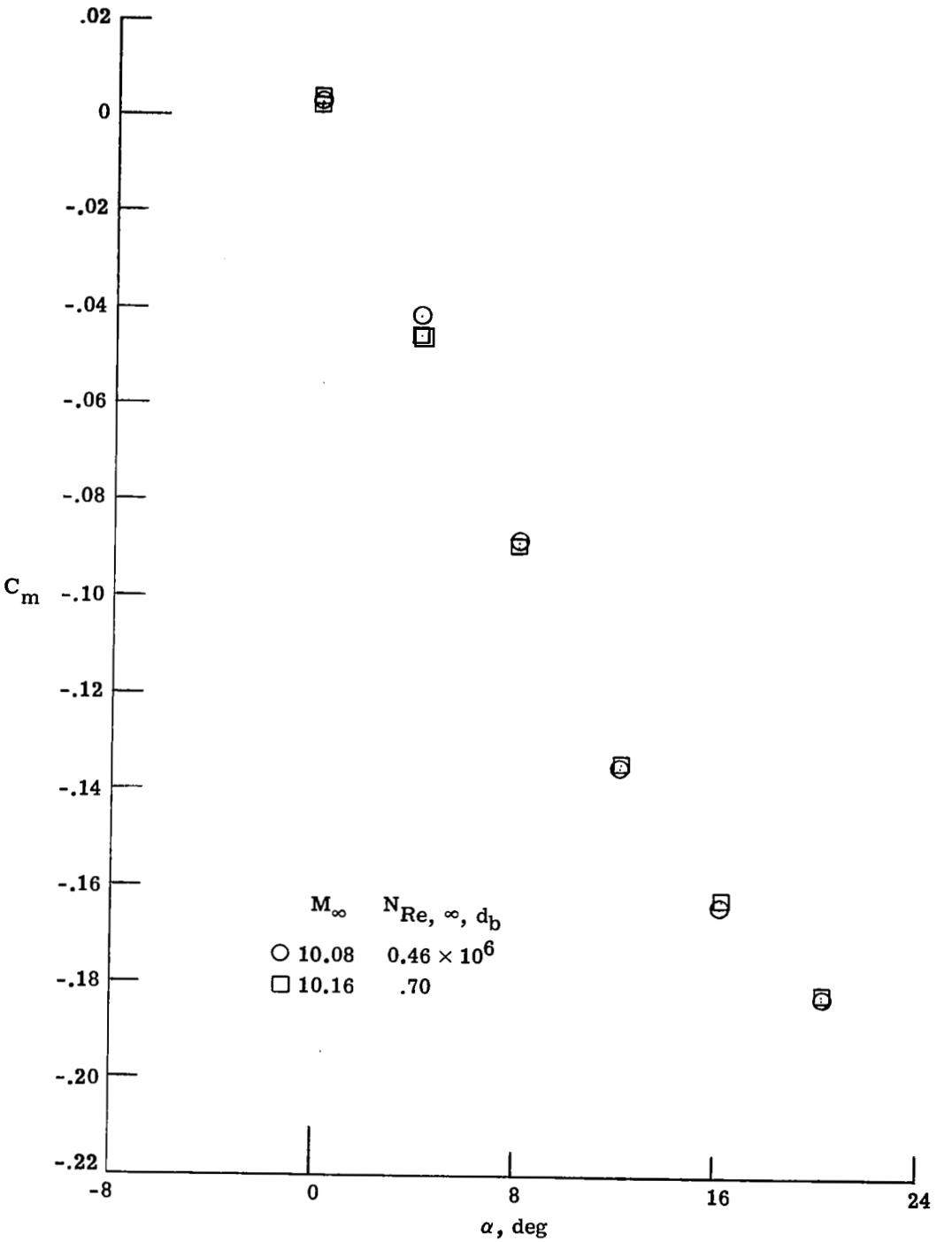

(c) Pitching-moment coefficient.

Figure 62.- Concluded.

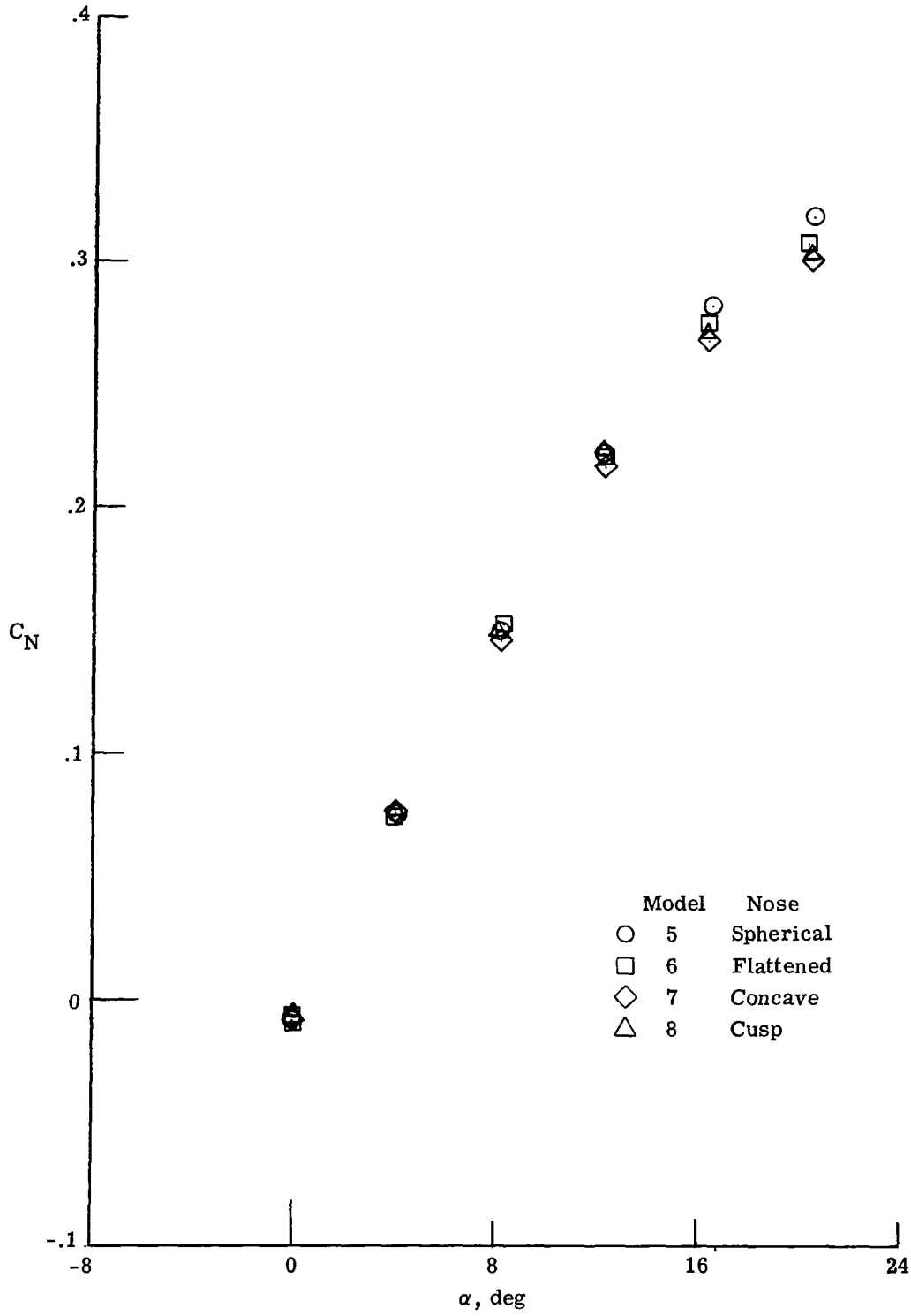

(a) Normal-force coefficient.

Figure 63.- Effect of nose shape of the cones (models 5 to 8) on aerodynamic coefficients in Mach 10 air. $N_{Re,\infty,d_b} = 0.70 \times 10^6$.

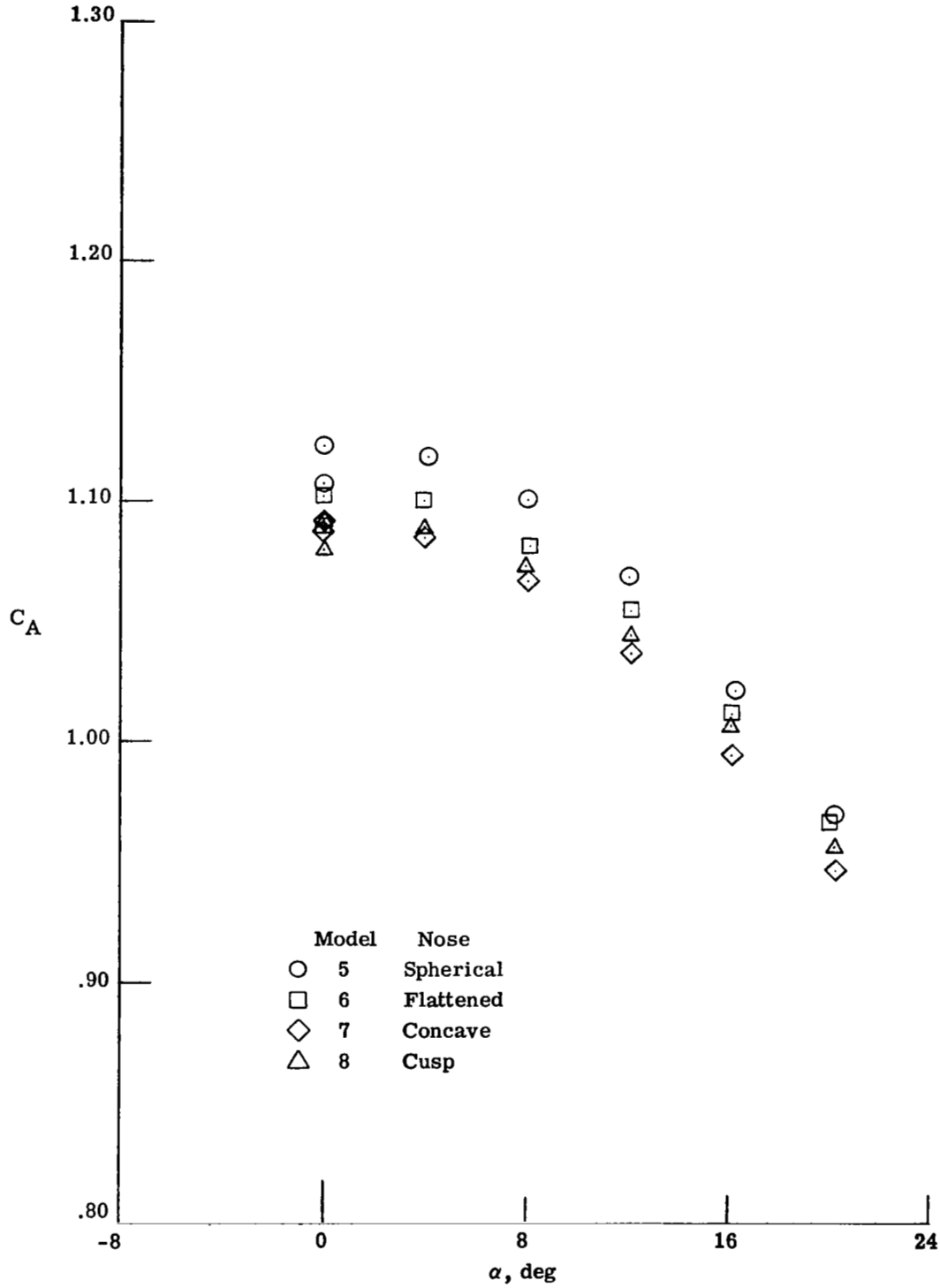

(b) Axial-force coefficient.

Figure 63.- Continued.

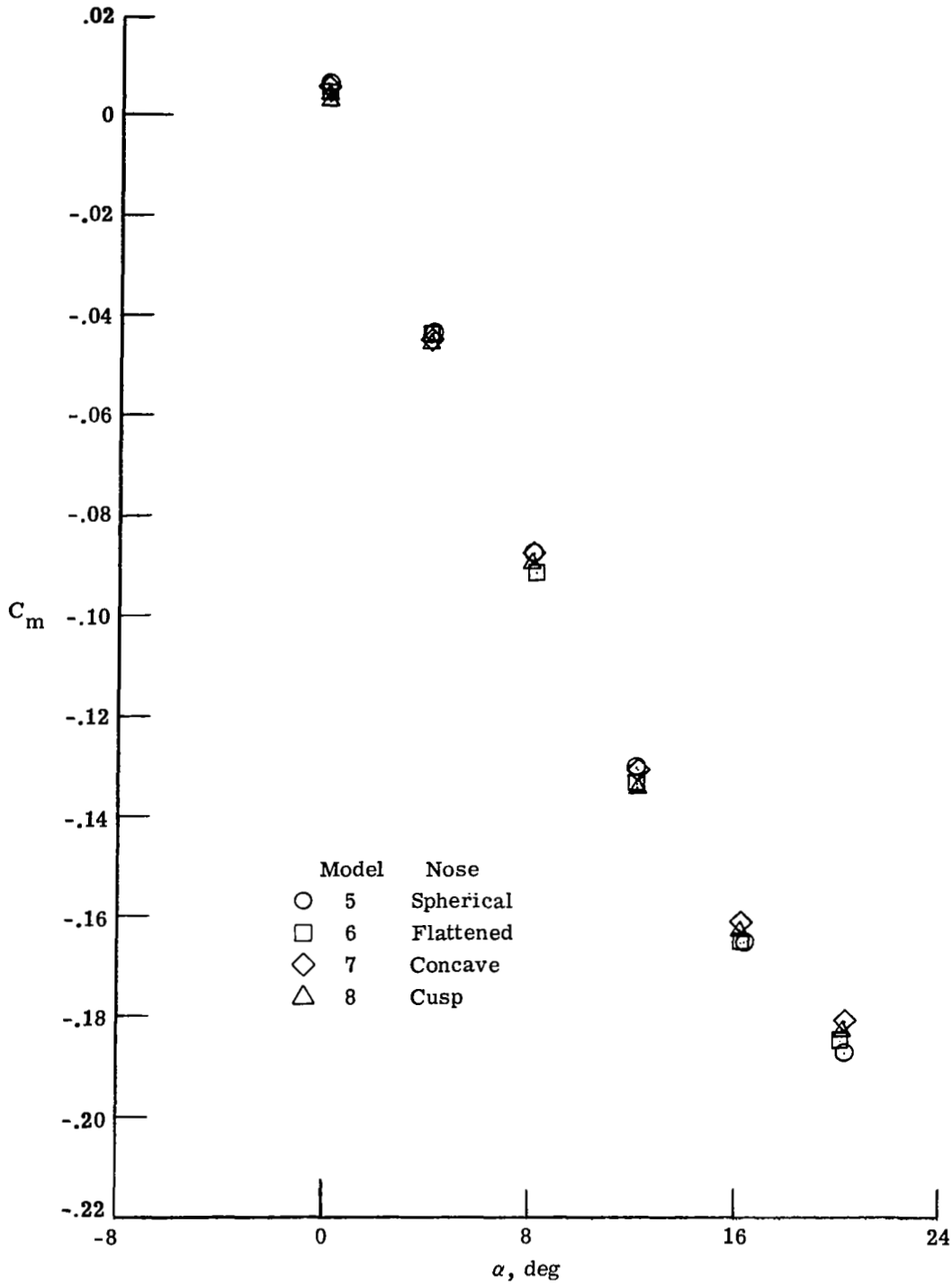

(c) Pitching-moment coefficient.

Figure 63.- Concluded.

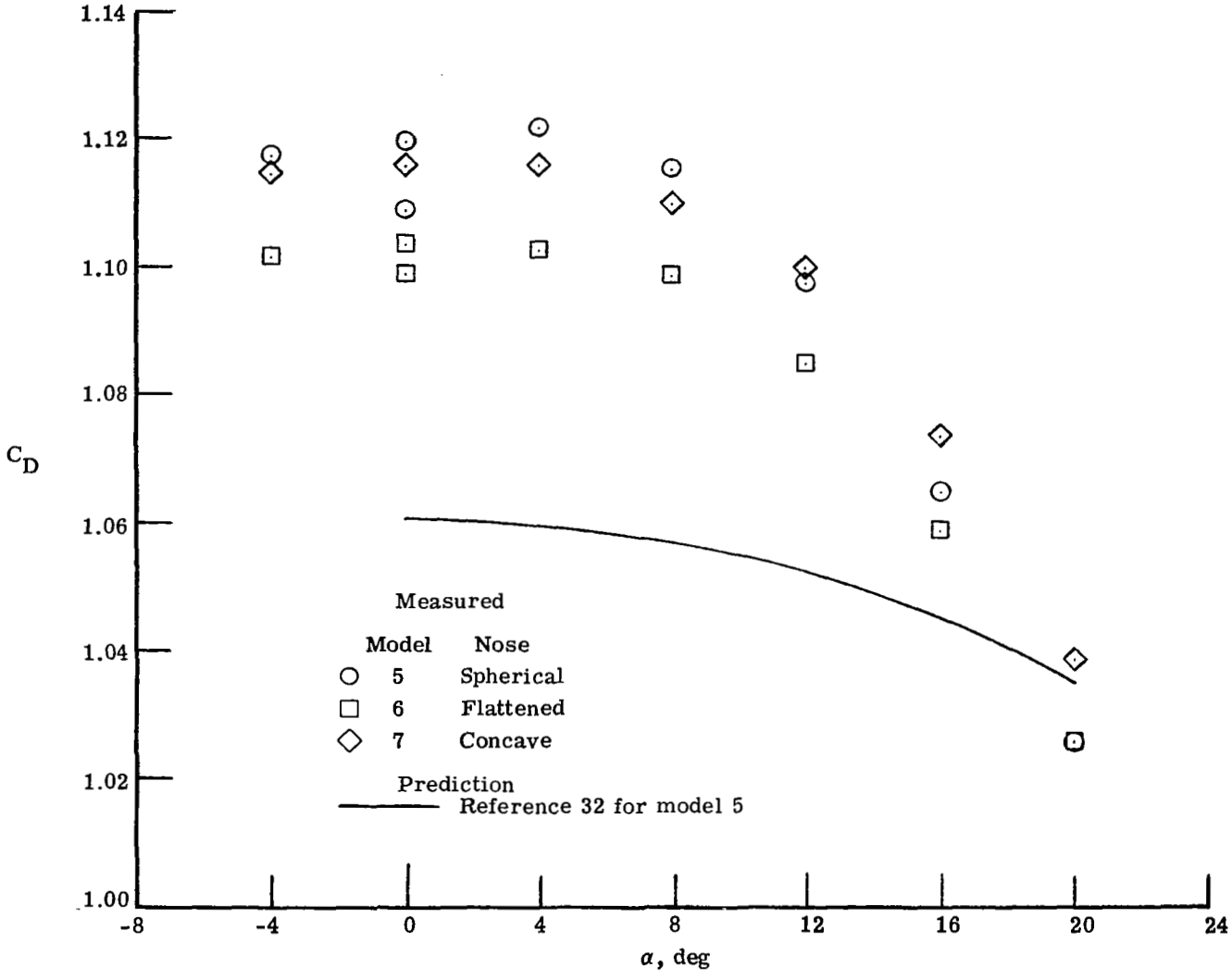

(a) Drag coefficient. $M_\infty = 5.9$.

Figure 64.- Drag and lift coefficients and lift-drag ratio for the cones (models 5 to 8) and hyperboloid (model 1, series 2) in Mach 5.9 and Mach 10.1 air. $N_{Re,\infty,d_b} = 0.46 \times 10^6$.

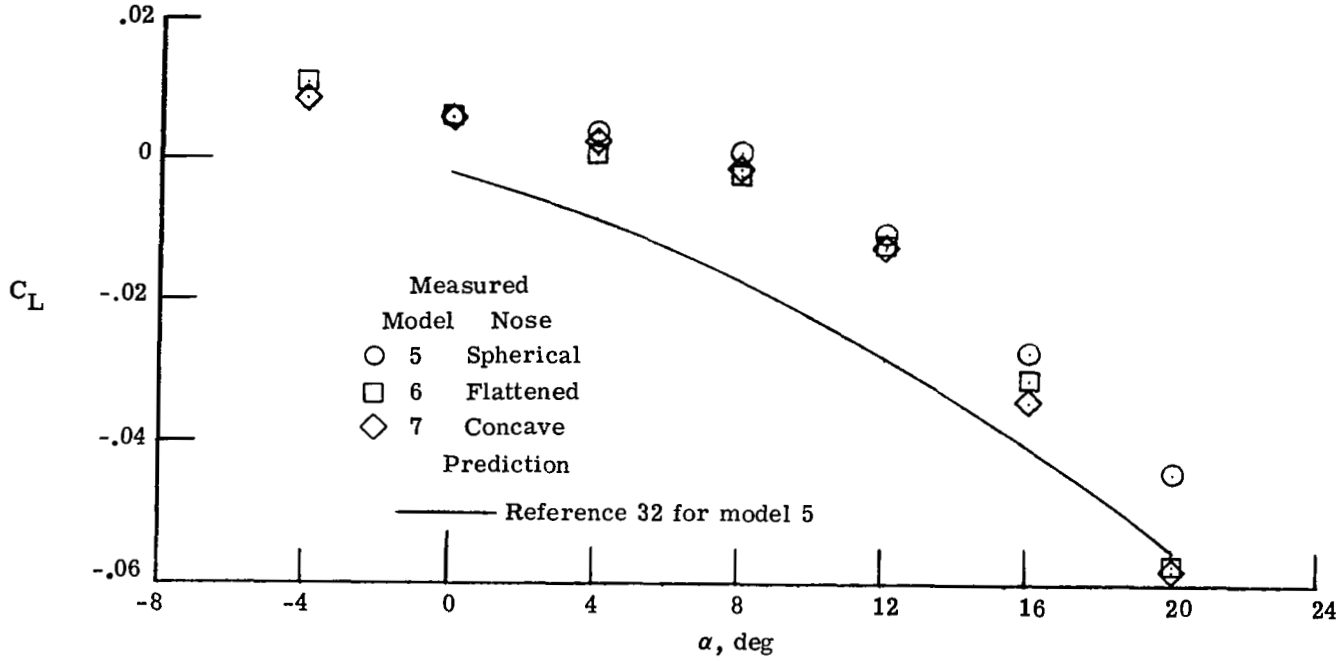

(b) Lift coefficient. $M_\infty = 5.9$.

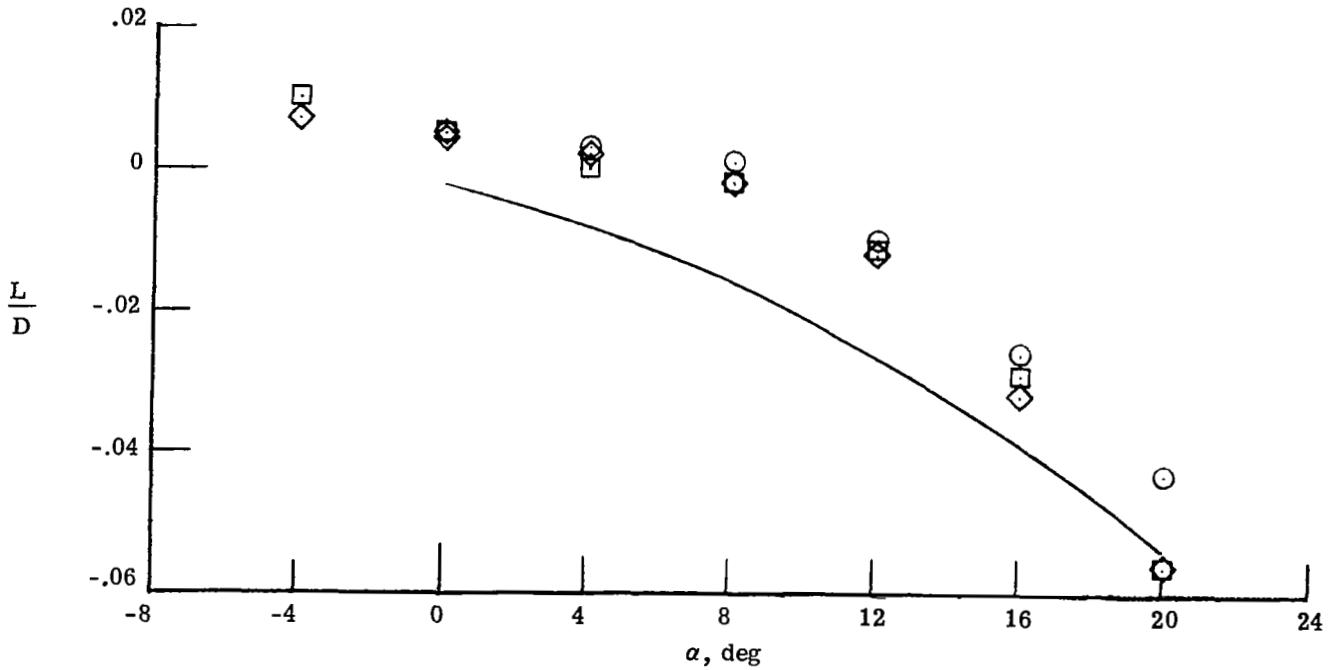

(c) Lift-drag ratio. $M_\infty = 5.9$.

Figure 64.- Continued.

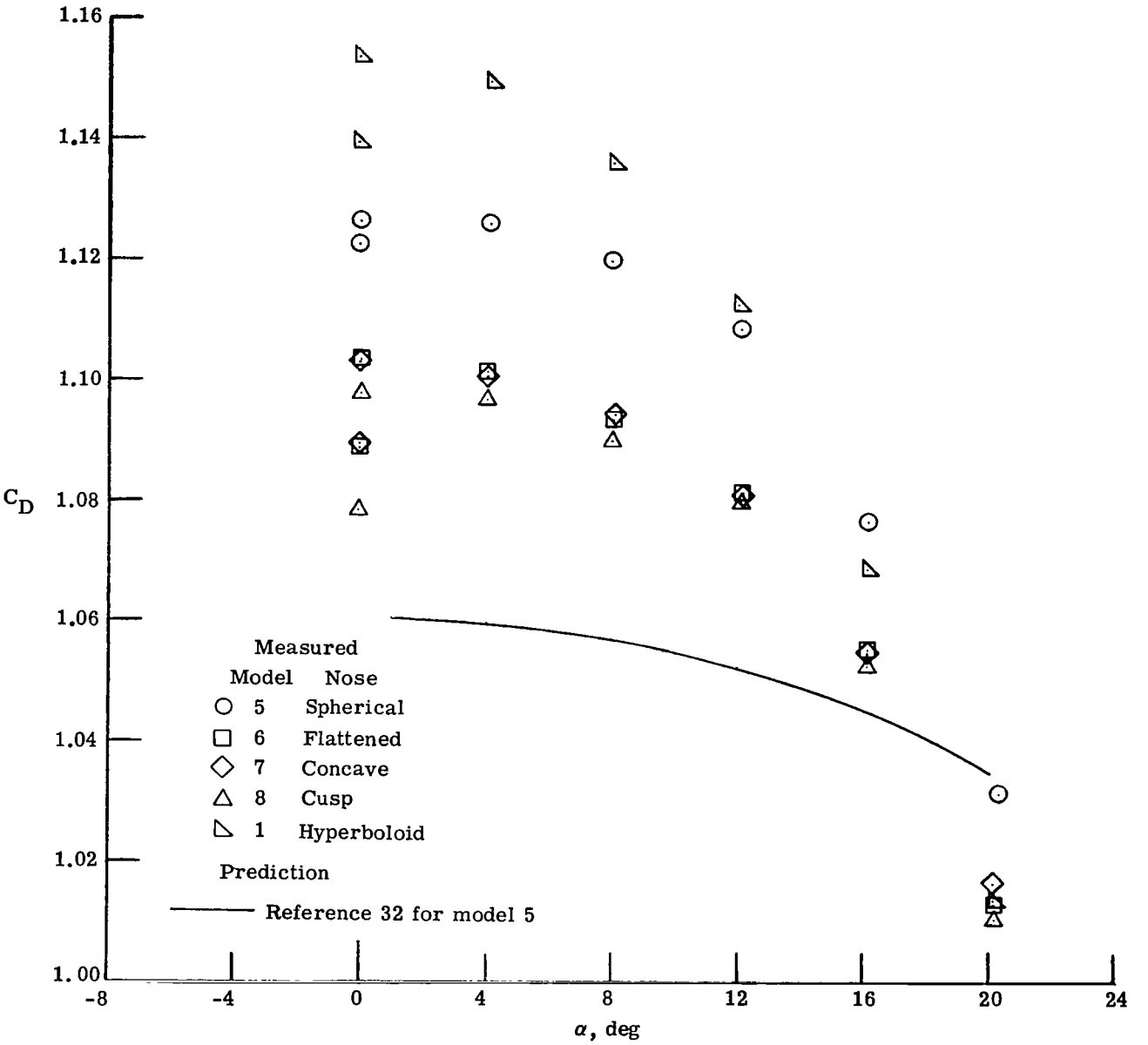

(d) Drag coefficient. $M_\infty = 10.1$.

Figure 64.- Continued.

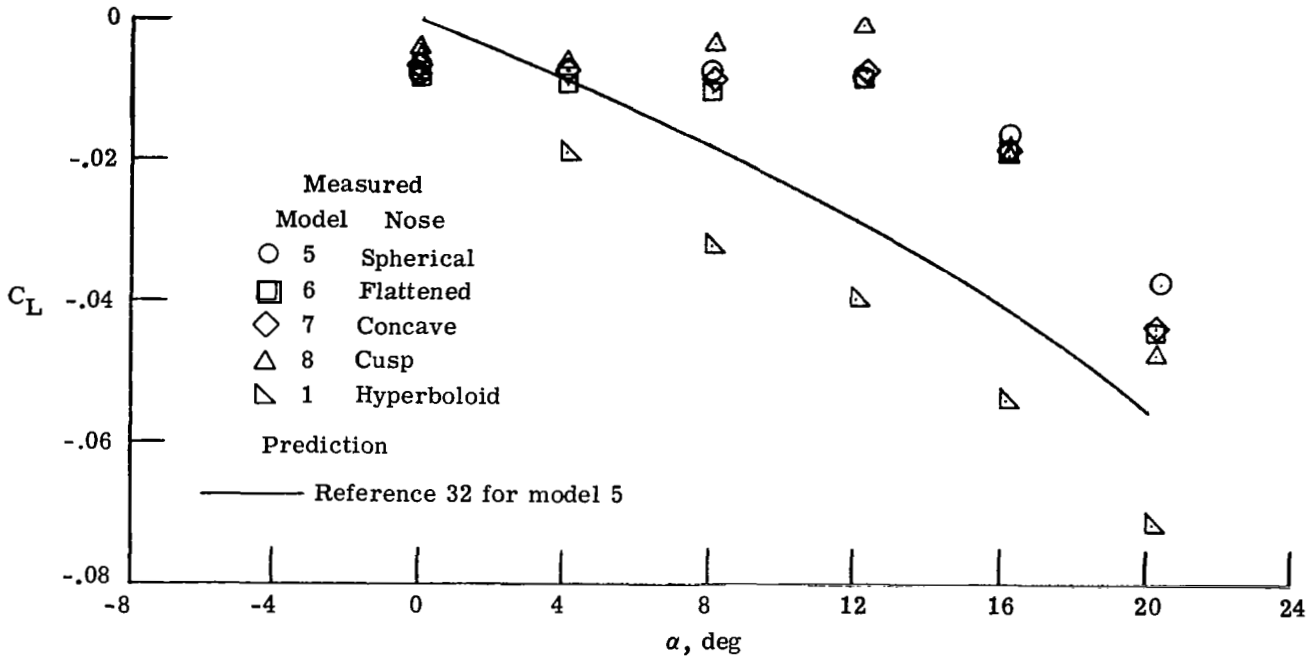

(e) Lift coefficient. $M_\infty = 10.1$.

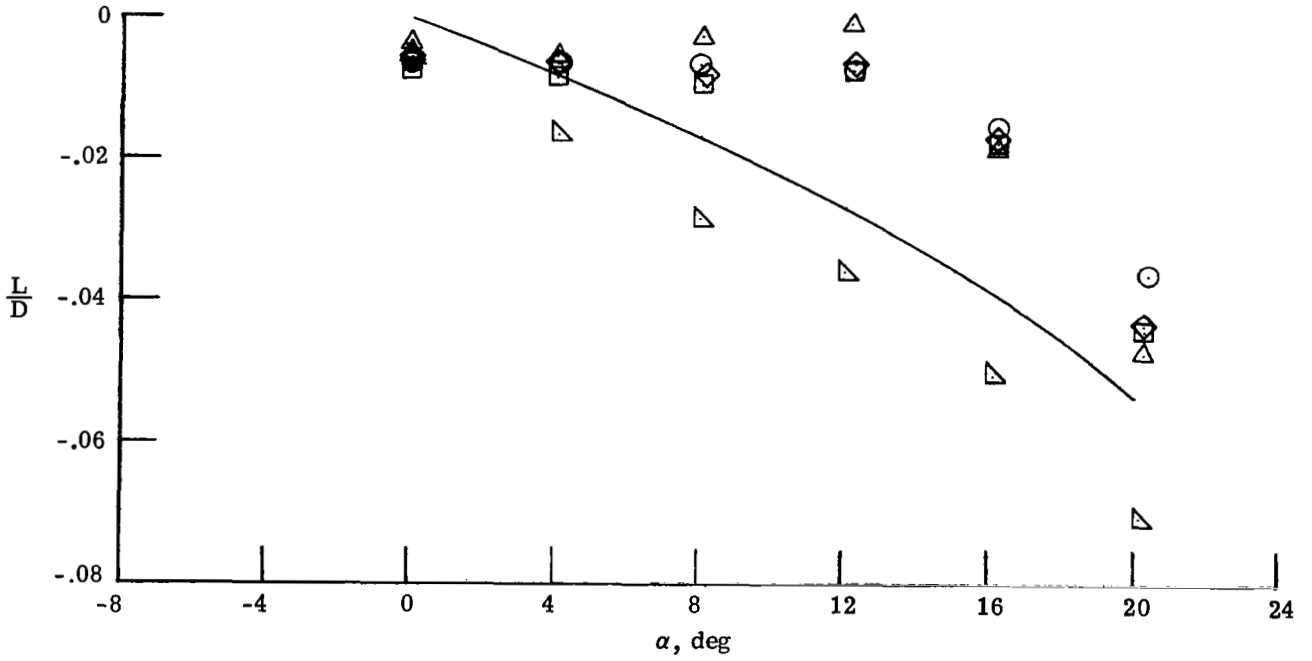

(f) Lift-drag ratio. $M_\infty = 10.1$.

Figure 64.- Concluded.

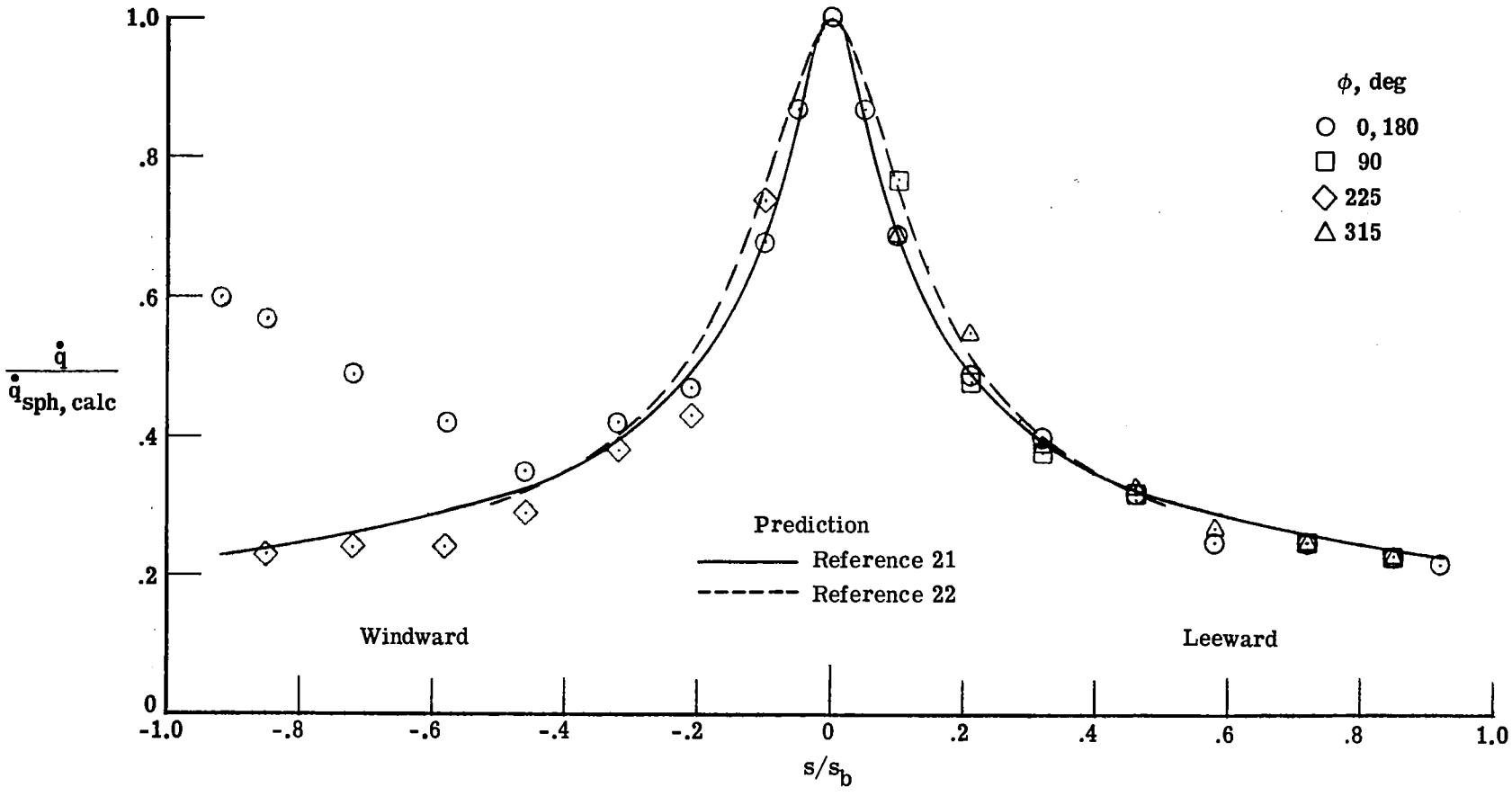

(a) $\alpha = 0°$; $\dot{q}_{sph,calc} = 140.6\ kW/m^2$.

Figure 65.- Heat-transfer distributions measured on hyperboloid (model 1, series 1) in Mach 6.0 air. $N_{Re,\infty,d_b} = 2.93 \times 10^6$.

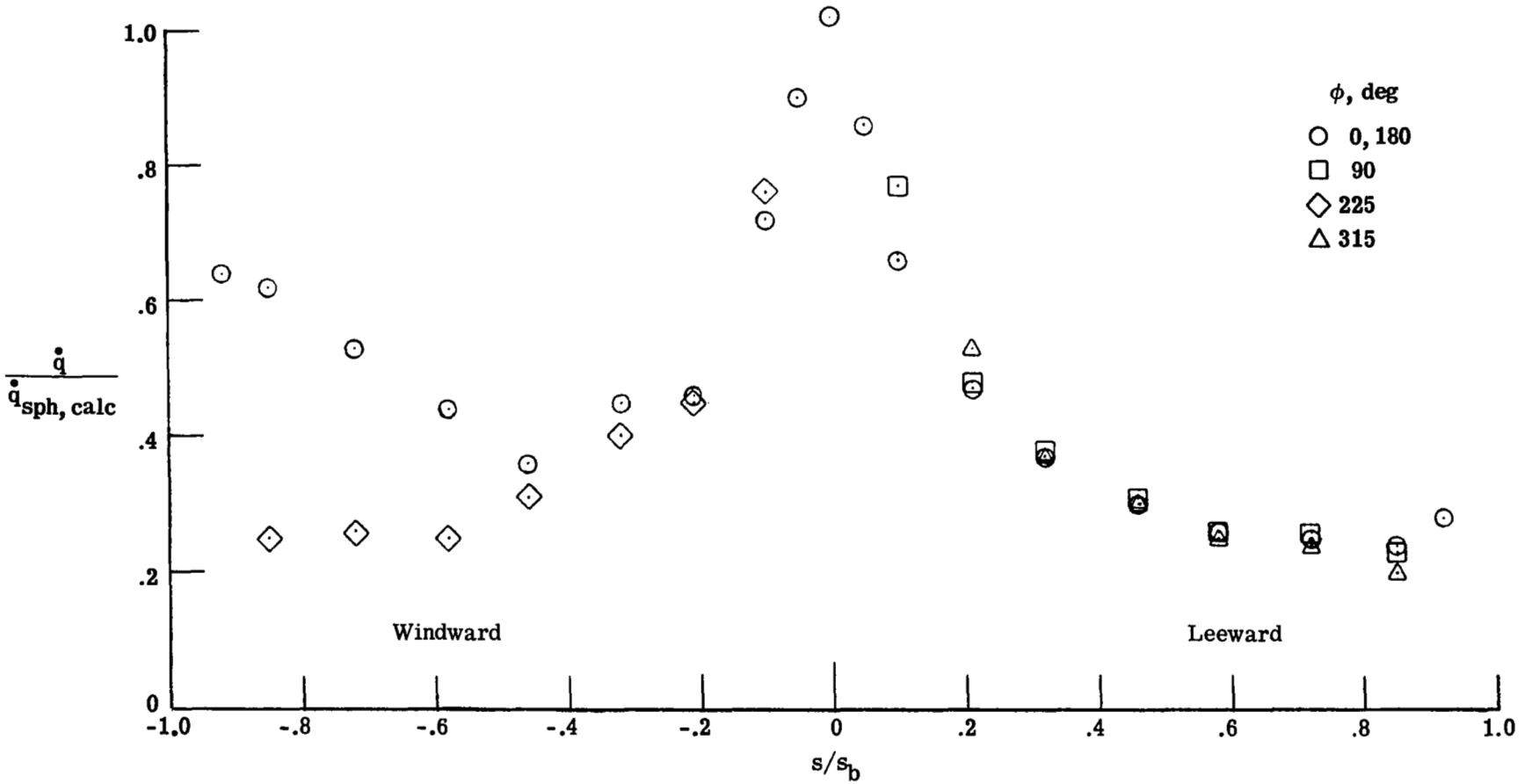

(b) $\alpha = 4°$; $\dot{q}_{sph,calc} = 141.2\ kW/m^2$.

Figure 65.- Continued.

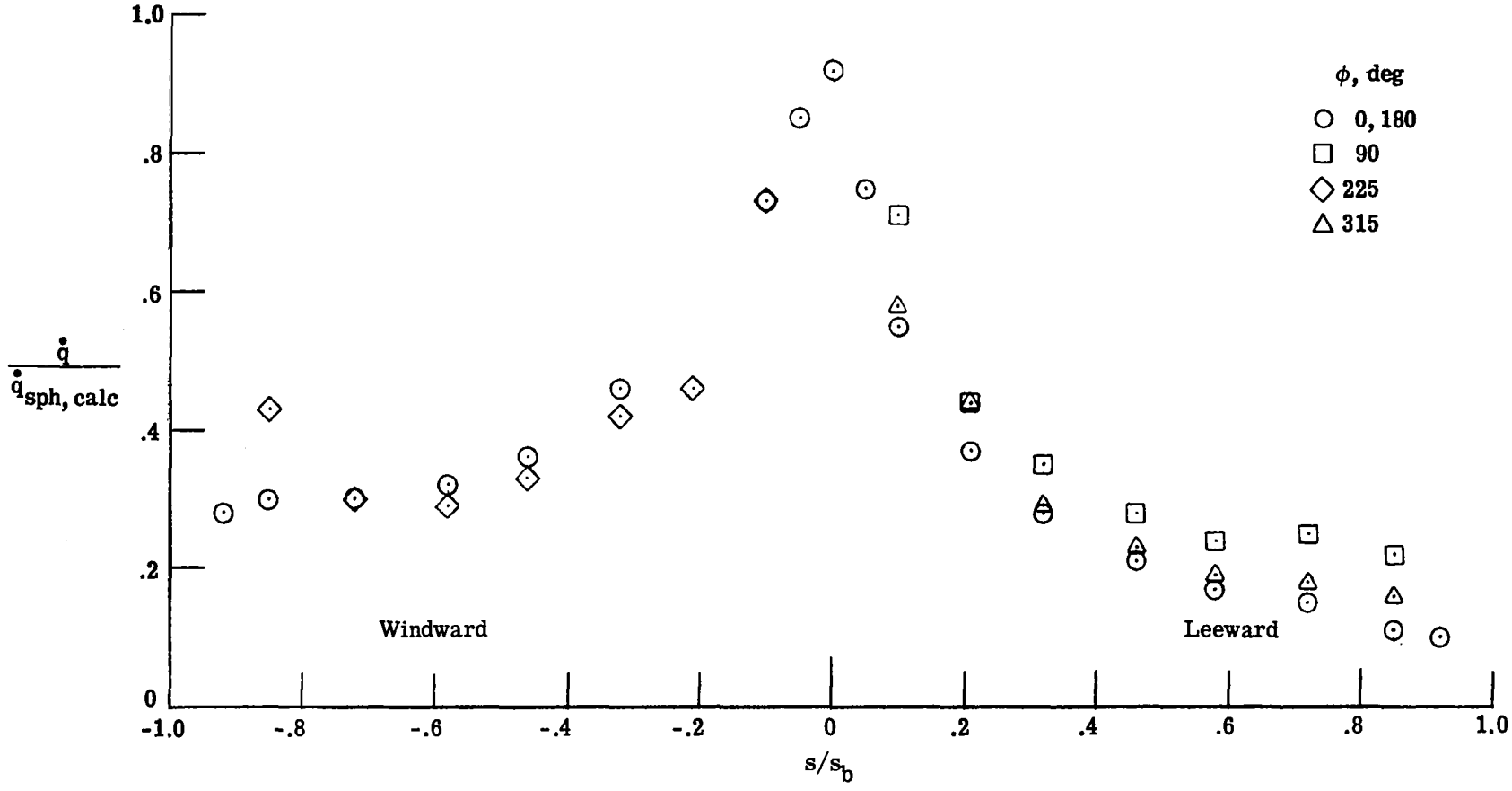

(c) $\alpha = 12°$; $\dot{q}_{sph,calc} = 132.7\ kW/m^2$.

Figure 65.- Continued.

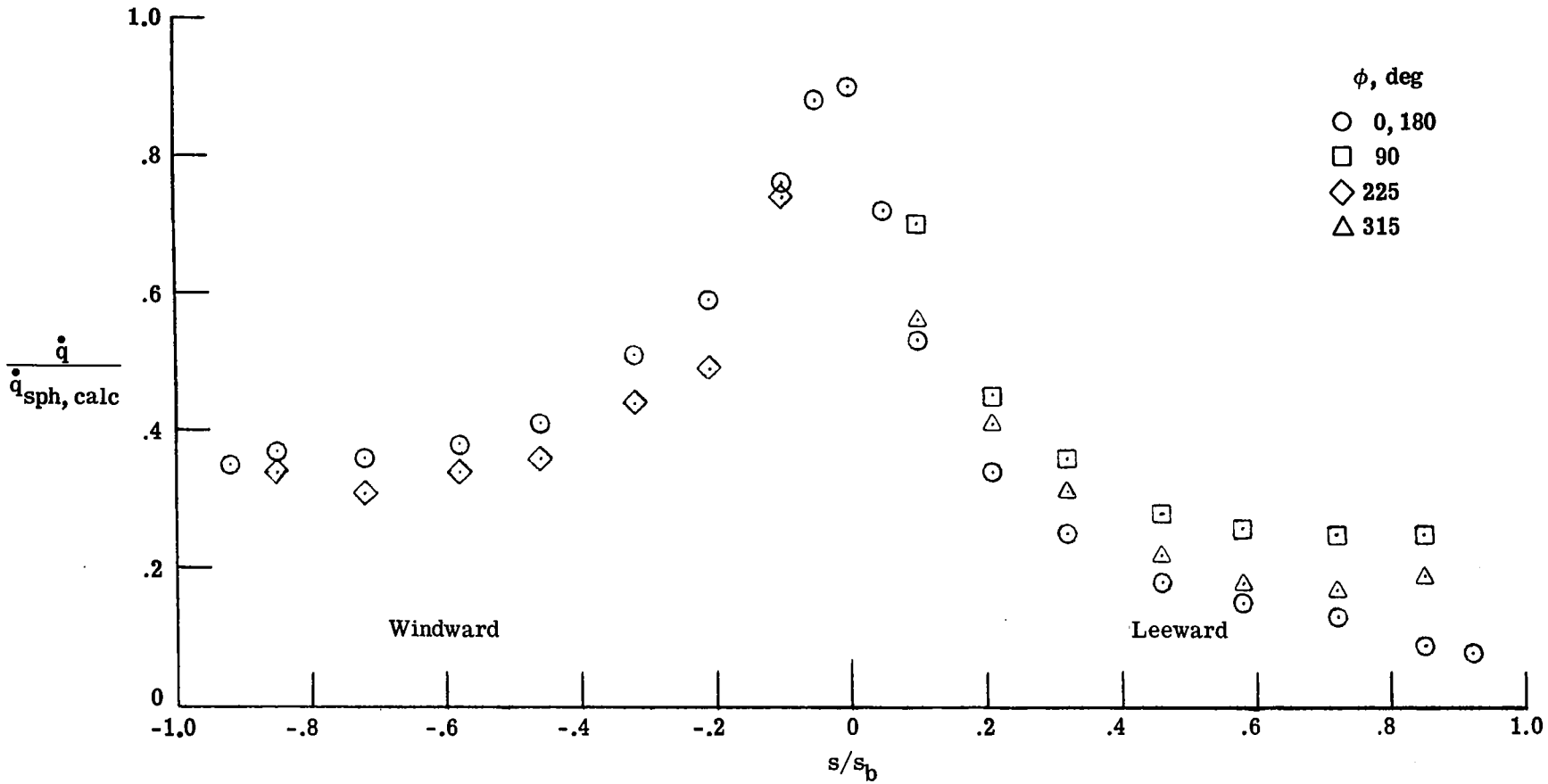

(d) $\alpha = 16°$; $\dot{q}_{sph,calc} = 134.6\ kW/m^2$.

Figure 65.- Continued.

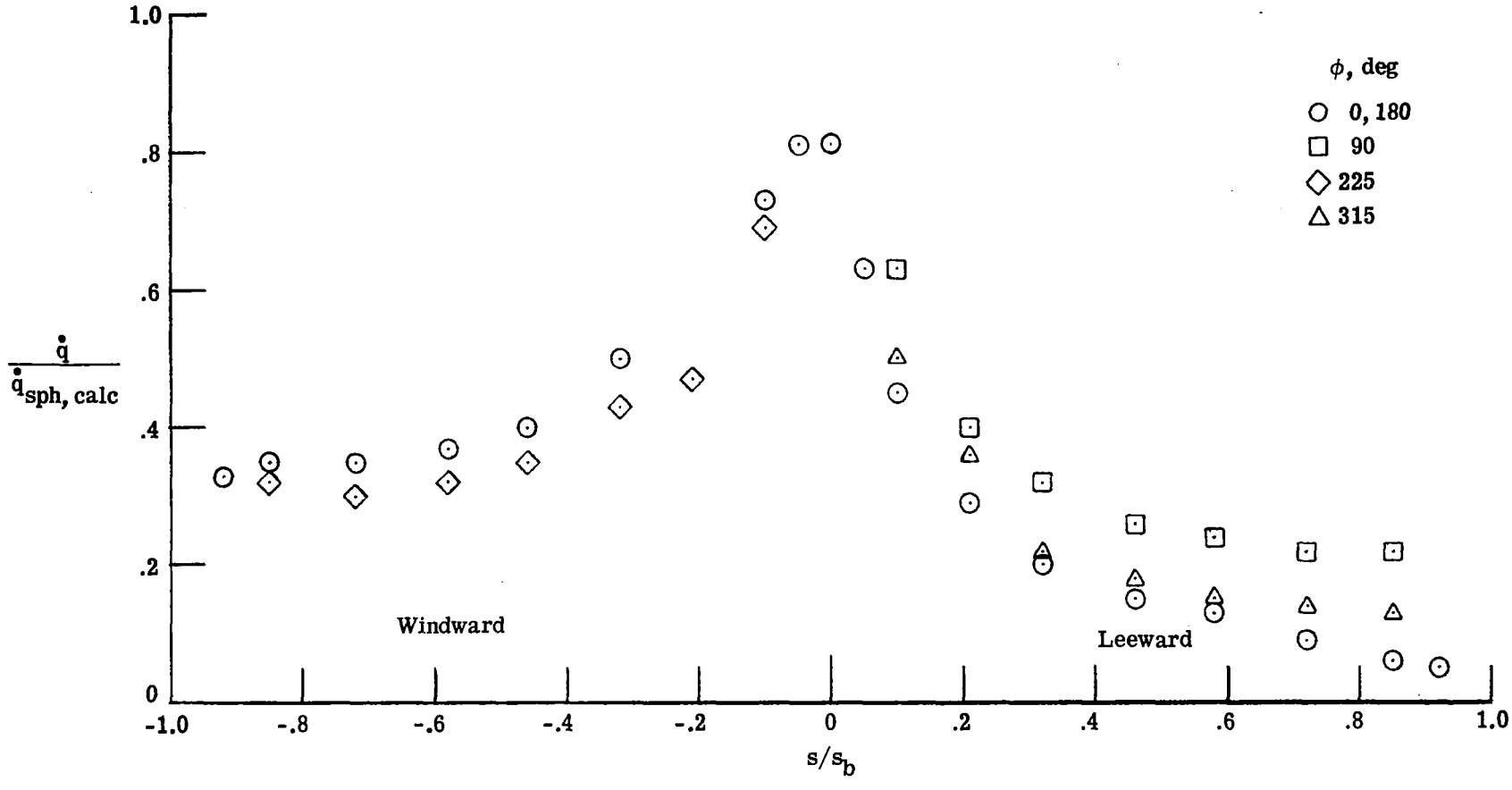

(e) $\alpha = 20°$; $\dot{q}_{sph,calc} = 136.0\ kW/m^2$.

Figure 65.- Concluded.

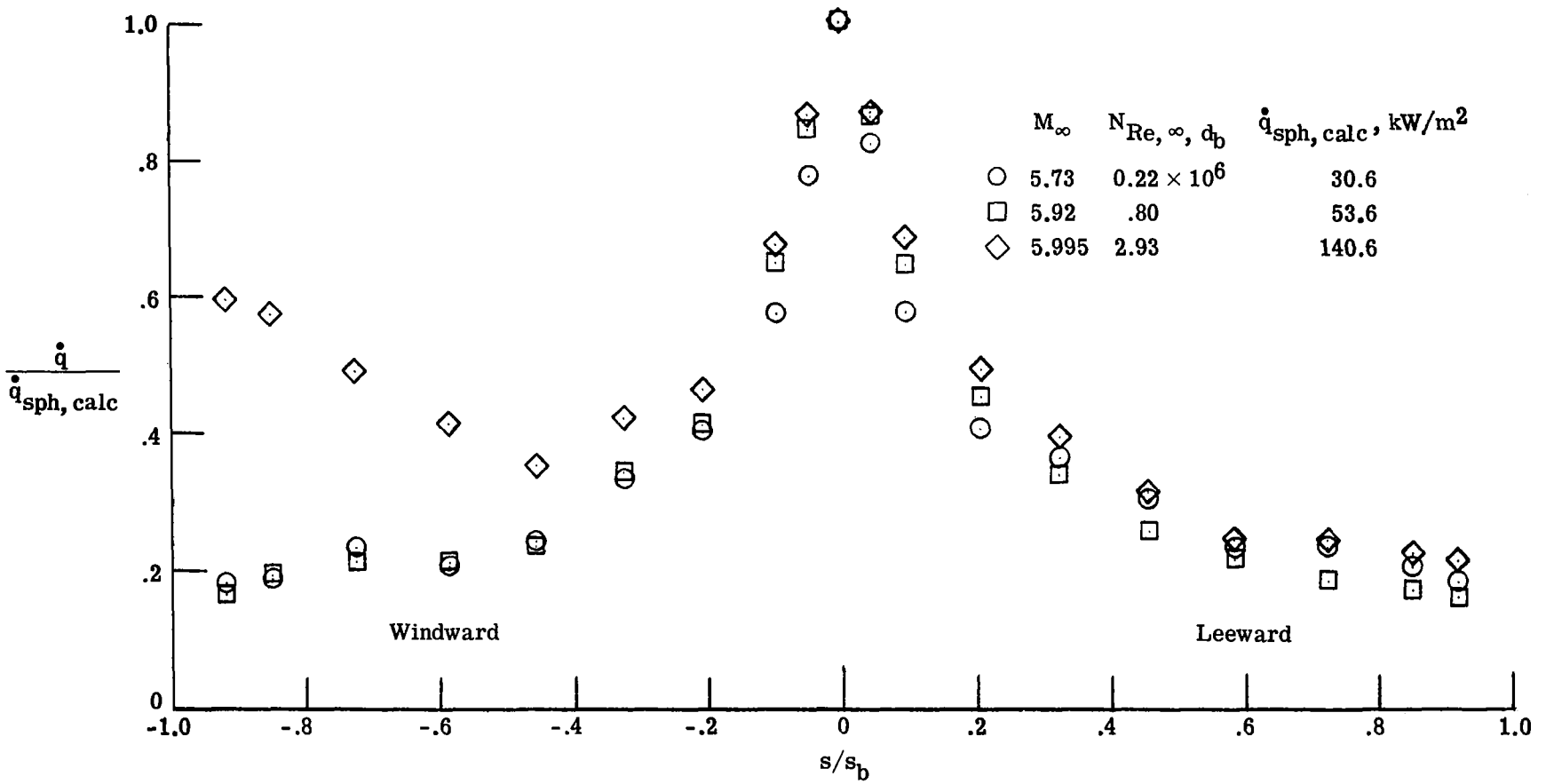

Figure 66.- Effect of free-stream Reynolds number on heat-transfer distributions for the most windward and leeward rays of the hyperboloid (model 1, series 1). $\alpha = 0°$.

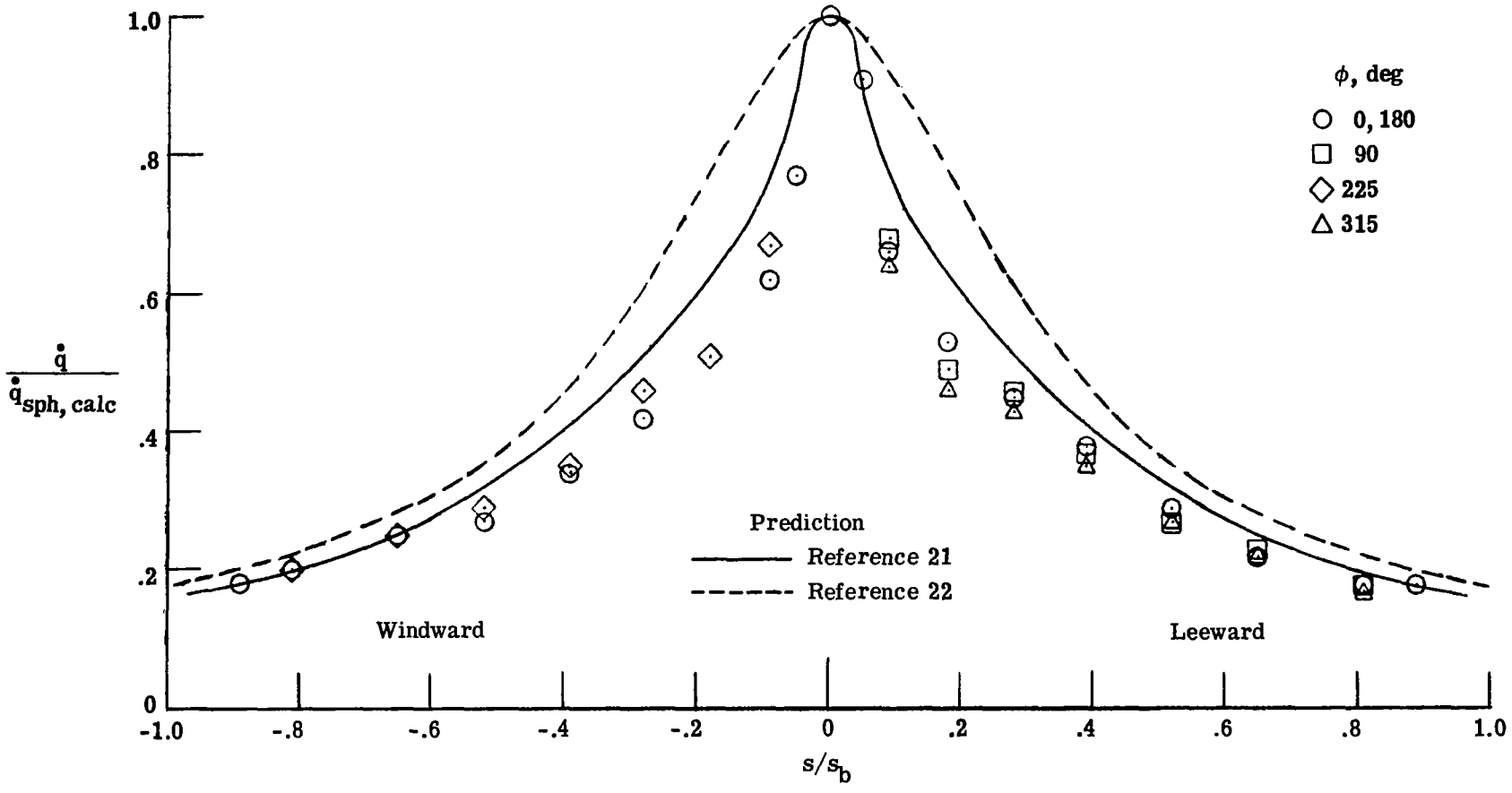

(a) $\alpha = 0°$; $\dot{q}_{sph,calc} = 97.25\ kW/m^2$.

Figure 67.- Heat-transfer distributions measured on the paraboloid (model 3, series 1) in Mach 5.985 air. $N_{Re,\infty,d_b} = 2.98 \times 10^6$.

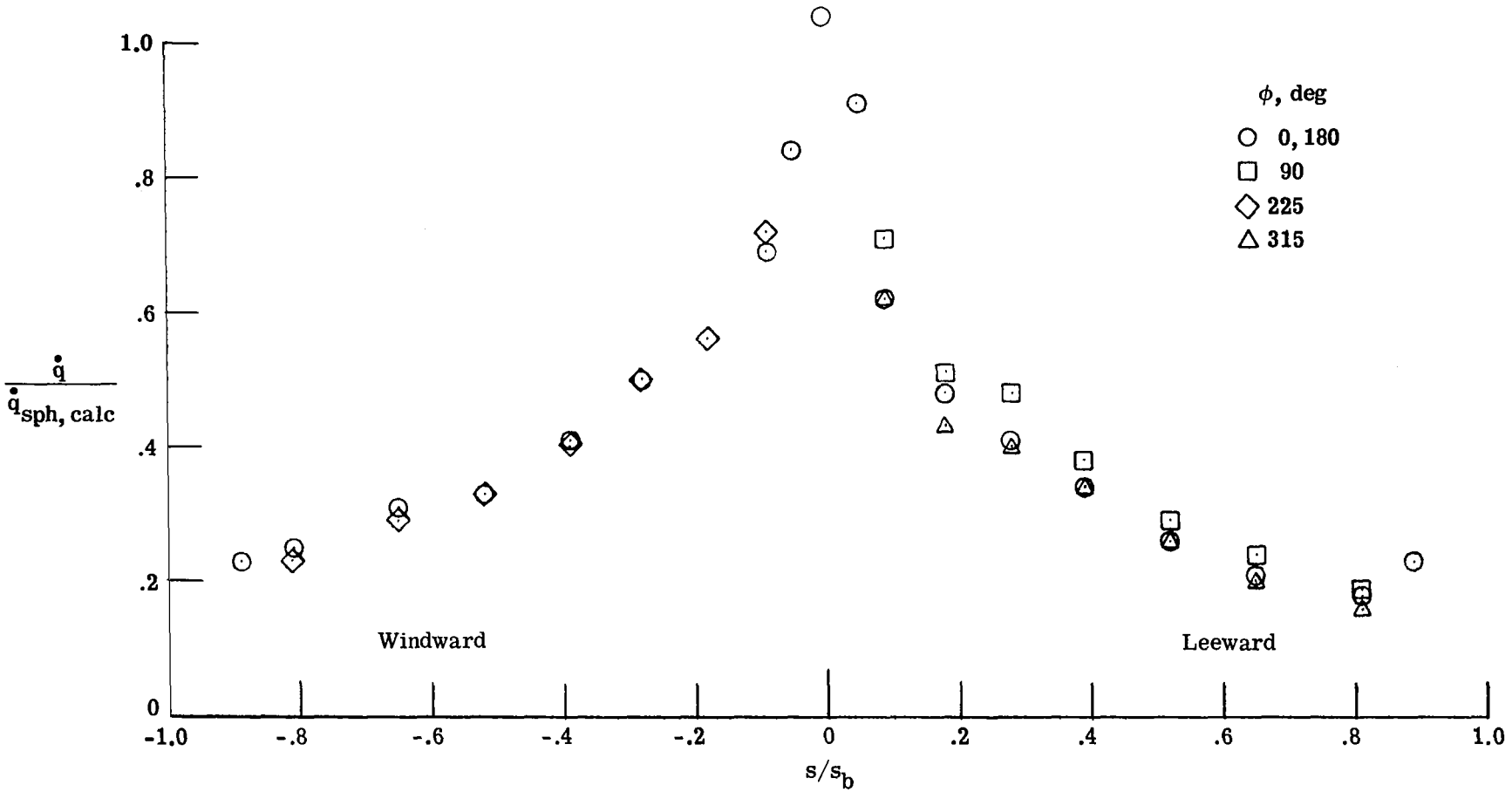

(b) $\alpha = 4°$; $\dot{q}_{sph,calc} = 100.6\ kW/m^2$.

Figure 67.- Continued.

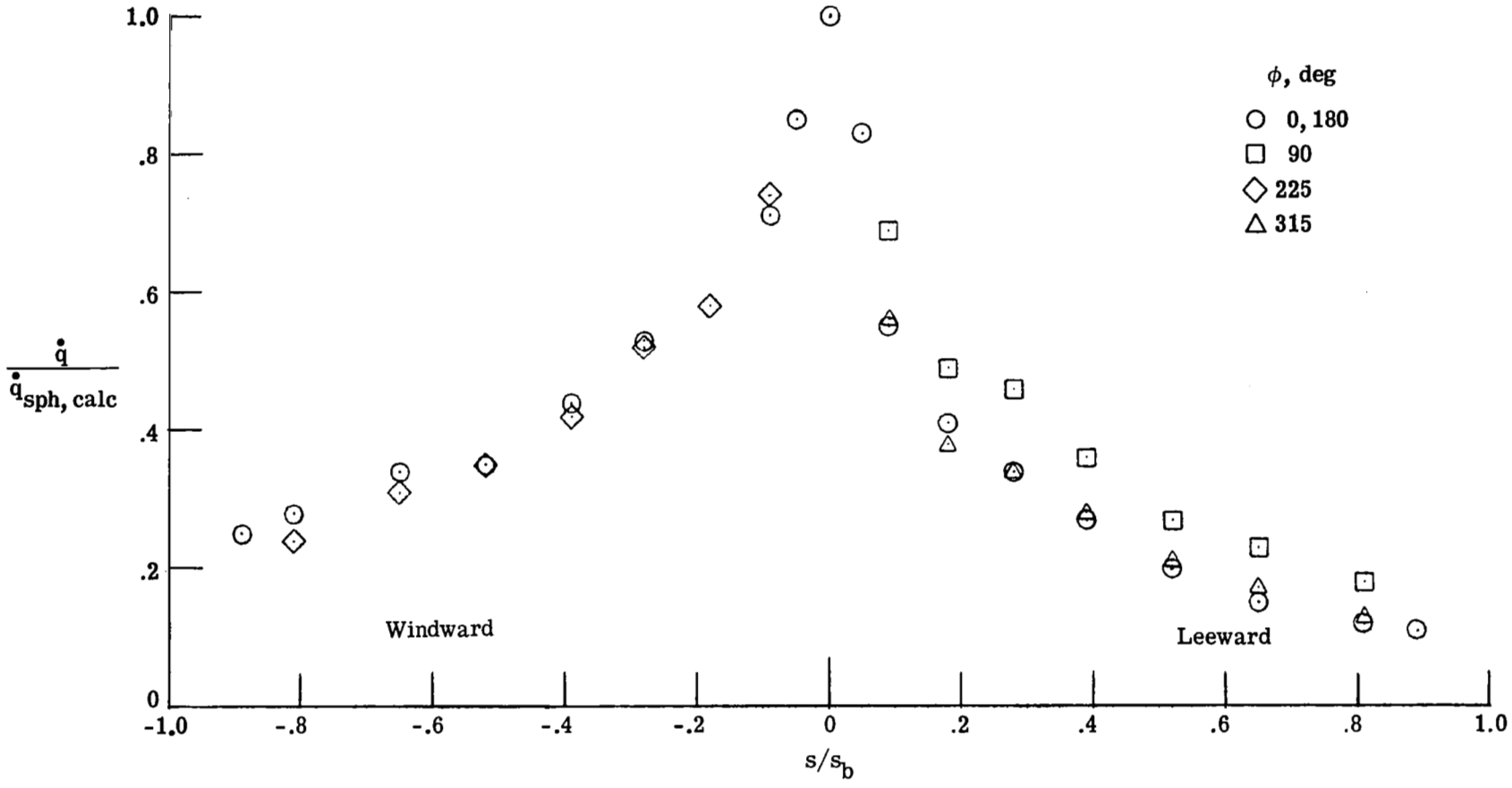

(c) $\alpha = 8°$; $\dot{q}_{sph,calc} = 96.7\ kW/m^2$.

Figure 67.- Continued.

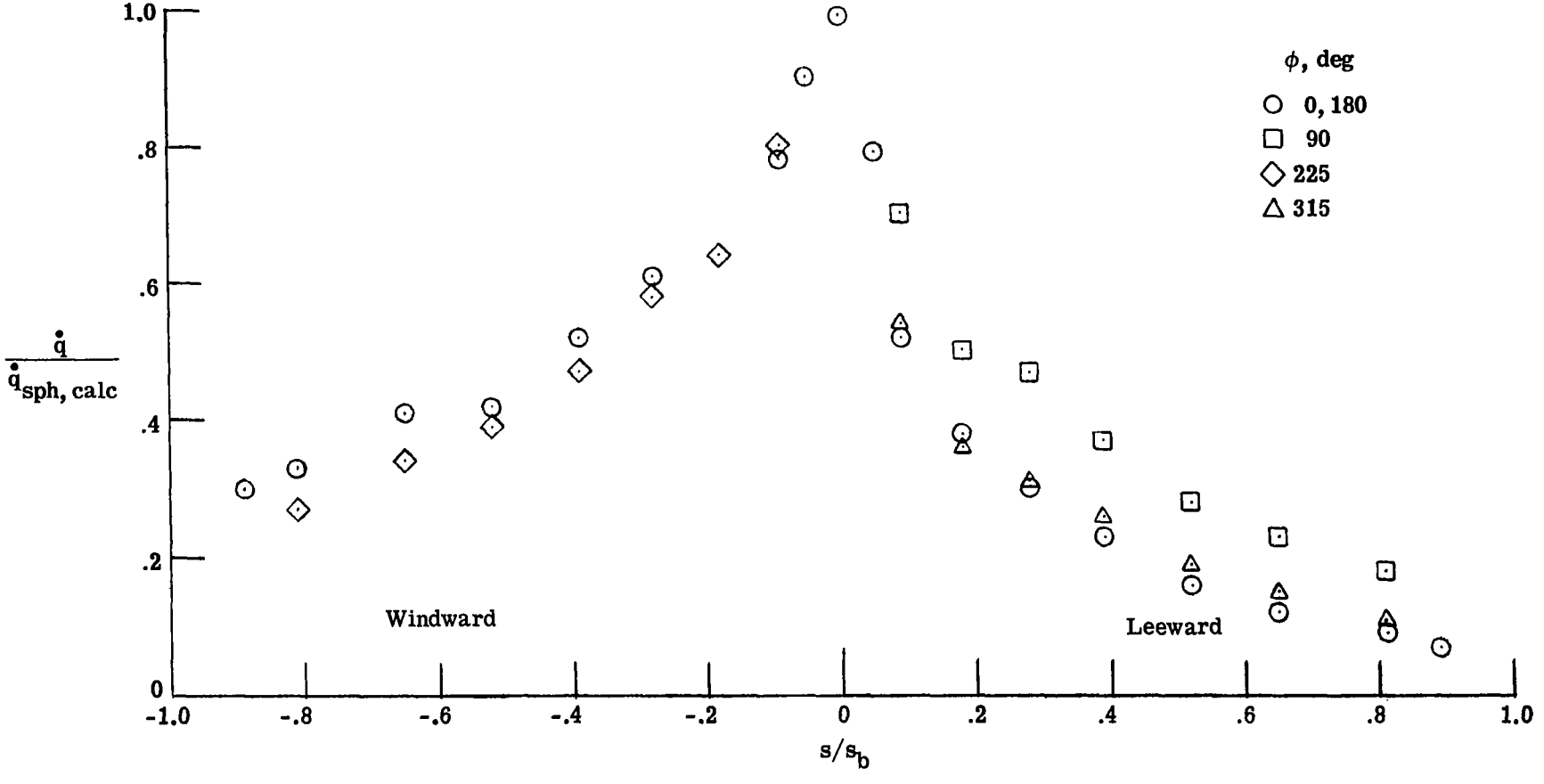

(d) $\alpha = 12°$; $\dot{q}_{sph,calc} = 100.25$ kW/m^2.

Figure 67.- Continued.

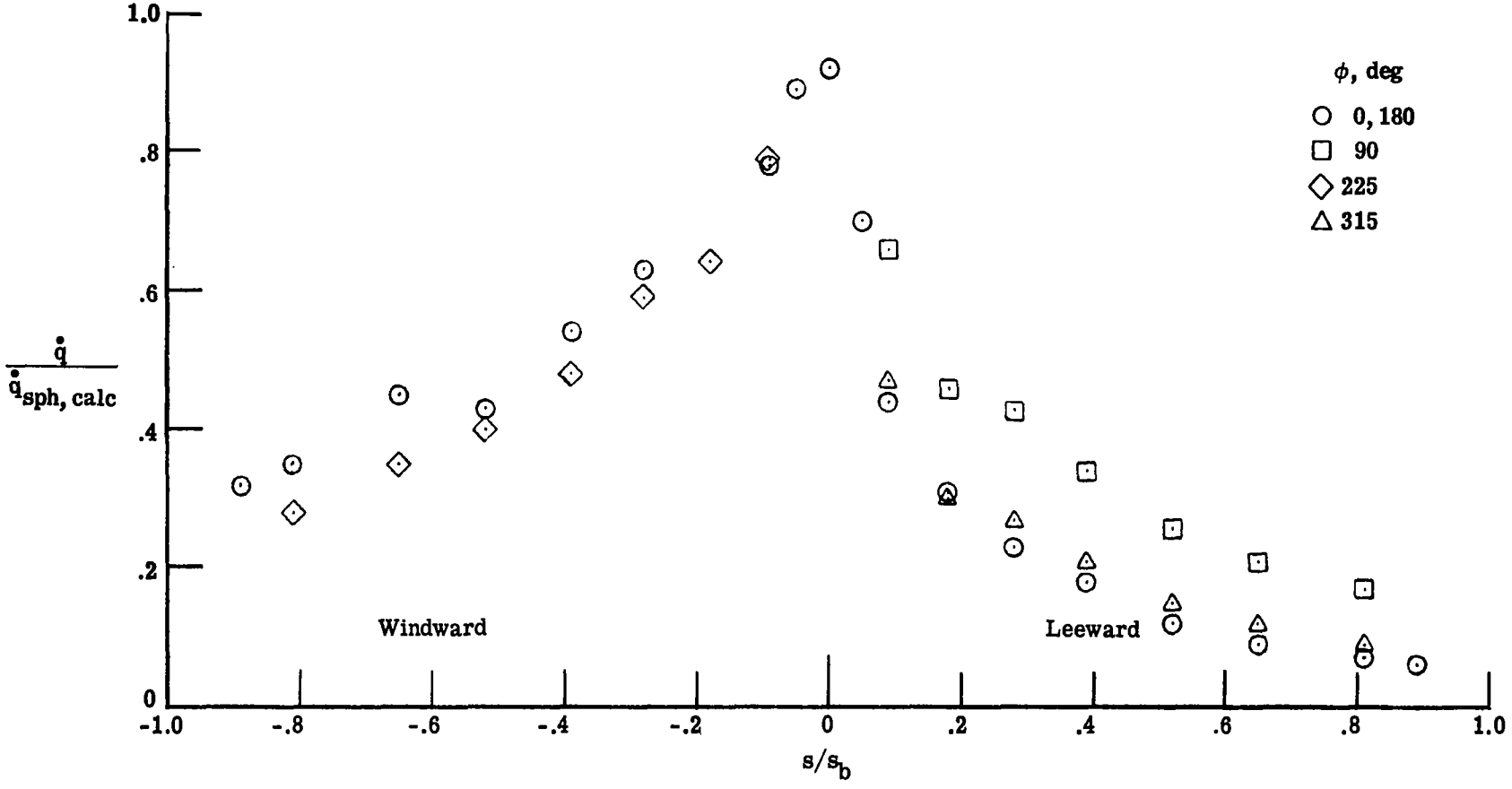

(e) $\alpha = 16°$; $\dot{q}_{sph,calc} = 96.6\ kW/m^2$.

Figure 67.- Continued.

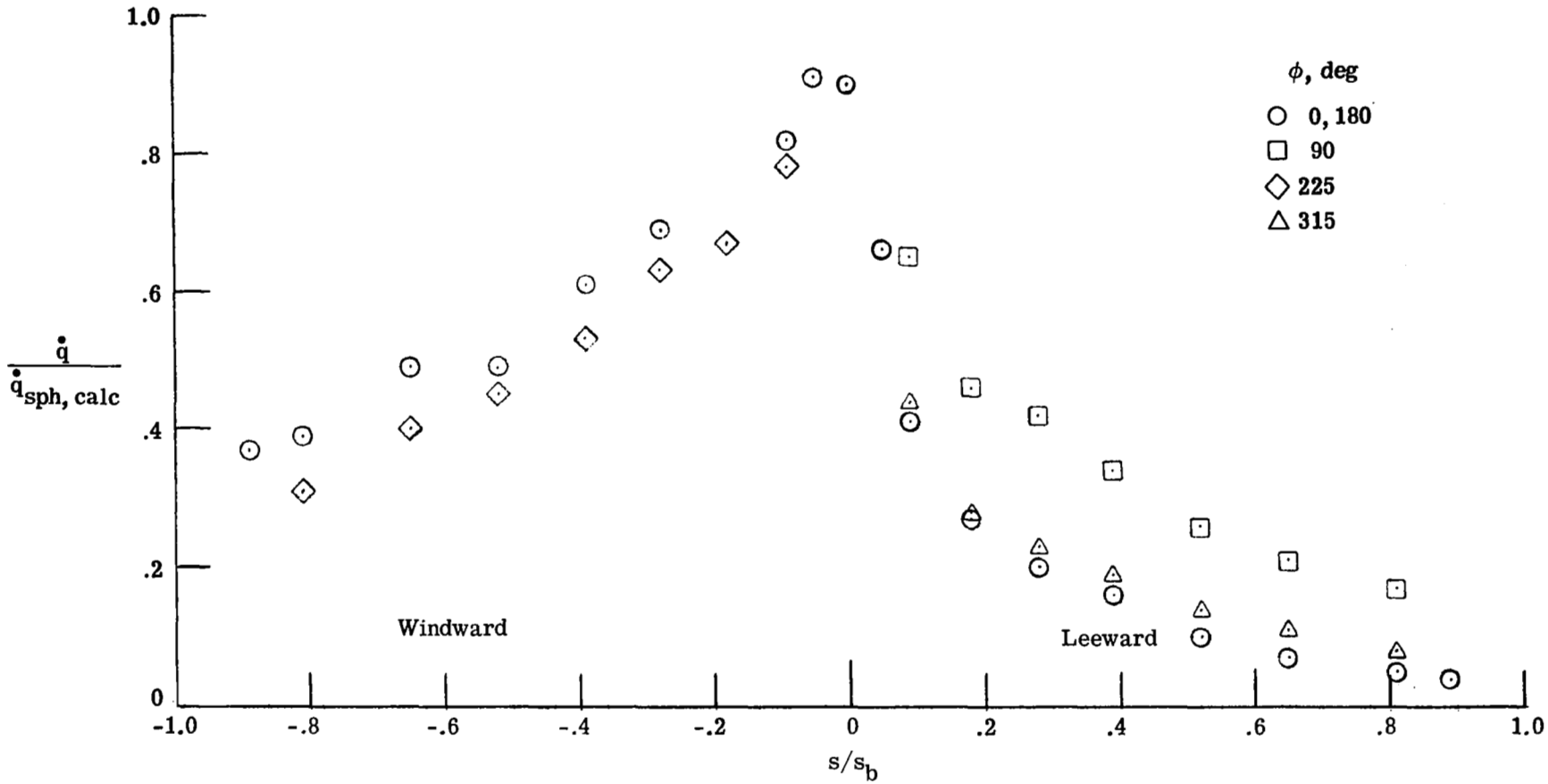

(f) $\alpha = 20°$; $\dot{q}_{sph,calc} = 104.6$ kW/m^2.

Figure 67.- Concluded.

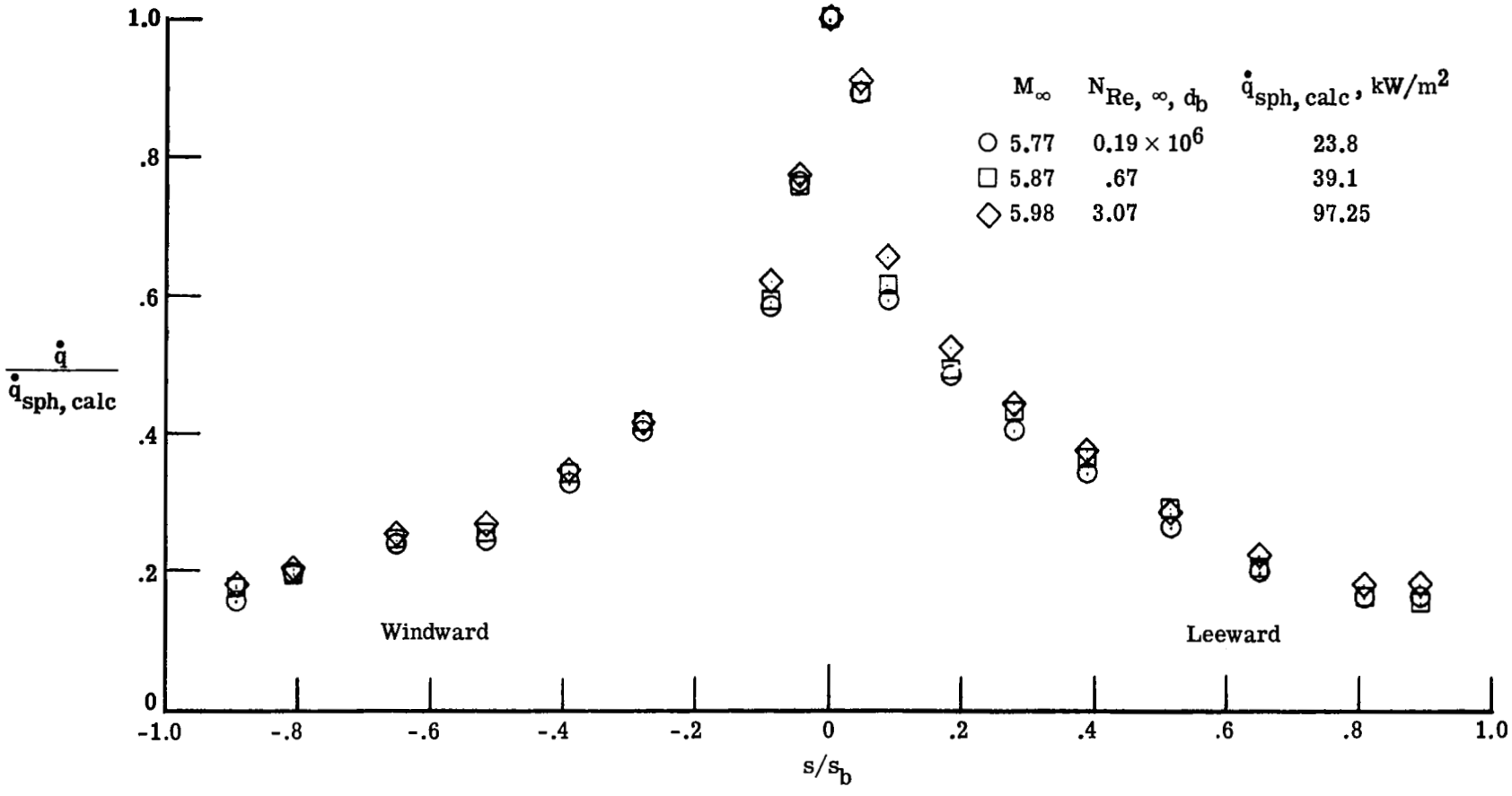

Figure 68.- Effect of free-stream Reynolds number on heat-transfer distribution for the most windward and leeward rays of the paraboloid (model 3, series 1). $\alpha = 0°$.

1. Report No.	2. Government Accession No.	3. Recipient's Catalog No.
NASA TM-84489		

4. Title and Subtitle	5. Report Date
MEASURED PRESSURE DISTRIBUTIONS, AERODYNAMIC COEFFICIENTS, AND SHOCK SHAPES ON BLUNT BODIES AT INCIDENCE IN HYPERSONIC AIR AND CF_4	September 1982
	6. Performing Organization Code 506-51-23-01
7. Author(s) Charles G. Miller III	8. Performing Organization Report No. L-15188
	10. Work Unit No.
9. Performing Organization Name and Address NASA Langley Research Center Hampton, VA 23665	11. Contract or Grant No.
	13. Type of Report and Period Covered Technical Memorandum
12. Sponsoring Agency Name and Address National Aeronautics and Space Administration Washington, DC 20546	14. Sponsoring Agency Code

15. Supplementary Notes

16. Abstract

Pressure distributions, aerodynamic coefficients, and shock shapes were measured on blunt bodies of revolution in Mach 6 CF_4 and in Mach 6 and Mach 10 air. The angle of attack was varied from 0° to 20° in 4° increments. Configurations tested were a hyperboloid with an asymptotic angle of 45°, a sonic-corner paraboloid, a paraboloid with an angle of 27.6° at the base, a Viking aeroshell generated in a generalized orthogonal coordinate system, and a family of cones having a 45° half-angle with spherical, flattened, concave, and cusp nose shapes. Real-gas effects were simulated for the hyperboloid and paraboloid models at Mach 6 by testing at a normal-shock density ratio of 5.3 in air and 12 in CF_4. Predictions from simple theories and numerical flow field programs are compared with measurement. It is anticipated that the data presented in this report will be useful for verification of analytical methods for predicting hypersonic flow fields about blunt bodies at incidence.

17. Key Words (Suggested by Author(s))	18. Distribution Statement
Pressure distributions Shock shapes Blunt bodies Hypersonic flow	Unclassified - Unlimited Subject Category 02

19. Security Classif. (of this report)	20. Security Classif. (of this page)	21. No. of Pages	22. Price
Unclassified	Unclassified	292	A13

For sale by the National Technical Information Service, Springfield, Virginia 22161 NASA-Langley, 1982

National Aeronautics and Space Administration

Washington, D.C.
20546

Official Business
Penalty for Private Use, $300

SPECIAL FOURTH CLASS MAIL
BOOK

Postage and Fees Paid
National Aeronautics and
Space Administration
NASA-451

4 1 1U,A, 820810 S00903DS
DEPT OF THE AIR FORCE
AF WEAPONS LABORATORY
ATTN: TECHNICAL LIBRARY (SUL)
KIRTLAND AFB NM 87117

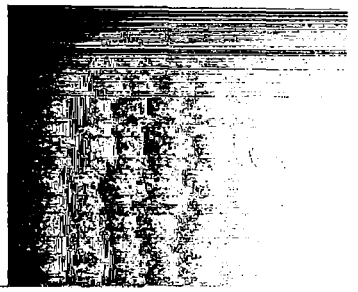

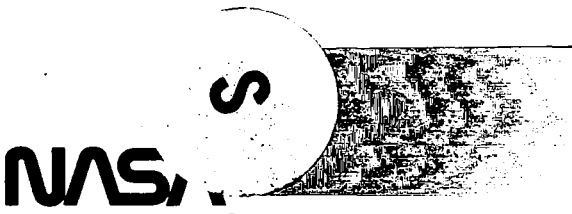

POSTMASTER: If Undeliverable (Section 158 Postal Manual) Do Not Return